



UNIVERSITAT DE  
BARCELONA

## Design, synthesis and study of coordination complexes with spin crossover or single-molecule magnet properties

Rosa Diego Creixenti

**ADVERTIMENT.** La consulta d'aquesta tesi queda condicionada a l'acceptació de les següents condicions d'ús: La difusió d'aquesta tesi per mitjà del servei TDX ([www.tdx.cat](http://www.tdx.cat)) i a través del Dipòsit Digital de la UB ([diposit.ub.edu](http://diposit.ub.edu)) ha estat autoritzada pels titulars dels drets de propietat intel·lectual únicament per a usos privats emmarcats en activitats d'investigació i docència. No s'autoritza la seva reproducció amb finalitats de lucre ni la seva difusió i posada a disposició des d'un lloc aliè al servei TDX ni al Dipòsit Digital de la UB. No s'autoritza la presentació del seu contingut en una finestra o marc aliè a TDX o al Dipòsit Digital de la UB (framing). Aquesta reserva de drets afecta tant al resum de presentació de la tesi com als seus continguts. En la utilització o cita de parts de la tesi és obligat indicar el nom de la persona autora.

**ADVERTENCIA.** La consulta de esta tesis queda condicionada a la aceptación de las siguientes condiciones de uso: La difusión de esta tesis por medio del servicio TDR ([www.tdx.cat](http://www.tdx.cat)) y a través del Repositorio Digital de la UB ([diposit.ub.edu](http://diposit.ub.edu)) ha sido autorizada por los titulares de los derechos de propiedad intelectual únicamente para usos privados enmarcados en actividades de investigación y docencia. No se autoriza su reproducción con finalidades de lucro ni su difusión y puesta a disposición desde un sitio ajeno al servicio TDR o al Repositorio Digital de la UB. No se autoriza la presentación de su contenido en una ventana o marco ajeno a TDR o al Repositorio Digital de la UB (framing). Esta reserva de derechos afecta tanto al resumen de presentación de la tesis como a sus contenidos. En la utilización o cita de partes de la tesis es obligado indicar el nombre de la persona autora.

**WARNING.** On having consulted this thesis you're accepting the following use conditions: Spreading this thesis by the TDX ([www.tdx.cat](http://www.tdx.cat)) service and by the UB Digital Repository ([diposit.ub.edu](http://diposit.ub.edu)) has been authorized by the titular of the intellectual property rights only for private uses placed in investigation and teaching activities. Reproduction with lucrative aims is not authorized nor its spreading and availability from a site foreign to the TDX service or to the UB Digital Repository. Introducing its content in a window or frame foreign to the TDX service or to the UB Digital Repository is not authorized (framing). Those rights affect to the presentation summary of the thesis as well as to its contents. In the using or citation of parts of the thesis it's obliged to indicate the name of the author.



# DESIGN, SYNTHESIS AND STUDY OF COORDINATION COMPLEXES WITH SPIN CROSSOVER OR SINGLE- MOLECULE MAGNET PROPERTIES

UNIVERSITAT DE BARCELONA

Facultat de Química

Departament de Química Inorgànica i Orgànica

Secció Inorgànica

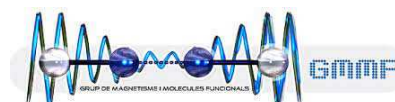
Institut de Nanociència i Nanotecnologia

Programa de doctorat en Nanociència

Grup de Magnetisme i Molècules Funcionals (GMMF)



UNIVERSITAT DE  
BARCELONA



**Rosa Diego Creixenti**

Directors: Dr. Guillem Aromí Bedmar

Dr. Jorge García Gómez

Tutor: Patrick Gámez Enamorado



**Als meus pares i al meu germà**



# CONTENTS

## Abbreviations and Symbols

### 1. INTRODUCTION

1.1. Nanotechnological background/context. Molecular Switches.	1
1.2. The Spin Crossover Phenomenon	2
1.3. Monitoring SCO.	6
1.3.1. Variable temperature magnetic susceptibility measurements	6
1.3.1.1. SQUID Magnetometry. Detection in solid state.	6
1.3.1.2. <sup>1</sup> H-Nuclear Magnetic Resonance (NMR). Detection in solution	8
Evans method	8
Temperature dependence of the NMR chemical shift	10
1.3.2. Crystallography	11
1.4. Pyrazole-pyridine based ligands used for Fe(II) SCO complexes	13
1.4.1. Mononuclear complexes of Fe(II) with tridentate ligands (bpp)	14
1.4.2. Metallo-Supramolecular architectures of Fe (II), multitopic ligands.	17
1.4.2.1. Dinuclear Fe <sub>2</sub> Triple stranded helicates. Host-guest chemistry and bifunctional systems.	20
1.4.2.2. Dimerized mononuclear Fe (jellyfish). (Metallosupramolecular hosts)	22
1.4.2.3. Grids: Supramolecular and Cluster chemistry.	24
1.5. Introduction to Single Molecule Magnets (SMMs)	26
1.5.1. Detecting SMMs behavior	30
1.6. Objectives and Scope of the Thesis	33
1.7. References	34

## **2. THE EFFECT OF LIGAND SUBSTITUENTS ON THE SPIN CROSSOVER OF Fe (II) COMPLEXES**

Abstract	45
2.1. Introduction	45
2.2. Results and discussion	47
Synthesis of 3-Methyl and 3,5-dimethyl substituted 1,3-bis-pyrazolylpyridine (1,3-bpp) ligands	47
Synthesis of the homoleptic Fe(II) complexes [Fe(1,3bpp) <sub>2</sub> ](ClO <sub>4</sub> ) <sub>2</sub> ( <b>1</b> ), [Fe(Me-1,3bpp) <sub>2</sub> ](ClO <sub>4</sub> ) <sub>2</sub> ( <b>2</b> ) and [Fe(Me <sub>2</sub> -1,3bpp) <sub>2</sub> ](ClO <sub>4</sub> ) <sub>2</sub> ( <b>3</b> )	49
Crystal structures of [Fe(Me-1,3bpp) <sub>2</sub> ](ClO <sub>4</sub> ) <sub>2</sub> ( <b>2</b> ) and [Fe(Me <sub>2</sub> -1,3bpp) <sub>2</sub> ](ClO <sub>4</sub> ) <sub>2</sub> ( <b>3</b> )	50
Comparison of the cation lattice arrangement between both compounds	52
Bulk magnetic measurements	54
Solution-phase measurements. Evan's method	57
DFT calculations	58
2.3. Conclusions	62
2.4. Experimental	62
2.5. References	65

## **3. THE EFFECT OF METAL COMPOSITION ON THE THERMAL SPIN TRANSITION OF [Fe(Me<sub>1</sub>-1,3bpp)<sub>2</sub>](ClO<sub>4</sub>)<sub>2</sub> MOLECULAR ALLOYS**

Abstract	71
3.1. Introduction	71
3.2. Results and discussion	75
Synthesis of [Zn(Me-1,3bpp) <sub>2</sub> ](ClO <sub>4</sub> ) <sub>2</sub> ( <b>4</b> ) and the series of metal solutions with the formula [Fe <sub>x</sub> Zn <sub>1-x</sub> (Me <sub>1</sub> -1,3bpp) <sub>2</sub> ](ClO <sub>4</sub> ) <sub>2</sub> ( <b>5x</b> )	75
Structure of [Fe(Me-1,3bpp) <sub>2</sub> ](ClO <sub>4</sub> ) <sub>2</sub> ( <b>2</b> ) and [Zn(Me-1,3bpp) <sub>2</sub> ](ClO <sub>4</sub> ) <sub>2</sub> ( <b>4</b> )	77
Structure of the series of solid solutions with formula [Fe <sub>x</sub> Zn <sub>1-x</sub> (Me-1,3bpp) <sub>2</sub> ](ClO <sub>4</sub> ) <sub>2</sub> ( <b>5x</b> )	79
Powder X-ray diffraction (PXRD) of the family of compounds	80



Solid-state magnetic properties	82
3.3. Conclusions	87
3.4. Experimental	88
3.5. References	90

#### **4. A MONONUCLEAR SPIN-CROSSOVER COMPLEX DESCRIBING FOUR DISTINCT THERMAL ROUTES**

Abstract	95
4.1. Introduction	95
4.2. Results and discussion	97
Synthesis	97
Crystal structure of [FeL(bbp)](ClO <sub>4</sub> ) <sub>2</sub> ·ac ( <b>6</b> ·ac)	98
Bulk magnetic measurements of [FeL(bbp)](ClO <sub>4</sub> ) <sub>2</sub> ·ac ( <b>6</b> ·ac)	100
XCSR Study of the thermal evolution of [FeL(bbp)](ClO <sub>4</sub> ) <sub>2</sub> ·ac ( <b>6</b> ·ac) and [FeL(bbp)](ClO <sub>4</sub> ) <sub>2</sub> ( <b>6</b> )	101
<b>6</b> ·ac [HS-LS] → <b>6</b> <sup>α</sup> [HS-HS] transformation	101
<b>6</b> <sup>α</sup> [HS-HS] → <b>6</b> <sup>β</sup> [LS-LS] transformation	104
<b>6</b> <sup>β</sup> [LS-LS] → <b>6</b> <sup>γ</sup> [HS-LS] transformation	106
Differential Scanning calorimetry (DSC) studies of the phase transition succession for <b>6</b> ·ac	109
DFT study of the Solid-State Transformations	111
Crystal structure of [FeL(bbp)](ClO <sub>4</sub> ) <sub>2</sub> ·ac ( <b>7</b> ·ac)	112
Probing the importance of intermolecular interactions on these systems	114
4.3. Conclusions	118
4.4. Experimental	118
4.5. References	120

#### **5. DESIGN, SYNTHESIS AND CHARACTERIZATION OF NEW BIS-PYRAZOLYL BASED LIGANDS TO ACCESS METALLOSUPRAMOLECULAR ARCHITECTURES**

Abstract	125
----------	-----

5.1. Introduction	125
5.2. Results and discussion	128
5.2.1. Description, synthesis and characterization of <b>H<sub>2</sub>L3</b> : 4,4''-bis(3-(pyridin-2-yl)-1 <i>H</i> -pyrazol-5-yl)-1,1':3',1''-terphenyl	128
5.2.2 Description, synthesis and characterization of <b>H<sub>2</sub>L4</b> : 6,6''-dimethyl-5,5''-bis(3-(pyridin-2-yl)-1 <i>H</i> -pyrazol-5-yl)- 2,2':6',2''-terpyridine	130
5.2.3. Description, synthesis and characterization of <b>H<sub>2</sub>L5</b> : 1,3-bis(3-(isoquinolin-3-yl)-1 <i>H</i> -pyrazol-5-yl)benzene	135
5.2.4. Description, synthesis and characterization of <b>H<sub>2</sub>L6</b> : 1,3-bis(3-(6-methylpyridin-2-yl)-1 <i>H</i> -pyrazol-5-yl)benzene	137
5.2.5. Description, synthesis and characterization of <b>H<sub>2</sub>L7</b> : 1,3-bis(3-(pyrazin-2-yl)-1 <i>H</i> -pyrazol-5-yl)benzene	138
5.2.6. Description, synthesis and characterization of <b>H<sub>2</sub>L8</b> : 5,5''-bis(4-(pyridin-2-yl)-4,5-dihydro-1 <i>H</i> -1,2,3-triazol-1-yl)- 2,2':6',2''-terpyridine	139
5.3. Conclusions	142
5.4. Experimental	142
5.5. References	149
<b>6. Cl@ [Co<sup>II</sup><sub>2</sub>(H<sub>2</sub>L)<sub>3</sub>]<sup>3+</sup> AND Cl@[Co<sup>II</sup> Zn<sup>II</sup> (H<sub>2</sub>L)<sub>3</sub>]<sup>3+</sup> TRIPLE-STRANDED HELICATES SHOWING SLOW MAGNETIC RELAXATION</b>	
Abstract	155
6.1. Introduction	155
6.2. Results and discussion	161
Synthesis and Mass Spectrometry of Cl@[Co <sub>2</sub> (H <sub>2</sub> L) <sub>3</sub> ]Cl(PF <sub>6</sub> ) <sub>2</sub> ( <b>11</b> ), Cl@[Zn <sub>2</sub> (H <sub>2</sub> L) <sub>3</sub> ]Cl(PF <sub>6</sub> ) <sub>2</sub> ( <b>12</b> ) and Cl@[Zn <sub>1.15</sub> Co <sub>0.85</sub> (H <sub>2</sub> L) <sub>3</sub> ]Cl(PF <sub>6</sub> ) <sub>2</sub> ( <b>13</b> )	161
Crystal structure of the [Co <sup>II</sup> <sub>2</sub> ] ( <b>11</b> ), [Zn <sup>II</sup> <sub>2</sub> ] ( <b>12</b> ) and [Co <sup>II</sup> Zn <sup>II</sup> ] ( <b>13</b> ) helicates	163
Magnetic study of the [Co <sup>II</sup> <sub>2</sub> ] ( <b>11</b> ) and [Co <sup>II</sup> Zn <sup>II</sup> ] ( <b>13</b> ) helicates. Combining phase-solution and solid-state techniques.	165
6.3. Conclusions	171
6.4. Experimental	172
6.5. References	173

## 7. EXPLORATION OF THE COORDINATION CHEMISTRY OF H<sub>2</sub>L<sub>2</sub>. THE DISCOVERY OF [Fe<sub>9</sub>] GRIDS.

Abstract	179
7.1. Introduction	179
7.2. Results and Discussion	182
Synthesis	182
Crystal structure description of Fe(C <sub>2</sub> O <sub>4</sub> ) <sub>3</sub> @[Fe <sub>2</sub> (H <sub>2</sub> L <sub>2</sub> )] <sup>3+</sup> helicate complexes	185
Crystal structure description of [Fe(C <sub>2</sub> O <sub>4</sub> ) <sub>3</sub> ]@[Fe <sub>2</sub> (H <sub>2</sub> L <sub>2</sub> ) <sub>3</sub> ](BF <sub>4</sub> )·5(C <sub>2</sub> H <sub>3</sub> N)·CH <sub>4</sub> O·3(H <sub>2</sub> O), ( <b>14</b> )	185
Crystal structure description of Fe(C <sub>2</sub> O <sub>4</sub> ) <sub>3</sub> @[Fe <sub>2</sub> (H <sub>2</sub> L <sub>2</sub> ) <sub>3</sub> ](BF <sub>4</sub> )·3(CH <sub>4</sub> O)·4.75(H <sub>2</sub> O), ( <b>15</b> )	187
Crystal structure description of Fe(C <sub>2</sub> O <sub>4</sub> ) <sub>3</sub> @[Fe <sub>2</sub> (H <sub>2</sub> L <sub>2</sub> ) <sub>3</sub> ](ClO <sub>4</sub> )·[H <sub>2</sub> O], ( <b>16</b> )	188
Crystal structure description of the grid [Fe <sub>9</sub> O <sub>4</sub> (OH) <sub>10</sub> (H <sub>2</sub> L <sub>2</sub> ) <sub>6</sub> (H <sub>2</sub> O) <sub>4</sub> ](BF <sub>4</sub> ) <sub>5</sub> , ( <b>17</b> )	189
Crystal structure description of the grid [Fe <sub>9</sub> O <sub>4</sub> Cl <sub>6</sub> (OH) <sub>8</sub> (H <sub>2</sub> L <sub>2</sub> ) <sub>6</sub> ](Cl) <sub>4</sub> , ( <b>18</b> )	192
Magnetic behavior of grid <b>17</b>	196
7.3. Conclusions	198
7.4. Experimental	198
7.5. References	200

## 8. MAGNETIC STUDY OF THE TRIPLE-STRANDED HELICATES [X@Fe<sub>2</sub>(H<sub>2</sub>L)<sub>3</sub>]<sup>4+</sup> IN SOLUTION AND ACCESS TO (X@[Fe(H<sub>2</sub>L<sub>5</sub>)<sub>3</sub>]<sub>2</sub>)<sup>3+</sup> COMPLEXES (X= I-, Br-, Cl-)

Abstract	205
8.1. Introduction	205
8.2. Results and discussion	210
Organic Synthesis	210
Inorganic Synthesis	210
Analysis of the NMR spectra for the Fe <sub>2</sub> (H <sub>2</sub> L) <sub>3</sub> helicates ( <b>19</b> and <b>20</b> )	211

Crystal structures of $(\text{I}@\text{[Fe}(\text{H}_2\text{L}_5)_3]_2)(\text{PF}_6)_3$ ( <b>24</b> ), $(\text{Br}@\text{[Fe}(\text{H}_2\text{L}_5)_3]_2)(\text{PF}_6)_3$ ( <b>25</b> ), and $(\text{Cl}@\text{[Fe}(\text{H}_2\text{L}_5)_3]_2)(\text{PF}_6)_3$ ( <b>26</b> )	217
Crystal structure of $(\text{I}@\text{[Fe}(\text{H}_2\text{L}_5)_3]_2)(\text{PF}_6)_3$ ( <b>24</b> )	217
Crystal structure of $(\text{Cl}@\text{[Fe}(\text{H}_2\text{L}_5)_3]_2)(\text{ClO}_4)_3$ ( <b>27</b> )	220
8.3. Conclusions	221
8.4. Experimental	222
8.5. References	223
<b>9. CONCLUSIONS AND FUTURE PERSPECTIVES</b>	227
<b>APPENDIX</b>	
Appendix 1	235
Appendix 2	242
Appendix 3	258
Appendix 4	267
Appendix 5	293
Appendix 6	314
Appendix 7	331
Appendix 8	362
<b>PHYSICAL TECHNIQUES</b>	381
<b>LIST OF PUBLICATIONS</b>	383

## Abbreviations and Symbols

<b>bbp</b>	<b>Bis(pyrazolyl-pyridine) = 2,6-di(pyrazolyl pyridine)</b>
<b>BVS</b>	Bond Valence Sum
<b>C<sub>p</sub></b>	Molar Heat Capacity at Constant Pressure
<b>D</b>	Axial Zero-Field Splitting Parameter
<b>DFT</b>	Density Functional Theory
<b>DSC</b>	Differential Scanning Calorimetry
<b>g</b>	Landé constant
<b>H</b>	Enthalpy
<b>HS</b>	High Spin
<b>k<sub>B</sub></b>	Boltzmann constant
<b>LS</b>	Low Spin
<b>M<sub>L</sub></b>	total angular momentum quantum number
<b>M<sub>S</sub></b>	total spin quantum number
<b>NMR</b>	Nuclear Magnetic Resonance
<b>ppm</b>	Parts Per Million
<b>PXRD</b>	Powder X-ray Diffraction
<b>QTM</b>	Quantum Tunneling Magnetization
<b>R</b>	Ideal Gas Constant
<b>R<sub>f</sub></b>	Rate factor
<b>S</b>	Entropy
<b>SCO</b>	Spin Crossover
<b>SOC</b>	Spin-Orbit Coupling
<b>SCSC</b>	Single-Crystal-to-Single Crystal
<b>SCXRD</b>	Single Crystal X-ray Diffraction
<b>SMM</b>	Single-molecule magnet
<b>SPT</b>	structural phase transitions
<b>SQUID</b>	Superconducting Quantum Interference Device
<b>T<sub>1/2</sub></b>	Spin Transition Temperature
<b>TAP</b>	Trigonal Antiprismatic
<b>terpy</b>	2,2':6',2''-terpyridine

<b>TMS</b>	Tetramethylsilane
<b>TP</b>	Trigonal Prismatic
<b><math>U_{\text{eff}}</math></b>	Barrier height for the magnetization reversal
<b>VT</b>	Variable-Temperature
<b>ZFS</b>	Zero-Field Splitting
<b><math>10Dq</math></b>	cubic crystal field splitting
<b><math>\gamma_{\text{HS}}</math></b>	Normalized High Spin Fraction
<b><math>\delta</math></b>	Chemical Shift
<b><math>\Delta E_{\text{elec}}</math></b>	Difference in Electrostatic Energy
<b><math>\Delta G</math></b>	Difference in Gibb's Free Energy
<b><math>\Delta H</math></b>	Difference in Enthalpy
<b><math>\Delta S</math></b>	Difference in Entropy
<b><math>\Delta</math></b>	Difference in
<b><math>\Delta_o</math></b>	Octahedral Crystal Field Splitting Parameter
<b><math>\Theta</math></b>	Trigonal Distortion Parameter of the Octahedron
<b><math>\mu_{\text{eff}}</math></b>	Effective Magnetic Moment
<b><math>\Sigma</math></b>	Octahedral Distortion Parameter of
<b><math>\chi_M</math></b>	Molar Magnetic Susceptibility

# CHAPTER 1

---

## INTRODUCTION







## 1. INTRODUCTION

### 1.1. Nanotechnological background/context. Molecular Switches.

Over the last few years, the speed of nanotechnology development has reached the promising theoretical principles established in the early 1960s. It was Richard Feynman who introduced the idea of manipulating information at the atomic level, thereby putting all of the Encyclopaedia Britannica on the head of a pin.<sup>1</sup> From that moment, the way of manufacturing new tiny devices faced a tremendous change. The bottom-up approach could overcome the limits of miniaturisation established by making the existing materials smaller, the so-called top-down approach.<sup>2</sup> For this reason, the generation of new nanomaterials turned towards molecule-based systems. At that molecular level, interesting physical properties arise due to quantum effects and the performance speed of the device is improved. Employing this approach, we can reproduce the conventional memories, modulators, transistors, switches and wires at a nanometric scale, which are reduced in size and are more efficient. To date, thousands of molecular magnetic materials based on the spin state control of magnetic coordinating complexes have been studied and proposed as new molecular switches.<sup>3-7</sup> A magnetic bistable behaviour is a fundamental feature of such prototypes to reach a binary requisite within the molecular scale.<sup>8,9</sup> Besides these materials, Spin Crossover (SCO) complexes are promising candidates by virtue of their possible interconversion between the high spin (HS) state and the low spin (LS) states when an external stimulus is applied.<sup>10,11</sup> Thus, taking advantage of the accessible ON/OFF positions (binary code) associated with the spin states, a new set of input and output signals were initially proposed to encode information. Indeed, one of the elementary logic operations, the cNOT gate, could be described through the SCO behaviour.<sup>12</sup> However, these molecular switches gain better technological applicability as promising entries for memory storage when hysteresis is present in the spin transition.<sup>13,14</sup> In this case, two magnetic responses may be retained under the same temperature range and these can be reached depending on the thermal "history". Another application is to employ them as spin based-sensors since they are highly sensitive to molecules from the environment. In some cases, solvent absorption/desorption and solvent exchange leads to a simultaneous change of the spin state, optical properties and crystallographic arrangements.<sup>15-17</sup> Hence, the construction of sensory and memory devices is the ultimate goal of this research. Other promising on-

off nano-switching systems are the single-molecule magnets (SMMs)<sup>18,19</sup>. For these complexes, the bistability arises from the flipping of the total spin orientation of the metal centres between the total magnetic moment up ( $+M_s$ ) or down ( $-M_s$ ), separated by a high energetic barrier preventing its fast reorientation below a certain blocking temperature. As also mentioned for SCO systems, the switching in magnetization accompanied with hysteresis provides many technological applications. In addition, SMMs have been proposed as qubits for quantum computing<sup>20,21</sup>, as prototypes for molecular spintronics<sup>22</sup> and high-density data storage<sup>23,24</sup>.

Although the SCO and SMMs systems have been intensely studied for many years<sup>25</sup> and an extensive “encyclopaedia” of compounds have been synthesized since they were discovered by Cambi and Szegö (1931)<sup>26</sup> and Gatteschi (1991)<sup>27</sup>, respectively, the research on this field is still significant<sup>23,24,28</sup>. While current research stages mostly tend to incorporate such molecules into functional nanostructured systems (nanoparticles<sup>29-31</sup>, thin films<sup>32-34</sup> or surfaces<sup>35-38</sup>, among others) to reach real operating devices, some lack understanding of theoretical and fundamental aspects of both phenomena persist. Currently, it remains challenging to envisage a robust design and synthesis for a desired or addressed magnetic performance. Following this conception, this work aims to moderately contribute to elucidating some elementary insights to the overall molecular magnetism community through the deliberate design, synthesis and study of new molecular SCO and SMM complexes through ligand design.

## 1.2. The Spin Crossover Phenomenon

Spin Crossover (SCO) is a fascinating phenomenon occurring in first-row transition metals with the configuration  $d^4$  to  $d^7$  due to their ability to switch the spin state when the ligands induce the appropriate crystal field splitting.<sup>39,40</sup> In an octahedral geometry, the degeneracy loss of the five  $3d$  orbital occurs, splitting them into two subsets, the  $e_g$  ( $d_{z^2}$  and  $d_{x^2-y^2}$ ) and the  $t_{2g}$  ( $d_{xy}$ ,  $d_{zy}$  and  $d_{zx}$ ). The difference in energy between them is defined as the ligand field splitting ( $\Delta$ ) and is symbolized by the  $10Dq$  parameter. This ligand field strength depends on the particular set of ligands, the metal ion and its oxidation state, and the metal-ligand distance ( $r$ ). When a set of ligands induces a weak-field strength,  $\Delta$  will be smaller than the interelectronic spin-pairing energy ( $P$ ), and the electrons will fill up the five orbitals according to Hund’s rule, exhibiting the maximum multiplicity and thus favouring the high spin (HS) ground state. For strong strong-ligand

field strengths,  $\Delta$  will be larger than  $P$ , and the pairing of the electrons in the lower orbital ( $t_{2g}$ ) is favoured, resulting in a low spin (LS) ground state. When the ligands display a ligand field splitting close to the critical ( $\Delta_c$ ) value, meaning that  $\Delta$  is comparable to the magnitude of  $P$ , a transition between LS and HS can be induced by applying an external stimulus such as temperature, light, pressure or magnetic field. Among the suitable metals, Fe(II) in an  $N_6$ -coordination environment is the most widely reported<sup>41-43</sup> and will be the focus of this thesis. This  $d^6$  metal ion experiences the most significant structural changes during SCO, toggling the complex between a  $^1A_1$  diamagnetic ( $S=0$ ) and a  $^5T_{2g}$  paramagnetic ( $S=2$ ) spin state. The degeneration of the ground state around the critical point is shown in the Tanabe-Sugano diagram<sup>44</sup> (Figure 1.1).

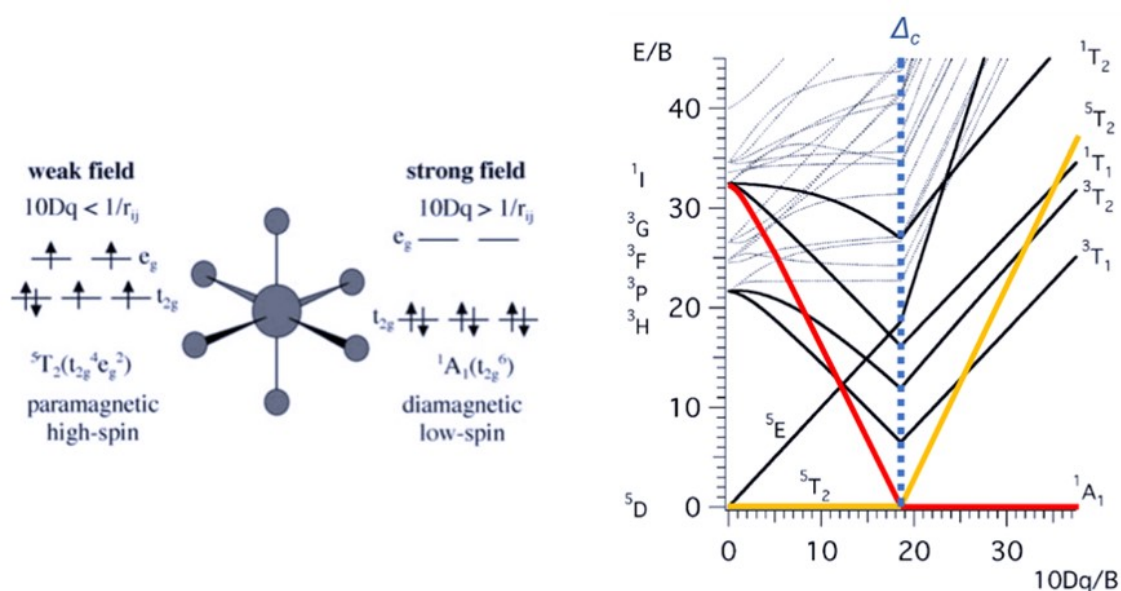


Figure 1.1. (Left): Representation of the two possible electronic configurations for an octahedral Fe(II) complex. (Right): Tanabe-Sugano diagram for a  $d^6$  transition metal ion. Figures adapted from reference 40.

As mentioned above, the ligand field splitting depends not only on the nature of the donor ligand but also on the Fe-L distance ( $r$ ). The difference in metal-ligand distance of the two states is due to the fact that two electrons occupy antibonding orbitals in the HS state ( $t_{2g}^4 e_g^2$  configuration), whereas the six d electrons occupy the non-bonding orbitals in the LS state ( $t_{2g}^6$  configuration). This is illustrated by plotting the potential electronic energies as a function of the symmetric metal-ligand stretch vibration for each spin state (Figure 1.2, left), where the  $^5T_{2g}$  (HS) potential well is horizontally shifted to higher (Fe-L) distances. The values of the HS Fe-N coordination bond lengths ( $r_{HS}$ ) are around 0.2 Å longer than the LS bond lengths ( $r_{LS}$ ), which lie between 1.95-2.0 Å. Thus, the typical

horizontal displacement is  $\Delta r_{HL} = r_{HS} - r_{LS} \approx 0.2 \text{ \AA}$ . On the contrary, the vertical shifting of the potential well strongly depends on the nature of the ligands. The thermal spin crossover takes place when the zero-point energy difference,  $\Delta E_{HL}^0 = E_{HS}^0 - E_{LS}^0$ , is in the order of magnitude of the thermally accessible energy ( $k_B T \approx \Delta E_{HL}^0$ ). In these conditions, the thermal population of the LS state with the lowest enthalpy is favoured at low temperatures. Instead, The HS state is thermodynamically more stable at higher temperatures since its associated entropy is larger than that for the LS state. The origin of this entropic enlargement is driven by the increase of spin multiplicity and the higher density of vibrational states in the HS state. In this sense, the  $10Dq$  parameter also depends on the respective Fe-L bond distances. Therefore, ranges for  $10Dq^{HS}$  and  $10Dq^{LS}$  can be estimated when considering the abovementioned conditions (Figure 1.2, right). SCO can only occur in a narrow range of conditions, explaining why the phenomenon is susceptible to tiny changes in the coordination sphere or in the crystal lattice.

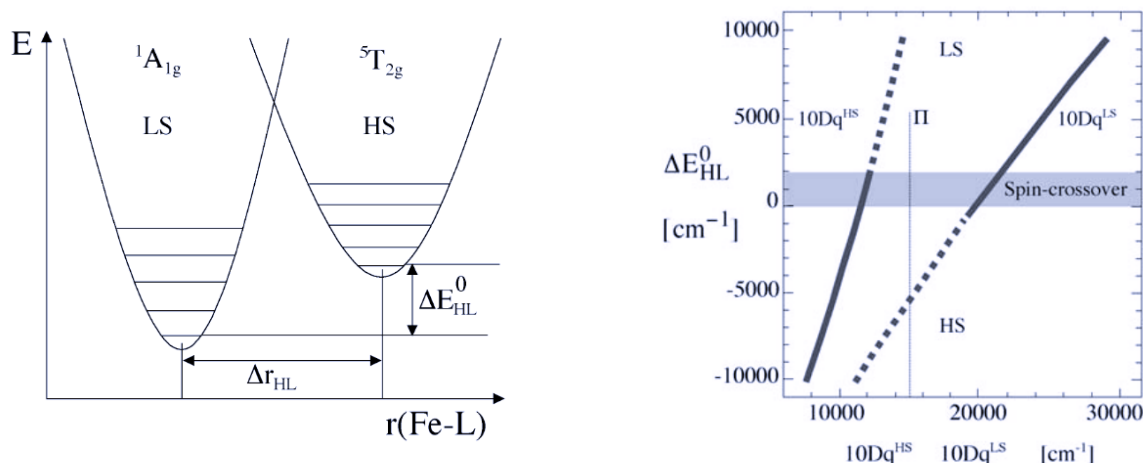
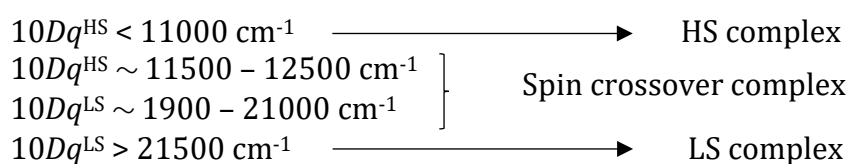


Figure 1.2. (Left): Schematic representation of the potential wells of the HS and the LS states for an Fe (II) complex along the symmetric metal-ligand stretch vibration (Fe-L). (Right): Regions where the HS state, the LS state or the SCO are stable as function of the ligand field strength ( $10Dq$ ). Taken from reference 40.

The spin transition is generally represented by plotting the high spin fraction ( $\gamma_{HS}$ ) as a function of temperature. The  $T_{1/2}$  parameter is used to define the temperature of the spin

transition, being the temperature at which the population of the HS and the LS species is the same (50%). Depending on the cooperativity, the spin-transition curves can be more or less abrupt and thus take different shapes (Figure 1.3). The degree of cooperativity is a measure of the propagation of the structural and electronic changes of the SCO-active metal centres through the crystal lattice. Usually, this communication arises from intermolecular interactions, which can convey the chemical pressure induced by the volume change around the metal ion when the spin changes.

For weak interactions, a gradual transition spanning a wide temperature range is observed (Figure 1.3 a). This type of transition occurs in solution or for isolated molecules such as SCO solid-diluted systems. In these cases, a Boltzmann distribution of both spin states with the temperature takes place. An abrupt transition (Figure 1.3 b) over a narrow temperature range is observed in more cooperative systems.<sup>14,45,46</sup> If the intermolecular interactions between SCO centers are strong enough, a thermal hysteresis loop may appear. Thus, a bistable system allows to encode an “on” or an “off” state due to the possibility to have two spin states at the same temperature depending on the thermal history. Although not shown in Figure 1.3, incomplete SCO or two-step transition may occur. The former occurs when only some metal centres can switch the spin state. The second one may happen on binuclear systems or mononuclear ones with different distinguished crystallographic centres.

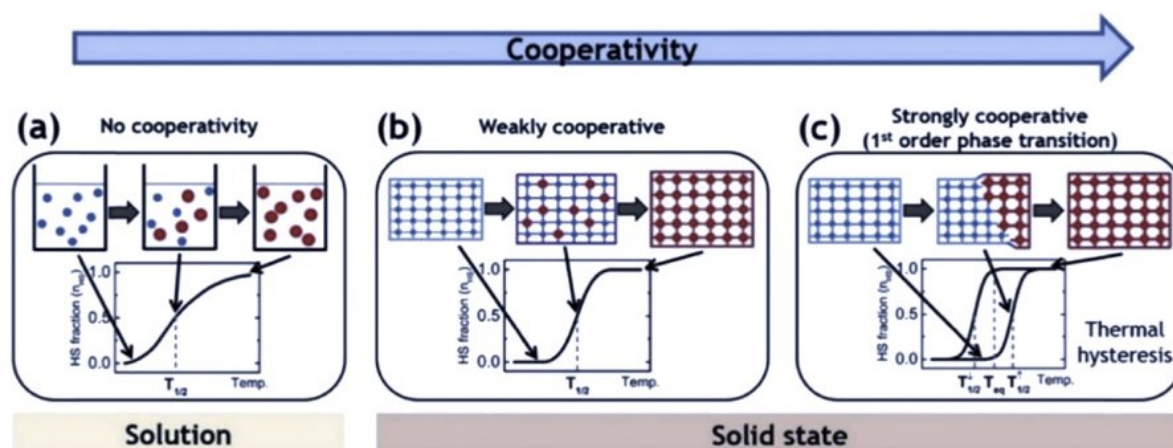


Figure 1.3. Representation of some of the more common types of SCO curves exhibiting different degrees of cooperativity. (a) Gradual transition in solution with no cooperativity. (b) More abrupt transition in solid state exhibiting weak cooperativity. (c) Abrupt transition with hysteresis in a solid state. A schematic representation of the cooperativity for each example is given in the upper part of the curve. LS and HS molecules are represented in blue and red circles, respectively. Taken from reference 14 and 46.

### 1.3. Monitoring SCO.

The redistribution of some d electrons among two possible electronic configurations causes a marked change in physical properties such as magnetism, structural, optical and vibrational properties. For this reason, several methods can be used to detect and follow the transition. Among them, only the techniques used in this thesis are briefly described.

#### 1.3.1. Variable temperature magnetic susceptibility measurements

The SCO transition is represented by plotting  $\chi_m T$  versus  $T$ ,  $\chi_m$  being the molar paramagnetic susceptibility (see below). The  $\chi_m T$  values derive from the  $\chi_{HS}$  and the  $\chi_{LS}$  contribution as determined by the mole fraction of each HS and LS species ( $\chi_m(T) = \gamma_{HS}\chi_{HS} + \gamma_{LS}\chi_{LS}$ ) at a given temperature. The magnetic susceptibility is determined using SQUID magnetometers in the solid-state and Evan's method in the solution phase.

##### 1.3.1.1. SQUID Magnetometry. Detection in solid state.

Superconducting Quantum Interference Devices (SQUID) magnetometers<sup>47</sup> provide a homogenous external magnetic field,  $H$ , which induces a magnetization,  $M$  in the sample. If the applied magnetic field is weak enough, the degree of magnetization can be expressed as the volume susceptibility ( $\chi_v$ ), following Equation 1.1<sup>48,49</sup>:

$$\chi_v = \frac{M}{H} \quad (1.1)$$

$$\chi_g = \frac{\chi_v}{\rho} \quad (1.2)$$

$$\chi_m = \chi_g \cdot Mr \quad (1.3)$$

$$\chi_m = \chi_m(\text{paramagnetic}) + \chi_m(\text{diamagnetic}) \quad (1.4)$$

$$\chi_m(\text{diamagnetic}) = -\frac{Mr}{2} \cdot 10^{-6} \text{ cm}^3 \cdot \text{mol}^{-1} \quad (1.5)$$

$$\chi_m = \chi_g \cdot \frac{Mr}{m} + \left( \frac{Mr}{2} \cdot 10^{-6} \right) \quad (1.6)$$

The magnetic susceptibility is adimensional. However, the use of molar magnetic susceptibility is quite common. Thus, the mass susceptibility ( $\chi_g$ ), in  $\text{cm}^3 \cdot \text{g}^{-1}$ , is determined by dividing the  $\chi_v$  by the density of the sample ( $\rho$ ) in  $\text{g} \cdot \text{cm}^{-3}$  (Equation 1.2). The molar magnetic susceptibility ( $\chi_m$ ) is calculated by multiplying the molecular weight ( $Mr$  in  $\text{g} \cdot \text{mol}^{-1}$ ) yielding  $\chi_g$ . (Equation 1.3). The measured susceptibility in  $\text{emu} \cdot \text{mol}^{-1}$  (or  $\text{cm}^3 \cdot \text{mol}^{-1}$ ) includes two components of the magnetic response of the sample, the paramagnetic and the diamagnetic one (Equation 1.4). The paramagnetic contribution arises from a permanent magnetic dipole moment of the unpaired valence electrons, which has the same applied magnetic field direction. On the contrary, the diamagnetic contribution arises from the paired electrons of the inner electron shells and causes a small magnetic moment against the applied field. The diamagnetic contribution can be approximately calculated using the expression shown in Equation 1.5 or using Pascal's constants.<sup>50</sup> Thus, Equation 1.6 is the expression for the corrected molar susceptibility corresponding only to the paramagnetic response of the sample, where  $m$  is the mass of the sample.

Curie's Law allows to calculate the paramagnetic susceptibility value for an isolated electron under an applied magnetic field ( $H$ ) at relatively high temperatures through equation 1.7:

$$\chi = \frac{M}{H} = \frac{N_A g^2 \mu_B^2}{4k_B T} \quad (1.7)$$

And, thus:

$$\chi_m = \frac{N_A g^2 \mu_B^2}{4k_B T} \cdot \frac{Mr}{\rho} \quad (1.8)$$

where  $N_A$  is Avogadro's number,  $g$  is the Landé g-factor for an electron ( $g=2.0023$ ),  $\mu_B$  is the effective magnetic moment,  $k_B$  is the Boltzmann constant, and  $T$  is the temperature. Considering a mononuclear compound of a metal transition without orbital contribution on the energetic term, Curie's law is described through the spin component ( $S$ ) of the molecule under study:

$$\chi_m T = \frac{N_A g^2 \mu_B^2}{3k_B} \cdot S(S+1) \quad (1.9)$$

The molar magnetic susceptibility product  $\chi_m T$  is directly proportional to the normalised HS fraction,  $\gamma_{HS}$ , since the HS state for Fe(II) is paramagnetic with an  $S=2$ , and the LS state is diamagnetic ( $S=0$ ). Therefore, the spin transition can be monitored by changing the temperature and measuring the  $\chi_m T$  variation.

### 1.3.1.2. $^1\text{H}$ -Nuclear Magnetic Resonance (NMR). Detection in solution

The study of SCO behaviour in solution, where the cooperative effects associated with the crystal packing in the solid-state are lost, provides direct insights into the electronic effect displayed by the coordinated ligands. Besides some solvent effects that could be significant on the resultant magnetic behaviour, the ligand field strength has the most considerable contribution to the SCO of the isolated molecules in the absence of intermolecular interactions.<sup>51</sup> Therefore, solution studies are the most used to establish correlations and trends relating SCO and the effect of ligand design when changing different substituent groups,<sup>52,53</sup> different aromatic groups<sup>53</sup> or anions<sup>54</sup>. Among all the techniques used to investigate the SCO in solution, the Evans method is the most extended.

#### Evans method

NMR spectroscopy is a valuable technique in the characterization of diamagnetic and paramagnetic complexes in solution. The Evans method,<sup>55</sup> which relies on NMR, can be used to determine the magnetic response of a paramagnetic species due to effect between the unpaired electrons and a nucleus of the system used as probe. The paramagnetic shift experienced by the probe can be directly measured using a diamagnetic reference of this probe (an independent compound such as TMS) when extracting the difference between its signals in pure solvent and the same solvent containing the paramagnetic material (Figure 1.4). The signal of the solvent itself can also be used as probe to track the magnetic influence. In this case, the signal from the solvent protons containing the dissolved paramagnetic species is compared with the pure solvent signal. For this, a coaxial NMR tube with two separate compartments for both solutions, solvent with paramagnetic species (outer tube) and solvent as reference (inner tube), is needed to acquire the composite spectrum simultaneously. The frequency difference ( $\Delta\nu$ ) between the solvent peaks is directly measured and related to the mass susceptibility ( $\chi_g$ ) using Equation 1.10.<sup>56,57</sup>



$$\chi_g = \frac{3\Delta\nu}{4\pi\nu_o c} \quad (1.10)$$

where,  $\nu_o$  is the spectrometer frequency in Hz, and  $c$  is the exact concentration of the paramagnetic solution in  $\text{g}\cdot\text{cm}^{-3}$ . Thus, this method requires a very pure paramagnetic sample. Again,  $\chi_g$  multiplied by the molar mass ( $Mr$ ) in  $\text{g}\cdot\text{mol}^{-1}$  gives the total molar susceptibility  $\chi_m$  (Equation 1.3). This total measured susceptibility must also be corrected using Equations 1.4 and 1.5.<sup>58,59</sup>

For SCO monitoring in solution, only narrow temperature ranges are suitable due to solvent melting and boiling point limitations. Therefore, the complete interconversion between both states HS and LS is not seen in some cases. One way to overcome this problem is by fitting the data set ( $\chi_M T$  versus  $T$ ) as a gradual and complete SCO using the ideal solution model<sup>48,60</sup> (Equation 1.11).

$$\chi_m T(T) = \frac{\chi_m T(max)}{1 + e^{\left(\frac{-\Delta H}{RT} + \frac{\Delta S}{R}\right)}} \quad (1.11)$$

The derived parameters, the thermodynamic enthalpy ( $\Delta H$ ) and entropy ( $\Delta S$ ) associated with the SCO transition are obtained by fitting each data set.  $\chi_m T(T)$  is the  $\chi_m T$  value measured at temperature  $T$ ,  $\chi_m T(max)$  is the maximum  $\chi_m T$  value ( $3.5 \text{ emu K mol}^{-1}$  for iron (II) complexes),<sup>51,61</sup>  $R$  is the ideal gas constant ( $8.314 \text{ K mol}^{-1} \text{ K}^{-1}$ ).  $T_{1/2}$  can be deduced from the thermodynamic values (Equation 1.12), as  $\Delta G=0$  at  $T_{1/2}$  and ( $\Delta G= \Delta H - T\Delta S$ ).

$$T_{1/2} = \frac{\Delta H}{\Delta S} \quad (1.12)$$

Typically, the Evans method has a relative error of 5%,<sup>62,63</sup> which arises from weighing error or impurities. Therefore, significant errors are associated with data fitting.

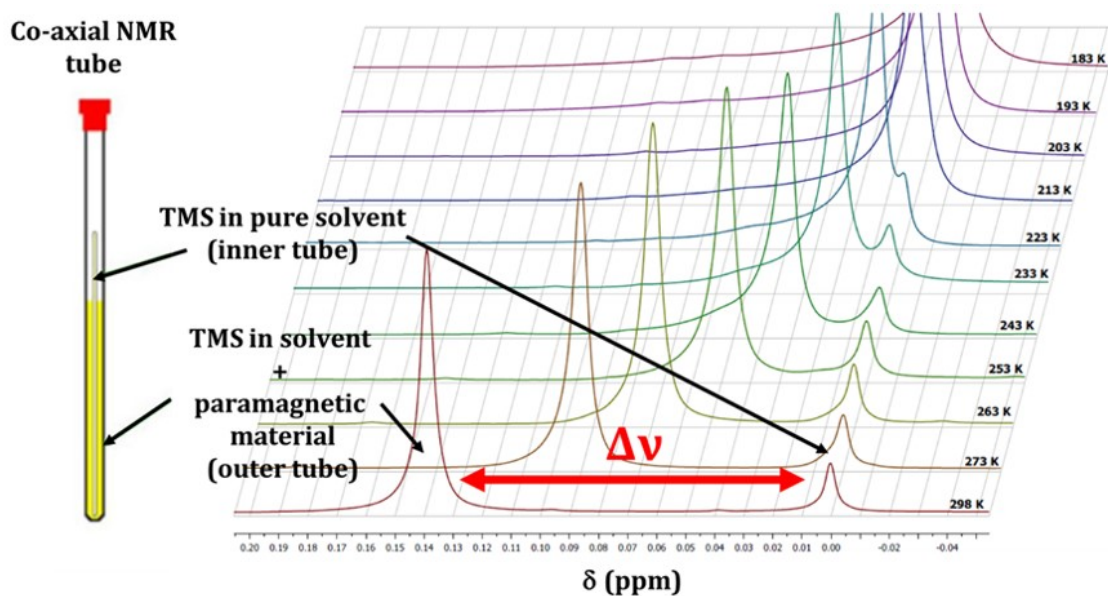


Figure 1.4. Schematic representation of the co-axial NMR tube used in Evan's method. The  $^1\text{H}$ -NMR outcome shows the paramagnetic shift ( $\Delta\nu$ ) between the TMS in pure solvent and TMS in the paramagnetic solution. The composite spectrum within 298-183K is shown. Decreasing of the frequency shift ( $\Delta\nu$ ) is easily appreciated when decreasing temperature since LS is stabilized at low temperature.

### Temperature dependence of the NMR chemical shift

An alternative to the Evans method is to directly track the paramagnetic shift ( $\Delta\nu$ ) as the difference of the proton signals for the LS and HS species of the complex itself when multiple NMR spectra are acquired in a variable temperature experiment.<sup>63,64</sup> This method was used by Weber and Walker to investigate Fe(II) SCO transitions in solution, avoiding the main limitations of the previous method, such as knowing the precise concentration of the paramagnetic compound and its highly pure availability. The chemical shifts were found to be strongly influenced by the iron (II) spin state for a series of mononuclear and dinuclear SCO-active complexes, showing an excellent temperature-dependence fitting to a Curie-like behaviour. The high-spin molar fraction can also be easily determined from the paramagnetic shift of several protons by normalizing plots of the  $(\Delta\nu) \cdot T$  as a function of temperature. Additionally, the results were in good agreement once compared with the obtained ones from the Evans method. However, this method is only suitable for Fe(II) containing SCO complexes, which have a diamagnetic LS state. Recently, Novikov and co-workers developed another NMR-based method to overcome this specific drawback.<sup>65</sup> This method is based on relating the chemical shift directly with the magnetic susceptibility of the species that carries the nucleus analysed. Three contributions are considered for the total observed chemical shift of a given nucleus

contained in paramagnetic species. The diamagnetic chemical shift, always present, arises from the internal paired electrons ( $\delta_{dia}$ ), the contact contribution for spin polarization mediated through the molecular orbitals ( $\delta_c$ ), and the pseudocontact contribution from the dipole-dipole coupling of the nucleus with the unpaired electrons ( $\delta_{PC}$ ). (See Chapter 9 and Appendix 9 for details of the method where equations and DFT calculations are explained.). Thus, the method is also applicable to compounds with a paramagnetic LS state. Considering the population of both spin states in the solution of temperature-induced SCO compound, the three contributions for both, the LS and HS species, participate in the observed chemical shift ( $\delta_{obs}$ ):

$$\delta_{obs} = (\delta_{dia}^{LS} + \delta_P^{LS} + \delta_{PC}^{LS})\eta^{LS} + (\delta_{dia}^{HS} + \delta_P^{HS} + \delta_{PC}^{LS})\eta^{HS} \quad (1.13)$$

where  $\eta^{LS}$  and  $\eta^{HS}$  are the fractional population of each spin state.  $\delta_{dia}^i$  values are measured from a diamagnetic analogue,  $\delta_P^i$  are obtained by DFT calculations and the  $\delta_{PC}^i$  equation depends on the metal ion. The method was used to estimate the total observed paramagnetic shift and test the SCO behaviour solution for a series of SCO-active compounds containing different transition metal ions such as Ni(II) and Co(II).

### 1.3.2. Crystallography

Single crystal X-ray diffraction (SCXRD) measurements are used to detect the SCO transition easily since this technique can discriminate different atomic positions with high precision. As mentioned above, the most significant change associated with SCO is the metal-ligand bond lengths, which increase up to 10% when the molecules switch from the LS to the HS state for Fe(II). In this way, the spin state can be deduced from the structural changes. Usually, the spin transition is also accompanied by a deformation of the FeN<sub>6</sub> octahedral geometry. The coordination geometry of the LS complexes is close to the ideal octahedron due to the stronger metal-ligand bonding, whereas HS state complexes are the most distorted. Guionneau and Halcrow used some structural parameters to elucidate general trends of the distortion within SCO-active compounds and correlated it with the measured magnetic response establishing interesting magneto-structural correlations.<sup>66-69</sup> The definition of four structural parameters:  $\theta$ ,  $\phi$ ,  $\Sigma$  and  $\Theta$ , which are the ones used in this thesis,<sup>70-72</sup> are given in this section. The first two parameters are only used to characterize complexes with two meridional tridentate

ligands coordinated to the metal centre, such as  $[\text{Fe}(\text{1bpp})_2]^{2+}$  (Figure 1.5, left). The distortion is assessed by the  $\theta$  angle between the least-squares planes defined by the two chelating ligands and the  $\phi$  parameter, which is the trans N-Fe-N angle corresponding to the nitrogen of the central pyridyl rings coordinated to Fe(II). Thus, the values are  $90^\circ$  and  $180^\circ$ , respectively, for an ideal octahedron.

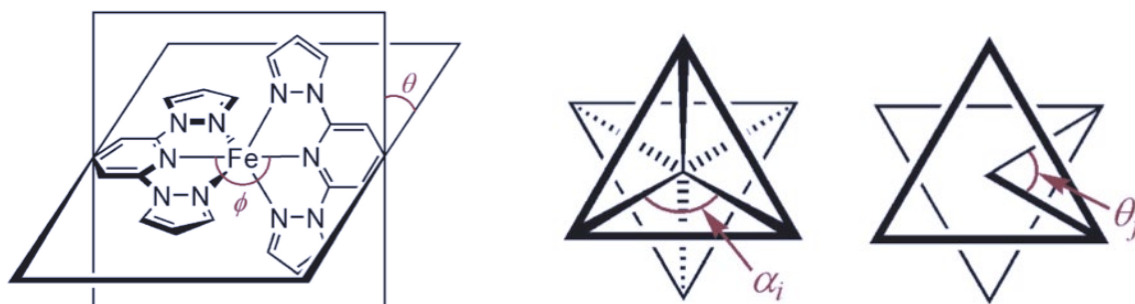


Figure 1.5. (Left) Representation of  $[\text{Fe}(\text{1bpp})_2]^{2+}$  complex in the HS state with the angular distortion parameters,  $\theta$  and  $\phi$ , illustrated. (Center and right) Definitions of the angles  $\alpha_i$  and  $\theta_j$  used to calculate the distortion indices  $\Sigma$  and  $\Theta$ , respectively, for an  $\text{ML}_6$  complex. Illustrations taken from reference 67.

Instead, the  $\Sigma$  and  $\Theta$  parameters consider the distortion of the  $\text{FeN}_6$  immediate coordination sphere without considering their connectivity through the ligands. The  $\Sigma$  parameter can be calculated from equation 1.14, which is the sum of the deviation from  $90^\circ$  of the twelve *cis*-N-Fe-N angles. The value for a perfect octahedral complex is  $\Sigma=0$ . The  $\Theta$  parameter indicates the distortion from a perfect octahedral symmetry towards a trigonal prismatic symmetry,  $D_{3h}$ , and can be calculated using equation 1.15. The  $\theta_j$  are the 24 N-Fe-N angles on the projection of two triangular faces of the octahedron along the eight threefold symmetry axis. When the octahedron is distorted by twisting towards  $D_{3h}$  symmetry (trigonal prismatic symmetry), the angles vary from  $60^\circ$  to  $0^\circ$ . Therefore, the high spin state complexes, which adopt more distorted octahedral geometry, display higher values for  $\Sigma$  and  $\Theta$ .

$$\Sigma = \sum_{i=1}^{12} |90 - \alpha_i| \quad (1.14)$$

$$\Theta = \sum_{j=1}^{24} |60 - \theta_j| \quad (1.15)$$

These parameters are easily calculated, as it is commonly done, by using the program Olex 2.0<sup>73</sup>. Firstly, the central metal ion with an octahedral environment is selected, followed by selecting the six donor atoms in a clockwise way and executing the distances and angles measurements from the geometry toolbar. Nevertheless, some discrepancies in the calculating method for  $\theta$  parameter in the literature lead to useless and non-homogenous data for structural studies. Consequently, Harding and co-workers have recently developed the OctaDist program.<sup>74</sup> It provides a consistent and straightforward way to calculate  $\theta$ , contributing to the obtention of reliable values to establish structural correlations among the SCO compounds. Besides these structural parameters, which define the local distortion of the metal coordination sphere, the SCXRD experiments give additional structural insights in light of the entire crystal packing. The overall magnetic response also depends on the intermolecular interactions between the SCO-active centres and other species in the crystal, such as solvent or counterions.<sup>16,54,67,75,76</sup> These interactions may promote the propagation of the SCO through the crystal lattice, which is known as the cooperative effect. Variable-temperature SCXRD experiments are highly relevant to precisely track the intermolecular changes, correlate them with the cooperativity and establish magneto-structural relationships. A detailed study of solid-state transformations coupled to SCO transitions is discussed in chapter 4.

#### 1.4. Pyrazole-pyridine based ligands used for Fe(II) SCO complexes

Most SCO-active iron (II) complexes are achieved by choosing the appropriate ligands, which generally contain aromatic heterocyclic rings with N-donors like pyridine, pyrazole, triazole or tetrazole.<sup>77</sup> In this thesis, we will focus on ligands derived from pyrazole and pyridine rings attached through C<sub>pyrazole</sub>-C<sub>pyridine</sub> or N<sub>pyrazole</sub>-C<sub>pyridine</sub> bonds.<sup>78</sup> The coordination of these pyrazole-pyridine derived ligands with iron, in turn, allows for the synthesis of several types of discrete SCO complexes. In this context, two main types of Fe(II) metal complexes depending on their nuclearity, are discussed through this thesis. Mononuclear SCO complexes, on the one hand, and polynuclear or supramolecular complexes (i.e. dinuclear triple-stranded helicate or, dimerized monomers of Fe). Therefore, a deliberate ligand design is crucial to address the synthesis of a desired molecular system.<sup>79,80</sup> When two-terminal pyrazole rings are bonded to a central pyridine (bis-(pyrazolyl)pyridine; bpp), tridentate ligands are produced, which can form, predictably, mononuclear iron (II) complexes with the cationic formula [Fe(bpp)<sub>2</sub>]<sup>2+</sup>

(Figure 1.6 a). In contrast, when isolated pyridinyl-pyrazolyl binding pockets are linked by organic spacers leading to a multidentate ligand, complexes with higher nuclearity are obtained. For example, H<sub>2</sub>L (Figure 1.6 b) is a ditopic ligand with two terminal pyridinyl-pyrazolyl moieties linked by a phenyl spacer forming two bidentate binding sites. Thus, triple stranded supramolecular host-guest helicates with the cationic formula  $\{X\text{C}[\text{Fe}_2(\text{H}_2\text{L})_3]\}^{3+}$  (X= Cl, Br) are formed by the assembly two Fe (II) metal centres and three such ligands, in order to fulfil the octahedral symmetry around the iron. In regard, two main directions have been pursued on the ligand design to access mononuclear (chapters 2 to 4) or polynuclear (chapters 8 to 11) molecular systems. Some representative complexes in the literature are described in the following sections.

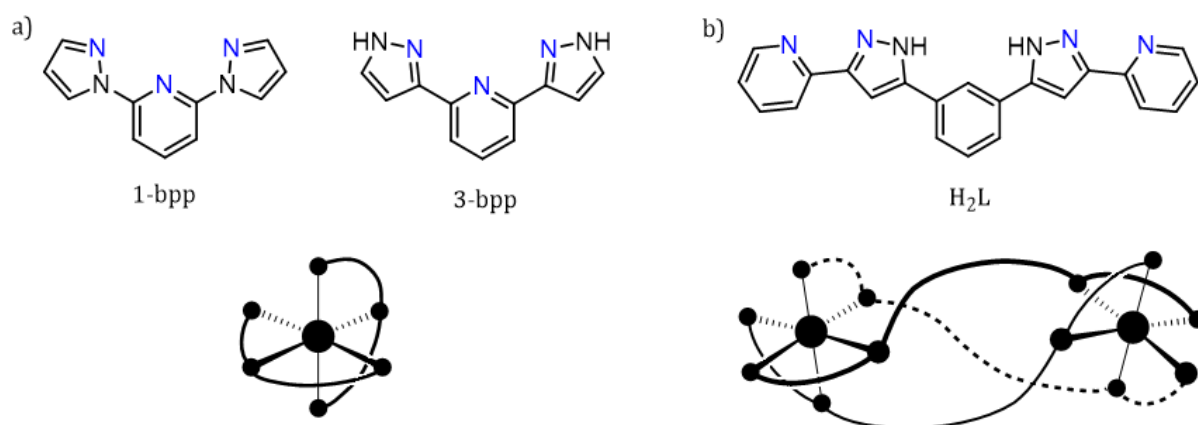


Figure 1.6 a) View of the two regio-isomers of the bis(pyrazolyl)pyridine ligands, 1-bpp and 3-bpp, respectively. Representation of the mononuclear complex from two ligands coordinated meridionally to the metal center in the bottom. b) View of the bis(pyridinyl-pyrazolyl) ligand and the respective possible ligand coordination for the synthesis of dinuclear ferrous SCO complex.

#### 1.4.1. Mononuclear complexes of Fe(II) with tridentate ligands (bpp)

Highlights of some relevant mononuclear SCO complexes based on bis-pyrazolyl pyridine (bpp) moieties are given in this section. The first application of 2,6-bis(pyrazol-3-yl)pyridine (3-bpp) into the SCO field was accomplished by Sugiyarto and Goodwin.<sup>81,82</sup> They presented the SCO-active compound,  $[\text{Fe}(3\text{-bpp})_2](\text{BF}_4)_2$ , which displays a 10K hysteresis loop around 175K. Its solvatomorph,  $[\text{Fe}(3\text{-bpp})_2](\text{BF}_4)_2 \cdot 2\text{H}_2\text{O}$ , presented instead a gradual SCO around 300K. The disparity of SCO behaviour between both complexes was attributed to the possible intermolecular interactions with the water within the lattice, which could influence the cooperativity of the system. However, no crystallographic data was available at that moment. Subsequently, the suggested

assumption was corroborated after crystallizing  $[\text{Fe}(\text{3-bpp})_2](\text{BF}_4)_2 \cdot 3\text{H}_2\text{O}$ .<sup>83</sup> From then on, more related systems were investigated,<sup>84-86</sup> and a large amount of different-substituted 3-bpp derivatives have been synthesized and coordinated to Fe(II), generating many relevant systems to the field.<sup>83-97</sup> Mainly, methyl<sup>89</sup>, hydroxyphenol<sup>90,92</sup>, methoxyphenol<sup>97</sup>, *tert*-butoxide<sup>89,93</sup>, amine<sup>89</sup>, *p*-toluoyloxy<sup>95</sup> and fluorophenyl<sup>95</sup> substituents, among others, have been introduced in C5 position of the side pyrazolyl ring (some symmetrically substituted and some unsymmetrically). The related literature also contains N1-alkylated 3-bpp derivatives, which usually give rise to HS complexes.<sup>91</sup> Additionally, the isomeric ligand (1-bpp) and its substituted-derivatives constitute a vast set of ligands used in the SCO field.<sup>98-112</sup> Indeed, both isomeric forms are the most widely instigated in the field, leading to a wide library of SCO complexes. The main difference between both categories relies on the accessible N-H free groups of 3-bpp, while in 1-bpp, the nitrogen N1 of the pyrazolyl ring is directly attached to the central pyridine moiety without any N-H free. Overall, depending on the functionalization, distinct spin-crossover transitions (ranging from gradual to abrupt with hysteresis) have been observed. This, in turn, has allowed to establish several magneto-structural correlations and unveil more insights intervening in the resulting magnetic behaviour.<sup>52,61,117</sup> Our research group has been greatly contributing to this research field.<sup>16,87,90,92,97,114,118-127</sup> In the work immediately preceding this thesis, the GMMF group reported two active-SCO complexes using the asymmetric 1,3bpp ligand (1,3bpp = 2-(pyrazol-1-yl)-6-(pyrazol-3-yl)pyridine), which combines both bpp isomeric moieties within the same ligand (Figure 1.7). Two solvent free polymorphs of compound  $[\text{Fe}(\text{1,3bpp})_2](\text{ClO}_4)_2$  displaying abrupt SCO transitions with a difference in SCO temperature of nearly 40K between them were reported.<sup>124</sup> One polymorph was directly obtained from a reaction using dried solvent, while the other was rationally prepared through a stepwise method of dehydration involving single-crystal-to-single-crystal (SCSC) transformations from a di-hydrated solvatomorph (Figure 1.7). The specific group of molecular interactions between the cationic metal centres within the lattice for each polymorph is directly associated with the different cooperativity and SCO behaviour. Notably, one polymorph has a more efficient crystal packing due to the amount of greater  $\pi \cdots \pi$  and C-H $\cdots$  $\pi$  intermolecular interactions, which enlarge the cooperativity. Additionally, since the N-H $\cdots$ O interactions involving perchlorates in this polymorph are much strong, a shift in  $T_{\text{SCO}}$  ( $\sim 40\text{K}$ ) is likely

promoted. Thus, the  $T_{\text{SCO}}$  was tuned utilizing the control of the different crystal organization for two compounds with the same empirical formula.

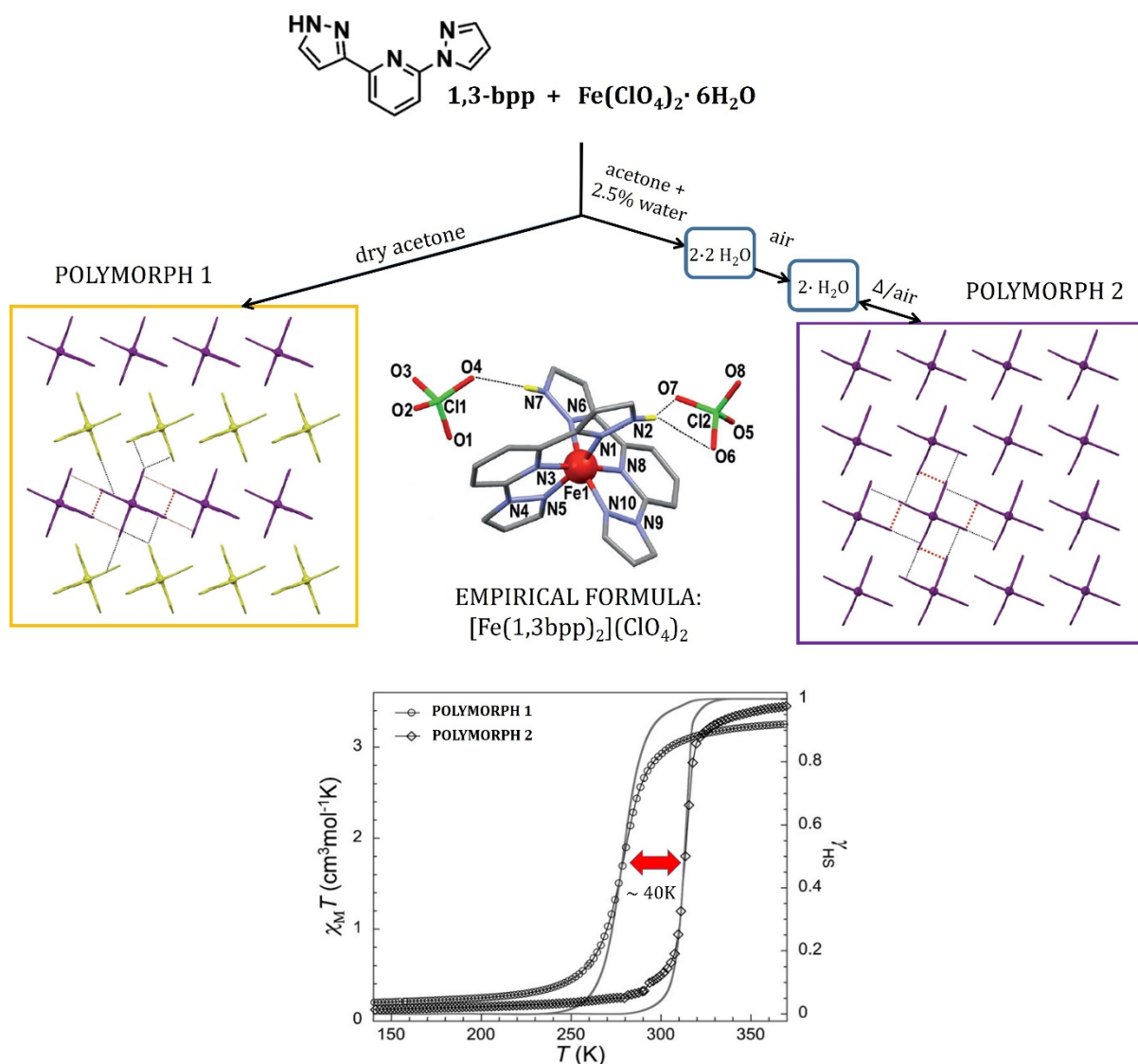


Figure 1.7. Schematic representation of the synthetic method for both polymorphs. Highlights on the different organization of the  $[\text{Fe}(\text{1,3-bpp})_2]_{2+}$  cations within the sheets of each polymorph. (Inside yellow and purple squares). Plot of the magnetic response of both polymorphism, emphasizing the difference of around 40 K between them. Adapted from reference 120.

Over the same period, a new synthetic approach for increasing the availability of novel active-SCO compounds was reported in our group. They showed the remarkable propensity to produce heteroleptic compounds with Fe (II) when combining the appropriate tris-imine chelating ligands. Series of 3-bpp ligands together with terpyridine-like and the 2-bbp (2,6-bis-(benzimidazol-2-yl)-pyridine) ligands were used to exploit this preferential ligand distribution (heteroleptic versus homoleptic) when



mixing pairs of them with the metal source. As a result, three new heteroleptic compounds that exhibit a versatile magnetic behaviour were described. In relation to these previous reports, chapter 2 to 4 were realized as a continuation of the research line of mononuclear SCO complexes using bpp-like ligands.

#### **1.4.2. Metallo-Supramolecular architectures of Fe (II), multitopic ligands.**

Bis-(pyridinyl-pyrazolyl) ligands have been significant actors in the field of coordination and supramolecular chemistry. This field encompasses the study of molecular structures which are held by weak and reversible non-covalent interactions. These include hydrogen bonding,  $\pi$ - $\pi$  interactions, van der Waals forces, electrostatic interactions and, according to some authors, metal coordination. As a result of these weak non-covalent interactions, the construction of assemblies beyond the molecule can be accomplished. The molecular self-assembly promoted by molecular recognition allows natural systems to assemble individual components into more complex structures that are thermodynamically favourable. Consequently, this strategy has been taken from nature to build up new artificial molecular structures. Metallo-supramolecular chemistry the part of supramolecular chemistry where metals and ligands are the fundamental components. Fortunately, metal-ligand interactions are highly directional, therefore, the incorporation of metals into such assemblies provides a more extensive series of geometries (square pyramidal, square planar, octahedral and others) which cannot be achieved with pure organic molecules. Thus, coordination chemistry together with a rational ligand design provides access to many predictable architectures. By considering these key concepts, a large number of discrete assemblies have become available. Among them, different polyhedra, helicates, grids, cages, wires, and rings are well known.

In this regard, bis-(pyridinyl-pyrazolyl) ligands have been previously used to achieve molecular arrays with various dimensionalities. Some ditopic ligands containing two terminal bidentate pyrazolyl-pyridine units with different aromatic spacers are shown in figure 1.8. Two types of derived bis-(3-(pyridin-2-yl)1*H*-pyrazol-*x*-yl) (*x*=1 or 5) ligands are distinguished depending on the connectivity of the spacer with the pyrazolyl ring. While the pyrazol-1-yl isomers display the aromatic spacer directly attached to the nitrogen donor through a methylene connector, the pyrazol-5-yl isomers have the deprotonable N-H (N1) group free. In this case, intermolecular interactions are promoted via hydrogen bonding, and host-guest features may play an important role. The

modulation of SCO behavior through encapsulation of guests will be discussed in section 1.4.2.1 and 1.4.2.2.

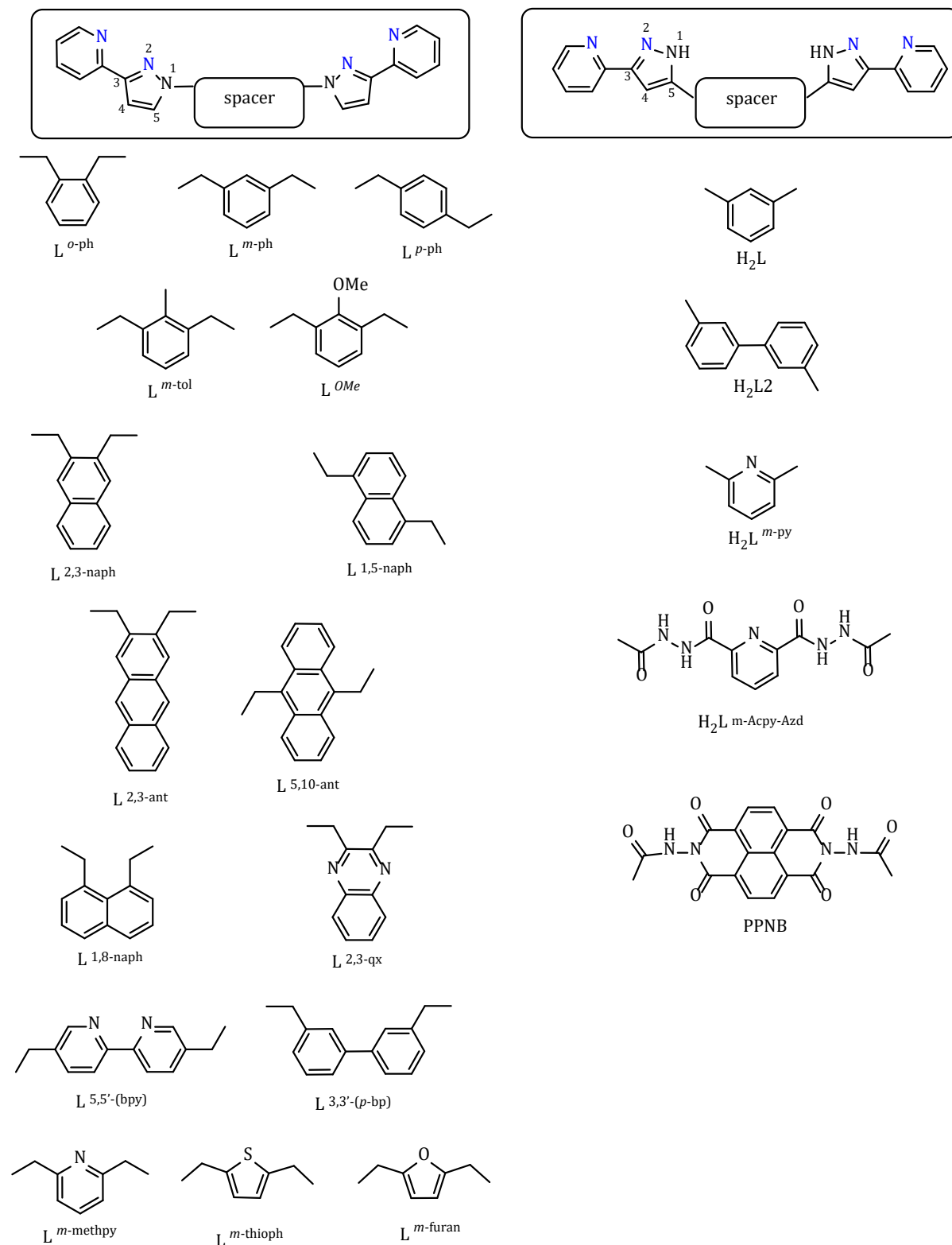


Figure 1.8. Representation of the bis-(3-(pyridin-2-yl)1H-pyrazol-x-yl) ( $x=1$  and  $5$ , on the left and right of the figure, respectively) derivative ligands with different spacer employed to explore several metallo-supramolecular architectures found in CDS database.

According to the CCDC database, the number of ligands containing the pyrazol-1-yl moiety is substantially higher than those containing the pyrazol-5-yl group. Thus, the amount of molecular architectures of the former is the largest. The majority of them are reported by Ward, who prepared  $M_4L_6$  tetrahedral cages<sup>128-131</sup>,  $M_8L_{12}$  octanuclear cubic cages<sup>132,133</sup>, one-dimensional helical polymers<sup>130,134</sup>, some helicates and mesocates,<sup>130,134</sup> and some other molecular arrangements such as a mixed-spin  $Fe_4$  grid,<sup>135</sup> 12 or 16-nuclear cages<sup>136</sup> and heteronuclear catenane systems<sup>137</sup>. In our group, we are interested in ligands containing the other isomeric unit and, the design and synthesis of five new derivatives are reported in chapter 8. Before that, only five ligands containing the pyrazol-5-yl were found in the literature. Two of them,  $H_2L$  and  $H_2L2$ , were synthesised and exploited in terms of supramolecular ensembles displaying SCO behavior in our group. These cases are discussed below. The ligand  $L^{m-py}$ , with two bidentate pockets formed by the terminal pyrazol-5-yl-pyridine parts and one central tridentate site, was used in Oshio's group to form a heptanuclear helicate  $[Fe^{III}_2Co^{II}_5(L^{m-py})_6O_6(H_2O)_6](BF_4)_4$  or a nonanuclear heterometallic [3x3] grid  $[Fe^{II}_4Fe^{III}Co^{II}_4(L^{m-py})_6(OH)_{12}(H_2O)_6](BF_4)_7$  depending on the stoichiometry of Fe:Co used.<sup>138</sup> For both clusters, the central tridentate cavity does not participate in the coordination with the metal centres. Instead, it takes part in several intermolecular interactions by establishing hydrogen bonds with water molecules. Additionally, they present a series of oxo and hydroxo bridges between some metal ions completing their octahedral coordination geometry. Later, the same ligand was used to prepare  $[Fe_5]$ ,  $[Fe_7]$  and  $[Fe_{17}]$  triple-stranded helical structures with pseudo threefold symmetry. The existing intramolecular magnetic interactions are mediated in part through additional oxo-bridges.<sup>139</sup> Two [3x3] grids were also obtained when all the binding pockets of  $L^{m-py}$  were directly coordinated to nine copper centres.<sup>140</sup> Finally,  $[Mn_5]$  and  $[Mn_8]$  structures with helical structures were reported.<sup>141</sup> While the former is formed by three  $L^{m-py}$  ligands, five manganese ions in a mixture of +2 and +3 oxidation states and  $\mu_3$ -oxo bridges, the latter is composed of six  $L^{m-py}$ , eight homovalent manganese ions 2+ and two  $\mu_3$ -chlorido bridges. Both complexes display antiferromagnetic interactions between the manganese ions. Ligands  $H_2L^{m-Acpy-Azd}$  and PPNB have not been used in the field of molecular magnetism. Instead, they have applications for wastewater purification by creating a metallogel with toxic heavy metals (Pb, Cd and Hg)<sup>142</sup>, and hydrogen production by the Ni(II)-PPNB complex on  $TiO_2$ .<sup>143</sup>

The ligand H<sub>2</sub>L (Figure 1.8) has been synthesized in our group and used to prepare triple-stranded helicates with SCO behaviour. These helicates contain a cavity able to encapsulate anion guests, such as Cl<sup>-</sup> and Br<sup>-</sup>. These, in turn, allow tuning the SCO response, which is a very rare case of host-guest inducing SCO in the field of supramolecular chemistry. Additionally, supramolecular assemblies with the cationic formula (X@[Fe(H<sub>2</sub>L)<sub>3</sub>]<sub>2</sub>)<sup>3+</sup> can be synthesized depending on the synthetic conditions. Ligand H<sub>2</sub>L2 holds a larger and more flexible spacer (biphenyl), which can form triple-stranded helicates with the ability to encapsulate bigger guests. Thus, a bifunctional system can be synthesized by encapsulating [Cr(ox)<sub>3</sub>]<sup>3-</sup>. A detailed description of these systems is given in detail in the following sections (1.4.2.1. and 1.4.2.2.)

#### **1.4.2.1. Dinuclear Fe<sub>2</sub> Triple stranded helicates. Host-guest chemistry and bifunctional systems.**

Dinuclear complexes are the simplest polynuclear structures where SCO and magnetic coupling interactions between metal centres can be studied. Although polymers are more suitable SCO systems to seek a bistable response promoted by strong covalent interactions between the metal centres, it remains challenging to crystallize them and establish insights into their cooperativity. For this reason, the interest in discrete dinuclear complexes, which are easier to crystallise and more convenient to unveil magneto-structural correlations, has increased in recent years. More interestingly, such complexes can provide a multi-step SCO behaviour by reaching three possible magnetic spin-paired states (HS-HS, HS-LS and LS-LS) when an external stimulus is applied. Therefore, the higher number of magnetic state combinations could be used to encode more complex logical operations or greater memory capacity.<sup>144</sup>

In this context, a series of [Fe<sub>2</sub>(H<sub>2</sub>L)<sub>3</sub>]<sup>4+</sup> metallohelicates were synthesized in our group (Figure 1.9).<sup>145</sup> Given their helical structure that offers a host cavity and the presence of free N-H groups that facilitates the host-guest interaction, the Cl<sup>-</sup> and Br<sup>-</sup> halides can be encapsulated inside. Due to the non-centric accommodation of this halide guests inside the cavity, two crystallographically inequivalent Fe<sup>II</sup> centres can be distinguished, which in turns allow reaching two possible magnetic states, [LS-HS] and [HS-HS] in the solid-state. The nature of the halides (Cl<sup>-</sup> versus Br<sup>-</sup>) influences the crystal field around the Fe centres shifting the gradual SCO around 40K (Figure 1.9, right). Additionally, the exposure to air of the ((X@[Fe<sub>2</sub>(H<sub>2</sub>L)<sub>3</sub>])<sup>3+</sup>(X: Cl, Br) complexes allows obtaining

solvatomorphs (e.g.  $\text{Cl}@\text{[Fe}_2(\text{H}_2\text{L})_3\text{]Cl}(\text{PF}_6)_2 \cdot 3\text{CH}_3\text{OH} \cdot \text{H}_2\text{O}$ ) through single-crystal-to-single-crystal (SCSC) transformations. For the latest compounds, a new possible spin state [LS-LS] is reached when cooling from the [HS-HS] state (at high temperatures) due to crystallographic equivalence of the Fe(II) centres.

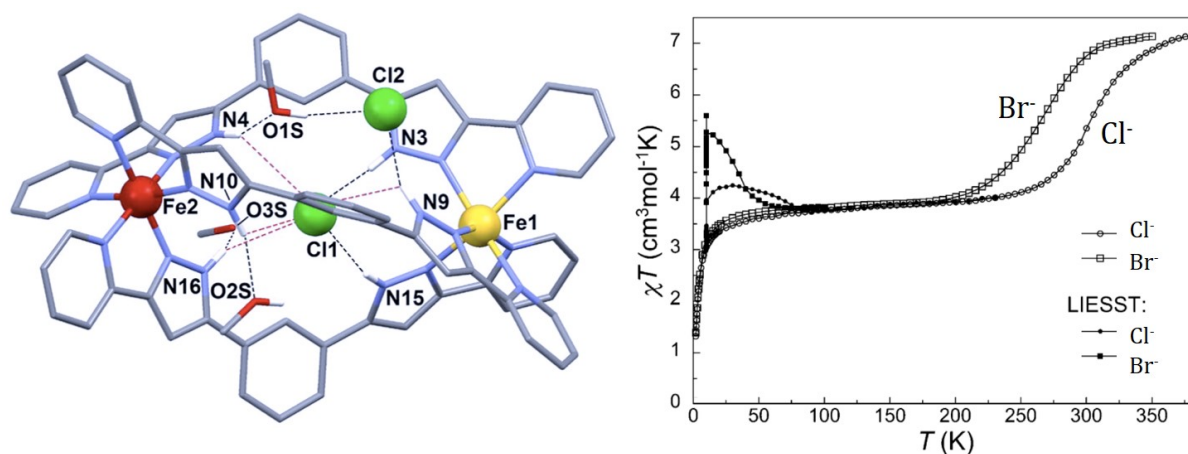


Figure 1.9. (Left) Representation of the cationic complex  $(\text{Cl}@\text{[Fe}_2(\text{H}_2\text{L})_3\text{]})^{3+}$  (**19**) at 100K. (Right) Magnetic response ( $\chi T$  plotted vs  $T$ ) for complexes with  $\text{Cl}^-$  and  $\text{Br}^-$  encapsulated. LIESST effect is also depicted in the graphic. Taken from reference 145.

At last, two more dinuclear helicates were achieved by changing the  $\text{PF}_6^-$  counterion for  $\text{I}_3^-$ . In fact, these were synthesised by mean of the failed tries on iodide encapsulation, which is too large to fit on the host cavity provided with the ligand  $\text{H}_2\text{L}$ . The complexes with the formula  $\text{X}@\text{[Fe}_2(\text{H}_2\text{L})_3\text{]}\text{(I}_3\text{)}_3 \cdot 3\text{Et}_2\text{O}$  ( $\text{X}=\text{Cl}, \text{Br}$ ) are found in the [HS-HS] state and any SCO transition was observed. In short, the  $(\text{X}@\text{[Fe}_2(\text{H}_2\text{L})_3\text{]})^{3+}$  is a versatile system which permits to access three possible spin states depending on the chemical nature of the halide, the amount of solvents and the counterion.

The magnetic study in solution of the helical compounds  $(\text{X}@\text{[Fe}_2(\text{H}_2\text{L})_3\text{]})^{3+}$ , labelled as **19** and **20** for  $\text{X}$ : Cl and Br, respectively, is presented in chapter 8.

Because of the encapsulating limitation governed by the respective volumes of the host-guest species, such as  $[\text{Fe}_2(\text{H}_2\text{L})_3]^{4+}$  and the biggest I- halide, ligand  $\text{H}_2\text{L}_2$  with a larger spacer was designed. Among the helicates synthesized with ligand  $\text{H}_2\text{L}_2$ , the unprecedented magnetic behaviour of the supramolecular  $([\text{Cr}(\text{ox})_3]@\text{[Fe}_2(\text{H}_2\text{L}_2)_3\text{]})\text{BF}_4$  assembly stands out.<sup>146</sup> This hybrid system, exhibits the SCO behaviour and LIESST effect of the  $[\text{Fe}_2(\text{H}_2\text{L}_2)_3]^{4+}$  helicate and the induced single-ion magnet (SIM) behaviour when

the  $[\text{Cr}(\text{ox})_3]^{3-}$  guest is encapsulated (Figure 1.10). Interestingly, the SIM behaviour could be attributed to the specific effects caused by the helicate host, since the  $\text{K}_3[\text{Cr}(\text{ox})_3]$  salt does not show any slow relaxation of the magnetization.

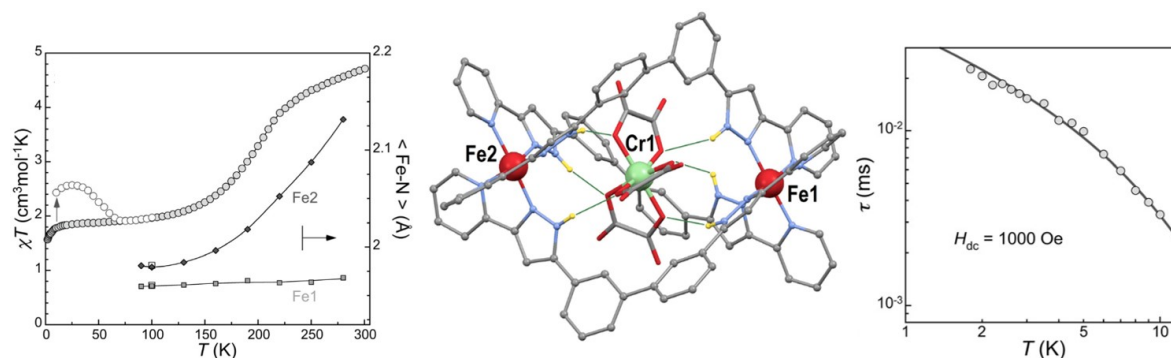


Figure 1.10. (Left): Temperature dependence of  $\chi T$  for  $[[\text{Cr}(\text{ox})_3]@[\text{Fe}_2(\text{H}_2\text{L}_2)_3]]\text{BF}_4$  complex (in full circles) and the average Fe-N bond lengths for both Fe centres (full squares). The empty circles correspond to the LIESST effect. (Middle): Molecular representation of the cationic  $[[\text{Cr}(\text{ox})_3]@[\text{Fe}_2(\text{H}_2\text{L}_2)_3]]^+$ . (Right): Plot of the temperature dependence of the characteristic relaxation time  $\tau$ . Taken from reference 146.

#### 1.4.2.2. Dimerized mononuclear Fe (jellyfish). (Metallosupramolecular hosts)

One of the main advantages of supramolecular chemistry is the ability to explore multiple molecular arrangements by using the same small building blocks. Depending on their molecular recognition and the self-assembly process, a different product may be thermodynamically stabilized. As a result, the metallo-supramolecular structure and the derived magnetic properties and ability to encapsulate guests can be tuned. In this particular case, the combination of  $\text{Fe}^{\text{II}}/\text{H}_2\text{L}/\text{X}^-$  components, which has been shown to yield triple-stranded helicates (above section), drives to the formation of the cationic supramolecular assembly  $(\text{X}@[\text{Fe}(\text{H}_2\text{L})_3]_2)^{3+}$ .<sup>147</sup> Its formation is ruled by the specific manner of introducing the counterion ( $\text{PF}_6^-$ ) into the complex. An aqueous solution of  $\text{NH}_4\text{PF}_6$  is layered with a methanolic solution of  $\text{H}_2\text{L}$  and  $\text{FeX}_2$  in the 3:2 molar ratio (X: Cl, Br). Since the ligand amount exceeds the required for the formation of the dimer, one can deduce that the water plays an essential role by favouring the partial oxidation of  $\text{Fe}(\text{II})$  and, therefore, changing the stoichiometry. In contrast, the dimetallic  $(\text{X}@[\text{Fe}_2(\text{H}_2\text{L})_3])^{3+}$  was obtained in a methanolic solution with the same initial molar ratio (3:2) of L vs  $\text{FeX}_2$  (X: Cl, Br) treated with a methanolic solution of  $\text{NBU}\text{PF}_6$ . Thus, it represents a clear example of structure tuning by changing the reaction conditions.

Like the Fe<sub>2</sub> helicates, these new supramolecular architectures can recognize and encapsulate guests, influencing the SCO process. However, the encapsulation of iodide, which is the bigger halide and was found unable to fit inside the helicate, is now reachable due to the higher flexibility of the assembly. These complexes consist of a dimer of two Fe(II) mononuclear cations forming the supramolecular architecture (X@[Fe(H<sub>2</sub>L)<sub>3</sub>]<sub>2</sub>)<sup>3+</sup> (X<sup>-</sup> = Cl<sup>-</sup>, Br<sup>-</sup>, I<sup>-</sup>) through several intermolecular interactions between the pendant arms (Figure 1.11). Therefore, three bidentate H<sub>2</sub>L ligands coordinate from one site, instead of acting as a bis-chelating ligand, with one Fe(II) centre accomplishing the octahedral geometry. The non-coordinating sites of the six ligands are involved in: i) six N–H···X<sup>-</sup> hydrogen bonds with the halide guests ii) twelve strong hydrogen bonds like N–H···N between pairs of an opposite and equivalent ligand of each mononuclear entity iii) fifteen π-stacking interactions between the five aromatic rings of a ligand with the five ones of a neighbouring ligand laying almost parallel. The overall contribution of all of these interactions probably induces the formation of the dimer complex instead of the helicate.

The influence of the guest on the SCO through bulk magnetic susceptibility measurements unveiled the following sequence on the transition: T<sub>SCO</sub>(I) < T<sub>SCO</sub>(Br) < T<sub>SCO</sub>(Cl). This thermal SCO shift correlates with the intensity decrease of the N–H···N interactions (involving directly N-pyrazole atoms bonded to the metals) when the size of the guest X<sup>-</sup> increases. Since the encapsulated halides establish hydrogen bonds with the non-coordinated N of the pyrazole ring, the contribution for the metal centres is reduced. Furthermore, solution studies give more insights on the dimerized complexes formation through the template effect of the guest X<sup>-</sup>. The size of the I<sup>-</sup> prevents the formation of dimetallic helicates, which were observed in the MS experiments for the Br<sup>-</sup> and Cl<sup>-</sup> guests. This work represents an illustrative case on the importance of the role of guest molecules in the self-assembly of metallo-architectures.

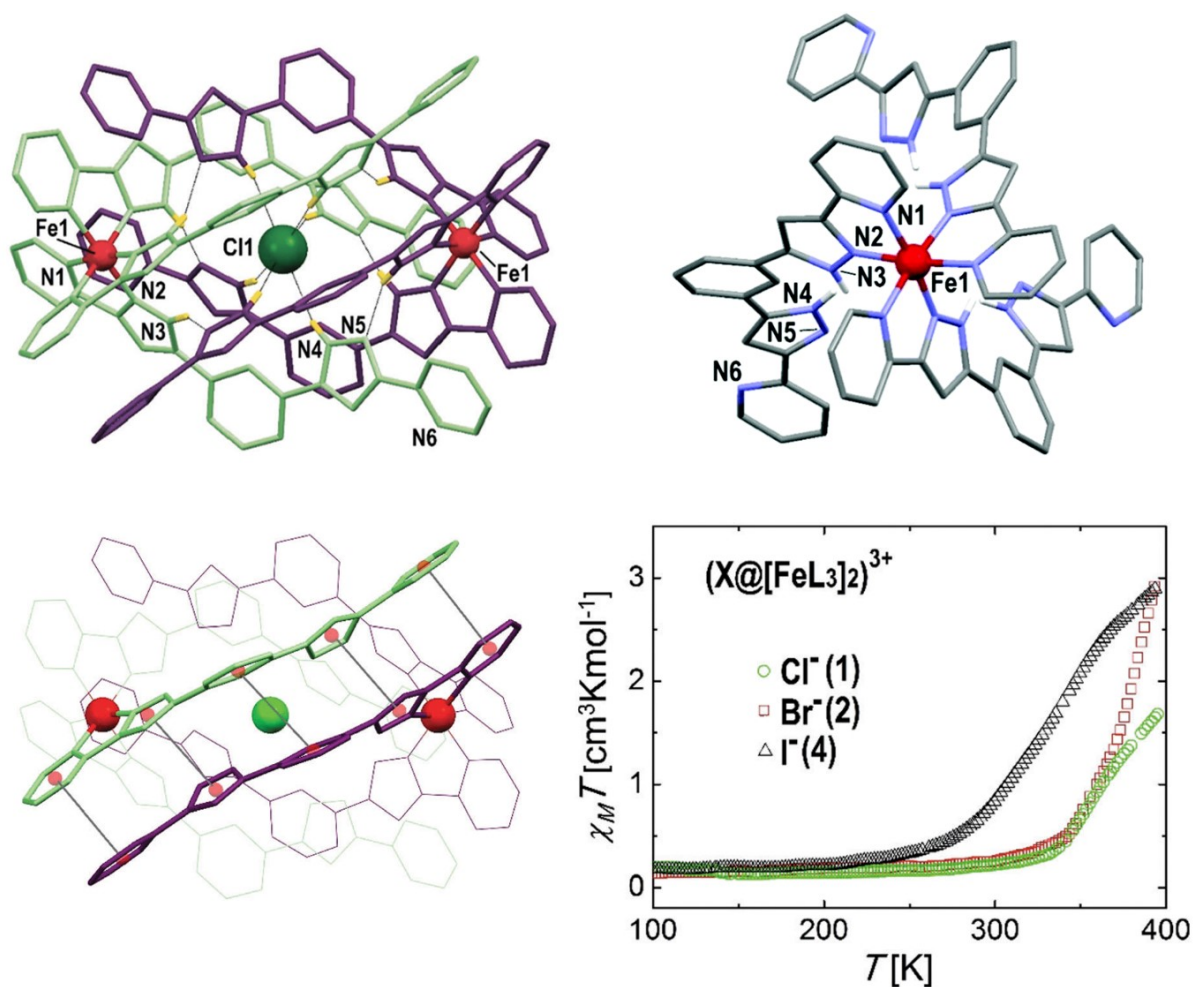


Figure 1.11. (Top left) Molecular representation of the dimerized  $(Cl@[Fe(H_2L)_3]_2)^{3+}$  complex. The ligands of each monomer are differentiated in green and purple. The same supramolecular arrangement is present when  $Br^-$  and  $I^-$  encapsulated. (Top right) Molecular representation of the mononuclear  $[Fe(H_2L)_3]^{2+}$  moiety. (Bottom left) Representation of the  $(Cl@[Fe(H_2L)_3]_2)^{3+}$  assembly, highlighting the  $\pi \cdots \pi$  interactions between one of the pairs of ligands from different monomer entities. (Bottom right) Temperature dependence of the  $\chi_m T$  for all the family of complexes with the formula  $(X@[Fe(H_2L)_3]_2)^{3+}$  ( $X = Cl^-, Br^-, I^-$ ). Taken from reference 147.

#### 1.4.2.3. Grids: Supramolecular and Cluster chemistry.

The study of  $[n \times n]$  grids is of great interest since a higher amount of spin active centres can be arranged within a discrete molecule and thereby used for information storage with high density. Indeed, a controllable spin-state switching in an SCO  $[2 \times 2]$   $Fe^{II}$  grid containing four crystallographically distinct irons was synthesized in Oshio's group. Three combinations of HS/LS-state (from 2HS-2LS to a 4HS) could be reached by selectively switching the iron centres using light irradiation or regulating the temperature.<sup>148</sup> The specific design of the ligand, which contains pyrazolyl-pyridyl moieties, plays a vital role in providing the appropriate electronic structure, hence,



allowing to control the “individual” magnetic components of the ternary data system. Only a few SCO active grids of Fe<sub>4</sub> and Co<sub>4</sub> coordinated with polypyridyl and Schiff-base ligands are reported in the literature.<sup>149–154</sup> However, in a grid-like supramolecular cluster, the metal centres may interact differently depending on the linkage between them. Different magnetic properties, such as single molecular magnetism, could emerge if the spin centres interact electronically more strongly through proper connections between them. A brief introduction of single molecule magnets (SMMs) is given in the following section. Several [*n* × *n*] grid-like clusters containing the same 3d transition metal<sup>155–157</sup> or 4f lanthanide<sup>158–161</sup>; and heterometallic ones by combining different 3d metals<sup>155,162</sup> and 3d-4f metals<sup>162,163</sup> have shown this particular behaviour. The metal ions in these polynuclear clusters are arranged in a controlled manner through a rational ligand design. The convenient and encoded topological and chemical features of the *n*-polytopic ligands ensure the predicted and desired [*n* × *n*] grid-like ensembles. Usually, grids are formed by arrays of ligands arranged in perpendicular directions connected with metal ions located at the intersections provided by the coordination sites. For example, a tritopic ligand with adequate denticity to coordinate the desired metal ions would lead to a [3×3] grid (Figure 1.12).<sup>164</sup>

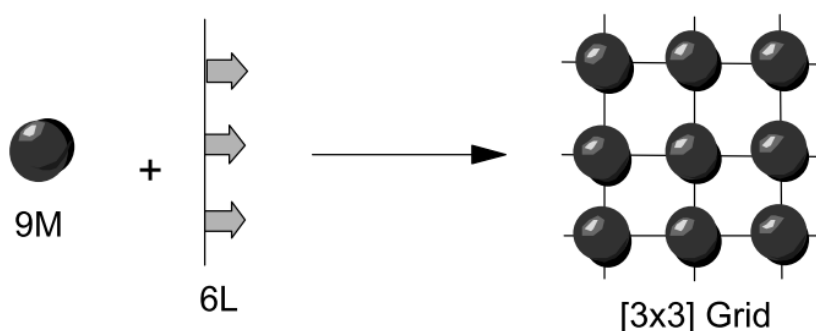


Figure 1.12. Schematic representation of the [3×3] squared grid organization by using a hypothetical tritopic ligand and nine metal ions. Taken from reference 164.

However, the majority of polynuclear systems exhibiting SMM behaviour have been made serendipitously. Usually, such clusters have oxide bridges acting as short connectors between the metal centres, which assists appropriate spin exchange and, in turn, can lead to the SMM behaviour. This is the case of the first SMM complex with the formula [Mn<sub>12</sub>O<sub>12</sub>(O<sub>2</sub>CMe)<sub>16</sub>](H<sub>2</sub>O)<sub>4</sub>, typically known as Mn<sub>12</sub> carboxylate cluster, which is formed by the combination of twelve oxide and acetate bridging ligands.<sup>27</sup> Since then, it

has been the basis for the production of a myriad of such clusters. Among these unpredicted self-assembly products with high nuclearity, iron-containing clusters are of interest in this thesis. Mainly, we focused on polyiron hydroxo(oxo) discrete molecules with brucite-like hydroxides, such as the exemplified structure of  $\text{Mg}(\text{OH})_2$ .<sup>165</sup> These inorganic moieties are formed by the aggregation of iron metal centres linked by oxide and hydroxide ions like in naturally occurring clusters; however, its growth is truncated by primary ligands used in the coordination reaction conditions. In this way, two regions can be distinguished in these structures. An “inner” inorganic region composed of the confined polyiron hydroxo(oxo) core, and the “external” organic region composed of the primary ligand acting as capping ligands. In our case, an unprecedented flat  $[\text{Fe}_9\text{O}_4(\text{OH})_8]$  core has been synthesized thanks to the crucial role as “pincers” of the  $\text{H}_2\text{L}$  ligands. Two  $[\text{Fe}_9]$  girds constituted by such inorganic core and differentiated by the axially coordinated ligands ( $\text{OH}^-$ ,  $\text{H}_2\text{O}$ , or  $\text{Cl}^-$ ) were obtained. Detailed information on this new family of clusters based on polynuclear transition metals is given in chapter 10.

### 1.5. Introduction to Single Molecule Magnets (SMMs)

Isolated molecules retaining all spins parallelly aligned or retaining the magnetization for a given time and below a specific temperature at zero external magnetic field are known as single molecule magnets. As the name indicates, they are magnets at the molecular scale, and in many aspects, they display the typical properties of “classical magnets”. However, additional quantum effects, such as quantum tunnelling of the magnetization, come to rise. The origin of the SMM behaviour relies on an energy barrier ( $U_{\text{eff}}$ ) between the two opposed orientations of the magnetization of the ground spin state, which impedes its spin reversal. The height of the barrier requires conditions in relation to two physical parameters: i) a large total spin state  $S$  in the ground state, ii) strong anisotropy or an easy-axis of the magnetic anisotropy, which is the preferential alignment of the magnetic moment along a specific direction. The expressions of this dependence are:  $U_{\text{eff}} = |D|S^2$  (for integer spins) or  $U_{\text{eff}} = (|D|S^2 - 1/4)$  (for half-integer spins).  $D$  is the axial zero-field splitting (ZFS) parameter associated with the anisotropy of the system. When  $D$  is negative, the energy levels with highest projection of the magnetization on the easy axis ( $M_s = \pm S$ ) are at the ground state, furnishing a double potential well diagram of energy where this doublet lies degenerated in the lowest energy, but separated by the barrier (Figure 1.13). The positive  $M_s$  are depicted in one potential well, and the negative ones

in the other. For this case, the  $U_{\text{eff}}$  is the energy difference between the  $M_S=0$  and  $M_S=\pm S$ .<sup>166-169</sup>

At low temperatures, both fundamental spin states  $M_S=\pm S$  are populated. Once an external magnetic field is applied on the z-axis, the  $M_S$  degeneracy is lost. The corresponding spin projection parallel to the applied field ( $M_S=-S$ ) is stabilized with respect to the one with magnetization against the field ( $M_S=+S$ ). Therefore, just only one  $M_S$  will be populated at low temperature. At this point, the magnetization is saturated, and upon removal of the magnetic field, the trapped system in the minimum potential well wants to return to thermal equilibrium. Fortunately, it has to overcome the energy barrier while reaching the equilibrium and reorientation of the magnetic moment, giving rise to the retention of the magnetization below the blocking temperature ( $K_B T$  smaller than  $U_{\text{eff}}$ ).

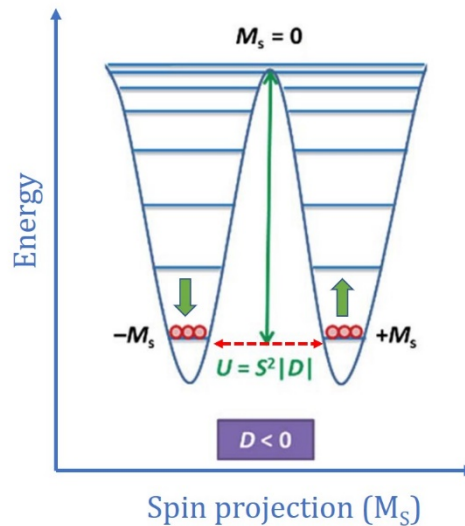


Figure 1.13. Energetic  $M_S$  levels for an SMMs with negative  $D$ .  $U$  represents the energetic barrier for the reversal magnetization. Dashed red line represents the quantum tunneling magnetization (QTM). Figure adapted from reference 168.

As a result of this process, the slow relaxation of the magnetization is the most remarkable feature of SMMs for storing information applications. Fast relaxation must be avoided for such a purpose. The study of the thermal relaxation in SMMs through adjusting the relaxation times as a function of temperature, which usually follows and Arrhenius-like behaviour (Equation 1.16), allows evaluating the energy barrier ( $U_{\text{eff}}$ ).

$$\tau^{-1} = \tau_0^{-1} \exp(-U_{\text{eff}}/K_B T) \quad (1.16)$$

where  $\tau$  is the relaxation rate,  $\tau_0$  is the preexponential factor, and  $k_B$  is the Boltzmann constant. Nevertheless, this situation contemplates a sole thermal process of relaxation, rarely observed in real systems since other factors participate in the relaxation. In the solid-state, we usually think on the study of the properties that arise from the motion of the electrons, from both classical and quantum views, and treat the lattice as a static or rigid with no participation of the bulk system. Instead, the lattice components (i.e. molecules) are not entirely fixed within the periodic lattice. From the mechanical point of view, the phonons are the collective vibrations within the lattice that also interact and contribute to the spin relaxation. Thus, the spin-lattice relaxation assumption completes a set three different mechanisms of magnetic relaxation that affect the relaxation time of the SMM molecules (Figure 1.14):

i) Direct relaxation. The process involves a single lattice phonon emission or absorption with the same quantum magnetic resonance between the  $-M_S$  and  $+M_S$  states. Its relaxation rate is dependent on the temperature ( $T$ ) and the applied magnetic field ( $H$ ) (Equation 1.17):

$$\tau^{-1} = AH^m T \approx AT \quad (1.17)$$

where  $A$  is a constant characteristic value for each system, and the  $m$  value is 2 or 4 for Kramer and no Kramer paramagnetic ion, respectively.

ii) Orbach relaxation. It originates when there is a phonon absorption and subsequent phonon emission (two-phonon process) from an excited state. Ideally, if a sequential spin-phonon transition (multi-phonon process) takes place, overcoming the whole anisotropic barrier ( $U_{\text{eff}}$ ), the relaxation is slower as the barrier is larger, and the SMM is better for storing information. The process shows exponential temperature dependence and follows equation 1.16.

iii) Raman relaxation. The process is similar to Orbach, while the relaxation goes through a virtual excited state. It can be identified by measuring the relaxation as a function of temperature. However, it has a temperature dependence different to that of the Arrhenius mechanism. Instead, the process follows the Power law (Equation 1.18):

$$\tau^{-1} = CT^n \quad (1.18)$$

Where  $C$  is a constant value, and the  $n$  value is 9 or 7 for Kramer and no Kramer paramagnetic ion, respectively. In addition to these temperature-dependent mechanisms, SMMs can exhibit show relaxation by quantum tunnelling of the magnetization (QTM). This process occurs through the ground states without overcoming the energetic barrier ( $U_{\text{eff}}$ ) due to the transversal anisotropy caused by distortions of the axial symmetry of the system. Since QTM-like relaxation is temperature independent (Equation 1.19), it can be easy detectable when plotting the relaxation rate versus temperature ( $\ln \tau$  vs  $1/T$ ):

$$\tau^{-1} = \tau_{QTM}^{-1} \quad (1.19)$$

This relaxation mechanism can also take place between excited sublevels of the same energy, known as relaxation by thermally assisted QTM (TA-QTM). It is also exponentially dependent on the temperature, being thus, indistinguishable from the Orbach process. All mechanisms of relaxation are depicted in Figure 1.14.

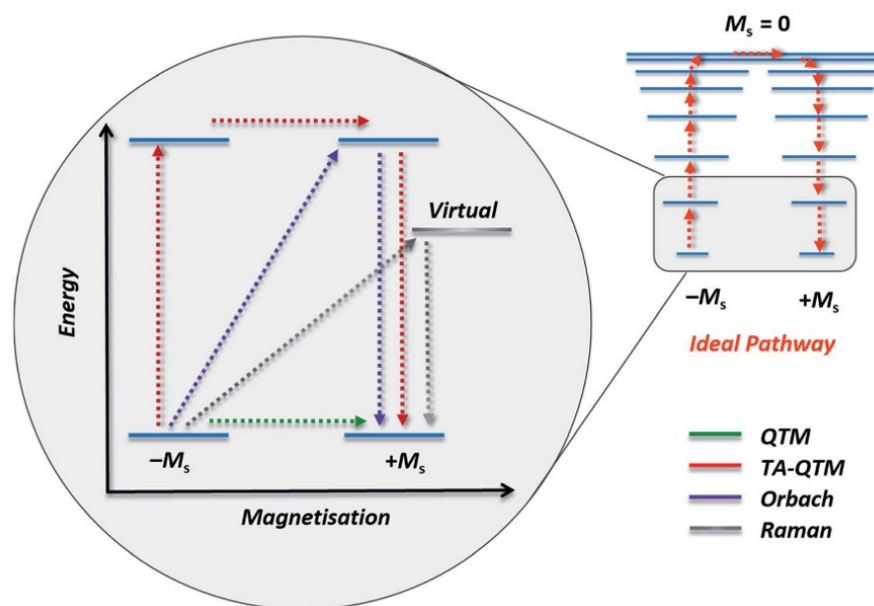


Figure 1.14. Schematic representation of the diverse relaxation processes. Blue lines are the spin levels and the grey represents a virtual state. Taken from reference 168.

### 1.5.1. Detecting SMMs behavior

Evidence of SMM behaviour is the exhibition of hysteresis loops below the blocking temperature ( $T_B$ ). The hysteresis is observable when plotting the magnetization versus the applied magnetic field (Figure 1.15A), and  $T_B$  is the maximum temperature that defines the functionality of the SMM.<sup>27,170,171</sup> However, the  $U_{\text{eff}}$  also serves as a criterion to characterize a SMM. From a practical viewpoint, the use of  $U_{\text{eff}}$  is more widespread and is determined through measurement of magnetic susceptibility out-of-phase ( $\chi_M''$ ) as a function of the temperature (Figure 1.15B).<sup>171,172</sup> Indeed, this is a way of studying the dynamic magnetic properties of the sample. This study consists of applying an alternating-current (AC) oscillating at particular frequencies ( $\nu$ ) and temperatures. If the spins cannot follow the changing direction of the oscillating magnetic field, the reallocation of spins over the spin levels follows a relaxation process characterized by a relaxation time  $\tau$ . (All mechanisms of relaxation and their relative  $\tau$  equations are described in the previous section). Treating the AC data with the Debye model provides a relationship between the angular frequency  $\omega$  ( $=2\pi\nu$ ,  $\nu$  is the frequency of the ac oscillating field) and the relaxation time  $\tau$ .<sup>166</sup>

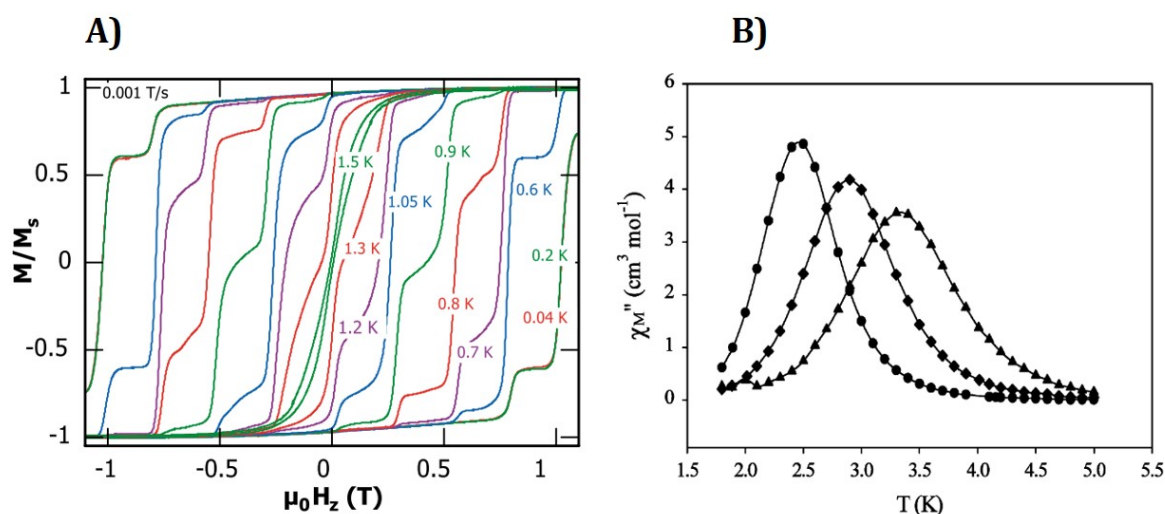


Figure 1.15. (A, left) Hysteresis measurement as function of magnetic field. (B, right) out-of-phase magnetic susceptibility as function of temperature for an SMM molecules. Taken from reference 171.

At low frequency ( $\omega\tau \ll 1$ ), the isothermal susceptibility ( $\chi_T$ ) is measured. In this frequency regime, the magnetic moments can exchange energy with the lattice, and the thermal equilibria of the system is observed. At high frequency ( $\omega\tau \gg 1$ ), the adiabatic susceptibility ( $\chi_s$ ) is measured, and the magnetic moments of the system can not respond

or exchange energy with the lattice since the field oscillates too fast. At intermediate frequency ( $\omega\tau \approx 1$ ), the frequency oscillation is comparable to the timescale of the magnetic relaxation. The measured susceptibility at his frequency regime follows equation 1.20. The susceptibility is made of two components: the in-phase (real) and the out-of-phase (imaginary) component, with the expression 1.21 and 1.22, respectively. A maximum on the  $\chi''$  and a concomitant decrease of  $\chi'$  are the characteristic fingerprints of the slow relaxation of the magnetization of a SMM. <sup>166,173</sup>

$$\chi(\omega) = \chi_s + \frac{\chi_T - \chi_s}{1 + i\omega\tau} \quad (1.20)$$

$$\chi'(\omega) = \frac{\chi_T - \chi_s}{1 + \omega^2\tau^2} + \chi_s \quad (1.21)$$

$$\chi''(\omega) = \frac{\omega\tau(\chi_T - \chi_s)}{1 + \omega^2\tau^2} \quad (1.22)$$

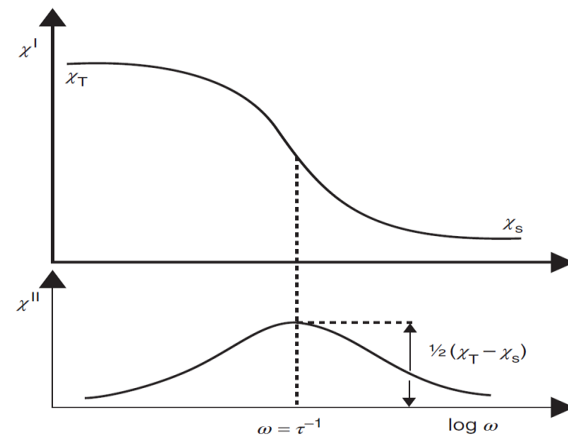


Figure 1.16. (Left) Formulae for the AC magnetic susceptibility. (Right) Schematic representation of the frequency dependence of  $\chi'$  and  $\chi''$ . The high and low limits of the  $\chi'$  correspond to the adiabatic and thermal susceptibility, respectively. Taken from reference 166.





## 1.6. Objectives and Scope of the Thesis

The aim of this thesis mainly deals with the synthesis and study of several magnetic compounds exhibiting Spin Crossover or SMM properties.

In the first stage, the ligand design and synthesis of different bis-pyrazolyl-pyridine (bpp) derivatives which are tridentate ligands were set out for accessing mononuclear Fe(II) compounds. This type of tris-imine-like ligands potentially produce SCO-active compounds with dense networks of intermolecular interactions. The series of new SCO compounds offers a valuable opportunity for the analysis and understanding of specific insights related to the behaviour in terms of:

- SCO transition tuning by ligand design (chapter 2).
- Study of the cooperative effects (chapter 3).
- Polymorphism and study of the intimate relation between the crystallographic and magnetic data over a succession of solid-state transformations (Chapter 4).

The following chapters are focused on the synthesis and study of supramolecular architectures. Firstly, we designed the appropriate polytopic ligands containing pyrazolyl-pyridine chelating units separated by a suitable aromatic spacer (Chapter 5).

The coordination of the ditopic ligand, H<sub>2</sub>L, with cobalt (II) ions allows to introduce the single-molecule magnet (SMM) behaviour and rationalize this response in relation with the ion geometry (Chapter 6).

The coordination chemistry exploration of the ligand H<sub>2</sub>L<sub>2</sub> with different sources of Fe(II) and conditions allow the discovery of new supramolecular cluster containing an almost flat grid of nine irons (Chapter 7).

The stability of SCO Fe(II) dinuclear helicates in solution, allow their characterization by using paramagnetic NMR. Additionally, the judicious ligand design H<sub>2</sub>L<sub>5</sub> allows the obtention of pure dimerized supramolecular architectures of iron (Chapter 8).

## 1.7. References

- (1) Feynman, R. P. *Eng. Sci.* **1960**, *23*, 22–36.
- (2) Balzani, V.; Credi, A.; Venturi, M. *Chem. - A Eur. J.* **2002**, *8*, 5524–5532.
- (3) Ferrando-Soria, J.; Vallejo, J.; Castellano, M.; Martínez-Lillo, J.; Pardo, E.; Cano, J.; Castro, I.; Lloret, F.; Ruiz-García, R.; Julve, M. *Coord. Chem. Rev.* **2017**, *339*, 17–103.
- (4) Aguilà, D.; Prado, Y.; Koumoussi, E. S.; Mathonière, C.; Clérac, R. *Chem. Soc. Rev.* **2016**, *45*, 203–224.
- (5) Shao, D.; Shi, L.; Yin, L.; Wang, B.; Wang, Z.; Zhang, Y.; Wang, X. *Chem. Sci.* **2018**, *9*, 7986–7991.
- (6) Rostamzadeh Renani, F.; Kirczenow, G. *Phys. Rev. B* **2013**, *87*, 121403.
- (7) Meng, Y. S.; Liu, T. *Acc. Chem. Res.* **2019**, *52*, 1369–1379.
- (8) Sato, O. *Proc. Jpn. Acad., Ser. B* **2012**, *88*, 213–225.
- (9) Yao, Z. S.; Tang, Z.; Tao, J. *Chem. Commun.* **2020**, *56*, 2071–2086.
- (10) Hayami, S.; Holmes, S. M.; Halcrow, M. A. *J. Mater. Chem. C* **2015**, *3*, 7775–7778.
- (11) Létard, J.-F.; Guionneau, P.; Goux-Capes, L. In *Spin Crossover in Transition Metal Compounds III*; 2006; Vol. 1, pp 221–249.
- (12) Raymo, F. M. *Adv. Mater.* **2002**, *14*, 401–414.
- (13) Kahn, O.; Jay Martinez, C. *Science*. **1998**, *279*, 44–48.
- (14) Ridier, K.; Molnár, G.; Salmon, L.; Nicolazzi, W.; Bousseksou, A. *Solid State Sci.* **2017**, *74*, A1–A22.
- (15) Renz, F.; de Souza, P. A.; Klingelhöfer, G.; Goodwin, H. A. *Hyperfine Interact.* **2002**, *139/140*, 699–704.
- (16) Costa, J. S.; Rodríguez-Jiménez, S.; Craig, G. A.; Barth, B.; Beavers, C. M.; Teat, S. J.; Aromí, G. *J. Am. Chem. Soc.* **2014**, *136*, 3869–3874.
- (17) Zuluaga, A. R.; Brock, A. J.; Pfrunder, M. C.; Phonsri, W.; Murray, K. S.; Harding, P.; Micallef, A. S.; Mullen, K. M.; Clegg, J. K.; Harding, D. J.; McMurtrie, J. C. *Chem. Mater.* **2020**, *32*, 10076–10083.
- (18) Woodruff, D. N.; Winpenny, R. E. P.; Layfield, R. A. *Chem. Rev.* **2013**, *113*, 5110–5148.
- (19) Aromí, G.; Brechin, E. K. In *Single-molecule magnets and related phenomena*; Winpenny, R. E. P., Ed.; Springer Berlin Heidelberg, 2006; Vol. 122, pp 1–67.
- (20) Timco, G. A.; Faust, T. B.; Tuna, F.; Winpenny, R. E. P. *Chem. Soc. Rev.* **2011**, *40*, 3067–3075.

- (21) Affronte, M.; Carretta, S.; Timco, G. A.; Winpenny, R. E. P. *Chem. Commun.* **2007**, 1789–1797.
- (22) Bogani, L.; Wernsdorfer, W. *Nat. Mater.* **2008**, 7, 179–186.
- (23) Guo, F. S.; Day, B. M.; Chen, Y. C.; Tong, M. L.; Mansikkamäki, A.; Layfield, R. A. *Angew. Chemie - Int. Ed.* **2017**, 56, 11445–11449.
- (24) Goodwin, C. A. P.; Ortu, F.; Reta, D.; Chilton, N. F.; Mills, D. P. *Nature.* **2017**, 548, 439–442.
- (25) Brooker, S.; Kitchen, J. A. *Dalt. Trans.* **2009**, 7331–7340.
- (26) Cambi, L.; Szegö, L. *Ber. Dtsch. Chem. Ges. A/B.* **1931**, 64, 2591–2598.
- (27) Sessoli, R.; Gatteschi, D.; Caneschi, A.; Novak, M. A. *Nature* **1993**, 365, 141–143.
- (28) Heras Ojea, M. J.; Van Raden, J. M.; Louie, S.; Collins, R.; Pividori, D.; Cirera, J.; Meyer, K.; Jasti, R.; Layfield, R. A. *Angew. Chemie - Int. Ed.* **2021**, 60, 3515–3518.
- (29) Piquer, L. R.; Sánchez, R. R.; Sañudo, E. C.; Echeverría, J. *Molecules* **2018**, 23, 1411.
- (30) Rosado Piquer, L.; Jiménez Romero, E.; Lan, Y.; Wernsdorfer, W.; Aromí, G.; Sañudo, E. C. *Inorg. Chem. Front.* **2017**, 4, 595–603.
- (31) Zoppellaro, G.; Tuček, J.; Herchel, R.; Šafařová, K.; Zbořil, R. *Inorg. Chem.* **2013**, 52, 8144–8150.
- (32) Shi, S.; Schmerber, G.; Arabski, J.; Beaufrand, J. B.; Kim, D. J.; Boukari, S.; Bowen, M.; Kemp, N. T.; Viart, N.; Rogez, G.; Beaurepaire, E.; Aubriet, H.; Petersen, J.; Becker, C.; Ruch, D. *Appl. Phys. Lett.* **2009**, 95, 2–5.
- (33) Clemente-leo, M.; Coronado, E.; Mingotaud, C.; Delhae, P. *Angew. Chem., Int. Ed.* **1998**, 37, 2842–2845.
- (34) Sundaresan, S.; Kitchen, J. A.; Brooker, S. *Inorg. Chem. Front.* **2020**, 7, 2050–2059.
- (35) Kumar, K. S.; Ruben, M. *Angew. Chemie - Int. Ed.* **2021**, 60, 7502–7521.
- (36) Mannini, M.; Pineider, F.; Sainctavit, P.; Danieli, C.; Otero, E.; Sciancalepore, C.; Talarico, A. M.; Arrio, M. A.; Cornia, A.; Gatteschi, D.; Sessoli, R. *Nat. Mater.* **2009**, 8, 194–197.
- (37) Brandl, T.; Johannsen, S.; Häussinger, D.; Suryadevara, N.; Prescimone, A.; Bernhard, S.; Gruber, M.; Ruben, M.; Berndt, R.; Mayor, M. *Angew. Chemie - Int. Ed.* **2020**, 59, 15947–15952.
- (38) Jasper-Tönnies, T.; Gruber, M.; Karan, S.; Jacob, H.; Tuczek, F.; Berndt, R. *J. Phys. Chem. Lett.* **2017**, 8, 1569–1573.
- (39) Gütlich, P.; Goodwin, H. A. In *Spin Crossover in Transition Metal Compounds*

- I, Topics in Current Chemistry*; Gütlich, P., Goodwin, H. A., Eds.; Springer, 2004; Vol. 233, pp 1–47.
- (40) Hauser, A. In *Spin Crossover in Transition Metal Compounds I, Topics in Current Chemistry*; Gütlich, P., Goodwin, H. A., Eds.; Springer, 2004; Vol. 233, pp 49–58.
- (41) Gütlich, P.; Garcia, Y.; Goodwin, H. A. *Chem. Soc. Rev.* **2000**, 29, 419–427.
- (42) Gütlich, P.; Hauser, A.; Spiering, H. *Angew. Chemie - Int. Ed.* **1994**, 33, 2024–2054.
- (43) Gütlich, P.; Gaspar, A. B.; Garcia, Y. *Beilstein J. Org. Chem.* **2013**, 9, 342–391.
- (44) Tanabe, Y.; Sugano, S. *J. Phys. Soc. Jpn.* **1954**, 9, 766–779.
- (45) Halcrow, M. A. *Chem. Lett.* **2014**, 43, 1178–1188.
- (46) Nicolazzi, W.; Bousseksou, A. *C. R. Chim.* **2018**, 21, 1060–1074.
- (47) Fagaly, R. L. *Rev. Sci. Instrum.* **2006**, 77, 101101.
- (48) Kahn, O. *Molecular Magnetism.*; VCH Publisher Inc.: New York, 1993.
- (49) Gispert, J. R. *Coordination Chemistry*; Wiley-VCH, Ed.; Weinheim, 2008.
- (50) Bain, G. A.; Berry, J. F. *J. Chem. Educ.* **2008**, 85, 532.
- (51) Shores, M. P.; Klug, C. M.; Fiedler, S. R. In *Spin-Crossover Materials*; Halcrow, M. A., Ed.; John Wiley & Sons Ltd: Oxford, UK, 2013; pp 281–301.
- (52) Halcrow, M. A.; Capel Berdiell, I.; Pask, C. M.; Kulmaczewski, R. *Inorg. Chem.* **2019**, 58, 9811–9821.
- (53) Rodríguez-Jiménez, S.; Yang, M.; Stewart, I.; Garden, A. L.; Brooker, S. *J. Am. Chem. Soc.* **2017**, 139, 18392–18396.
- (54) Barrett, S. A.; Halcrow, M. A. *RSC Adv.* **2014**, 4, 11240–11243.
- (55) Evans, D. F. *J. Chem. Soc.* **1959**, 2003–2005.
- (56) Sur, S. K. *J. Magn. Reson.* **1989**, 82, 169–173.
- (57) Schubert, E. M. *J. Chem. Educ.* **1992**, 69, 62.
- (58) Turner, J. W.; Schultz, F. A. *Inorg. Chem.* **2001**, 40, 5296–5298.
- (59) Piguet, C. *J. Chem. Educ.* **1997**, 74, 815.
- (60) Slichter, C. P.; Drickamer, H. G. *J. Chem. Phys.* **1972**, 56, 2142–2160.
- (61) Kershaw Cook, L. J.; Kulmaczewski, R.; Mohammed, R.; Dudley, S.; Barrett, S. A.; Little, M. A.; Deeth, R. J.; Halcrow, M. A. *Angew. Chem., Int. Ed.* **2016**, 55, 4327–4331.
- (62) Yatsunyk, L. A.; Walker, F. A. *Inorg. Chem.* **2004**, 43, 757–777.
- (63) Weber, B. *Coord. Chem. Rev.* **2009**, 253, 2432–2449.
- (64) Weber, B.; Walker, F. A. *Inorg. Chem.* **2007**, 46, 6794–6803.

- (65) Pavlov, A. A.; Denisov, G. L.; Kiskin, M. A.; Nelyubina, Y. V.; Novikov, V. V. *Inorg. Chem.* **2017**, *56*, 14759–14762.
- (66) Guionneau, P.; Marchivie, M.; Bravic, G.; Létard, J. F.; Chasseau, D. In *Spin Crossover in Transition Metal Compounds II, Topics in Current Chemistry*; Gütllich, P., Goodwin, H. A., Eds.; Springer, 2004; Vol. 234, pp 97–128.
- (67) Halcrow, M. A. *Chem. Soc. Rev.* **2011**, *40*, 4119–4142.
- (68) Money, V. a; Evans, R.; Halcrow, M. a; Goeta, E.; Howard, a K. *Chem Com* **2003**, 158–159.
- (69) Kershaw Cook, L. J.; Mohammed, R.; Sherborne, G.; Roberts, T. D.; Alvarez, S.; Halcrow, M. A. *Coord. Chem. Rev.* **2015**, *289–290*, 2–12.
- (70) Marchivie, M.; Guionneau, P.; Létard, J. F.; Chasseau, D. *Acta Crystallogr. Sect. B Struct. Sci.* **2003**, *59*, 479–486.
- (71) McCusker, J. K.; Rheingold, A. L.; Hendrickson, D. N. *Inorg. Chem.* **1996**, *35*, 2100–2112.
- (72) Drew, M. G. B.; Harding, C. J.; McKee, V.; Morgan, G. G.; Nelson, J. *J. Chem. Soc., Chem. Commun.* **1995**, 1035–1038.
- (73) Dolomanov, O. V.; Bourhis, L. J.; Gildea, R. J.; Howard, J. A. K.; Puschmann, H. *J. Appl. Crystallogr.* **2009**, *42*, 339–341.
- (74) Ketkaew, R.; Tantirungrotechai, Y.; Harding, P.; Guionneau, P.; Marchivie, M.; Harding, D. J. *Dalt. Trans.* **2021**, *50*, 1086–1096.
- (75) Tao, J.; Wei, R. J.; Huang, R. Bin; Zheng, L. S. *Chem. Soc. Rev.* **2012**, *41*, 703–737.
- (76) Guionneau, P. *Dalt. Trans.* **2014**, *43*, 382–393.
- (77) Boillot, M. L.; Weber, B. C. *R. Chim.* **2018**, *21*, 1196–1208.
- (78) Olguín, J.; Brooker, S. *Coord. Chem. Rev.* **2011**, *255*, 203–240.
- (79) Halcrow, M. A. *Dalt. Trans.* **2009**, 2059–2073.
- (80) Halcrow, M. A. *New J. Chem.* **2014**, *38*, 1868–1882.
- (81) Goodwin, H. A.; Sugiyarto, K. H. *Chem. Phys. Lett.* **1987**, *139*, 470–474.
- (82) Sugiyarto, K. H.; Goodwin, H. A. *Aust. J. Chem.* **1988**, *41*, 1645–1663.
- (83) Sugiyarto, K.; Craig, D.; Rae, A.; Goodwin, H. *Aust. J. Chem.* **1994**, *47*, 869–890.
- (84) Buchen, T.; Gütllich, P.; Sugiyarto, K. H.; Goodwin, H. A. *Chem. - Eur. J.* **1996**, *2*, 1134–1138.
- (85) Scudder, M. L.; Craig, D. C.; Goodwin, H. A. *CrystEngComm.* **2005**, *7*, 642–649.
- (86) Barrett, S. A.; Kilner, C. A.; Halcrow, M. A. *Dalt. Trans.* **2011**, *40*, 12021–12024.

- (87) Craig, G. A.; Roubeau, O.; Aromí, G. *Coord. Chem. Rev.* **2014**, *269*, 13–31.
- (88) King, P.; Henkelis, J. J.; Kilner, C. A.; Halcrow, M. A. *Polyhedron* **2013**, *52*, 1449–1456.
- (89) Roberts, T. D.; Little, M. A.; Kershaw Cook, L. J.; Halcrow, M. A. *Dalt. Trans.* **2014**, *43*, 7577–7588.
- (90) Craig, G. A.; Costa, J. S.; Roubeau, O.; Teat, S. J.; Aromí, G. *Chem. - A Eur. J.* **2012**, *18*, 11703–11715.
- (91) Roberts, T. D.; Little, M. A.; Kershaw Cook, L. J.; Barrett, S. A.; Tuna, F.; Halcrow, M. A. *Polyhedron* **2013**, *64*, 4–12.
- (92) Craig, G. A.; Costa, J. S.; Roubeau, O.; Teat, S. J.; Aromí, G. *Eur. J. Inorg. Chem.* **2013**, 745–752.
- (93) Cook, B. J.; Chen, C. H.; Pink, M.; Lord, R. L.; Caulton, K. G. *Inorganica Chim. Acta* **2016**, *451*, 82–91.
- (94) Djemel, A.; Stefanczyk, O.; Marchivie, M.; Trzop, E.; Collet, E.; Desplanches, C.; Delimi, R.; Chastanet, G. *Chem. - A Eur. J.* **2018**, *24*, 14760–14767.
- (95) Pavlov, A. A.; Aleshin, D. Y.; Nikovskiy, I. A.; Polezhaev, A. V.; Efimov, N. N.; Korlyukov, A. A.; Novikov, V. V.; Nelyubina, Y. V. *Eur. J. Inorg. Chem.* **2019**, 2819–2829.
- (96) Nikovskiy, I.; Polezhaev, A.; Novikov, V.; Aleshin, D.; Pavlov, A.; Saffiulina, E.; Aysin, R.; Dorovatovskii, P.; Nodaraki, L.; Tuna, F.; Nelyubina, Y. *Chem. - A Eur. J.* **2020**, *26*, 5629–5638.
- (97) Barrios, L. A.; Bartual-Murgui, C.; Peyrecave-Lleixà, E.; Le Guennic, B.; Teat, S. J.; Roubeau, O.; Aromí, G. *Inorg. Chem.* **2016**, *55*, 4110–4116.
- (98) Holland, J. M.; McAllister, J. A.; Lu, Z.; Kilner, C. A.; Thornton-Pett, M.; Halcrow, M. A. *Chem. Commun.* **2001**, 577–578.
- (99) Holland, J. M.; Barrett, S. A.; Kilner, C. A.; Halcrow, M. A. *Inorg. Chem. Commun.* **2002**, *5*, 328–332.
- (100) Holland, J. M.; McAllister, J. A.; Kilner, C. A.; Thornton-Pett, M.; Bridgeman, A. J.; Halcrow, M. A. *J. Chem. Soc., Dalt. Trans.* **2002**, 548–554.
- (101) Money, V. A.; Evans, I. R.; Halcrow, M. A.; Goeta, A. E.; Howard, J. A. K. *Chem. Commun.* **2003**, 158–159.
- (102) Elhaïk, J.; Evans, D. J.; Kilner, C. A.; Halcrow, M. A. *Dalt. Trans.* **2005**, 1693–1700.
- (103) Elhaïk, J.; Kilner, C. A.; Halcrow, M. A. *Dalt. Trans.* **2006**, *5*, 823–830.

- (104) Carbonera, C.; Kilner, C. A.; Létard, J. F.; Halcrow, M. A. *J. Chem. Soc. Dalt. Trans.* **2007**, 1284–1292.
- (105) Halcrow, M. A. *Coord. Chem. Rev.* **2009**, *253*, 2493–2514.
- (106) Hasegawa, Y.; Sakamoto, R.; Takahashi, K.; Nishihara, H. *Inorg. Chem.* **2013**, *52*, 1658–1665.
- (107) Vela, S.; Novoa, J. J.; Ribas-Arino, J. *Phys. Chem. Chem. Phys.* **2014**, *16*, 27012–27024.
- (108) Cook, L.; Halcrow, M. *Magnetochemistry* **2015**, *1*, 3–16.
- (109) Cook, L. J. K.; Shepherd, H. J.; Comyn, T. P.; Baldé, C.; Cespedes, O.; Chastanet, G.; Halcrow, M. A. *Chem. - A Eur. J.* **2015**, *21*, 4805–4816.
- (110) Fumanal, M.; Jiménez-Grávalos, F.; Ribas-Arino, J.; Vela, S. *Inorg. Chem.* **2017**, *56*, 4474–4483.
- (111) Halcrow, M. A.; Chastanet, G. *Polyhedron* **2017**, *136*, 5–12.
- (112) Kumar, K. S.; Šalitroš, I.; Moreno-Pineda, E.; Ruben, M. *Dalt. Trans.* **2017**, *46*, 9765–9768.
- (113) Bridonneau, N.; Rigamonti, L.; Poneti, G.; Pinkowicz, D.; Forni, A.; Cornia, A. *Dalt. Trans.* **2017**, *46*, 4075–4085.
- (114) García-López, V.; Palacios-Corella, M.; Gironés-Pérez, V.; Bartual-Murgui, C.; Real, J. A.; Pellegrin, E.; Herrero-Martín, J.; Aromí, G.; Clemente-León, M.; Coronado, E. *Inorg. Chem.* **2019**, *58*, 12199–12208.
- (115) Senthil Kumar, K.; Del Giudice, N.; Heinrich, B.; Douce, L.; Ruben, M. *Dalt. Trans.* **2020**, *49*, 14258–14267.
- (116) Kulmaczewski, R.; Bamiduro, F.; Shahid, N.; Cespedes, O.; Halcrow, M. A. *Chem. - A Eur. J.* **2021**, *27*, 2082–2092.
- (117) Kulmaczewski, R.; Howard, M. J.; Halcrow, M. A. *Dalt. Trans.* **2021**, *50*, 3464–3467.
- (118) Gamez, P.; Costa, J. S.; Quesada, M.; Aromí, G. *Dalt. Trans.* **2009**, 7845–7853.
- (119) Craig, G. A.; Sánchez Costa, J.; Roubeau, O.; Teat, S. J.; Aromí, G. *Chem. - A Eur. J.* **2011**, *17*, 3120–3127.
- (120) Craig, G. A.; Costa, J. S.; Teat, S. J.; Roubeau, O.; Yufit, D. S.; Howard, J. A. K.; Aromí, G. *Inorg. Chem.* **2013**, *52*, 7203–7209.
- (121) Barrios, L. A.; Peyrecave-Lleixà, E.; Craig, G. A.; Roubeau, O.; Teat, S. J.; Aromí, G. *Eur. J. Inorg. Chem.* **2014**, *2014*, 6013–6021.
- (122) Craig, G. A.; Costa, J. S.; Roubeau, O.; Teat, S. J.; Shepherd, H. J.; Lopes, M.; Molnár,

- G.; Bousseksou, A.; Aromí, G. *Dalt. Trans.* **2014**, *43*, 729–737.
- (123) Bartual-Murgui, C.; Vela, S.; Roubeau, O.; Aromí, G. *Dalt. Trans.* **2016**, *45*, 14058–14062.
- (124) Bartual-Murgui, C.; Codina, C.; Roubeau, O.; Aromí, G. *Chem. Eur. J.* **2016**, *22*, 12767–12776.
- (125) Aromí, G.; Beavers, C. M.; Sánchez Costa, J.; Craig, G. A.; Mínguez Espallargas, G.; Orera, A.; Roubeau, O. *Chem. Sci.* **2016**, *7*, 2907–2915.
- (126) Bartual-Murgui, C.; Pérez-Padilla, C.; Teat, S. J.; Roubeau, O.; Aromí, G. *Inorg. Chem.* **2020**, *59*, 12132–12142.
- (127) Costa, J. S.; Rodríguez-Jiménez, S.; Craig, G. A.; Barth, B.; Beavers, C. M.; Teat, S. J.; Gagnon, K. J.; Barrios, L. A.; Roubeau, O.; Aromí, G. *Inorg. Chem. Front.* **2020**, 3165–3175.
- (128) Tidmarsh, I. S.; Taylor, B. F.; Hardie, M. J.; Russo, L.; Clegg, W.; Ward, M. D. *New J. Chem.* **2009**, *33*, 366–375.
- (129) Hall, B. R.; Manck, L. E.; Tidmarsh, I. S.; Stephenson, A.; Taylor, B. F.; Blaikie, E. J.; Vander Gridend, D. A.; Ward, M. D. *Dalt. Trans.* **2011**, *40*, 12132–12145.
- (130) Argent, S. P.; Adams, H.; Riis-Johannessen, T.; Jeffery, J. C.; Harding, L. P.; Clegg, W.; Harrington, R. W.; Ward, M. D. *J. Chem. Soc. Dalt. Trans.* **2006**, 4996–5013.
- (131) Najar, A. M.; Tidmarsh, I. S.; Adams, H.; Ward, M. D. *Inorg. Chem.* **2009**, *48*, 11871–11881.
- (132) Tidmarsh, I. S.; Faust, T. B.; Adams, H.; Harding, L. P.; Russo, L.; Clegg, W.; Ward, M. D. *J. Am. Chem. Soc.* **2008**, *130*, 15167–15175.
- (133) Champness, N. R. *Dalt. Trans.* **2011**, *40*, 10311–10315.
- (134) Stephenson, A.; Ward, M. D. *RSC Adv.* **2012**, *2*, 10844–10853.
- (135) Li, F.; Clegg, J. K.; Goux-Capes, L.; Chastanet, G.; D'Alessandro, D. M.; Létard, J. F.; Kepert, C. J. *Angew. Chemie - Int. Ed.* **2011**, *50*, 2820–2823.
- (136) Stephenson, A.; Sykes, D.; Ward, M. D. *Dalt. Trans.* **2013**, *42*, 6756–6767.
- (137) Li, F.; Clegg, J. K.; Price, D.; Kepert, C. J. *Inorg. Chem.* **2011**, *50*, 726–728.
- (138) Newton, G. N.; Onuki, T.; Shiga, T.; Noguchi, M.; Matsumoto, T.; Mathieson, J. S.; Nihei, M.; Nakano, M.; Cronin, L.; Oshio, H. *Angew. Chem., Int. Ed.* **2011**, *50*, 4844–4848.
- (139) Oshio, H.; Matsumoto, T.; Shiga, T.; Newton, G. N.; Sato, H.; Noguchi, M. *Dalt. Trans.* **2013**, *42*, 16185.



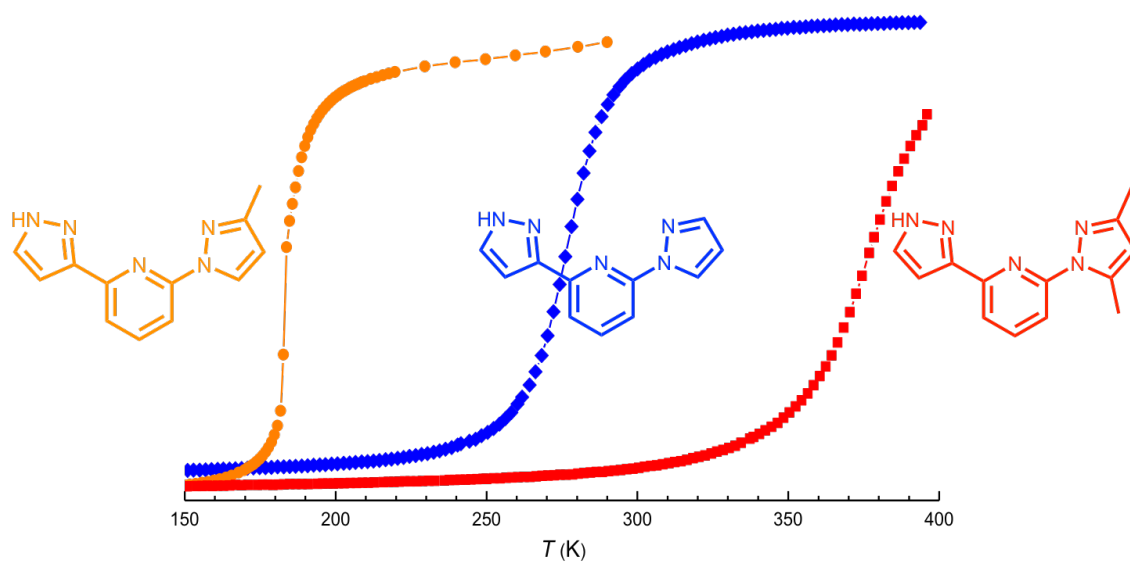
- (140) Sato, H.; Miya, L.; Mitsumoto, K.; Matsumoto, T.; Shiga, T.; Newton, G. N.; Oshio, H. *Inorg. Chem.* **2013**, *52*, 9714–9716.
- (141) Sato, H.; Yamaguchi, M.; Onuki, T.; Noguchi, M.; Newton, G. N.; Shiga, T.; Oshio, H. *Eur. J. Inorg. Chem.* **2015**, *2015*, 2193–2198.
- (142) De, A.; Mondal, R. *ACS Omega* **2018**, *3*, 6022–6030.
- (143) Bala, S.; Mondal, I.; Goswami, A.; Pal, U.; Mondal, R. *Dalt. Trans.* **2014**, *43*, 15704–15707.
- (144) Olguín, J.; Brooker, S. In *Spin-Crossover Materials: Properties and Applications*; Halcrow, M. A., Ed.; John Wiley & Sons, 2013; pp 77–120.
- (145) Darawsheh, M.; Barrios, L. A.; Roubeau, O.; Teat, S. J.; Aromí, G. *Chem. - A Eur. J.* **2016**, *22*, 8635–8645.
- (146) Aromi, G.; Darawsheh, M.; Barrios, L. A.; Roubeau, O.; Teat, S. J. *Angew. Chemie Int. Ed.* **2018**, *57*, 13509–13513.
- (147) Darawsheh, M. D.; Barrios, L. A.; Roubeau, O.; Teat, S. J.; Aromí, G. *Chem. Commun.* **2017**, *53*, 569–572.
- (148) Matsumoto, T.; Newton, G. N.; Shiga, T.; Hayami, S.; Matsui, Y.; Okamoto, H.; Kumai, R.; Murakami, Y.; Oshio, H. *Nat. Commun.* **2014**, *5*, 1–8.
- (149) Breuning, E.; Ruben, M.; Lehn, J. M.; Renz, F.; Garcia, Y.; Ksenofontov, V.; Gütlich, P.; Wegelius, E.; Rissanen, K. *Angew. Chem. Int. Ed. Engl.* **2000**, *39*, 2504–2507.
- (150) Schneider, B.; Demeshko, S.; Dechert, S.; Meyer, F. *Angew. Chemie - Int. Ed.* **2010**, *49*, 9274–9277.
- (151) Steinert, M.; Schneider, B.; Dechert, S.; Demeshko, S.; Meyer, F. *Inorg. Chem.* **2016**, *55*, 2363–2373.
- (152) Steinert, M.; Schneider, B.; Dechert, S.; Demeshko, S.; Meyer, F. *Angew. Chem., Int. Ed.* **2014**, *53*, 6135–6139.
- (153) Wang, Y. T.; Li, S. T.; Wu, S. Q.; Cui, A. L.; Shen, D. Z.; Kou, H. Z. *J. Am. Chem. Soc.* **2013**, *135*, 5942–5945.
- (154) Shen, F.; Huang, W.; Wu, D.; Zheng, Z.; Huang, X. C.; Sato, O. *Inorg. Chem.* **2016**, *55*, 902–908.
- (155) Dawe, L. N.; Shuvaev, K. V.; Thompson, L. K. *Chem. Soc. Rev.* **2009**, *38*, 2334–2359.
- (156) Shiga, T.; Matsumoto, T.; Noguchi, M.; Onuki, T.; Hoshino, N.; Newton, G. N.; Nakano, M.; Oshio, H. *Chem. - An Asian J.* **2009**, *4*, 1660–1663.
- (157) Tong, J.; Demeshko, S.; John, M.; Dechert, S.; Meyer, F. *Inorg. Chem.* **2016**, *55*,

- 4362–4372.
- (158) Anwar, M. U.; Thompson, L. K.; Dawe, L. N.; Habib, F.; Murugesu, M. *Chem. Commun.* **2012**, *48*, 4576–4578.
- (159) Huang, W.; Shen, F. X.; Wu, S. Q.; Liu, L.; Wu, D.; Zheng, Z.; Xu, J.; Zhang, M.; Huang, X. C.; Jiang, J.; Pan, F.; Li, Y.; Zhu, K.; Sato, O. *Inorg. Chem.* **2016**, *55*, 5476–5484.
- (160) Wu, S. Q.; Xie, Q. W.; An, G. Y.; Chen, X.; Liu, C. M.; Cui, A. L.; Kou, H. Z. *Dalt. Trans.* **2013**, *42*, 4369–4372.
- (161) Randell, N. M.; Anwar, M. U.; Drover, M. W.; Dawe, L. N.; Thompson, L. K. *Inorg. Chem.* **2013**, *52*, 6731–6742.
- (162) Yang, Q.; Tang, J. *Dalt. Trans.* **2019**, *48*, 769–778.
- (163) Thompson, L. K.; Dawe, L. N. *Coord. Chem. Rev.* **2015**, *289–290*, 13–31.
- (164) Thompson, L. K.; Dawe, L. N.; Shuvaev, K. V. In *Molecular Cluster Magnets*; Winpenny, R., Ed.; World Scientific, 2011; pp 1–58.
- (165) Mandel, A.; Schmitt, W.; Womack, T. G.; Bhalla, R.; Henderson, R. K.; Heath, S. L.; Powell, A. K. *Coord. Chem. Rev.* **1999**, *190–192*, 1067–1083.
- (166) Benelli, C.; Gatteschi, D. *Introduction to Molecular Magnetism. From Transition Metals to Lanthanides*; Wiley-VC, 2015.
- (167) Craig, G. A.; Murrie, M. *Chem. Soc. Rev.* **2015**, *44*, 2135–2147.
- (168) Frost, J. M.; Harriman, K. L. M.; Murugesu, M. *Chem. Sci.* **2016**, *7*, 2470–2491.
- (169) Rosado Piquer, L.; Sañudo, E. C. *Dalt. Trans.* **2015**, *44*, 8771–8780.
- (170) Thomas, L.; Lionti, F.; Ballou, R.; Gatteschi, D.; Sessoli, R.; Barbara, B. *Nature* **1996**, *383*, 145–147.
- (171) Brechin, E. K.; Soler, M.; Christou, G.; Davidson, J.; Hendrickson, D. N.; Parsons, S.; Wernsdorfer, W. *Polyhedron* **2003**, *22*, 1771–1775.
- (172) Brechin, E. K.; Sañudo, E. C.; Wernsdorfer, W.; Boskovic, C.; Yoo, J.; Hendrickson, D. N.; Yamaguchi, A.; Ishimoti, H.; Concolino, T. E.; Rheingold, A. L.; Christou, G. *Indian J. Chem.* **2008**, *47*, 32–36.
- (173) Topping, C. V.; Blundell, S. J. *J. Phys. Condens. Matter* **2019**, *31*, 013001.

# CHAPTER 2

---

## THE EFFECT OF LIGAND SUBSTITUENTS ON THE SPIN CROSSOVER OF Fe (II) COMPLEXES





## 2. THE EFFECT OF LIGAND SUBSTITUENTS ON THE SPIN CROSSOVER OF Fe (II) COMPLEXES

### Abstract

Identifying the individual factors affecting the SCO temperature is a challenging task since many variables are involved. We present a series of Fe(II) complexes with three derivatives of (2-(pyrazol-1-yl)-6-(1H-pyrazol-3-yl)pyridine (1,3-bpp): [Fe(1,3-bpp)<sub>2</sub>](ClO<sub>4</sub>)<sub>2</sub> (**1**), [Fe(Me-1,3-bpp)<sub>2</sub>](ClO<sub>4</sub>)<sub>2</sub> (**2**), [Fe(Me<sub>2</sub>-1,3-bpp)<sub>2</sub>](ClO<sub>4</sub>)<sub>2</sub> (**3**). We thereby unveil how the ligand substituents (containing none, one or two methyl groups) can modulate drastically the SCO temperature through intramolecular non-covalent interactions as the main factor. This modulation of the SCO temperature was observed in solid-state and in solution (with T<sub>SCO</sub> (**3**) > T<sub>SCO</sub> (**1**) > T<sub>SCO</sub> (**2**)), which allows quantifying the influence of the methyl substituents on the SCO temperature. The origin of these effects was demonstrated by DFT calculations, helping to separate the crystal packing effects and focus on the intramolecular non-covalent or steric interactions.

### 2.1. Introduction

The phenomenon of SCO is still widely studied in part because the temperature and type of transition vary extraordinarily with just subtle changes between similar compounds. Despite the molecular origin of SCO, many reports highlight the chemical and structural factors that also affect directly the overall macroscopic behaviour in the solid-state.<sup>1,2</sup> Such studies are thus important if one wants to dominate the phenomenon and design systems with customized behaviour. Generally, the ligand effect,<sup>3</sup> crystal packing,<sup>4</sup> intermolecular interactions<sup>5-7</sup> or secondary bonding interactions<sup>8-10</sup> are superimposed. Thus, unveiling the individual influence of each factor is very challenging. Therefore, it continues to be arduous to predict and control the spin state through a reliable molecular design. Over time, an extensive literature has developed relating the nature of the ligands and the SCO.<sup>3</sup> Solution phase measurements are ideal to identify the pure ligand contribution since the molecules undergoing SCO are isolated and unrestrained<sup>11</sup>, thus avoiding lattice effects, the importance of which has been established with the study of solvatomorphs<sup>12-21</sup> and, most importantly, polymorphs.<sup>4,22</sup> Previous

## 2. The effect of ligand substituents on the Spin Crossover of Fe (II) complexes

studies have shown several ways to control the spin state by making proper chemical modifications of the ligands. Several studies have drawn the difference between  $\sigma$ -donating and  $\pi$ -accepting groups into the ligand moiety.<sup>23,24</sup> The dependence on the substituent position and the opposite effect of both bonding properties has been reported.<sup>25</sup> Furthermore, a common strategy to induce SCO behaviour when non-substituted ligands complexes display LS state is to increase the steric demand by adding bulky substituents close to the coordinating nitrogen atoms.<sup>3,26-29</sup> In some cases, the high-spin state is fully stabilized by preventing the Fe-N bonds contraction.<sup>30-35</sup> Counterintuitively, the steric effect can also promote the low-spin state stabilization. This effect takes place in Fe(II) scorpionates, where steric intra-ligand repulsions impede the transition.<sup>36</sup> This has also been explored with the cation  $[\text{Fe}(\text{Me}_4\text{-1bpp})_2]^{2+}$  ( $\text{Me}_4\text{-1bpp}$ =2,6-bis-(3,5-dimethyl-pyrazol-1-yl)-pyridine), whose intra-ligand repulsion between methyl group at position 5 and the central pyridine in the 1bpp induce the low-spin of the complex. These opposite steric effects can be proved in an analogues series of Fe(II) complexes. We were interested in adding additional insights into the ability of using internal steric effects to modulate the SCO properties in a family of complexes. With such an aim, we designed three ligands showing zero, one and two methyl substituent on the pyrazol-1-yl ring of the 1,3bpp parent ligand; 2-(pyrazol-1-yl)-6-(1H-pyrazol-3-yl)pyridine (1,3bpp),<sup>22</sup> 2-(3-methylpyrazol-1-yl)-6-(1H-pyrazol-3-yl)pyridine (Me-1,3bpp) and 2-(3,5-dimethylpyrazol-1-yl)-6-(1H-pyrazol-3-yl)pyridine (Me<sub>2</sub>-1,3bpp). All ligands are depicted in Figure 2.1. The respective homoleptic Fe(II) complexes were prepared;  $[\text{Fe}(1,3\text{bpp})_2](\text{ClO}_4)_2$  (previously published, **1**),  $[\text{Fe}(\text{Me-1,3bpp})_2](\text{ClO}_4)_2$  (**2**) and  $[\text{Fe}(\text{Me}_2\text{-1,3bpp})_2](\text{ClO}_4)_2$  (**3**).

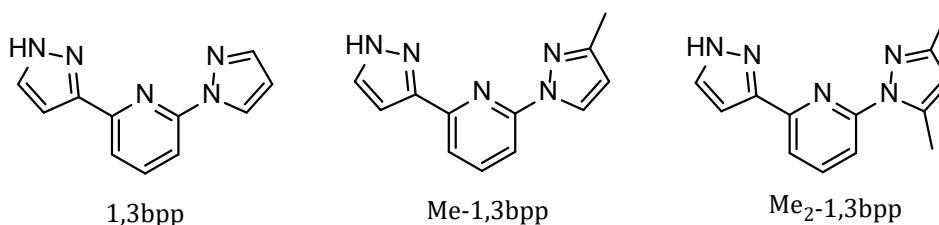


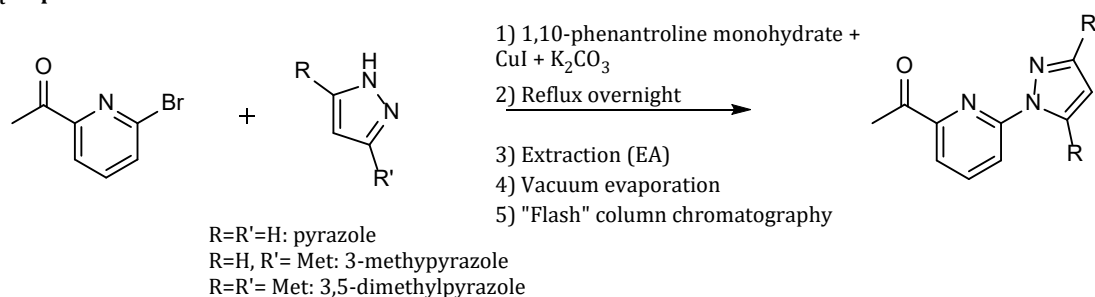
Figure 2.1. Molecular structure of ligands 1,3bpp, Me-1,3bpp (with the methyl in the position 3 in the pyrazole) and Me<sub>2</sub>-1,3bpp (with both position 3 and 5 methylated).

## 2.2. Results and discussion

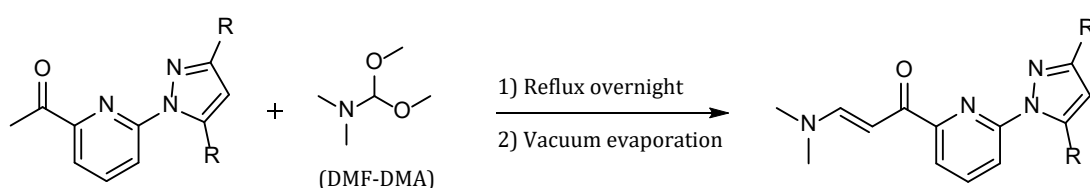
### Synthesis of 3-Methyl and 3,5-dimethyl substituted 1,3-bis-pyrazolylpyridine (1,3-bpp) ligands

The synthetic route used to prepare ligands Me-1,3bpp and Me<sub>2</sub>-1,3bpp (Figure 2.2) was the same. The three steps procedure is analogous to that previously reported for 1,3bpp.<sup>22</sup> Hence, the proper substituted pyrazole ring was first coupled to 2-acetyl-6-bromopyridine through an Ullman reaction. In the case of Me-1,3bpp, a mixture of regioisomers is obtained (**i** and **i'**), since the pyrazole precursor is unsymmetrical and it can couple through either of both N atoms. However, the coupling takes places mainly through the less hindered nitrogen of the pyrazole giving rise to 1-(6-(3-methylpyrazol-1-yl)pyridin-2-yl)ethenone (**i**) as the major product and one easy to purify (Figure 2.3, top). See Figure A2.1 in Appendix 2 for characterization of the crude.

#### 1<sup>st</sup> step: Ullman reaction



#### 2<sup>nd</sup> step: Enaminone formation



#### 3<sup>rd</sup> step: Ring closure

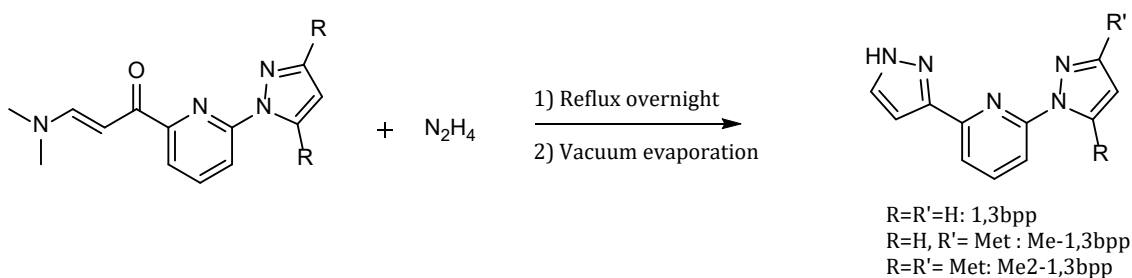


Figure 2.2. General synthetic route used to reach 1,3bpp ligand and the derivatives: Me-1,3bpp and Me<sub>2</sub>-1,3bpp.

## 2. The effect of ligand substituents on the Spin Crossover of Fe (II) complexes

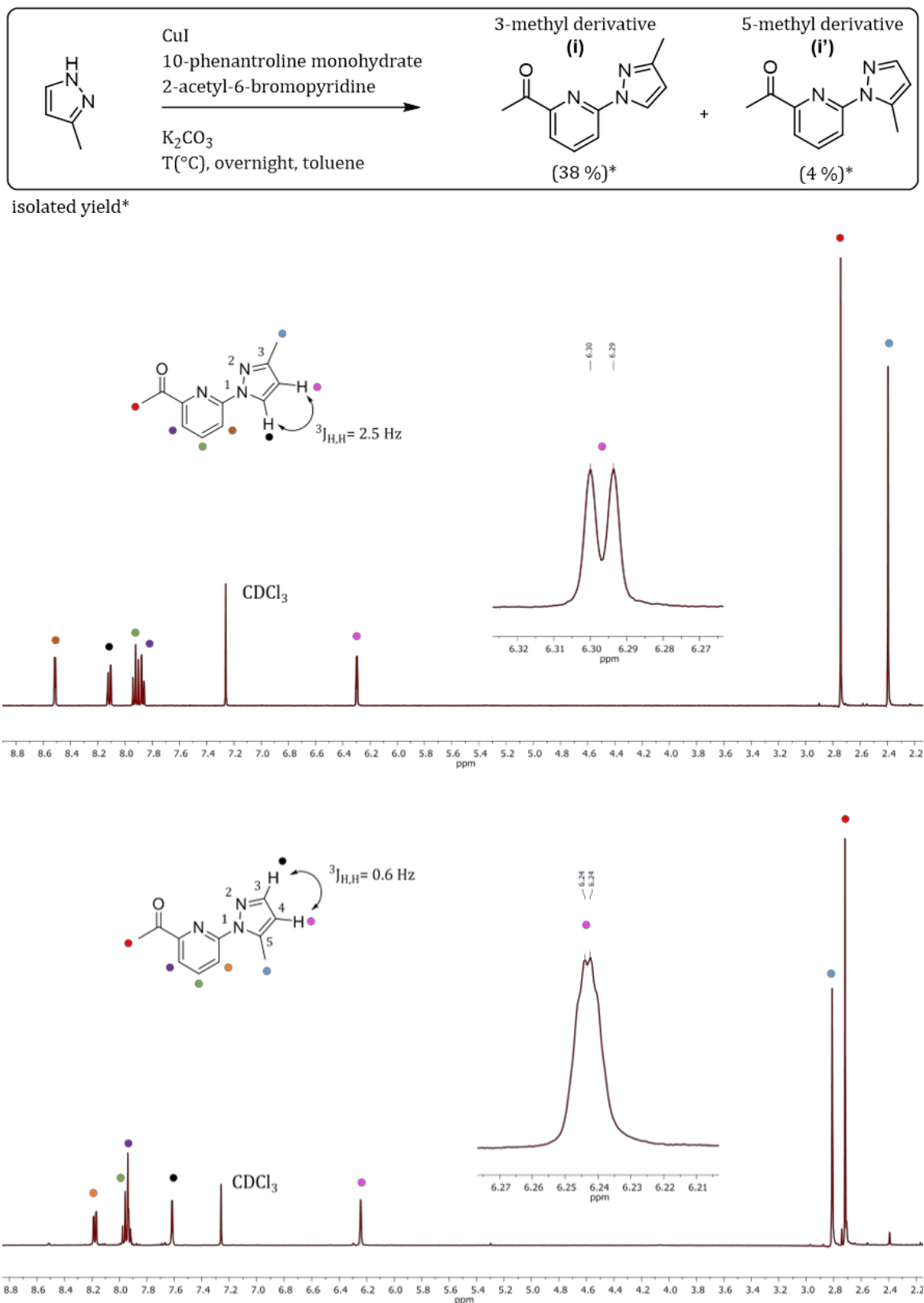


Figure 2.3. (Top) N-arylation conditions for the unsymmetrical 3-methyl-pyrazole regioisomer. (Top spectrum): <sup>1</sup>H-NMR of 3-methyl derivative. (Bottom spectrum): <sup>1</sup>H-NMR of 5-methyl-pyrazole regioisomer.



The 5-methyl derivative was isolated in a small amount after “flash” column chromatography purification (hexane/ ethyl acetate (8:2)) of the crude. The isolated yield was 4%, proving that the analogue with one methyl on position 5 is not easily affordable with our synthetic procedure. The reaction outcome is initially assessed by  $^1\text{H-NMR}$ . Singling out each regioisomer can be easily accomplished through the measured coupling constants of the hydrogen atoms in the pyrazole ring. As has been previously reported in the literature,  $^3J_{\text{H,H}}$  2.4-2.9 Hz is characteristic for pyrazoles substituted on position 3, while  $^3J_{\text{H,H}}$  1.5-1.9 Hz is observed when the methyl is on position 5 (Figure 2.3).<sup>37</sup> The second synthetic step is treating the appropriate product with N,N-dimethylformamide-dimethyl acetal (DMFDMA) providing the corresponding 3-(dimethylamino)prop-2-en-1-one moiety. DMFDMA is a broadly used reagent in the synthesis of heterocyclic compounds.<sup>38</sup> In this case, the formylation of the active acetyl group gives the desired enaminone while, in a third step, hydrazine monohydrate allows the ring closure to yield the sought pyrazole.

### **Synthesis of the homoleptic Fe(II) complexes $[\text{Fe}(\mathbf{1,3\text{bpp}})_2](\text{ClO}_4)_2$ (**1**), $[\text{Fe}(\text{Me-1,3\text{bpp}})_2](\text{ClO}_4)_2$ (**2**) and $[\text{Fe}(\text{Me}_2\text{-1,3\text{bpp}})_2](\text{ClO}_4)_2$ (**3**)**

The complex  $[\text{Fe}(\mathbf{1,3\text{bpp}})_2](\text{ClO}_4)_2$  (**1**) was prepared as previously published by our group.<sup>22</sup> It was obtained following two distinct procedures as two different polymorphs, **1a** and **1b**. The former was obtained using dry acetone while the other comes from extruding the lattice water molecules by single-crystal-to-single-crystal SCSC transformations of a hydrated solvatomorph. Complexes  $[\text{Fe}(\text{Me-1,3\text{bpp}})_2](\text{ClO}_4)_2$  (**2**) and  $[\text{Fe}(\text{Me}_2\text{-1,3\text{bpp}})_2](\text{ClO}_4)_2$  (**3**) were obtained by direct reaction of hydrated  $\text{Fe}(\text{ClO}_4)_2$  with the Me-1,3bpp and Me<sub>2</sub>-1,3bpp ligands, respectively, in the presence of catalytic amounts of ascorbic acid to prevent the oxidation of Fe(II) to Fe(III). Compound **2** was obtained from a reaction in absolute ethanol that produced a yellow solution, using hexane as the crystallization medium. The pair of solvents used for the preparation of **3** as red crystals are acetone and diethyl ether.

**Crystal structures of [Fe(Me-1,3bpp)<sub>2</sub>](ClO<sub>4</sub>)<sub>2</sub> (2) and [Fe(Me<sub>2</sub>-1,3bpp)<sub>2</sub>](ClO<sub>4</sub>)<sub>2</sub> (3)**

The structure of complex **1** has been already described in a previous publication.<sup>22</sup> This compound can be obtained following two different procedures, respectively as two polymorphs, **1a** and **1b**, showing two different organizations of the Fe(II) complex cations closely related to these observed for compounds **2** and **3**, respectively (see below).

**[Fe(Me-1,3bpp)<sub>2</sub>](ClO<sub>4</sub>)<sub>2</sub> (2)**. The structure of **2** was determined at 100 K, on crystals that had turned red from their original yellow colour at room temperature. Their solvent-free lattice is found in the monoclinic space group C2/c. The asymmetric unit consists of one formula unit, with eight such moieties present in the unit cell. The complex cation features a distorted octahedral Fe(II) center coordinated to two Me-1,3bpp tris-imine ligands lying approximately perpendicular to each other (Figure 2.4). As a result of the asymmetric character of the ligands, this complex is chiral, both enantiomers being present in the lattice, which is racemic. The average of the Fe–N bond distances is 1.96(4) Å, corroborating the LS state of the compound at this temperature. The spin state is also evident from the distortion parameters  $\Sigma$  and  $\Theta$ ,<sup>2,39,40</sup> which here amount to 93.2 and 367.8, respectively, within the region expected for LS compounds.<sup>41</sup> The structure was also determined at 300K, on crystals that had turned pale yellow upon heating, due to a LS to HS conversion. As a result of the SCO expansion, the unit cell experiences an isotropic growth, with a volume expansion of 5%, a Fe-N bond distance average of 2.16 (2) Å, and distortion parameters of  $\Sigma = 147.5$  and  $\Theta = 378.2$ . These numbers confirm the HS configuration of the compound at 300K (Table A2.1, Appendix 2).

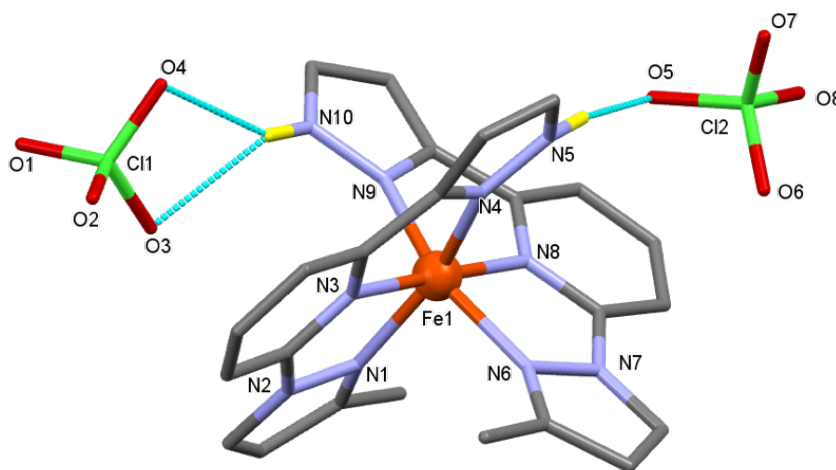


Figure 2.4. Molecular representation of  $[\text{Fe}(\text{Me-1,3bpp})_2](\text{ClO}_4)_2$  (**2**) at 100 K with heteroatoms labelled. Only H atoms of N–H groups shown (in yellow). Cyan blue dashed lines are H-bonds.

**$[\text{Fe}(\text{Me}_2\text{-1,3bpp})_2](\text{ClO}_4)_2$  (**3**)**. The molecular structure of **3** was determined at 100 and 296 K. At both temperatures, the lattice exhibits the monoclinic  $P2_1/n$  space group, the asymmetric unit coinciding with the empirical formula and the unit cell enclosing four such moieties. The complex cation  $[\text{Fe}(\text{Me}_2\text{-1,3bpp})_2]^{2+}$  is analogous to that of **2**, now with the ligand  $\text{Me}_2\text{-1,3bpp}$  (Figure 2.5). The average of the Fe–N distances (1.95(4) at both temperatures) and the  $\Sigma/\theta$  distortion parameters (88.7/367.2 and 90.0/367.1 respectively) show that the Fe(II) centres are in the LS state at 100 and 296 K. Attempts to obtain the structure of **3** in the HS (>400 K) were unsuccessful because of crystal damage. From 100 to 296K, the cell dimension experiences an isotropic expansion purely of thermal origin, with a volume increase of 4%. (Table A2.1, Appendix 2).

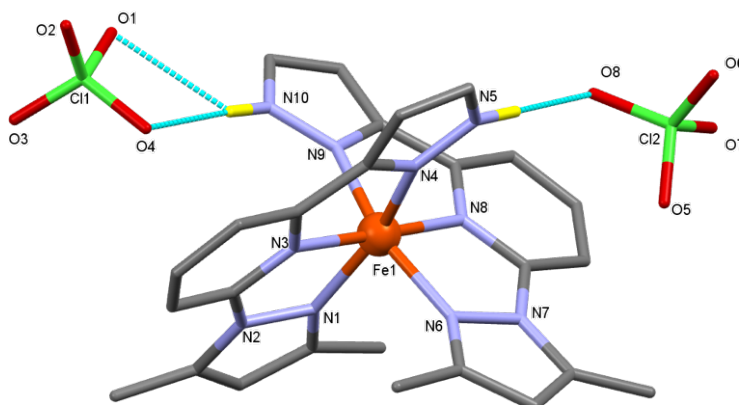


Figure 2.5. Molecular representation of  $[\text{Fe}(\text{Me}_2\text{-1,3bpp})_2](\text{ClO}_4)_2$  (**3**) at 100 K with heteroatoms labelled. Only H atoms of N–H groups shown (in yellow). Cyan blue dashed lines are H-bonds.

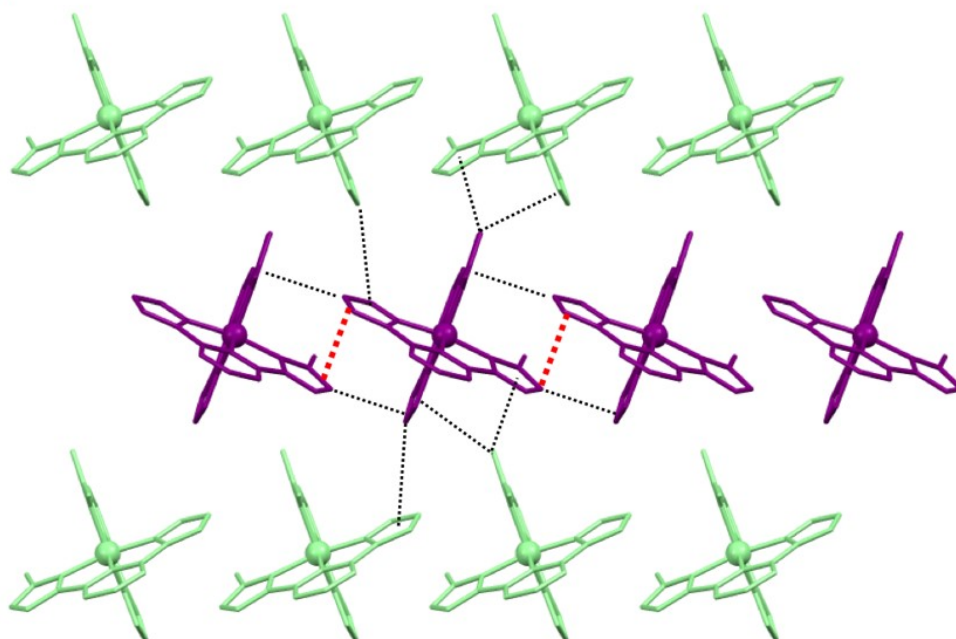
### Comparison of the cation lattice arrangement between both compounds

The Fe<sup>II</sup> metal centre of the cationic [Fe(Me-1,3bpp)<sub>2</sub>]<sup>2+</sup> and [Fe(Me<sub>2</sub>-1,3bpp)<sub>2</sub>]<sup>2+</sup> complexes is chelated with two neutral 1,3bpp ligand type providing a *mer* coordination environment. Due to the asymmetric feature of Me-1,3bpp and Me<sub>2</sub>-1,3bpp, their complexes are chiral with both enantiomers equally present in the lattice (racemic mixture). Both complexes in these compounds are part of solvent-free structures, perhaps because the ClO<sub>4</sub><sup>-</sup> counterions establish hydrogen bonding interactions with the N-H groups of the ligands preventing the accommodation of other proton acceptors at these locations of the lattice. Interestingly, complexes **2** and **3** are arranged in the crystal lattice as the previously reported polymorphs **1a** and **1b**, respectively (Figure 2.6). Selected bond lengths and angles and intermolecular distances are given in Tables A2.1-A2. and Figure A2.2 in the Appendix 2.

The main difference between both crystal packings is, as easily perceived, the organization within sheets of the respective cations. The parallel arrays within the layers alternate [Fe(Me-1,3bpp)<sub>2</sub>]<sup>2+</sup> cations with different orientations, whereas [Fe(Me<sub>2</sub>-1,3bpp)<sub>2</sub>]<sup>2+</sup> cations are oriented in the same direction. Consequently, the orientation of the first neighbours and the intermolecular interactions within the sheets (Figure 2.6) of the Fe complex in compounds **2** and **3**, respectively, are different. Thus, each [Fe(Me-1,3bpp)<sub>2</sub>]<sup>2+</sup> moiety interacts with two neighbours *via* two π···π and six C-H···π interactions within the sheets. Each cation establishes a total of six weak C-H···π contacts with two nearby congeners in between the sheets (Figure 2.6 Top). The angle between complexes in the two orientations (measured using idealized planes of two equivalent ligands) is 41.40°. There are two types of very similar interlayer separations (Figure A2.3, Appendix 2) 9.640 Å and 9.887 Å. Instead, each [Fe(Me<sub>2</sub>-1,3bpp)<sub>2</sub>]<sup>2+</sup> interacts with four first neighbours (within the sheets), establishing four π···π and eight C-H···π interactions (Figure 2.6 Bottom). The layers feature separations (Figure A2.4, Appendix 2) of 9.420/9.499 and 9.636/9.598 Å at both temperatures, respectively. Furthermore, the homogeneity and the purity of the bulk material for compounds **2** and **3** was proved through powder X-ray diffraction (PXRD) methods. This technique

was also previously used to provide proof of the two polymorphic phases of compound 1. (Figure A2.5, Appendix 2)

Complex 2



Complex 3

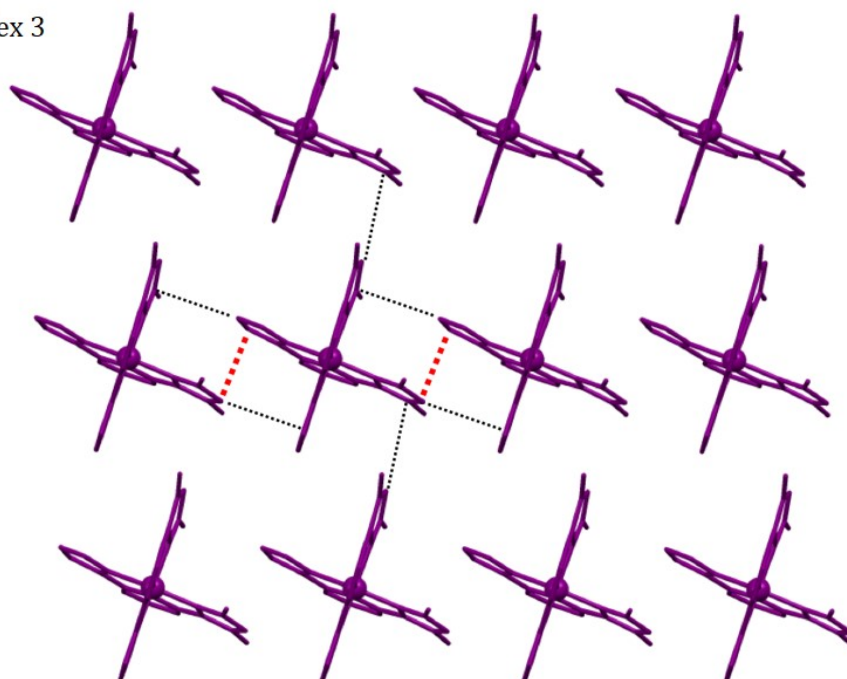


Figure 2.6. Sheet organization of the cations in **2** (top) and **3** (bottom), emphasizing their cationic sheet orientation. Two different orientations for **2** and the sole orientation for **3**. The  $\pi \cdots \pi$  and C-H  $\cdots \pi$  interactions formed by each complex with its immediate neighbours within the sheet.

### Bulk magnetic measurements

Magnetic susceptibility measurements of compounds **2** and **3** were carried out on polycrystalline samples in the temperature range between 5 and 400K in the warming and cooling modes under a constant magnetic field. The data were compared with the response from polymorphs **1a** and **1b**. Thus, first insights of the influence of the metal substituents on the SCO of the complexes analogous to  $[\text{Fe}(\text{1,3bpp})_2](\text{ClO}_4)_2$  were acquired in the solid-state. The plots of  $\chi_M T$  vs.  $T$  ( $\chi_M$  is the molar paramagnetic susceptibility) for all the compounds are shown in Figure 2.7. At low temperatures, all the complexes are diamagnetic, with  $\chi_M T$  values ranging from 0.06 to 0.17  $\text{cm}^3 \cdot \text{K} \cdot \text{mol}^{-1}$  (100 K). An abrupt transition takes places in all the cases with  $\chi_M T$  reaching values (in  $\text{cm}^3 \cdot \text{K} \cdot \text{mol}^{-1}$ ) of 3.01 (**2**), 3.26 (**1a**) and 3.4  $\text{cm}^3 \cdot \text{K} \cdot \text{mol}^{-1}$  (**1b**), while for **3**, with a value of 2.64  $\text{cm}^3 \cdot \text{K} \cdot \text{mol}^{-1}$ , it was still increasing at 400 K (the maximum temperature reached by the magnetometer). These SCO profiles collected under warming mode are quasi-superimposable with the ones recorded in the cooling mode, indicating the absence of hysteresis. Inspection of the plots reveals that the transitions of **2** and **1b** are more abrupt than those of **1a** and **3**. Additionally, their transition temperatures are considerably different, with  $T_{1/2}$  values of 183 (**2**), 278 (**1a**), 314 (**1b**) and 378 K (**3**).

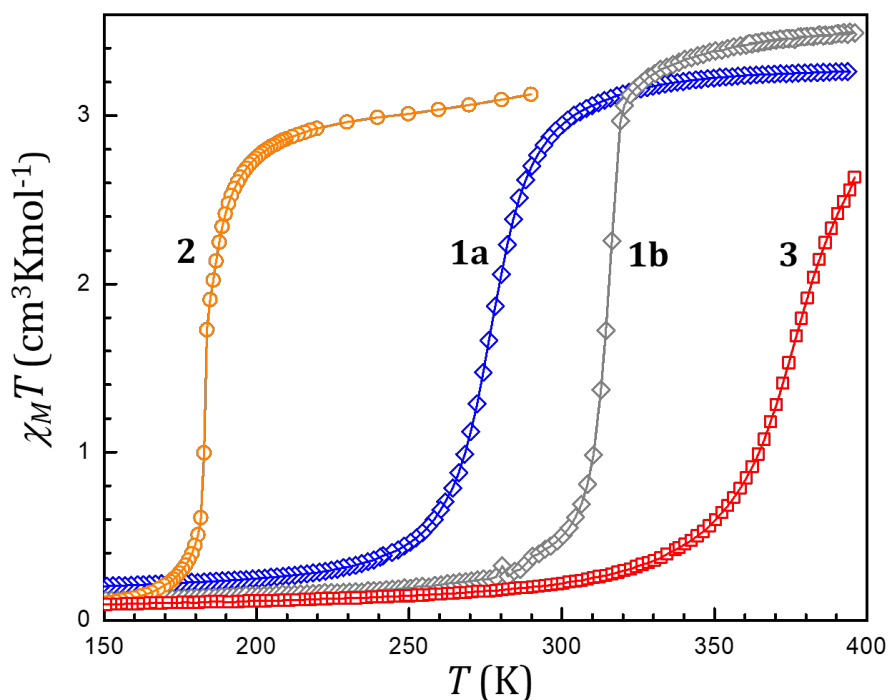


Figure 2.7. Thermal SCO properties of compounds **1a**, **1b**, **2** and **3**:  $\chi_M T$  vs.  $T$  plots. All data correspond to the warming mode.

These results are entirely consistent with the differential scanning calorimetry (DSC) results since the  $T_{SCO}$  values deduced from the maxima of the molar heat capacity vs temperature curves match very well the values observed from magnetic measurements. The anomalies associated with the SCO processes are substantially sharp, sharp and relatively broad for **2**, **1b** and **1a/3**, respectively. (Figure 2.8). The thermodynamic sum (the excess entropy and enthalpy) associated to the SCO provides a qualitative measure of the related cooperativity of each SCO process. In our case, the integration of  $\Delta C_p$  respect to  $T$  gives an excess of entropies larger than the expected entropy gain  $\Delta S = R \ln 5 = 13.38 \text{ J K}^{-1} \text{ mol}^{-1}$  for the (Table 2.1) spin multiplicity change (from the  $^1A_{1g}$  LS to the  $^5T_{2g}$  HS state).

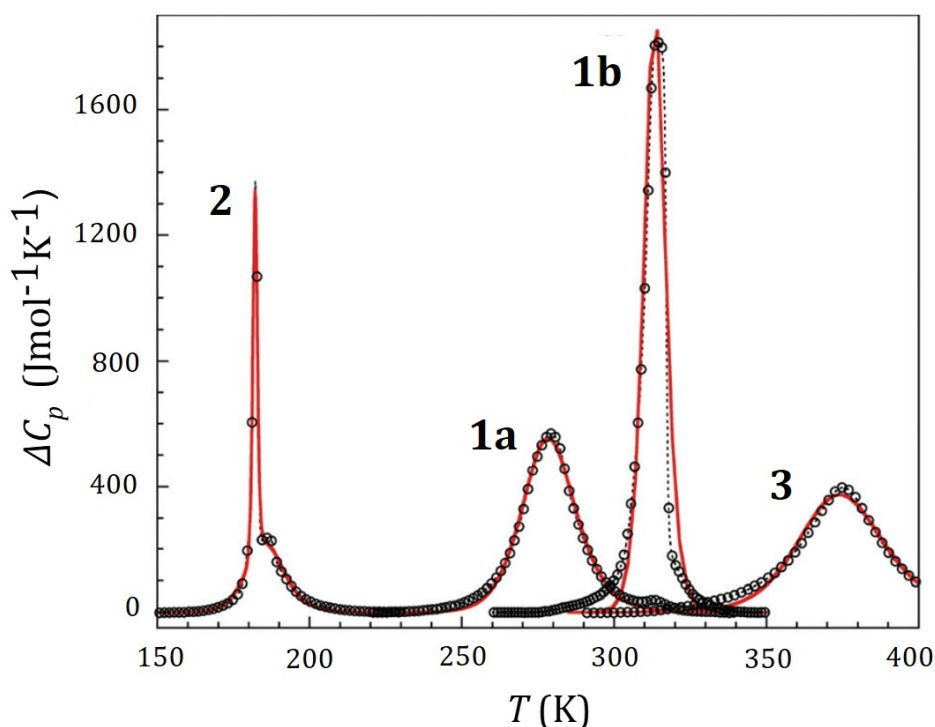


Figure 2.8. Molar heat capacity vs.  $T$  plots derived from DSC measurements. All data correspond to the warming mode. Black circles and red lines are experimental data and fits to Sorai's domain, respectively. See Appendix 2 for further information.

Thus, additional intramolecular vibrations perturb the lattice vibrations which is translated into a phonon contribution coupled with the SCO process in the solid state. Since these thermodynamic parameters vary drastically along with the present series of compounds, fitting the experimental  $\Delta C_p$  vs  $T$  data to Sorai's domain model allowed us to get more quantitative insights into the cooperativity.<sup>42,43</sup> (See Appendix 2, Equation S1 and Figure A2.6). This model relates

## 2. The effect of ligand substituents on the Spin Crossover of Fe (II) complexes

Table 2.1. Thermodynamic parameter of compounds **1a**, **1b**, **2** and **3**.

	<b>1a</b>	<b>1b</b>	<b>2</b>	<b>3</b>
$\Delta H_{SCO}$ (KJ mol <sup>-1</sup> )	13.57	17.74	5.87	14.11
$\Delta S_{SCO}$ (J mol <sup>-1</sup> K <sup>-1</sup> )	48.7	56.8	31.7	38.0
$n^a$	8.5(1)	20.0(2)	128.7(3)	9.0(1)
$T_{SCO}$ (K) <sup>a</sup>	278.8(3)	313.4(3)	182.1(1)	375.0(3)
$T_{1/2}$ (K) <sup>b</sup>	278	314	184	378
$T_{1/2}$ (K) <sup>c</sup>	262	262	232	281

<sup>a</sup> Solid-state, from fit of  $\Delta C_p$  vs. T the domain model (see Appendix 2). <sup>b</sup> Solid-state, from  $\chi_M T$  vs. T.

<sup>c</sup> Solution, from the <sup>1</sup>H NMR (un solution, **1a** and **1b** become, to a very good approximation, the same system).

the thermodynamic values with the cooperative nature of the SCO through the domain size  $n$  (number of SCO-like molecules in each interacting domain). As the number  $n$  increases, the transition is more cooperative. Values of  $n$  close to 1 are characteristic for gradual SCO while values above 20 are for highly cooperative systems.<sup>43–45</sup> Compounds **1a** and **3** have values of 8.5 and 9.0, respectively, while for **1b** is 20.0, corresponding to the medium to high cooperativity of the SCO. In contrast, compound **2** with  $n=128.7$  exhibits very strong cooperativity. The influential coupling between SCO and the induced structural changes (large variation of the crystallographic cell parameters) at the SCO are the roots for this highly cooperative system. In fact, two components of the SCO were fitted for the sharp and the broader (below the former) anomalies for compound **2**, giving a good simulation for the coexistence of both processes.

While the substituents on the bare 1,3bpp ligand impact dramatically on the  $T_{1/2}$  in solid-state, further studies to establish how the nature and location of the methyl substituents influence the SCO temperature are required where the packing does not play a role. Indeed, different crystal packing alone of the same substance, as seen in polymorphs **1a** and **1b** cause very different magnetic responses (eg. a disparity of about 40K in SCO temperature) and behave as different materials. Thus, while solid-state measurements are significant for investigating the molecular packing and intermolecular interactions (cooperativity), solution-phase measurements are appropriate to quantify exclusively local electronic effects.<sup>11</sup>



### **Solution-phase measurements. Evan's method**

The influence of ligand modifications on the temperature of the spin transition is screened in solution through NMR spectroscopy. Using the Evans method<sup>46-48</sup>, the variable temperature paramagnetic susceptibility of a dissolved paramagnetic substance can be calculated. A detailed description of the technique is given in the introduction (section 1.2.3). Firstly, <sup>1</sup>N-NMR spectra of complexes **1**, **2** and **3** were collected at room temperature in CD<sub>3</sub>OD (Figure A2.7, Appendix 2). As expected for a paramagnetic compound, the proton peaks are strongly shifted (wide spectral window) and broadened due to coupling between nuclear spin and the magnetic moment of the unpaired electrons of the Fe(II) centre. Because of their stability in solution, the spectra of the three compounds could be recorded between 193 and 298 K. (Figures A2.8-A2.16, Appendix 2). The TMS paramagnetic shift and the calculated  $\chi_M$  in solution as a function of temperature for **1**, **2** and **3** are provided in Appendix 2 (Table A2.5). The plot of  $\chi_M T$  vs.  $T$  is shown in Figure 2.9. Each data set was modelled as a gradual and complete SCO using the regular solution model (Equation 1.8; introduction) yielding good fits (Table A2.6; Appendix 2). For each data set, the fit allows to extract values for  $\Delta H$  and  $\Delta S$ , the thermodynamic enthalpy and entropy changes associated with the SCO. By dividing  $\Delta H/\Delta S$ , as  $\Delta G = 0$  at the SCO transition,  $T_{1/2}$  can be easily calculated (equation 1.9; introduction). These temperatures are approximately (in K) 232 (**2**), 262 (**1**) and 281 (**3**) and are found to be correlated with the temperatures obtained from the bulk measurements. The solution experiments corroborate that one sole methyl substituent, if it is the position 3 of the pyrazolyl ring, stabilizes the HS state, thus reducing the SCO temperature. When two methyl groups (on positions 3 and 5), the opposite result is observed. Hence, the SCO temperature increases instead. Together, the present findings suggest that a methyl on position 5 opposes the influence of the one located in position 3, in a stronger manner. From this standpoint, this could be demonstrated by the compound with only one methyl group located in position 5. Unfortunately, it has not yet been possible to prepare the corresponding derivative to verify this.

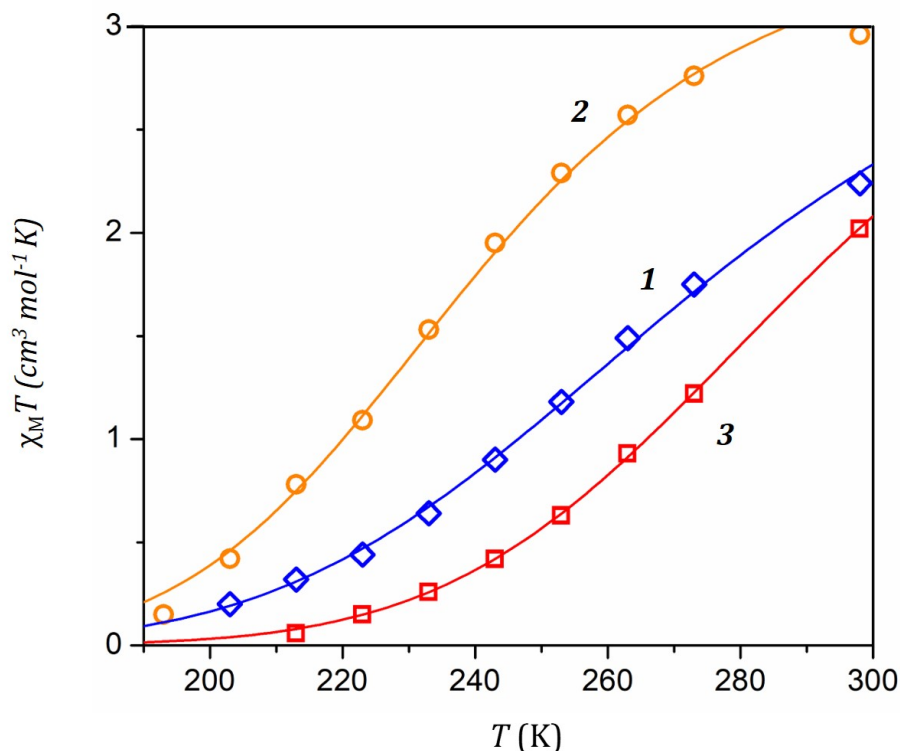


Figure 2.9.  $\chi_M T$  vs.  $T$  plots for each of the three complexes at 0.005M in methanol- $d_4$  solution by employing the Evans method. Data points (Table A2.5, Appendix 2); curves are fitted to the regular solution model (see the text and Table A2.6; Appendix 2 for details).

Table 2.2. Summary of the thermodynamic parameters,  $\Delta H$  (kJ mol $^{-1}$ ) and  $\Delta S$  (J mol $^{-1}$  K $^{-1}$ ) resulting from the regular solution fitting, the  $T_{1/2}$  (K) calculated from  $\Delta H/\Delta S$ , and the  $R^2$  for the fit.

Compound	$T_{1/2}$	$\Delta H$	$\Delta S$	$R^2$
<b>1</b>	273.8 (262)	-18072	-66	0.997
<b>2</b>	238.9(232)	-20780	-87	0.994
<b>3</b>	291 (281)	-24732	-85	0.999

### DFT calculations

Overall, our results demonstrate a strong effect of the methyl group position over the SCO temperature. Furthermore, the experimental results have been entirely rationalized and quantified with DFT+ $U$ +D2 calculations in terms of inter- and intra-ligand interaction effects. The computational method has been used to calculate the relative stability of the HS and LS state in the gas phase for complexes **2** (3-methyl derivative), **3** (3,5-dimethyl derivative) and for its hypothetical analogue with only one methyl on position 5 ("**4**"), which is not experimentally accessible through our synthetic procedure. The results were compared with those for the bare cationic

## 2. The effect of ligand substituents on the Spin Crossover of Fe (II) complexes

complex of **1**.<sup>35</sup> The computed enthalpic difference between the HS and LS total energies ( $\Delta H_{\text{elec}}$ ) reached from the energies of the optimized structures are consistent with the experimental results (Table 2.3). By comparing these computed values, the effect of adding methyl groups on different positions can be directly reasoned. When adding the methyl substituent at position 3 (complex **2**),  $\Delta H_{\text{elec}}$  decreases around  $2.0 \text{ KJ mol}^{-1}$  ( $\Delta H_{\text{elec}} = 9.9 \text{ KJ mol}^{-1}$ ) with regard to the unsubstituted complex **1** with  $\Delta H_{\text{elec}} = 11.9 \text{ KJ mol}^{-1}$ . On the contrary, the value increases notably by  $7.7 \text{ KJ mol}^{-1}$  ( $\Delta H_{\text{elec}} = 19.6 \text{ KJ mol}^{-1}$ ) when substituted at position 5 ("**4**"). The introduction of both methyl groups, one at each position (3 and 5, complex **3**) gives a value of  $\Delta H_{\text{elec}} = 16.4 \text{ KJ mol}^{-1}$ . The value difference ( $\Delta H_{\text{elec}} = 4.5 \text{ KJ mol}^{-1}$ ) between **3** and **1** lies close to the one calculated for the combination of both individual effects ( $7.7 - 2.0 = 5.7 \text{ KJ mol}^{-1}$ ). Because these effects partially cancel each other, this indicates of the opposite effects displayed by methyl substituents at the different positions 3 and 5.

Table 2.3. Averaged orbital energies of the  $t_{2g}$  and  $e_g$  subsets for compound **1-3** and the hypothetical "**4**", energy difference between them ( $\Delta E$ , in eV), and electronic enthalpy ( $\Delta H$ , in  $\text{KJ mol}^{-1}$ ).

	<b>1</b>	<b>2</b>	<b>3</b>	" <b>4</b> "
$t_{2g}$	-1.48	-1.45	-1.41	-1.48
$e_g$	2.26	2.28	2.31	2.28
$\Delta E$	-3.74	-3.73	-3.72	-3.76
$\Delta H$	11.9	9.9	16.4	19.6

The correlation of computed  $\Delta H_{\text{elec}}$  with experimental  $T_{\text{SCO}}$  has been previously used to analyse the effect of different ligand substituents. Indeed, the ligand effect was quantified by their effect on the the 3d-orbital energies.<sup>25</sup> In our case, we analysed the effect of the addition of one (**2** and "**4**") and two (**3**) methyl groups on the  $t_{2g}$  and  $e_g$  orbitals. While the  $e_g$  orbital are destabilized, no pattern is observed for the  $t_{2g}$  orbitals of all the complexes. Furthermore, there is no correlation between the orbital energy splitting ( $\Delta E$ ) and  $\Delta H_{\text{elec}}$ . For these reasons, the effect of the methyl groups related to the ligand field seems to be negligible, which, in turn, indicates that the  $\Delta H_{\text{elec}}$  differences must be ascribed to a large extent, to inter- and /or intra-ligand interactions within the cationic complexes. The methyl groups are involved with these out of the coordination sphere of Fe(II) interactions, which are further

linked to changes in the Fe-N distances occurring upon SCO. These effects contribute to the  $\Delta H_{\text{elec}}$  in two ways: i) causing a strain to the overall structure of the cationic  $[\text{Fe}(1,3\text{-bpp})_2]^{2+}$ , and ii) through direct inter- and intra-ligand interactions within the complex. Calculations were performed on the optimized structures of  $\mathbf{2}^{\text{LS}}$  and  $\mathbf{2}^{\text{HS}}$  with the methyl group substituted by an H atom with the purpose of analyse the influence of the 3-methyl substituent. These structures labelled as  $\mathbf{2}^{\text{core}}$  are equivalent to the bare one ( $\mathbf{1}$ ). When comparing their computed  $\Delta H_{\text{elec}}$ , the one for  $\mathbf{2}^{\text{core}}$  is one unit larger than for  $\mathbf{1}$ . This indicates a higher destabilization of the HS which is the opposite effect seen experimentally for this substituent. In order to rationalize this contradictory result, the optimized geometries for  $\mathbf{2}$  and  $\mathbf{1}$  were compared (Figure A2.17, Appendix 2). Indeed, it reveals that the HS structures are much more distant from each other than the LS geometries. The planes of the 1,3bpp are more perpendicular to each other in  $\mathbf{2}$ . It seems that the 3-methyl pushes the other ligand back imposing a steric effect and perhaps also favours an attractive C-H $\cdots$   $\pi$  interaction between the methyl and the central pyridine of the other ligand (Figure 2.10). This last interaction was analysed for the optimized structures  $\mathbf{2}^{\text{HS}}$  and  $\mathbf{2}^{\text{LS}}$ . The HS exhibits a close contact between the 3-methyl and its perpendicular 1,3bpp ligand (the mentioned C-H $\cdots$   $\pi$  interaction) of 2.7 Å. On the contrary, in the LS, this attractive interaction may not be favourable or have turned repulsive (the Fe-N bond distance is shorter for the 3-pyrazole than for the 1-pyrazole ring). In this case, the contraction of the FeN<sub>6</sub> core by the SCO to the LS state enforces the rotation of the methyl group, which now display too close contacts with the other ligand of 2.8 Å for each. Together, the present computed findings confirm the overall stabilization of the HS state.

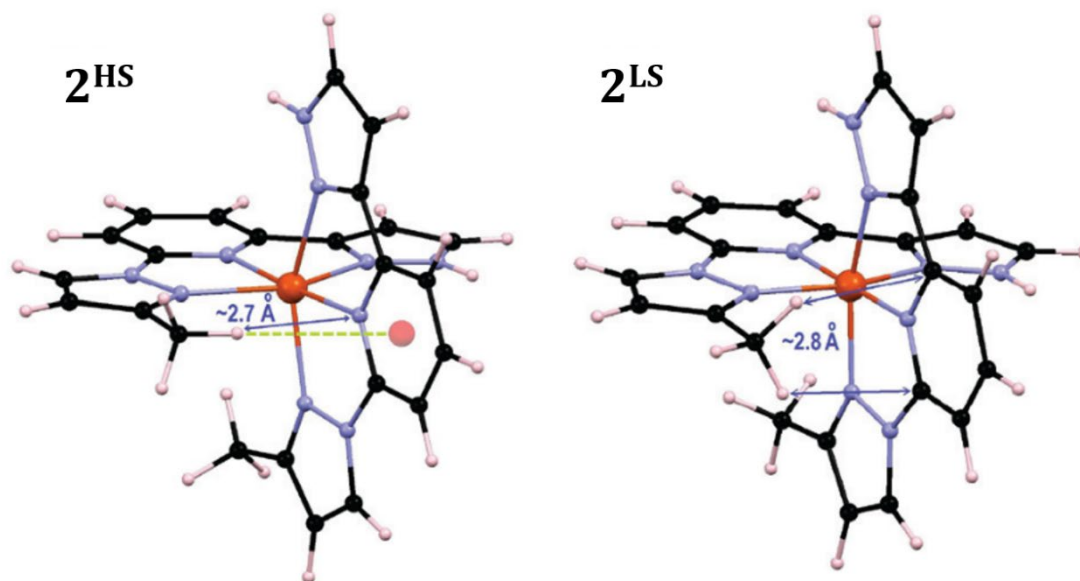


Figure 2.10. Optimized structures by DFT+U+D2 of complex **2** in both spin states. The closest contact between the 3-methyl and the pyridine of the other ligand is emphasized for the HS state structure. The two closest inter-ligand interaction are highlighted of the LS state structure.

The effect of the methyl group at position 5 was also studied by using an analogous procedure to the mentioned above. Firstly, the **4**<sup>core</sup> complex, which is the methyl free structure of the hypothetical compound “**4**” was optimized to quantify: i) the strain of the cationic [Fe(1,3-bpp)<sub>2</sub>]<sup>2+</sup> core and ii) the direct intramolecular interactions. When comparing **4**<sup>core</sup> with **1**, the HS state is 4.7 KJ mol<sup>-1</sup> less stable for the former, being  $\Delta H_{\text{elec}}$  16.6 and 11.8 KJ mol<sup>-1</sup> for each, respectively. This must be understood as the strain of the [Fe(1,3-bpp)<sub>2</sub>]<sup>2+</sup> core when it accommodates partial steric congestion between the 5-methyl group and the central pyridine. Additionally, the difference between “**4**” (19.6 KJ mol<sup>-1</sup>) and “**4**<sup>core</sup>” allows to quantify directly the impact of the intraligand interactions related to the methyl on position 5 (Figure 2.11). This contribution of 3 KJ mol<sup>-1</sup> on the  $\Delta H_{\text{elec}}$  completes the total  $\Delta H_{\text{elec}}$  difference of 7.7 KJ mol<sup>-1</sup> between “**4**” and **1**. Accordingly, the stabilization of the LS state through intra-ligand repulsion is theoretically confirmed for the first time. Overall, the theoretical results suggests that the HS vs LS state stability is influenced by inter-ligand interactions that affect the Fe(II) coordination sphere.

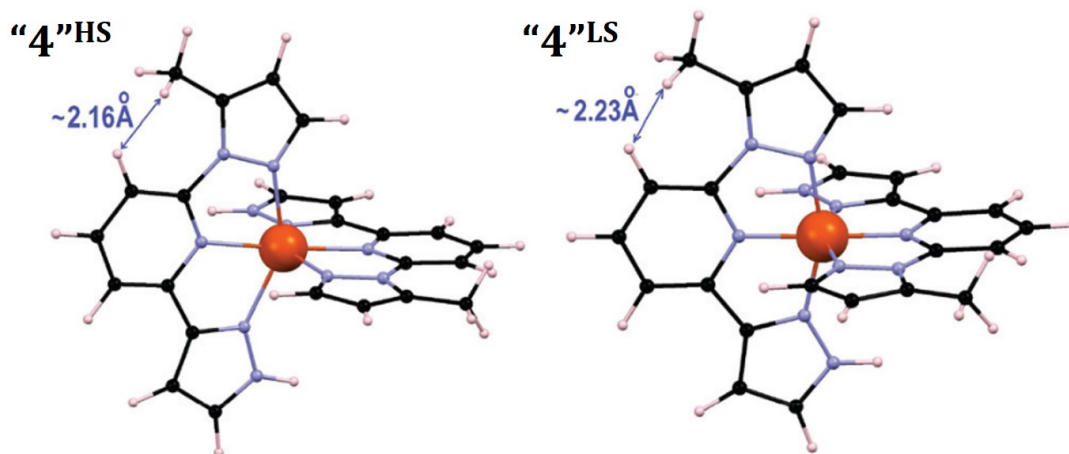


Figure 2.10. Optimized structures by DFT+U+D2 of complex “4” in both spin states. The closest contact between the 3-methyl and the pyridine of the other ligand is emphasized for the HS state structure. The two closest inter-ligand interaction are highlighted of the LS state structure

### 2.3. Conclusions

We demonstrate that the temperature of the spin transition can be fine-tuned by ligand design. The specific location of the methyl groups into the ligands, with 1,3-bbp being non-substituted, 3-methyl or 3,5 dimethyl substituted 1,3-bis-pyrazolylpyridine, is crucial on the effect of the SCO temperature of the analogous family of  $\text{Fe}(1,3\text{bpp})_2(\text{ClO}_4)_2$  complexes. The results show that the methyl in position 3 favours the HS state compared to the unsubstituted system and that the same substituent on position 5 favours the LS state, with a more substantial incidence. This influence is manifested on the solid-state thermal behaviour of the concerned systems and most significantly on their SCO in solution, where packing effects are absent.

### 2.4. Experimental

#### Synthesis

The ligand 2-(pyrazol-1-yl)-6-(1H-pyrazol-3-yl)pyridine (1,3bpp) was synthesized as published,<sup>22</sup> using a slight modification of a previously reported procedure.<sup>49</sup> The corresponding complex  $[\text{Fe}(1,3\text{bpp})_2](\text{ClO}_4)_2$  (**1**) was prepared as previously published.<sup>22</sup> **Caution:** Perchlorate salts of metal complexes are potentially

explosive. Only small quantities of material should be prepared, and the samples should be handled with care.

**1-(6-(3-Methylpyrazol-1-yl)pyridin-2-yl)ethanone. (i)** To a solution of 1-(6-bromo-pyridin-2-yl)ethanone (2.5 g, 12.5 mmol) in toluene (15 mL) were added, under a N<sub>2</sub> atmosphere, 3-methyl-pyrazole (1.53 g, 18.75 mmol), 1,10-phenanthroline monohydrate (0.5 g, 2.5 mmol), CuI (0.24 g, 1.25 mmol) and K<sub>2</sub>CO<sub>3</sub> (1.9 g, 12.5 mmol). The resulting black mixture was heated to reflux and vigorously stirred overnight. After cooling to room temperature, ethyl acetate (20 mL) and water (20 mL) were added and the organic layer was isolated. The aqueous solution was extracted two additional times with ethyl acetate and the organic phases were recombined, washed with brine, dried with MgSO<sub>4</sub> and evaporated under vacuum to afford the product as a brown liquid (2.4 g, 96%). **i/i' = 2.33:1**. The crude was purified by "flash" column chromatography (hexane/ethyl acetate (8:2)) to afford (i) and (i') as white powders. (i) (0.95 g, 38%). Rf: 0.73. (i') (0.10 g, 4%) Rf: 0.62. <sup>1</sup>H-NMR (400 MHz, CDCl<sub>3</sub>, ppm), (i): δ 8.51 (d, J = 2.4 Hz, 1H), 8.12 (dd, J = 8.0, 1.22 Hz, 1H), 7.83–7.97 (m, 2H), 6.31 (d, J = 2.5 Hz, 1H), 2.74 (s, 3H), 2.40 (s, 3H). (i') δ 8.18 (dd, J = 7.47, 1.81 Hz, 1H), 7.86–8.00 (m, 2H), 7.62 (d, J = 1.66 Hz, 1H), 6.24 (d, J = 0.88 Hz, 1H), 2.81 (s, 3H), 2.72 (s, 3H).

**1-(6-(3-Methylpyrazol-1-yl)-pyridin-2-yl)-3-(dimethylamino)-prop-2-en-1-one. (ii)** N,N-Dimethylformamide-dimethyl acetal (2.5 mL, 24 mmol) was added to 1-(6-(3-methylpyrazol-1-yl) pyridin-2-yl)ethanone (2.4 g, 11.9 mmol) and the mixture was heated to reflux (120 °C) and stirred overnight. After cooling to room temperature, the resulting dark yellow solution was concentrated under vacuum to obtain the crude as a brown powder (2.77 g, 91%). <sup>1</sup>H-NMR (400 MHz, CDCl<sub>3</sub>, ppm): 8.46 (d, J = 2.0 Hz, 1H), 6.42 (m, 1H), 7.97–7.77 (m, 4H), 6.46–6.34 (m, 1H), 6.24–6.11 (m, 1H), 3.13 (s, 3H), 2.93 (s, 3H), δ 2.32 (s, 3H).

**2-(3-Methylpyrazol-1-yl)-6-(1H-pyrazol-3-yl)pyridine (Me-1,3bpp).** A large excess of hydrazine monohydrate (2.5 mL, 50 mmol) was added to a methanolic solution (25 mL) of 1-(6-(3-methyl-pyrazol-1-yl)-pyridin-2-yl)-3-(dimethylamino) prop-2-en-1-one (2.77 g, 10.8 mmol) and the mixture stirred and refluxed overnight.

Subsequently, the resulting solution was cooled to room temperature, producing a pale-yellow precipitate that was filtered, washed with water and diethyl ether and dried in air to afford the product as a white powder (1.5 g, 62%). <sup>1</sup>H-NMR (400 MHz, CDCl<sub>3</sub>, ppm): δ 11.11–10.20 (m, 1H), 8.45 (d, J = 2.4 Hz, 1H), 7.83–7.72 (m, 1H), 7.60 (d, J = 1.9 Hz, 1H), 7.51 (s, 1H), 6.78 (s, 1H), 6.22 (d, J = 2.5 Hz, 1H), 2.33 (s, 1H).

**1-(6-(3,5-Dimethylpyrazol-1-yl)pyridin-2-yl)ethanone. (iii)** To a solution of 1-(6-bromopyridin-2-yl)ethanone (2.25 g, 11.3 mmol) in toluene (5 mL) were added, under a N<sub>2</sub> atmosphere, 3,5-di-methylpyrazole (0.9 g, 9.36 mmol), 1,10-phenanthroline monohydrate (0.37 g, 1.9 mmol), CuI (0.1 g, 0.5 mmol) and K<sub>2</sub>CO<sub>3</sub> (3.2 g, 23.15 mmol). The resulting dark brown mixture was heated to reflux and vigorously stirred overnight. After cooling to room temperature, ethyl acetate (20 mL) and water (20 mL) were added and the organic layer isolated. The aqueous solution was extracted two additional times with ethyl acetate and the organic phases were recombined, washed with brine, dried with MgSO<sub>4</sub> and evaporated under vacuum. Column chromatography (7:3 hexanes/ethyl acetate) provided 0.66 g (32% yield) of the title compound as a white solid. <sup>1</sup>H-NMR (400 MHz, CDCl<sub>3</sub>, ppm): δ 8.13 (dd, J = 7.8, 1.4 Hz, 1H), 8.00–7.87 (m, 2H), 7.97–7.8 (m, 2H), 6.04 (s, 1H), 2.76 (s, 3H), 2.76 (s, 3H), 2.70 (s, 3H), 2.31 (s, 3H).

**1-(6-(3,5-Dimethylpyrazol-1-yl)-pyridin-2-yl)-3-(dimethylamino)prop-2-en-1-one. (iv)** N,N-Dimethylformamide-dimethyl acetal (0.3 mL, 2.23 mmol) was added to 1-(6-(3,5-dimethylpyrazol-1-yl)-(1H-pyrazol-1-yl)pyridin-2-yl)ethanone (0.66 g, 3.1 mmol) and the mixture was heated to reflux (110 °C) and stirred overnight. After cooling to room temperature, the resulting dark yellow solution was concentrated under vacuum to yield the product as a pale brown solid (0.83 g, 87%). <sup>1</sup>H-NMR (400 MHz, CDCl<sub>3</sub>, ppm): δ 8.02–7.86 (m, 4H), 6.45 (d, J = 12.7 Hz, 1H), 6.02 (s, 1H), 3.19 (s, 3H), 2.96 (s, 3H), 2.78 (s, 3H), 2.31 (s, 3H).

**2-(3,5-Dimethylpyrazol-1-yl)-6-(1H-pyrazol-3-yl)pyridine (Me<sub>2</sub>-1,3bpp).** An excess of hydrazine monohydrate (0.1 mL, 1.35 mmol) was added to an ethanolic solution (5 mL) of 1-(6-(3,5-dimethylpyrazol-1-yl)-pyridin-2-yl)-3-(dimethylamino)prop-2-en-1-one (0.72 g, 0.27 mmol) and the mixture was stirred and



refluxed overnight. The resulting solution was cooled to room temperature and water (5 mL) was added. The organic phase was separated by decantation. The aqueous phase was extracted three times with CH<sub>2</sub>Cl<sub>2</sub> (10 ml), and the organic layers were then combined, washed with brine, dried with MgSO<sub>4</sub> and evaporated under vacuum to afford the product as a pale brown solid (0.52 g, 80%). <sup>1</sup>H-NMR (400 MHz, CDCl<sub>3</sub>, ppm): δ 10.67 (s, 1H), 7.83–7.82 (m, 2H), 7.66 (d, J = 2.1, 1H), 7.6 (s, 1H), 6.82 (d, J = 2.0, 1H), 6.04 (s, 1H), 2.74 (s, 3H), 2.32 (s, 3H).

**[Fe(Me-1,3bpp)<sub>2</sub>](ClO<sub>4</sub>)<sub>2</sub> (2).** To a solution of Fe(ClO<sub>4</sub>)<sub>2</sub>·6H<sub>2</sub>O (0.023 g, 0.065 mmol) and ascorbic acid (~2 mg) in absolute ethanol (10 mL) was added dropwise a solution of met1,3bpp (0.027 g, 0.12 mmol) in absolute ethanol (10 mL). The resulting dark yellow solution was stirred for 40 minutes at room temperature. The solution was then filtered and layered with hexane (1:1 vol.). Yellow crystals of the product suitable for single crystal X-ray diffraction were obtained after 4 days. Yield: 43.2%. EA, calcd (%) for C<sub>24</sub>H<sub>22</sub>Cl<sub>2</sub>FeN<sub>10</sub>O<sub>8</sub> (found): C, 40.87 (41.04); H, 3.14 (3.01); N, 19.86 (19.06).

**[Fe(Me<sub>2</sub>-1,3bpp)<sub>2</sub>](ClO<sub>4</sub>)<sub>2</sub> (3).** To a solution of Fe(ClO<sub>4</sub>)<sub>2</sub>·6H<sub>2</sub>O (0.023 g, 0.065 mmol) and ascorbic acid (~2 mg) in dry acetone (10 mL) was added dropwise a solution of 2met1,3bpp (0.029 g, 0.12 mmol) in dry acetone (10 mL). In this case, the resulting red solution was stirred for 40 minutes, filtered, and layered with diethyl ether. 3–4 days later, red crystals of the product of good quality for single crystal X-ray diffraction were obtained. Yield: 60.1%. EA, calcd (%) for C<sub>26</sub>H<sub>26</sub>Cl<sub>2</sub>FeN<sub>10</sub>O<sub>8</sub> (found): C, 42.59 (43.03); H, 3.57 (3.22); N, 19.10 (18.96).

## 2.5. References

- (1) Real, J. A.; Gaspar, A. B.; Muñoz, M. C. *Dalt. Trans.* **2005**, 12, 2062–2079.
- (2) Gütlich, P.; Goodwin, H. A. In *Spin Crossover in Transition Metal Compounds I, Topics in Current Chemistry*; Gütlich, P., Goodwin, H. A., Eds.; Springer, 2004; Vol. 233, pp 1–47.
- (3) Halcrow, M. *Crystals* **2016**, 6, 58.
- (4) Tao, J.; Wei, R. J.; Huang, R. Bin; Zheng, L. S. *Chem. Soc. Rev.* **2012**, 41, 703–737.
- (5) Halcrow, M. A. In *Spin-Crossover Materials: properties and Applications*; John Wiley

- & Sons, Ltd., 2013; pp 147–169.
- (6) Guionneau, P. *Dalt. Trans.* **2014**, *43*, 382–393.
- (7) Fumanal, M.; Jiménez-Grávalos, F.; Ribas-Arino, J.; Vela, S. *Inorg. Chem.* **2017**, *56*, 4474–4483.
- (8) Ni, Z.; Shores, M. P. *J. Am. Chem. Soc.* **2009**, *131*, 32–33.
- (9) Barrett, S. A.; Halcrow, M. A. *RSC Adv.* **2014**, *4*, 11240–11243.
- (10) Young, M. C.; Liew, E.; Ashby, J.; McCoy, K. E.; Hooley, R. J. *Chem. Commun.* **2013**, *49*, 6331–6333.
- (11) Shores, M. P.; Klug, C. M.; Fiedler, S. R. In *Spin-Crossover Materials*; Halcrow, M. A., Ed.; John Wiley & Sons Ltd: Oxford, UK, 2013; pp 281–301.
- (12) Bonnet, S.; Molnár, G.; Costa, J. S.; Siegler, M. A.; Spek, A. L.; Bousseksou, A.; Fu, W. T.; Gamez, P.; Reedijk, J. *Chem. Mater.* **2009**, *21*, 1123–1136.
- (13) Wei, R. J.; Tao, J.; Huang, R. Bin; Zheng, L. S. *Inorg. Chem.* **2011**, *50*, 8553–8564.
- (14) Zhang, W.; Zhao, F.; Liu, T.; Yuan, M.; Wang, Z. M.; Gao, S. *Inorg. Chem.* **2007**, *46*, 2541–2555.
- (15) Craig, G. A.; Costa, J. S.; Roubeau, O.; Teat, S. J.; Aromí, G. *Chem. - A Eur. J.* **2012**, *18*, 11703–11715.
- (16) Costa, J. S.; Rodríguez-Jiménez, S.; Craig, G. A.; Barth, B.; Beavers, C. M.; Teat, S. J.; Aromí, G. *J. Am. Chem. Soc.* **2014**, *136*, 3869–3874.
- (17) Barrios, L. A.; Bartual-Murgui, C.; Peyrecave-Lleixà, E.; Le Guennic, B.; Teat, S. J.; Roubeau, O.; Aromí, G. *Inorg. Chem.* **2016**, *55*, 4110–4116.
- (18) Cook, L. J. K.; Kulmaczewski, R.; Cespedes, O.; Halcrow, M. A. *Chem. - A Eur. J.* **2016**, *22*, 1789–1799.
- (19) Miller, R. G.; Brooker, S. *Chem. Sci.* **2016**, *7*, 2501–2505.
- (20) Rodríguez-Jiménez, S.; Feltham, H. L. C.; Brooker, S. *Angew. Chem., Int. Ed.* **2016**, *55*, 15067–15071.
- (21) Steinert, M.; Schneider, B.; Dechert, S.; Demeshko, S.; Meyer, F. *Angew. Chem., Int. Ed.* **2014**, *53*, 6135–6139.
- (22) Bartual-Murgui, C.; Codina, C.; Roubeau, O.; Aromí, G. *Chem. Eur. J.* **2016**, *22*, 12767–12776.
- (23) Park, J. G.; Jeon, I. R.; Harris, T. D. *Inorg. Chem.* **2015**, *54*, 359–369.
- (24) Nakano, K.; Suemura, N.; Yoneda, K.; Kawata, S.; Kaizaki, S. *Dalt. Trans.* **2005**, *2*, 740–743.
- (25) Kershaw Cook, L. J.; Kulmaczewski, R.; Mohammed, R.; Dudley, S.; Barrett, S. A.; Little, M. A.; Deeth, R. J.; Halcrow, M. A. *Angew. Chem., Int. Ed.* **2016**, *55*, 4327–4331.
- (26) Hoselton, M. A.; Wilson, L. J.; Drago, R. S. *J. Am. Chem. Soc.* **1975**, *97*, 1722–1729.

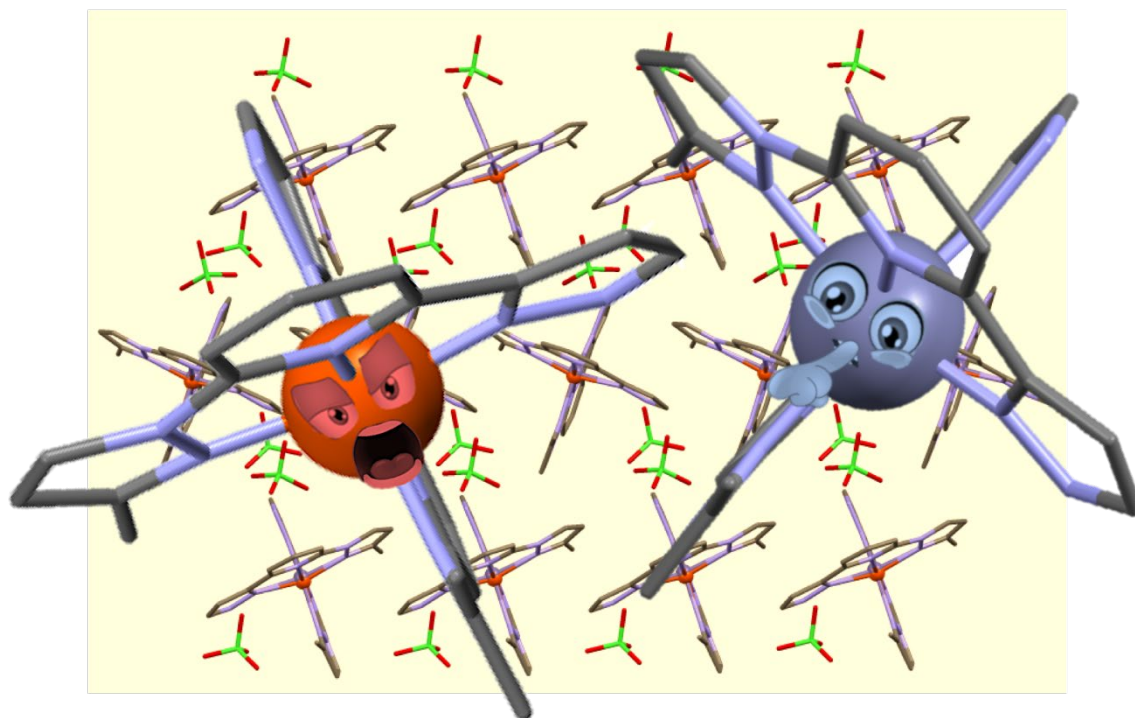
- (27) Onggo, D.; Hook, J. M.; Rae, A. D.; Goodwin, H. A. *Inorg. Chim. Acta.* **1990**, *173*, 19–30.
- (28) Goodwin, H. A. *Aust. J. Chem.* **1991**, *44*, 1539–1551.
- (29) Zang, Y.; Kim, J.; Dong, Y.; Wilkinson, E. C.; Appelman, E. H.; Que, L. *J. Am. Chem. Soc.* **1997**, *119*, 4197–4205.
- (30) Holland, J. M.; McAllister, J. A.; Kilner, C. A.; Thornton-Pett, M.; Bridgeman, A. J.; Halcrow, M. A. *J. Chem. Soc., Dalt. Trans.* **2002**, 548–554.
- (31) Roberts, T. D.; Little, M. A.; Tuna, F.; Kilner, C. A.; Halcrow, M. A. *Chem. Commun.* **2013**, *49*, 6280.
- (32) Holland, J. M.; Barrett, S. A.; Kilner, C. A.; Halcrow, M. A. *Inorg. Chem. Commun.* **2002**, *5*, 328–332.
- (33) Elhaïk, J.; Evans, D. J.; Kilner, C. A.; Halcrow, M. A. *Dalt. Trans.* **2005**, 1693–1700.
- (34) Santoro, A.; Kershaw Cook, L. J.; Kulmaczewski, R.; Barrett, S. A.; Cespedes, O.; Halcrow, M. A. *Inorg. Chem.* **2015**, *54*, 682–693.
- (35) Bartual-Murgui, C.; Vela, S.; Roubeau, O.; Aromí, G. *Dalt. Trans.* **2016**, *45*, 14058–14062.
- (36) Hamon, P.; Thépot, J. Y.; Le Floch, M.; Boulon, M. E.; Cador, O.; Golhen, S.; Ouahab, L.; Fadel, L.; Saillard, J. Y.; Hamon, J. R. *Angew. Chem., Int. Ed.* **2008**, *47*, 8687–8691.
- (37) Cristau, H. J.; Cellier, P. P.; Spindler, J. F.; Taillefer, M. *Eur. J. Org. Chem.* **2004**, 695–709.
- (38) Abu-Shanab, F. A.; Sherif, M. S.; Mousa, S. A. S. *J. Heterocycl. Chem.* **2009**, *46*, 801–827.
- (39) Guionneau, P.; Marchivie, M.; Bravic, G.; Létard, J. F.; Chasseau, D. *J. Mater. Chem.* **2002**, *12*, 2546–2551.
- (40) Marchivie, M.; Guionneau, P.; Létard, J. F.; Chasseau, D. *Acta Crystallogr., Sect. B Struct. Sci.*, **2005**, *61*, 25–28.
- (41) Craig, G. A.; Roubeau, O.; Aromí, G. *Coord. Chem. Rev.* **2014**, *269*, 13–31.
- (42) Sorai, M.; Seki, S. *J. Phys. Chem. Solids* **1974**, *35*, 555–570.
- (43) Sorai, M.; Nakazawa, Y.; Nakano, M.; Miyazaki, Y. *Chem. Rev.* **2013**, *113*.
- (44) Roubeau, O.; Castro, M.; Burriel, R.; Haasnoot, J. G.; Reedijk, J. *J. Phys. Chem. B* **2011**, *115*, 3003–3012.
- (45) Arcis-Castillo, Z.; Zheng, S.; Siegler, M. A.; Roubeau, O.; Bedoui, S.; Bonnet, S. *Chem. - A Eur. J.* **2011**, *17*, 14826–14836.
- (46) Evans, D. F. *J. Chem. Soc.* **1959**, 2003–2005.
- (47) Sur, S. K. *J. Magn. Reson.* **1989**, *82*, 169–173.
- (48) Grant, D. H. *J. Chem. Educ.* **1995**, *72*, 39.
- (49) Tan, D.; Xie, J.; Li, Q.; Li, H.; Li, J.; Li, H.; Lang, J. *Dalt. Trans.* **2014**, *43*, 14061–14071.



# CHAPTER 3

---

## THE EFFECT OF METAL COMPOSITION ON THE THERMAL SPIN TRANSITION OF $[\text{Fe}_x\text{Zn}_{1-x}(\text{Me-bpp})_2](\text{ClO}_4)_2$ MOLECULAR ALLOYS





### 3. THE EFFECT OF METAL COMPOSITION ON THE THERMAL SPIN TRANSITION OF $[\text{Fe}(\text{Me-bpp})_2](\text{ClO}_4)_2$ MOLECULAR ALLOYS

#### Abstract

Metal dilution effects on the spin-crossover (SCO) thermal transition of the  $[\text{Fe}(\text{Me-1,3bpp})_2](\text{ClO}_4)_2$  (**2**) compound are reported. Diluted solid solutions with the formula  $[\text{Fe}_x\text{Zn}_{1-x}(\text{Me-1,3bpp})_2](\text{ClO}_4)_2$  (**5x**; x: 0.1, 0.153, 0.219, 0.333, 0.412, 0.476, 0.559 and 0.636) and the non-active SCO complex with Zn(II),  $[\text{Zn}(\text{Me-1,3bpp})_2](\text{ClO}_4)_2$  (**4**) were synthesised and characterized by single-crystal X-ray diffraction. Comparisons of the structural data and powder diffraction patterns for all the compounds with the reported compound **2** demonstrate the isostructurality among them. The cooperativity of the parent SCO-active Fe(II) complex diminishes monotonically upon dilution. The increase of Zn amounts also cause a decrease of  $T_{1/2}$  ( $T_{1/2} = 183\text{K}$ , compound **2**) in line with the negative chemical pressure when the Zn(II) complexes are incorporated into the Fe(II) lattice. The gradual variation of the magnetic properties as the composition changes correlate with the evolution of the structural parameters at the molecular, intermolecular and crystal lattice scales. Upon warming, the relaxation temperature of the metastable states is nearly constant for all compositions when a portion of the Fe(II) are thermally trapped by quenching the crystals at 2K.

#### 3.1. Introduction

Salient nanotechnological applications such as room temperature data storage within SCO materials<sup>1-3</sup> are feasible when these prototypes display high cooperativity, conferring even hysteresis to the system.<sup>4</sup> Achieving bistable molecular architectures or predicting the SCO behaviour by chemical design in terms of thermodynamic parameters and kinetic properties is still challenging since a large number of superimposed variables play a role. Regarding the specific property of cooperativity, some theoretical models have been proposed to rationalize the properties of spin-change propagation through the lattice.<sup>5,6</sup> From the experimental viewpoint, several synthetic approaches have been proposed to reach the target SCO systems with highly effective cooperativity. These synthetic

efforts focus on influencing the type, nature and strength of the interactions between the spin active species (*i.e.* Fe(II) centres). One approach is to introduce covalent links between them, building extended 1-,2- or 3D polymeric systems.<sup>2,7-9</sup> Another relevant strategy relies on the increase of weak intermolecular interactions like hydrogen bonds<sup>10</sup> or  $\pi\cdots\pi$  stacking interactions between the Fe(II) complexes.<sup>10-12</sup> With regard to this, the precise role of crystal packing of a given set of components can be studied when some polymorphs of a given SCO-active compound are available. Such studies are rare and have evidenced the dramatic impact of the specific lattice organization on the various SCO parameters, including the cooperativity.<sup>13-15</sup> One case is exemplified in the previous chapter.<sup>16</sup> Another pertinent study to investigate the cooperative of SCO-active complexes deals with the monitorization of the doping effect of their lattice with different amounts of non-active SCO complexes with the same molecular structure as the parent ones. Ideally, the resulting molecular alloys are isostructural to the active ones. Most often, networks of Fe(II) complexes have been doped with their silent Zn(II) analogue,<sup>17-27</sup> but other metal ions ( $\text{Mn}^{2+}$ ,  $\text{Co}^{2+}$ ,  $\text{Ni}^{2+}$ ,  $\text{Cd}^{2+}$ ) have also been introduced as a dopant into the Fe(II) lattice.<sup>17,19,24-26,28-33</sup> The main effect of doping with a silent metal is a decrease in cooperativity ascribed to the inclusion of complexes that do not undergo structural changes while the spin active species experience the SCO, thus disrupting its propagation. The solid dilution also shifts the  $T_{1/2}$  to lower temperatures. This decrease occurs because the ionic radius of the M(II) center of the dopant,  $r(\text{M}^{2+})$ , is either larger than that of HS Fe(II), ( $r(\text{Fe}_{\text{HS}}^{2+}) = 78$  pm), or in between the latter and that of LS Fe(II), ( $r(\text{Fe}_{\text{LS}}^{2+}) = 61$  pm). This causes a negative chemical pressure on the Fe(II) centres of the lattice that encumbers their HS-to-LS transition, effectively stabilizing the HS state. Additionally, the negative chemical pressure exerted by the dopant can cause a remaining amount of residual HS centres at low temperature upon thermal SCO to the LS state. This residual HS increases as the concentration of the dopant is larger. It is well-known that the HS state can be trapped at low temperature as a metastable excited state by irradiating the material when laying in a stable LS state with light. This phenomenon is called light-induced excited spin state trapping (LIESST).<sup>34,35</sup> The LIESST effect may be characterized by the  $T(\text{LIESST})$  temperature at which the metastable HS state relaxes back to the stable LS state when increasing the temperature up to a certain value that activates a



thermal relaxation regime.<sup>36</sup> The  $T_{1/2}$  and  $T(\text{LIESST})$  are related according to the so-called inverse energy-gap law,<sup>37</sup> by which if  $T_{1/2}$  decreases,  $T(\text{LIESST})$  increases.<sup>38</sup> In a similar way, the HS state may also be retained as a metastable state when decreasing suddenly and sufficiently the temperature in a system lying initially in the HS state.<sup>39,40</sup> This HS state quenching assisted thermally is known as thermally-induced excited spin state trapping (TIESST), and its relative temperature of the thermal relaxation is the  $T(\text{TIESST})$ . The  $T(\text{LIESST})$  dependence with the composition of the metal dilutions of SCO systems has been investigated.<sup>21,41</sup> In the case where Zn(II) ( $r(\text{Zn}^{2+}) = 74$  pm) was used as dopant, contrary to  $T_{1/2}$ ,  $T(\text{LIESST})$  remains almost the same, which contradicts the inverse energy-gap law.<sup>21,41</sup> Conversely, if Ni(II) (with smaller  $r(\text{Ni}^{2+})$ ; 69 pm) is used,  $T(\text{LIESST})$  decreases upon increasing the amount of dopant.<sup>19,28</sup> Instead, doping the  $[\text{Fe}(\text{phen})_2(\text{NCS})_2]$  (phen = phenantroline) lattice with Cd(II) complexes, which causes a markedly shift of  $T_{1/2}$  towards lower temperatures due to the large chemical pressure exerted by the bigger metal ion ( $r(\text{Cd}^{2+}) = 95$  pm), cause an increase of the  $T(\text{LIESST})$ .<sup>19</sup> In the same way, doping the  $[\text{Fe}(\text{bpp})_2](\text{BF}_4)_2$  (bpp = 2,6-bis-pyrazolylpyridine) lattice with HS Mn(II), ( $r(\text{Mn}_{\text{HS}^{2+}}) = 78$  pm) a similar behaviour was revealed, *ie.* an increase of  $T(\text{LIESST})$  with the dopant.<sup>24</sup> These observations highlight that several factors influence the relaxation of the metastable state induced by light in molecular alloys; i) the cooperativity, which is reduced dramatically with the doping, plays a role in propagating the relaxation, ii) the inverse energy-gap law is explained with local thermodynamic arguments based on the relation between the potential well of both states, iii) the internal chemical pressure caused by the doping plays an important role on the spin transition processes, including this thermal relaxation. The influence of the composition of doped Fe(II) lattices on the relaxation of their thermally trapped HS state, specifically on  $T(\text{TIESST})$ , has been very little explored, although the trends are expected to be the same as for  $T(\text{LIESST})$ . One of the few cases investigated is that of Mn(II) doped  $[\text{Fe}(\text{bpp})_2](\text{BF}_4)_2$ , which reveals indeed that the relaxation of the metastable state produced by thermal quenching exhibits the same tendency as that seen for the photoinduced HS state.<sup>33</sup> However, more studies are needed to confirm this parallelism.

In Chapter 2, the SCO properties of complexes  $[\text{Fe}(\text{Me-1,3bpp})_2](\text{ClO}_4)_2$  (**2**) and  $[\text{Fe}(\text{Me}_2\text{-1,3bpp})_2](\text{ClO}_4)_2$  (**3**) (Me-1,3bpp = 2-(3-methyl-pyrazol-1-yl)-6-(pyrazol-3-yl)pyridine; Me<sub>2</sub>-1,3bpp = 2-(3,5-dimethyl-pyrazol-1-yl)-6-(pyrazol-3-yl)pyridine, Figure 3.1) were presented. We elucidated the effect of the methyl substituents of the bpp ligand on the parameters of the spin transition and its cooperativity.<sup>16</sup> Both complexes display abrupt SCO transitions at very distinct temperatures ( $T_{1/2}$  = 183 and 378 K, respectively). In turn, the properties of a series of the crystalline solid solution containing complexes with both ligands combined in different ratios were studied by the group, revealing a fascinating allosteric effect to the SCO.<sup>42</sup> Since all crystalline compounds are solvent-free (*i.e.* no crystallization solvent is present in their lattice), they are ideal for studying solid solutions. Changing only the metal centre on the lattice along with a series of compounds, would allow for a tangible solid dilution. Therefore, we prepared a series of solid solutions of  $[\text{Fe}(\text{Me-1,3bpp})_2](\text{ClO}_4)_2$  (**2**) and  $[\text{Zn}(\text{Me-1,3bpp})_2](\text{ClO}_4)_2$  (**4**) with different metal compositions described by the formula  $[\text{Fe}_x\text{Zn}_{1-x}(\text{Me-1,3bpp})_2](\text{ClO}_4)_2$  (**5x**; x: 0.1, 0.153, 0.219, 0.333, 0.412, 0.476, 0.559 and 0.636). The molecular structure of all the composite system of **5x** was determined and analysed by single crystal X-ray diffraction (SCXRD). Thus, the structural evolution of the molecular materials was fully monitored in detail as the composition gradually changes. This detailed structural knowledge represents an unprecedented development among studies of doped SCO materials. The exact amount of the metal composition for **5x** was determined from inductively coupled plasma-optical emission spectrometry (ICP-OES) results. All compounds have also been characterized by elemental analysis, powder X-ray diffraction (PXRD) and mass spectrometry. In light of the structural changes associated to the increase of the Zn(II) amount as dopant into **2**, the effect on the SCO process has been analysed by means of bulk magnetic measurements at variable temperature. All members of this series were thermally quenched at 2K, generating a small portion of their Fe(II) complexes trapped as a metastable HS state, which partially relaxes to the LS state upon warming. This is the first analysis of the dependence of the temperature of relaxation (determined approximately and called  $T_{\text{relax}}$ ) carried in SCO doped lattices.



$[\text{Fe}_x\text{Zn}_{1-x}(\text{Me-1,3bpp})_2](\text{ClO}_4)_2$  (**4** or **5x**). The Fe:Zn ratios of the crystalline samples (**5x**) were quantitatively determined by (ICP-OES) metal trace analysis (Table A3.1; Appendix 3) and were consistent with the SCXRD data (see below). The amount of iron found for each isolated crystalline sample ( $x$ ) was found to be slightly lower than the original Fe-to Zn ratio used experimentally (Figure 3.2). It reflects the relative thermodynamic stabilities of the various mixtures in the solid-state versus the solution phase. Indeed, a change of regime in the ratio seems to occur when the reactions solvent changes from only acetone to the 1:1 mixture of ethanol/acetone.

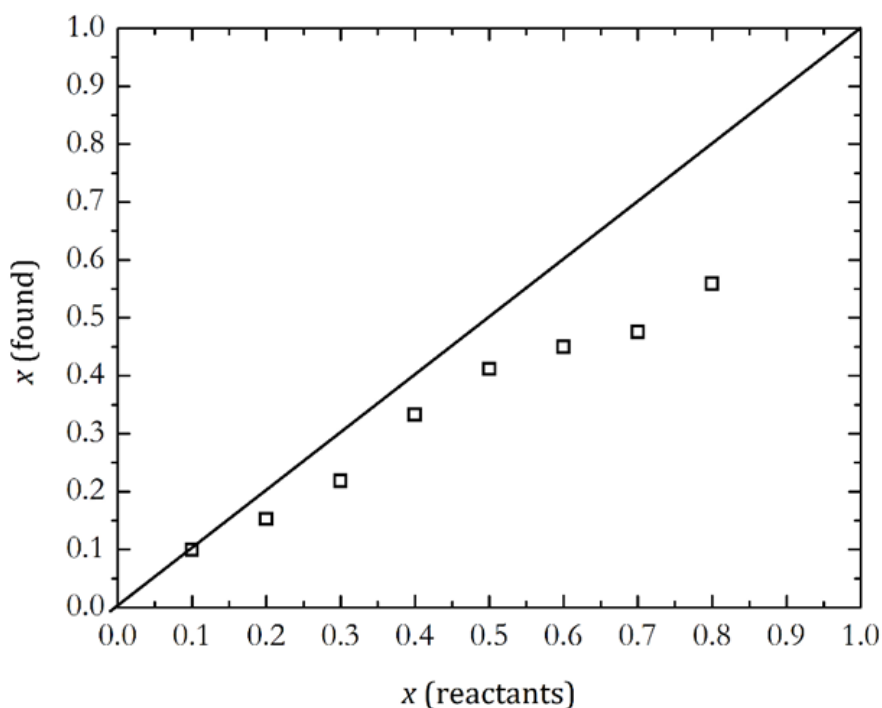


Figure 3.2. Iron fractions ( $x$ ) present in the series  $[\text{Fe}_x\text{Zn}_{1-x}(\text{Me-1,3bpp})_2](\text{ClO}_4)_2$  (**5x**) as detected by ICP-OES plotted versus the fractions employed in the reactants for their preparation. The diagonal line is a reference.

Elemental analysis matches the chemical compositions of all crystals (**4** and **5x**), considering that the samples absorb a small amount of water from the atmosphere (<1equiv, Table A3.2; Appendix 3). Additionally, the positive-ion MALDI MS spectra of the alloy with  $x=0.22$  was compared with that of compounds **2** and **4**, respectively. The solid solution has both peak of the corresponding individual molecular components at  $m/z = 505.1$  for  $[\text{FeC}_{24}\text{H}_{21}\text{N}_{10}]^+$  and  $m/z = 513.1$  for  $[\text{ZnC}_{24}\text{H}_{21}\text{N}_{10}]^+$ , respectively, with their respective isotropic distribution (Figure A3.2; Appendix 3). All these observations confirmed that homogeneous solid solutions of complexes of  $[\text{Fe}(\text{Me-1,3bpp})_2](\text{ClO}_4)_2$  (**2**) and  $[\text{Zn}(\text{Me-1,3bpp})_2](\text{ClO}_4)_2$  (**4**) with a wide range of

compositions can be prepared to study the effect of the composition on the key parameters and cooperativity of the SCO of Fe (II).

### Structure of $[\text{Fe}(\text{Me-1,3bpp})_2](\text{ClO}_4)_2$ (**2**) and $[\text{Zn}(\text{Me-1,3bpp})_2](\text{ClO}_4)_2$ (**4**)

The molecular structure of the complex  $[\text{Fe}(\text{Me-1,3bpp})_2](\text{ClO}_4)_2$  (**2**) has been previously reported in chapter 2.

$[\text{Zn}(\text{Me-1,3bpp})_2](\text{ClO}_4)_2$  (**4**). Complex **4** was found in the monoclinic  $C2/c$  space group at 100K. The asymmetric unit consists of one formula unit, with eight such moieties present in the unit cell. The cationic complex displays a distorted octahedral Zn(II) center coordinated to two Me-1,3bpp tris-imine ligands lying in a *mer*-fashion (Figure 3.3). Since the ligands are asymmetric, the complex is chiral and both enantiomers are present in the lattice, which is a racemate. The average of the Zn–N bond distances is 2.16(1) Å, which is coherent with the ionic radius of zinc (II) ( $r=74$  pm) more similar to the HS iron (II) metal radius ( $r=78$  pm), than the LS one ( $r=61$  pm). The distortion parameters  $\Sigma$  and  $\Theta$ , are 137.1(3) and 445.7(6), respectively. Each cation of **4** interacts with its two  $\text{ClO}_4^-$  anions *via* hydrogen bonds with the N–H groups of both Me-1,3bpp ligands (Figure 3.3). The compound is isostructural with the Fe analogue (**2**); an overlay of both asymmetric units shows only subtle atomic displacements between them (Figure A3.3, Table A3.3 Appendix 3).

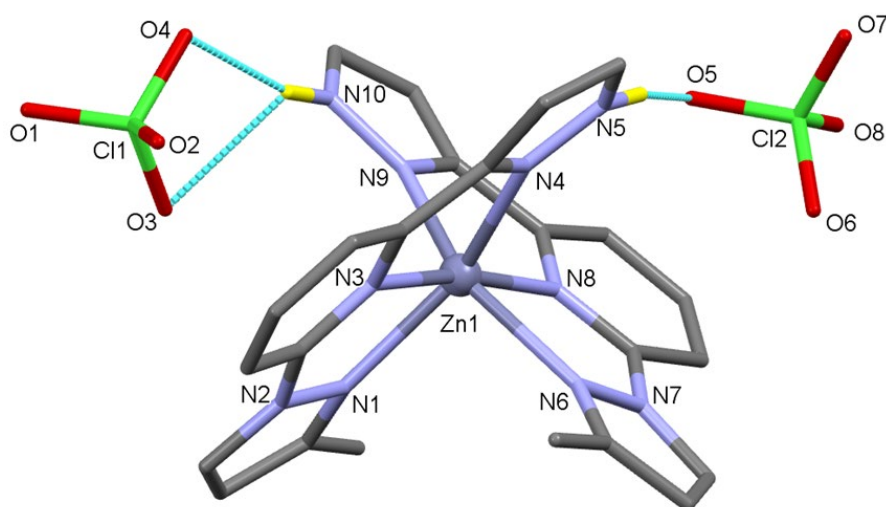


Figure 3.3. Molecular representation of  $[\text{Zn}(\text{Me-1,3bpp})_2](\text{ClO}_4)_2$  (**2**) at 100 K with heteroatoms labelled and C atoms shown in grey. Only H atoms of N–H groups shown (in yellow). Dashed cyan lines are H-bonds.

The  $[\text{Zn}(\text{Me-1,3bpp})_2]^{2+}$  cations are organized in sheets (Figure 3.4 and A3.2, Appendix 2), which alternate arrays of cations in two different orientations (with an angle of  $41.59^\circ$ , Figure A3.5; Appendix 3) and opposite chirality, as seen before with related Fe(II) complexes. Thus, each complex displays the same amount of intermolecular interactions within and between sheets. The former set is established mainly with four first-neighbors (Figure 3.4) in form of two  $\pi\cdots\pi$  contacts and four  $\text{C-H}\cdots\pi$  interactions (see details in Table A3.2 and Figure A3.4; Appendix 3). In between sheets, weaker  $\text{C-H}\cdots\pi$  interactions are established.

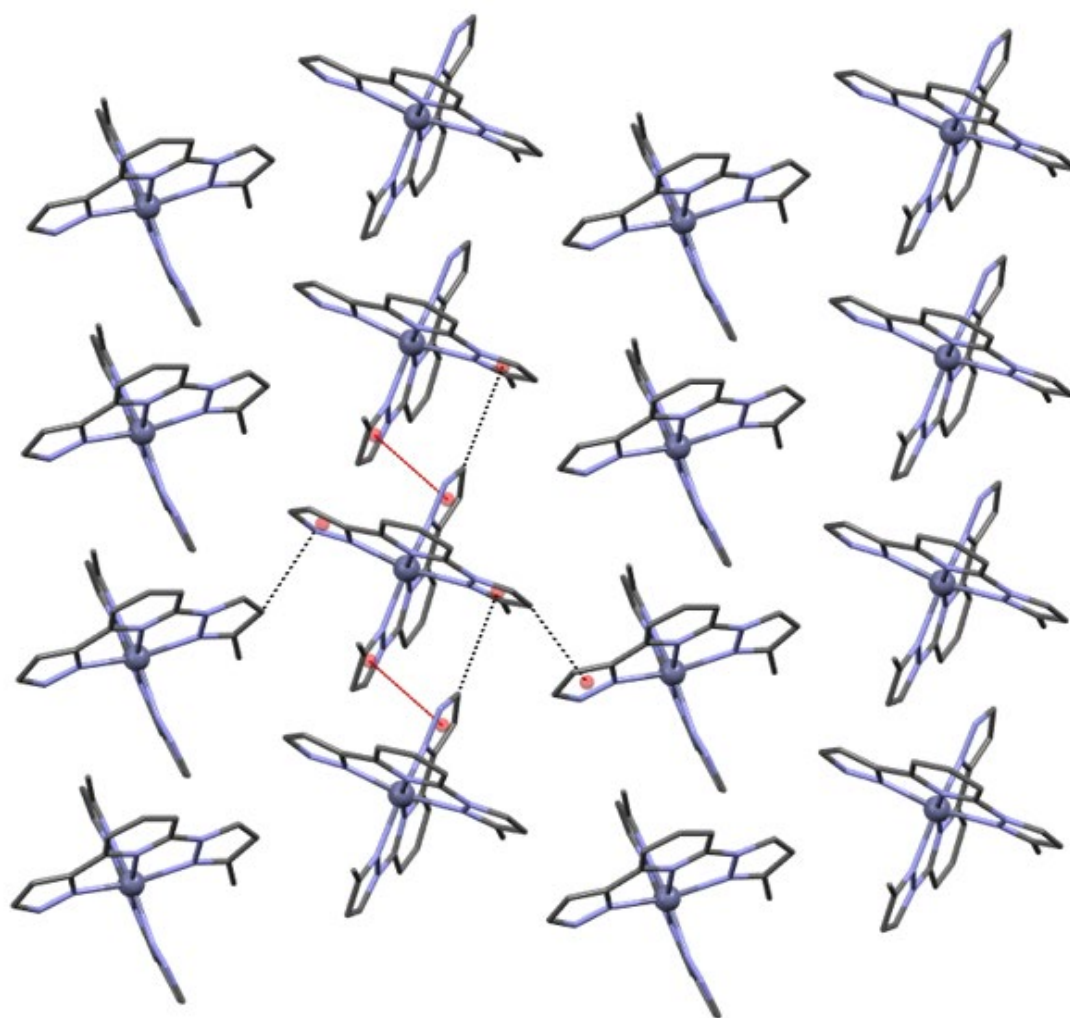


Figure 3.4. Representation of one sheet the cationic  $[\text{Zn}(\text{Me-1,3bpp})_2]^{2+}$  complexes of **4**, emphasizing their two different orientations and the main interatomic interactions that one complex establishes with its neighbors; four  $\text{C-H}\cdots\pi$  contacts (black dashed lines) and two  $\pi\cdots\pi$  bonds (red dashed lines). The centroids of the pyrazolyl rings involved are red balls.

**Structure of the series of solid solutions with formula  $[\text{Fe}_x\text{Zn}_{1-x}(\text{Me-1,3bpp})_2](\text{ClO}_4)_2$  (**5x**)**

**$[\text{Fe}_x\text{Zn}_{1-x}(\text{Me-1,3bpp})_2](\text{ClO}_4)_2$  (**5x**)**. The structural details of the series of solid solutions **5x** ( $x = 0.10, 0.15, 0.22, 0.33, 0.41, 0.48, 0.56, 0.64$ ) were determined by SCXRD at 100 K. The crystals had a pale-yellow colour that fades upon dilution. All the alloys are isostructural among them and with **2** and **4**, displaying very similar cell parameters and the monoclinic  $C2/c$  space group (see the crystal data in Table A3.5; Appendix 3). The simultaneous presence at the position of the metal of both, iron and zinc ions in the averaged model was detected by anomalous thermal parameters at that position. However, their precise atomic positions of each metal could not be discriminated in view of their proximity. The presence of a unique homogeneous crystallographic phase and a sole metal site suggest that both atoms, Fe and Zn, are randomly distributed within the structure. Performing the refinement with a free occupancy factors for Fe and Zn at the same metallic position gave the best model for Zn/Fe ratios that were close to these determined with metal analysis. In two cases ( $x=0.15$  and  $x=0.64$ ) larger deviations were observed. This may result from the refinement, affected by additional restrains introduced due to further disorder of the perchlorate anions (see details in table A3.5; Appendix 3). For all fractions, good quality models were reached (with  $R1$  and  $wR2$  typically of 0.04 and 0.09, respectively). Because of their isostructural nature, the whole arrangement of the components of the alloy within the lattice is identical as in the parent components (**2** and **4**), as are the intermolecular interactions. Most geometric parameters show an appreciable gradual evolution from the values for one end composition,  $[\text{Zn}(\text{Me-1,3bpp})_2](\text{ClO}_4)_2$  ( $x = 0$ ; **4**) to the other  $[\text{Fe}(\text{Me-1,3bpp})_2](\text{ClO}_4)_2$  ( $x = 1$ ; **2**), as a consequence of the progressive replacement of Zn(II) ( $r = 74$  pm) by LS Fe(II) ( $r = 61$  pm). Interestingly, these variations are perceived at the atomic, the molecular and the unit cell scales (Figure 3.5). These observations underly the acquired multiscale dimension of the collective local changes within a crystal lattice when the crystal components are connected through intermolecular interactions.<sup>43</sup>

### 3. The effect of metal dilution on the thermal spin transition

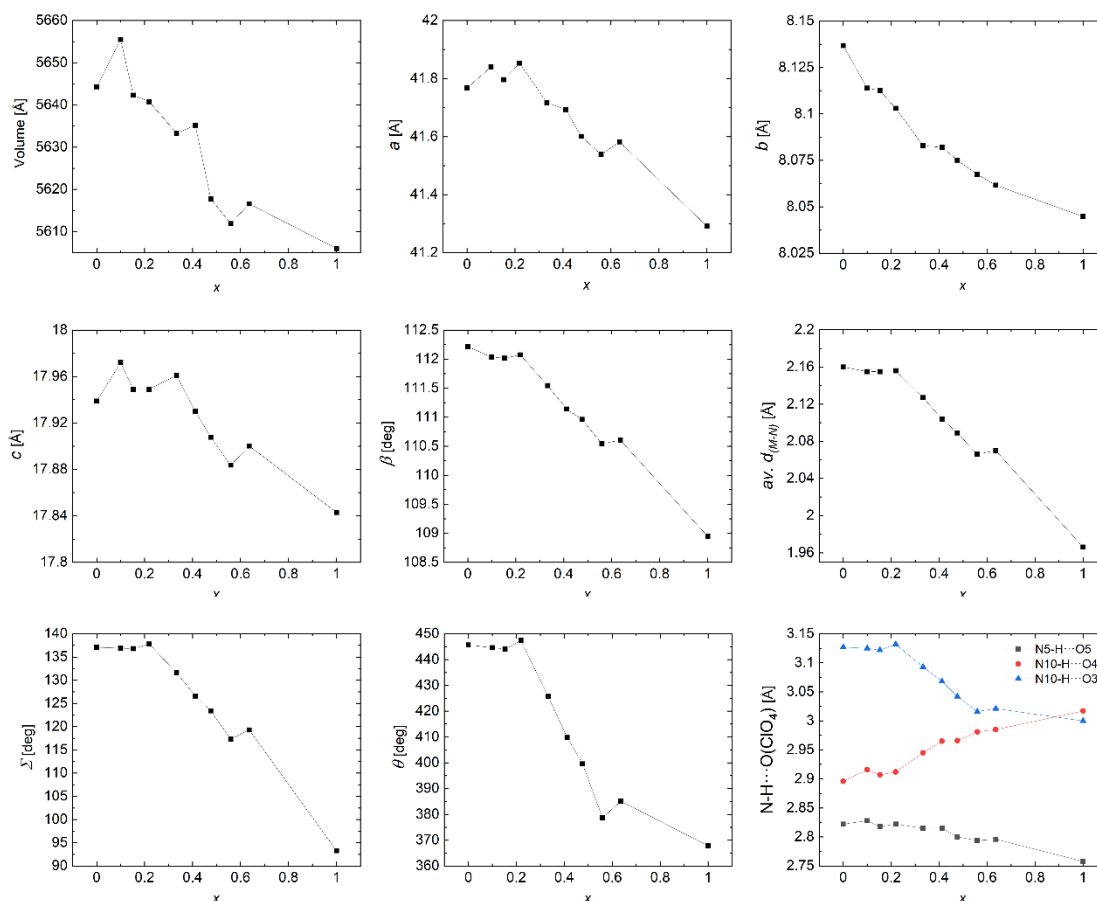


Figure 3.5. Plots of (from left to right and top to bottom) unit cell volume, unit cell parameters  $a$ ,  $b$ ,  $c$  and  $\beta$ , average M-N bond distances (M= Fe/Zn position), distortion parameters  $\Sigma$  and  $\theta$  and N-H...O hydrogen bond distances to perchlorates *versus*  $x$  for the solid solutions  $[\text{Fe}_x\text{Zn}_{1-x}(\text{Me-1,3bpp})_2](\text{ClO}_4)_2$  (**5x**) and compounds **2** and **4**. The systematic anomaly for  $x = 0.636$  coincides with the fact that this data set was refined differently because of the presence of disorder on the  $\text{ClO}_4^-$  anions.

#### Powder X-ray diffraction (PXRD) of the family of compounds

PXRD data were collected in the range  $2\theta = 5-60$  for all the **5x** alloys, as well as for compounds **2** and **4**. Very sharp signals are observed for all the patterns, manifesting the high crystallinity of the phases. All PXRD measures have very similar patterns and show a remarkable continuity in going from one terminal of the composition spectrum to the other (*i.e.* from **2** to **4**, through the successive **5x** compositions), proving that the series of  $[\text{Fe}_x\text{Zn}_{1-x}(\text{Me-1,3bpp})_2](\text{ClO}_4)_2$  are well-defined crystalline solid solutions (Figure 3.6). A direct comparison between the calculated from SCXRD data and PXRD is no possible since the latest were performed at 300K, and the SCXRD were determined at 100K. Additionally, the Fe centres in these systems have a different spin state at each of these two temperatures, which varies the



diffraction patterns significantly. However, the comparison at 300K (where the Fe centres are in the HS state) satisfactorily suits complex **2**, and there is continuity on the 300K over the entire range of compositions. The few additional peaks present in all the compounds of the **5x** series with respect to both pure compounds are attributed to the effect of the disorder at the perchlorate anion featured by all the members of the series and not by the pure compounds. These observations confirm that the crystal lattice is the correct one and it is preserved for the entire series of compounds under study.

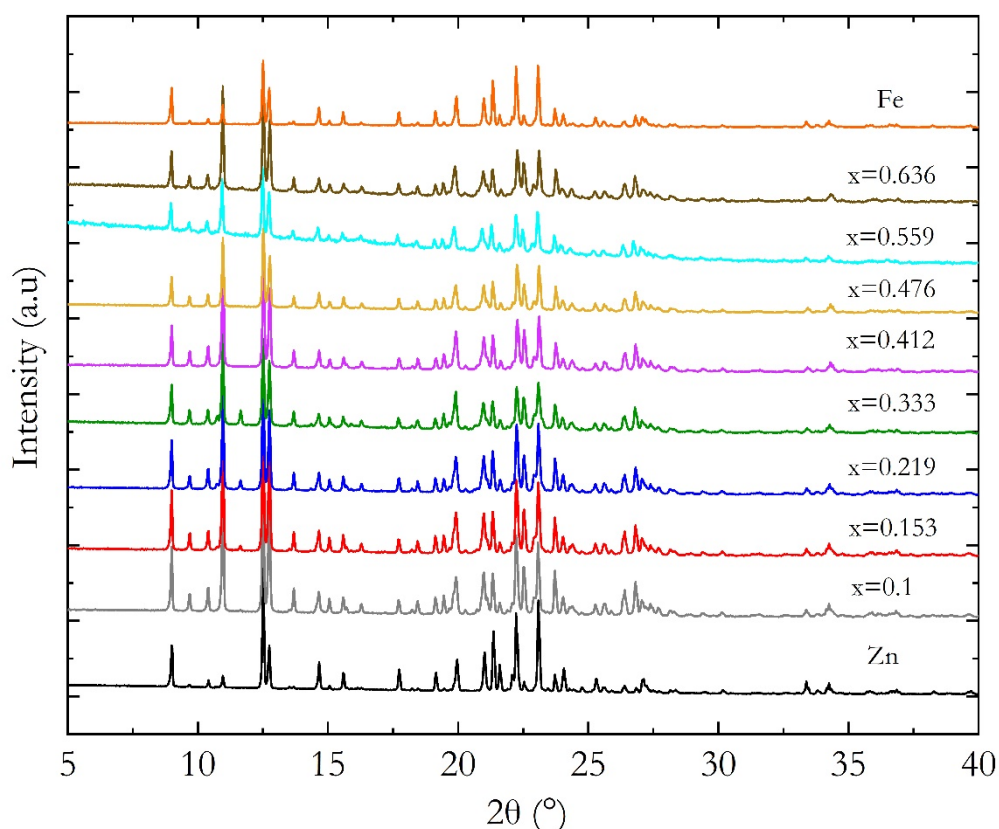


Figure 3.6. Experimental powder X-ray diffractograms of complexes  $[\text{Fe}(\text{Me-1,3bpp})_2](\text{ClO}_4)_2$  (**2**),  $[\text{Zn}(\text{Me-1,3bpp})_2](\text{ClO}_4)_2$  (**4**) and solid solutions  $[\text{Fe}_x\text{Zn}_{1-x}(\text{Me-1,3bpp})_2](\text{ClO}_4)_2$  (**5x**).

#### **Solid-state magnetic properties**

The magnetic properties of the solid solutions of **5x** were investigated using bulk magnetic susceptibility measurements at variable temperature. Notably, we were interested in the resulting SCO behavior of the complex  $[\text{Fe}(\text{Me-1,3bpp})_2](\text{ClO}_4)_2$  when gradually introduced with increasing concentrations into the lattice of  $[\text{Zn}(\text{Me-1,3bpp})_2](\text{ClO}_4)_2$ . Polycrystalline samples of all **5x** compounds were quenched directly from room temperature to 2K. Then, the magnetization was measured upon warming until reaching 300K under a constant external magnetic field of 0.5T. Afterward, the data was collected upon cooling back to 2K in the same conditions, and then, upon warming again to 300K. The data for all compounds are represented as  $\chi T$  vs  $T$  plots. Figure 3.7 (left) shows the first jump of  $\chi T$  in the warming mode from 2K. It reaches a plateau until around 74K that drops at 80K approximately. Then, it reaches a minimum upon further warming followed by an immediate increase of  $\chi T$  vs  $T$ , which levels off around 175K and remains approximately constant until 300K. Upon cooling, the  $\chi T$  vs  $T$  plots follow the inverse path as for the warming mode until it reaches the minimum. Below this point, this time, the decrease is succeeded directly by a lower plateau (Figure 3.7, right). The  $\chi T$  vs  $T$  plots of the following warming mode (from 2 to 300K) superimposes to the previous cooling (from 300 to 2K). The first increase follows from the consequences of the initial quenching, causing results the thermal trapping of some of the  $[\text{Fe}(\text{Me-1,3bpp})_2]^{2+}$  species in a metastable high-spin (HS) state, subject to zero-field splitting effects<sup>44,45</sup> at the lowest temperature. The subsequent decline of  $\chi T$  towards a minimum results from the thermal relaxation of the species trapped in the HS state to the low-spin (LS) state, which is stable in this temperature range. The subsequent  $\chi T$  increase is the thermal SCO transition of the Fe (II) centres. This SCO transition is reversed upon cooling back from 300K, concluding at around 80K. Now, the  $\chi T$  values of the low temperature plateau are lower than the ones obtained after the first thermal quenching. The molar paramagnetic response of all the **5x** solid solutions is proportional to the fraction content of iron (x). For instance,  $\chi T$  ranges 2.24 to 0.34  $\text{cm}^3\text{Kmol}^{-1}$  in changing x from 0.64 to 0.10, at 300K (Figure 3.7).

### 3. The effect of metal dilution on the thermal spin transition

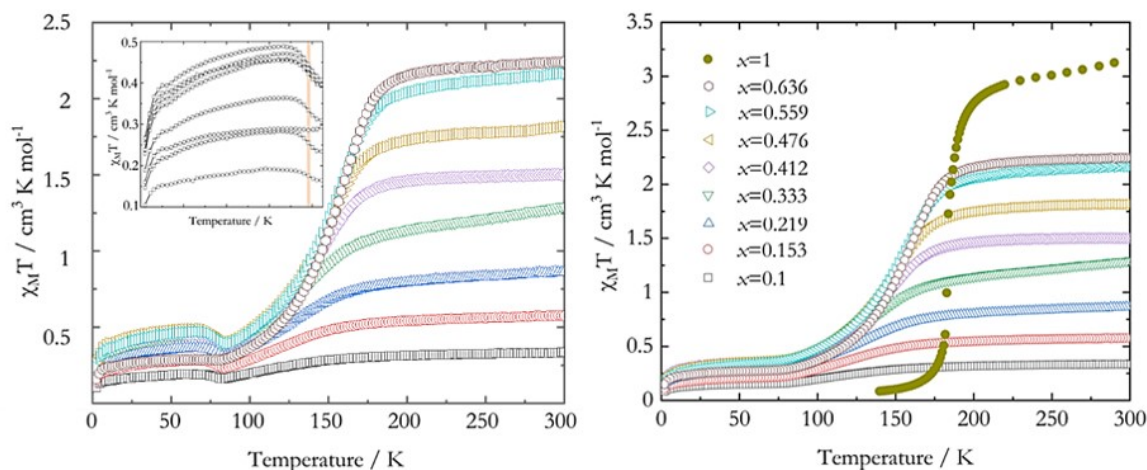


Figure 3.7. (left) Plots of  $\chi T$  vs  $T$  for solid solutions  $[\text{Fe}_x\text{Zn}_{1-x}(\text{Me-1,3bpp})_2](\text{ClO}_4)_2$  (**5x**), measured from 2 K to 300 K after quenching the polycrystalline samples from room temperature. The inset is the part of the plot emphasizing the response of a small portion of Fe(II) trapped in a metastable HS state, following the thermal quenching, that relax to the LS state. The orange band is the narrow range of temperatures containing  $T_{\text{relax}}$  (the approximate temperature of relaxation) for all compositions. (right) Plots of  $\chi T$  vs  $T$  for compounds **5x** and  $[\text{Fe}(\text{Me-1,3bpp})_2](\text{ClO}_4)_2$  (**2**) recorded during the 300 K  $\rightarrow$  2 K temperature cycle, after the first warming.

Qualitatively, it is clear that the decrease of the iron concentration within the  $[\text{Fe}_x\text{Zn}_{1-x}(\text{Me-1,3bpp})_2](\text{ClO}_4)_2$  lattice reduces the cooperativity of the SCO, by producing more and more gradual SCO curves (the SCO curve of the pure  $[\text{Fe}(\text{Me-1,3bpp})_2](\text{ClO}_4)_2$  (**2**) is included in the plots of figures 3.7, right and 3.8, left, for comparison). This expected feature emerges in all the studies of solid solutions of SCO-active complexes of iron diluted with a non-active and isomorphous complex.<sup>17-33</sup> The rationale is that the cooperativity of the spin transition depends on the propagation of the structural changes taking place upon the SCO at the molecular level. Elastic interactions among the spin-switching complexes ensure this propagation through the crystalline lattice. The insertion of non-active or silent species implies the intercalation of complexes that do not experience these changes, thus disrupting the propagation of the molecular breathing and drastically reducing the cooperativity. The fraction of the Fe(II) centres in the HS state,  $\gamma_{\text{HS}}$ , has been used to analyse this effect qualitatively. It has been derived from the magnetic data above 50K (*i.e.* a temperature at which the SCO process is completed). It has been realized by normalizing the  $\chi T$  value at a given temperature with those at the beginning and the end, respectively, of the SCO process. This was done for each composition using

### 3. The effect of metal dilution on the thermal spin transition

the expression  $\chi_{HS}(T) = (\chi T(T) - \chi T_{LS}(T)) / (\chi T_{HS}(T) - \chi T_{LS}(T))$ . This normalization empirically considers the effects of the ZFS of remaining HS species and slight variation in the  $\chi T$  caused by the temperature-independent magnetism or unideal diamagnetic corrections. Plots of the normalized HS fraction vs  $T$  are shown in Figure 3.8, left. For an approximate evaluation of the SCO cooperativity, the phenomenological Sorai's domain model was used to fit the  $\gamma_{HS}(T)$  data (Figure A3.6; Appendix 3), using the expression eq.3.1:

$$\gamma_{HS}(T) = \gamma_{HS}^{residual} + \frac{\gamma_{HS}^{residual}}{1 + e^{\left[\frac{n\Delta_{SCO}H}{R} \left(\frac{1}{T} - \frac{1}{T_{SCO}}\right)\right]}} \quad (3.1)$$

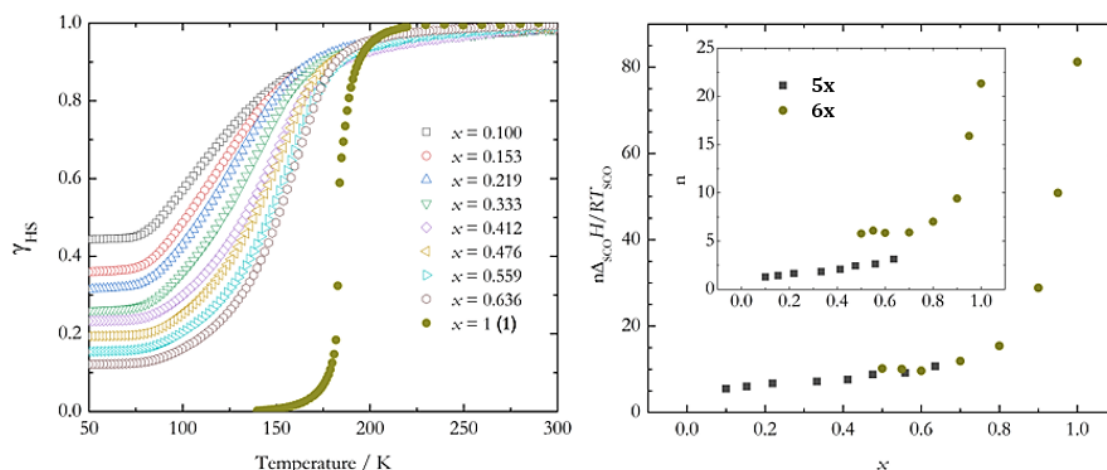


Figure 3.8. (left) Plots of  $\gamma_{HS}$  vs.  $T$  for solid solutions  $[\text{Fe}_x\text{Zn}_{1-x}(\text{Me-1,3bpp})_2](\text{ClO}_4)_2$  (**5x**) and compound  $[\text{Fe}(\text{Me-1,3bpp})_2](\text{ClO}_4)_2$  (**2**). (right) Variation of the cooperative character of the SCO for the solid solutions  $[\text{Fe}_x\text{Zn}_{1-x}(\text{Me-1,3bpp})_2](\text{ClO}_4)_2$  (**5x**),  $[\text{Fe}(\text{Me-1,3bpp})_{2x}(\text{Me}_2\text{-1,3bpp})_{2-2x}](\text{ClO}_4)_2$  (**5'x**) and compound  $[\text{Fe}(\text{Me-1,3bpp})_2](\text{ClO}_4)_2$  (**2**) as derived through Sorai's domain model (see text).

The model gives a measure of cooperativity by determining the number of spin-like molecules (here, the SCO-active centres),  $n$ , in each interacting domain. As  $n$  increases or the larger the domain, the cooperativity of the transition increases.<sup>46,47</sup> The same model was previously used to analyze the doping effect of complex **2** with another SCO-active analogue,  $[\text{Fe}(\text{Me}_2\text{-1,3bpp})_2](\text{ClO}_4)_2$  (**4**).<sup>42</sup> Nevertheless, the excess enthalpy associated with the SCO process,  $\Delta_{SCO}H$ , has not been experimentally determined here. Therefore, we evaluate the product  $n\Delta_{SCO}H$  together. Additionally, the term  $\gamma_{HS}^{residual}$  has been included to consider the fraction of Fe(II) remaining in their HS state. This was unnecessary for the **5'x** series, where an allosteric SCO took place for all the Fe(II) centres simultaneously in the solid solutions. As expected, the

product  $n\Delta_{\text{SCO}}H$  decreases when decreasing  $x$  — extrapolating to *ca.* 4.4 kJ/mol for infinite dilution, we deal with a situation corresponding to isolated SCO centres and thus  $n=1$ . Then, an estimation of  $n$  using  $\Delta_{\text{SCO}}H = 4.4$  kJ/mol actually shows that it is already close to the unit for  $x=0.10$ . Comparing the  $n\Delta_{\text{SCO}}H/RT_{\text{SCO}}$  values derived for the series **5x** with those obtained for the analogue series **5'x** doping with  $[\text{Fe}(\text{Me}_2\text{-1,3bpp})_2](\text{ClO}_4)_2$  exhibit excellent agreement (Figure 3.8, right). This comparison confirms that the effect of the dilution in the range of the  $x$  reachable for the **5x** series is rather monotonous and reasonably weak, since the cooperativity has been lost even at the highest values of  $x$ . Indeed, while the  $n$  value has decreased from *ca.* 2.1 for pure **2** to *ca.* 3.1 for  $x=0.64$ , further dilution only results in an almost linear decrease of  $n$  down to *ca.* 1.3 for  $x=0.10$ . This is reasonable since the slightest modifications of the lattice composition when doping can be expected to strongly affect the long-range elastic interactions at the root of the efficient propagation of the structural changes associated with the SCO at the molecular scale. Surprisingly, a perhaps more original remark is that this effect appears to be similar whether the doping involves the breakdown of some intermolecular interactions between some active spin network as in the **5'x** series or the introduction of inactive spin centres as in the series **5x**. It appears that different types of doping have a similar destructive effect on the cooperative nature of the host SCO process for the same host.

Another effect on the SCO properties arising from the negative chemical pressure seen when reducing the concentration of the active complexes within the Fe/Zn alloys is the stabilization of the HS state. This results in a decrease of the SCO temperature and the partial hampering of the HS to LS state transition, which causes an increase of the residual fraction of the Fe(II) remaining in the HS state below the SCO temperature.<sup>19,21,24,25,28,30</sup> Both consequences are here qualitatively perceived in figure 3.7 and quantified in Figure 3.9, left. The  $T_{\text{SCO}}$  decreases linearly while the residual HS fractions increase with lowering  $x$ . The latter effect may be resulting from the additive influence of two phenomena occurring with the increase of Zn content; the  $T_{\text{SCO}}$  reduction and the loss of cooperativity. Indeed, the residual fraction of HS is often observed in systems with a gradual SCO transition, especially when it occurs at relatively low temperatures. To put the linear decrease of  $T_{\text{SCO}}$  for the series **5x** into perspective, we compared the relative decrease  $\Delta T_{\text{SCO}}$  (defined as

### 3. The effect of metal dilution on the thermal spin transition

$T_{SCO}(x)/T_{SCO}(x=1)$ , with four other Fe(II) SCO systems also doped with a Zn analogue. These complexes with a similar coordination environment include a bis-tris-imine-like ligand in  $[Fe_xZn_{1-x}(bpp)_2](NCSe)_2$  ( $bpp = 2,6$ -bis(pyrazol-3-yl)pyridine),<sup>40</sup> a tris-amineimine chromophore in  $[Fe_xZn_{1-x}(2-pic)_3]Cl_2 \cdot EtOH$  ( $2-pic = 2$ -picolylamine)<sup>23</sup> and two complexes with a bis-imine equatorial environment and additional axial thiocyanate donors in  $[Fe_xZn_{1-x}(phen)_2](NCS)_2$  ( $phen = 1,10$ -phenantroline),<sup>21</sup> or a tetra-imine chelate in  $[Fe_xZn_{1-x}(bapbpy)(NCS)_2] \cdot 3DMF$  ( $bapbpy = N6,N6'$ -di(pyridin-2-yl)-2,2'-bipyridine-6,6'-diamine).<sup>48</sup> Extraordinarily, despite the different temperature ranges for the SCO and types of SCO processes, the data of all five families of doped complexes follow approximately a general linear trend described by  $\Delta T_{SCO}(x) = 62.3 + 37.1x$ . This trend suggests that the dilution effect with the silent Zn(II) ions on the SCO temperature of Fe(II) complexes seems to be quite independent on the topology/ composition of the complex, and thus essentially resulting from the ionic radii difference. Although this may be surprising, it agrees with previous studies that have pointed to a dominant role for the lattice, the volume change that accompanies the spin transition, and the connected elastic energies.<sup>17</sup> In fact, all molecular SCO systems compared can be expected to have similar lattice (Debye constant) and interaction energies. More rigid materials (2D or 3D-like arrays) may not follow the linear trend observed here.

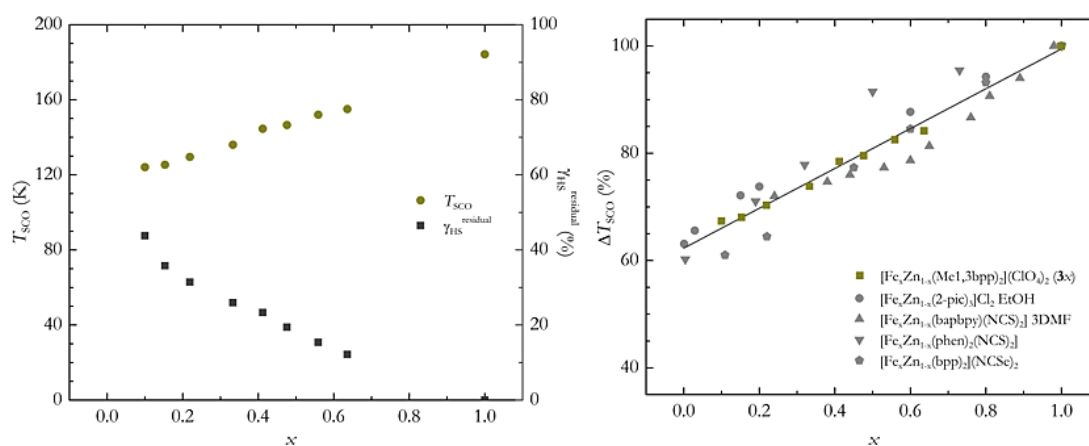


Figure 3.9. (left) Variation of the spin crossover temperature  $T_{SCO}$  for solid solutions  $[Fe_xZn_{1-x}(Me-1,3bpp)_2](ClO_4)_2$  (**5x**) together with the values of low temperature  $\gamma_{HS}^{residual}$  for all compositions. (right) Relative variation of the spin crossover temperature upon doping for **5x** and the series  $[Fe_xZn_{1-x}(2-pic)_3]Cl_2 \cdot EtOH$  ( $2-pic = 2$ -picolylamine),<sup>23</sup>  $[Fe_xZn_{1-x}(bapbpy)(NCS)_2] \cdot 3DMF$  ( $bapbpy = N6,N6'$ -di(pyridin-2-yl)-2,2'-bipyridine-6,6'-diamine),<sup>48</sup>  $[Fe_xZn_{1-x}(phen)_2](NCS)_2$  ( $phen = 1,10$ -phenantroline)<sup>21</sup> and  $[Fe_xZn_{1-x}(bpp)_2](NCSe)_2$  ( $bpp = 2,6$ -bis(pyrazol-3-yl)pyridine).<sup>40</sup>

Furthermore, it was also observed that the thermal relaxation of the small fraction of the Fe (II) complexes that are trapped in the HS state after being thermally quenched (Figure 3.7 left, inset) occurs at a temperature (here called  $T_{relax}$ ) around 77K, falling for the ensemble of compounds within a very narrow range (about 2K wide). This contrasts with the 40 K temperature variation range (when  $x$  varies from 0.10 to 0.64) observed for  $T_{1/2}$  in this series. The models used to describe the effects of dilution of active Fe (II) complexes when they are part of solid solutions associate this dependence of  $T_{1/2}$  vs concentration with a decrease in cooperativity after dilution. Conversely, the  $T(TIESST)$  or the  $T_{relax}$  dependence with the composition is expected to be more complex. For the  $T(LIESST)$  in molecular alloys, this dependence is affected by the reduction of cooperativity as the Fe(II) amounts decrease, the inverse energy-gap and principally, the effect of the internal pressure.<sup>19,21,28,41</sup> For the Fe/Zn systems, this results into a small variation of  $T(LIESST)$  with the composition. While the relaxation effects of the  $T(TIESST)$  are expected to display similar behavior, very few data are available.<sup>24</sup> Thus, the present work represents one of the first contributions towards the confirmation of this trend.

### 3.3. Conclusions

Mixing perchlorate salts of Zn(II) and Fe(II) with Me-1,3bpp in acetone with increasing amounts of iron, produces homogeneous phases of crystalline solid solutions with the formula  $[Fe_xZn_{1-x}(Me-1,3bpp)_2](ClO_4)_2$  (**5x**;  $x = 0.10, 0.15, 0.22, 0.33$ ). Using this solvent, reactant Zn/Fe ratios aiming at  $x > 0.33$  results in the segregation of the crystalline phase. However, using a mixture of acetone/ethanol (1:1 in volume) allows increasing the amount of iron within the pure crystalline phases, giving access to alloys with compositions of  $x = 0.41, 0.48, 0.56$  and  $0.64$ . Molecular solid solutions with higher iron content cannot be prepared, possibly because these are not the preferred option thermodynamically. The nature of true homogeneous solid solution for all the compositions was demonstrated by SCXRD together with PXRD. The analysis of the crystallographic data shows a gradual evolution of the structural parameters with the composition at three levels: i) at the local scale; ii) at the level of intermolecular interactions; iii) in terms of the crystal lattice parameters. Using magnetization measurements, it was possible to analyse the effect of the composition within these lattices on the cooperativity and the

thermodynamic parameters of the SCO of the Fe (II) complexes. The decrease of  $T_{1/2}$  of the SCO and the presence of larger amounts of residual HS Fe(II) ions during the thermal HS to LS transition is easily understood due to the negative chemical pressure that the Zn(II) exerts into the active iron lattice. Curiously, the analysis of literature data, together with present results unveiled that the variation of  $T_{1/2}$  seems independent of the complex studied as long as the metal of the dopant is the same (when comparing the variation in terms of  $\Delta T_{SCO}(x) = T_{SCO}(x)/T_{SCO}(x = 1)$ ). Additionally, the disruption of the molecular interactions between the spin active species within the network as originated from the intercalation of spin silent complexes result in a decrease in cooperativity. For the highest iron-containing sample ( $x=0.64$ ), the major disruption of cooperativity has already taken place; thus, the variation of cooperativity with  $x$  (gauged here by the expression  $n\Delta_{SCO}H/RT_{SCO}$  based on the Sorai model) is weak and linear. Interestingly, a small amount of Fe(II) can be thermally trapped in the HS state when quickly quenching the samples at 2K from their initial HS state at room temperature. This procedure allows determining the  $T(TIESST)$  for the various doped complexes, which provides rare experimental proof of the fact that the temperature of thermal relaxation of the metastable state reached in this manner is unaffected by the composition (*ie.* the different values of  $x$ ).

#### 3.4. Experimental

The ligand 2-(3-methyl-pyrazol-1-yl)-6-(pyrazol-3-yl)pyridine (Me-1,3bpp) and the complex  $[\text{Fe}(\text{Me-1,3bpp})_2](\text{ClO}_4)_2$  (**2**) were prepared as previously reported in chapter 2.

**$[\text{Zn}(\text{Me-1,3bpp})_2](\text{ClO}_4)_2$  (**4**)**. To a solution of  $\text{Zn}(\text{ClO}_4)_2 \cdot 6\text{H}_2\text{O}$  (12 mg, 0.03 mmol) in acetone (10 ml) was added dropwise a solution of Me-1,3bpp (13.5 mg, 0.06 mmol) in acetone (10ml). The resulting colourless solution was stirred for 40 minutes at room temperature. The solution was then filtered and layered with diethyl ether (1:1 vol). Colourless needles of the product suitable for single crystal X-ray diffraction were obtained after a week. Yield: 40%. Anal. Calcd (found) for  $\text{ZnC}_{24}\text{H}_{22}\text{Cl}_2\text{N}_{10}\text{O}_8$ : C, 39.96 (40.63); H, 3.18 (3.30); N, 19.41 (18.74).



**[Fe<sub>x</sub>Zn<sub>1-x</sub>(Me-1,3bpp)<sub>2</sub>](ClO<sub>4</sub>)<sub>2</sub> (5x; 0.10 ≤ x ≤ 0.33).** Depending on the dilution degree *x*, various quantities of Fe(ClO<sub>4</sub>)<sub>2</sub>·6H<sub>2</sub>O and Zn(ClO<sub>4</sub>)<sub>2</sub>·6H<sub>2</sub>O (in mg, using the Fe/Zn format, 3.2/41.7, 6.3/36.9, 9.5/32.3 and 12.6/27.7 for *x* = 0.10, 0.15, 0.22 and 0.33, respectively) and ascorbic acid (~2 mg) were dissolved in acetone (20 ml). A solution of Me-1,3bpp (56 mg, 0.25 mmol) in acetone (20 ml) was added dropwise to each metal mixture solution. The resulting yellow solutions were stirred for 45 minutes at room temperature. The solutions were then filtered and layered with diethyl ether (1:1 vol). Yellow needles of the products suitable for single crystal X-ray diffraction were obtained in a week. Typical yields: ~ 39 %. Anal. Calcd (found) for [Fe<sub>0.10</sub>Zn<sub>0.9</sub>(C<sub>12</sub>H<sub>11</sub>N<sub>5</sub>)<sub>2</sub>](ClO<sub>4</sub>)<sub>2</sub>: C, 39.7 (40.27); H, 3.24 (3.16); N, 19.29(18.71). Anal. Calcd (found) for [Fe<sub>0.15</sub>Zn<sub>0.847</sub>(C<sub>12</sub>H<sub>11</sub>N<sub>5</sub>)<sub>2</sub>](ClO<sub>4</sub>)<sub>2</sub>: C, 39.66 (40.39); H, 3.26 (3.2); N, 19.27 (18.54). Anal. Calcd (found) for [Fe<sub>0.22</sub>Zn<sub>0.781</sub>(C<sub>12</sub>H<sub>11</sub>N<sub>5</sub>)<sub>2</sub>](ClO<sub>4</sub>)<sub>2</sub>: C, 39.75 (40.53); H, 3.25 (3.19); N, 19.31 (18.53). Anal. Calcd (found) for [Fe<sub>0.33</sub>Zn<sub>0.667</sub>(C<sub>12</sub>H<sub>11</sub>N<sub>5</sub>)<sub>2</sub>](ClO<sub>4</sub>)<sub>2</sub>: : C, 40.27 (40.51); H, 3.16 (3.19); N, 19.56 (19.32).

**[Fe<sub>x</sub>Zn<sub>1-x</sub>(Me-1,3bpp)<sub>2</sub>](ClO<sub>4</sub>)<sub>2</sub> (5x; 0.41 ≤ x ≤ 0.64).** Depending on the dilution degree *x*, various quantities of Fe(ClO<sub>4</sub>)<sub>2</sub>·6H<sub>2</sub>O and Zn(ClO<sub>4</sub>)<sub>2</sub>·6H<sub>2</sub>O (in mg, using the Fe/Zn format, 15.8/23.1, 19/18.5, 22.1/13.8 and 25.3/9.2 for *x* = 0.41, 0.48, 0.56 and 0.64, respectively) and ascorbic acid (~2 mg) were dissolved in a mixture of ethanol and acetone (1:1 vol; 20 ml). A solution of Me-1,3bpp (56 mg, 0.25 mmol) in acetone (20 ml) was added dropwise to the former metal mixture solution. The resulting yellow solutions were stirred for 45 minutes at room temperature. The solutions were then filtered and layered with diethyl ether (1:1 vol). Yellow needles of the products suitable for single crystal X-ray diffraction were obtained in a week. Typical yields: ~ 39 %. Anal. Calcd (found) for [Fe<sub>0.41</sub>Zn<sub>0.558</sub>(C<sub>12</sub>H<sub>11</sub>N<sub>5</sub>)<sub>2</sub>](ClO<sub>4</sub>)<sub>2</sub>: C, 40.2 (40.46); H, 3.19 (3.15); N, 19.53 (19.27). Anal. Calcd (found) for [Fe<sub>0.48</sub>Zn<sub>0.524</sub>(C<sub>12</sub>H<sub>11</sub>N<sub>5</sub>)<sub>2</sub>](ClO<sub>4</sub>)<sub>2</sub>: C, 40.32 (40.51); H, 3.18 (3.14); N, 19.59 (19.4). Anal. Calcd (found) for [Fe<sub>0.56</sub>Zn<sub>0.441</sub>(C<sub>12</sub>H<sub>11</sub>N<sub>5</sub>)<sub>2</sub>](ClO<sub>4</sub>)<sub>2</sub>: C, 40.04 (40.35); H, 3.24 (3.16); N, 19.45 (19.14). Anal. Calcd (found) for [Fe<sub>0.64</sub>Zn<sub>0.364</sub>(C<sub>12</sub>H<sub>11</sub>N<sub>5</sub>)<sub>2</sub>](ClO<sub>4</sub>)<sub>2</sub>: C, 40.46 (40.74); H, 3.17 (3.13); N, 19.66 (19.38).

### 3.5. References

- (1) Gamez, P.; Costa, J. S.; Quesada, M.; Aromí, G. *Dalt. Trans.* **2009**, 7845–7853.
- (2) Kahn, O.; Jay Martinez, C. *Science.* **1998**, 279, 44–48.
- (3) Larionova, J.; Salmon, L.; Guari, Y.; Tokarev, A.; Molvinger, K.; Molnár, G.; Bousseksou, A. *Angew. Chemie - Int. Ed.* **2008**, 47, 8236–8240.
- (4) Halcrow, M. A. *Chem. Lett.* **2014**, 43, 1178–1188.
- (5) Spiering, H. In *Spin Crossover in Transition Metal Compounds III*; Gülich, P., Goodwin, H. A., Eds.; Springer Berlin Heidelberg, 2006; pp 171–195.
- (6) Popa, A. I.; Stoleriu, L.; Enachescu, C. *J. Appl. Phys.* **2021**, 129, 131101.
- (7) Real, J. A.; Gaspar, A. B.; Muñoz, M. C. *Dalt. Trans.* **2005**, 12, 2062–2079.
- (8) Roubeau, O. *Chem. - A Eur. J.* **2012**, 18, 15230–15244.
- (9) Weber, B. *Coord. Chem. Rev.* **2009**, 253, 2432–2449.
- (10) Wannarit, N.; Roubeau, O.; Youngme, S.; Teat, S. J.; Gamez, P. *Dalt. Trans.* **2013**, 42, 7120–7130.
- (11) Barrios, L. A.; Peyrecave-Lleixà, E.; Craig, G. A.; Roubeau, O.; Teat, S. J.; Aromí, G. *Eur. J. Inorg. Chem.* **2014**, 2014, 6013–6021.
- (12) Arcis-Castillo, Z.; Zheng, S.; Siegler, M. A.; Roubeau, O.; Bedoui, S.; Bonnet, S. *Chem. - A Eur. J.* **2011**, 17, 14826–14836.
- (13) Bartual-Murgui, C.; Codina, C.; Roubeau, O.; Aromí, G. *Chem. Eur. J.* **2016**, 22, 12767–12776.
- (14) Bartual-Murgui, C.; Piñeiro-López, L.; Valverde-Munoz, F. J.; Muñoz, M. C.; Seredyuk, M.; Real, J. A. *Inorg. Chem.* **2017**, 56, 13535–13546.
- (15) Tao, J.; Wei, R. J.; Huang, R. Bin; Zheng, L. S. *Chem. Soc. Rev.* **2012**, 41, 703–737.
- (16) Bartual-Murgui, C.; Vela, S.; Darawsheh, M.; Diego, R.; Teat, S. J.; Roubeau, O.; Aromí, G. *Inorg. Chem. Front.* **2017**, 4, 1374–1383.
- (17) Adler, P.; Wiehl, L.; Meibner, E.; Köhler, C. P.; Spiering, H.; Gülich, P. *J. Phys. Chem. Solids* **1987**, 48, 517–525.
- (18) Jung, J.; Schmitt, G.; Wiehl, L.; Hauser, A.; Knorr, K.; Spiering, H.; Gülich, P. *Zeitschrift für Phys. B-Condensed Matter.* **1996**, 100, 523–534.
- (19) Sylla, M. S.; Baldé, C.; Daro, N.; Desplanches, C.; Marchivie, M.; Chastanet, G. *Eur. J. Inorg. Chem.* **2018**, 297–304.

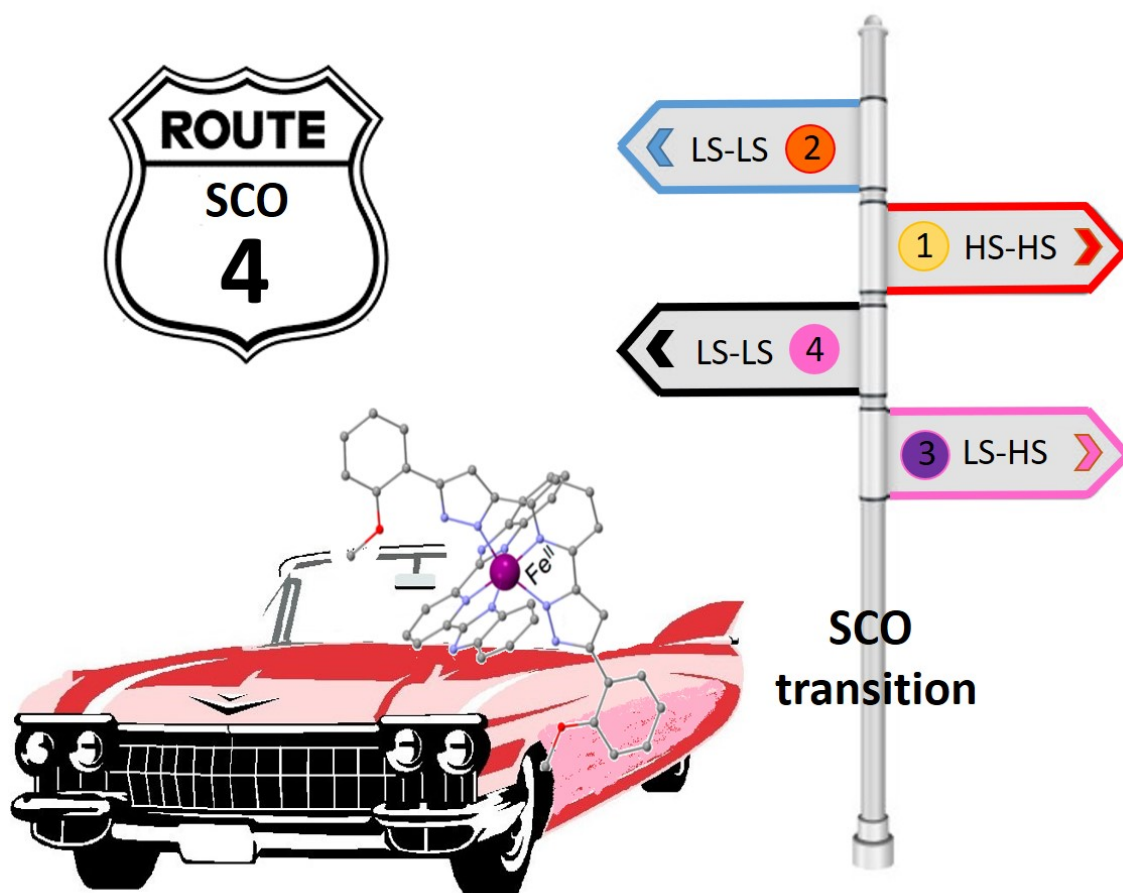
- (20) Buchen, T.; Poganiuch, P.; Gütlich, P. *J. Chem. Soc. Dalton Trans.* **1994**, 2285–2288.
- (21) Baldé, C.; Desplanches, C.; Wattiaux, A.; Guionneau, P.; Gütlich, P.; Létard, J. F. *J. Chem. Soc. Dalton Trans.* **2008**, 2702–2707.
- (22) Jakobi, R.; Spiering, H.; Wiehl, L.; Gütlich, P.; Gmelin, E. *Inorg. Chem.* **1988**, *27*, 1823–1827.
- (23) Gütlich, P.; Link, R.; Steinhäuser, H. G. *Inorg. Chem.* **1978**, *17*, 2509–2514.
- (24) Baldé, C.; Desplanches, C.; Gütlich, P.; Freysz, E.; Létard, J. F. *Inorg. Chim. Acta.* **2008**, *361*, 3529–3533.
- (25) Zhong, Y.; Takayoshi, K.-S.; Hiroaki, K.; Takashi, O.; Masahiko, M.; Megumu, M. *Bull. Chem. Soc. Jpn.* **2009**, *82*, 333–337.
- (26) Rotaru, A.; Dîrtu, M. M.; Enachescu, C.; Tanasa, R.; Linares, J.; Stancu, A.; Garcia, Y. *Polyhedron.* **2009**, *28*, 2531–2536.
- (27) Lefter, C.; Tricard, S.; Peng, H.; Molnár, G.; Salmon, L.; Demont, P.; Rotaru, A.; Bousseksou, A. *J. Phys. Chem. C.* **2015**, *119*, 8522–8529.
- (28) Baldé, C.; Desplanches, C.; Létard, J. F.; Chastanet, G. *Polyhedron* **2017**, *123*, 138–144.
- (29) Sanner, I.; Meissner, E.; Köppen, H.; Spiering, H.; Gütlich, P. *Chem. Phys.* **1984**, *86*, 227–233.
- (30) Ganguli, P.; Gütlich, P.; Müller, E. W. *Inorg. Chem.* **1982**, *21*, 3429–3433.
- (31) Martin, J. P.; Zarembowitch, J.; Dworkin, A.; Haasnoot, J. G.; Coddjovi, E. *Inorg. Chem.* **1994**, *33*, 2617–2623.
- (32) Martin, J. P.; Zarembowitch, J.; Bousseksou, A.; Dworkin, A.; Haasnoot, J. G.; Varret, F. *Inorg. Chem.* **1994**, *33*, 6325–6333.
- (33) Paradis, N.; Chastanet, G.; Létard, J. F. *Eur. J. Inorg. Chem.* **2012**, 3618–3624.
- (34) Decurtins, S.; Gütlich, P.; Köhler, C. P.; Spiering, H.; Hauser, A. *Chem. Phys. Lett.* **1984**, *105*, 1–4.
- (35) Chastanet, G.; Desplanches, C.; Baldé, C.; Rosa, P.; Marchivie, M.; Guionneau, P. *Chem. Sq.* **2018**, *2*, 1–18.
- (36) Létard, J. F.; Guionneau, P.; Rabardel, L.; Howard, J. A. K.; Goeta, A. E.; Chasseau, D.; Kahn, O. *Inorg. Chem.* **1998**, *37*, 4432–4441.
- (37) Hauser, A. *Coord. Chem. Rev.* **1991**, *111*, 275–290.
- (38) Létard, J. F.; Guionneau, P.; Nguyen, O.; Costa, J. S.; Marcén, S.; Chastanet, G.;

- Marchivie, M.; Goux-Capes, L. *Chem. - A Eur. J.* **2005**, *11*, 4582–4589.
- (39) Craig, G. A.; Sánchez Costa, J.; Roubeau, O.; Teat, S. J.; Aromí, G. *Chem. - A Eur. J.* **2011**, *17*, 3120–3127.
- (40) Marchivie, M.; Guionneau, P.; Létard, J. F.; Chasseau, D.; Howard, J. A. K. *J. Phys. Chem. Solids* **2004**, *65*, 17–23.
- (41) Baldé, C.; Desplanches, C.; Le Gac, F.; Guionneau, P.; Létard, J. F. *Dalt. Trans.* **2014**, *43*, 7820–7829.
- (42) Bartual-Murgui, C.; Pérez-Padilla, C.; Teat, S. J.; Roubeau, O.; Aromí, G. *Inorg. Chem.* **2020**, *59*, 12132–12142.
- (43) Guionneau, P.; Marchivie, M.; Chastanet, G. *Chem. - A Eur. J.* **2021**, *27*, 1483–1486.
- (44) Craig, G. A.; Costa, J. S.; Teat, S. J.; Roubeau, O.; Yufit, D. S.; Howard, J. A. K.; Aromí, G. *Inorg. Chem.* **2013**, *52*, 7203–7209.
- (45) Halcrow, M. A. *Chem. Soc. Rev.* **2008**, *37*, 278–289.
- (46) Sorai, M.; Seki, S. *J. Phys. Chem. Solids* **1974**, *35*, 555–570.
- (47) Sorai, M. In *Spin Crossover in Transition Metal Compounds III*; Gülich, P., Goodwin, H. A., Eds.; Springer Berlin Heidelberg, 2004; pp 153–170.
- (48) Zheng, S.; Siegler, M. A.; Costa, J. S.; Fu, W. T.; Bonnet, S. *Eur. J. Inorg. Chem.* **2013**, 1033–1042.

# CHAPTER 4

---

## A MONONUCLEAR SPIN-CROSSOVER COMPLEX DESCRIBING FOUR DISTINCT THERMAL ROUTES





## 4. A MONONUCLEAR SPIN-CROSSOVER COMPLEX DESCRIBING FOUR DISTINCT THERMAL ROUTES

### Abstract

The origin of the SCO transition lies in the molecular scale even so structural phase transitions (SPTs) influence greatly the behaviour within crystalline structures due to different effects of cooperativity. Coordinating tris-imine like ligands with Fe (II) often produces dense networks of intermolecular interactions that offer the possibility of analysing the crystal breathing and the understanding of the solid-state transformations. The heteroleptic complex, [FeL(bpp)](ClO<sub>4</sub>)<sub>2</sub> (**6**; L and bpp are tris-imine ligands) is an ideal robust system that allows making a connection between SCO and SPTs through single crystal X-ray diffraction (SCXRD). Magnetometry and SCXRD measurements unveil a succession of SCO and crystallographic phase transformations never seen before. Starting from a fresh crystal of **6** (a mixed spin state HS-LS) containing one molecule of acetone per Fe center (**6**·ac), a fully HS (**6**<sup>α</sup> phase) state is reached upon warming. This crystallographic phase converts into another one (**6**<sup>β</sup>) upon cooling, simultaneously converting to the LS state. Warming of **6**<sup>β</sup> induces a new SCO coupled to another crystallographic phase and spin transition, **6**<sup>β</sup>→**6**<sup>γ</sup> (HS-LS). This last phase cycles thermally between the HS-LS and the LS states through superimposable pathways. Here, four different thermal SCO routes give rise to four different magnetic responses within a range of temperatures near to ambient conditions.

### 4.1. Introduction

The switching between the two possible electronic configurations for Fe(II) compounds is directly tracked from the changes in the size of the metal center (contraction for the LS state and expansion for the HS state) during the transition.<sup>1</sup> Moreover, a distortion of the FeN<sub>6</sub> coordination sphere takes place upon the transition, being the HS state the more distorted rather than the LS one.<sup>2,3</sup> More detailed explanations about this aspect are given in the Introduction. In the solid-state, each iron centre induces a pressure effect to the nearest neighbour in the lattice that propagates all the changes of the complex throughout the crystal. If large

#### 4. A mononuclear spin-crossover complex describing four distinct thermal routes

---

rearrangements of the molecules at the molecular level take place, then a structural phase transition (SPT) may also occur. Then, a fascinating coupling between SCO and SPTs can be established. The connection between them is related to the efficiency in spreading structural changes through the lattice (cooperativity). Indeed, the presence of hysteresis is most favoured when both, SCO and SPTs, are concomitant.<sup>4</sup> There are several types of SPTs reported in the literature.<sup>5</sup> Very often, SPTs involve a crystallographic symmetry breaking consisting in a change of the space group symmetry.<sup>6-9</sup> These are more easily detectable since the structural modifications are more significant (higher different molecular dispositions). Nevertheless, none all of the SPTs exist with this specific variation.<sup>10,11</sup> Pronounced changes in the magnetic behaviour can take place without significant modifications of the unit cell but still considered as a result due to interplay between SCO and SPT. In this respect, some controversial arguments related to the existence of SPTs have been seen in the literature.<sup>12,13</sup> These disagreements arise from the ambiguity in establishing the limits of the significative changes that could define an SPT. For example, no structural phase change is considered to be involved with the SCO transition of the complex  $[\text{Fe}(\text{H}_4\text{L})_2][\text{ClO}_4]_2 \cdot 2(\text{CH}_3)_2\text{CO}$  ( $\text{H}_4\text{L} = 2,6\text{-Bis}\{5\text{-(2-hydroxyphenyl)-pyrazol-3-yl}\}\text{pyridine}$ ) since there is no change in space group.<sup>13</sup> However this compound exhibits an abrupt SCO at 153K with a wide hysteresis (40K) and large changes in ligand conformation that could be the major contribution to its bistability.<sup>10</sup> Atomic displacements up to 1.5 Å between the metal centres arise from the large conformational rearrangement of the terminal phenoxy groups.<sup>3,13</sup> For this reason, this drastic structural rearrangements within the crystal lattice are equivalent to a full SPT. Polymorphic transformations constitute the vast majority of the SCO coexistence with SPTs and are rarely irreversible among molecular crystals, at least for the well described examples.<sup>14</sup> These occurrences lead to suggest that SCO may serve as the starting motion (or trigger) to the relaxation of a metastable crystallographic state. Furthermore, these materials may be designed as time-temperature devices capable of generating a thermal history.<sup>15</sup> For the study of these important issues, it was of interest to exploit the unique properties of tris-imine Fe(II) complexes.<sup>16-19</sup> This family of compounds features two main important characteristics: i) they display the appropriate crystal field around the metal centre giving rise to SCO almost systematically<sup>20</sup> and ii) usually, these materials arrange-



through a large number of intermolecular interactions generating a compact packing, favouring high cooperativity. This dense material allows the persistence of crystal integrity under variable temperature studies, allowing the use of single-crystal X-ray diffraction (SCXRD) to study the SPTs in detail.<sup>16,21,22</sup>

In this chapter, a succession of SCO events, most of them associated to SPTs for a novel heteroleptic Fe(II) complex [FeL(bbp)](ClO<sub>4</sub>)<sub>2</sub> (**6**, L = 2,6-bis-(5-(2-methoxyphenyl)-pyrazol-3-yl)-pyridine<sup>21</sup>, bbp = 2,6-bis-(benzimidazol-2-yl)-pyridine);<sup>23,24</sup> Figure 4.1), are reported. Since the phase transitions occur in a single-crystal-to-single-crystal (SCSC) way, the structural changes are screened using SCXRD diffraction. The results show a first SCO transition associated with desorption of acetone, which acts as a template during the formation stage, establishing a new solvent-free phase upon desorption from the lattice. Another abrupt SCO path occurs upon cooling this phase. The last phase shows another SCO upon warming with a marked rearrangement of the phenoxy groups of the ligand L. Finally, this crystallographic phase does not change anymore being a reversible SCO transition upon several thermal cycles.

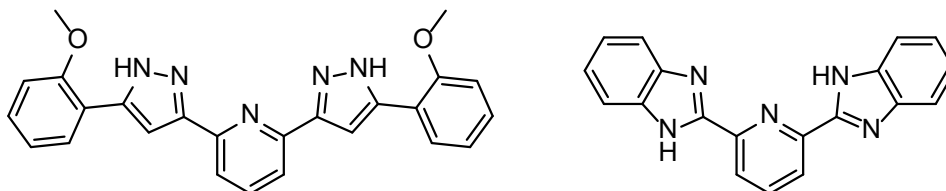


Figure 4.1. Structure of ligands **L** (left) and **bbp** (right).

## 4.2. Results and discussion

### Synthesis

Ligand 2,6-bis-(5-(2-methoxyphenyl)-pyrazol-3-yl)-pyridine (**L**) was synthesized as described in the literature.<sup>21</sup> Firstly, a Claisen condensation between 2-methoxyacetophenone and ethyl 2,6-pyridinedicarboxylate was performed to obtain the corresponding bis- $\beta$ -diketone. Secondly, this precursor was subjected to chemical cyclizing by using hydrazine. The ligand, 2,6-bis-(benzimidazol-2-yl)-pyridine(**bbp**) was prepared through condensation of pyridine-2,6-dicarboxylic acid with *o*-phenylenediamine in polyphosphoric acid solution under microwave conditions.<sup>25</sup> Stoichiometric amounts of L and bbp with the hydrated version of the

#### 4. A mononuclear spin-crossover complex describing four distinct thermal routes

---

salt  $\text{Fe}(\text{ClO}_4)_2$  were firstly mixed in acetone and layered in diethyl ether to provide the desired compound  $[\text{FeL}(\text{bbp})](\text{ClO}_4)_2 \cdot \text{ac}$  (**6**·ac; ac = acetone). The compound was obtained as dark-red large crystals. However, another type of crystals, light orange-yellow needles, were obtained under these reaction conditions. Fortunately, the mixture of crystals was easy to separate manually. (Figure A4.1(left), Appendix 4). Poor diffraction of this additional yellow needles did not allow obtaining any structure from them. By comparing the IR spectra of the ligand (**L**) with that of the two types of crystals, together with the  $^1\text{H}$  NMR of the orange-yellow crystals, evidence was gathered that they could correspond to a salt of the protonated **bbp** ligand  $\text{H}_2\text{bbp}(\text{ClO}_4)_2$  (Figure A4.2 and A4.3, Appendix 4). With the aim to obtain clean compound **6**·ac, the sodium salt of deprotonated **bbp** ( $\text{Na}_2\text{bbp}$ ) was used instead, following the same stoichiometry and reaction conditions explored in the first attempt. A first visual inspection suggested that pure isolated crystals of **6**·ac had formed. To our surprise, we discovered another type of crystals with deep shiny red colour (compound **7**·ac) mixed with the original compound **6**·ac when checking the homogeneity of the sample under the microscope (See Figure A4.1(right), Appendix 4). Again, we were not able to isolate the desired compound by means of direct crystallization. Despite this, a new interesting compound was identified. Crystallographic description of compound **7**·ac is given below. Finally, the pure obtention of dark large crystals of  $[\text{FeL}(\text{bbp})](\text{ClO}_4)_2 \cdot \text{ac}$  (**6**·ac; ac = acetone) was pursued by screening different solvent conditions for the crystallization reaction, being the mixture acetone/ethanol (1:1) the suitable one.

##### **Crystal structure of $[\text{FeL}(\text{bbp})](\text{ClO}_4)_2 \cdot \text{ac}$ (**6**·ac)**

At 100 K, the compound **6**·ac crystallizes in the triclinic space group *P*-1. Two asymmetric units are confined into the unit cell with two  $[\text{FeL}(\text{bbp})](\text{ClO}_4)_2$  moieties and two crystallographically unequal molecules of acetone in each unit. The lattice features an ordered mixed-spin state since two distinct average Fe–N bond distances are present. The average Fe1–N bond distance is 2.172(9) Å and it is 1.956(9) Å for Fe2–N at 100K. Thus, Fe1 and Fe2 are in the HS and LS states, respectively. (Figure 4.2; see also Table A4.1, Appendix 4). The same parameters are similar at 30 and 280K, as determined also by SCXRD. Each heteroleptic cation consists of two different planar tri-dentate ligands coordinated to the Fe (II) in a

#### 4. A mononuclear spin-crossover complex describing four distinct thermal routes

*mer*-fashion. Each type of ligand lies approximately parallel to its counterpart in the other cationic complex. The methoxyphenyl groups of L display different conformation in both complexes. In the Fe1 complex, the phenol groups are oriented opposite to each other (*syn,anti*) whereas in the Fe2 complex, both phenol groups point toward the coordination pocket of L (*syn,syn*). Each pyrazolyl and imidazolyl ring of their respective ligands (L and bbp) holds a free N-H group able to interact with the counterion and lattice solvent molecule through hydrogen bonds.

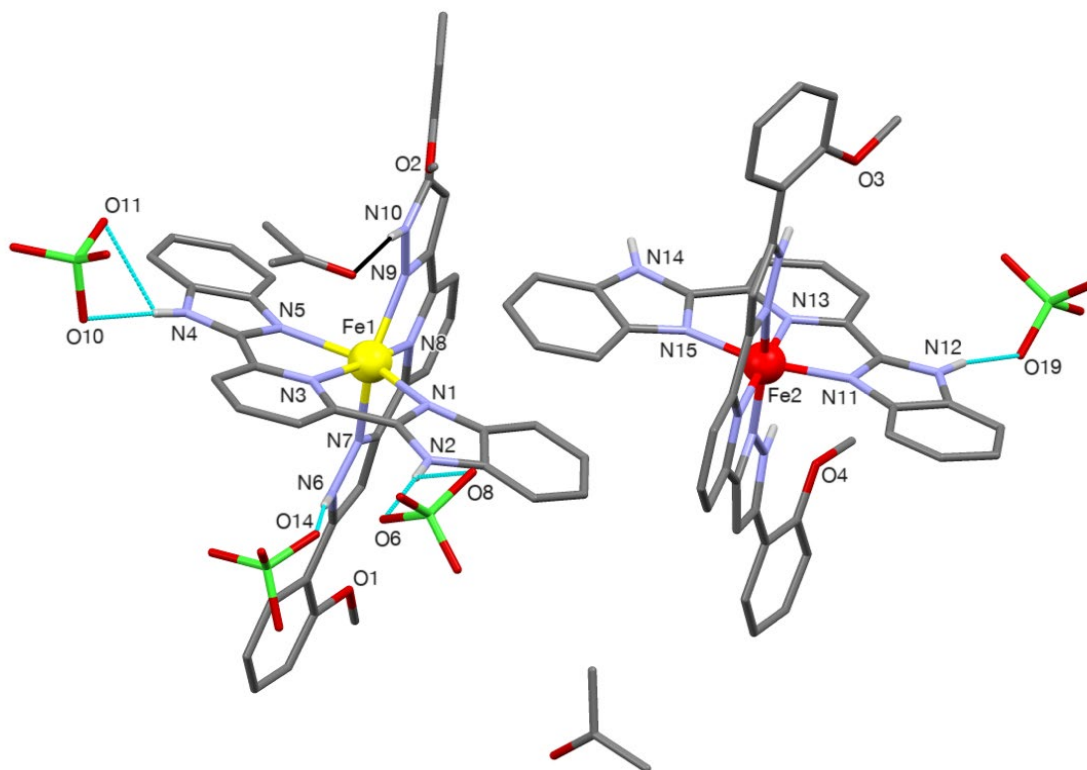


Figure 4.2. Molecular representation of  $[\text{FeL}(\text{bbp})](\text{ClO}_4)_2 \cdot \text{ac}$  ( $6 \cdot \text{ac}$ ) with certain heteroatoms labelled. Only hydrogen atoms of the heteroatoms are shown. Hydrogen bonds between perchlorate ions (dashed cyan lines) are emphasised. Carbon, oxygen and hydrogen atoms are coloured in gray, red and white, respectively. Acetone interaction with N-H group is shown with black line. The HS Fe is in yellow while the LS one is red.

In fact, all of them establish hydrogen bonds with six  $\text{ClO}_4^-$  anions and two molecules of acetone (Figure A4.4 and Table A4.3, Appendix 4). The  $[\text{FeL}(\text{bbp})]^{2+}$  cationic sheet organization is shown in the Appendix 4 (Figure A4.5 and Table A4.2). The Fe1 complexes interact with six neighbours through  $\pi \cdots \pi$  interactions while the Fe2 ones with five in the formation of sheets. Within these sheets, the complexes are disposed in a characteristic sequence. The LS and HS ions are alternated in one direction. While the perpendicular direction alternates pairs of HS and LS iron

#### 4. A mononuclear spin-crossover complex describing four distinct thermal routes

centers. (Figure A4.6, Appendix 4). Among all the crystallographic features, no clear structural evidence explains the different magnetic behaviour of Fe1 and Fe2. Hence, this divergence may be due to a subtle effect.

##### Bulk magnetic measurements of [FeL(bbp)](ClO<sub>4</sub>)<sub>2</sub>·ac (**6**·ac)

Magnetic data were collected from a polycrystalline sample of **6**·ac over various warming and cooling processes till an steady and cyclic magnetic response was observed. The plot of  $\chi_M T$  vs  $T$  ( $\chi_M$  is the molecular paramagnetic susceptibility per Fe center) is shown in Figure 4.3.

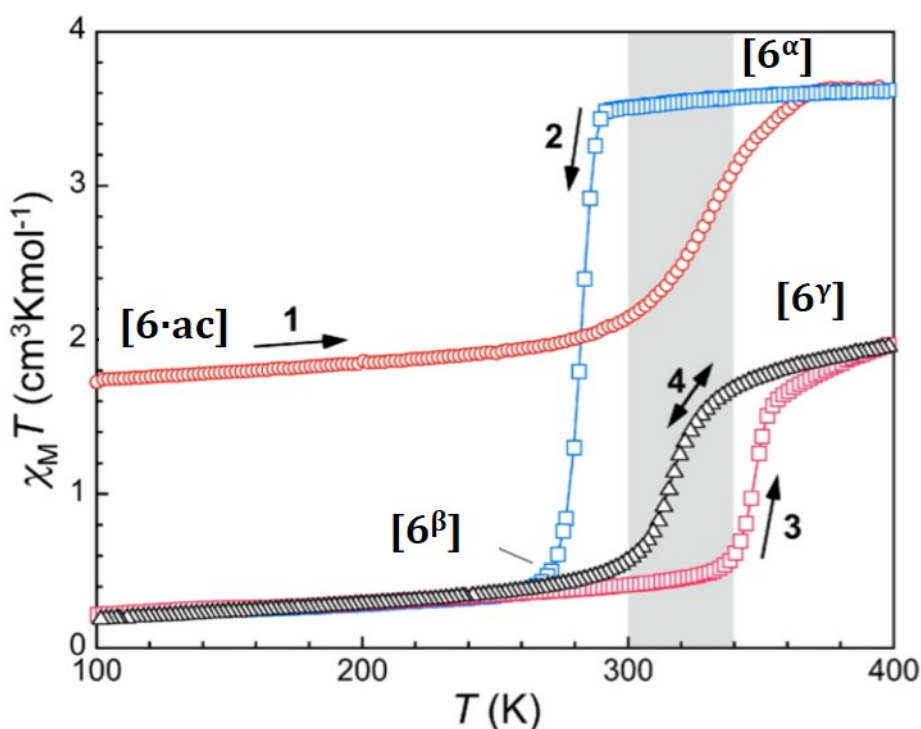


Figure 4.3.  $\chi_M T$  vs  $T$  plot showing the **6**·ac ( $\chi_M$ :the molar paramagnetic susceptibility per Fe center) thermal evolution. A succession of phase transformations are indicated in brackets. These go from **6**·ac until reaching **6** $\gamma$  following other the sequence: **6**·ac  $\rightarrow$  **6** $\alpha$   $\rightarrow$  **6** $\beta$   $\rightarrow$  **6** $\gamma$ . The thermal history of the crystal is shown by increasing numbers (1 to 4). The first warming mode is indicated in red, followed by the cooling one in blue. Second warming mode is pink and the final bidirectional branch is in black. The gray zone indicates the temperature range where four different magnetic responses exist depending on the thermal route.

From low temperature to near room temperature, the complex **6**·ac is maintained in an ordered [LS–HS] state with a nearly constant  $\chi_M T$  value of 1.74 cm<sup>3</sup> K mol<sup>-1</sup>. Then, the value gradually increases until reaching 3.63 cm<sup>3</sup> K mol<sup>-1</sup> at 374 K. The complex is subject to SCO reaching a fully [HS–HS] state with  $T_{1/2\uparrow} = 330$  K. Around

#### 4. A mononuclear spin-crossover complex describing four distinct thermal routes

---

342K, a slight change of the slope is observed, which can be associated to the acetone desorption from the crystal lattice (see below). Subsequently, the value of  $\chi_M T$  remains nearly constant upon decreasing the temperature to 280K. At this temperature, the magnetic response suddenly decreases reaching  $0.41 \text{ cm}^3 \text{ K mol}^{-1}$  at 266 K, drawing a very sharp transition. The quasi diamagnetic response is constantly maintained upon further cooling (labelled 2 in Figure 4.3). When warming again, the [LS-LS] state remains immutable up to around 330K. At this point, the  $\chi_M T$  value rises to  $2.0 \text{ cm}^3 \text{ K mol}^{-1}$  at 398 K ( $T_{1/2\uparrow} = 345 \text{ K}$ ), thus reaching a [LS-HS] state again. Upon a second cooling mode, the system goes back to a diamagnetic state showing a lower temperature transition ( $T_{1/2\downarrow} = 318 \text{ K}$ ). Finally, the latter SCO transition (labelled 4 in Figure 4.3) is repeated in both thermal directions after a third warming and cooling mode. The above described succession of magnetic pathways is completely reproducible, when beginning with new fresh samples. From the results, it is clear the complex can exhibit four markedly different magnetic states *at a same temperature* (for the range in between 240 and 300K, approximately). Due to the several magnetic responses associated to structural phase transitions, compound **6·ac** is an ideal candidate to understand the behaviour in this type of molecular materials and the related mechanisms depending exclusively the thermal history. The analysis of crystallographic data is the best way to get insights into these relevant issues.

#### **XCSR D Study of the thermal evolution of of [FeL(bbp)](ClO<sub>4</sub>)<sub>2</sub>·ac (**6·ac**) and [FeL(bbp)](ClO<sub>4</sub>)<sub>2</sub> (**6**)**

Variable-temperature SCXRD measurements were recorded on different crystals of **6·ac** from several batches confirming the same sequences of phase transitions. The confirmed thermal phase transitions succession was **6·ac** → **6<sup>α</sup>** → **6<sup>β</sup>** → **6<sup>γ</sup>** occurring as SCSC transformations. The crystallographic study of each transition is shown below.

#### **6·ac [HS-LS] → 6<sup>α</sup> [HS-HS] transformation**

The SCO with  $T_{1/2}=330\text{K}$  coupled to this SPT is related to the desorption of acetone, since the crystallographic phase of [FeL(bbp)](ClO<sub>4</sub>)<sub>2</sub> (**6<sup>α</sup>**) is solvent-free. The structure of the latter was determined at 390K (Figure 4.4; and Table A4.1, Appendix 4). The lattice is still found in the same triclinic space group P-1 with two

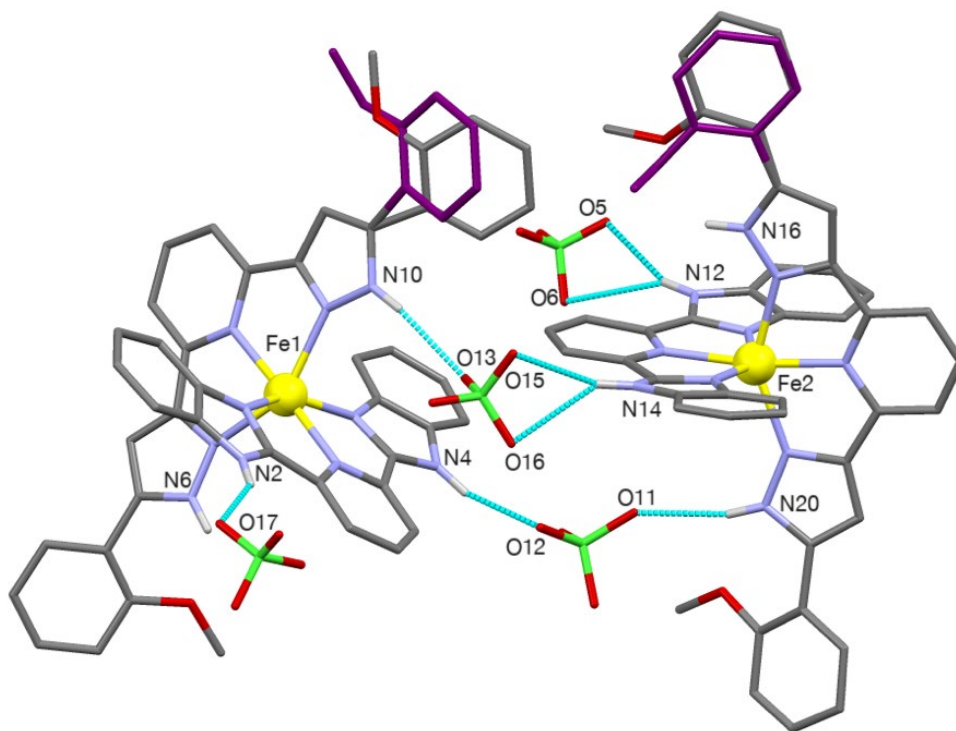


Figure 4.4. Representation of one asymmetric unit of the molecular structure of  $[\text{FeL}(\text{bbp})](\text{ClO}_4)_2$  ( $6^\alpha$ , HS), emphasizing the hydrogen bonds between perchlorate ions and the N–H groups of the complexes, and (in purple) the disorder of some of the methoxyphenyl groups. Both HS Fe centers are in yellow. Only hydrogen atoms on heteroatoms are shown.

$\text{FeL}(\text{bbp})](\text{ClO}_4)_2$  groups in the unit cell. Both iron centres are in the HS state with average Fe–N bond distances at this temperature of 2.183 and 2.151 Å for Fe1 and Fe2, respectively. Thus, the crystallographic data corroborate the [HS–HS] shown by the magnetic measurements. The same conformation of the methoxy groups on ligand L was found here, being *syn, anti* for Fe1 and *syn, syn* for Fe2. Nevertheless, some slight disorder on 50% of the phenyl rings is present. Moreover, all the N–H groups keep their hydrogen bonds with  $\text{ClO}_4^-$  anions. Only the N–H groups that were bonded to acetone molecules in  $6\cdot\text{ac}$  are now free. (Figure A4.7 and Table A4.3, Appendix 4). The inspection of the crystal packing confirms the overall findings. The  $6^\alpha$  lattice arrangement is almost identical to  $6\cdot\text{ac}$ . Thus, the  $[\text{FeL}(\text{bbp})]^{2+}$  cations (Figures 4.5 and A4.8 in Appendix 4) are closely placed like in the previous compound showing only slight differences and some disorder. Analogous intermolecular interactions between the complexes are also observed. However, these are slightly diminished, since there is one less  $\pi\cdots\pi$  interaction. This can be seen in the Appendix 4 (Figure A4.9), where Fe1 is surrounded with four neighbours and Fe2 with six.

#### 4. A mononuclear spin-crossover complex describing four distinct thermal routes

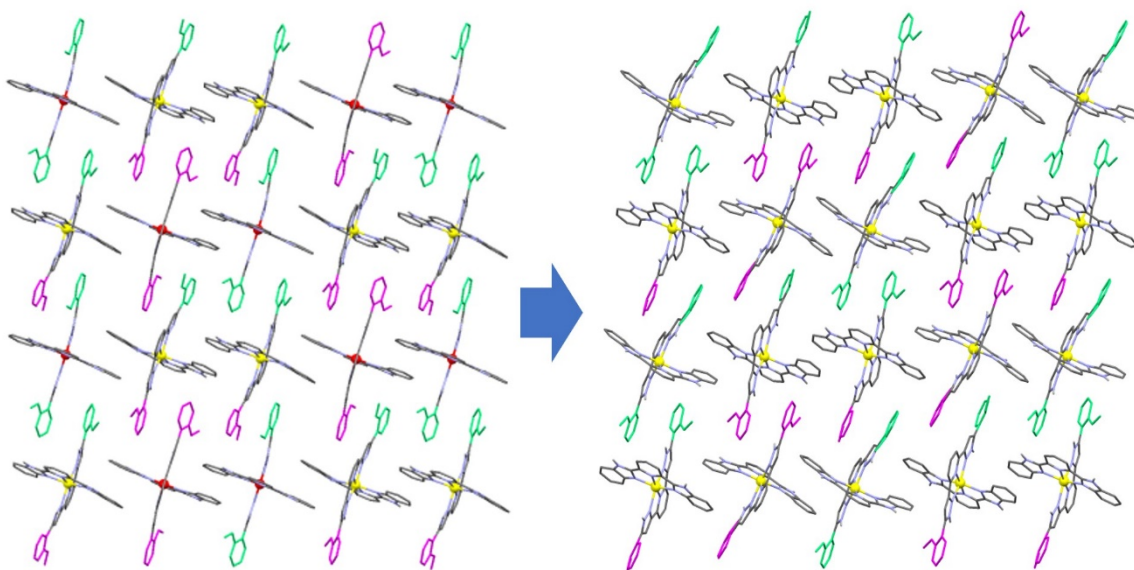


Figure 4.5. Representation of one asymmetric unit of the molecular structure of  $[\text{FeL}(\text{bbp})](\text{ClO}_4)_2$  ( $6^\alpha$ , HS), emphasizing the hydrogen bonds between perchlorate ions and the N–H groups of the complexes, and (in purple) the disorder of some of the methoxyphenyl groups. Both HS Fe centers are in yellow. Only hydrogen atoms on heteroatoms are shown.

The overall cell volume decreases slightly (0.1%), which agrees with the contraction expected from the solvent extrusion in compensation with the effect of the [LS- HS] to [HS-HS] SCO and the thermal expansion. Furthermore, the  $6\text{-ac}$  [HS-LS]  $\rightarrow 6^\alpha$  [HS-HS] transformation was monitored through a VT-SCXRD study. Therefore, SCXRD data were collected at several temperatures (100, 150, 200, 250, 280, 320, 340, 360 and 390K) from the same crystal using synchrotron radiation. (Table A4.1, Appendix 4). The resulting crystallographic results are consistent with the findings observed in the bulk magnetic data. Plots of the cell parameter, volume and the Fe–N bond lengths vs. temperature for both iron centers are shown in Figure 4.6. For Fe1, the average Fe–N bond length stays approximately constant around 2.18 Å for all temperatures (*i.e.* HS), while for Fe2, the value exhibits a noticeable change from 1.96 Å (*i.e.* LS) below 280 K and starts to increase at 320K to reach 2.14 Å (*i.e.* HS) at 390K. Another interesting finding was that the SCO process takes place before the acetone desorption since the solvent molecules are present in all structures up to 340K. Additionally, the unit cell volume gradually increases with warming up to 340K, and it suddenly drops to almost the same value at 100K at higher

temperatures. This value decrease is associated with the acetone extrusion. After completion of the  $6\cdot\text{ac}$  [HS-LS]  $\rightarrow$   $6^\alpha$  [HS-HS] transformation, the crystal was submitted again to low temperatures. The crystal structure of  $6^\alpha$  was again determined at 280K with structural parameters remaining practically constant, and thus, maintaining the HS state.

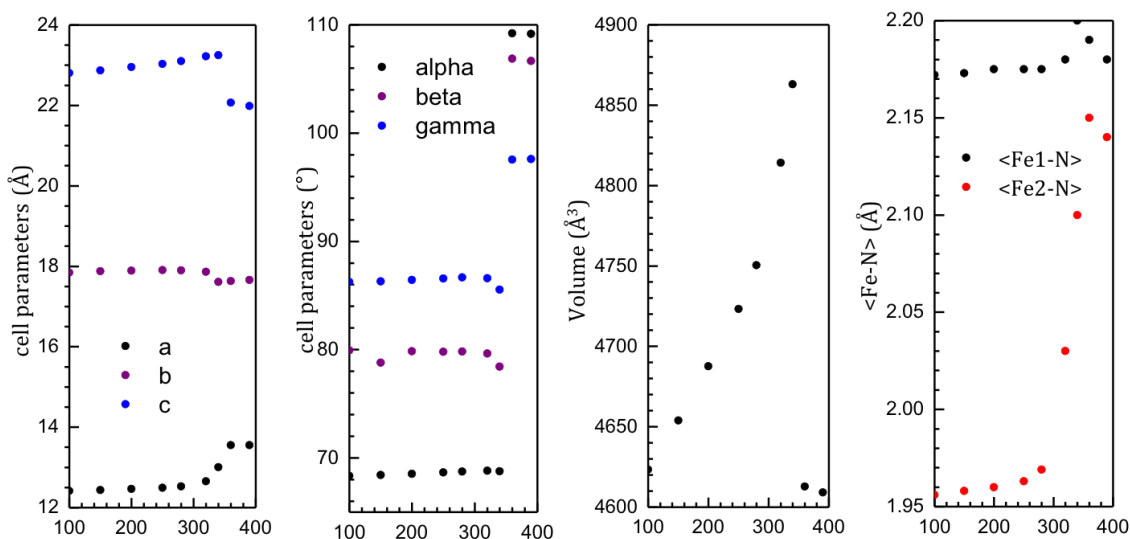


Figure 4.6. Thermal evolution of the cell parameters and volume and of the Fe-N bond lengths throughout the first warming from 100 to 390 K of a single crystal of  $6\cdot\text{ac}$  [LS-HS] to  $6^\alpha$  [HS-HS].

### $6^\alpha$ [HS-HS] $\rightarrow$ $6^\beta$ [LS-LS] transformation

Just below 280K, an abrupt phase transition related to a [HS-HS] to [LS-LS] SCO is observed (Figure 4.3). Structural results from SCXRD at 250 K reveal a new phase of the compound  $[\text{FeL}(\text{bbp})](\text{ClO}_4)_2$ ,  $6^\beta$ , associated with this drastic transition (Figure 4.7). The formation of the different crystallographic phase  $6^\beta$  confirms that the parent phase  $6^\alpha$  can be found only as [HS-HS] state, as reached following solvent vaporization. In this new phase, the space group ( $P-1$ ) and the content of the unit cell are the same as in  $6^\alpha$  (Table A4.2, Appendix 4). Thus, all the N-H groups in the complex cations are interacting with the  $\text{ClO}_4^-$  anions through hydrogen bonds in the same way as previously described and with the exception of two of them (Figure A4.10 and Table A4.3, Appendix 4). Despite their apparent structural resemblance, the Fe-N average bond distances in the new phase ( $6^\beta$ ; 1.964 and 1.955 Å for Fe1 and Fe2) proved the SCO transition between the [HS-HS] and [LS-LS] states, as shown by the magnetic data. Overall, the present crystallographic results provide evidence for the occurrence of major structural rearrangements during this



#### 4. A mononuclear spin-crossover complex describing four distinct thermal routes

transition through conformation changes. Although the configurations of the rings of L ligands of the complexes do not change (still *syn,anti* and *syn,syn* for Fe1 and Fe2, respectively; Figure A4.11, Appendix 4), an overlay of the complexes with the  $6^{\alpha}$  unveil very large molecular displacements. (Figure 4.8).

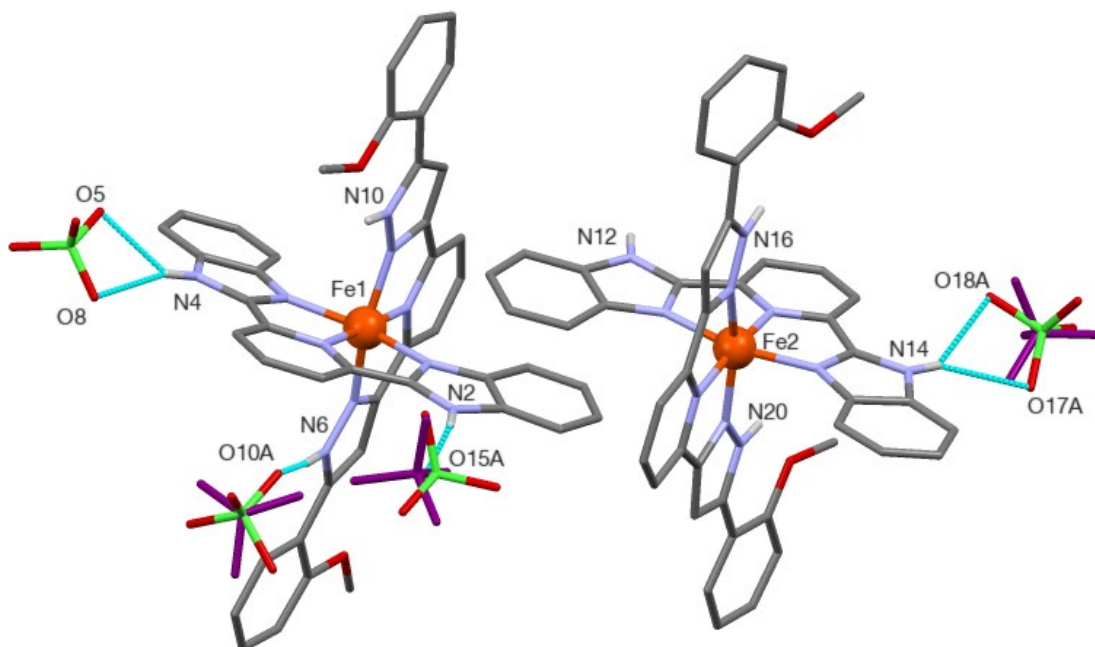


Figure 4.7. Representation of one asymmetric unit of the molecular structure of  $[\text{FeL}(\text{bbp})](\text{ClO}_4)_2$  ( $6^{\beta}$ , LS), emphasizing the hydrogen bonds between perchlorate ions and the N–H groups of the complexes, and (in purple) the disorder of some of these anions. Only hydrogen atoms on heteroatoms are shown.

This drastic reorganization merged with the SCO suggests that the molecules of  $[\text{FeL}(\text{bbp})](\text{ClO}_4)_2$  find themselves better packed in the  $6^{\beta}$  (LS state) rather than in other phases. Actually, there is one extra  $\pi\cdots\pi$  interaction involving the complexes of the asymmetric unit, now with a total of six (Fe1) and five (Fe2) interactions. Additionally, the stronger  $\pi\cdots\pi$  interaction are now shorter than in the cationic arrangement of other phases previously described (Figure A4.12, Appendix 4). This more efficient packing of the complex could be at the root of increased stability of the LS state phase. Additionally, hydrogen bonds with the perchlorate anions also be a driving force of the more compact packing (Appendix 4, Figures A4.13 and A4.14).

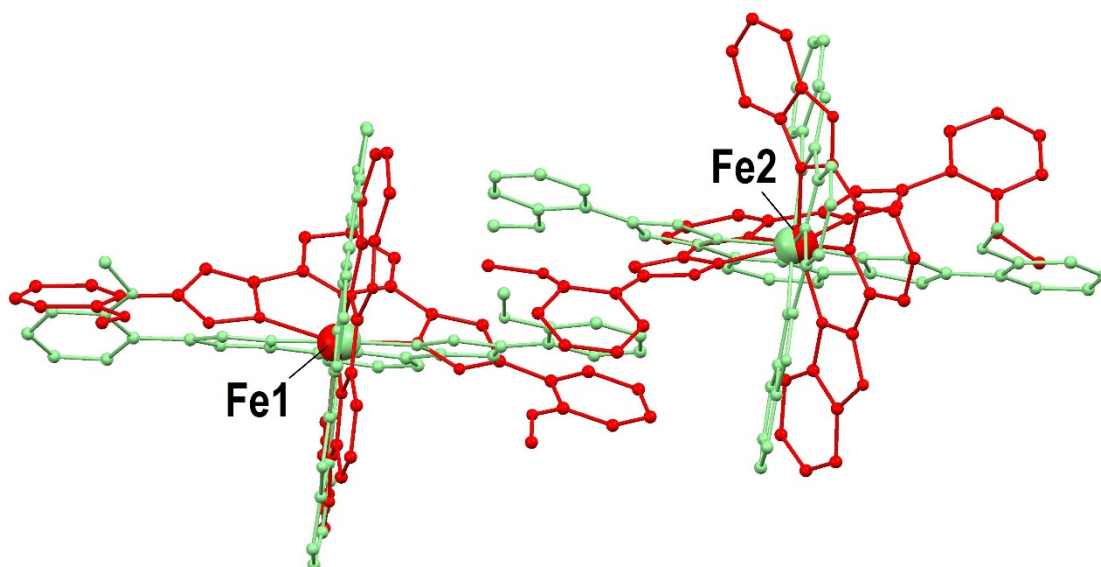


Figure 4.8. Last-squares overlay of the pair of structures of  $[\text{FeL}(\text{bpp})]^{2+}$  complexes in phase  $6^\alpha$  (red) and  $6^\beta$  (green) by displaying multiple structures simultaneously in Mercury program. The picture emphasizes the large atomic displacements of the cations while occurring the  $6^\alpha \rightarrow 6^\beta$ .

#### $6^\beta$ [LS-LS] $\rightarrow$ $6^\gamma$ [HS-LS] transformation

Phase  $6^\beta$  (LS state) persists upon increasing temperature up to 350K, when an abrupt SCO takes places. SCXRD at 360K was used to determine this new transition to the [LS-LS]  $\rightarrow$  [LS-HS] revealing a new phase of the system,  $6^\gamma$  (Figure 4.9). The same space group ( $P-1$ ) and asymmetric unit persist in the new phase. Evidences of the SCO are tracked through the structural parameters around the iron centres. In this case, the average of Fe–N distances is 1.954 and 2.111 for Fe1 and Fe2, respectively. Also, as seen previously, the unit cell varies slightly (increasing 2%, to  $4650.64 \text{ \AA}^3$ , table A4.2 and Figure A4.15, Appendix 4).

The most noticeable feature observed during the  $6^\beta$  [LS-LS]  $\rightarrow$   $6^\gamma$  [HS-LS] transformation is the rotation of 50% of all the methoxyphenyl rings of the  $[\text{FeL}(\text{bpp})]^{2+}$  complexes by approximately  $180^\circ$  (Figure 4.10 and A4.16, Appendix 4). Nevertheless, the overall configuration of the L ligands does not change since the Fe1 centre continues being *syn,anti* and Fe2 *syn,syn*.

#### 4. A mononuclear spin-crossover complex describing four distinct thermal routes

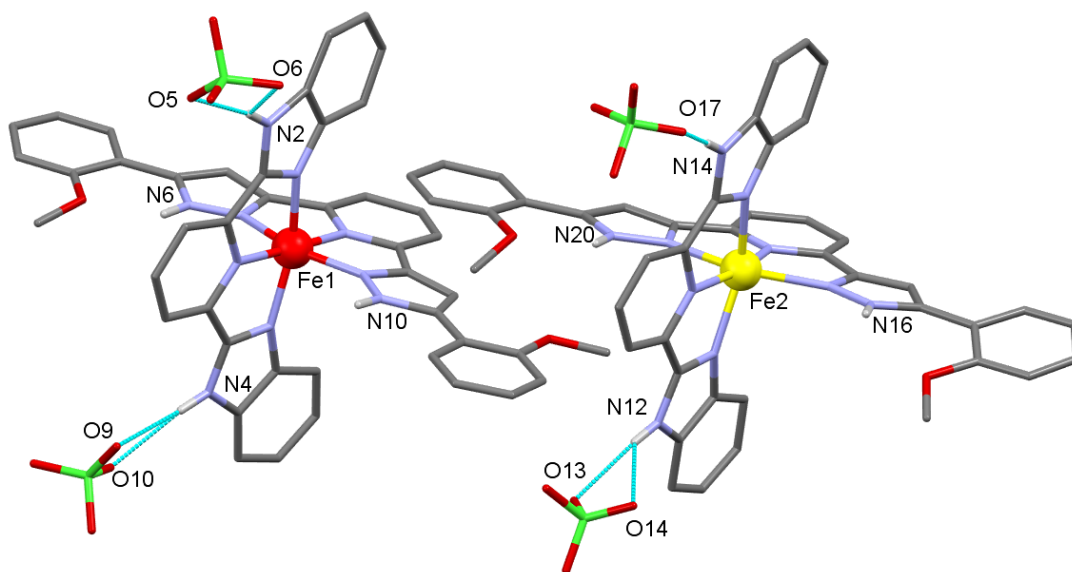


Figure 4.9. Molecular representation of one asymmetric unit of  $[\text{FeL}(\text{bbp})](\text{ClO}_4)_2$  ( $6\nu$ , [LS-HS], emphasizing the hydrogen bonds between the N-H groups of the complexes and the perchlorates. The HS Fe center is in yellow and the LS one in red. Only hydrogen atoms on heteroatoms are shown.

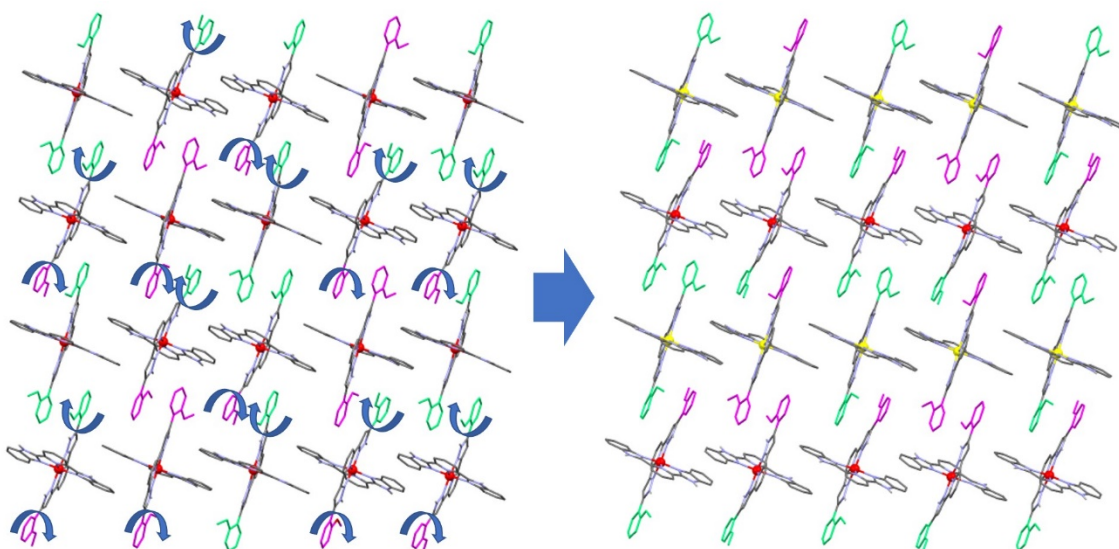


Figure 4.10. Representation of the cationic  $[\text{FeL}(\text{bbp})]^{2+}$  in phases  $6^\beta$  (left) and  $6^\nu$  (right). The blue arrows emphasise the rotation of 50% of the methoxyphenyl rings of the complexed ligand L when the transformation  $6^\beta \rightarrow 6^\nu$  takes place. Green and pink colors of the methoxyphenyl represents their two orientations with respect to the plane of the cations sheet (green toward the reader and pink away from the reader). LS centres are in red, while HS Fe are in yellow.

#### 4. A mononuclear spin-crossover complex describing four distinct thermal routes

Comparison of both structures revealed that the spin centers distribution in the [LS-HS] structure of  $6^\gamma$  is completely different from the one observed in the [LS-HS] system of  $6\cdot ac$ . While in this last phase the Fe complexes are arranged in alternative LS-LS and HS-HS pairs, adjacent arrays of HS and LS rows are observed in  $6^\gamma$ . Table 4.1 provides a summary of the crystallographic data for all the phases of the succession  $6\cdot ac \rightarrow 6^\alpha \rightarrow 6^\beta \rightarrow 6^\gamma$ .

Table 4.1. Summary of the Main Crystallographic Information and Spin States of the Phases Studied.

	$6\cdot ac$	$6^\alpha$	$6^\beta$	$6^\gamma$	$6^\gamma$
Spin state	[HS-LS]	[HS]	[LS]	[HS-LS]	[LS]
$T$ (K)	100K	280K	280K	360K	100K
$a$ (Å)	12.4111	13.4514	11.9586	11.9943	11.7737
$b$ (Å)	17.8454	17.6667	18.7168	17.2248	17.0662
$c$ (Å)	22.8090	21.724	22.6188	23.3508	22.6962
$\alpha$ (°)	68.355	109.064	67.058	98.696	97.611
$\beta$ (°)	79.941	106.922	77.756	97.990	97.009
$\gamma$ (°)	86.244	97.541	84.491	98.576	99.037
$V$ (Å <sup>3</sup> )	4623.4	4519.6	4555.7	4650.6	4416.3
$Z$	2	2	2	2	2
$d_{Fe1-N}$ (Å)	2.172	2.16	1.95	1.95	1.94
$d_{Fe2-N}$ (Å)	1.956	2.11	1.95	2.11	1.96

Since the crystal was subjected to a large succession of temperature cycles accompanied by crystallographic transformation, single-crystal mosaicity was used to prove the integrity of the crystals upon these changes. Furthermore, this notion can be used to follow the modification of the crystal.<sup>26</sup> In our case, all the transformations take place with small variation in the crystal relative mosaicity (Figure A4.17, Appendix 4). The largest variation (around 10% increase) occurs upon the  $6\cdot ac \rightarrow 6^\alpha$  transformation, which is reasonable due to the loss of the acetone molecules from the crystalline lattice. Overall, the mosaicity is not significantly modified which suggest that the integrity of the crystals remains over the cycles.

### Differential Scanning calorimetry (DSC) studies of the phase transition succession for $6 \cdot ac$

The DSC data are consistent with the sequence of transformations of  $6 \cdot ac$  (Figure 4.11). The derived temperatures and the estimation of the energies involved in each transformation is given in table 4.2. The broad anomaly (280 to 365K) of the first warming mode is attributed to the  $6 \cdot ac$  [LS-HS]  $\rightarrow 6^\alpha$  [HS-HS] transformation. The whole enthalpy associated with it can be attributed to the sum contribution of the desorption of two molecules of acetone,<sup>27</sup> the electronic contribution of the SCO of one Fe(II) and minimal structural changes. Two maxima, 316 and 345K, are clearly observed. The first one is attributed to the SCO of  $6 \cdot ac$  and to the loss of acetone molecules, while the second to the SPT. The desorption of acetone is likely observed at lower temperatures together with the SCO transition in  $6 \cdot ac$  concomitant to it. The connection between these two processes is not necessarily established. Indeed, their independence is corroborated by the magnetic and crystallographic data. A slope change around 345K in the  $\chi_M T$  vs  $T$  plot (Figure 4.3) is ascribed to the vaporization of acetone. Additionally, an increase in average Fe1-N bond lengths is already shown at 320 and 340K (Figure 4.6 right) in the VT-SCXRD study, while both acetone molecules are still fully present in the crystal lattice.

0

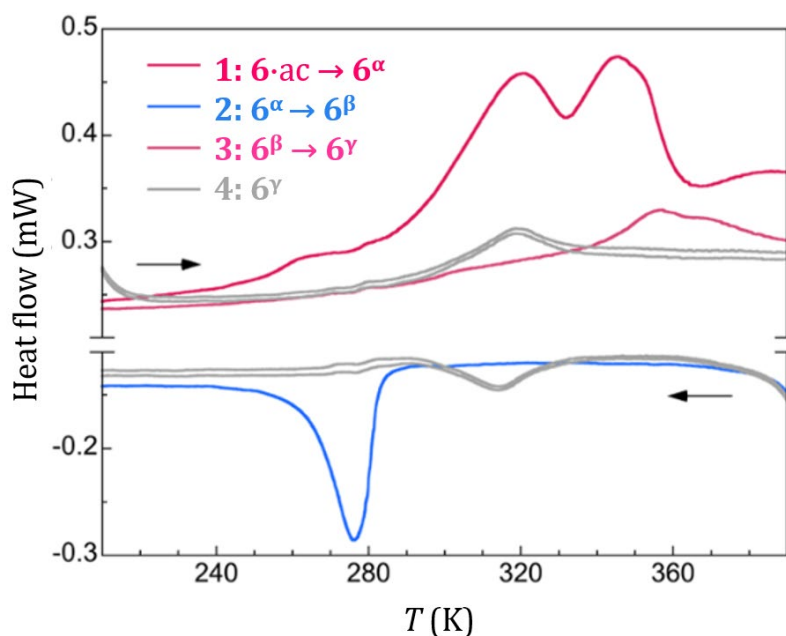


Figure 4.11. DSC patterns for  $5 \cdot ac$  upon four successive thermal cycles. The successive transformations  $6 \cdot ac \rightarrow 6^\alpha \rightarrow 6^\beta \rightarrow 6^\gamma$  are depicted. The last  $6^\gamma$  reversible SCO is also indicated.

#### 4. A mononuclear spin-crossover complex describing four distinct thermal routes

Table 4.2. Summarized temperatures and associated enthalpies for each phase transition.<sup>a</sup>

	$T_{1/2}$ (K) <sup>b</sup>	$T_{\max}$ (K) <sup>c</sup>	$\Delta H$ (kJ·mol <sup>-1</sup> ) <sup>d</sup>
<b>6·ac</b> [LS-HS] → <b>6·ac</b> [HS-HS]	318	316	
<b>6·ac</b> [HS-HS] → <b>6<sup>α</sup></b> [HS-HS]	345	345	69 <sup>e</sup>
<b>6<sup>α</sup></b> [HS-HS] → <b>6<sup>β</sup></b> [LS-LS]	280	276	28.6
<b>6<sup>β</sup></b> [LS-LS] → <b>6<sup>γ</sup></b> [LS-HS]	360	357	12.4
<b>6<sup>γ</sup></b> [LS-HS] ↔ <b>6<sup>γ</sup></b> [LS-LS] <sup>f</sup>	318	319	11.0

<sup>a</sup>All transformations are irreversible except the last one. <sup>b</sup>Temperature at which the corresponding change in  $\chi T$  is halfway from the magnetometry data. <sup>c</sup>Temperature derived from the peak maxima of the heat flow anomalies. <sup>d</sup>Enthalpy derived from the integration of the heat flow anomalies and considering the formula from the single-crystal structures with two Fe sites per mol. <sup>e</sup> The separate enthalpy contributions of the two maxima peaks (clearly observed) cannot be estimated with accuracy. <sup>f</sup>The SCO transition is reversible.

When cooling, the **6<sup>α</sup>** [HS-HS] → **6<sup>β</sup>** [LS-LS] transition takes place with a sharp exothermic peak at 276K. The large enthalpy (28.6 kJ·mol<sup>-1</sup>) associated with it comes up from the SCO of two Fe(II) centres and the largest crystallographic rearrangement among all transitions. In contrast, a smaller enthalpy (12.4 kJ·mol<sup>-1</sup>) for the less pronounced rearrangement when **6<sup>β</sup>** [LS-LS] → **6<sup>γ</sup>** [LS-HS] is observed. Apparently, this is constituted by two separate processes from the thermal perspective: the anomaly presents a small shoulder at ca. 368K and a more intuitive peak at 357K, which could be intuitively associated to the succession **6<sup>β</sup>** [LS-LS] → **6<sup>β</sup>** [LS-HS] and **6<sup>β</sup>** [LS-HS] → **6<sup>γ</sup>** [LS-HS], respectively. The last thermal scans are superimposable. Thus, one of the Fe centres of **6<sup>γ</sup>** shows a reversible SCO with an unexpected similar temperature to **6·ac**. Further heating of **6<sup>γ</sup>** up to 460K does not show any anomaly. Therefore, its [HS-HS] state cannot be reached before decomposition or probable explosion of the compound containing perchlorate. The excess enthalpy and entropy derived from the integration of  $\Delta C_p$  with respect to  $T$  and  $\ln T$ , respectively, associated to the SCO of the Fe2 centre depicted in Figure 4.11 have values of 11.0 kJ·mol<sup>-1</sup> and 31.6 11.0 kJ·mol<sup>-1</sup>, respectively. Since the excess entropy is much larger than the electronic component of the transition ( $R \ln 5 = 13.38$  J K<sup>-1</sup>mol<sup>-1</sup>), the SCO is significantly coupled to lattice phonons. The fitted data to Sorai's domain model confirmed this coupling.<sup>28,29</sup> The number of interacting molecules per domain are  $n=17.0$ , which corresponds to medium to high

#### 4. A mononuclear spin-crossover complex describing four distinct thermal routes

cooperativity of the SCO transition (Figure A4.18, Appendix 4). As mentioned previously in chapter 2, values of  $n$  close to one are characteristic for gradual SCO, while values above 20 are for highly cooperative systems.<sup>30,31</sup>

##### DFT study of the Solid-State Transformations

The free-energy ( $G$ ) of the [HS-HS], [HS-LS] and [LS-LS] states for **6**·ac, **6**<sup>α</sup>, **6**<sup>β</sup> and **6**<sup>γ</sup> were screened along the temperature range 1-400K by means of DFT calculations in order to estimate the associated energy difference involved in each transformation (see Appendix 4 for extended computational details). Usually, the difference in electronic enthalpy ( $\Delta H_{\text{elec}}$ ), the main component of  $G$ , is often used in SCO calculations to complete the evolution of the free-energy (Table 4.3). Thus, both calculated values for all the accessible spin-state combinations of all the crystallographic phases were analysed. For the first transformation, [LS-HS]-to-[HS-HS], its  $G$  evolution shows that **6**·ac is more stable in the [LS-HS] along all the temperature range (Figure A4.19, Appendix 4). This agrees also with the small computed value of  $\Delta H_{\text{elec}}^{[\text{LS-HS}]-[\text{LS-LS}]} = 2.2 \text{ kJ mol}^{-1}$ . For this transition, the predicted temperature is 688K, while the experimental value is 340K. This large difference can be attributed to the extrusion of acetone rather than an error on choosing the appropriate DFT method to simulate the SCO phenomena.<sup>32,33</sup>

Table 4.3. Summary of the electronic enthalpy difference on the SCO transitions in **6**·ac, **6**<sup>α</sup>, **6**<sup>β</sup> and **6**<sup>γ</sup> (kJ mol<sup>-1</sup>).

	$\Delta H_{\text{elec}}^{[\text{HS-HS}]-[\text{LS-LS}]}$	$\Delta H_{\text{elec}}^{[\text{LS-HS}]-[\text{LS-LS}]}$
<b>6</b> ·ac	21.9	2.2
<b>6</b> <sup>α</sup>	7.2	2.5
<b>6</b> <sup>β</sup>	30.9	16.3
<b>6</b> <sup>γ</sup>	14.9	12.3

The [HS-HS] state was preferred for the **6**<sup>α</sup> phase above 76K and the [LS-HS] state below this temperature. The observed value for the [HS-HS]- to [LS-LS] transition is 280K. Thus, the abrupt transition cannot be exclusively based on spin conversion. In fact, SCXRD results on the **6**<sup>α</sup> to **6**<sup>β</sup> transition evidenced its coupling with a SPT. This proven fact is also confirmed by the DFT calculations, since the phase **6**<sup>β</sup> is more

stable (5.2 KJ mol<sup>-1</sup>) than the **6<sup>α</sup>** in the [LS-LS] state (Figure A4.19, Appendix 4). Then, the computed study for [LS-LS] conversion to [HS-HS] of **6<sup>β</sup>** indicates that it would occur at ca. 500K (not accessible, too high temperature). Again, the abrupt SCO transition must be associated with the coupling between SCO and the SPT for the **6<sup>β</sup>** → **6<sup>γ</sup>** transformation. Nevertheless, this computed [HS-HS] state does not match with the experimentally accessed [LS-HS]. Two assumptions could explain this disagreement: (i) the [LS-HS] is kinetically trapped or (ii) the computational model failed for this case. For the first case, the computed unit cell would suffer a much larger volume increase (5.6%) upon the [LS-LS]-to-[HS-HS] SCO than upon [LS-LS]-to-[LS-HS] (1.8%, see Table A4.4, Appendix 4). For the second case, the used approximation for the evaluation of the vibrational enthalpy and entropy might be erroneous. However, the proposed computational method predicted accurately the rest of the phase transitions. Finally, the computations validate the last reversible transition of **6<sup>γ</sup>** (i.e., purely SCO based). The predicted SCO temperature (350K) for the [LS-LS]-to [LS-HS] transition agrees with the observed transition at 318K, since the value difference is within the margin of expected error.

After this detailed study of a succession of different crystallographic phases giving rise to an unprecedented mixed-states molecular complex, we present a similar interesting compound (**7·ac**) obtained as side product from the attempts on isolation of **6·ac** (See synthesis discussion above and Figure A4.1, Appendix 4).

#### **Crystal structure of [FeL(bpp)](ClO<sub>4</sub>)<sub>2</sub>·ac (**7·ac**)**

The molecular structure of **7·ac** was determined by SCXRD at 100K. The compound crystallizes in the triclinic space group *P*-1. The unit cell encloses two asymmetric units, each containing four [FeL(bpp)](ClO<sub>4</sub>)<sub>2</sub> ensembles and four crystallographic inequivalent molecules of acetone (Figure 4.12). The volume unit cell is 9167.03 Å<sup>3</sup>. Within each cation, both tridentate imine ligand coordinate with the Fe (II) metal in a *mer* fashion, giving a distorted octahedral geometry to each center. At this temperature, the average Fe-N bond distances are 2.17 Å (Fe1), 1.98 Å (Fe2), 2.0 Å (Fe3) and 2.16 Å (F4). The corresponding parameters of distortion Σ and Θ are given in Table 4.2. Thus, Fe1 and Fe4 are HS state, while Fe2 and Fe3 are LS.



#### 4. A mononuclear spin-crossover complex describing four distinct thermal routes

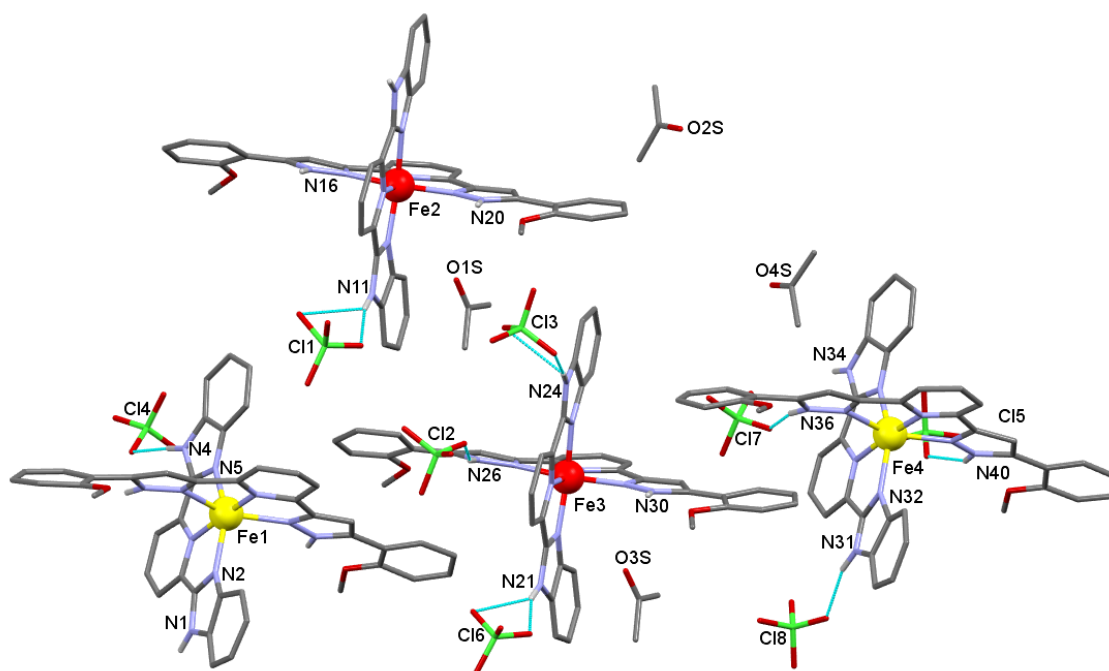


Figure 4.12. Molecular representation of  $[\text{FeL}(\text{bbp})](\text{ClO}_4)_2 \cdot \text{ac}$  ( $7 \cdot \text{ac}$ ) with certain heteroatoms labelled. Only hydrogen atoms of the heteroatoms are shown. Hydrogen bonds between perchlorate ions (dashed cyan lines) are emphasised. Carbon, oxygen and hydrogen atoms are coloured in gray, red and white, respectively. The HS Fe is in yellow while the LS one is red.

Table 4.4. Summarized Average Fe-N bond lengths, distortion parameters and assigned spin states for the four inequivalent Fe atoms of compound 7.

Irons of complex 6	$\langle \text{Fe-N} \rangle$ bond average	$\Sigma$	$\Theta$	Spin state
Fe1	2.17	142(3)	469(7)	HS
Fe2	1.98	92(3)	301(7)	LS
Fe3	2.0	92(2)	302(7)	LS
Fe4	2.165	141(2)	463(6)	HS

The conformation of the methoxyphenyl groups of L in all complexes is the same. One methoxy group points towards the coordination pocket of L and the other to the opposite side, being (*syn, anti*) for all irons. The free N-H groups of the pyrazolyl and imidazolyl rings of ligands L and bbp allow the formation of hydrogen bonds. A total of sixteen hydrogen bonds between them and perchlorate ions and two molecules of acetone are established (Figure A4.20 and Table A4.5, Appendix 4). The cationic  $[\text{FeL}(\text{bbp})]^{2+}$  moieties are organized in sheets stabilising  $\pi \cdots \pi$  interactions. Two  $\pi$ -stacking interactions are depicted in Figure A4.21 with the distances with Olex2 in Table A4.6 and A4.7, Appendix 4. The rest of the rest of the distances between the

selected centroids are also depicted in green. Within the sheets, the complexes describe different successions of distinct crystallographic iron centres and HS and LS states. In one direction, Fe1 and Fe4 alternates in one row of the sheet, being all of the centres in the HS state. The other row is formed by alternated Fe2 and Fe3 in the LS state. In the other direction, all metal centres (Fe1-Fe4) are alternated. Thus, the HS-LS states are alternated too (Figure A4.22, Appendix 4). Since no evident structural and electronic features are present, the difference of magnetic behaviour ascribed to the irons may be due to subtle factors.

Compound **7·ac** represents another extraordinary mononuclear complex with high number of ordered mixed-spin states as previously seen for compound **6·ac**. The findings mentioned above provides a good starting point for discussion and further magnetic and crystallographic research of such kind of compounds.

#### **Probing the importance of intermolecular interactions on these systems**

The cationic  $[\text{FeL}(\text{bbp})]^{2+}$  in **6·ac** are connected with perchlorate anions and solvent molecules giving a highly dense network of intermolecular interactions. Therefore, the compounds are prone to display cooperativity. Small variations of these connections in between the well-organized layers of cations can lead to different cooperative effects and different magnetic behaviour. One way to probe the importance of this intermolecular interactions within the molecular material would be to disrupt them. With such a purpose, the N-H free nitrogen sites of the bbp ligand were N-acetylated to introduce methyl groups (ligand  $\text{NMe}_2\text{bbp}$ ). Thus, the formation hydrogen bonds derived from the bbp ligand could be prevented, therefore, the packing would be necessary affected. Furthermore, the change on the ligand field could play a role too. In order to obtain a derivative of compound to **6·ac**, stoichiometric amounts of L and  $\text{NMe}_2\text{bbp}$  with hydrated  $\text{Fe}(\text{ClO}_4)_2$  salt mixed in dry acetone and layered in diethyl ether, which is an analogous procedure to **6·ac**. Nevertheless, the formation of each homoleptic compound was preferred over the heteroleptic one. Thus, two type of crystal, yellow needles and deep purple blocks, were obtained under these mentioned conditions. Although yellow needles have been obtained, the crystal structure has not, as yet, fully solved due to a disordered perchlorate and additional solvent molecules which couldn't be definitively identified. However, the homoleptic compound  $[\text{FeL}_2](\text{ClO}_4)_2$  (**8**) could be identified (Figure 4.13 and Table

#### 4. A mononuclear spin-crossover complex describing four distinct thermal routes

A4.8, Appendix 4). The compound crystallises in the triclinic space group P-1, and the asymmetric unit consists in one  $[\text{FeL}_2]^{2+}$  cation, two perchlorates to balance the charge, two molecules of water, and some unidentified solvent. Although, the synthesis was performed in dry acetone, some molecules of adventitious water are present, perhaps coming from the hydrated salt employed. Therefore, the crystal easily absorbs water molecules from air moisture. For this compound, there is one ligand L with a *syn,syn* conformation of the phenol groups towards the central coordination pocket. The other ligand, has only one methoxyphenol group disordered over two positions of equal occupancy.

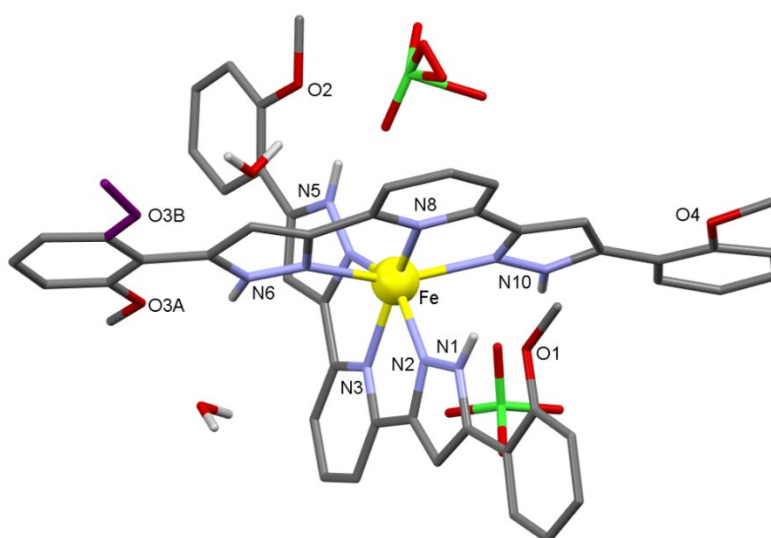


Figure 4.13. Molecular representation of  $[\text{FeL}_2](\text{ClO}_4)_2 \cdot 2\text{H}_2\text{O}$  (**8**) with certain heteroatoms labelled. Both disordered orientations on one methoxyphenyl ring are shown. Carbon, oxygen and hydrogen atoms are coloured in gray, red and white, respectively. The HS Fe is in yellow.

From the average of Fe-N distances and the deformation around the Fe(II) center ( $\Sigma$ ), 2.18 and 171.4, respectively, the compound resulted in a HS state at 100K. No further investigations on this compound were carried since it is another crystallographic phase of similar compounds previously reported in our group (Tables A4.8 and A4.9). All these compounds remain stable in the HS state, not displaying any SCO.

The other co-crystallized crystals, the deep purple blocs, were found to be from the other homoleptic compounds, now with ligand bbp. Compound **9** crystallizes in the tetragonal space group *P*-4b2, and the unit cell contains one  $[\text{Fe}(\text{bbp})_2]^{2+}$  and two

#### 4. A mononuclear spin-crossover complex describing four distinct thermal routes

perchlorate anions with disorder in one of them (Figure 4.14 and Table A4.8, Appendix 4). As yet, the fully solution has not been carried out. Nevertheless, the homoleptic compound  $[\text{Fe}(\text{bbp})_2](\text{ClO}_4)_2$  (**8**) could be identified and the description of the deformation around the coordination sphere allows to predict the LS state of the compound at 100K, having a Fe–N bond distances average and  $\Sigma$  of 1.93 and 81, respectively. This is consistent with the dark red colour of the crystals.

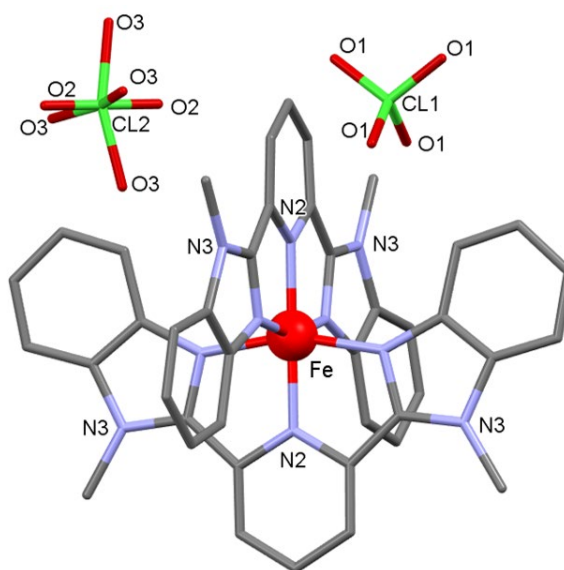


Figure 4.14. Molecular representation of complex  $[\text{Fe}(\text{NMe}_2\text{bbp})_2](\text{ClO}_4)_2$  (**9**). The LS Fe center is in red.

In order to assist the formation of the heteroleptic compounds, other solvents were tested. The use of not dried acetone gives similar results. Two type of crystals were obtained. In this case however, compound **10** was obtained instead of the homoleptic compound, as yellow needles (Figure 4.15 and Table A4.8, Appendix 4). The complex crystallizes in the monoclinic space group  $P2_1/c$  and it is formed by one ligand L coordinated to the iron centre together with 2 molecules of water and one of acetone. Two perchlorates compensate the positive charge and two additional acetone molecules establish hydrogen bonds with water and one free N-H group. The other co-crystallized crystals, the deep purple blocks, corresponded to the previously obtained homoleptic  $[\text{Fe}(\text{bbp})_2](\text{ClO}_4)_2$  (**9**). Similar results were obtained when using ethanol and dmf as solvents.

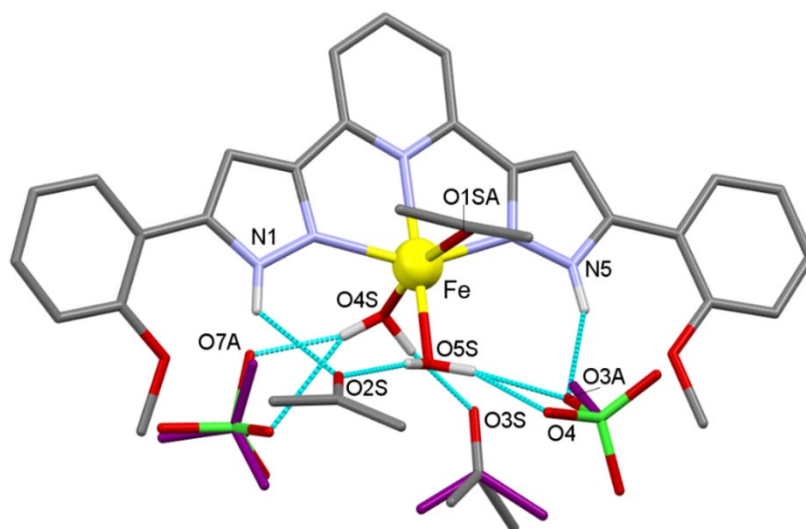


Figure 4.15. Molecular representation of complex  $[\text{FeL}(\text{H}_2\text{O})_2(\text{C}_3\text{H}_6\text{O})](\text{ClO}_4)_2 \cdot 2\text{C}_3\text{H}_6\text{O}$  (**10**) emphasizing the hydrogen bonds between the N-H groups of the complexes and the perchlorates and the acetone and water molecules. The HS Fe center is in yellow. Only hydrogen atoms on heteroatoms are shown.

Unfortunately, obtaining of the corresponding heteroleptic complex was not possible after screening several crystallization conditions. The formation of each homoleptic compound with ligands L and NMe<sub>2</sub>bbp, respectively, is favoured in the solid state. Previously, it was demonstrated that the preferred distribution in solution is not always the one favoured in solid estate.<sup>16</sup> Still, we don't have insights on the presence of the hypothetical heteroleptic complex  $[\text{FeL}(\text{NMe}_2\text{bbp})](\text{ClO}_4)_2$  in solution. Nevertheless, the difference in reactivity between both systems ( with bpp or with NMe<sub>2</sub>bbp) can be unambiguously attributed to the disruption of the N-H interactions. The free N-H groups of bbp in compound **6**·ac and the other crystallographic phases (**6**<sup>α</sup>, **6**<sup>β</sup> and **6**<sup>γ</sup>) contribute extensively to the construction of a dense intermolecular network, which in turn, may facilitate its easy isolation in the solid state. Assuming that the hypothetical  $[\text{FeL}(\text{NMe}_2\text{bbp})](\text{ClO}_4)_2$  complex would display a less dense molecular network due the lack of the significant hydrogen bonds, its isolation in solid-state might be prevented.

### 4.3. Conclusions

[FeL(bbp)](ClO<sub>4</sub>)<sub>2</sub>·ac (**6**·ac) is a molecular material organized as a dense arrangement of intermolecular interactions which gives a highly compact lattice as a result. This discrete material allows the diffusion of acetone molecules out of the crystal lattice through heating without any crystallinity loss. Although this feature is quite rarely observed in non-porous materials, the robustness of its lattice allows to access to a novel phase formed through the template effect caused by the leaving solvent. Since four different thermal transitions can be observed through magnetometry measurements, SCXRD studies are the best technique to unveil their origin and connect the magnetic behaviour with the associated SPTs. After the acetone desorption, another SCO transition takes place (from [HS-HS] to [LS-LS] upon cooling). Interestingly, another SCO (now [LS-LS] to [LS-HS]) is observed upon warming the latter phase. This transformation into a third phase has never been seen before since it is even rare to find irreversible SPTs coupled to SCO. Thus, [FeL(bbp)](ClO<sub>4</sub>)<sub>2</sub> (**6**) is a unique compound exhibiting four different magnetic responses within a determinate temperature range (300–340K) depending on the thermal history of the sample. All of these features make these compounds valuable as potential new smart materials responsive to complex thermal itineraries. A similar compound (**7**·ac) is presented as good candidate for further SCO exploration. The mixed-spin states compound could give rise to similar magnetic behaviour. The direct effect of disrupting hydrogen bonds interactions could not be reached. Nevertheless, after several attempts to access the methylated derivative of **6**·ac, we can have some insights on the importance of these interaction within the complex.

### 4.4. Experimental

#### Synthesis

Ligand 2,6-bis-(5-(2-methoxyphenyl)-pyrazol-3-yl)pyridine (L) was synthesized as the group published before, by ring closure of a bis-β-diketone precursor using hydrazine.<sup>21</sup> The ligand, 2,6-bis-(benzimidazol-2-yl)pyridine (bbp) was prepared through a condensation of pyridine-2,6-dicarboxylic acid with *o*-phenylenediamine in polyphosphoric acid solution assisted with microwave irradiation.<sup>25,34</sup> The disodium salt of 2,6-bis(benzimidazole-2-yl)pyridine was synthesised by following

#### 4. A mononuclear spin-crossover complex describing four distinct thermal routes

---

the reported procedure.<sup>35</sup> The NMe<sub>2</sub>-bbp derivative was synthesized by substituting both N-H nitrogen sites of bbp using methyl iodide as alkylating agent.<sup>36</sup> **Caution:** Perchlorate salts of metal complexes are potentially explosive. Only small quantities of material should be prepared, and the samples should be handled with care.

**[FeL(bbp)](ClO<sub>4</sub>)<sub>2</sub>·ac (6·ac).** A suspension of L (0.026g, 0.06 mmol) and bbp (0.019 g, 0.06 mmol) in dry acetone and absolute ethanol (10 mL; 1:1 vol.) was added dropwise with stirring to a solution of Fe(ClO<sub>4</sub>)<sub>2</sub>·6H<sub>2</sub>O (0.034 g, 0.13 mmol) and ascorbic acid (~3 mg) in dry acetone and absolute ethanol (10 mL; 1:1 vol.). The resulting red solution was stirred for 45 min at room temperature. The solution was then filtered and layered with diethyl ether (1:1 vol.). Dark red crystals (0.018 mg, 8%) suitable for SCXRD were obtained after a few days.

**[FeL(bbp)](ClO<sub>4</sub>)<sub>2</sub>·ac (7·ac).** A suspension of L (0.026g, 0.06 mmol) and Na<sub>2</sub>bbp (0.021 g, 0.06 mmol) in dry acetone (10 mL) was added dropwise with stirring to a solution of Fe(ClO<sub>4</sub>)<sub>2</sub>·6H<sub>2</sub>O (0.034 g, 0.13 mmol) and ascorbic acid (~3 mg) in dry acetone (10 mL). The resulting red solution was stirred for 45 min at room temperature. The solution was then filtered and layered with diethyl ether (1:1 vol.). Shining red crystals suitable for SCXRD were obtained after a few days. The crystals were easily separated manually under microscope.

**[FeL<sub>2</sub>](ClO<sub>4</sub>)<sub>2</sub>·2H<sub>2</sub>O(8) and [Fe(Me<sub>2</sub>bbp)<sub>2</sub>](ClO<sub>4</sub>)<sub>2</sub> (9).** A suspension of L (0.026g, 0.06 mmol) and NMe<sub>2</sub>bbp (0.020 g, 0.06 mmol) in dry acetone (10 mL) was added dropwise with stirring to a solution of Fe(ClO<sub>4</sub>)<sub>2</sub>·6H<sub>2</sub>O (0.034 g, 0.13 mmol) and ascorbic acid (~3 mg) in dry acetone (10 mL). The resulting red-violet solution was stirred for 45 min at room temperature. The solution was then filtered and layered with hexane (1:1 vol.). Yellow needles and deep-purple block crystals were obtained after a few days. The crystals were easily separated manually under microscope.

## 4.5. References

- (1) Gütlich, P.; Gaspar, A. B.; Garcia, Y. *Beilstein J. Org. Chem.* **2013**, *9*, 342–391.
- (2) Guionneau, P.; Marchivie, M.; Bravic, G.; Létard, J. F.; Chasseau, D. In *Spin Crossover in Transition Metal Compounds II, Topics in Current Chemistry*; Gütlich, P., Goodwin, H. A., Eds.; Springer, 2004; Vol. 234, pp 97–128.
- (3) Halcrow, M. A. *Chem. Soc. Rev.* **2011**, *40*, 4119–4142.
- (4) Halcrow, M. A. *Chem. Lett.* **2014**, *43*, 1178–1188.
- (5) Shatruk, M.; Phan, H.; Chrisostomo, B. A.; Suleimenova, A. *Coord. Chem. Rev.* **2015**, *289–290*, 62–73.
- (6) Carbonera, C.; Sánchez Costa, J.; Money, V. A.; Elhaïk, J.; Howard, J. A. K.; Halcrow, M. A.; Létard, J. F. *Dalt. Trans.* **2006**, No. 25, 3058–3066.
- (7) Pritchard, R.; Kilner, C. A.; Halcrow, M. A. *Chem. Commun.* **2007**, 577–579.
- (8) Tailleur, E.; Marchivie, M.; Daro, N.; Chastanet, G.; Guionneau, P. *Chem. Commun.* **2017**, *53*, 4763–4766.
- (9) Ortega-Villar, N.; Muñoz, M.; Real, J. *Magnetochemistry* **2016**, *2*, 16.
- (10) Craig, G. A.; Sánchez Costa, J.; Roubeau, O.; Teat, S. J.; Aromí, G. *Chem. - A Eur. J.* **2011**, *17*, 3120–3127.
- (11) Phan, H. V.; Chakraborty, P.; Chen, M.; Calm, Y. M.; Kovnir, K.; Keniley, L. K.; Hoyt, J. M.; Knowles, E. S.; Besnard, C.; Meisel, M. W.; Hauser, A.; Achim, C.; Shatruk, M. *Chem. - A Eur. J.* **2012**, *18*, 15805–15815.
- (12) Salje, E. K. H. *Acta Crystallogr. Sect. A* **1991**, *47*, 453–469.
- (13) Halcrow, M. A. In *Spin-Crossover Materials: properties and Applications*; John Wiley & Sons, Ltd., 2013; pp 147–169.
- (14) Salmon, L.; Molnár, G.; Cobo, S.; Oulié, P.; Etienne, M.; Mahfoud, T.; Demont, P.; Eguchi, A.; Watanabe, H.; Tanaka, K.; Bousseksou, A. *New J. Chem.* **2009**, *33*, 1283–1289.
- (15) Cavallini, M.; Melucci, M. *ACS Appl. Mater. Interfaces* **2015**, *7*, 16897–16906.
- (16) Barrios, L. A.; Bartual-Murgui, C.; Peyrecave-Lleixà, E.; Le Guennic, B.; Teat, S. J.; Roubeau, O.; Aromí, G. *Inorg. Chem.* **2016**, *55*, 4110–4116.
- (17) Craig, G. A.; Roubeau, O.; Aromí, G. *Coord. Chem. Rev.* **2014**, *269*, 13–31.
- (18) Goodwin, H. A. In *Spin Crossover in Transition Metal Compound I. Top. Curr. Chem.*; Springer-Verlag Berlin Heidelberg 2004, 2004; pp 59–90.
- (19) Halcrow, M. A. *Coord. Chem. Rev.* **2009**, *253*, 2493–2514.



- (20) Halcrow, M. A. *New J. Chem.* **2014**, *38*, 1868–1882.
- (21) Costa, J. S.; Rodríguez-Jiménez, S.; Craig, G. A.; Barth, B.; Beavers, C. M.; Teat, S. J.; Aromí, G. *J. Am. Chem. Soc.* **2014**, *136*, 3869–3874.
- (22) Li, B.; Wei, R. J.; Tao, J.; Huang, R. Bin; Zheng, L. S.; Zheng, Z. *J. Am. Chem. Soc.* **2010**, *132*, 1558–1566.
- (23) Boča, R.; Renz, F.; Boča, M.; Fuess, H.; Haase, W.; Kickelbick, G.; Linert, W.; Vrbová-Schikora, M. *Inorg. Chem. Commun.* **2005**, *8*, 227–230.
- (24) Boča, R.; Baran, P.; Dlhán, L.; Fuess, H.; Hasse, W.; Renz, F.; Linert, W.; Svoboda, I.; Wemer, R. *Inorg. Chim. Acta.* **1997**, *260*, 129–136.
- (25) Niknam, K.; Fatehi-Raviz, A. *J. Iran. Chem. Soc.* **2007**, *4*, 438–443.
- (26) Guionneau, P.; Lakhroufi, S.; Lemée-Cailleau, M. H.; Chastanet, G.; Rosa, P.; Mauriac, C.; Létard, J. F. *Chem. Phys. Lett.* **2012**, *542*, 52–55.
- (27) Pennington, R. E.; Kobe, K. A. *J. Am. Chem. Soc.* **1957**, *79*, 300–305.
- (28) Sorai, M.; Nakano, M.; Miyazaki, Y. *Chem. Rev.* **2006**, *106*, 976–1031.
- (29) Sorai, M.; Seki, S. *J. Phys. Chem. Solids* **1974**, *35*, 555–570.
- (30) Roubeau, O.; Castro, M.; Burriel, R.; Haasnoot, J. G.; Reedijk, J. *J. Phys. Chem. B* **2011**, *115*, 3003–3012.
- (31) Bartual-Murgui, C.; Vela, S.; Darawsheh, M.; Diego, R.; Teat, S. J.; Roubeau, O.; Aromí, G. *Inorg. Chem. Front.* **2017**, *4*, 1374–1383.
- (32) Cirera, J.; Paesani, F. *Inorg. Chem.* **2012**, 8194–8201.
- (33) Piçeiro-lópez, L.; Ortega-villar, N.; Muçoz, M. C.; Molnár, G.; Cirera, J.; Moreno-esparza, R.; Ugalde-saldívar, V. M.; Bousseksou, A. *Chem. - Eur. J.* **2016**, *22*, 12741–12751.
- (34) Addison, A. W.; Burke, P. J. *J. Heterocycl. Chem.* **1981**, *18*, 803–805.
- (35) Cenicerós-Gómez, A. E.; Ramos-Organillo, A.; Hernández-Díaz, J.; Nieto-Martínez, J.; Contreras, R.; Castillo-Blum, S. E. *Heteroat. Chem.* **2000**, *11*, 392–398.
- (36) Golesorkhi, B.; Guénée, L.; Nozary, H.; Fürstenberg, A.; Suffren, Y.; Eliseeva, S. V.; Hauser, A.; Piguet, C. *Chem. - A Eur. J.* **2018**, *24*, 13158–13169.



# CHAPTER 5

---

## DESIGN, SYNTHESIS AND CHARACTERIZATION OF NEW BIS-PYRAZOLYL BASED LIGANDS TO ACCESS METALLOSUPRAMOLECULAR ARCHITECTURES





## 5. DESIGN, SYNTHESIS AND CHARACTERIZATION OF NEW BIS-PYRAZOLYL BASED LIGANDS TO ACCESS METALLOSUPRAMOLECULAR ARCHITECTURES

### Abstract

Five new derivatives of bis-pyrazolyl based ligands containing different spacers (terphenyl: **H<sub>2</sub>L3** and dimethyl-terpyridine: **H<sub>2</sub>L4**) and terminal moieties (isoquinoline: **H<sub>2</sub>L5**, methyl-pyridine: **H<sub>2</sub>L6** and pyrazine: **H<sub>2</sub>L7**) have been synthesized. All ligands, 4,4''-bis(3-(pyridin-2-yl)-1H-pyrazol-5-yl)-1,1':3',1''-terphenyl, **H<sub>2</sub>L3**; 1,3-bis(3-(isoquinolin-3-yl)-1H-pyrazol-5-yl)benzene, **H<sub>2</sub>L5**; 1,3-bis(3-(6-methylpyridin-2-yl)-1H-pyrazol-5-yl)benzene, **H<sub>2</sub>L6**; 1,3-bis(3-(pyrazin-2-yl)-1H-pyrazol-5-yl)benzene, **H<sub>2</sub>L7** are ditopic except 6,6''-dimethyl-5,5''-bis(3-(pyridin-2-yl)-1H-pyrazol-5-yl)-2,2':6',2''-terpyridine, **H<sub>2</sub>L4** which is tritopic. The description, synthesis and characterization of all organic compounds are reported. All ligands were obtained in acceptable to high yields. This is important for the further exploration of its coordination chemistry. Exploration of a new synthetic route to achieve organic ligand containing triazole-pyridine chelating moieties; 5,5''-bis(4-(pyridin-2-yl)-4,5-dihydro-1H-1,2,3-triazol-1-yl)-2,2':6',2''-terpyridine, **H<sub>2</sub>L8** is reported.

### 5.1. Introduction

The rational design of ligands is fundamental to access desired polynuclear structures with interesting magnetic properties and potential applications. Several strategies and relevant experience learned on ligand design to intentionally achieve the predicted molecular assemblies have been reported.<sup>1-4</sup> In general, a multitopic ligand with certain backbone rigidity and the appropriate orientation and geometrical placement of the binding sites is required to coordinate with the adequate supply of metal ions. The metal also has to display the right coordination geometry and lability to provide both subunits proposed self-assembly. Using this directing approach, considerably control on the molecular recognition is offered. However, it should be borne in mind that some degree of serendipity may play a role in discovering new polynuclear architectures. The exploration of unexpected

molecular systems has been the way of producing such fascinating assemblies in most cases. In this regard, most of the presented organic ligands containing pyrazolyl-pyridine moieties are intentionally designed to reach new dinuclear triple-stranded helicates with SCO magnetic properties. In previous works, ligands H<sub>2</sub>L and H<sub>2</sub>L2 were synthesized showing that are suitable for the formation of helical systems. Both ligands display the right rigidity within the binding sites and some rotating C-C bonds in the central spacer (phenyl and biphenyl respectively) which provide their helical twist when wrapped with two metal centres. These assemblies are metallosupramolecular hosts since their cavities can encapsulate different guests that influence the whole complex's magnetic properties. The main host-guest chemistry related to SCO tuning behaviour of these systems is described in section 1.4.2.1. Here, the new **H<sub>2</sub>L3** ligand is similar to previously designed ligands (H<sub>2</sub>L and H<sub>2</sub>L2), but it contains a larger spacer group providing a bigger cavity for encapsulating larger guests. Within the spacer moieties, nitrogen atoms were included in ligand H<sub>2</sub>L4. Another coordination site (terpyridine) into the ligand may enable a more significant opportunity to coordinate or encapsulate even more than one guest. **H<sub>2</sub>L6** contains two methyl groups in the terminal C6-pyridinyl position. The addition of methyl close to the iron is often used to tune the T<sub>SCO</sub> of a derivative complex. **H<sub>2</sub>L7** has terminal pyrazines acting as external coordinating units which could further coordinate with other metals, such as transition metals or lanthanides, to produce heterometallic compounds. Ligand **H<sub>2</sub>L5** with two additional extended aromatic rings on each terminal sides of the ligand was also designed to reach helicates. Nevertheless, its formation could be prevented, and only dimerized mononuclear products thermodynamically stabilized due to the enhancement of  $\pi\cdots\pi$  interaction between the pendant components of the mononuclear complexes. All ligands are depicted in Figure 5.1. Our synthetic approach towards the preparation of these ligands involves the formation of bis- $\beta$ -diketone precursors, which are easily converted into a pyrazole ring by its ring closure with hydrazine. The bis- $\beta$ -diketone chelating ligands have been widely used to prepare a large number of helicates.<sup>5,6</sup> The considerable versatility derives from the use of different ester and ketone joined through a Claisen condensation.<sup>7</sup> Thus, several derivatives can be afforded by choosing suitable starting materials. As this chelating moiety containing oxygen donor atoms is prone to oxidase divalent metal ions such as

Fe(II), it was envisioned to incorporate nitrogen atoms through cyclization with hydrazine. The resulting polypyrazolyl ligands display the appropriate crystal field to provide novel SCO-active complexes and are also able to form helicates. Figure 5.2 illustrates the general synthetic route used in the present work.

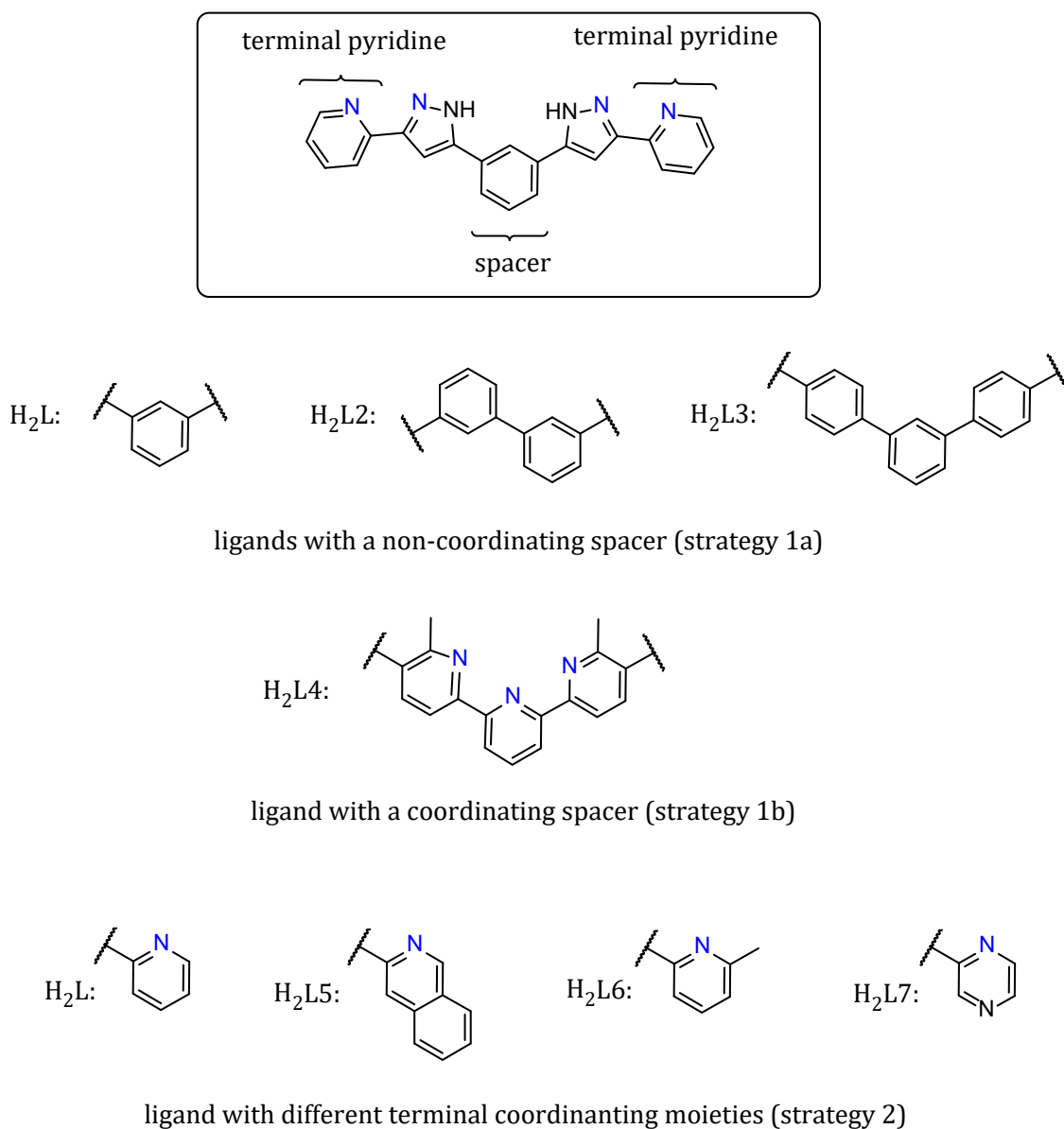


Figure 5. 1. Molecular representation of all designed ligands with the nitrogen coordinating donor atoms highlighted in blue. The ligands are classified depending on the used synthetic strategy.

The presented ligands can be divided into two main categories depending on the strategy used when constructing the bis- $\beta$ -diketone precursor. The first strategy (1a) consists in changing the space group between the pyrazolyl-pyridine moieties. An *m*-terphenyl (1,3-diphenylbenzene) moiety and an analogous one containing

nitrogen donor atoms (1b, terpyridine) constitute the structural core of ligands **H<sub>2</sub>L3** and **H<sub>2</sub>L4**, respectively. Accordingly, the appropriate diacetyl core for each enlarged spacer must be synthesised to obtain the desired bis- $\beta$ -diketone able to form helicates. The second strategy consists of replacing the terminal pyridine rings by other nitrogen-containing heterocycles, like isoquinoline and pyrazine, and a substituted pyridine. For this reason, the adequate ester of each moiety is condensed through a Claisen with the 1,3-diacetylbenzene core. In the following, the synthesis and characterization of all ligands are described.

One practical advantage of the synthetic method is preparing a large amount of poly- $\beta$ -diketone by replacing different spacers and terminal groups. While only one component per ligand is changed in this work, both moieties could be replaced in the same ligand simultaneously. Then, the synthetic advantage envisages more significant versatility when combining both structural changes.

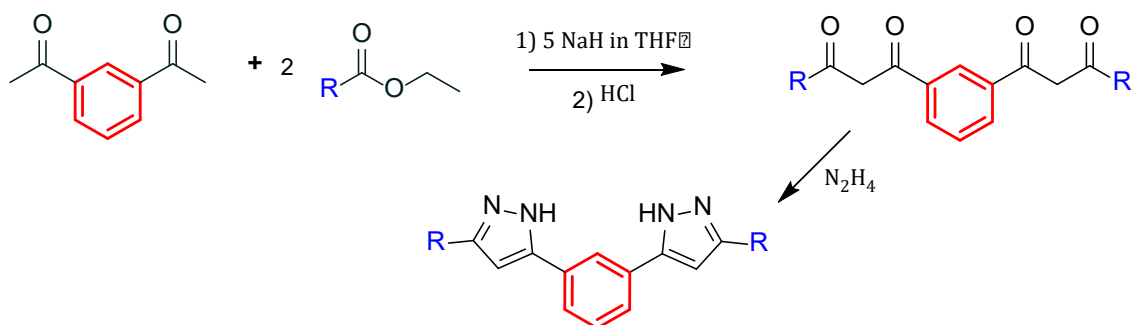


Figure 5.2. General synthetic route for the preparation of bis- $\beta$ -diketones through the Claisen condensation and the final polypyrazolyl ligands after condensation with hydrazine. The central benzene highlighted in red represents the aromatic spacer group which could be changed by the other new proposed cores; terphenyl and 6,6''-dimethyl-terpyridine for **H<sub>2</sub>L3** and **H<sub>2</sub>L4**, respectively. The terminal moieties are R: isoquinolinyl, 6-methylpyridinyl and pyrazinyl for **H<sub>2</sub>L5**, **H<sub>2</sub>L6** and **H<sub>2</sub>L7**, respectively.

## 5.2. Results and discussion

### 5.2.1. Description, synthesis and characterization of **H<sub>2</sub>L3**: 4,4''-bis(3-(pyridin-2-yl)-1H-pyrazol-5-yl)-1,1':3',1''-terphenyl

Ligand **H<sub>2</sub>L3** was designed to access to larger triple-stranded helicates capable of hosting bigger molecules or multiple guests such as halide ions. The extended ligand contains a terphenyl moiety as a larger spacer between the coordinating pockets. The combination of several aromatic groups in the core should provide the proper balance between rigidity and flexibility to access bigger triple-standard helicates.



Furthermore, the single bonds between the phenyl groups can twist along themselves and provide such supramolecular moieties. This ternary structure is present in various natural products<sup>8</sup> and has been used to enhance the fluorescence of supramolecular assemblies since it is well-known as fluorophore.<sup>9-13</sup> Many applications arise from this motif such as pharmacological substances<sup>12,14</sup>, fluorescent labels<sup>9,10</sup> and for the fabrication of organic light-emitting diodes (OLED's)<sup>13,15</sup>. For this reason, a large number of terphenyl derivatives synthetic approaches has been purposed.<sup>16-18</sup> Among them, the aryl-aryl coupling reactions are the most exploit to reach symmetrical polyaryls. The combination of the aromatic groups may be arranged in *ortho*-, *meta*- or *para*- configurations. The *m*- and *p*- terphenyl structures have more relevance in supramolecular coordination chemistry. While *p*-terphenyl containing ligands and related linear derivatives are more prone to provide tetrahedral cages<sup>19,20</sup>, the *m*-terphenyl fashion accomplishes more the geometrical requirements to reach helical complexes. Here, a reported synthesis for 4,4''-diacetyl-*m*-terphenyl (**A1**) has been used (Figure 5.3). The reaction is a classical Suzuki-Miyaura coupling reaction between 1,3-dibromobenzene and two equivalents of 4-acetylphenylboronic acid as the transmetallating reagent, using Pd(PPh<sub>3</sub>)<sub>2</sub>Cl<sub>2</sub> as a catalyst. The 4,4''-position of the ketones is also relevant to furnish helicates. Thus, the desired diacetylated polyarene core was obtained in good yield.

The reaction of one equivalent of **A1** with two equivalents of 2-picolinate in THF and the presence of five equivalents of sodium hydride leads to the bis- $\beta$ -diketone precursor (**A2**). In the <sup>1</sup>H NMR spectrum, a broad peak at 16.53 ppm corresponding to the enol form of the symmetric **A2** ligand is present in chloroform. Usually, this enolic signal is used to track the formation of bis- $\beta$ -diketone in solution since it is more stable at room temperature.<sup>21</sup> Nevertheless, the <sup>1</sup>H NMR characterization of bis- $\beta$ -diketone might be sometimes arduous due to the presence of both keto and enol tautomers in equilibria.<sup>22</sup> The ligand **H<sub>2</sub>L3** was then obtained through the ring closure of both beta-diketone units of **A2** with hydrazine in methanol. Generally, ten excess of hydrazine and around 20h of refluxing heating are used in our group to complete de cyclisation. However, the reaction as firstly carried out in excess hydrazine and heated overnight. The <sup>1</sup>H NMR of the product was unclear, and the bond between carbonyl groups seems to break. This was justified by the mass

spectrum (Figure A5.6; Appendix), displaying the proposed fragments of the molecule. Therefore, the reaction was done in 5 fold excess of hydrazine and was only refluxed for 3 hours when the solution changed from yellow to white. For the final **H<sub>2</sub>L3** ligand, all the expected protons except the NH protons of the pyrazole rings were observed in the <sup>1</sup>H NMR spectrum in chloroform. Exchangeable protons like N-H may give a broad signal or completely disappear in the NMR spectra. The ligand was also characterized in dms-*d*<sub>6</sub> containing traces of water where all the protons were assigned. See experimental section and Appendix A5.4 -A5.7 for completed characterization.

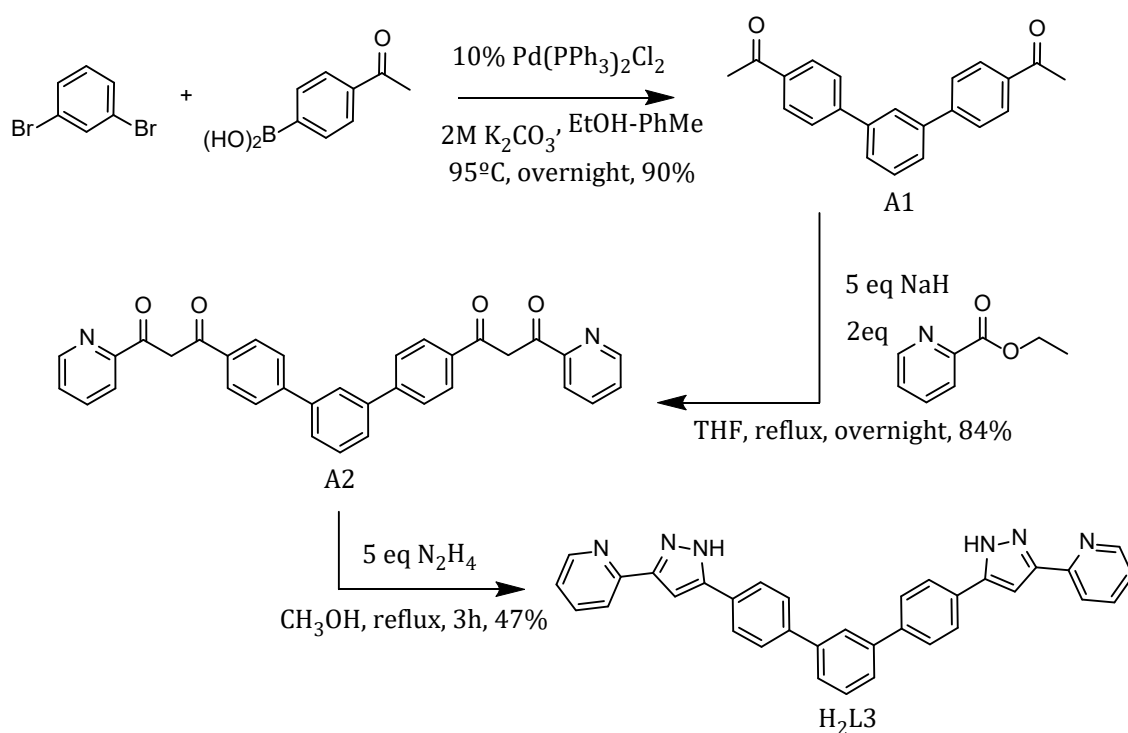


Figure 5.3. Synthetic route of the coordinating ligand **H<sub>2</sub>L3**.

### 5.2.2. Description, synthesis and characterization of **H<sub>2</sub>L4**: 6,6''-dimethyl-5,5''-bis(3-(pyridin-2-yl)-1H-pyrazol-5-yl)-2,2':6',2''-terpyridine

For the new ligand **H<sub>2</sub>L4**, the addition of nitrogen donor atoms into the terphenyl core leads to a new coordination pocket. The introduction of 2,2':6',2''-terpyridine (terpy) as a central core is the right candidate due to its richness in coordination chemistry. Among them are lanthanide-terpyridine complexes with a large variety

of properties which lead to many potential applications. These include luminescence<sup>23-29</sup>, magnetic behaviour<sup>30,31</sup> (along with SMM behaviour)<sup>32-34</sup>, extraction and separation of nuclear waste<sup>31,35,36</sup>, medical chemistry<sup>37-39</sup> and catalysis<sup>40</sup>. The tritopic ligand H<sub>2</sub>L4 contains a central tridentate terpyridine pocket and two terminal bidentate pyrazolyl-pyridine sites. The combination of two different coordination sites provide different environments for the metal ions and therefore, access to heterometallic complexes more easily. In this way, bifunctional systems might be accessible by combining the exhibited properties of the lanthanide in the central pocket and the SCO in the terminal sides. The helical assembly could be reached by combining three H<sub>2</sub>L4, two iron metal ions. The lanthanide with a high coordination number can bind to multiple ligands could be wrapped within the central terpyridines. The suggested coordination chemistry of the ligand is depicted in Figure 5.4.

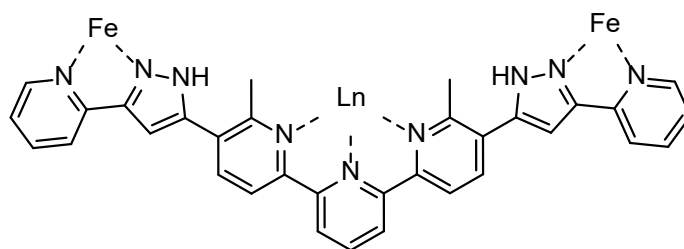


Figure 5.4. Representation of the suggested coordination for ligand **H<sub>2</sub>L4**.

Other systems might be achieved by coordinating two H<sub>2</sub>L4 ligands with one central metal ion giving a *mer*-fashion mononuclear unit. Here, two tridentate ligands are nearly perpendicular to each other, and the two additional bidentate pyrazolyl-pyridine chelating groups would act as pendant binding sites. Three-dimensional metallosupramolecular architectures can be produced through the post-coordination of the bidentate pendant units. This approach consisting of the sequential occupation of different binding sites of a multitopic ligand has also been explored to achieve heterometallic complexes.<sup>41-44</sup>

For the synthesis of the new ligand incorporating the nitrogen in the centre via our established synthetic route a 5,5''-diacetyl-2,2':6',2''-terpyridine as starting material for the Claisen condensation was required (Figure 5.5.) While the ease functionalization of terpyridines at 4'-position and the symmetrical disubstituted terpyridines at 6,6''- position, scarce examples of 5,5''-disubstituted-2,2':6',2''-

terpyridines are reported.<sup>45-47</sup> Only the synthesis of the more readily accessible 6,6''-diacetyl analogue was reported.<sup>48</sup> Since the geometry of the ligand changes considerably when functionalized in the 5,5' (meta) or 6,6'' (ortho) and the latter causes a hindered environment around the metal ion, its possible consideration as a core was completely discarded (Figure 5.5).

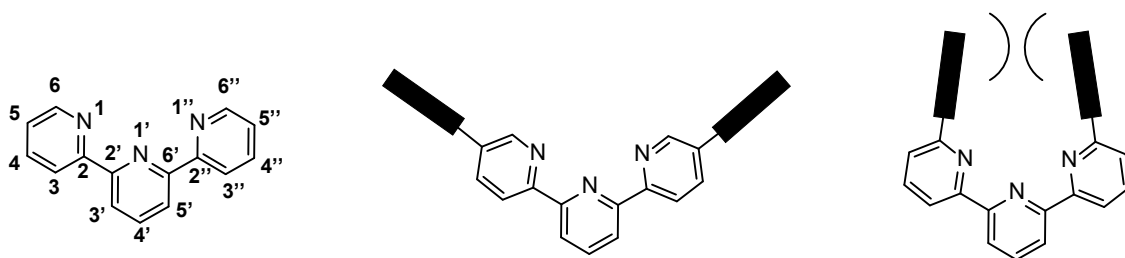


Figure 5.5. (Left) A view of the terpyridine moiety; and the two regio-isomers of the disubstituted terpyridine ligands, the less sterically hindered 5,5''- or meta-substituted system (middle) and the more sterically hindered 6,6''- or ortho-substituted system.

However, its substituted-terpyridine ring construction through Stille cross-coupling inspired us to use another synthetic route to achieve only a 5,5''-disubstituted terpyridine. The different disconnection and synthetic approaches are depicted in Figure 5.6. In section 5.2.6, we report the synthesis of a new 2,2':6,2''-terpyridine derivative with a distinct chemical route.

Another alternative option was to use 1,1'-(6,6''-dimethyl-[2,2':6,2''-terpyridine]-5,5''-diyl)bis(ethan-1-one) (**B2**) as a reagent for the following Claisen condensation. The compound B2 contains a functional 5,5''-diacetyl groups but additional 6,6''-dimethyl groups that may cause some steric hindrance.<sup>49</sup> Nevertheless, despite the steric concern mentioned above and given its easily accessible synthesis, we decide to use B2 to form the bis- $\beta$ -diketone.

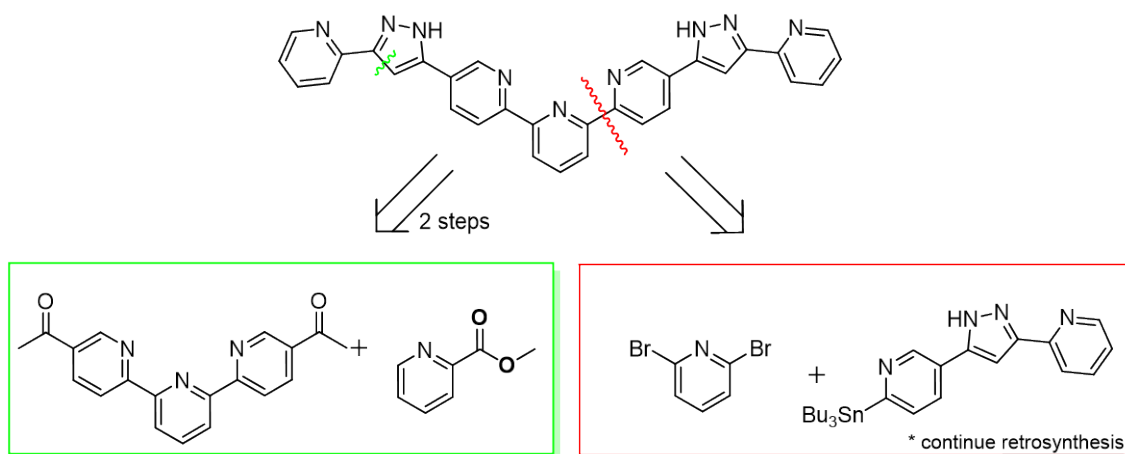
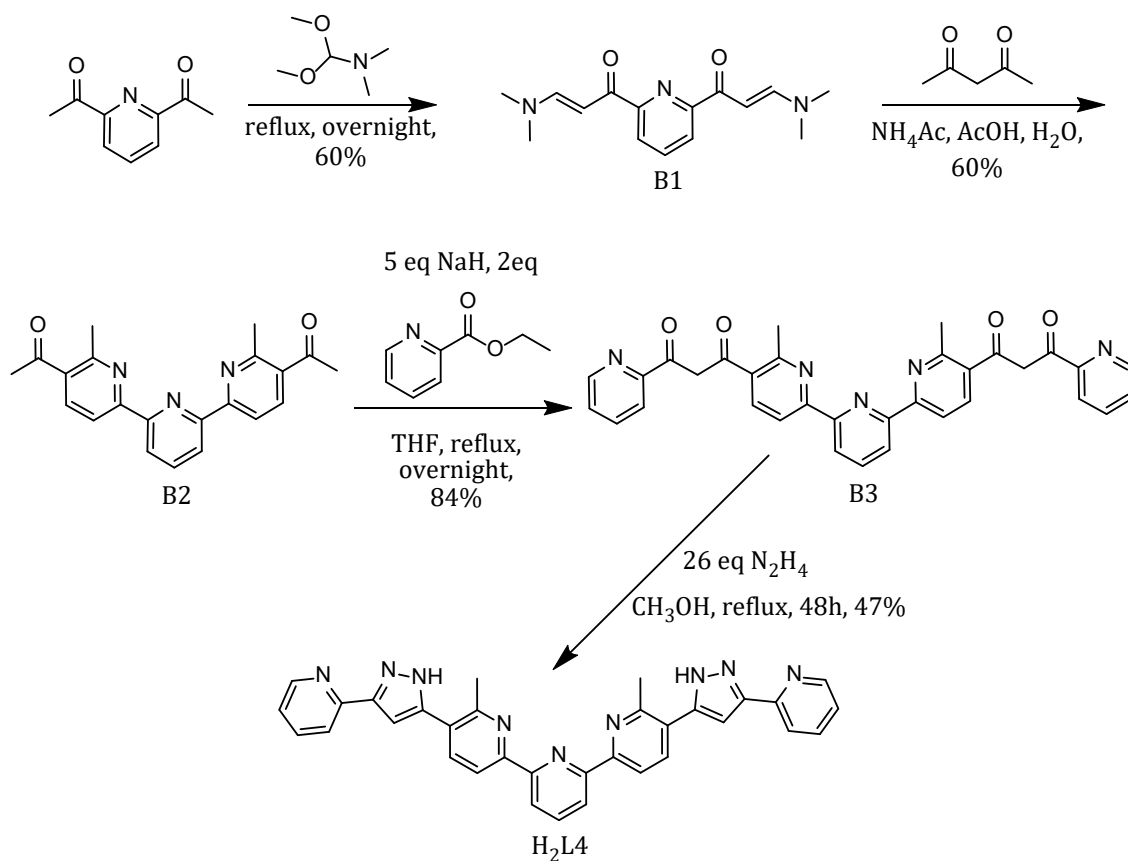
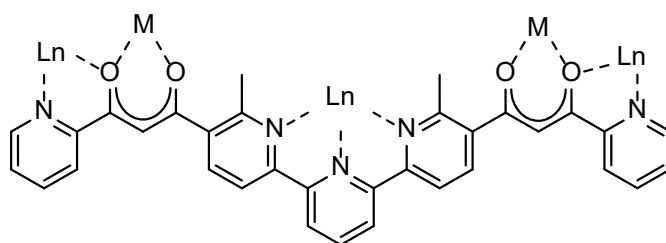


Figure 5.6. Proposed retrosynthesis for the formation of 5,5''-disubstituted terpyridine. (Left in green) Disconnection of the pyrazolyl ring. Synthesis through a bis- $\beta$ -diketone followed by ring closure with hydrazine. The depicted 5,5''-diacetyl (hypothetical/ideal) wasn't furnished. Instead **B2** was used. (Right in red) Disconnection of the central terpyridine. Synthesis through Stille cross-coupling. Synthesis of the stannyl compound is discussed in section 5.2.6.

The synthesis of the **B2** involved two reactions (Figure 5.7). Firstly, the enaminone **B1** is easily prepared by treating 2,6-diacetylpyridine with DMFDMA. Enaminones are widely used for the synthesis of heterocyclic compounds. In fact, this building block was used in section chapter 2 to construct the pyrazolyl ring when treated with hydrazine. Instead, we use acetylacetonate with acetic acid, followed by the addition of ammonium acetate to yield the terminal pyridinyl ring of the terpyridine. This second reaction involves two steps. A Michael adduct (bis-1,5-diketone) is formed when the active methylene (acetylacetonate) reacts with the double bond of **B1**. Without isolating the bis-1,5-diketone intermediate, the ring closure is followed by adding ammonium acetate. The compound **B2** was obtained in moderate to high yield and characterized by  $^1\text{H}$  NMR. Then, one equivalent of **B2**, two equivalents of 2-picolinate with five equivalents of sodium hydride in THF lead to the desired bis- $\beta$ -diketone. As mentioned previously, this precursor was characterized by  $^1\text{H}$  NMR where the broad peaks of the enolates can be easily observed, and all protons were assigned. It was further characterized by positive ESI. See experimental section and Appendix A5.8 – A5.12 for more detail.

Figure 5.7. Synthetic route of the coordinating ligand **H<sub>2</sub>L4**.

Among all the reported bis- $\beta$ -diketone intermediates, **B3** is more interesting since it also displays differentiated binding pockets. Its suggested coordination is highlighted because it can serve as a final ligand (Figure 5.8). The linear heterometallic chain-like cluster synthesis with 3d and 4f ions are promising prototypes as molecular qubits. Indeed, our research group is involved in developing such kind of complexes. Thus, ligand **B3** is an excellent candidate to reach arrays of paramagnetic ions with quantum computing applications.

Figure 5.8. Representation of the suggested coordination for the intermediated ligand **B3**.

The final step to accomplish the ligand **H<sub>2</sub>L<sub>4</sub>** involves the ring formation by condensation of the 1,3- diketone moieties with hydrazine. The amount of hydrazine monohydrate and the refluxing time is greatly influenced depending on the starting bis- $\beta$ -diketone. In this case, up to 20 equivalents of hydrazine (64% in H<sub>2</sub>O) and two days of refluxing were required before the reaction was completed. In the first attempts on monitoring the reaction course, TLC and <sup>1</sup>H NMR were not clear. Due to partial solubility of the final crudes in chloroform-*d* and dms<sub>o</sub>-*d*<sub>6</sub>, broad peaks of the protons were observed in both deuterated solvents. This result suggested the presence in the crude of both compounds **B3** and **H<sub>2</sub>L<sub>4</sub>**. Therefore, mass spectrometry was used to confirm that the cyclisation required more time and equivalents than initially perceived (see Appendix A5.15). The ligand was finally characterized by <sup>1</sup>H NMR in dms<sub>o</sub>-*d*<sub>6</sub> and positive ion electrospray ionization (ESI<sup>+</sup>) using CHCl<sub>3</sub> as a solvent. See experimental section and Appendix A5.13-A515.

### 5.2.3. Description, synthesis and characterization of **H<sub>2</sub>L<sub>5</sub>: 1,3-bis(3-(isoquinolin-3-yl)-1H-pyrazol-5-yl)benzene**

The ligand **H<sub>2</sub>L<sub>5</sub>** consists in a central benzene ring bonded to two terminal pyrazolyl-isoquinoline chelating units in the *meta* position. In the first instance, the ligand was pre-designed to reach dinuclear iron (II) triple-stranded helicates.<sup>50</sup> In this particular case, the ligand acts as bis-chelating units between both metal centers. Nevertheless, the formation of another supramolecular assembly composed by dimerized mononuclear units may be preferred instead. In this case, only one Fe(II) center is octahedrally coordinated to one bidentate chelating site of three pyrazolyl-pyridine (Figure 5.9). The other chelating site of the ligand is not coordinated and contributes to extensive series of  $\pi\cdots\pi$  interactions holding whole structure with the formula  $(X@[Fe(H_2L)_3]_2)^{3+}$  ( $X^- = Cl^-, Br^-, I^-$ ).<sup>51</sup> If compared with ligand **H<sub>2</sub>L**, an important feature of **H<sub>2</sub>L<sub>5</sub>** is the additional aromatic group provided by the isoquinoline moiety. The sequence of seven aromatic groups into the ligand can contribute to a total of twenty-one  $\pi\cdots\pi$  stacking interactions between parallel pairs of ligands from different  $[Fe(H_2L_3)]^{2+}$  components. The enhancement of such intermolecular interactions (six additional  $\pi$ -stacking interactions) could enforce the formation such dimerized mononuclear assemblies and prevent the formation of helicates.

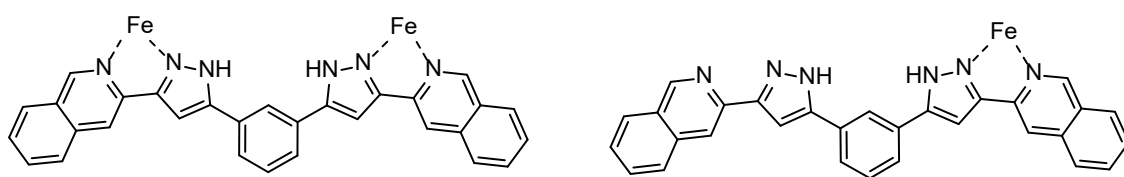


Figure 5.9. Representation of the suggested coordination for ligand **H<sub>2</sub>L5**. Binuclear (left) and mononuclear (right) forms are depicted.

For the synthesis of **H<sub>2</sub>L5** (Figure 5.10), the commercially available ethyl isoquinoline-3-carboxylate was condensed to 1,3-diacetylbenzene following the procedure for the Claisen reaction shown in the previous ligands. However, additional refluxing time was required to complete the reaction. The bis- $\beta$ -diketone (**C1**) was purely isolated in good yield after 48h. Cyclization of **C1** with hydrazine following the usual procedure led to the final ligand **H<sub>2</sub>L5**. Both products were characterized by <sup>1</sup>H NMR in chloroform-*d* and dms-*d*<sub>6</sub>, respectively. ESI<sup>+</sup> also confirmed the presence of each ligand. (See experimental section and Appendix A5.17-A5.18).

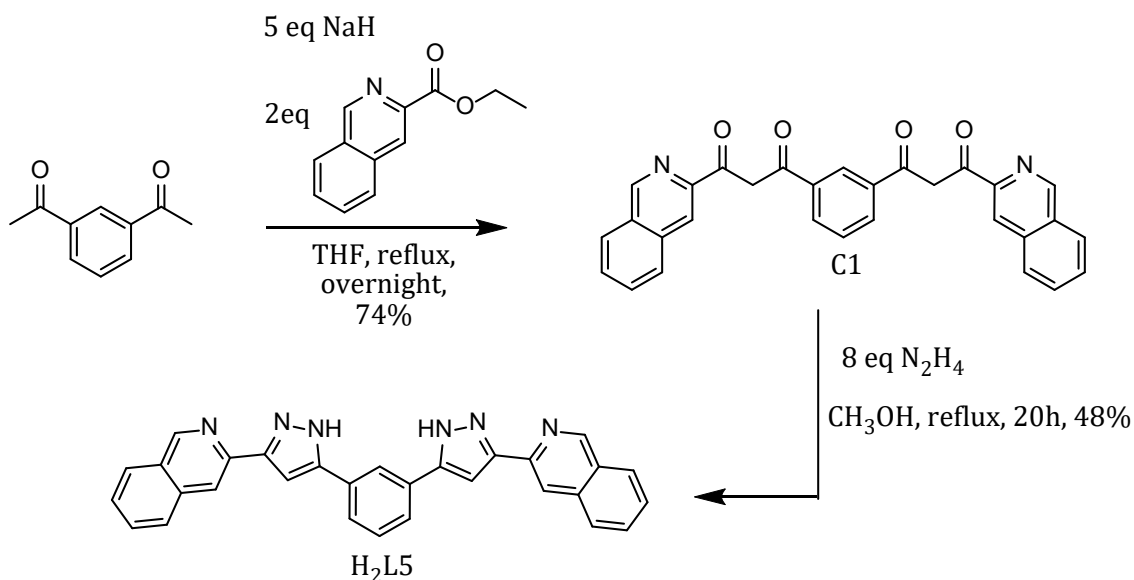


Figure 5.10. Synthetic route of the coordinating ligand **H<sub>2</sub>L5**.



#### 5.2.4. Description, synthesis and characterization of **H<sub>2</sub>L6**: 1,3-bis(3-(6-methylpyridin-2-yl)-1H-pyrazol-5-yl)benzene

The ligand **H<sub>2</sub>L6** consists of bis-pyrazolylpyridine ligand with two additional methyl groups adjacent to the nitrogen of the terminal pyridine. As mentioned in chapter 2, the addition of a steric group near the binding sites is a widely used approach to tune the SCO behaviour.<sup>52</sup> The steric effect of ligand substituents enforces longer M-L bonds and therefore, favours the HS state of the complex. Therefore, the sterically crowded ligands are usually used to induce thermal SCO when its bare derivative is fully stabilized in the LS. In the present case, the possibility to reach different possible magnetic states, such as [LS-HS] and [HS-HS], might be induced directly by the ligand.

Ligand **H<sub>2</sub>L6** was synthesized following the same procedure shown in previous ligands (Figure 5.11). The ethyl 6-methylpicolinate (**D1**) was obtained from 6-methylpicolinic acid in high yield.<sup>53</sup> Then, the Claisen reaction between **D1** and 1,3-diacetylbenzene afforded the desired bis- $\beta$ -diketone (**D2**), which was cyclized with hydrazine. The final bis-pyrazolylpyridine derivative (**H<sub>2</sub>L6**) was obtained in good yield. See experimental section and Appendix A5.19-A5.23 for characterization.

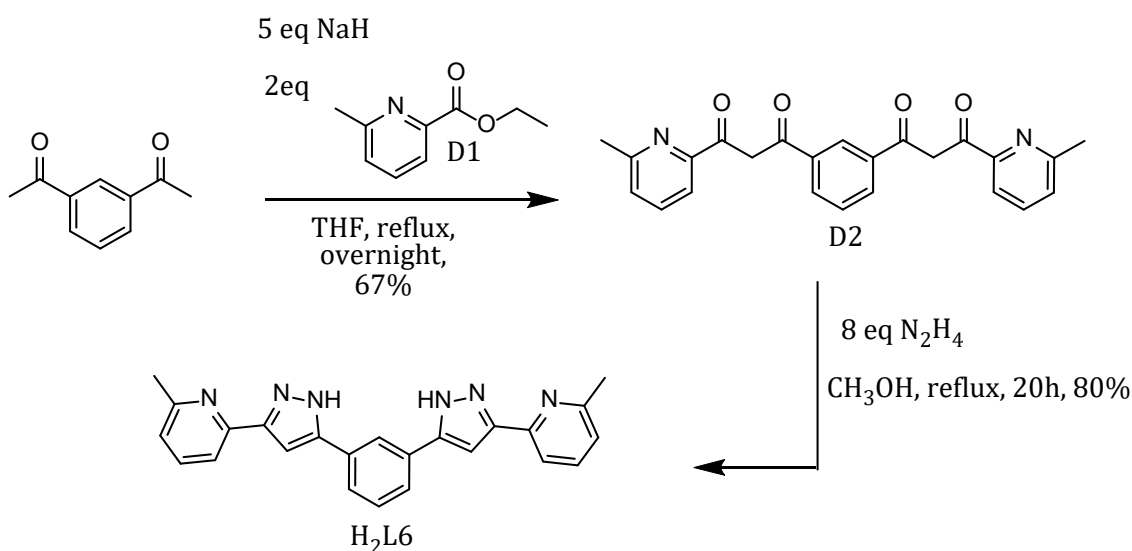


Figure 5.11. Synthetic route of the coordinating ligand **H<sub>2</sub>L6**.

### 5.2.5. Description, synthesis and characterization of **H<sub>2</sub>L7**: 1,3-bis(3-(pyrazin-2-yl)-1*H*-pyrazol-5-yl)benzene

An additional donor nitrogen atom is introduced into the 4-position of the terminal pyridines for ligand **H<sub>2</sub>L7**, creating a ditopic bis-pyrazolylpyrazine ligand with two additional binding sides from behind the former primary chelating moieties. This ligand could also afford triple-stranded helicates when coordinated to two Fe(II) centers. Additionally, heterometallic structures might be reached after a post-coordination through the two extra nitrogen donors of the pyrazine (Figure 5.12).

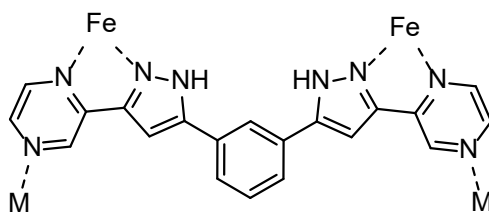
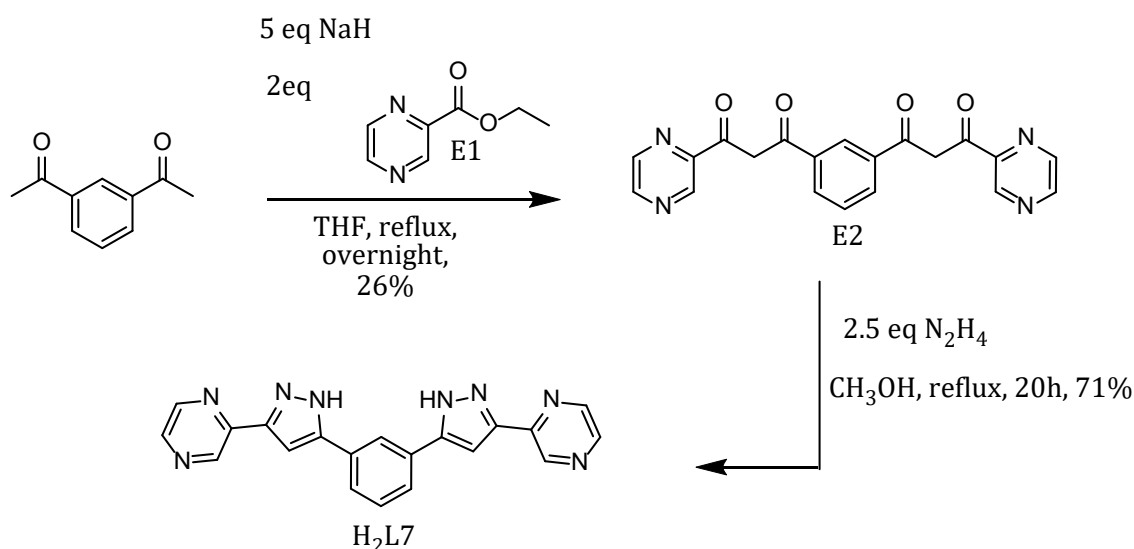


Figure 5.12. Representation of the suggested coordination for ligand **H<sub>2</sub>L7**.

Ligand **H<sub>2</sub>L7** was synthesized following a synthetic scheme similar to that shown in previous ligands (Figure 5.13). The ethyl pyrazine-2-carboxylate (**E1**) was obtained by Fischer esterification of pyrazinecarboxylic acid. Then, the Claisen reaction between **E1** and 1,3-diacetylbenzene using NaH as base led to the disodium salt of the adduct. While all the presented bis- $\beta$ -diketones are usually obtained by precipitation at pH 2-3, the bis- $\beta$ -diketone (**E2**) was obtained by acidifying the mixture to pH 5-6 using hydrochloric acid. The gummy product was left stirring with ethyl acetate overnight, which allows getting the product as a brown solid. The final bis-pyrazolylpyrazine derivative was obtained after **E2** cyclization with hydrazine. See experimental section and Appendix A5.24-A5.28 for characterization.

Figure 5.13. Synthetic route of the coordinating ligand **H<sub>2</sub>L7**.

### 5.2.6. Description, synthesis and characterization of **H<sub>2</sub>L8**: 5,5''-bis(4-(pyridin-2-yl)-4,5-dihydro-1H-1,2,3-triazol-1-yl)-2,2':6',2''-terpyridine

The design of ligand **H<sub>2</sub>L8** was developed to achieve an intended tritopic ligand analogous to **H<sub>2</sub>L4** without the methyl groups in the 6,6''-positions. Nevertheless, the two bidentate terminal pyrazolyl-pyridine were replaced by triazolyl-pyridine. This change was considered due to more accessible and affordable synthesis while preserving the geometry and binding type modes of **H<sub>2</sub>L4**. The 1,4-disubstituted-1,2,3-triazole has been generally seen to bind a metal ion via the N3. This pyridine-type nitrogen-containing a free electron pair is the more basic, and therefore, the predominant site for coordination. Additionally, the N3 takes part of the five-member ring chelating unit with the terminal pyridine. This enhances its preferred coordination over the N2. This is exemplified in a series of binuclear complexes displaying a helical structure when combining three bis-chelating triazolylpyridine ligands with two metal centres.<sup>54-56</sup> In terms of intermolecular interactions, the main difference between the pyrazolyl and triazolyl rings within our ligands, is the nature of the adjacent nitrogen to the coordinating one. The adjacent N-H for the pyrazolyl containing ligands is usually involved in hydrogen-bonding interactions with guests. Instead, the adjacent uncoordinated N2 with a lone electron pair of the triazolyl ring could bring some lone pair-lone pair repulsion between them once coordinated.<sup>55</sup> Ligand **H<sub>2</sub>L8** do not own any N-H actin as hydrogen bond donor. Considering the mentioned reasoning, the suggested coordination of **H<sub>2</sub>L8** is

depicted in Figure 5.14. Like H<sub>2</sub>L<sub>4</sub>, heterometallic triple-stranded helicates are possible structures to access. Similar architectures are reported in the literature by using two-terminal triazolylpyridine cheating units and a central bidentate 2,2'-bipyridine.<sup>57,58</sup>

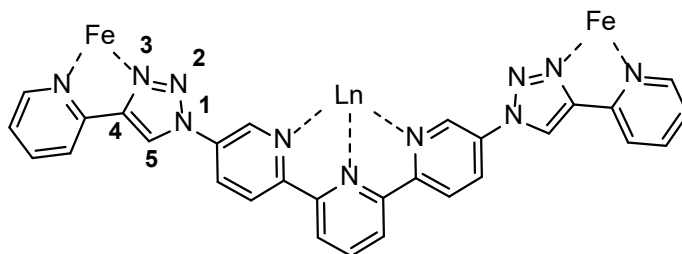


Figure 5.14. Representation of the suggested coordination for the ligand **H<sub>2</sub>L<sub>8</sub>**.

For the synthesis of H<sub>2</sub>L<sub>8</sub> a three-step synthetic route comprising a copper(I)-catalysed azide–alkyne cycloaddition (CuAAC), a thin derivative formation and a double Stille coupling was designed. Thus, the side triazolylpyridine pockets are firstly formed, and the central terpyridine core is constructed in the final step (Figure 5.15).

The CuAAC reaction, typically known as “click reaction”, is a Huisgen 1,3-dipolar cycloaddition improved by Sharpless and Meldal which provides 1,4-disubstituted-1,2,3-triazoles as a unique product.<sup>59,60</sup> The reaction offers high regioselectivity, high yields, working under mild conditions and an easy opportunity to include a wide range of functional groups. All of these advantages make this reaction-type particularly valuable for the synthesis of the desired fragment **F1**. The literature review shows that a series of ten 1,4-disubstituted 1,2,3-triazole derivatives structurally similar to our desired **F1** were synthesized.<sup>61</sup> Only 3 and 4-iodopyridine were used as pyridyl mono-halides. This implies that all reported 1,2,3-triazole analogues do not have additional functionalities, which is required in our case to form the terpyridine futher. Nevertheless, in the original one-pot two-step procedure,<sup>62</sup> *p*-bromo iodobenzene was converted to the mono-triazole product without affecting the aryl bromide group. At this point, it was of interest to know whether 2-bromo-5-iodopyridine still would be selective and give the desired **F1** product. Fortunately, the new derivative (**F1**) was obtained by following a simple and efficient method. It consists in mixing and stirring 2-bromo-5-iodopyridine, 2-

ethynylpyridine and the rest of required reagents in a sealed vial at 65 °C (Figure 5.15). The pure **F1** compound was easily isolated by filtration in 57% yield.

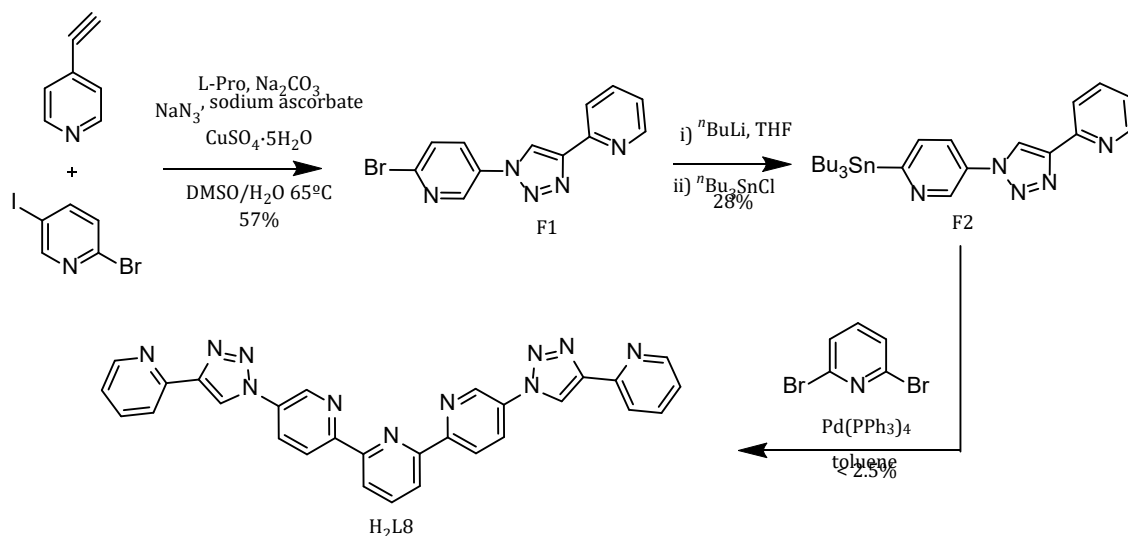


Figure 5.15. Synthetic route of the coordinating ligand **H<sub>2</sub>L8**.

The second step of the synthetic route consists of the formation of the tributylstannyl intermediate. The bromide of compound **F1** was converted through a nucleophilic substitution with tributyltin chloride into the organotin compound. In our case, a modification of the reported protocol for the preparation of 2-tributylstannyl pyridine<sup>63</sup> and 2-tributylstannyl-5-methylpyridine<sup>64</sup> was followed. The desired stannyl compound **F2** was obtained using an excess of *n*BuLi into a more concentrated mixture. Nevertheless, it was obtained in low yield (~28%) after purification by column chromatography. Additionally, it was not possible to isolate a significant sample of pure intermediate. Remaining tributyltin chloride was present in the <sup>1</sup>H NMR as a part from some side products. For this reason, the product was fully characterized by 2D-COSY, 2D-HSQC and <sup>13</sup>C NMR. (See Appendix A5.29-A5.39). The proton signals corresponding to the desired **F2** were assigned. However, due to the presence of the impurity, some carbons remained unassigned. Although further optimization of the reaction should be required, we decided to test the last coupling reaction with the obtained crude.

The formation of ligand **H<sub>2</sub>L8** through the double Stille coupling of **F2** with 2,6-dibromopyridine with the presence of Pd(PPh<sub>3</sub>)<sub>4</sub> was observed after refluxing overnight in dry toluene. Unfortunately, the yield, after several tries, was generally

low (less than 2 mg). See experimental section and Appendix A5.39. for  $^1\text{H}$  NMR characterization. Nonetheless, we believe that this is a promising synthetic route to achieve H<sub>2</sub>L8 like ligand if we further make more efforts for optimization.

Future research could examine trimethylstannyl compound instead of the tributylstannyl since the former is more reactive than the second. Another option to explore would be the formation of 2,6-distannylpyridine to couple with the easily obtained F1 fragment.

### 5.3. Conclusions

This chapter reports the synthesis of five new multitopic ligands H<sub>2</sub>L3- H<sub>2</sub>L7. The synthetic route established in our group provides an efficient way to access multidentate ligand containing nitrogen donor atoms in high yields. However, it appears to be limited for the synthesis of tritopic ligand (H<sub>2</sub>L4) without methyl groups. A new synthetic route for the synthesis of ligand H<sub>2</sub>L8 has been attempted. The first step, based on the click chemistry, allows a large fragment F1 of the final molecule with an additional bromide functionality. The optimization of the next steps is required. The contributions made should be of a broad interest in synthesizing new multitopic ligands by using a new promising synthetic route.

### 5.4. Experimental

Ligands H<sub>2</sub>L and H<sub>2</sub>L2 were synthesis as previously reported by our group.<sup>50,65</sup>

**1,1'-([1,1':3',1''-terphenyl]-4,4''-diyl)bis(ethan-1-one), A1:** A mixture of 1,3-dibromobenzene (513  $\mu\text{L}$ , 4.24 mmol), 4-acetylphenylboronic acid (1.8 g, 11.02 mmol) and bis-triphenylphosphine palladium (II) chloride (297 mg, 0.42 mmol) were placed in a round-bottom flask. A 1:1:1 mixture of aqueous 2M K<sub>2</sub>CO<sub>3</sub>: ethanol: toluene (24 mL) was then added. The solution was purged with N<sub>2</sub> for 10 minutes and stirred. After stirring for a few minutes, the solution went from yellow to red and finally to black. Once the colour changing process was complete, it was refluxed overnight (95°C). The solution was cooled down and methanol was added to encourage precipitation of the solid. The tan solid was filtered via a Sartorius funnel and recrystallized in dichloromethane. The yield was 1.2 g (90%).  $^1\text{H}$  NMR (400 MHz, CDCl<sub>3</sub>, ppm):  $\delta$  8.07 (dt,  $J = 4.7, 1.9$  Hz, 4H), 7.85 (t,  $J = 1.8$  Hz, 1H), 7.75 (dt,  $J =$

4.7, 1.9 Hz, 4H), 7.66 (dd,  $J = 8.3, 1.5$  Hz, 2H), 7.58 (dd,  $J = 8.5, 6.7$  Hz, 1H), 2.66 (s, 6H).

**3,3'-([1,1':3',1''-terphenyl]-4,4''-diyl)bis(1-(pyridin-2-yl)propane-1,3-dione),**

**A2:** To a suspension of 60% NaH oil dispersion (0,54 g, 13.5 mmol) in 46 ml THF was added A1 (0,85 g, 2,65 mmol). The mixture was stirred for 15 minutes until the suspension turned yellow, indicating the formation of the enolate. Then, 2-ethylpicolinate (0.73 mL, 5.4 mmol) was then added in THF (16 mL) dropwise and the mixture was left under N<sub>2</sub> conditions to reflux overnight. A green-mustard solution was formed, which was cooled to room temperature and quenched with ethanol (5 mL). The resulting solid was filtered and suspended in water (150 mL). The pH was then adjusted to 2-3 using 12% HCl and the mixture was left 30 minutes stirring. The resulting yellow solid was filtered and dried in the air. The yield was 1.3 g (84%). <sup>1</sup>H NMR (400 MHz, CDCl<sub>3</sub>, ppm):  $\delta$  16.53 (s, 2H), 8.74 (d,  $J = 4.6$  Hz, 2H), 8.19 (d,  $J = 8.3$  Hz, 6H), 7.93 – 7.85 (m, 3H), 7.79 (d,  $J = 8.3$  Hz, 4H), 7.71 – 7.66 (m, 2H), 7.64 (s, 2H), 7.62 – 7.55 (m, 1H), 7.46 (dd,  $J = 7.5, 4.9$  Hz, 2H). MS (ESI<sup>+</sup>): calc. C<sub>34</sub>H<sub>24</sub>N<sub>2</sub>O<sub>4</sub> 524.17; found, 525.18 (M+H)<sup>+</sup>.

**4,4''-bis(3-(pyridin-2-yl)-1H-pyrazol-5-yl)-1,1':3',1''-terphenyl, H<sub>2</sub>L3:** The A2 bis- $\beta$ -diketone (1.3 g, 2.48 mmol) was suspended in methanol (61 mL) and 64% hydrazine (1 mL, 13.2 mmol) was added dropwise. The yellow solution was then heated to reflux and left for 3 hours. Once cooled from reflux, the white solid was then filtered and dried via a Sartorius funnel. The yield was 0.6 g (47%). <sup>1</sup>H NMR (400 MHz, CDCl<sub>3</sub>, ppm):  $\delta$  8.64 (d,  $J = 4.9$  Hz, 2H), 7.96 (d,  $J = 8.3$  Hz, 4H), 7.92 (s, 1H), 7.76 (d,  $J = 8.5$  Hz, 9H), 7.65 (d,  $J = 8.5$  Hz, 2H), 7.58 – 7.51 (m, 1H), 7.11 (s, 2H). MS (ESI<sup>+</sup>): calc. C<sub>34</sub>H<sub>24</sub>N<sub>6</sub> 516,21; found, 517.21 (M+H)<sup>+</sup>.

**1,1'-(pyridine-2,6-diyl)bis(3-(dimethylamino)prop-2-en-1-one), B1:** DMADMF (3.5 mL, 26.3 mmol) was added to 2, 6-diacetylpyridine (1 g, 6.13 mmol). The reaction was then placed under reflux (120°C) and left overnight. The solvent was then removed and the solid was recrystallized with a 1:1 mixture of THF: ether. This yellow solid was then filtered via a Sartorius funnel. The yield was 1.6 g (95%).

$^1\text{H}$  NMR (400 MHz,  $\text{CDCl}_3$ , ppm):  $\delta$  8.21 (d,  $J = 7.7$  Hz, 2H), 7.92 (d,  $J = 12.8$  Hz, 2H), 7.89 (t,  $J = 7.7$  Hz, 1H), 6.61 (d,  $J = 12.4$  Hz, 2H), 3.18 (s, 6H), 2.99 (s, 6H).

**1,1'-(6,6''-dimethyl-[2,2':6',2''-terpyridine]-5,5''-diyl)bis(ethan-1-one), B2:** A mixture of 1,1'-pyridine-2,6-diyl)bis(3-(dimethylamino)prop-2-en-1-one) (1.36 g, 4.98 mmol) and ammonium acetate (1 g, 14.3 mmol) were placed in acetic acid (10 mL, 183 mmol). Pentane-2,4-dione (1.2 mL, 11.69 mmol) was then added and the mixture was heated to reflux for 4 hours. The solvent was then removed and the remaining solid was recrystallized using ethanol. The yield was 1.16 g (67%).  $^1\text{H}$  NMR (400 MHz,  $\text{CDCl}_3$ , ppm):  $\delta$  8.59 (d,  $J = 7.8$  Hz, 2H), 8.52 (d,  $J = 8.2$  Hz, 2H), 8.15 (d,  $J = 8.1$  Hz, 2H), 7.99 (t,  $J = 7.8$  Hz, 1H), 2.87 (s, 6H), 2.66 (s, 6H). MS (ESI<sup>+</sup>): calc.  $\text{C}_{21}\text{H}_{19}\text{N}_3\text{O}_2$  345.15; found, 346.18 (M+H)<sup>+</sup>.

**3,3'-(6,6'-dimethyl-[2,2':6',2''-terpyridine]-5,5''-diyl)bis(1-pyridin-2-yl)propane-1,3-dione, B3:** THF (55 mL) was added to 60% NaH oil (0.6 g, 15.92 mmol) followed by 1,1'-(6,6''-dimethyl-[2,2':6',2''-terpyridine]-5,5''-diyl)bis(ethan-1-one) (1.1 g, 3.18 mmol). The mixture was then stirred for 15 minutes. The solution then appeared black. Ethyl 2-picolinate (0.86 mL, 6.37 mmol) was then added in THF (20 mL) dropwise and the mixture was left under  $\text{N}_2$  conditions refluxing overnight. By the next day, a brown solution had formed. The solvent was removed and the resulting brown solid was suspended in water (150 mL). The pH was adjusted to 2-3 using 12% HCl and stirred for 30 minutes. Extractions with DCM afforded a maroon solution. The volatiles were removed on a rotary evaporator to gain a brown solid. The yield was 0.9 g (51%).  $^1\text{H}$  NMR (400 MHz,  $\text{CDCl}_3$ , ppm):  $\delta$  16.25 (s, 2H), 8.72 (d,  $J = 4.6$  Hz, 2H), 8.59 (d,  $J = 7.8$  Hz, 2H), 8.54 (d,  $J = 8.2$  Hz, 2H), 8.19 (d,  $J = 7.9$  Hz, 2H), 8.16 (d,  $J = 8.2$  Hz, 2H), 7.99 (t,  $J = 7.9$  Hz, 1H), 7.92 – 7.85 (m, 2H), 7.47 (dd,  $J = 7.1, 5.2$  Hz, 2H), 7.36 (s, 2H), 2.92 (s, 6H). MS (ESI<sup>+</sup>): calc.  $\text{C}_{33}\text{H}_{25}\text{N}_5\text{O}_4$  555.19; found, 556.20 (M+H)<sup>+</sup>.

**6,6''-dimethyl-5,5''-bis(3-(pyridin-2-yl)-1H-pyrazol-5-yl)-2,2':6',2''-terpyridine, H<sub>2</sub>L4:** 3,3'-(6,6'-dimethyl-[2,2':6',2''-terpyridine]-5,5''-diyl)bis(1-pyridin-2-yl)propane-1,3-dione (0.9 g, 1.64 mmol) was suspended in methanol (42 mL) and excess hydrazine (64% in  $\text{H}_2\text{O}$ , 3.3 mL, 43.54 mmol) was added dropwise. The



resulting brown solution was heated to reflux and left for 2 days. Once cooled from reflux, the beige solid was filtered and dried via a Sartorius funnel. The yield was 0.5 g (56%).  $^1\text{H}$  NMR (400 MHz,  $\text{dms}\text{-}d_6$ , ppm):  $\delta$  8.65 (d,  $J$  = 4.1 Hz, 2H), 8.58 (d,  $J$  = 8.1 Hz, 2H), 8.51 (d,  $J$  = 7.8 Hz, 2H), 8.23 (d,  $J$  = 8.1 Hz, 2H), 8.14 (t,  $J$  = 7.8 Hz, 1H), 8.00 (d,  $J$  = 7.9 Hz, 2H), 7.92 (td,  $J$  = 7.7, 1.8 Hz, 2H), 7.38 (dd,  $J$  = 7.5, 4.9 Hz, 2H), 7.31 (s, 2H), 2.85 (s, 6H). MS (ESI<sup>+</sup>): calc.  $\text{C}_{33}\text{H}_{25}\text{N}_9$  547.22; found, 548.23 (M+H)<sup>+</sup>.

**3,3'-(1,3-phenylene)bis(1-(isoquinolin-3-yl)propane-1,3-dione), C1.** To a suspension of 60% NaH oil dispersion (2.5 g, 104 mmol) in 100 ml THF was added a solution of 1,3-diacetylbenzene (2 g, 12.3 mmol) in THF (40 ml) and the mixture was stirred for 15 minutes (the white suspension turns yellow). Then, ethyl isoquinoline-3-carboxylate (4.5 g, 22.6 mmol) in 40 ml THF was added dropwise, (the solution turns brown) and the mixture brought and left to reflux 2 days. A green-mustard suspension was formed after that, which was quenched with 5 ml EtOH and the resulting solid was then collected by filtration. The solid was suspended in 150 ml  $\text{H}_2\text{O}$ , the pH was adjusted to 2-3 using 12% HCl and the mixture was left 30 minutes under stirring. The yellow solid was collected by filtration, washed with water and dried under vacuum. The yield was 3.4 g (74%).  $^1\text{H}$  NMR (400 MHz,  $\text{CDCl}_3$ , ppm):  $\delta$  16.67 (s, 2H), 9.34 (s, 2H), 8.82 (t,  $J$  = 1.7 Hz, 1H), 8.63 (s, 2H), 8.31 (dd,  $J$  = 7.8, 1.7 Hz, 2H), 8.09 – 8.07 (m, 2H), 8.03 (d,  $J$  = 7.8 Hz, 2H), 7.82 (s, 2H), 7.79 – 7.73 (m, 4H), 7.66 (t,  $J$  = 7.7 Hz, 1H). MS (ESI<sup>+</sup>): calc.  $\text{C}_{30}\text{H}_{20}\text{N}_2\text{O}_4$  472.14; found, 473.12 (M+H)<sup>+</sup>.

**1,3-bis(3-(isoquinolin-3-yl)-1H-pyrazol-5-yl)benzene, H<sub>2</sub>L5:** Solid C1 (1.5 g, 4 mmol) was suspended in  $\text{CH}_3\text{OH}$  (70 ml) and hydrazine (64% in  $\text{H}_2\text{O}$ , 2.6 ml, 34.3 mmol) was added to the mixture dropwise. The mixture turned with time to clear orange solution to yield a white solid through reflux for 20h. The mixture is cooled to room temperature and the solid was collected by filtration, washed with  $\text{CH}_3\text{OH}$  and water and dried under vacuum. The yield was 0.70 g (48 %).  $^1\text{H}$  NMR (400 MHz,  $\text{dms}\text{-}d_6$ , ppm):  $\delta$  13.70 (s, 2H), 9.40 (s, 2H), 8.43 (s, 1H), 8.41 (s, 2H), 8.17 (d,  $J$  = 8.3 Hz, 2H), 8.03 (d,  $J$  = 8.3 Hz, 2H), 7.88 (d,  $J$  = 7.6 Hz, 2H), 7.82 (t,  $J$  = 7.8 Hz, 2H), 7.68 (t,  $J$  = 7.7 Hz, 2H), 7.57 (d,  $J$  = 7.7 Hz, 1H), 7.54 (s, 2H). MS (ESI<sup>-</sup>): calc.  $\text{C}_{30}\text{H}_{20}\text{N}_6$  464.17; found, 463.17(M-H)<sup>-</sup>.

**ethyl 6-methyl-2-picolinate, D1:**

6-methyl-2-picolinic acid (5 g, 36.46 mmol) was dissolved in absolute ethanol (40 ml) and the solution was saturated with HCl gas. The solution was allowed to reflux for 2h. The excess of solvent was evaporated and the residue washed with a cold saturated solution of K<sub>2</sub>CO<sub>3</sub>. The product was extracted with diethyl ether and the extracts were dried over MgSO<sub>4</sub>, filtrated and evaporated. The pure compound was obtained as a colourless liquid after distillation under vacuum. The yield was 5.5 g (91%). <sup>1</sup>H NMR (400 MHz, CDCl<sub>3</sub>, ppm): δ 7.96 – 7.90 (m, 1H), 7.71 (t, *J* = 7.7 Hz, 1H), 7.36 – 7.29 (m, 1H), 4.47 (q, *J* = 7.1 Hz, 2H), 2.66 (s, 3H), 1.43 (t, *J* = 7.1 Hz, 3H).

**3,3'-(1,3-phenylene)bis(1-(6-methylpyridin-2-yl)propane-1,3-dione), D2:** To a suspension of 60% NaH (oil dispersion, 0.51 g, 12.75 mmol) in THF (50 mL), 1,3-diacetylbenzene (0.38 g, 2.34 mmol) was added and the mixture was stirred for 15 min. Then ethyl 6-methylpicolinate (0.78 g, 4.7 mmol) in THF (10 mL) was added dropwise, and the mixture was heated under reflux overnight. A dark brown suspension was formed. The solvent was removed in vacuo and the resulting brown solid was suspended in water (40 mL). The aqueous mixture was acidified to a pH 3-4 using 12% HCl and left for 30 min under stirring. The yellow solid was collected by filtration, washed with water, and dried under vacuum. The yield was 0.63 g (67%). <sup>1</sup>H NMR (400 MHz, CDCl<sub>3</sub>, ppm): δ 16.52 (s, 1H), 8.72 (s, 1H), 8.25 (d, *J* = 7.9 Hz, 2H), 7.99 (d, *J* = 8.1 Hz, 2H), 7.76 (t, *J* = 7.2 Hz, 2H), 7.67 (s, 2H), 7.65 – 7.61 (m, 2H), 7.32 (d, *J* = 8.1 Hz, 2H), 2.68 (s, 6H). MS (ESI<sup>+</sup>): calc. C<sub>24</sub>H<sub>20</sub>N<sub>6</sub>O<sub>2</sub> 400.14; found, 401.14 (M+H)<sup>+</sup>.

**1,3-bis(3-(6-methylpyridin-2-yl)-1H-pyrazol-5-yl)benzene, H<sub>2</sub>L6:** Solid D2 (0.62 g, 1.6 mmol) was suspended in a mixture of methanol and chloroform (4:1, 50 ml) and hydrazine (64% in H<sub>2</sub>O, 0.76 mL, 9.42 mmol) was added to the mixture dropwise, which was then heated under reflux overnight. After that, the mixture was cooled to room temperature and the solvents were removed by rotary evaporation. A brown oily residue was collected and suspended in water (50 ml). A white solid formed after stirring for 30 min. It was collected by filtration, washed with diethyl ether (50 mL), and dried under vacuum. The yield was 0.49g (80%). <sup>1</sup>H NMR (400 MHz, CDCl<sub>3</sub>, ppm): 7.84 (dd, *J* = 7.7, 1.5 Hz, 2H); 7.65 (t, *J* = 7.7, 2H); 7.52 (3, 3H); 7.12-

10 (m, 3H); 7.11 (s, 2H); 2.61 (s, 6H). MS (ESI<sup>+</sup>): calc. C<sub>24</sub>H<sub>20</sub>N<sub>6</sub> 392.17; found, 393.18(M+H)<sup>+</sup>.

**Ethyl pyrazine-2-carboxylate, E1:** Pyrazinecarboxylic acid (2 g, 16.11 mmol) was dissolved in ethanol (50 ml) and sulfuric acid (2.5 mL, 46.90 mmol) was added. The mixture was refluxed for 48 hours. The solution was allowed to cool at room temperature and the pH was adjusted to 8 using a saturated solution of K<sub>2</sub>CO<sub>3</sub>. The solvent was removed under reduced pressure. The residue was extracted with dichloromethane (3 x 20 ml). The extracts were washed with water (3 x 20 ml) and dried over MgSO<sub>4</sub>, filtrated and evaporated. The product was obtained as dark brown crystals after removing the solvent in vacuo. The yield was 1.94 (79%). <sup>1</sup>H NMR (400 MHz, CDCl<sub>3</sub>, ppm): δ 9.32 (d, *J* = 1.5 Hz, 1H), 8.76 (d, *J* = 2.4 Hz, 1H), 8.73 (dd, *J* = 2.4, 1.5 Hz, 1H), 4.51 (q, *J* = 7.2 Hz, 2H), 1.46 (t, *J* = 7.1 Hz, 3H).

**3,3'-(1,3-phenylene)bis(1-(pyrazin-2-yl)propane-1,3-dione), E2:** To a suspension of 60% NaH (oil dispersion, 0.64 g, 26.55 mmol) in dry THF (60 mL), ethyl pyrazine-2-carboxylate, E1 (1.966 g, 12.96 mmol) in dry THF (15ml) was added. Then, a solution of 1,3-diacetylbenzene (1.049 g, 6.47 mmol) in dry THF (25 mL) was added dropwise to the suspension, which was refluxed overnight. The solvent was removed in vacuo, followed by the addition of water (75 mL). The aqueous mixture was acidified to a pH of 5-6 using 12% HCl and left for 30 min under stirring. The precipitate was filtered, ethyl acetate (25 mL) was added and the mixture was left stirring overnight. The orange precipitate was filtrated. Yield 26%. <sup>1</sup>H NMR (400 MHz, dms<sub>o</sub>-*d*<sub>6</sub>, ppm) δ 9.29 (s, 2H), 8.89 (s, 2H), 8.85 (s, 2H), 8.58 (s, 1H), 8.31 (d, *J* = 6.4 Hz, 1H), 7.74 (m, 1H), 7.54 (s, 2H). MS (ESI<sup>+</sup>): calc. C<sub>24</sub>H<sub>14</sub>N<sub>4</sub>O<sub>4</sub> 374.10; found, 375.11(M+H)<sup>+</sup>.

**1,3-bis(3-(pyrazin-2-yl)-1H-pyrazol-5-yl)benzene, H<sub>2</sub>L7:** 3,3'-(1,3-phenylene)bis(1-(pyrazin-2-yl)propane-1,3-dione) (E2) (0.500 g, 1.34 mmol) was suspended in methanol (50 mL) and a hydrazine solution (0.18 mL, 3.19 mmol) was added. The suspension was brought to reflux and left overnight. Methanol was removed in vacuo, followed by the addition of water (25 mL). The suspension was stirred. After one hour the solid was filtered, washed with diethyl ether and dried in vacuo. The obtained solid was 1,3-bis(3-(pyrazin-2-yl)-1H-pyrazol-5-yl)benzene

(H<sub>2</sub>L7). Yield 71%. NMR (400 MHz, dms<sub>o</sub>-d<sub>6</sub>) δ 13.84 (s, 2H), 9.24 (s, 2H), 8.70 (s, 2H), 8.61 (s, 2H), 8.41 (s, 1H), 7.87 (d, *J* = 6.2 Hz, 2H), 7.62 – 7.54 (m, 3H). MS (ESI<sup>+</sup>): calc. C<sub>24</sub>H<sub>14</sub>N<sub>8</sub> 366.13; found, 365.14(M-H).

**2-bromo-5-(4-(pyridin-2-yl)-1H-1,2,3-triazol-1-yl)pyridine, F1:** 2-Bromo-5-iodopyridine (1 g, 3.52 mmol) and 2-ethynylpyridine (0.36 ml, 3.52 mmol) were mixed in a sealable round bottom vial. To the mixture were added *L*-proline (81 mg, 0.76 mmol), Na<sub>2</sub>CO<sub>3</sub> (75 mg, 0.76 mmol), NaN<sub>3</sub> (274.6 mg, 4.22 mmol), sodium ascorbate (69 mg, 0.35 mmol), 20 ml (9:1) DMSO/H<sub>2</sub>O and CuSO<sub>4</sub>·5H<sub>2</sub>O (44 mg, 0.18 mmol). The vial was sealed and the mixture was stirred overnight at 65 °C. The brown crude was poured into ice-cold water and a white precipitate formed. It was isolated by filtration and washed with dilute aq NH<sub>3</sub> to remove any traces of explosive copper azides. The solid was dried when filtrated in the air. The yield was 0.606g (57%). <sup>1</sup>H NMR (400 MHz, CDCl<sub>3</sub>, ppm): δ 8.86 (d, *J* = 2.7 Hz, 1H), 8.64 (s, 1H), 8.66 – 8.60 (m, 1H), 8.25 (d, *J* = 7.9 Hz, 1H), 8.10 (dd, *J* = 8.6, 2.8 Hz, 1H), 7.84 (td, *J* = 7.7, 1.8 Hz, 1H), 7.71 (d, *J* = 8.5 Hz, 1H), 7.31 (ddd, *J* = 7.6, 4.9, 1.2 Hz, 1H). <sup>13</sup>C NMR (400 MHz, CDCl<sub>3</sub>, ppm): δ 149.87, 149.76, 149.41, 141.74, 141.46, 137.21, 133.23, 130.37, 129.18, 123.61, 120.68, 119.78. MS (ESI<sup>+</sup>): calc. C<sub>12</sub>H<sub>8</sub>BrN<sub>5</sub> 301.00 (100%), 303.00 (97.3%); found, 302.00 and 304.00 (M+H)<sup>+</sup>.

**5-(4-(pyridin-2-yl)-1H-1,2,3-triazol-1-yl)-2-(tributylstannyl)pyridine, F2:** <sup>n</sup>BuLi (0.35 ml, 0.87 mmol, 2.5 M in hexane) was added dropwise to a solution of F1 (0.250 g, 0.83 mmol) in dry THF (10 ml) at -78°C. The mixture was stirred at this temperature for 1 hour before the addition of tributyltin chloride (0.23 ml, 0.84 mmol). The mixture was additionally stirred for 3 hours at -78°C before it was allowed to warm to room temperature. The solution turned deep yellow when quenched with NH<sub>4</sub>Cl (10 ml). The mixture was extracted with ethyl acetate (3 x 15 ml), then washed with brine (10 ml), and dried over MgSO<sub>4</sub>. The solvent was evaporated in vacuo yielding a yellow solid. The compound was afforded as a yellow oil after purification via column chromatography (8:2 hexane/ethyl acetate). The yield was 120 mg (28%). <sup>1</sup>H NMR (400 MHz, CDCl<sub>3</sub>, ppm): δ 8.76 (dd, *J* = 4.8, 1.6 Hz, 1H), 8.73 (d, *J* = 2.4 Hz, 1H), 8.50 (d, *J* = 4.8 Hz, 1H), 8.26 (d, *J* = 6.8 Hz, 1H), 7.86 (ddd, *J* = 8.1, 2.7, 1.4 Hz, 1H), 7.83 – 7.73 (m, 1H), 7.50 (dd, *J* = 8.1, 4.8 Hz, 1H), 7.21 (ddd, *J* = 7.6, 4.9, 1.3 Hz, 1H), 1.36 – 1.19 (m, 12H), 1.16 – 1.06 (m, 6H), 0.81 (s, 9H).

**5,5''-bis(4-(pyridin-2-yl)-4,5-dihydro-1H-1,2,3-triazol-1-yl)-2,2':6',2''-terpyridine, H<sub>2</sub>L<sub>8</sub>:** 2,6-dibromopyridine (19 mg, 0.08 mmol) and F2 (120 mg, 0.23 mmol) were dissolved in dry toluene (3ml). Pd(PPh<sub>3</sub>)<sub>4</sub> (38 mg, 0.03 mmol) was added and the solution was refluxed for 24 hours. After cooling to room temperature, the solvent was removed under reduced pressure. The product was purified by column chromatography (gradient elution 9:1 ethyl acetate/hexane to 1% methanol in ethyl acetate). The product was obtained as a yellow solid. The yield was about 1 mg (<2.5%). <sup>1</sup>H NMR (400 MHz, CDCl<sub>3</sub>, ppm): δ 8.62 (d, *J* = 2.1 Hz, 2H), 8.48 (d, *J* = 1.5 Hz, 2H), 8.17 (d, *J* = 9.3 Hz, 2H), 7.87 – 7.77 (m, 4H), 7.62 (d, *J* = 9.3 Hz, 2H), 7.36 (d, *J* = 1.9 Hz, 1H), 7.35 – 7.31 (m, 1H), 7.31 – 7.26 (m, 2H), 7.04 (s, 2H).

## 5.5. References

- (1) Steel, P. J. *Acc. Chem. Res.* **2005**, *38*, 243–250.
- (2) Holliday, B. J.; Mirkin, C. A. *Angew. Chemie - Int. Ed.* **2001**, *40*, 2022–2043.
- (3) Caulder, D. L.; Raymond, K. N. *Acc. Chem. Res.* **1999**, *32*, 975–982.
- (4) Caulder, D. L.; Raymond, K. N. *J. Chem. Soc. - Dalt. Trans.* **1999**, No. 8, 1185–1200.
- (5) Aromí, G.; Gamez, P.; Reedijk, J. *Coord. Chem. Rev.* **2008**, *252*, 964–989.
- (6) Aromí, G.; Aguilà, D.; Gamez, P.; Luis, F.; Roubeau, O. *Chem. Soc. Rev.* **2012**, *41*, 537–546.
- (7) Claisen, L.; Ehrhardt, E. F. *Berichte der Dtsch. Chem. Gesellschaft* **1889**, *22*, 1009–1019.
- (8) Liu, J. K. *Chem. Rev.* **2006**, *106*, 2209–2223.
- (9) Bogie, P. M.; Lyon, Y.; Holloway, L. R.; Julian, R. R.; Hooley, R. J. *Supramol. Chem.* **2017**, *29*, 936–945.
- (10) Cuppoletti, A.; Cho, Y.; Park, J. S.; Strässler, C.; Kool, E. T. *Bioconjug. Chem.* **2005**, *16*, 528–534.
- (11) Ferrand, Y.; Crump, M. P.; Davis, A. P. *Science (80- )*. **2007**, *318*, 619–622.
- (12) Rajakumar, P.; Padmanabhan, R.; Rajesh, N. *Bioorganic Med. Chem. Lett.* **2012**, *22*, 3770–3775.
- (13) Kim, D.; Coropceanu, V.; Brédas, J. L. *J. Am. Chem. Soc.* **2011**, *133*, 17895–17900.
- (14) Sawayama, Y.; Tsujimoto, T.; Sugino, K.; Nishikawa, T.; Isobe, M.; Kawagishi,

- H. Biosci. Biotechnol. Biochem.* **2006**, *70*, 2998–3003.
- (15) Sasabe, H.; Seino, Y.; Kimura, M.; Kido, J. *Chem. Mater.* **2012**, *24*, 1404–1406.
- (16) Adrio, L. A.; Antelo Mfguez, J. M.; Hii, K. K. *Org. Prep. Proced. Int.* **2009**, *41*, 331–358.
- (17) Rocchi, D.; González, J. F.; Gómez-Carpintero, J.; González-Ruiz, V.; Martín, M. A.; Sridharan, V.; Menéndez, J. C. *ACS Comb. Sci.* **2018**, *20*, 722–731.
- (18) Raghukumar, V.; Murugan, P. *Synth. Commun.* **2001**, *31*, 3497–3505.
- (19) Bell, Z. R.; McCleverty, J. A.; Ward, M. D. *Aust. J. Chem.* **2003**, *56*, 665–670.
- (20) Tidmarsh, I. S.; Taylor, B. F.; Hardie, M. J.; Russo, L.; Clegg, W.; Ward, M. D. *New J. Chem.* **2009**, *33*, 366–375.
- (21) Lowrey, A. H.; George, C.; D'Antonio, P.; Karle, J. *J. Am. Chem. Soc.* **1971**, *93*, 6399–6403.
- (22) Aromí, G.; Gamez, P.; Boldron, C.; Kooijman, H.; Spek, A. L.; Reedijk, J. *Eur. J. Inorg. Chem.* **2006**, No. 10, 1940–1944.
- (23) Batrice, R. J.; August Ridenour, J.; Lee Ayscue, R.; Bertke, J. A.; Knope, K. E. *CrystEngComm* **2017**, *19*, 5300–5312.
- (24) Wang, Y.; Shen, P. P.; Ren, N.; Zhang, J. J.; Geng, L. N.; Wang, S. P.; Shi, S. K. *RSC Adv.* **2016**, *6*, 70770–70780.
- (25) Huo, J. X.; Wang, Y.; Zhang, D. H.; Ren, N.; Zhang, J. J. *J. Therm. Anal. Calorim.* **2016**, *124*, 1575–1585.
- (26) Carter, K. P.; Zulato, C. H. F.; Rodrigues, E. M.; Pope, S. J. A.; Sigoli, F. A.; Cahill, C. L. *Dalt. Trans.* **2015**, *44*, 15843–15854.
- (27) Zhu, B. H.; Liu, Y. H.; Jin, X. Y.; Xu, H. Y.; Han, Y. Y.; Zhao, Q. *Polyhedron* **2014**, *74*, 67–71.
- (28) Andreiadis, E. S.; Gauthier, N.; Imbert, D.; Demadrille, R.; Pécaut, J.; Mazzanti, M. *Inorg. Chem.* **2013**, *52*, 14382–14390.
- (29) Smith, P. A.; Crawford, C.; Beedoe, N.; Assefa, Z.; Sykora, R. E. *Inorg. Chem.* **2012**, *51*, 12230–12241.
- (30) Carter, K. P.; Thomas, K. E.; Pope, S. J. A.; Holmberg, R. J.; Butcher, R. J.; Murugesu, M.; Cahill, C. L. *Inorg. Chem.* **2016**, *55*, 6902–6915.
- (31) Messimeri, A.; Papadimitriou, C.; Raptopoulou, C. P.; Escuer, A.; Perlepes, S. P.; Boudalis, A. K. *Inorg. Chem. Commun.* **2007**, *10*, 800–804.
- (32) Petrosyants, S. P.; Ilyukhin, A. B.; Efimov, N. N.; Gavrikov, A. V.; Novotortsev,

- V. M. *Inorganica Chim. Acta* **2018**, *482*, 813–820.
- (33) Petrosyants, S. P.; Ilyukhin, A. B.; Gavrikov, A. V.; Mikhlina, Y. A.; Puntus, L. N.; Varaksina, E. A.; Efimov, N. N.; Novotortsev, V. M. *Inorganica Chim. Acta* **2019**, *486*, 499–505.
- (34) Kumar, K.; Stefańczyk, O.; Chorazy, S.; Nakabayashi, K.; Sieklucka, B.; Ohkoshi, S. I. *Inorg. Chem.* **2019**, *58*, 5677–5687.
- (35) Ahrens, B.; Cotton, S. A.; Feeder, N.; Noy, O. E.; Raithby, P. R.; Teat, S. J. *J. Chem. Soc. Dalton Trans.* **2002**, No. 9, 2027–2030.
- (36) Lewis, F. W.; Harwood, L. M.; Hudson, M. J.; Drew, M. G. B.; Sypula, M.; Modolo, G.; Whittaker, D.; Sharrad, C. A.; Videva, V.; Hubscher-Bruder, V.; Arnaud-Neu, F. *Dalt. Trans.* **2012**, *41*, 9209–9219.
- (37) Shen, P. P.; Wu, X. H.; Ren, N.; Zhang, J. J.; Wang, S. P. *Zeitschrift für Anorg. und Allg. Chemie* **2017**, *643*, 889–894.
- (38) Sarkar, T.; Banerjee, S.; Mukherjee, S.; Hussain, A. *Dalt. Trans.* **2016**, *45*, 6424–6438.
- (39) Hussain, A.; Somyajit, K.; Banik, B.; Banerjee, S.; Nagaraju, G.; Chakravarty, A. *Dalt. Trans.* **2013**, *42*, 182–195.
- (40) Young, K.; Xiao, Q.; Zakarian, A. *European J. Org. Chem.* **2015**, *2015*, 2337–2341.
- (41) Wei, Q. H.; Argent, S. P.; Adams, H.; Ward, M. D. *New J. Chem.* **2008**, *32*, 73–82.
- (42) Encinas, S.; Flamigni, L.; Barigelletti, F.; Constable, E. C.; Housecroft, C. E.; Schofield, E. R.; Figgemeier, E.; Fenske, D.; Neuburger, M.; Vos, J. G.; Zehnder, M. *Chem. - A Eur. J.* **2002**, *8*, 137–150.
- (43) Sénéchal-David, K.; Pope, S. J. A.; Quinn, S.; Faulkner, S.; Gunnlaugsson, T. *Inorg. Chem.* **2006**, *45*, 10040–10042.
- (44) Li, F.; Clegg, J. K.; Price, D.; Kepert, C. J. *Inorg. Chem.* **2011**, *50*, 726–728.
- (45) Cargill Thompson, A. M. W. *Coord. Chem. Rev.* **1997**, *160*, 1–52.
- (46) Constable, E. C.; Davies, J. E.; Phillips, D.; Raithby, P. R. *Polyhedron* **1998**, *17*, 3989–3997.
- (47) Synthesis, I. **2001**, 271–272.
- (48) Champouret, Y. D. M.; Chaggar, R. K.; Dadhiwala, I.; Fawcett, J.; Solan, G. A. *Tetrahedron* **2006**, *62*, 79–89.
- (49) Zeid, A.; El, A.; Hassanien, B. *J. Chem. Res.* **2004**, No. 8, 536–540.

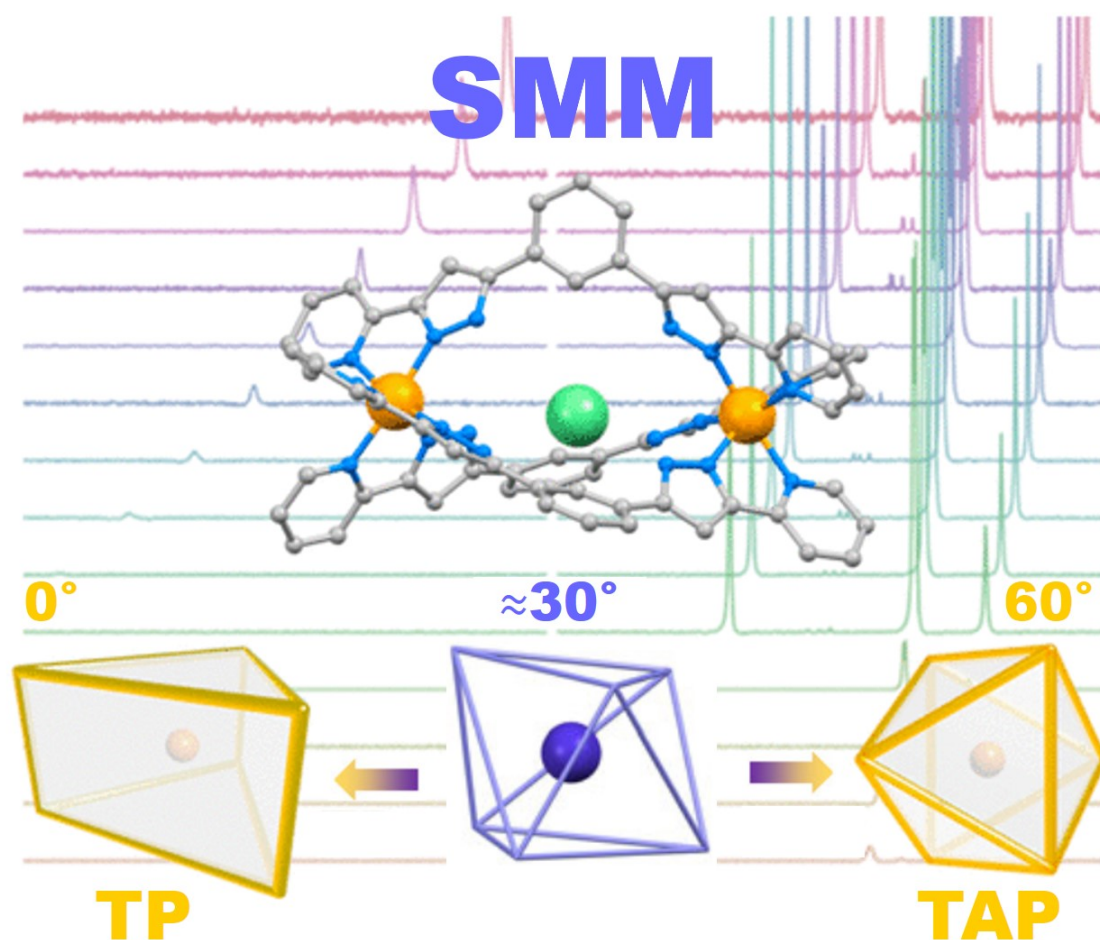
- (50) Darawsheh, M.; Barrios, L. A.; Roubeau, O.; Teat, S. J.; Aromí, G. *Chem. - A Eur. J.* **2016**, *22*, 8635–8645.
- (51) Darawsheh, M. D.; Barrios, L. A.; Roubeau, O.; Teat, S. J.; Aromí, G. *Chem. Commun.* **2017**, *53*, 569–572.
- (52) Bartual-Murgui, C.; Vela, S.; Darawsheh, M.; Diego, R.; Teat, S. J.; Roubeau, O.; Aromí, G. *Inorg. Chem. Front.* **2017**, *4*, 1374–1383.
- (53) Overberger, C. G.; Shalati, M. D. *Eur. Polym. J.* **1983**, *19*, 1055–1065.
- (54) Stevenson, K. A.; Melan, C. F. C.; Fleischel, O.; Wang, R.; Petitjean, A. *Cryst. Growth Des.* **2012**, *12*, 5169–5173.
- (55) Vellas, S. K.; Lewis, J. E. M.; Shankar, M.; Sagatova, A.; Tyndall, J. D. A.; Monk, B. C.; Fitchett, C. M.; Hanton, L. R.; Crowley, J. D. *Molecules* **2013**, *18*, 6383–6407.
- (56) Wu, N.; Melan, C. F. C.; Stevenson, K. A.; Fleischel, O.; Guo, H.; Habib, F.; Holmberg, R. J.; Murugesu, M.; Mosey, N. J.; Nierengarten, H.; Petitjean, A. *Dalt. Trans.* **2015**, *44*, 14991–15005.
- (57) Akhuli, B.; Cera, L.; Jana, B.; Saha, S.; Schalley, C. A.; Ghosh, P. *Inorg. Chem.* **2015**, *54*, 4231–4242.
- (58) Jana, B.; Cera, L.; Akhuli, B.; Naskar, S.; Schalley, C. A.; Ghosh, P. *Inorg. Chem.* **2017**, *56*, 12505–12513.
- (59) Rostovtsev, V. V.; Green, L. G.; Fokin, V. V.; Sharpless, K. B. *Angew. Chemie - Int. Ed.* **2002**, *41*, 2596–2599.
- (60) Tornøe, C. W.; Christensen, C.; Meldal, M. *J. Org. Chem.* **2002**, *67*, 3057–3064.
- (61) Rizzi, L.; Gotti, C.; De Amici, M.; Dallanoce, C.; Matera, C. *Chem. Biodivers.* **2018**, *15*, 2–9.
- (62) Feldman, A. K.; Colasson, B.; Fokin, V. V. *Org. Lett.* **2004**, *6*, 3897–3899.
- (63) Scattergood, P. A.; Roberts, J.; Omar, S. A. E.; Elliott, P. I. P. *Inorg. Chem.* **2019**, *58*, 8607–8621.
- (64) Hanan, G. S.; Schubert, U. S.; Volkmer, D.; Rivière, E.; Lehn, J. M.; Kyritsakas, N.; Fischer, J. *Can.J.Chem* **1997**, *75*, 169–182.
- (65) Aromi, G.; Darawsheh, M.; Barrios, L. A.; Roubeau, O.; Teat, S. J. *Angew. Chemie Int. Ed.* **2018**, *57*, 13509–13513.



# CHAPTER 6

---

## Cl@[Co<sup>II</sup><sub>2</sub>(H<sub>2</sub>L)<sub>3</sub>]<sup>3+</sup> AND Cl@[Co<sup>II</sup> Zn<sup>II</sup> (H<sub>2</sub>L)<sub>3</sub>]<sup>3+</sup> TRIPLE-STRANDED HELICATES SHOWING SLOW MAGNETIC RELAXATION





## 6. Cl@ [Co<sup>II</sup><sub>2</sub>(H<sub>2</sub>L)<sub>3</sub>]<sup>3+</sup> AND Cl@[Co<sup>II</sup> Zn<sup>II</sup> (H<sub>2</sub>L)<sub>3</sub>]<sup>3+</sup> TRIPLE-STRANDED HELICATES SHOWING SLOW MAGNETIC RELAXATION

### Abstract

Among the 3d-block metal ions, Co(II) often behaves as single-molecule magnets (SMMs) due to its large intrinsic magnetic anisotropy arising from the zero-field splitting (ZFS), which in turn comes to rise from the spin-orbit coupling (SOC). Lately, for six-coordinated Co(II)-based ions, the trigonal prismatic (TP) geometry emerged as a new source of axial magnetic anisotropy and, therefore, as a new type of SMM complexes. On the other hand, Co(II) complexes in a trigonal antiprismatic (TAP) geometry, which is on the other extreme of the Bailar isomeric twist along the C<sub>3</sub> symmetry axis, only show SMM behaviour when a magnetic field is applied. Here, the moderate SMM behaviour of new [Co<sub>2</sub>(H<sub>2</sub>L)<sub>3</sub>]<sup>4+</sup> (**11**) and [CoZn(H<sub>2</sub>L)<sub>3</sub>]<sup>4+</sup> (**13**) coordination helicates [L is a bis(pyrazolylpyridine) ligand] was investigated. The cobalt ions in these compounds display an intermediate geometry between the trigonal prismatic and antiprismatic, which gives rise to a small axial anisotropy. This property was previously predicted and later unveiled by solution paramagnetic <sup>1</sup>H NMR and solid-state magnetization measurements.

### 6.1. Introduction

The pursuit of interesting magnetic properties in molecular compounds has lately increased considerably since these systems open vast possibilities for creating devices with high-density information storage or for quantum computing applications.<sup>1-4</sup> Molecules displaying bistable magnetic behaviour<sup>5</sup> are ideal candidates for realizing such potential applications. In light of previous work from the group, we could effectively tune and control the bistable magnetism through guests, light and thermal modulation of the spin crossover in Fe<sup>II</sup><sub>2</sub> triple-stranded helicates.<sup>6</sup> However, the use of 3d-metal ions, such as Co<sup>2+</sup> and 4f-metal ions, can offer the coexistence of different stable states (bistability) through a different magnetic strategy; by exploiting the slow relaxation of the magnetization of individual ions.<sup>7-10</sup> These magnetic properties arise from the metal ion in a suitable ligand field, geometry and electronic structure that creates magnetic anisotropy. In

this sense, single-molecule magnets (SMMs) are paramagnetic complexes that hold an axial bistable magnetic moment. These systems retain the orientation of the magnetization in the absence of a magnetic field below a given temperature (blocking temperature). Thus, highly anisotropic systems are required, which implies a larger size of the barrier associated with the reversal of the magnetization. Detailed information about the SMM behaviour is given in section 1.5 in the Introduction. Although many SMMs complexes have been studied during the last decade, the control of this behaviour remains a relevant goal. Getting more insights into the factors that govern the magnetic anisotropy is important to control the magnetic states and achieve new SMMs by rational design. Among first-row transition metals, cobalt is an excellent candidate for SMMs synthesis due to its strong spin-orbit coupling (SOC) in the 2+ oxidation state. Generally, the Co (II)  $d^7$  ion adopts a high spin ( $S=3/2$ ) configuration and different coordination geometry (distorted octahedra, trigonal prismatic, tetrahedral, distorted squared pyramid or linear; being usually the SOC and the anisotropy stronger when lowering in symmetry) depending on the ligands used. Thus, the symmetry around the 3d metal ion and the electronic structure exhibited by HS Co(II) is essential to understand their slow magnetic relaxation. However, in each geometry mentioned above, the spin ground state can be subject to zero-field splitting (ZFS; except for a trigonally-distorted octahedron). This effect is known as the energy gap ( $2D$ ;  $D$ : axial zero-field splitting parameter) causing the loss of the  $M_s$  ( $2S+1$ ) spin microstates degeneracy associated with a ground state  $S \geq 1$  in the presence of unquenched orbital angular momentum ( $L$ ) and absence of an external magnetic field. The  $L$  contribution arises from the odd number of electrons in degenerate  $d$  orbitals.<sup>11</sup> For  $S=3/2$ , the  $M_s = \pm 1/2$  sub-levels are separated from the  $M_s \pm 3/2$  by  $2D$ .<sup>12</sup> In the yellow column in Figure 6.1, the  $D$  parameter is considered positive since  $M_s = \pm 1/2$  are low in energy. Contrarily, if  $D$  is negative, the  $M_s \pm 3/2$  sub-levels lie below in energy. The ZFS is magnetically visible when the thermal population of the sub-levels is unequal causing a breach of the Curie-Law. Thus, it is detected at low temperatures where  $KT$  is lower than the energy gap. Additionally, to this explanation,<sup>13,14</sup> an example of a classic case of Co(II) is described below to illustrate the origin of the SOC. In the absence of ligand field (purple column in Figure 6.1), the  $d^7$  metal with a  $^4F$  Russell-Saunders free-ion term due to electronic repulsion ( $L=3$ ,  $S=3/2$ ) is 28-fold

degenerate (seven orbitally degenerated levels,  $M_L = \pm 3, \pm 2, \pm 1, 0$ ; and each has four spin degenerated  $M_S = \pm 3/2, \pm 1/2$ ). Introducing a weak  $O_h$  ligand field (orange column in Figure 6.1), this  $^4F$  free-ion term loses its orbital degeneracy and splits into two orbital triplets (T) and one orbital singlet (A), being  $^4T_{1g}$  the ground state and,  $^4T_{2g}$  and  $^4A_{2g}$  the excited ones. If SOC is considered at this level, the ground  $^4T_{1g}$  term further splits into a doublet, a quartet and a sextet. Nevertheless, in this illustrative case, we considered an additional distortion. The ideal  $O_h$  geometry is rarely found in real systems. Depending on the structural distortion (direction on-axis or off-axis), the ground state orbital degeneracy can be removed differently. Usually, an axially elongated distortion ( $D_{4h}$ , green column in Figure 6.1) of the octahedron takes place and gives rise to the  $^4T_{1g}$  ground term splitting into  $^4A_{2g}$  and  $^4E_{2g}$  terms. SOC further splits these terms into six Kramers doublets (yellow column in Figure 6.1). If  $^4A_{2g}$  is electronically isolated from  $^4E_{2g}$ , the former splits into two Kramers doublets ( $M_S = \pm 1/2$  or  $\pm 3/2$ ) separated by  $2D$  in the absence of a magnetic field. As mentioned above, if  $D > 0$ , the  $M_S = \pm 1/2$  is lowest in energy. Thus, a highly anisotropic system is reached. Furthermore, when an external field is applied (blue column in Figure 6.1), the energy levels of each spin projection further splits, through the phenomenon known as the Zeeman effect.

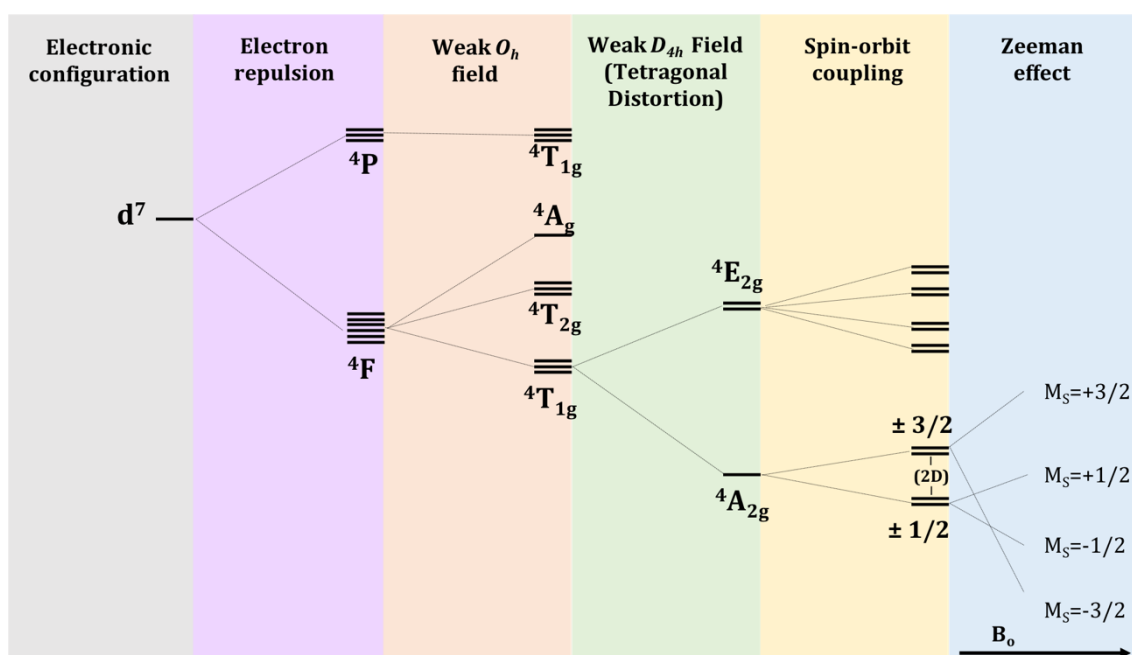


Figure 6.1. Schematic energy-level diagram for Co(II) illustrating the effects described in the text. The diagram is adapted from several references.<sup>11–16</sup>

In this way, Co(II) systems, which are strongly anisotropic, feature the highest barrier of magnetization reversal ( $U_{\text{eff}}$ ) of all the first-row transition metal SMMs.<sup>17-20</sup> To date, a two-coordinate linear cobalt(II) complex<sup>21</sup> exhibits the highest  $U_{\text{eff}}$  theoretical limit of  $450\text{cm}^{-1}$  in such an environment. In this case, magnetic data and theoretical simulation unveil that this close-to-maximal magnetic anisotropy is due to the significant orbital angular momentum coming from equally occupied ( $d_{x^2-y^2}$ ,  $d_{xy}$ ) and ( $d_{xz}$ ,  $d_{yz}$ ) orbital sets. However, this type of low-coordinate cobalt(II) complexes, together with their cobalt(I)<sup>22</sup>, iron(I)<sup>23</sup> and iron(II)<sup>24</sup> analogues, are unstable. Consequently, their possible technological purpose as molecular devices is exceptionally arduous. Recently, a trigonal prism (TP) coordination environment around the Co(II) metal centre emerged as an ideal geometry that also guarantees a source of large magnetic anisotropy while keeping the complex chemically stable.<sup>19,25</sup> Despite some efficient SMMs of Co(II)-TP lately synthesized,<sup>20,26,27</sup> TP remains an unusual geometry. Such an environment is ensured by a limited type of rigid cage ligands known as clathrochelates.<sup>28</sup> Instead, scorpionate-like ligands commonly lead to trigonal-antiprism (TAP) geometries.<sup>29</sup> Nevertheless, such Co(II)-TAP complexes only display slow relaxation when an external magnetic field is applied.<sup>30-32</sup> An illustrative chart containing one example of each Co(II)-SMM with different geometry (TP vs TAP) and their respective main geometrical and magnetic features is given in Figure 6.2. Each particular geometry represents one of the opposite limits of the Bailar twist, which involves an octahedron twist through the C3 axis of the molecule. From the C3 view, the octahedron (also namely trigonal antiprismatic, TAP) geometry with opposite triangular faces twists to the eclipsed arrangement trigonal prismatic (TP). As this twist occurs, the  $\varphi$  angle formed between the cis-vertices on the projection of the faces varies. Therefore, the  $\varphi$  value for the ideal TP is  $60^\circ$ , while the eclipsed TAP is  $0^\circ$  (Figure 6.3)<sup>33</sup>. Several reported six-coordinated Co(II) SMMs with different TAP and TP configurations were analysed in order to establish correlations between structural ( $\varphi$ ) and magnetic (axial anisotropy) factors.<sup>34</sup> The study evidences the slow magnetization in a zero dc field for complexes with symmetries close to TP, while field-induced SMMs corresponds to complexes with TAP symmetry. Furthermore, it unveils the worsening of SMMs behaviour compared to ideal geometries when distorting from a Co(II)-TP geometry towards a Co(II)TAP geometry.

## 6. [Co2] and [CoZn] triple-stranded helicates showing slow magnetic relaxation

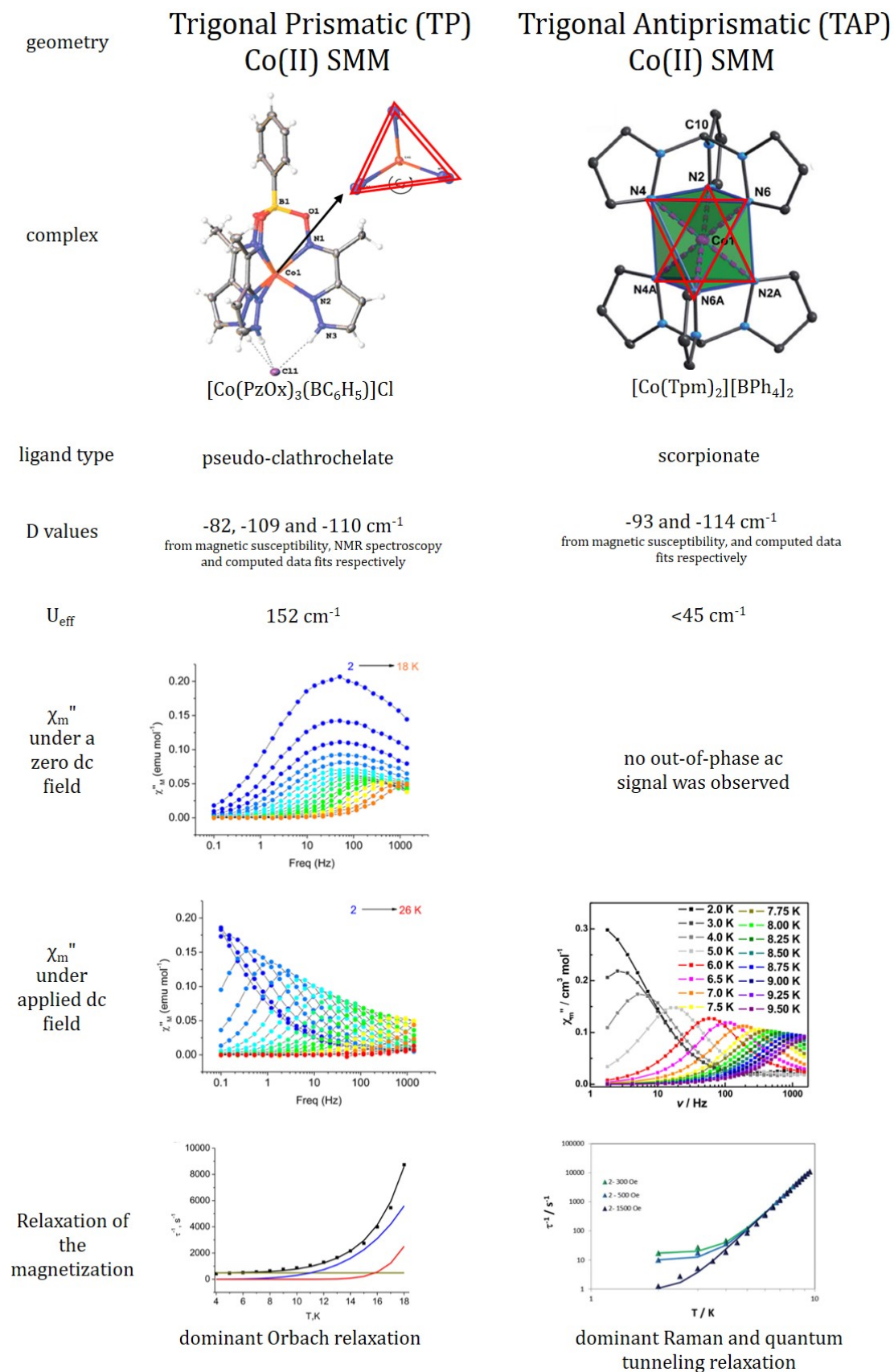


Figure 6.2. Illustrative chart of two examples of Co(II) displaying a TP (left)<sup>19,35</sup> and TAP(right)<sup>30</sup> geometry together with their geometrical and magnetic features summarized.

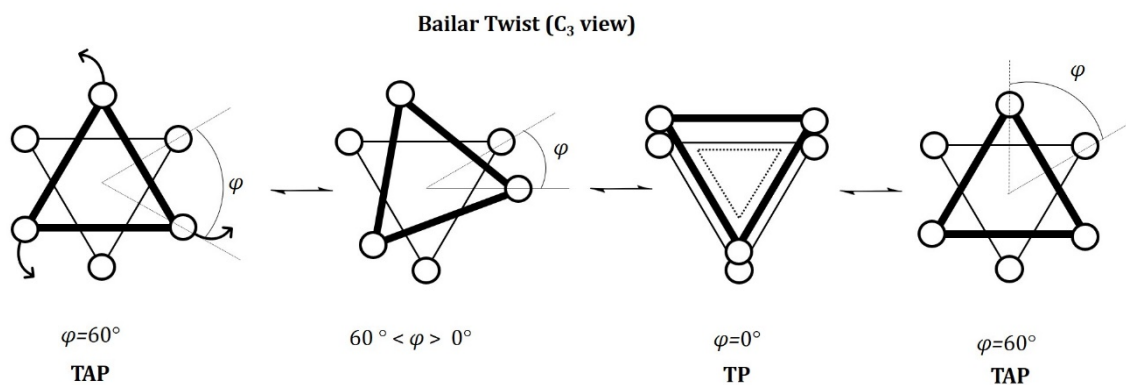


Figure 6.3. Bailar twist for the conformation transformation. The bite angle ( $\varphi$ ) used to difference the distortion of an ideal octahedron towards a trigonal prismatic symmetry is illustrated.

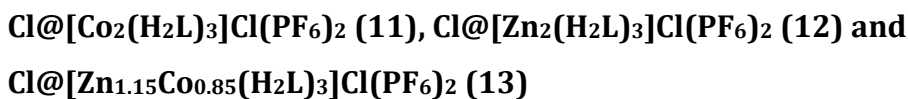
In a previous study, the anisotropy parameter for six-coordinated Co(II) was found to be highly sensitive to the local geometry of the metal center. Computationally the change in sign was predicted for an the axial parameter (D) around  $\varphi=42^\circ$  when twisting the Co(II) geometry from 0 to  $60^\circ$ .<sup>36</sup> However, to date, there is no previous experimental data on Co(II)- SMMS with trigonal symmetry and angular distortions ( $\varphi$ ) between 24 and  $57^\circ$ . It would be of special interest to provide Co(II)based SMM holding an  $\varphi$  value between this non-studied range to get more insights and understating of its magnetostructural correlations. The benefit of using coordination helicates<sup>37,38</sup> is expected to accomplish such structural demand.

In light of all the discussions above, we decided to coordinate cobalt(II) with a bis(pyrazolylpyridine) ligand (L, 1,3-bis[1-(pyridine-2-yl)-pyrazol-3-yl]benzene).<sup>6</sup> The new resulting Co(II) dinuclear triple-stranded helicate, [Co<sub>2</sub>(H<sub>2</sub>L)<sub>3</sub>]<sup>4+</sup> (**11**), ensures the intermediate geometry between TP and TAP around the metal ion. The analogous Fe<sup>II</sup><sub>2</sub> helicates display  $\varphi \approx 30^\circ$  values.<sup>6,39</sup> While the desired coordination geometry is acquired, the complex contains two Co<sup>II</sup> ions, which could affect the SMM properties through exchange bias between both metals.<sup>40</sup> Thus, to analyse the mutual effect of both ions within the [Co<sub>2</sub>] (**11**) complex, we also synthesized the mixed-metal [CoZn] (**13**) complex, which can be obtained as part of a solid solution with the homometallic [Zn<sub>2</sub>] complex by performing the reaction with larger amounts of Zn(II) compared with Co(II). Additionally, the pure [Zn<sub>2</sub>] (**12**) was prepared and characterized to provide further support and a source of comparison.



## 6.2. Results and discussion

### Synthesis and Mass Spectrometry of



The bis-(pyrazolylpyridine) ligand (H<sub>2</sub>L, 1,3-bis[1-(pyridine-2-yl)-pyrazol-3-yl]benzene) was synthesized by following our previously reported procedure.<sup>6</sup> Complexes **11**<sup>41</sup> and **12** were prepared from the reaction of CoCl<sub>2</sub>·6H<sub>2</sub>O or ZnCl<sub>2</sub> salts, respectively, with ligand H<sub>2</sub>L (3:2 stoichiometry) in methanol at room temperature. The resulting orange and white solutions, respectively, were treated with two equivalents of NBu<sub>4</sub>PF<sub>6</sub>. Suitable single crystals, orange (**11**) and colourless (**12**), respectively, were isolated in both cases via vapour diffusion of diethyl ether into the methanolic solution. Compound **12** was obtained in a lower yield due to its higher solubility. The colourless crystals were collected once formed. If left in the crystallization solution for few days, redissolution occurs; instead, orange crystals (**11**) remained crystalline in the methanol/ether solution. After several attempts, we were able to prepare the [CoZn] analogue by exploring different stoichiometric ratios of cobalt and zinc sources under the same crystallization conditions of **11** and **12**. Obtaining it is not straightforward since H<sub>2</sub>L is a symmetrical ligand, without any differentiated chelating pocket, therefore not displaying any structural feature to promote the formation of a heterometallic compound. In fact, the homometallic [Co<sup>II</sup><sub>2</sub>] helicate was mainly isolated (orange crystals) as part of a solid solution within a matrix of [CoZn] when using an equimolar mixture of the cobalt and zinc salts. Its presence was confirmed by the MS technique (Figure 6.4), which suggests a higher propensity of the [Co<sub>2</sub>] over the [Zn<sub>2</sub>] to crystallize, as inferred from their formation procedures. Therefore, the higher robustness of the homoleptic [Co<sub>2</sub>] over any Zn containing analogous in the MS conditions was taken into consideration. Despite the similarity of both ionic radii ( $r(\text{Zn}^{2+}) = 74.0 \text{ pm}$  and  $r(\text{Co}^{2+};\text{HS}) = 74.5 \text{ pm}$ )<sup>42</sup> the heterometallic [CoZn] species was only obtained by increasing substantially the amount of zinc salt. A 1:9 ratio of cobalt *versus* zinc salts was necessary to observe it with clarity. The MS spectrum of the sample unveiled the prominent presence of [Zn<sub>2</sub>] and [CoZn]

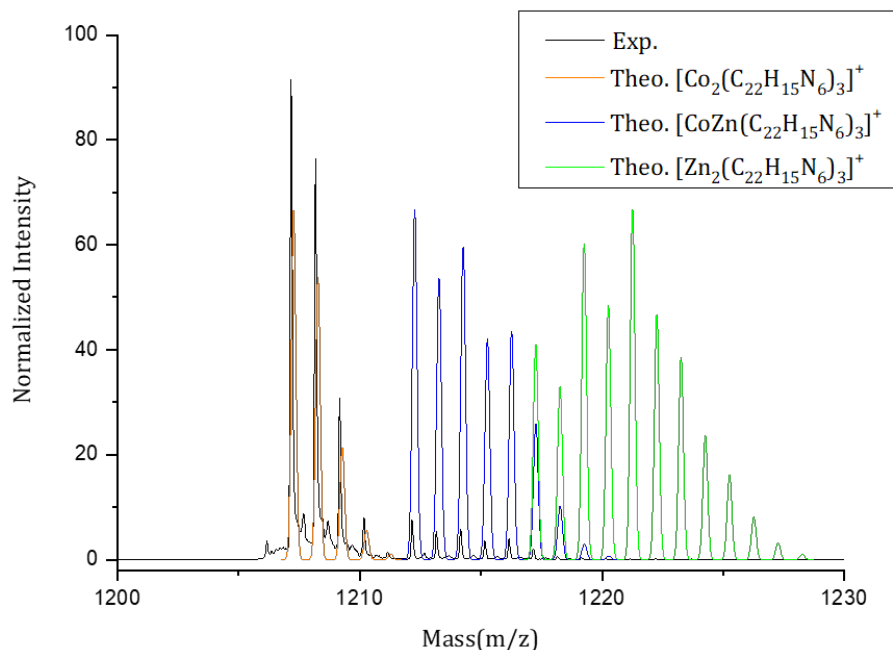


Figure 6.4. The mass spectrometry for detecting compound **13** of crystals form the reaction using an equimolar ratio of Co(II) and Zn(II) salts was measured in a mixture of MeOH/DMSO using a positive-ion MALDI. The selected region of the diagram (black line) show a peak for the fragments  $[\text{Co}_2(\text{H}_2\text{L})_3]^+$  and a marginal signal for  $[\text{CoZn}(\text{H}_2\text{L})_3]^+$ . The corresponding peak of  $[\text{Zn}_2(\text{H}_2\text{L})_3]^+$  was not observed. The superimposed colored lines are the theoretical patterns for the three fragments; orange line for  $[\text{Co}_2]$ , blue for  $[\text{CoZn}]$  and green for  $[\text{Zn}_2]$ . Only empty specimens were detected.

helicates and a residual, marginal amount of the  $[\text{Co}_2]$  within the solid matrix (Figure 6.5). This was consistent with ICP-OES metal analysis and the SCXRD, which propose the formula  $\text{Cl}@\text{[Co}_{0.19}\text{Zn}_{0.81}\text{L}_3]\text{Cl}(\text{PF}_6)_2$  (**13**) for the alloy (see below). Overall, the results corroborate that  $[\text{CoZn}]$  is present, and the segregation of the metals into homometallic species is not favoured in the system. Additionally, the presence of a marginal amount of  $[\text{Co}_2]$  in the mixture was revealed in the  $^1\text{H}$  NMR spectrum (see below). The apparent gradation of the cobalt amount within the various samples of complexes in going from **11** to **13** (solid dilution) was also visualized from the crystal colour of the samples. Orange, pale-orange and colourless crystals were obtained upon cobalt “solid dilution” (Figure A6.1- Appendix).

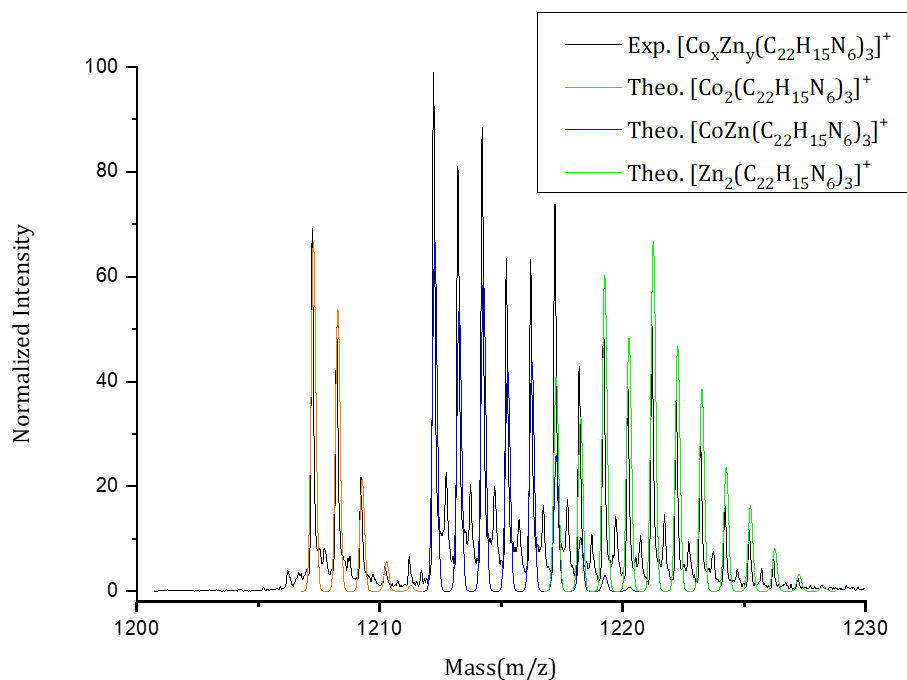


Figure 6.5. The mass spectrometry for detecting compound **12** of crystals from the reaction using an 1:9 ratio of Co(II) and Zn(II) salts was measured in a mixture of MeOH/DMSO using a positive-ion MALDI. The selected region of the diagram (black line) show a peak for the fragments  $[\text{Zn}_2(\text{H}_2\text{L})_3]^+$ ,  $[\text{CoZn}(\text{H}_2\text{L})_3]^+$  and a lesser signal for  $[\text{Co}_2(\text{H}_2\text{L})_3]^+$ . The superimposed colored lines are the theoretical patterns for the three fragments; orange line for  $[\text{Co}_2]$ , blue for  $[\text{CoZn}]$  and green for  $[\text{Zn}_2]$ . Only empty specimens were detected.

### Crystal structure of the [Co<sup>II</sup><sub>2</sub>] (**11**), [Zn<sup>II</sup><sub>2</sub>] (**12**) and [Co<sup>II</sup> Zn<sup>II</sup>] (**13**) helicates

All series of crystals were suitable for SCXRD. The three compounds (**11-13**) are isostructural if minor differences in lattice solvent molecules and some crystallographic disorder are not considered. For this reason, a detailed crystallographic description is only given for compound **11**. Detailed crystallographic information for all three compounds is summarized in Figures A6.2-A6.5 and Tables A6.1-A6.3. The triple-stranded [Co<sub>2</sub>] helicate, formulated as Cl@[Co<sub>2</sub>(H<sub>2</sub>L)<sub>3</sub>]Cl(PF<sub>6</sub>)<sub>2</sub> (**11**), has a cationic helical structure [Co<sub>2</sub>(H<sub>2</sub>L)<sub>3</sub>]<sup>4+</sup> with one Cl<sup>-</sup> anion encapsulated inside the cavity, together with one external Cl<sup>-</sup> and two PF<sub>6</sub><sup>-</sup> counter-ions. The inner Cl<sup>-</sup> anion is acting as a guest since it participates in six hydrogen-bonding interactions with the free N-H groups of the pyrazolyl moieties. Interestingly, the helical structure has never been isolated without a halide guest. These species are likely to provide a templating effect which is usually seen on other host helical examples.<sup>43</sup> Empty helicates have only been observed through MS. At 100K, compound **11** crystallizes in the tetragonal space group *I4<sub>1</sub>cd*. Its asymmetric

unit contains one cationic Cl@[Co<sub>2</sub>(H<sub>2</sub>L)<sub>3</sub>]<sup>3+</sup> species, one Cl<sup>-</sup> and two PF<sub>6</sub><sup>-</sup> distorted anions, four MeOH molecules and one ether molecule partially occupied (0.25%). The unit cell contains sixteen asymmetric units. The Cl@[Co<sub>2</sub>(H<sub>2</sub>L)<sub>3</sub>]<sup>3+</sup> moiety (Figure 6.6) is formed by two Co<sup>II</sup> metal centres defining the central helical axis and three H<sub>2</sub>L ligands acting as holding strands. Both cobalt centres have a Co-N average distance of 2.139 Å, typical for the HS state. The intra-helical distance between both cobalt ions is 9.771 Å. Thanks to the coordination of Co ions with the H<sub>2</sub>L ligands through their two pyrazolylpyridyl chelating pockets, these metals feature a distorted trigonal environment lying in between the TP and the TAP ideal geometries. Thus, we reached in an accidental manner a desired Co complex displaying an intermediate geometry with a  $\varphi \approx 38^\circ$ . Continuous shape measures were conducted with the program SHAPE to evaluate the distances between the polyhedra described by **11** (also for compounds **12** and **13**) and both the ideal geometries for both, TP and TAP coordination symmetries.<sup>33</sup> The resulting values indicate closer proximity to the TAP geometry than could be inferred from the experimental angles due to considerably disparate Co-N bond distances. In view of this geometry, where the signal D is expected to change (see above),<sup>36</sup> this compound is particularly valuable for this type of study.

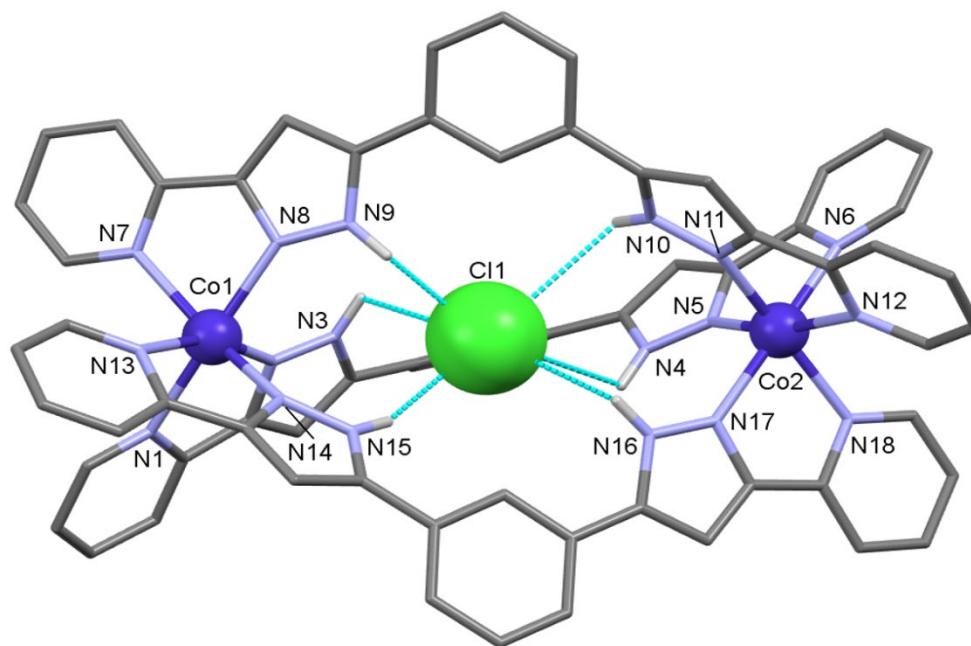


Figure 6.6. Molecular representation of the cationic (Cl@[Co<sub>2</sub>L<sub>3</sub>])<sup>3+</sup> assembly in compound **11**. PF<sub>6</sub><sup>-</sup> and Cl<sup>-</sup> counterions and MeOH and diethyl ether molecules are omitted for clarity. Only heteroatoms are labelled and H atoms that are part of N-H groups shown. H-bonds are shown with dashed cyan lines.

Both metal ions have the same chirality. By symmetry, two possible enantiomers ( $\Delta$ - $\Delta$  and  $\Lambda$ - $\Lambda$ ) are present within the lattice, leading to a racemic mixture. The helical architectures are nearly disposed of in sheets along the *ab* plane, with the PF<sub>6</sub><sup>-</sup> counterions in between them. (Figure A6.4, Appendix 6). These sheets are connected through several  $\pi\cdots\pi$  and C-H $\cdots\pi$  involving some aromatic rings of the Cl@[Co<sub>2</sub>(H<sub>2</sub>L)<sub>3</sub>]<sup>3+</sup> species, in which five close neighbours surround each helicate.

### **Magnetic study of the [Co<sup>II</sup><sub>2</sub>] (**11**) and [Co<sup>II</sup> Zn<sup>II</sup>] (**13**) helicates. Combining phase-solution and solid-state techniques.**

By combining paramagnetic NMR and SQUID magnetometry data, we unveil and verify the predicted SMMs behaviour of compounds **11** and **13**.

Regarding the first technique, an alternative NMR-based method developed by Novikov et al. was used to analyse the paramagnetic shifts in the NMR spectra.<sup>44</sup> In fact, all magnetic studies in solution were done in collaboration with his group. Since this solution's approach allows us to overcome some limitations, such as to avoid knowing the exact concentration of the paramagnetic compound and its immunity to the presence of other paramagnetic impurities, we deemed this method ideal to study compound **13**. This material is formed by [ZnCo] molecules within a matrix of [Zn<sub>2</sub>] helicates, in the presence of a small amount of [Co<sub>2</sub>] (negligible traces, see NMR results below) within a solid solution. Details on the NMR-based analysis of paramagnetic shifts for both cobalt compounds are summarized in Appendix 6.

The idealized trigonal symmetry of the Cl@[Co<sub>2</sub>(H<sub>2</sub>L)<sub>3</sub>]<sup>3+</sup> (**11**) and Cl@[CoZn(H<sub>2</sub>L)<sub>3</sub>]<sup>3+</sup> (**13**) helicates was corroborated from the paramagnetic <sup>1</sup>H NMR data acquired in methanol-*d*<sub>4</sub> (Figure 6.7, A6.6 and A6.7 in Appendix 6). Collectively, these results are consistent with MS, EA, the crystalline structures and the magnetic properties.

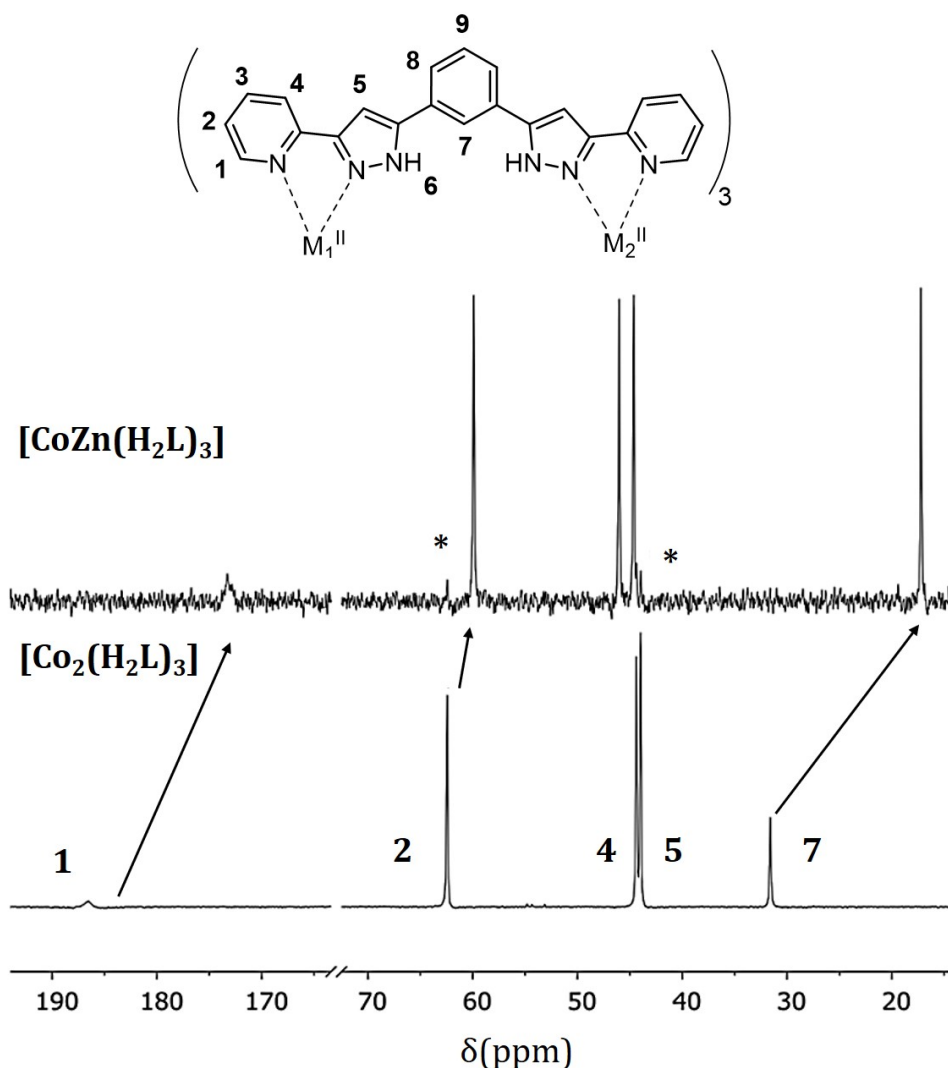


Figure 6.7. Stacked spectra (zoom) from the paramagnetic  $^1\text{H}$  NMR spectra of  $\text{Cl}@\text{[Co}_2(\text{H}_2\text{L})_3\text{]}^{3+}$  (bottom) and  $\text{Cl}@\text{[CoZn}(\text{H}_2\text{L})_3\text{]}^{3+}$  (top) in methanol- $d_4$ . Asterisks are non-detected peaks of  $\text{Cl}@\text{[Co}_2(\text{H}_2\text{L})_3\text{]}^{3+}$  in the top spectrum.

As expected, significant paramagnetic shifts ( $\delta$ ) are observed for an SMM molecule.<sup>45,46</sup> In our case, all large  $\delta_{\text{obs}}$  values for the [Co<sub>2</sub>] compound at several temperatures are summarized and compared with the calculated ones in Figure A6.8, Appendix 6. Details and a more comprehensive description for analysing the paramagnetic shifts in the  $^1\text{H}$  NMR spectra and the quantum chemical calculations are given in Appendix 6. However, the resulting axial anisotropy  $\Delta\chi_{ax} = 0.05\text{\AA}^3$  (Figure A6.9, Appendix 6), determined by the fit between the measured and the calculated chemical shifts, was moderate at room temperature. This value is smaller than those found for complexes with both, the TP ( $\Delta\chi_{ax} = 0.26\text{\AA}^3$ )<sup>20</sup> and TAP ( $\Delta\chi_{ax} = 0.21\text{\AA}^3$ )<sup>47</sup> geometries, respectively. Two possible reasons may contribute to

this - the intermediate TP-TAP geometry and the presence of intramolecular magnetic interactions. Since the molecules in solution are isolated, intermolecular interactions do not intervene in the magnetic analysis. However, intramolecular magnetic interactions between Co(II) ions of the dinuclear [Co<sub>2</sub>] assembly may lead to an overall quasi-nonmagnetic response. Thus, the small anisotropy due to an antiferromagnetic exchange between the cobalt ions.

To evaluate the intramolecular-interaction contribution, we studied the heterometallic Cl@[CoZn(H<sub>2</sub>L)<sub>3</sub>]<sup>3+</sup> helicate of the solid admixture mentioned above. The amount of the desired species [CoZn] was determined to be 13% from <sup>1</sup>H NMR spectrum, with 87% of the [Zn<sub>2</sub>] helicate and only traces of the [Co<sub>2</sub>] complex (Figures A6.10 and A6.11, Appendix 6). When comparing the [CoZn] <sup>1</sup>H NMR spectrum with that of [Co<sub>2</sub>], significant differences can be appreciated (Figure 6.7 and A6.7, Appendix 6). While the signals for the protons near Co(II) (H<sub>1</sub>, H<sub>2</sub>, H<sub>4</sub>, H<sub>5</sub>) are paramagnetically shifted similarly, the ones close to the Zn(II) ion are differently shifted. Additionally, the  $\delta_{\text{obs}}$  for proton 7 shows different shifts in [CoZn] and [Co<sub>2</sub>] species because this nucleus is equidistant from both metal ions, located on the bridging phenyl moiety of the ligand. In [CoZn], it is affected by only one cobalt paramagnetic ion. Thus, the paramagnetic shift is half as much that seen in [Co<sub>2</sub>]. This feature allows distinguishing both paramagnetic complexes by <sup>1</sup>H NMR. The estimated value of  $\Delta\chi_{\text{ax}}$  for [CoZn] from the NMR spectrum was 0.05 Å<sup>3</sup>, essentially the same as that observed for the [Co<sub>2</sub>] derivative. Therefore, the low magnetic anisotropy  $\Delta\chi_{\text{ax}}$  is not derived from the intramolecular magnetic interactions. Instead, the distorted TP-TAP geometry must be the determining factor.

Direct-current (dc) magnetometry data was used to support the NMR-based findings. Molar magnetic susceptibility ( $\chi_m$ ) of compound **11**, [Co<sub>2</sub>], was measured for a polycrystalline sample in the 2-300K temperature range under a constant magnetic field of 1kOe. The Co(II) ion is HS over the whole temperature range. At 300K, the measured  $\chi_m T$  value (5.7 cm<sup>3</sup> mol<sup>-1</sup> K) exceeds the spin-only value for two noninteracting Co(II) ions in the HS (spin-only value 3.75 cm<sup>3</sup> mol<sup>-1</sup> K). Therefore, there is spin-orbit coupling contribution displayed by the Co(II) ions. The  $\chi_m T$  value decreases reaching 3.5 cm<sup>3</sup> mol<sup>-1</sup> K at 2K, which also can be ascribed to the spin-orbit coupling effects. This is consistent with the field dependence of the

magnetization measurements (Figure 6.8), which show a magnetic saturation of 4.2  $\mu_B$  at 2K. Plots of  $\chi_m T$  vs.  $T$  and  $M$  vs.  $H$  for compound [CoZn] are superimposable to those of [Co<sub>2</sub>] once the data were scaled for the number of Co(II) ions per molecule and the dilution by the isostructural diamagnetic compound [Zn<sub>2</sub>] (Figures A6.12 and A6.13, Appendix 6). Thus, both complexes show the same magnetic behaviour, which in turns proves the absence of some relevant inter- or intramolecular magnetic interactions for the [Co<sub>2</sub>] complex.

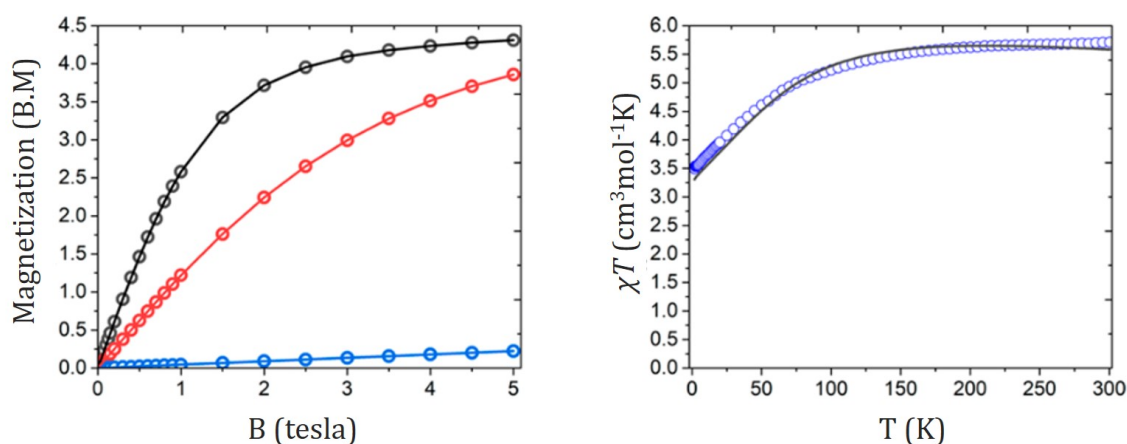


Figure 6.8. (Left) Plot of isothermal magnetization versus magnetic field of Cl@[Co<sub>2</sub>(H<sub>2</sub>L)<sub>3</sub>]<sup>3+</sup> at 2K (black), 5K (red) and 100K (blue). (Right) VT- magnetic susceptibility under an applied dc field of 1kOe. Black line corresponds to fit explained in Appendix 6.

As mentioned in the introduction of the chapter, unveiling the electronic structure of the ground term for a complex, which governs the magnetic properties of the material, is essential to rationalize the behaviour of a new magnetic compound, such as the SMMs. By jointly employing NMR spectroscopy and dc magnetometry and fitting simultaneously their VT data to the appropriate spin Hamiltonians (see table A6.5 in Appendix 6 for details), the energy of the first excited magnetic state was estimated (see table A6.6 in Appendix 6 for details), giving a value of at least 174 cm<sup>-1</sup> for Cl@[Co<sub>2</sub>(H<sub>2</sub>L)<sub>3</sub>]<sup>3+</sup> and establishing an Ising-like type magnetic anisotropy which leads to SMM behaviour. Additionally, X-band paramagnetic resonance (EPR) was used to provide more insights into the magnetic structure. However, both spectra of Cl@[Co<sub>2</sub>(H<sub>2</sub>L)<sub>3</sub>]<sup>3+</sup> and Cl@[CoZn(H<sub>2</sub>L)<sub>3</sub>]<sup>3+</sup> diverge from the ones seen in TAP-Co(II) complexes. Their X-band shown in Appendix 6, Figure A6.14, exclude the possibility for showing slow magnetic relaxation in zero field since SMMs are usually EPR-



silent due to the selection rules forbidding transitions between the states of the ground Kramers doublet. Instead of precise EPR spectra with a clear axial component,<sup>48-50</sup> the complexes Cl@[Co<sub>2</sub>(H<sub>2</sub>L)<sub>3</sub>]<sup>3+</sup> and Cl@[CoZn(H<sub>2</sub>L)<sub>3</sub>]<sup>3+</sup> give the same set of broad lines, as an indication of the symmetry lower than trigonal as a result of the complicated magnetic behaviour.

Alternating-current (ac) magnetic susceptibility measures were also performed to probe the spin dynamics of complexes **11** and **13**. In zero magnetic field, no out-of-phase ac susceptibility signals were observed even down to 2K. This result is consistent with the small anisotropy of the system, which was previously expected for an angle of  $\varphi \approx 40^\circ$ . Nevertheless, the lack of an out-of-phase signal might also be ascribed to the presence of QTM relaxation. To probe this effect, an external dc magnetic field is usually used to quench the QTM process. Indeed, the application dc field of 100 Oe (Figure A6.15. in Appendix 6) gives rise to a signal for both [Co<sub>2</sub>] and [CoZn] complexes, characteristic of the slow dynamics of the magnetization.

Fitting the frequency dependence of the ac susceptibility yields the field dependence of the relaxation time  $\tau$ , which is very similar for both complexes (Figure 6.9). Initially,  $\tau$  increases with the magnetic field and decreases at high fields. The latter is characteristic of the direct relaxation mechanism expected for a Kramer system since  $\tau^{-1}$  is nearly proportional to  $H^4$ .<sup>51</sup> The slight differences between both complexes might be ascribed to large intermolecular dipolar interactions in [Co<sub>2</sub>].

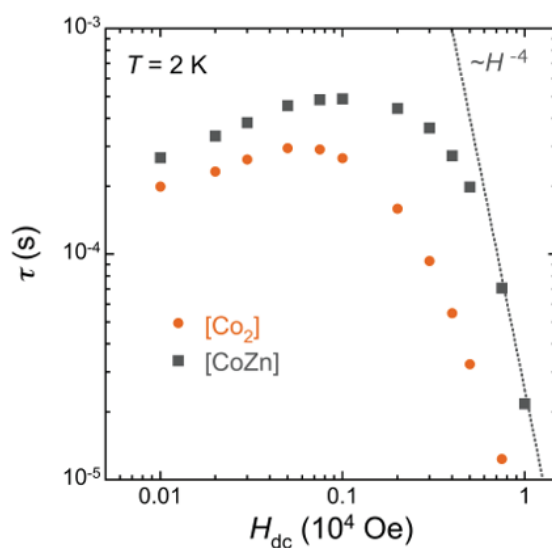


Figure 6.9. Field dependence of  $\tau$  at 2K for [Co<sub>2</sub>] (orange) and [CoZn] (grey).

The maximum in the  $\chi''$  (out-of-phase) vs frequency curve is only observed for certain fields. Therefore, further measurements were done in the range of 100–10000 Hz to find an ideal dc field. Under the optimal dc field of 1000 Oe, the variable-temperature measurements were done for compounds **11** and **13** at increasing temperatures (Figure 6.10).

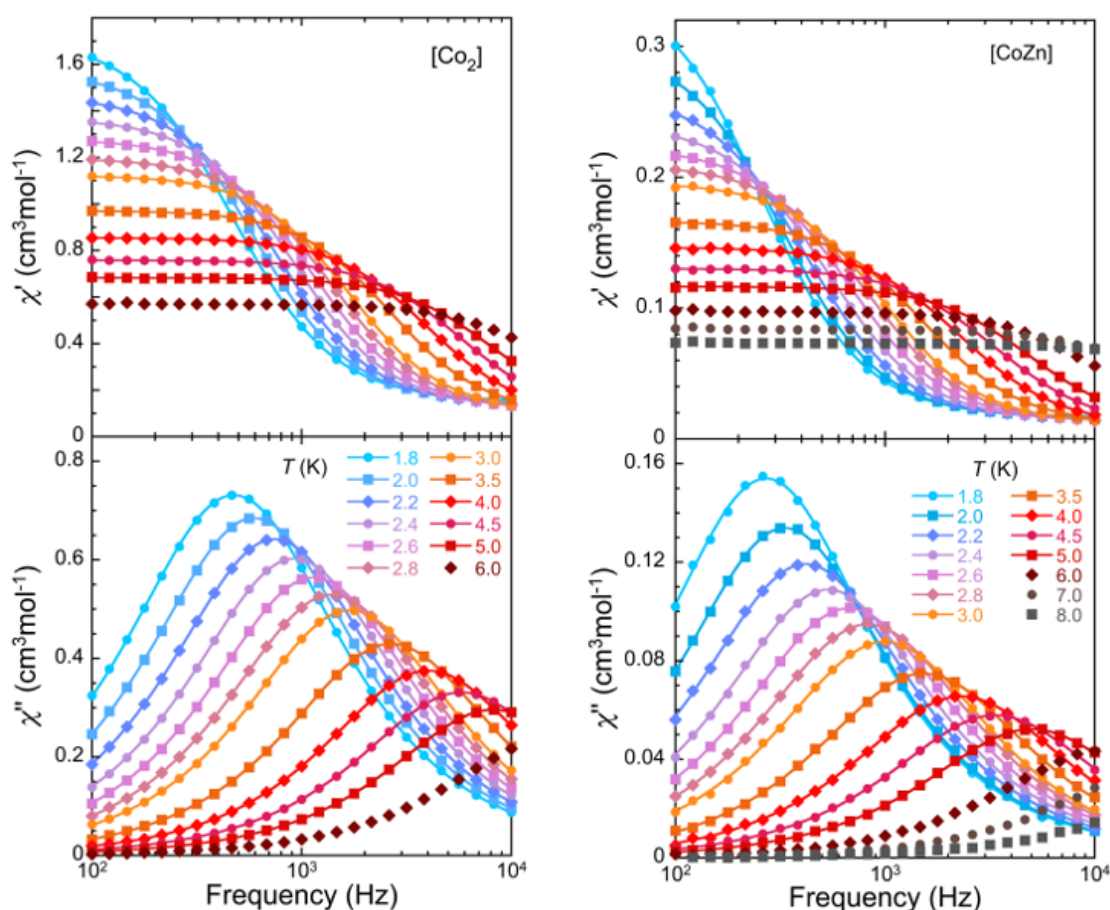


Figure 6.10. Field dependence study of the spin dynamics. In-phase ( $\chi'$ ) and out-of-phase ( $\chi''$ ) ac magnetic susceptibility for [Co<sub>2</sub>] (**11**, left) and [CoZn] (**13**, right) at a dc external magnetic field of 1000 Oe and at various temperatures. The solid lines are fit of the Cole-Cole expressions.

Fitting these data to the Cole-Cole expressions for the real and imaginary susceptibility (solid lines Figure 6.10) allows deriving the temperature dependence of the spin-lattice relaxation time  $\tau$ . These dependencies produced nonlinear Arrhenius plots (Figure 6.11) and similar curves for both complexes. These dependencies can be reproduced by combining the quantum tunnelling [ $B_1/(1+B_2H^2)$ ], the direct ( $AB^nT$ ), the Raman ( $CT^m$ ) and the Orbach ( $\tau_0\exp(-\Delta/K_B T)$ ) relaxation processes. Details and obtained values are in Appendix 6 and table A6.7.

Smaller values for the Orbach relaxation barrier ( $\Delta$ ) were obtained from the fits, according to the expected from the dc magnetometry and NMR data. However, the  $\Delta$  values are in accordance with other cobalt (II)-based SMMs previously reported. The magnetic relaxation was attributed to the Raman, and direct relaxation combined paths with no Orbach contribution<sup>27,52,53</sup> or where the much small Orbach barrier was predicted by other methods.<sup>54-56</sup> Since these values result from a fit with eight parameters, they should be carefully taken.

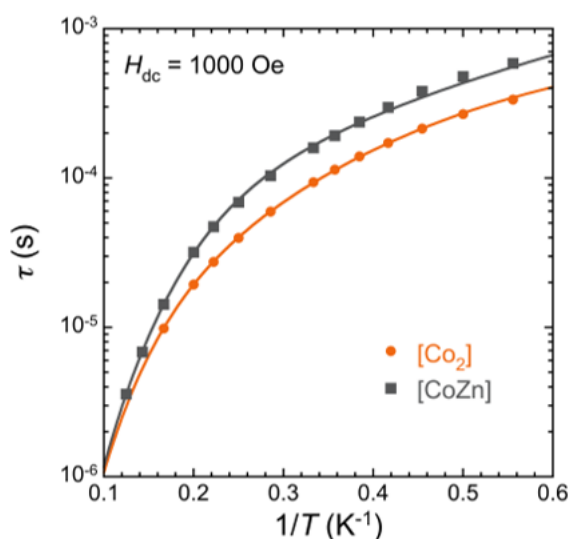


Figure 6.11. Temperature dependence for complexes [Co<sub>2</sub>] (orange) and [CoZn] (grey) in an optimal field of 1000 Oe.

### 6.3. Conclusions

The new [Co<sub>2</sub>(H<sub>2</sub>L)<sub>3</sub>]<sup>4+</sup> and [CoZn(H<sub>2</sub>L)<sub>3</sub>]<sup>4+</sup> helical complexes with the cobalt metal centers in a trigonal intermediate geometry between TP and TAP have been used to corroborate the reduction of the magnetic anisotropy expected for either or both ideal extreme geometries. Complexes with TP geometry are ideally pursued since the TAP geometry facilitates high magnetic anisotropy but large contributions from non-Orbach relaxation mechanisms. Here, we provide an intriguing and completed study of the elusive intermediate geometry. Introducing capping fragments into the pyridine moieties of H<sub>2</sub>L or modifying the bridging phenylene might allow us to exploit and tune the magnetic behaviour through the torsion variation for future research.

## 6.4. Experimental

**Cl@[Co<sub>2</sub>(H<sub>2</sub>L)<sub>3</sub>]Cl(PF<sub>6</sub>)<sub>2</sub>·4CH<sub>3</sub>OH·0.25C<sub>4</sub>H<sub>10</sub>O (11):** A suspension of H<sub>2</sub>L (25 mg, 0.069 mmol) in methanol (10 mL) was added dropwise to a methanolic solution (10 mL) of CoCl<sub>2</sub>·6H<sub>2</sub>O (10.9 mg, 0.046 mmol). An orange solution formed, which was stirred for 45 minutes and filtered and the filtrate was treated with a methanolic (2 mL) solution of NBu<sub>4</sub>PF<sub>6</sub> (14 mg, 0.036 mmol), followed by ten minutes of stirring. The resulting solution was layered with ether, which yielded orange crystals after four days. The yield was 19 mg (48%). Anal. Calc. (Found) for 1(+1.65H<sub>2</sub>O): C, 48.91 (48.78); H, 4.18 (4.02); N, 14.27 (14.42). <sup>1</sup>H NMR (CD<sub>3</sub>OD): 5.92 (br. s, 2H, 8, 8'), 11.05 (br. s, 2H, 3, 3'), 11.30 (br. s, 1H, 9), 31.24 (br. s, 1H, 7), 43.7 (br. s, 2H, 4, 4'), 44.1 (br. s, 2H, 5, 5'), 61.9 (br. s, 2H, 2, 2'), 184.6 (br. s, 2H, 1, 1')

**Cl@[Zn<sub>2</sub>(H<sub>2</sub>L)<sub>3</sub>]Cl(PF<sub>6</sub>)<sub>2</sub>·4CH<sub>3</sub>OH·C<sub>4</sub>H<sub>10</sub>O·H<sub>2</sub>O (12):** A suspension of HL (25 mg, 0.069 mmol) in methanol (10 mL) was added dropwise to a methanolic solution (5 mL) of ZnCl<sub>2</sub> (6.3 mg, 0.046 mmol). A colorless solution formed, which was stirred for 45 minutes, filtered and the filtrate treated with a methanolic (2 mL) solution of NBu<sub>4</sub>PF<sub>6</sub> (14 mg, 0.036 mmol), followed by ten minutes of stirring. The resulting solution was layered with ether, which yielded white crystals after four days. The yield was 15.5 mg (38%). Anal. Calc. (Found) for (2-3CH<sub>3</sub>OH-C<sub>4</sub>H<sub>10</sub>O+7H<sub>2</sub>O): C, 45.70 (45.32); H, 3.89 (3.48); N, 14.32 (13.91). <sup>1</sup>H (CD<sub>3</sub>CN): 7.43 (s, 2H, 7), 7.53 (ps-t, JHH = 6.3 Hz, 2H, 3), 7.62 (ps-t, JHH = 7.5 Hz, 1H, 9), 7.67 (d, JHH = 4.6 Hz, 2H, 8), 7.79 (d, JHH = 7.5 Hz, 2H, 4), 8.15 (d, JHH = 8.1 Hz, 2H, 1), 8.2 (ps-t, JHH = 7.8 Hz, 2H, 2), 9.41 (s, 2H, 5), 13.41 (br. s, 2H, 6).

**Cl@[Zn<sub>1.15</sub>Co<sub>0.85</sub>(H<sub>2</sub>L)<sub>3</sub>]Cl(PF<sub>6</sub>)<sub>2</sub>·2 CH<sub>3</sub>OH·3H<sub>2</sub>O (13):** A suspension of H<sub>2</sub>L (50 mg, 0.139 mmol) in methanol (20 mL) was added dropwise to a methanolic solution (20 mL) of CoCl<sub>2</sub>·6H<sub>2</sub>O (2.2 mg, 0.009 mmol) and ZnCl<sub>2</sub> (11.22 mg, 0.082 mmol). A colorless solution formed, which was stirred for 45 minutes, filtered and the filtrate treated with a methanolic (4 mL) solution of NBu<sub>4</sub>PF<sub>6</sub> (27 mg, 0.07 mmol) and stirred for ten minutes. The resulting solution was layered with ether, which yielded pale orange crystals after four days. The yield was 26.8 mg (35%). Anal. Calc. (Found) for (3-2CH<sub>3</sub>OH+8H<sub>2</sub>O): C, 44.72 (45.00); H, 3.98 (3.54); N, 14.22 (13.76); Zn, 5.39 (5.90); Co, 1.40 (1.28). <sup>1</sup>H (CD<sub>3</sub>CN): 7.91 (d, 1H, 4'), 8.31 (ps-t, 1H, 3'), 8.80

(d, 1H, 1'), 8.94 (ps-t, 1H, 2'), 9.11 (s, 1H, 5'), 9.25 (d, 1H, 8'), 9.31 (s, 1H, 3), 10.34 (br. s, 1H, 9), 19.09 (br. s, 1H, 7), 42.95 (br. s, 1H, 4/5), 44.35 (br. s, 1H, 4/5), 60.47 (br. s, 1H, 2), 179 (br. s, 1H, 1).

## 6.5. References

- (1) Kahn, O.; Jay Martinez, C. *Science*. **1998**, *279*, 44–48.
- (2) Halder, G. J.; Kepert, C. J.; Moubaraki, B. **2002**, *298*, 1762–1766.
- (3) Bogani, L.; Wernsdorfer, W. *Nat. Mater.* **2008**, *7*, 179–186.
- (4) Winpenny, R. E. P. *Angew. Chemie - Int. Ed.* **2008**, *47*, 7992–7994.
- (5) Feng, M.; Ruan, Z.; Chen, Y.; Feng, M. *Chem Com* **2020**, 13702–13718.
- (6) Darawsheh, M.; Barrios, L. A.; Roubeau, O.; Teat, S. J.; Aromí, G. *Chem. - A Eur. J.* **2016**, *22*, 8635–8645.
- (7) Craig, G. A.; Murrie, M. *Chem. Soc. Rev.* **2015**, *44*, 2135–2147.
- (8) Aromí, G.; Brechin, E. K. In *Single-molecule magnets and related phenomena*; Winpenny, R. E. P., Ed.; Springer Berlin Heidelberg, 2006; Vol. 122, pp 1–67.
- (9) Liddle, S. T.; Van Slageren, J. *Chem. Soc. Rev.* **2015**, *44*, 6655–6669.
- (10) Goodwin, C. A. P.; Ortu, F.; Reta, D.; Chilton, N. F.; Mills, D. P. *Nature*. **2017**, *548*, 439–442.
- (11) Carlin, R. L. *Magnetochemistry*; Springer, Berlin, 1986.
- (12) Murrie, M. *Chem. Soc. Rev.* **2010**, *39*, 1986–1995.
- (13) Frost, J. M.; Harriman, K. L. M.; Murugesu, M. *Chem. Sci.* **2016**, *7*, 2470–2491.
- (14) Baum, R. R.; James, C. D.; Tierney, D. L. In *Future Directions in Metalloproteins and Metalloenzyme Research*; Springer, 2017; pp 33–54.
- (15) Boča, R. *Coord. Chem. Rev.* **2004**, *248*, 757–815.
- (16) Lloret, F.; Julve, M.; Cano, J.; Ruiz-garcía, R.; Pardo, E. *Inorganica Chim. Acta* **2008**, *361*, 3432–3445.
- (17) Yao, X. N.; Du, J. Z.; Zhang, Y. Q.; Leng, X. B.; Yang, M. W.; Jiang, S. Da; Wang, Z. X.; Ouyang, Z. W.; Deng, L.; Wang, B. W.; Gao, S. *J. Am. Chem. Soc.* **2017**, *139*, 373–380.
- (18) Rechkemmer, Y.; Breitgoff, F. D.; Van Der Meer, M.; Atanasov, M.; Hakl, M.; Orlita, M.; Neugebauer, P.; Neese, F.; Sarkar, B.; Van Slageren, J. *Nat. Commun.* **2016**, *7*, 1–8.

- (19) Novikov, V. V.; Pavlov, A. A.; Nelyubina, Y. V.; Boulon, M. E.; Varzatskii, O. A.; Voloshin, Y. Z.; Winpenny, R. E. P. *J. Am. Chem. Soc.* **2015**, *137*, 9792–9795.
- (20) Pavlov, A. A.; Nelyubina, Y. V.; Kats, S. V.; Penkova, L. V.; Efimov, N. N.; Dmitrienko, A. O.; Vologzhanina, A. V.; Belov, A. S.; Voloshin, Y. Z.; Novikov, V. V. *J. Phys. Chem. Lett.* **2016**, *7*, 4111–4116.
- (21) Bunting, P. C.; Atanasov, M.; Damgaard-Møller, E.; Perfetti, M.; Crassee, I.; Orlita, M.; Overgaard, J.; Van Slageren, J.; Neese, F.; Long, J. R. *Science*. **2018**, *362*, eaat7319.
- (22) Meng, Y. S.; Mo, Z.; Wang, B. W.; Zhang, Y. Q.; Deng, L.; Gao, S. *Chem. Sci.* **2015**, *6*, 7156–7162.
- (23) Zadrozny, J. M.; Xiao, D. J.; Atanasov, M.; Long, G. J.; Grandjean, F.; Neese, F.; Long, J. R. *Nat. Chem.* **2013**, *5*, 577–581.
- (24) Zadrozny, J. M.; Atanasov, M.; Bryan, A. M.; Lin, C. Y.; Rekker, B. D.; Power, P. P.; Neese, F.; Long, J. R. *Chem. Sci.* **2013**, *4*, 125–138.
- (25) Zhu, Y. Y.; Cui, C.; Zhang, Y. Q.; Jia, J. H.; Guo, X.; Gao, C.; Qian, K.; Jiang, S. Da; Wang, B. W.; Wang, Z. M.; Gao, S. *Chem. Sci.* **2013**, *4*, 1802–1806.
- (26) Pavlov, A. A.; Savkina, S. A.; Belov, A. S.; Nelyubina, Y. V.; Efimov, N. N.; Voloshin, Y. Z.; Novikov, V. V. *Inorg. Chem.* **2017**, *56*, 6943–6951.
- (27) Pavlov, A. A.; Aleshin, D. Y.; Savkina, S. A.; Belov, A. S.; Efimov, N. N.; Nehr Korn, J.; Ozerov, M.; Voloshin, Y. Z.; Nelyubina, Y. V.; Novikov, V. V. *ChemPhysChem* **2019**, *20*, 1001–1005.
- (28) Novikov, V. V.; Ananyev, I. V.; Pavlov, A. A.; Fedin, M. V.; Lyssenko, K. A.; Voloshin, Y. Z. *J. Phys. Chem. Lett.* **2014**, *5*, 496–500.
- (29) Churchill, M. R.; Gold, K.; Maw, C. E. *Inorg. Chem.* **1970**, *9*, 1597–1604.
- (30) Zhang, Y. Z.; Gómez-Coca, S.; Brown, A. J.; Saber, M. R.; Zhang, X.; Dunbar, K. R. *Chem. Sci.* **2016**, *7*, 6519–6527.
- (31) Villa-Pérez, C.; Oyarzabal, I.; Echeverría, G. A.; Valencia-Urbe, G. C.; Seco, J. M.; Soria, D. B. *Eur. J. Inorg. Chem.* **2016**, 4835–4841.
- (32) Li, J.; Han, Y.; Cao, F.; Wei, R. M.; Zhang, Y. Q.; Song, Y. *Dalt. Trans.* **2016**, *45*, 9279–9284.
- (33) Alvarez, S.; Avnir, D.; Llunell, M.; Pinsky, M. *New J. Chem.* **2002**, *26*, 996–1009.
- (34) Zhang, J.; Li, J.; Yang, L.; Yuan, C.; Zhang, Y. Q.; Song, Y. *Inorg. Chem.* **2018**, *57*,

- 3903–3912.
- (35) Varzatskii, O. A.; Penkova, L. V.; Kats, S. V.; Dolganov, A. V.; Vologzhanina, A. V.; Pavlov, A. A.; Novikov, V. V.; Bogomyakov, A. S.; Nemykin, V. N.; Voloshin, Y. Z. *Inorg. Chem.* **2014**, *53*, 3062–3071.
- (36) Ozumerzifon, T. J.; Bhowmick, I.; Spaller, W. C.; Rappé, A. K.; Shores, M. P. *Chem. Commun.* **2017**, *53*, 4211–4214.
- (37) Mai, H. D.; Tran, N. M.; Yoo, H. *Coord. Chem. Rev.* **2019**, *387*, 180–198.
- (38) Zhang, Z.; Dolphin, D. *Chem. Commun.* **2009**, No. 45, 6931–6933.
- (39) Darawsheh, M. D.; Barrios, L. A.; Roubeau, O.; Teat, S. J.; Aromí, G. *Chem. Commun.* **2017**, *53*, 569–572.
- (40) Lodi Rizzini, A.; Krull, C.; Balashov, T.; Mugarza, A.; Nistor, C.; Yakhou, F.; Sessi, V.; Klyatskaya, S.; Ruben, M.; Stepanow, S.; Gambardella, P. *Nano Lett.* **2012**, *12*, 5703–5707.
- (41) Darawsheh, M. D. Universitat de Barcelona, 2016.
- (42) Hartman, P.; Chan, H. K. *Acta Crystallogr. Sect. A* **1976**, *32*, 751–767.
- (43) Albrecht, M. *Top. Curr. Chem.* **2005**, *248*, 105–139.
- (44) Pavlov, A. A.; Denisov, G. L.; Kiskin, M. A.; Nelyubina, Y. V.; Novikov, V. V. *Inorg. Chem.* **2017**, *56*, 14759–14762.
- (45) Hiller, M.; Krieg, S.; Ishikawa, N.; Enders, M. *Inorg. Chem.* **2017**, *56*, 15285–15294.
- (46) Morita, T.; Damjanović, M.; Katoh, K.; Kitagawa, Y.; Yasuda, N.; Lan, Y.; Wernsdorfer, W.; Breedlove, B. K.; Enders, M.; Yamashita, M. *J. Am. Chem. Soc.* **2018**, *140*, 2995–3007.
- (47) Pavlov, A. A.; Nehr Korn, J.; Pankratova, Y. A.; Ozerov, M.; Mikhalyova, E. A.; Polezhaev, A. V.; Nelyubina, Y. V.; Novikov, V. V. *Phys. Chem. Chem. Phys.* **2019**, *21*, 8201–8204.
- (48) Myers, W. K.; Duesler, E. N.; Tierney, D. L. *Inorg. Chem.* **2008**, *47*, 6701–6710.
- (49) Myers, W. K.; Scholes, C. P.; Tierney, D. L. *J. Am. Chem. Soc.* **2009**, *131*, 10421–10429.
- (50) Marts, A. R.; Greer, S. M.; Whitehead, D. R.; Woodruff, T. M.; Breece, R. M.; Shim, S. W.; Oseback, S. N.; Papish, E. T.; Jacobsen, F. E.; Cohen, S. M.; Tierney, D. L. *Appl. Magn. Reson.* **2011**, *40*, 501–511.
- (51) Abragam, A.; Bleaney, B. *Electron Paramagnetic Resonance of Transition Ions*;

OUP Oxford, 2012.

- (52) Gómez-Coca, S.; Urtizberea, A.; Cremades, E.; Alonso, P. J.; Camón, A.; Ruiz, E.; Luis, F. *Nat. Commun.* **2014**, *5*, 1–8.
- (53) Lunghi, A.; Totti, F.; Sessoli, R.; Sanvito, S. *Nat. Commun.* **2017**, *8*, 1–7.
- (54) Colacio, E.; Ruiz, J.; Ruiz, E.; Cremades, E.; Krzystek, J.; Carretta, S.; Cano, J.; Guidi, T.; Wernsdorfer, W.; Brechin, E. K. *Angew. Chemie Int. Ed.* **2013**, *52*, 9130–9134.
- (55) Huang, X. C.; Zhou, C.; Shao, D.; Wang, X. Y. *Inorg. Chem.* **2014**, *53*, 12671–12673.
- (56) Zhu, Y. Y.; Zhu, M. S.; Yin, T. T.; Meng, Y. S.; Wu, Z. Q.; Zhang, Y. Q.; Gao, S. *Inorg. Chem.* **2015**, *54*, 3716–3718.



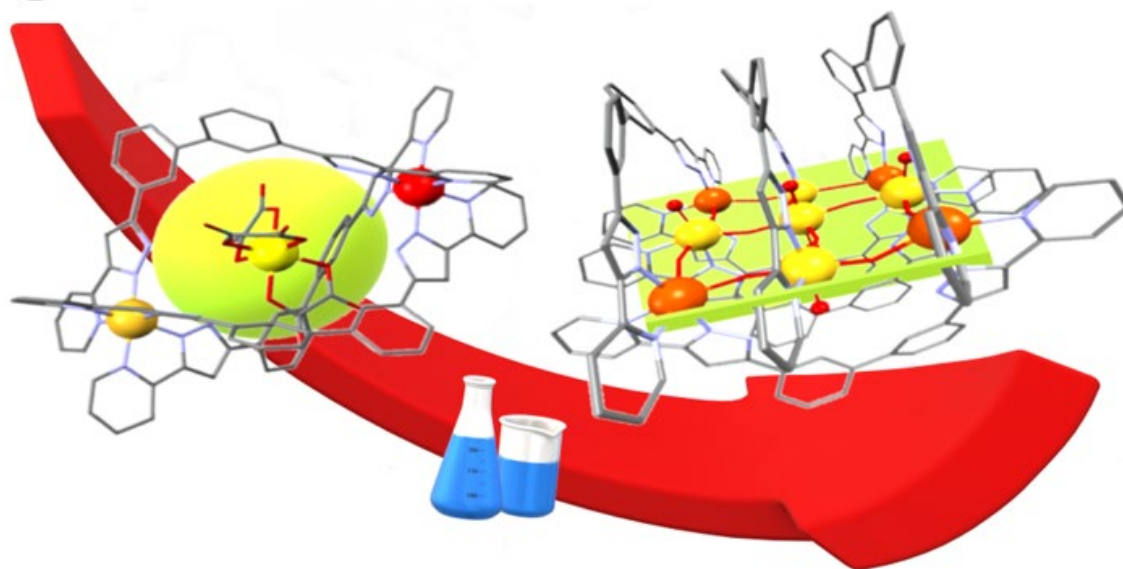
# CHAPTER 7

---

**EXPLORATION OF THE COORDINATION  
CHEMISTRY OF H<sub>2</sub>L2.**

**THE DISCOVERY OF [Fe<sub>9</sub>] GRIDS.**

**H<sub>2</sub>L2**





## 7. Exploration of the coordination chemistry of H<sub>2</sub>L<sub>2</sub>. The discovery of [Fe<sub>9</sub>] grids.

### Abstract

The exploration of the coordination chemistry of ligand H<sub>2</sub>L<sub>2</sub> with different iron (II) sources in various solvents and atmospheric conditions allowed the formation of three triple-stranded helicates with the formula [Fe(C<sub>2</sub>O<sub>4</sub>)<sub>3</sub>]@[Fe<sub>2</sub>(H<sub>2</sub>L<sub>2</sub>)<sub>3</sub>]X·S (X:BF<sub>4</sub>, S:5(C<sub>2</sub>H<sub>3</sub>N), CH<sub>4</sub>O, 3(H<sub>2</sub>O) for **14**, X:BF<sub>4</sub>, S: 3(CH<sub>4</sub>O), 4.75(H<sub>2</sub>O) for **15** and X: ClO<sub>4</sub> and S: (H<sub>2</sub>O) for **16**) displaying different spin-states, and the discovery of a new fascinating supramolecular cluster-type based on a planar iron nanosheet. They consist of two new [Fe<sub>9</sub>] squared grids composed by hydroxo(oxo) bridges in between the metal ions with formulae [Fe<sub>9</sub>O<sub>4</sub>(OH)<sub>8</sub>]<sup>7+</sup> (**17**) and [Fe<sub>9</sub>O<sub>4</sub>(OH)<sub>8</sub>]<sup>10+</sup> (**18**). The main differences of both coordination clusters are the occupation of the remaining axial positions of the metal centres in this Fe/O<sup>2-</sup>/OH<sup>-</sup> core. Water and hydroxide ligands are present in these positions for grid **17**, while chloride ligands are placed in grid **5**. Thus, based on the crystalline structure, charge balance, the valence bond sum (VBS), the elemental analysis (EA) and magnetometry, the whole compounds are formulated as [Fe<sub>9</sub>O<sub>4</sub>(OH)<sub>10</sub>(H<sub>2</sub>L<sub>2</sub>)<sub>6</sub>(H<sub>2</sub>O)<sub>4</sub>](BF<sub>4</sub>)<sub>5</sub> (**17**) and [Fe<sub>9</sub>O<sub>4</sub>Cl<sub>6</sub>(OH)<sub>8</sub>(H<sub>2</sub>L<sub>2</sub>)<sub>6</sub>]Cl<sub>4</sub> (**18**). Considering the formation of these unprecedented flat polynuclear complexes, this chapter deals with their formation in pure manner and elucidation of their interesting magnetic behaviour.

### 7.1. Introduction

The generation of clusters based on polynuclear transition metals has strongly contributed to the progress of diverse research fields thanks to the interesting properties coming from their suitable metallic organizations. A large area of interest is that of molecular magnetism, where these systems have been deeply studied.<sup>1,2</sup> Particularly, many of them are high-spin molecules<sup>3-5</sup>, which could lead to a single molecule magnets (SMMs)<sup>3,6,7</sup> or cryogenic magnetic complexes for refrigerating applications at the nanoscale.<sup>8,9</sup> Since the transition metals tend to aggregate into oxide and hydroxide networks displaying single oxygen atom bridges between the metal centres, complexes containing such network fragments represent the vast

## 7. Exploration of the coordination chemistry of H2L2. The discovery of [Fe9] grids.

---

majority among all classes of polynuclear cluster assemblies. Their stabilization as discrete polynuclear species arises from the blocked or impeded growth of the oxide coordination lattice by capping ligands. Thus, they are composed by an inner piece of the classic magnetic oxides with short distances and intense electronic interactions between the metals, and external blocking ligands that also ensure the stability of the complexes. First remarkable examples are the hydroxo(oxo)polyiron [Fe<sub>19</sub>] and [Fe<sub>17</sub>] complexes<sup>10,11</sup> in which a ring-like [Fe<sub>9</sub>O<sub>2</sub>(OH)<sub>10</sub>]<sup>13+</sup> core is confined within a armour of carboxylate-type ligands. Its connected-iron units (iron cubes with one of it missing in one corner) can be recognized as a part of a 2D network M(OH)<sub>2</sub>, typically found in AX<sub>2</sub>-type structures of Mg(OH)<sub>2</sub>, α-Ni(OH)<sub>2</sub> or α-Co(OH)<sub>2</sub>, also known as brucite-like hydroxides.<sup>12-14</sup> This core is surrounded by [Fe/heidi] units (where heidi is a carboxylate-type blocking ligand) drawing an external circle and supplementary O<sup>2-</sup> and OH<sup>-</sup> ligands.

Indeed, dozens of works that contain the [M<sub>7</sub>(OH)<sub>6</sub>(OR)<sub>6</sub>] disk-like moiety reproducing perfectly the brucite layers (when R is a proton or neglected) have been published. These heptanuclear clusters has been found for several metal ions, such as Mn<sup>2+</sup>,<sup>15</sup> Fe<sup>2+</sup>,<sup>16</sup> Co<sup>2+</sup>,<sup>17,18</sup> Ni<sup>2+</sup>,<sup>19,20</sup> Cu<sup>2+</sup>,<sup>21</sup> and Zn<sup>2+</sup>,<sup>15,19</sup> being in some cases selectively achieved depending on the metal ion. For all of them, the brucite lattice growth is blocked by the capping ligands. Additionally, similar iron/oxide fragments of various forms of Fe<sub>2</sub>O<sub>3</sub> or Fe<sub>3</sub>O<sub>4</sub> oxides,<sup>22</sup> such as [Fe<sub>4</sub>O<sub>4</sub>] cubanes or the [Fe(μ-O)<sub>2</sub>Fe]<sub>n</sub> motif of various lengths, are incorporated into poly(oxo)iron complexes of a large nuclearity synthesised and studied.<sup>23-27</sup> In these complexes, the structural features of the trapped oxide lattice are preserved as a small piece of the extended network. Specifically, for octahedral Fe ions, the Fe-O-Fe angles lie in the range of 80 to 110° and the Fe...Fe distances are in between 2.8 and 3.0 Å. Thus, the constituent ligands only contribute on preventing the growth of the lattice, acting as blocking ligands without influencing the naturally occurring self-assembly process of the hydroxide(oxo)polymetallic fragment. Here, we report the obtention of a two unique hydroxo/oxo/Fe(II/III) squared grids of composition [Fe<sub>9</sub>O<sub>4</sub>(OH)<sub>8</sub>]<sup>x+</sup> with a different combination of mixed oxidations states of the iron centres and different ligands in the six available axial positions regarding the plane nano-sheet. While water and hydroxide ligands are axially coordinated in grid **17**, chloride ligands are present in grid **18**. The whole grid structure of both compounds is held by six

gripper H<sub>2</sub>L<sub>2</sub> ligands coordinating to the metal centres on the opposite sides of the square. In this way, they provide some strain on the perpendicular directions within the main plane. Consequently, this hydroxide/oxide polyiron fragments display several Fe-O-Fe angles larger than 150° and long Fe...Fe distances (close to 3.8 Å). Particularly, these structural features for hydroxide/oxide iron clusters are very unusual. One comparable polyiron example to our compounds is the mixed Fe(II)/Fe(III) grid with a [Fe<sub>9</sub>O<sub>12</sub>] core also held by six ligands.<sup>28</sup> However, in this case, the [3x3] grid is achieved by pre-encoding the driving force for the preferential self-assembly of the cluster using six tritopic ligands. Specifically, each ligand has three picolinic coordination pockets. The alkoxide O-atoms of the N<sub>2</sub>O tridentate side connects the iron atoms. Thus, the ligands are themselves the bridges between the overall metallic organization. Nevertheless, this extraordinary supramolecular grid has a different nature. It is not a piece of mineral Fe/OH<sup>-</sup>/O<sup>2-</sup> trapped inside a cluster. In contrast, and heterometallic [3x3] grid with a closer arrangement to our compounds was synthesised in Oshio's group.<sup>29</sup> The [Fe<sub>5</sub>Co<sub>4</sub>(OH)<sub>6</sub>]<sup>7+</sup> was still obtained despite the tritopic nature of the ligand which previously ensured the pre-designed formation of [Cu<sub>9</sub>] and [Co<sub>9</sub>] without any piece of a Fe/OH<sup>-</sup>/O<sup>2-</sup> lattice.<sup>30</sup> In the former case, the central N<sub>3</sub> coordinating pocket do not interact in bridging the metal ions, acting as non-directing ligand. The alkoxide bridges between the metal centers have a different nature from our growth of the classical inorganic crystal lattice inside the cluster.

Typically, our ditopic bis-pyrazole-pyridine ligands and other analogous ones display the appropriate flexibility and the functional pockets locate at remote positions to each other, which ideally lead to the formation of guest@[M<sub>2</sub>L<sub>3</sub>] dinuclear triple-stranded helicates.<sup>31-34</sup> As previously mentioned through this thesis, these supramolecular architectures are prone to encapsulate guests inside the central cavity.<sup>35,36</sup> Indeed, this fact was observed for ligand H<sub>2</sub>L<sub>2</sub> with the formation of the [Cr(ox)<sub>3</sub>] @[Fe<sub>2</sub>(H<sub>2</sub>L<sub>2</sub>)<sub>3</sub>]BF<sub>4</sub>, in which a *tris*-oxalate chromium(III) complex is encapsulated inside the helical cavity (see section 1.4.2.1).<sup>37</sup> Many factors regarding the proper guest determine the connectivity of the final supramolecular architecture. In our case, an anionic templating effect seems to govern the formation of the helicates. Thus, the anionic guest must possess the adequate size, shape, and chemical properties to fit into the provided cavity of the host using non-covalent

interactions.<sup>38</sup> Ligand H<sub>2</sub>L2 has free N-H groups available for establish several hydrogen bonds (Figure 7.1).

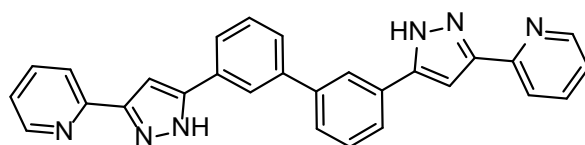


Figure 7.1. Molecular structure of ligand H<sub>2</sub>L2.

In this work, we observed the formation of several helicates with the general formula  $[\text{Fe}(\text{C}_2\text{O}_4)_3]@[\text{Fe}_2(\text{H}_2\text{L}_2)_3]^+$  (**14**, **15** and **16**) depending on the coordination chemistry conditions. This versatile system allows to access three different spin - states, [LS-LS] or [LS-HS], depending on the counterion and the solvents. These were elucidated crystallographically through SCXRD at 100 and 280K and. Compound (**14**) was purely obtained as a unique crystalline sample. However, co-crystallized crystals of different colour, size and shape were observed for (**15**) and (**16**). Analysis of the byproducts allowed the identification of the remarkable new  $[\text{Fe}_9\text{O}_4(\text{OH})_{10}(\text{H}_2\text{L}_2)_6(\text{H}_2\text{O})_4](\text{BF}_4)_5$  (**17**) molecular complex. Additionally, we synthesized an analogous cluster,  $[\text{Fe}_9\text{O}_4\text{Cl}_6(\text{OH})_8(\text{H}_2\text{L}_2)_6]\text{Cl}_4$  (**18**) with chloride ligands at the available axial positions instead, in order to influence the electronic properties of the nanosheet. Here, we describe the experimental conditions used to explore the H<sub>2</sub>L2 coordination chemistry and the optimization of the grid-like clusters formation, the structural details and their magnetic response.

## 7.2. Results and Discussion

### Synthesis

Ligand H<sub>2</sub>L2 was prepared in two steps, a Claisen condensation followed by cyclization of the bis-1,3-diketone intermediate with hydrazine, as previously reported in our group. As mentioned in the general introduction (section 1.4.2.1), the fascinating  $[[\text{Cr}(\text{ox})_3]@[\text{Fe}_2(\text{H}_2\text{L}_2)_3]]\text{BF}_4$  supramolecular assembly was achieved by encapsulating the  $[\text{Cr}(\text{ox})_3]^{3-}$  guest into the helical cavity provided by the triple-stranded helicate of Fe(II)<sub>2</sub>. Motivated by its unprecedented magnetic behaviour, where SCO and SMMs responses are both present in the system, and its feasible preparation by inducing the guest encapsulation, we decide to test different

## 7. Exploration of the coordination chemistry of H<sub>2</sub>L<sub>2</sub>. The discovery of [Fe<sub>9</sub>] grids.

---

guests to interact within the [Fe<sub>2</sub>(H<sub>2</sub>L<sub>2</sub>)<sub>3</sub>]<sup>4+</sup> host. In the first attempts, the encapsulation of several halides was pursued. Since the shorter ligand H<sub>2</sub>L<sub>1</sub> with a small cavity, could encapsulate Cl<sup>-</sup> and Br<sup>-</sup>, we were expecting to encapsulate several of them into the bigger cavity or even the larger halide I<sup>-</sup>, which cannot fit inside the former [Fe<sub>2</sub>(H<sub>2</sub>L<sub>1</sub>)<sub>3</sub>]<sup>4+</sup> helical host. Secondly, we pursued the encapsulation of bigger guest such as BF<sub>4</sub><sup>-</sup>, ClO<sub>4</sub><sup>-</sup>, PF<sub>6</sub><sup>-</sup>. And thirdly, [M(ox)<sub>3</sub>]<sup>3-</sup> (M<sup>3+</sup>: V<sup>3+</sup>, Mn<sup>3+</sup>, Al<sup>3+</sup>, Ru<sup>3+</sup>, Co<sup>3+</sup>; ox: oxalate; C<sub>2</sub>O<sub>4</sub><sup>2-</sup>) anionic complexes encapsulated since these are direct analogous to [Cr(ox)<sub>3</sub>]<sup>3-</sup>. Unfortunately, we did not obtain any the pursued complexes. Instead, we obtained a family of complexes with an anionic *tris*-oxalatoferrate(III) ion encapsulated within the helical moiety with the general formula [Fe(C<sub>2</sub>O<sub>4</sub>)<sub>3</sub>]@[Fe<sub>2</sub>(H<sub>2</sub>L<sub>2</sub>)<sub>3</sub>](X)·S, X:BF<sub>4</sub>, S:5(C<sub>2</sub>H<sub>3</sub>N), CH<sub>4</sub>O, 3(H<sub>2</sub>O) for **14**, X:BF<sub>4</sub>, S: 3(CH<sub>4</sub>O), 4.75(H<sub>2</sub>O) for **15** and X: ClO<sub>4</sub> and S: (H<sub>2</sub>O) for **16**. All coordination reactions and complexes are summarized in Appendix 7, Table A7.1. For all of them, the iron (II) source is oxidized due to the presence of oxygen of the air and the ascorbic acid is decomposed to its oxalate form leading to the formation [Fe(C<sub>2</sub>O<sub>4</sub>)<sub>3</sub>]<sup>3-</sup>. As it turns out, the derived Fe(III) *tris*-oxalate anion fits perfectly inside the cavity of the [Fe<sub>2</sub>(H<sub>2</sub>L<sub>2</sub>)<sub>3</sub>]<sup>4+</sup>, favouring the formation of the helical complexes.

Surprisingly, a completely different molecular architecture was obtained when using the BF<sub>4</sub><sup>-</sup> ion in the coordination reaction. The new cluster [Fe<sub>9</sub>O<sub>4</sub>(OH)<sub>10</sub>(H<sub>2</sub>L<sub>2</sub>)<sub>6</sub>(H<sub>2</sub>O)<sub>4</sub>](BF<sub>4</sub>)<sub>5</sub> was found to co-crystallize with the previously mentioned helical complexes. As an example, both helical and grid complexes were obtained from the reaction of Fe(BF<sub>4</sub>)<sub>2</sub> salt with H<sub>2</sub>L<sub>2</sub> (3:2 stoichiometry) in methanol under nitrogen. When the resulting solution was layered with an aqueous solution of K<sub>3</sub>[V(C<sub>2</sub>O<sub>4</sub>)<sub>3</sub>], a mixture of red and yellow crystals suitable for X-ray structure determination were collected after four weeks. This suggested that a side reaction could be favoured due to the unfavorable fit of the desired guest into the helical cavity. Once identified, the discovery of the grid opened a new research avenue focused on isolating this extraordinary complex. Initially, the appropriate stoichiometry (6:9) of H<sub>2</sub>L<sub>2</sub> ligand and the hydrated Fe(BF<sub>4</sub>)<sub>2</sub> was used with several reaction conditions. However, we only got viscous solutions and amorphous precipitates rather than crystalline compounds. With the aim of isolating the crystalline grid, we carried out the same reactions in the presence of added base

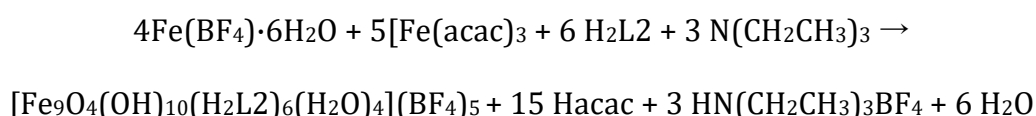
## 7. Exploration of the coordination chemistry of H<sub>2</sub>L<sub>2</sub>. The discovery of [Fe<sub>9</sub>] grids.

---

(triethylamine) since it should neutralize the possible acidic media formed from the equilibria of the reaction. Unfortunately, none of the direct approaches used to get pure grid were successful. Detailed analysis (see below) of compound **17** unveiled the presence of Fe(III) arising from the Fe(II) source oxidation in the air. Thus, different ratios of Fe(III) and Fe(II) sources were combined to achieve the target. Again, we could not isolate the compound through these attempts.

Parallel attempts of encapsulating other guests into the helical host [Fe<sub>2</sub>(H<sub>2</sub>L<sub>2</sub>)<sub>3</sub>]<sup>4+</sup>, reactions with [Fe(acac)<sub>3</sub>] (acac:acetylacetonate) were performed. This complex displays a similar structure to [Cr(ox)<sub>3</sub>]<sup>3-</sup> and was thought to fit into the volume of the helical cavity, while the acac ligands could easily point out of the host through the windows between the H<sub>2</sub>L<sub>2</sub> ligand strands.

Surprisingly, after many unsuccessful attempts and using an approach aimed to form helical complexes, pure crystalline grid. The hydrated Fe(BF<sub>4</sub>)<sub>2</sub> salt and H<sub>2</sub>L<sub>2</sub> were mixed in a solution of methanol and acetonitrile (1:1) in presence of basic media (trimethylamine). After stirring 30 minutes, the solution was layered with Fe(acac)<sub>3</sub> in water in a 1:1 ratio. Rhomboid orange-yellow crystals suitable for X-ray diffraction were obtained as a homogeneous phase and characterized, yielding to the pure grid [Fe<sub>9</sub>O<sub>4</sub>(OH)<sub>10</sub>(H<sub>2</sub>L<sub>2</sub>)<sub>6</sub>(H<sub>2</sub>O)<sub>4</sub>](BF<sub>4</sub>)<sub>5</sub> (**17**). Thus, the Fe(acac)<sub>3</sub> participates in this reaction as source of Fe(III) rather than being an anionic guest. From this successful procedure, the following balanced equation can be rationalized:



Accordingly, without wishing to take away any merit from the “undirect” synthetic approach used to reach pure grid, this is a great example on getting promising results without hesitating on combining the exploration of experimental conditions and addressed molecular design.

An analogous [Fe<sub>9</sub>] grid to (**17**) with chloride ligands in the axial positions with the formula [Fe<sub>9</sub>(O<sub>4</sub>Cl<sub>6</sub>(OH)<sub>8</sub>)Cl<sub>4</sub> (**18**) was obtained when a methanolic solution of ligand H<sub>2</sub>L<sub>2</sub> was added to a solution of FeCl<sub>2</sub>·4H<sub>2</sub>O in methanol and treated with NBu<sub>4</sub>BF<sub>4</sub>.



The resulting red solution was flushed with pressure air, causing the evaporation one third of the solution to ensure the oxidation of most of the Fe(II) ions. Suitable red crystals for X-ray diffraction were obtained after leaving the solution to slowly evaporate, reaching almost dryness, for one month.

### **Crystal structure description of Fe(C<sub>2</sub>O<sub>4</sub>)<sub>3</sub>@[Fe<sub>2</sub>(H<sub>2</sub>L<sub>2</sub>)<sub>3</sub>]<sup>+</sup> helicate complexes**

Among all the analogous Fe(C<sub>2</sub>O<sub>4</sub>)<sub>2</sub>@[Fe<sub>2</sub>(H<sub>2</sub>L<sub>2</sub>)<sub>3</sub>]<sup>+</sup>, a detailed structural description is given for compounds **14**, **15** and **16** since their structures show more disparity between their molecular structure. We did not further characterize these compounds since the majority of them co-crystallize with the grid-like compound, which changed the direction of the work.

#### **Crystal structure description of**

#### **[Fe(C<sub>2</sub>O<sub>4</sub>)<sub>3</sub>]<sup>3-</sup>@[Fe<sub>2</sub>(H<sub>2</sub>L<sub>2</sub>)<sub>3</sub>]<sup>+</sup>(BF<sub>4</sub>)<sup>-</sup>·5(C<sub>2</sub>H<sub>3</sub>N)·CH<sub>4</sub>O·3(H<sub>2</sub>O), (**14**)**

Compound **14** crystallizes in the triclinic space group *P*-1. At 100K, the asymmetric unit comprises a cationic supramolecular helical moiety with the formula {[Fe(C<sub>2</sub>O<sub>4</sub>)<sub>3</sub>]<sup>3-</sup>@[Fe<sub>2</sub>(H<sub>2</sub>L<sub>2</sub>)<sub>3</sub>]<sup>+</sup>}, one BF<sub>4</sub><sup>-</sup> compensating the overall charge and five molecules of acetonitrile, one of methanol and three of water (Figure 7.2, and Figure A7.1 and Table A7.2 in Appendix 7). The unit cell encloses two of such ensembles. The helical moiety is formed by three H<sub>2</sub>L<sub>2</sub> ligands wrapped around the principal axis between the two Fe(II) metal ions. Each metal center is octahedrally coordinated through the one pyrazolyl-pyridine chelating pocket of each ditopic ligand. This architecture arises from the appropriate flexibility of the ligand, which twists around the five C-C bonds between six aromatic rings. The averages of the C-C torsion angles are 38.11° (phen-phen), 18.90° (phen-pz) and 10.60° (pz-py), phen, pz and py being phenylene, pyrazolyl and pyridyl, respectively (Table A7.3, Appendix 7). The Fe1... Fe2 distance is 10.63 Å. The average Fe-N distances are 1.97 Å approximately for both metal centres, thus indicating the low spin at this temperature. In between them and almost equidistant (5.3 Å), the central guest [Fe(C<sub>2</sub>O<sub>4</sub>)<sub>3</sub>]<sup>3-</sup> displays the expected octahedral geometry with an Fe-O average bond distance of 2.03 Å. The guest stabilization inside the helical cavity is favoured by six N-H...O hydrogen bonds between the oxalate oxygen atoms and the free N-H groups

## 7. Exploration of the coordination chemistry of H<sub>2</sub>L<sub>2</sub>. The discovery of [Fe<sub>9</sub>] grids.

of the ligands. While the Fe(III) metal centre is completely inside the cavity, part of the oxalate ligands are pointing toward the three windows formed between the ligands of the stranded helicate. In this way, the oxalates reach the exterior of the cage and interact with water molecules. Thus, the [Fe(C<sub>2</sub>O<sub>4</sub>)<sub>3</sub>]<sup>3-</sup> guests of neighbouring assemblies are connected via O⋯HO hydrogen bonds between the non-coordinating oxygen atoms in each oxalate and two molecules of water which bridge the guests in an anti-anti fashion. (Figure A7.2; Appendix 7). Therefore, the resulting packing constitutes a 2D network of supramolecular interactions (Figure A7.3; Appendix 7). Furthermore, within this network, the helical assemblies interact to each other through weak C-H⋯π interactions. (Figure A7.4, Appendix 7).

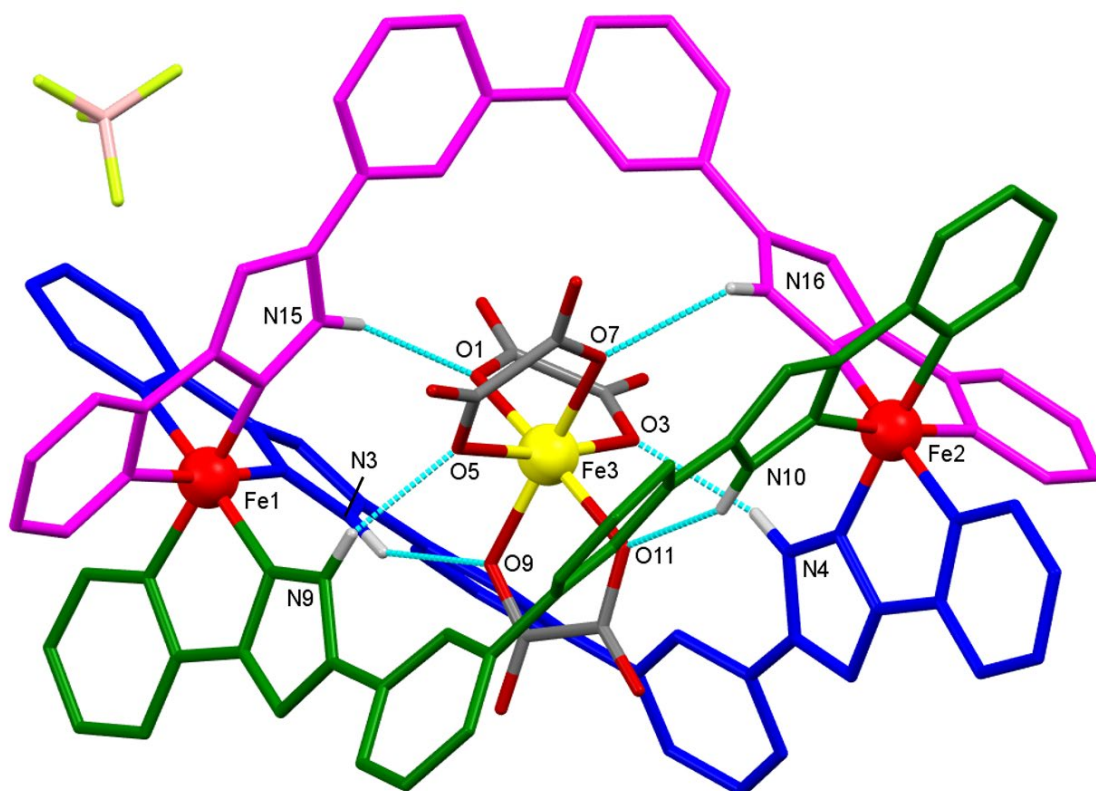


Figure 7.2. Molecular representation of the supramolecular  $\text{Fe}(\text{C}_2\text{O}_4)_2@[\text{Fe}_2(\text{H}_2\text{L}_2)_3](\text{BF}_4)_2$  architecture of compound **14**. Solvent molecules are omitted to clarify. Metals and heteroatoms involved in hydrogen bonding are labeled. Cyan lines are hydrogen bonds between the free NH groups of the ligand H<sub>2</sub>L<sub>2</sub> and the oxygen atoms of the oxalate.

The crystallographic data were also recorded at 280K (Table A7.2 and Figure A7.5; Appendix 7). Firstly, the data were refined using the model from the 100K structure of the same crystal. Two molecules of acetonitrile seemed too diffuse or be distorted

according to the refinement. Thus, it was modelled without these molecules (acetonitrile molecules containing N4S and N5S). Once refined as mentioned, the void space generated from the diffused acetonitrile of the lattice was analysed using the PLATON SQUEEZE function.<sup>39</sup> One void of 362 Å<sup>3</sup> with 89 electrons per void was found. This finding, reasonably corresponds to two diffused acetonitrile molecules concerning the 100K structure. Thus, the same chemical formula of 100K structure was used to refine. No other significant crystallographic difference was found at 280K with respect to the 100K structure. The average Fe-N distances are again around 1.97 Å for both Fe(II) of the helical moiety at 280K. Therefore, the metal centres remind in the low spin configuration suggesting the absence of SCO transition.

#### Crystal structure description of

#### **Fe(C<sub>2</sub>O<sub>4</sub>)<sub>3</sub>@[Fe<sub>2</sub>(H<sub>2</sub>L<sub>2</sub>)<sub>3</sub>](BF<sub>4</sub>) · 3(CH<sub>4</sub>O) · 4.75(H<sub>2</sub>O), (15)**

Another helical structure, compound **15**, was determined at 100 and 280K. In this case, the compound crystallizes as red blocks together with yellow needles of grid (see below). Compound **15** crystallizes in the monoclinic space group P2<sub>1</sub>/n. At 100K, the asymmetric unit comprises the helical moiety {Fe(C<sub>2</sub>O<sub>4</sub>)<sub>3</sub>@[Fe<sub>2</sub>(H<sub>2</sub>L<sub>2</sub>)<sub>3</sub>]}<sup>+</sup>, one BF<sub>4</sub><sup>-</sup> counterion, 3 molecules of methanol and 4.75 of water (Table A7.2 and Figure A7.6; Appendix 7). The unit cell encloses four of such ensembles. Like in compound **14**, the triple stranded host encapsulates a [Fe(C<sub>2</sub>O<sub>4</sub>)<sub>3</sub>]<sup>3-</sup> complex in the central cavity. The average of the C-C torsion angles are 37.29° (phen-phen), 19.03° (phen-pz) and 10.71° (pz-py), being phen, pz and py, phenylene, pyrazolyl and pyridyl, respectively (Table A7.4; Appendix 7). The Fe1... Fe2 distance is 10.76 Å. The average Fe-N distances are 1.97 Å for both metal centres, thus indicating the low spin configuration at this temperature. In general terms, the structure is closely similar to **14**. The structure was also collected at 280K and solved in a similar way since the methanol molecules of the lattice proved to diffuse (Figure A7.7; Appendix 7). The PLATON SQUEEZE function found two main voids of 308 Å<sup>3</sup> with 60 electrons per void, which reasonably correspond to three methanol and one partial water molecule missing with respect to the 100K structure. Thus, the same formula at 100K was used. However, Fe-N bond average for Fe1 and Fe2 were 1.96 Å and

2.14 Å, respectively, at this temperature. Therefore, a SCO transition associated to the Fe<sub>2</sub> metal centre is suggested through the crystallographic data.

### Crystal structure description of

#### **Fe(C<sub>2</sub>O<sub>4</sub>)<sub>3</sub>@[Fe<sub>2</sub>(H<sub>2</sub>L<sub>2</sub>)<sub>3</sub>](ClO<sub>4</sub>)·[H<sub>2</sub>O], (16)**

Compound **16** crystallizes in the monoclinic space group *P*2<sub>1</sub>/*n*. At 100 K, the asymmetric unit comprises a cationic helical moiety with formula {Fe(C<sub>2</sub>O<sub>4</sub>)<sub>3</sub>@[Fe<sub>2</sub>(H<sub>2</sub>L<sub>2</sub>)<sub>3</sub>]}<sup>+</sup>, one ClO<sub>4</sub><sup>-</sup> compensating the overall charge and several water molecules (Table A7.2 and Figure A7.8; Appendix 7). While one water molecule was directly determined from the electronic density the rest was calculated through the solvent mask function. The solvent mask function found two voids of 424.6 Å<sup>3</sup> with 106.9 electrons per void and four voids of 61.2 Å<sup>3</sup> with 10.3 electrons per void. The first void reasonably corresponds to ten molecules of water, and the second to two molecules. Thus, the total amount of water is 29. The unit cell encloses four of such ensembles. The helical ensemble is formed by three H<sub>2</sub>L<sub>2</sub> ligands wrapped around the principal axis between the two Fe(II) metal ions. Each metal center is octahedrally coordinated through the each pyrazoly-pyridine chelating pocket of the ditopic ligand. This architecture arises from the appropriate flexibility of the ligand, which twists around the five C-C bonds between the six aromatic rings. The average of the C-C torsion angles are 37.80° (phen-phen), 18.54° (phen-pz) and 10.83° (pz-py), being phen, pz and py, phenylene, pyrazolyl and pyridyl, respectively (Table A7.5; Appendix 7). The Fe1... Fe2 distance is 10.726 Å. The average Fe-N distances are 1.97 Å for Fe1 and 2.00 Å for Fe2, thus indicating the low spin for both metal centres at this temperature. In between them, the central guest [Fe(C<sub>2</sub>O<sub>4</sub>)<sub>3</sub>]<sup>3-</sup> displays the expected octahedral geometry with an Fe-O average bond distance of 2.06 Å. The iron (III) of the [Fe(C<sub>2</sub>O<sub>4</sub>)<sub>3</sub>]<sup>3-</sup> guest is slightly closer to Fe1, with distances of 5.440 and 5.291 Å with respect to Fe1 and Fe2, respectively. In this case, the crystal packing is different to **14** and **15** since the inner oxalate guest reach the exterior of the cage and interacts with one oxalate via two water bridges and with five helical complexes through weak O...H-C interactions (Figure A7.9; Appendix 7) instead of forming the 2D network. Unfortunately, we could not obtain the crystal structure of **16** at 280K due to the loss of crystallinity and poor resolution

## 7. Exploration of the coordination chemistry of H<sub>2</sub>L<sub>2</sub>. The discovery of [Fe<sub>9</sub>] grids.

(~1.7 Å) of the sample. However, we obtained the unit cell parameters which coincides with the ones at 100K.

Overall, the crystallographic data for compounds **14**, **15** and **16** gives insights on their magnetic behaviour. The helical compound **14** maintains the [LS-LS] at 280K while Fe<sub>2</sub> is in the HS at 280K for compound **15**, being the paired spin state [LS-HS]. Since the {Fe(C<sub>2</sub>O<sub>4</sub>)<sub>3</sub>@[Fe<sub>2</sub>(H<sub>2</sub>L<sub>2</sub>)<sub>3</sub>]}<sup>+</sup> moiety and the crystal packing are almost identical for both complexes, the main magnetic difference might be ascribed to the different solvent within the lattice and their respective intermolecular interactions. Compounds **14**, **15** and **16** display the same spin-state pair at 100 K. All spin-state pairs and averages of the Fe-N bond distances are summarized in table 7.1.

Table 7.1. Summary of the Spin States and the bond distance average Fe-N for the three helical complexes at 100 and 280K.

Compound	Temperature (K)	spin state	d <sub>Fe1-N</sub> (Å)	d <sub>Fe2-N</sub> (Å)
<b>14</b>	100	[LS-LS]	1.97	1.97
	280	[LS-LS]	1.97	1.97
<b>15</b>	100	[LS-LS]	1.97	1.97
	280	[LS-HS]	1.96	2.14
<b>16</b>	100	[LS-LS]	1.97	2.00

### Crystal structure description of the grid

#### [Fe<sub>9</sub>O<sub>4</sub>(OH)<sub>10</sub>(H<sub>2</sub>L<sub>2</sub>)<sub>6</sub>(H<sub>2</sub>O)<sub>4</sub>](BF<sub>4</sub>)<sub>5</sub>, (**17**)

Compound **17** crystallizes in the monoclinic space group P 2<sub>1</sub>/c with an asymmetric unit containing one [Fe<sub>9</sub>O<sub>4</sub>(OH)<sub>10</sub>(H<sub>2</sub>L<sub>2</sub>)<sub>6</sub>(H<sub>2</sub>O)<sub>4</sub>]<sup>5+</sup> grid, five BF<sub>4</sub><sup>-</sup> counterions (one disordered) compensating the overall positive charge and, one methanol and seven water lattice molecules. The unit cell encloses four of such ensembles. The [Fe<sub>9</sub>] structure comprises a nearly planar squared grid of nine iron metal ions connected through μ-oxide or -hydroxide bridging ligands and six H<sub>2</sub>L<sub>2</sub> capping ligands (Figure 7.3 and Table A7.6 in Appendix 7). Each oxidation state was analysed by valence

## 7. Exploration of the coordination chemistry of H<sub>2</sub>L<sub>2</sub>. The discovery of [Fe<sub>9</sub>] grids.

bond sum (VBS) approach, giving Fe(II) for the irons in the vertices of the grid and Fe(III) for the rest of metal ions (Tables A7.7, A7.8 and A7.9; Appendix 7).

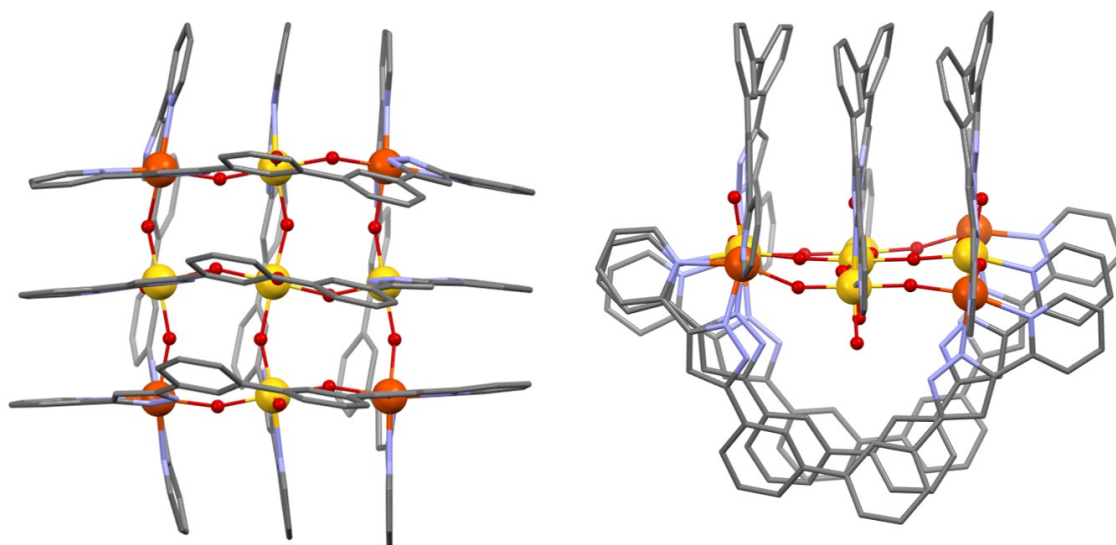


Figure 7.3. Two views of the cationic  $[\text{Fe}_9\text{O}_4(\text{OH})_{10}(\text{H}_2\text{L}_2)_6(\text{H}_2\text{O})_4]^{5+}$  moiety of grid **17**. Blue, red, yellow and grey are nitrogen, oxygen and carbon. Big red and yellow spheres are Fe(II) and Fe(III) atoms, respectively.  $\text{BF}_4^-$  counterions and H atoms are omitted for clarity.

Additionally, the bond distances around the iron ions give an average of 1.98 Å and 2.12 Å for Fe(III) and Fe(II), respectively (Table A7.7, Appendix 7). The latter indicates the HS state of the Fe(II) ions. Within the core of the molecule,  $[\text{Fe}_9\text{O}_4(\text{OH})_8]^{7+}$ , the iron centers are held by eight oxygen atoms mutually interacting as four pairwise  $\text{O}^{2-}/\text{OH}^-$  groups, by establishing hydrogen bonds in between them (Figure 7.4). The remaining four oxygen atoms lie in the edge of the grid and belong to hydroxide groups. This flat core is held by six ditopic H<sub>2</sub>L<sub>2</sub> ligands with the side binding pockets coordinated at opposite edges of the cluster. Two sets of three gripper ligands perpendicular to each other hold the grid on opposite sides of the metallic plane. The ligands within the same set are parallel to each other and establish several  $\pi\cdots\pi$  interactions. In this way, the Fe(II) ions lying at the vertices are coordinated to two ligands, one from each set, while the Fe(III) ions at the edges are only coordinated to one ligand. Therefore, the Fe(II) coordination sphere is

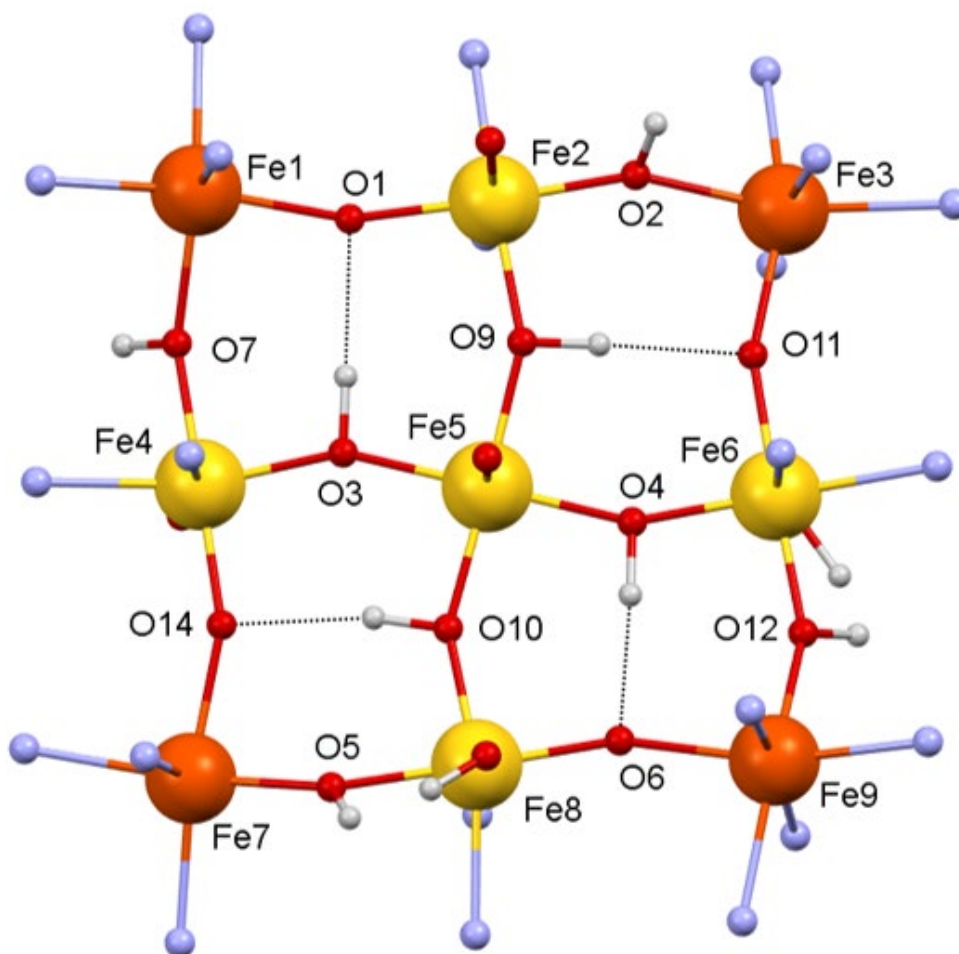


Figure 7.4. Molecular representation of the core of  $[\text{Fe}_9\text{O}_4(\text{OH})_{10}(\text{H}_2\text{L}_2)_6(\text{H}_2\text{O})_4]^{5+}$  in grid **17**. H, N and O atoms are white, blue and red (small spheres), respectively. Red and yellow spheres (big) are Fe(II) and Fe(III), respectively. Oxygen and iron atoms are labelled.

octahedral  $\text{O}_2\text{N}_4$  and the Fe(III) centres fulfil the six-coordinating  $\text{O}_4\text{N}_2$  environment with one terminal  $\text{H}_2\text{O}$  or  $\text{OH}^-$  ligand. The Fe(III) at the centre is geometrically octahedral  $\text{O}_6$  since two additional  $\text{H}_2\text{O}$  ligands to the four core O atoms are axially coordinated (Figure A7.10; Appendix 7).

The chemical features and the structural geometry of ligand  $\text{H}_2\text{L}_2$  facilitate the formation of the unprecedented ferrous/ic oxide/hydroxide block displaying a planar structure. Indeed, the atoms within the core lie almost within an ideal plane the largest distances to it being 0.482 Å and 0.339 Å for Fe1 and O5, respectively. This square grid displays twelve Fe-O-Fe angles ranging from 150.17 to 161.83° and Fe...Fe distances ranging from 3.785 to 3.928 Å (Tables A7.10 and A7.11; Appendix 7). The grid edges span 7.683 to 7.765 Å and the two diagonals are 10.797 and 10.907 Å. The O-Fe-O angles are in the 88.46 to 90.22° range. These parameters

describe a nearly ideal squared grid. The capping ligands solder the [Fe<sub>9</sub>] molecular structure. Indeed, several intramolecular non-covalent interactions between ligands of the same set contribute to holding the metallic grid. Particularly, the three ligands of each set establishes six series of  $\pi\cdots\pi\cdots\pi$  stacking interactions involving all the aromatic rings (per ligand, two phenylene, two pyridyl and two pyrazolyl rings). These series of interactions are depicted in figure A7.11, Appendix 7, together with the corresponding distances between the calculated centroids in Table A7.12. Additionally, the free N-H groups of the H<sub>2</sub>L<sub>2</sub> ligands interact with the terminal H<sub>2</sub>O or OH<sup>-</sup> ligands of the central core through twelve hydrogen bonds (Figure A7.12 and Table A7.13, Appendix 7). Each complex cation [Fe<sub>9</sub>O<sub>4</sub>(OH)<sub>10</sub>(H<sub>2</sub>L<sub>2</sub>)<sub>6</sub>(H<sub>2</sub>O)<sub>4</sub>]<sup>5+</sup> species is connected through twelve  $\pi\cdots\pi$  interactions with its close eight neighbours (Figure A7.13 and Table A7.13, Appendix 7).

### Crystal structure description of the grid

#### [Fe<sub>9</sub>O<sub>4</sub>Cl<sub>6</sub>(OH)<sub>8</sub>(H<sub>2</sub>L<sub>2</sub>)<sub>6</sub>]Cl<sub>4</sub>, (**18**)

Compound **18** crystallizes in the cubic space group *I-43d* with an asymmetric unit containing three different iron metals, being Fe1 the central ion, Fe2 the edge one and Fe3 the corner one, two different chloride ligands, one chloride counterion, and one H<sub>2</sub>L<sub>2</sub> ligand and a half (Table A7.15 and Figures A7.14 and A7.15). The corresponding atomic occupation of each atom is summarized in Table A7.16). The space group has 48 symmetry operators and once these symmetry operations are applied to the asymmetric unit, the complete grid [Fe<sub>9</sub>O<sub>4</sub>Cl<sub>6</sub>(OH)<sub>8</sub>(H<sub>2</sub>L<sub>2</sub>)<sub>6</sub>]Cl<sub>4</sub> structure is generated. The unit cell encloses eighteen of such grid moieties (Figure A7.16; Appendix 7). As seen in the previous compound, the grid **18** contains an analogous nonanuclear Fe/O<sup>2-</sup>/OH<sup>-</sup> grid. Indeed, the core [Fe<sub>9</sub>O<sub>4</sub>(OH)<sub>8</sub>]<sup>10+</sup> is similarly formulated to grid **17** with different oxidation states of the central and vertex Fe metals (see below). Additionally, the protons within the core are part of four O-H $\cdots$ O interactions, like in grid **17**. The main distinctive structural feature of grid **18** is the coordination of all the available axial positions by chloride ligands. Thus, the two neutral H<sub>2</sub>O ligands in the central Fe of grid **17**, are now Cl<sup>-</sup> ligands. Similarly, the H<sub>2</sub>O and OH<sup>-</sup> coordinated on the edge's Fe of the grid **17**, are now occupied by Cl<sup>-</sup> ions (Figure 7.5 and Table A7.17 in Appendix 7.).



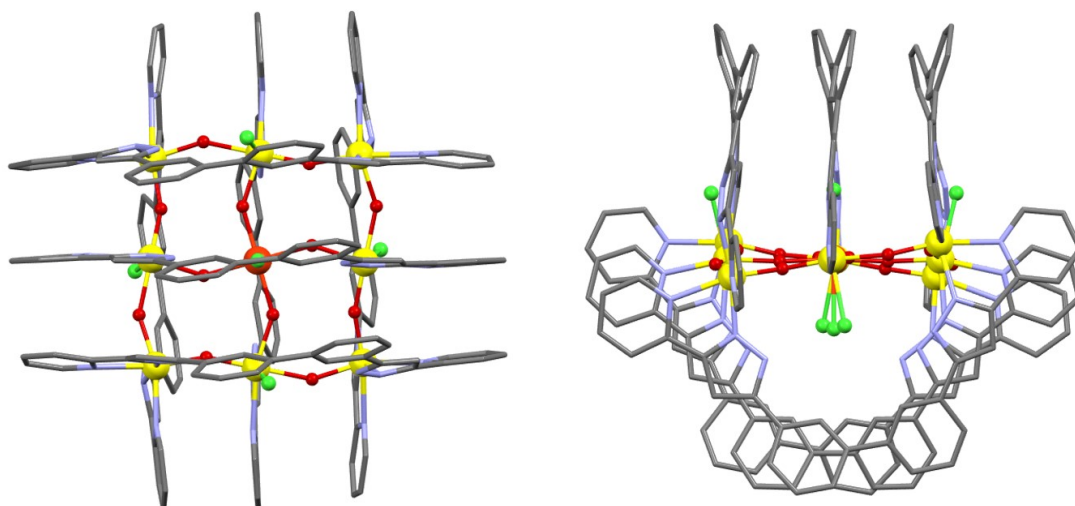


Figure 7.5. Two views of the cationic  $[\text{Fe}_9\text{O}_4\text{Cl}_6(\text{OH})_8(\text{H}_2\text{L}_2)_6]^{4+}$  moiety of grid **18**. Blue, red, yellow, green and grey are nitrogen, oxygen, chloride and carbon. Big spheres in red and yellow are Fe(II) and Fe(III) atoms, respectively.  $\text{BF}_4^-$  counterions and H atoms are omitted for clarity.

Considering the crystalline structure, the elemental analysis and the VBS analysis, and magnetometry (see below), the oxidation state of the central Fe is 2+ (less probable through VBS calculation, Tables A7.18 and A7.19; Appendix 7), while the rest of the Fe centres are 3+. Comparative details between both obtained grids are summarized in table 7.2. The bond distances around the iron ions average 2.14, 2.10 and 2.08 Å for Fe1, Fe2 and Fe3, respectively. As the six H<sub>2</sub>L<sub>2</sub> gripper ligands also act like grid scaffolding, the vertex Fe(III) centres display the same coordination sphere O<sub>2</sub>N<sub>4</sub> as in grid **17**. However, the Fe(III) on the edges exhibit the octahedral O<sub>3</sub>N<sub>2</sub>Cl coordination geometry and the central Fe(II) one an octahedral O<sub>4</sub>Cl<sub>2</sub> environment when adding the two trans chloride ligands to the four oxygen atoms of the core (Figure 7.6 and Figure A7.17 in Appendix 7).

7. Exploration of the coordination chemistry of H2L2. The discovery of [Fe9] grids.

Table 7.1. Comparative structural features of grids **17** and **18**.

	Compound <b>17</b>			Compound <b>18</b>		
core	[Fe <sub>9</sub> O <sub>4</sub> (OH) <sub>8</sub> ] <sup>7+</sup>			[Fe <sub>9</sub> O <sub>4</sub> (OH) <sub>8</sub> ] <sup>10+</sup>		
Planar nanosheet without ligands	[Fe <sub>9</sub> O <sub>4</sub> (OH) <sub>10</sub> (H <sub>2</sub> O) <sub>4</sub> ] <sup>5+</sup>			[Fe <sub>9</sub> O <sub>4</sub> Cl <sub>6</sub> (OH) <sub>8</sub> ] <sup>4+</sup>		
description	Metal ion	Ox. state	Coord. sphere	Metal ion	Ox. state	Coord. sphere
Central	Fe5	3+	O <sub>6</sub>	Fe1	2+	O <sub>4</sub> Cl <sub>2</sub>
Edges	Fe2, Fe4, Fe6, Fe8	3+	O <sub>4</sub> N <sub>2</sub>	Fe2	3+	O <sub>3</sub> N <sub>2</sub> Cl
vertices	Fe1, Fe3, Fe7, Fe9	2+	O <sub>2</sub> N <sub>4</sub>	Fe3	3+	O <sub>2</sub> N <sub>4</sub>

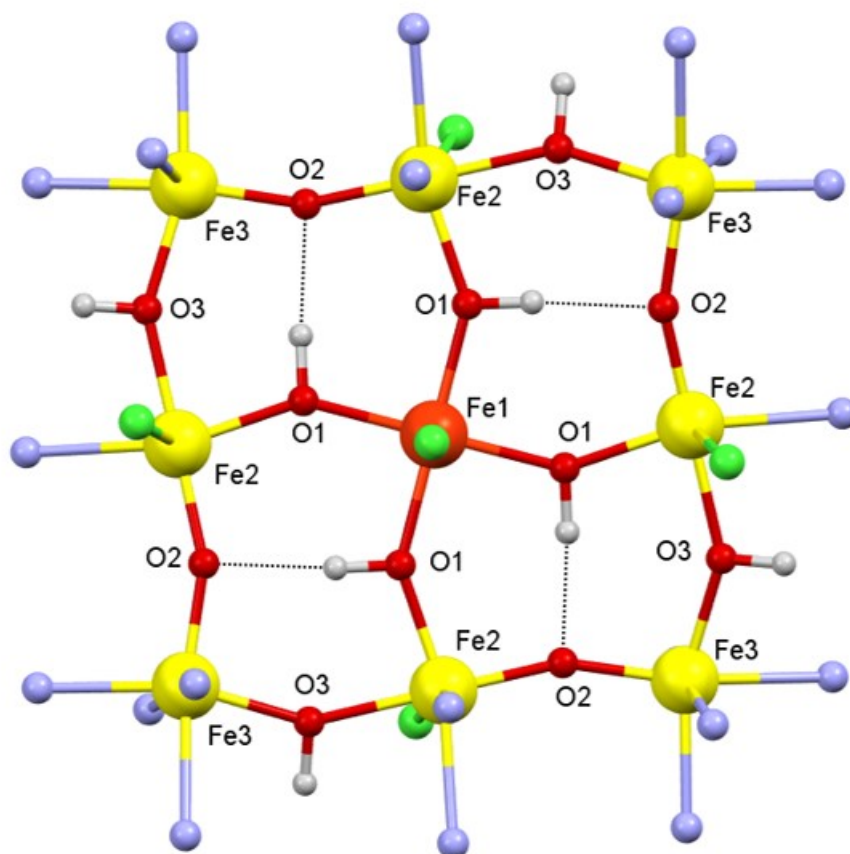


Figure 7.6. Molecular representation of the core of [Fe<sub>9</sub>O<sub>4</sub>Cl<sub>6</sub>(OH)<sub>8</sub>(H<sub>2</sub>L2)<sub>6</sub>]<sup>4+</sup> in grid **18**. H, N and O atoms are white, blue and red (small spheres), respectively. Red and yellow spheres (big) are Fe(II) and Fe(III), respectively. Oxygen and iron atoms are labelled.

## 7. Exploration of the coordination chemistry of H<sub>2</sub>L<sub>2</sub>. The discovery of [Fe<sub>9</sub>] grids.

---

The Fe-O-Fe angles within the three different iron centres are 164.4, 159.2 and 169.6 °, while the three shortest Fe...Fe distances are 3.745 Å, 3.801 Å and 3.566 Å. These values are reproduced by symmetry throughout the grid (Tables A7.20 and A7.21; Appendix 7). Thus, all the edges of the Fe<sub>9</sub> grid are 7.364 Å and the diagonal measures 10.278 Å as result of a perfect squared geometry. The H<sub>2</sub>L<sub>2</sub> ligands also hold the flat metallic core and interact in series of  $\pi\cdots\pi\cdots\pi$  stacking interactions (Figure A7.18 and Table A7.22; Appendix 7). In this case, the free N-H groups of the H<sub>2</sub>L<sub>2</sub> ligands interact with the six axial chloride ligands of the central core through twelve hydrogen bonds (Figure A7.19 and Table A7.23; Appendix 7). Each supramolecular [Fe<sub>9</sub>O<sub>4</sub>Cl<sub>6</sub>(OH)<sub>8</sub>(H<sub>2</sub>L<sub>2</sub>)<sub>6</sub>]<sup>4+</sup> species is connected through eight  $\pi\cdots\pi$  interactions with its close eight neighbours (Figure A7.20 and Table A7.24, Appendix 7).

Compounds **17** and **18** represent an unprecedented polynuclear cluster-type since their structural features have virtually never been seen in previous coordinating compounds. For instance, Fe-O-Fe angles larger than 150° are rarely found in hydroxo(oxo)polyiron clusters. It is observed in the central FeO<sub>6</sub> octahedron within a Lindqvist like cages with [Fe<sub>6</sub>O<sub>19</sub>] core,<sup>26,40,41</sup> or in clusters including such fragments through  $\mu_5$ - or  $\mu_4$ -O<sup>2-</sup> bridges.<sup>42</sup> Such angle is also displayed by the [Fe<sub>2</sub>OCl<sub>6</sub>]<sup>-</sup> anion<sup>43</sup> and as part of the bridge between mono- or dinuclear Fe(III) complexes linked by  $\mu$ -O<sup>2-</sup> moieties.<sup>44,45</sup>

This new inorganic organization is clearly a result from the structural features imposed by the six H<sub>2</sub>L<sub>2</sub> ligands. These capping ligands favour the formation of a squared of eight iron atoms connected pairwise by oxygen atoms. Then, the central position is completed by an additional Fe metal. The twelve  $\pi\cdots\pi\cdots\pi$  stacking interactions in between the aromatic rings of the ligands contribute to the self-assembly of the [Fe<sub>9</sub>] complexes. Some intramolecular  $\pi$  stacking interactions have been reported as the key factor for the stabilization of particular supramolecular architectures (e.g. cages), assembled from bis- or *tris*-pyrazolylpyridine ligands.<sup>46</sup>

### **Magnetic behavior of grid 17**

Bulk magnetic measurements were performed on a polycrystalline samples of compounds **17** and **18** to study the magnetic exchange between the electronic spin moments of the nine iron metal centres.

For compound **17**, the field dependence of the magnetization measured at 2 K is nearly straight at low temperature as field increases, levelling off and reaching a value of 4.2 Bohr magnetons at 5T (Figure 7.7 left). This data is consistent with the total spin ground  $S_T=3/2$  and  $g=2.57$  when fitted to the Brillouin function (See Appendix 7 for further explanation and fittings). This result can be rationalized considering predominant antiferromagnetic interactions between the nine iron centres linked through the twelve oxo/hydroxo bridges (Figure 7.3). Thus, all iron centres are considered in the high-spin state, being  $S=2$  for Fe(II) and  $S=5/2$  for Fe(III), except the central Fe(III), which should be in the low-spin state with  $S=1/2$ . The large value of  $g$  ( $2.57 > g_e=2.00$ ) is explained by the orbital angular momentum contribution expected for the nearly octahedral Fe centres of the grid. The measurement of the magnetic susceptibility ( $\chi$ ) under a constant magnetic field of 0.5 T and a variable temperature range of 2-350K, elucidates and proves the antiferromagnetic nature of the magnetic exchange interactions, being also consistent with the predicted ground spin state (Figure 7.7 right). The plot of  $\chi T$  vs  $T$  unveils a value of  $11.21 \text{ cm}^3\text{Kmol}^{-1}$  at 350K, far below the expected figure for a spin-only system ( $29.88 \text{ cm}^3\text{Kmol}^{-1}$ ) of four Fe(II) with  $S=2$ , four Fe(III) with  $S=5/2$  and one Fe(III) with  $S=1/2$ . This value decreases constantly upon cooling, reaching  $3.2 \text{ cm}^3\text{Kmol}^{-1}$  at the lowest temperature (2K). This value is very close to the one expected for an  $S=3/2$  system with  $g=2.57$  following the Curie law.

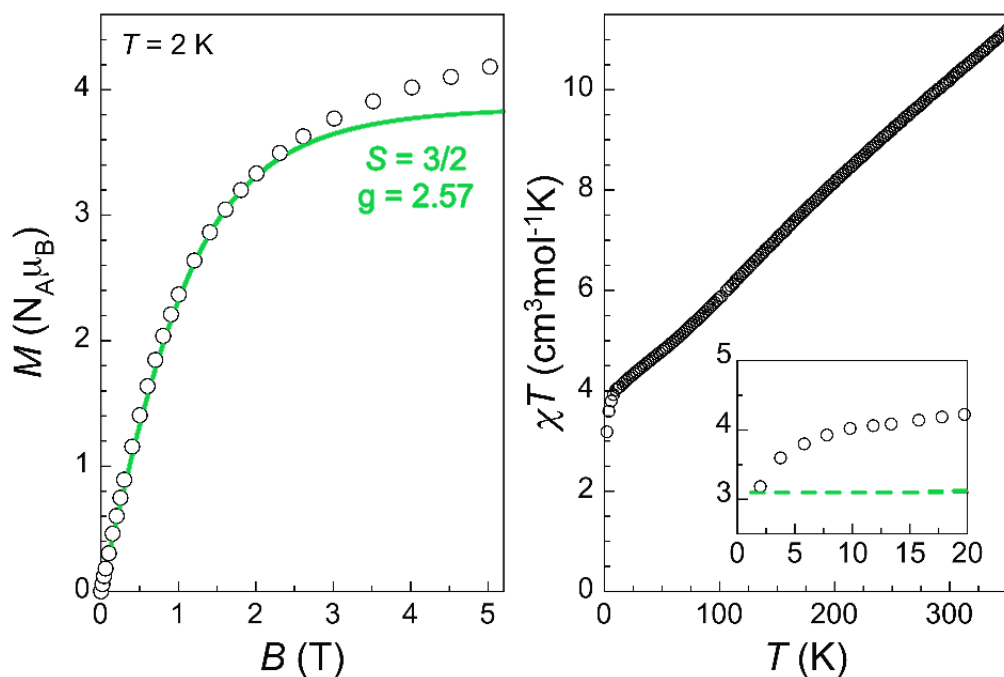


Figure 7.7. (left) Plot of reduced magnetization versus magnetic field of **17** at 2K. The fitting to the Brillouin function for  $S=3/2$  and  $g=2.57$  is shown in red. (right) Plot of  $\chi T$  vs  $T$  for grid **17** at 0.5T. Zoom of the plot at low temperature is shown in the inset.

In order to determine the spin ground state for compound **18**, preliminary magnetic data were collected at 2K varying the magnetic field from 0 to 5T, and plotting the data as reduced magnetization ( $M/N_A\mu_B$ ) versus  $H/T$  (Figure 7.8). Considering that the compound populates entirely the ground state and no ZFS, the observed saturated value indicates a  $S_T=2$ . This result can be rationalized considering also antiferromagnetic interaction between the irons. Thus, all iron centres are considered in the high-spin state, being  $S=5/2$  for all the external Fe(III), except the central Fe(II), which should be in the high-spin state with  $S=2$ . However, future investigations are necessary to validate the assumptions reported here. Our next goal is to fully characterize the grids through Mössbauer spectroscopy.

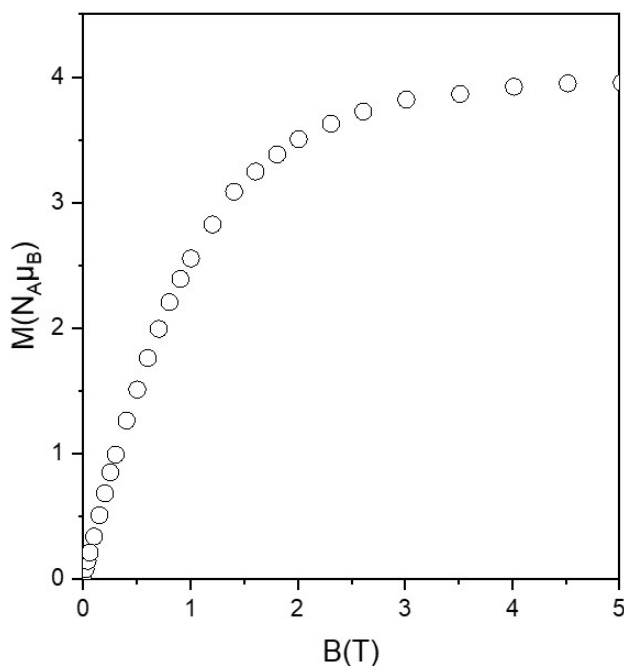


Figure 7.8. Plot of reduced magnetization versus magnetic field of **18** at 2K.

### 7.3. Conclusions

Combining the ligand design and the exploration of several experimental conditions allows the discovery of a new and unique grid-like cluster. This chapter describes the synthetic conditions influencing the two different self-assembled architectures from the ditopic ligand H<sub>2</sub>L. In conclusion, we found three triple-stranded helicates with an anionic ferrioxalate complex encapsulated inside the helical cavity displaying different spin-paired states and two grid-like complexes with an unprecedented flat shape. These compounds, **17** and **18**, display strong antiferromagnetic interactions between the iron neighbours, having a total ground spin state of 3/2 and 2, respectively. Due to the H<sub>2</sub>L<sub>2</sub> ligand geometry, both compounds display Fe-O-Fe angles rarely seen in nature. Further characterization is required.

### 7.4. Experimental

Ligand H<sub>2</sub>L<sub>2</sub> following our reported synthetic procedure.<sup>37</sup>

**Fe(C<sub>2</sub>O<sub>4</sub>)<sub>3</sub>@[Fe<sub>2</sub>(H<sub>2</sub>L<sub>2</sub>)<sub>3</sub>](BF<sub>4</sub>)·5(C<sub>2</sub>H<sub>3</sub>N)·CH<sub>4</sub>O·3(H<sub>2</sub>O), (**14**).** A methanolic solution (10 ml) of H<sub>2</sub>L<sub>2</sub> (20 mg, 0.05 mmol) was added dropwise with stirring to a methanolic solution (10 ml) containing Fe(BF<sub>4</sub>)<sub>2</sub>·6H<sub>2</sub>O (10.4 mg, 0.07 mmol) under nitrogen. This red solution was stirred for 1 hour and filtered off. The resulting

## 7. Exploration of the coordination chemistry of H<sub>2</sub>L2. The discovery of [Fe<sub>9</sub>] grids.

---

solution was combined with acetonitrile (15ml) and left for slow evaporation. Crystals were collected after two weeks.

**Fe(C<sub>2</sub>O<sub>4</sub>)<sub>3</sub>@[Fe<sub>2</sub>(H<sub>2</sub>L2)<sub>3</sub>](BF<sub>4</sub>)·3(CH<sub>4</sub>O)·4.75(H<sub>2</sub>O), (15).** A methanolic solution (10 ml) of H<sub>2</sub>L2 (20 mg, 0.05 mmol) was added dropwise with stirring to a methanolic solution (5ml) containing Fe(BF<sub>4</sub>)<sub>2</sub>·6H<sub>2</sub>O (10.4 mg, 0.07 mmol) under nitrogen. The resulting solution was stirred for 45 min. under inert conditions and at room temperature. Then, it was filtered and layered with an aqueous solution of K<sub>3</sub>V(Ox)<sub>3</sub> (5mg). Crystals were obtained after one month.

**Fe(C<sub>2</sub>O<sub>4</sub>)<sub>3</sub>@[Fe<sub>2</sub>(H<sub>2</sub>L2)<sub>3</sub>](ClO<sub>4</sub>)·29[H<sub>2</sub>O], (16).** A methanolic solution (10 ml) of H<sub>2</sub>L2 (25 mg, 0.06 mmol) was added dropwise with stirring to a methanolic solution (5ml) containing Fe(ClO<sub>4</sub>)<sub>2</sub>·xH<sub>2</sub>O (10.2 mg, 0.04 mmol) and ascorbic acid (~3 mg). The resulting solution was stirred for 45 min at room temperature, filtered, and layered with an aqueous solution of NBU<sub>4</sub>I (11.1 mg, 0.03 mmol). Two types of crystals, red needles and yellow rhomboid corresponding to the helicate and grid-like compounds, respectively, were collected after three weeks.

**[Fe<sub>9</sub>O<sub>4</sub>(OH)<sub>10</sub>(H<sub>2</sub>L2)<sub>6</sub>(H<sub>2</sub>O)<sub>4</sub>](BF<sub>4</sub>)<sub>5</sub>, (17).** A solution of H<sub>2</sub>L2 (25 mg, 0.06 mmol) and trimethylamine (0.02 ml, 0.12 mmol) in 1:1 (vol.) methanol:acetonitrile (10 mL) was added dropwise with stirring to a solution of Fe(BF<sub>4</sub>)<sub>2</sub>·6H<sub>2</sub>O (40.5 mg, 0.12 mmol) in the same medium (5 mL). The resulting solution was stirred for 45 minutes, filtered and layered with Fe(III) acetylacetonate (10.6 mg, 0.03 mmol) dissolved in water (15 mL). This yielded yellow crystals of **4** after 30 days. Yield: 12. Anal. Calcd (found) for **17** ·22 H<sub>2</sub>O: C, 50.77 (49.71); H, 4.51 (3.44); N, 12.69 (11.28).

**[Fe<sub>9</sub>O<sub>4</sub>Cl<sub>6</sub>(OH)<sub>8</sub>(H<sub>2</sub>L2)<sub>6</sub>]Cl<sub>4</sub>, (18).** A solution of ligand H<sub>2</sub>L2 (25 mg, 0.057 mmol) in methanol (10ml) was added dropwise with stirring to a methanolic (10 ml) solution of FeCl<sub>2</sub>·4H<sub>2</sub>O (17 mg, 0.085 mmol). The resulting solution was stirred for 45 min. and filtered. The solution was treated with a methanolic solution (10 ml) of NBU<sub>4</sub>BF<sub>4</sub> (10 mg, 0.03 mmol) and flushed with pressured air until two-thirds of the total solution were reduced. The resulting solution was leaved for slow evaporation. Red crystals were obtained after one month by leaving the solution to almost reach

dryness. Red crystals were obtained after one month. Yield: 13.5%. Anal. Calcd (found) for  $18 \cdot 0.9\text{CH}_4\text{O} \cdot 28.7 \text{H}_2\text{O}$ : C, 47.19 (47.78); H, 3.89 (4.49); N, 11.28 (11.88).

## 7.5. References

- (1) Winpenny, R. *Molecular Cluster Magnets*; Scientific, W., Ed.; 2012.
- (2) Gatteschi, D.; Sessoli, R.; Villain, J. *Molecular Nanomagnets*; 2006.
- (3) Sessoli, R.; Tsai, H. L.; Schake, A. R.; Wang, S.; Vincent, J. B.; Folting, K.; Gatteschi, D.; Christou, G.; Hendrickson, D. N. *J. Am. Chem. Soc.* **1993**, *115*, 1804–1816.
- (4) Baniodeh, A.; Magnani, N.; Lan, Y.; Buth, G.; Anson, C. E.; Richter, J.; Affronte, M.; Schnack, J.; Powell, A. K. *npj Quantum Mater.* **2018**, *3*, 10.
- (5) Brechin, E. K. *Chem. Commun.* **2005**, 5141–5153.
- (6) Sessoli, R.; Gatteschi, D.; Caneschi, A.; Novak, M. A. *Nature* **1993**, *365*, 141–143.
- (7) Aromí, G.; Brechin, E. K. In *Single-molecule magnets and related phenomena*; Winpenny, R. E. P., Ed.; Springer Berlin Heidelberg, 2006; Vol. 122, pp 1–67.
- (8) Zheng, Y. Z.; Evangelisti, M.; Tuna, F.; Winpenny, R. E. P. *J. Am. Chem. Soc.* **2012**, *134*, 1057–1065.
- (9) Zheng, Y. Z.; Zhou, G. J.; Zheng, Z.; Winpenny, R. E. P. *Chem. Soc. Rev.* **2014**, *43*, 1462–1475.
- (10) Heath, S. L.; Powell, A. K. *Angew. Chemie Int. Ed. English* **1992**, *31*, 191–193.
- (11) Powell, A. K.; Heath, S. L.; Gatteschi, D.; Pardi, L.; Sessoli, R.; Spina, G.; Del Giallo, F.; Pieralli, F. *J. Am. Chem. Soc.* **1995**, *117*, 2491–2502.
- (12) Brindley, G. W.; Kao, C. C. *Phys. Chem. Miner.* **1984**, *10*, 187–191.
- (13) Duffy, T. S.; Shu, J.; Mao, H. kwang; Hemley, R. J. *Phys. Chem. Miner.* **1995**, *22*, 277–281.
- (14) Yin, H.; Tang, Z. *Chem. Soc. Rev.* **2016**, *45*, 4873–4891.
- (15) Zhang, S. H.; Feng, C. *J. Mol. Struct.* **2010**, *977*, 62–66.
- (16) Menelaou, M.; Vournari, E.; Psycharis, V.; Raptopoulou, C. P.; Terzis, A.; Tangoulis, V.; Sanakis, Y.; Mateescu, C.; Salifoglou, A. *Inorg. Chem.* **2013**, *52*, 13849–13860.
- (17) Na, H. X.; Yang, P. Y.; Yin, Z.; Wang, Y. H.; Chang, L. X.; Si, R.; Kurmoo, M.; Zeng,



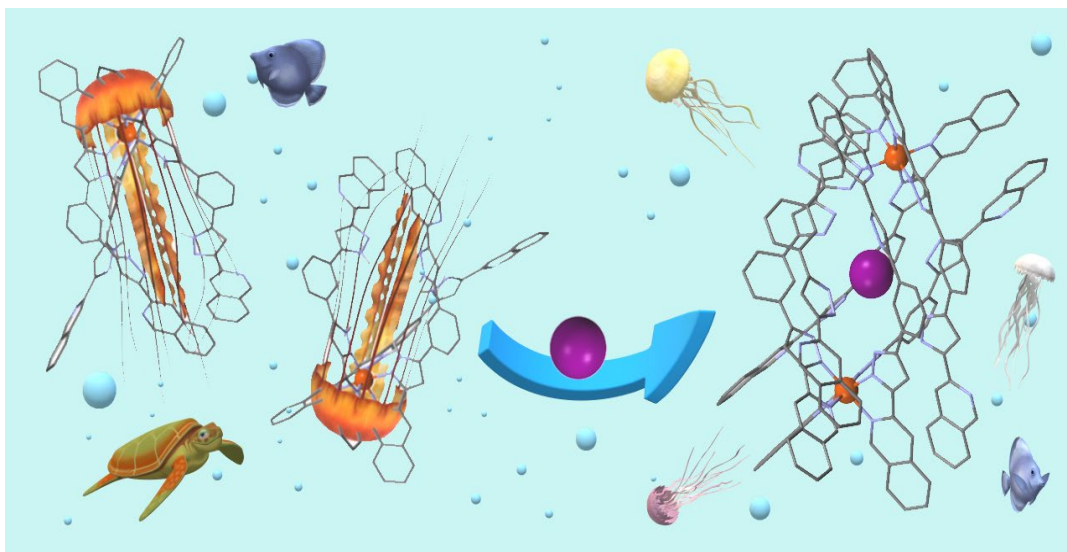
- M. H. *Chem. - A Eur. J.* **2016**, *22*, 18404–18411.
- (18) Zhou, Y. L.; Zeng, M. H.; Wei, L. Q.; Li, B. W.; Kurmoo, M. *Chem. Mater.* **2010**, *22*, 4295–4303.
- (19) Hill, S.; Datta, S.; Liu, J.; Inglis, R.; Milios, C. J.; Feng, P. L.; Henderson, J. J.; Del Barco, E.; Brechin, E. K.; Hendrickson, D. N. *Dalt. Trans.* **2010**, *39*, 4693–4707.
- (20) Meally, S. T.; Karotsis, G.; Brechin, E. K.; Papaefstathiou, G. S.; Dunne, P. W.; McArdle, P.; Jones, L. F. *CrystEngComm* **2010**, *12*, 59–63.
- (21) Pérez-Aguirre, R.; Beobide, G.; Castillo, O.; De Pedro, I.; Luque, A.; Pérez-Yáñez, S.; Rodríguez Fernández, J.; Román, P. *Inorg. Chem.* **2016**, *55*, 7755–7763.
- (22) Parkinson, G. S. *Surf. Sci. Rep.* **2016**, *71*, 272–365.
- (23) Dearle, A. E.; Cutler, D. J.; Fraser, H. W. L.; Sanz, S.; Lee, E.; Dey, S.; Diaz-Ortega, I. F.; Nichol, G. S.; Nojiri, H.; Evangelisti, M.; Rajaraman, G.; Schnack, J.; Cronin, L.; Brechin, E. K. *Angew. Chemie - Int. Ed.* **2019**, *58*, 16903–16906.
- (24) Micklitz, W.; Mckee, V.; Rardin, R. L.; Pence, L. E.; Papaefthymiou, G. C.; Bott, S. G.; Lippard, S. J. *J. Am. Chem. Soc.* **1994**, No. 24, 8061–8069.
- (25) Foguet-Albiol, D.; Abboud, K. A.; Christou, G. *Chem. Commun.* **2005**, *2*, 4282–4284.
- (26) Nachtigall, O.; Kusserow, M.; Clérac, R.; Wernsdorfer, W.; Menzel, M.; Renz, F.; Mrozinski, J.; Spandl, J. *Angew. Chemie - Int. Ed.* **2015**, *54*, 10361–10364.
- (27) Zhao, J. W.; Jia, H. P.; Zhang, J.; Zheng, S. T.; Yang, G. Y. *Chem. - A Eur. J.* **2007**, *13*, 10030–10045.
- (28) Anwar, M. U.; Dawe, L. N.; Parsons, S. R.; Tandon, S. S.; Thompson, L. K.; Dey, S. K.; Mereacre, V.; Reiff, W. M.; Bunge, S. D. *Inorg. Chem.* **2014**, *53*, 4655–4668.
- (29) Newton, G. N.; Onuki, T.; Shiga, T.; Noguchi, M.; Matsumoto, T.; Mathieson, J. S.; Nihei, M.; Nakano, M.; Cronin, L.; Oshio, H. *Angew. Chem., Int. Ed.* **2011**, *50*, 4844–4848.
- (30) Shiga, T.; Newton, G. N.; Oshio, H. *Dalton Transactions*. Royal Society of Chemistry 2018, pp 7384–7394.
- (31) Archer, R. J.; Scott, H. S.; Polson, M. I. J.; Williamson, B. E.; Mathonière, C.; Rouzières, M.; Clérac, R.; Kruger, P. E. *Dalt. Trans.* **2018**, *47*, 7965–7974.

- (32) Archer, R. J.; Hawes, C. S.; Jameson, G. N. L.; Mckee, V.; Moubaraki, B.; Chilton, N. F.; Murray, K. S.; Schmitt, W.; Kruger, P. E. *Dalt. Trans.* **2011**, *40*, 12368–12373.
- (33) Tuna, F.; Lees, M. R.; Clarkson, G. J.; Hannon, M. J. *Chem. - A Eur. J.* **2004**, *10*, 5737–5750.
- (34) Estrader, M.; Salinas Uber, J.; Barrios, L. A.; Garcia, J.; Lloyd-Williams, P.; Roubeau, O.; Teat, S. J.; Aromí, G. *Angew. Chemie - Int. Ed.* **2017**, *56*, 15622–15627.
- (35) Diego, R.; Pavlov, A.; Darawsheh, M.; Aleshin, D.; Nehr Korn, J.; Nelyubina, Y.; Roubeau, O.; Novikov, V.; Aromí, G. *Inorg. Chem.* **2019**, *58*, 9562–9566.
- (36) Darawsheh, M.; Barrios, L. A.; Roubeau, O.; Teat, S. J.; Aromí, G. *Chem. - A Eur. J.* **2016**, *22*, 8635–8645.
- (37) Aromi, G.; Darawsheh, M.; Barrios, L. A.; Roubeau, O.; Teat, S. J. *Angew. Chemie Int. Ed.* **2018**, *57*, 13509–13513.
- (38) Vilar, R. *Angew. Chemie - Int. Ed.* **2003**, *42*, 1460–1477.
- (39) Spek, A. L. *Acta Crystallogr. Sect. C Struct. Chem.* **2015**, *71*, 9–18.
- (40) Hegetschweiler, K.; Schmale, H.; Streit, H. M.; Schneider, W. *Inorg. Chem.* **1990**, *29*, 3625–3627.
- (41) Hegetschweiler, K.; Schmale, H.; Streit, H. M.; Gramlich, V.; Hund, H. U.; Erni, I. *Inorg. Chem.* **1992**, *31*, 1299–1302.
- (42) Glaser, T.; Lügger, T.; Hoffmann, R. D. *Eur. J. Inorg. Chem.* **2004**, 2356–2362.
- (43) Neuba, A.; Akin, E.; Herres-Pawlis, S.; Flörke, U.; Henkel, G. *Acta Crystallogr. Sect. C Cryst. Struct. Commun.* **2008**, *64*, 194–197.
- (44) Moon, D.; Lah, M. S.; Del Sesto, R. E.; Miller, J. S. *Inorg. Chem.* **2002**, *41*, 4708–4714.
- (45) Miyazato, Y.; Ohba, M.; Sakiyama, H.; Ōkawa, H. *Bull. Chem. Soc. Jpn.* **2007**, *80*, 1534–1541.
- (46) Stephenson, A.; Sykes, D.; Ward, M. D. *Dalt. Trans.* **2013**, *42*, 6756–6767.

# CHAPTER 8

---

## MAGNETIC STUDY OF TRIPLE-STRANDED HELICATES $[\text{Fe}_2(\text{H}_2\text{L})_3]^{4+}$ IN SOLUTION AND ACCESS TO $(\text{X}@[Fe(\text{H}_2\text{L}_5)_3]_2)^{3+}$ ( $\text{X} = \text{I}^-, \text{Br}^-, \text{Cl}^-$ ) COMPLEXES





## 8. MAGNETIC STUDY OF THE TRIPLE-STRANDED HELICATES $[X@Fe_2(H_2L)_3]^{4+}$ IN SOLUTION AND ACCESS TO $(X@[Fe(H_2L_5)_3]_2)^{3+}$ COMPLEXES (X= I<sup>-</sup>, Br<sup>-</sup>, Cl<sup>-</sup>)

### Abstract

The magnetic study of two metallohelicats with the formula  $X@[Fe_2(H_2L)_3]^{3+}$  (X: Cl and Br, for compounds **19** and **20**, respectively) is studied in solution by analysing changes in the NMR spectra expected for a SCO transition. The NMR-based method used allows to discriminate the magnetic response of **19** and **20** from their respective dimerized complexes  $(X@[Fe(H_2L)_3]_2)^{3+}$  (X= Cl and Br, for compounds **21** and **22**, respectively), also present in solution. Two magnetic states [HS-HS], [HS-LS] of the three possible ones (including the [LS-LS] state) are accessed over a large temperature range for **19** and **20**. Surprisingly, an unprecedented spin equilibrium for the simultaneous spin-state change of both iron in the paired mixed-spin [HS-LS] and [LS-HS] was perceived on a millisecond timescale for both compounds. Both mixed-states arise from the rarely seen broken-symmetry spin state (non-equivalence of the Fe(II) metal centres) in binuclear complexes. Thus, the dynamics of the [HS-LS]  $\leftrightarrow$  [LS-HS] interconversion were successfully studied by paramagnetic NMR spectroscopy in solution for the first time, thanks to the slow exchange between the two identified states.

Additionally, we present four new dimerized mononuclear complexes with the formula  $(X@[Fe(H_2L_5)_3]_2)(A)_3$  (A= PF<sub>6</sub><sup>-</sup>; X= I, Br and Cl; for **24**, **25** and **26**, respectively, and A=ClO<sub>4</sub><sup>-</sup>; X= Cl for **27**). The deliberate obtention of this supramolecular architecture is achieved by the rational ligand design of H<sub>2</sub>L<sub>5</sub>. Compounds **24-27** are more desirable than **21** and **22** for NMR studies since the formation of their respective helical counterparts is prevented (perhaps for steric reasons) making the characterization and study simpler.

### 8.1. Introduction

The “pre-programed” geometrical requirements of small chemical moieties determine the nature of the supramolecular architectures arising from the self-assembly process. In the solid-state, the stabilization of the most thermodynamic

product mainly depends on the ligand nature (considering its denticity, orientation of the binding pockets and compromise between its flexibility and rigidity, among other) and the chemical features of the metals. However, additional factors, such as the reaction conditions (involving use of different solvent, counterions, atmosphere type or basicity), may be important in defining a reaction pathway leading to other possible supramolecular architectures. Previously, in our group, we observed such tuning of the final product obtained through the use of slightly different synthetic conditions, which proved to be a valuable tool in coordination supramolecular chemistry. The specific manner in which the small building blocks  $\text{Fe}^{\text{II}}/\text{H}_2\text{L}/\text{X}^-$  (X: Cl and Br) rearrange (helicates versus dimerized mononuclear complexes, termed “jellyfish” complexes in our group because the appearance of the structure) is conditioned by the use of different solvents. Undoubtedly, the use of water favours the “jellyfish” when using ligand  $\text{H}_2\text{L}$ , perhaps due to the stoichiometric  $\text{FeX}_2/\text{H}_2\text{L}$  change and the increase of the basicity of the medium. These two specific arrangements,  $[\text{X}@\text{Fe}_2(\text{H}_2\text{L})_3]^{3+}$  (X: Cl and Br for compound **19** and **20**, respectively) and  $(\text{X}@[Fe(\text{H}_2\text{L})_3]_2)^{3+}$  (X: Cl and Br for compound **21** and **22**, respectively), are distinguished, separately isolated and magnetically studied in the solid-state (Figure 8.1A).<sup>1,2</sup> As described in detail in sections 1.4.2.1 and 1.4.2.2 (for helicates and jellyfishes, respectively), the SCO transition is modulated through the encapsulated halide guest. Nevertheless, attempts on accurately studying such behaviour in solution by using Evans method were impeded since both assemblies coexist. When dissolving the  $[\text{X}@\text{Fe}_2(\text{H}_2\text{L})_3]^{3+}$  helicates, some of the mononuclear  $(\text{X}@[Fe(\text{H}_2\text{L})_3]_2)^{3+}$  complexes are generated, and vice versa (Figure 8.1B). Thus, the solution system consists of an equilibrium between both supramolecular complexes, the major species being the one originally dissolved.<sup>1,2</sup> Fortunately, an alternative paramagnetic  $^1\text{H}$  NMR spectroscopy technique customized in Novikov’s group is suitable to probe the spin transition in solution of our paramagnetic admixtures of compounds. Considering that we can overcome the disadvantages of Evans method through the close collaboration with Novikov’s group, we studied the SCO in solution of the helical complexes with the formula  $[\text{X}@\text{Fe}_2(\text{H}_2\text{L})_3]^{4+}$  (**19** and **20**).

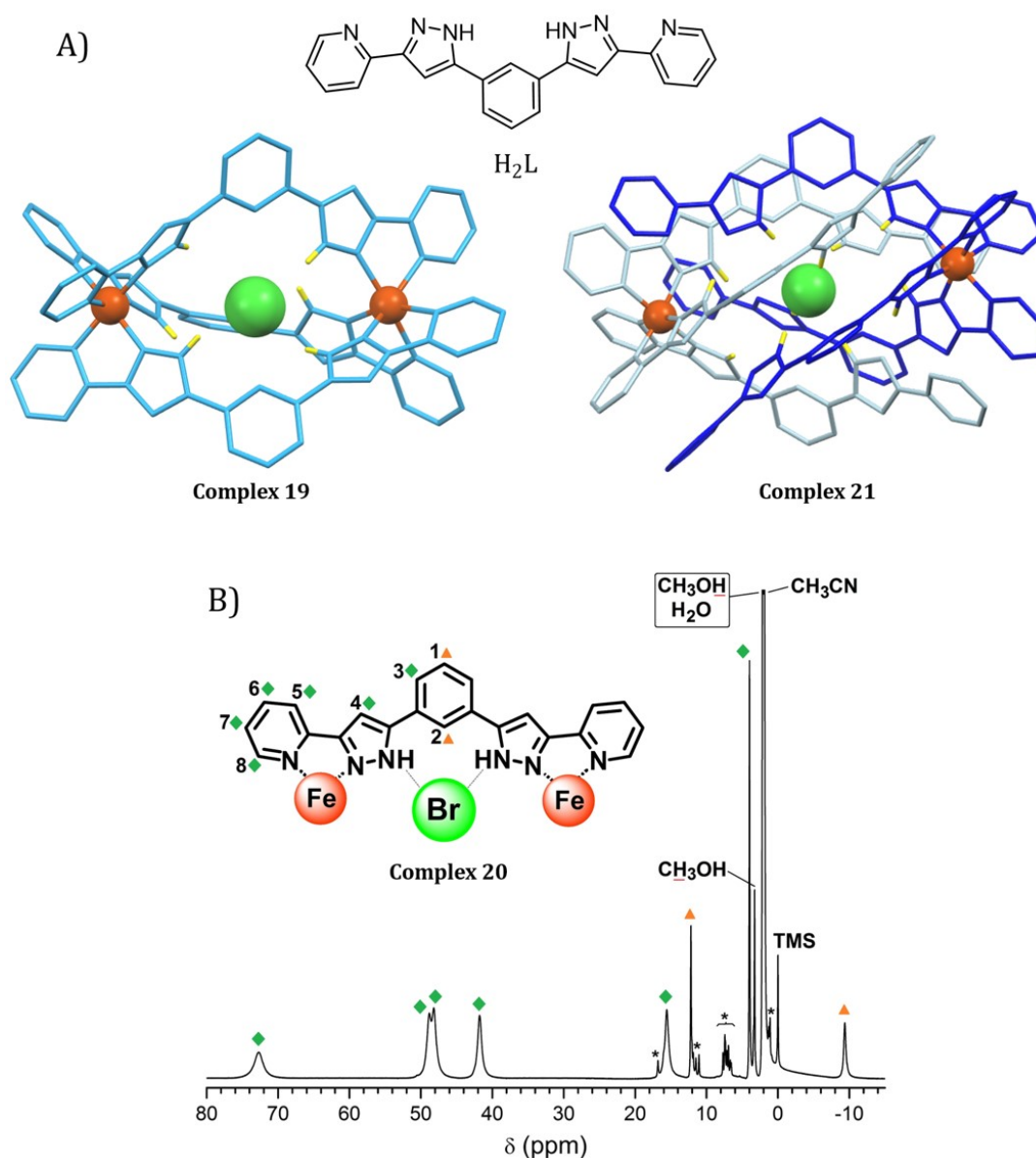


Figure 8.1. A) Molecular representation of both supramolecular architectures, helicate (**19**) and jellyfish (**21**), achieved independently by using different reaction conditions with ligand H<sub>2</sub>L. B) <sup>1</sup>H NMR of compound **20** in CD<sub>3</sub>CN. Peaks assigned with asterisk are ascribed to the minor specie of **22** (see manuscript for details). Image adapted from reference 1.

Three different mixed-spin states can possibly be reached for binuclear compounds, providing a multi-step SCO behavior. Among these, the fully high-spin [HS-HS] and low-spin [LS-LS] states are usually perceived. However, the intermediate [HS-LS] state<sup>3</sup> displaying a broken-symmetry has been observed in a few solids.<sup>4</sup> For these scarce cases,<sup>5,6</sup> the intermediate state is usually favoured by a structural symmetry breaking determined crystallographically.<sup>7</sup> More improbable is the case where the broken-symmetry state is mediated and stabilized by large structural

rearrangements that modify the ligand-field strength of one iron site when the other iron centre changes the spin state in solution.<sup>8</sup> In a symmetrical (two-fold symmetry) binuclear complex, there is an equal possibility to generate both intermediate [HS-LS] or [LS-HS] species. This situation could allow to observe transformation between both equivalent species, which is really arduous. To our knowledge, no prior studies have examined or detected this equilibrium.

In this chapter, the first attempt on identifying the temperature-dependent dynamics between the two [HS-LS] and [LS-HS] states exchange of the helicates [X@Fe<sub>2</sub>(H<sub>2</sub>L)<sub>3</sub>]X·(PF<sub>6</sub>)<sub>2</sub> (X: Cl and Br for compound **19** and **20**, respectively. See Figure 8.1) in solution is presented. As previously shown in the main introduction (section 1.4.2.1), the existence of the stable [HS-LS] state over large temperature ranges in the solid state represents a unique and ideal candidate to detect and study the intermediate state in solution unambiguously.<sup>1</sup>

The potential [HS-LS] ↔ [LS-HS] equilibrium can be theoretically tracked by paramagnetic NMR spectroscopy, which has been vastly used to follow the SCO behavior in solution.<sup>9</sup> The approach is based on the analysis of the paramagnetic chemical shift temperature dependence for the protons of the Fe(II) helicates.<sup>10</sup>

It is well established in molecular magnetism that, in the case of a HS ion in the absence of strong spin-orbit coupling (*e.g.* Fe(II) in the HS), the chemical paramagnetic shifts in the NMR spectra depends linearly on the inverse temperature, being the slope specific for each nucleus according to the Curie Law (left side on Figure 8.2A).<sup>11</sup> In the case of a SCO-active compound at high temperatures, the paramagnetic shift of the HS complex shows the same linear dependence; however, as the temperature decreases, the LS state population gradually increases causing deviations from the linearity. If the exchange between the HS and LS states is quite fast in the NMR timescale, which is mostly seen,<sup>12,13</sup> the observed paramagnetic shift is a weighted average of the HS and LS species.<sup>14,15</sup> Below a certain temperature, only the diamagnetic LS state (S=0 for Fe<sup>II</sup> at LS) is populated, featuring temperature-independent chemical shifts (right side on Figure 8.2A).



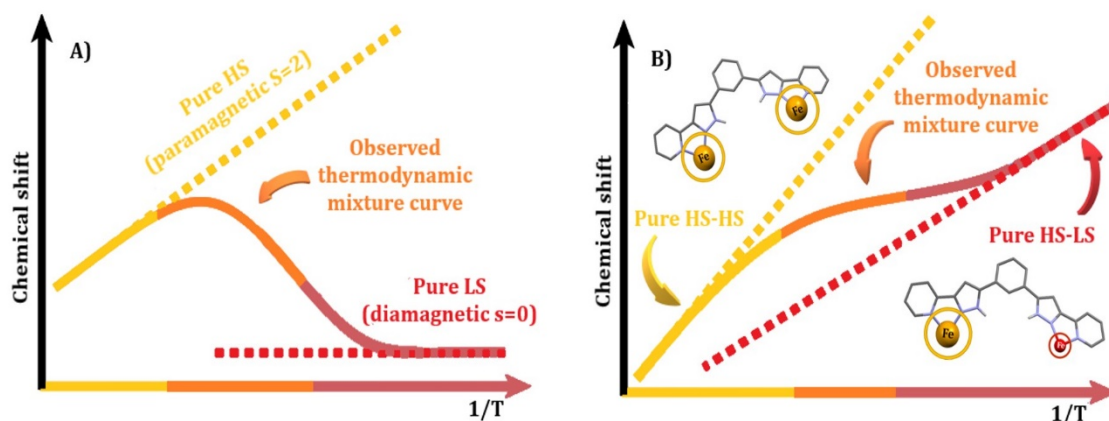


Figure 8.2. Dependence of the paramagnetic shifts on the inverse temperature for: A) a spin-crossover Fe(II) complex. B) the transition  $[\text{Fe}^{\text{HS}}\text{-Fe}^{\text{HS}}] \leftrightarrow [\text{Fe}^{\text{HS}}\text{Fe}^{\text{LS}}]$  in the case of the fast equilibrium  $[\text{HS-LS}] \leftrightarrow [\text{LS-HS}]$ .

In the case of a SCO involving two paramagnetic states, like  $[\text{HS-LS}] \leftrightarrow [\text{HS-HS}]$ , the spin crossover for the binuclear helicate  $X@[\text{Fe}_2(\text{H}_2\text{L})_3]^{3+}$  would be expected to look like the transition between two straight lines with non-zero slope, where the NMR spectra features a weighted average of the chemical shifts for the two states. Since both states are paramagnetic, the chemical shift of each stable state would follow the linear dependence on the  $1/T$  corresponding to the species  $[\text{HS-HS}]$  and  $[\text{HS-LS}]$ , having indeed different slopes (Figure 8.4B).

In addition to this study in solution, we present in this chapter four new supramolecular structure with the molecular formula  $(X@[\text{Fe}(\text{H}_2\text{L}_5)_3]_2)(\text{A})_3$  ( $\text{A} = \text{PF}_6$ ;  $\text{X} = \text{I}, \text{Br}$  and  $\text{Cl}$ ; for **24**, **25** and **26**, respectively, and  $\text{A} = \text{ClO}_4$ ;  $\text{X} = \text{Cl}$  for **27**) characterized through SCXRD. The obtention of these new “jellyfishes” assemblies opens up a future collaboration for the elucidation of the SCO behavior in solution, aside from the study in solid-state. Accomplishing the complete study in solution of the whole family of compounds (**19** to **22**), incorporating compounds **21** and **22**, accessed by using ligand  $\text{H}_2\text{L}$  can be really arduous. Aside from the more complex  $^1\text{H}$  NMR, as 16 independent protons are expected for its mononuclear moieties due to the loss of the  $\text{C}_2$  symmetry of the  $\text{H}_2\text{L}$  ligand, additional signals corresponding to the minor species **19** and **20** in equilibria are present.<sup>2</sup> Thus, the SCO study in solution for **24** to **27**, whose  $X@[\text{Fe}_2]$  helicates formation in solution could be prevented (see below) can facilitate the investigation.

## 8.2. Results and discussion

### Organic Synthesis

The bis(pyrazolylpyridine) ligand H<sub>2</sub>L and the [X@Fe(H<sub>2</sub>L)<sub>3</sub>]<sup>4+</sup> (X= Cl, Br) helicates were synthesized following the previously reported procedure by our group.<sup>1</sup> The ligand 1,3-bis(3-(isoquinolin-3-yl)-1*H*-pyrazol-5-yl)benzene, H<sub>2</sub>L5, was obtained by an analogous synthetic route to H<sub>2</sub>L. The detailed procedure is reported in chapter 5 (Figure 8.3).

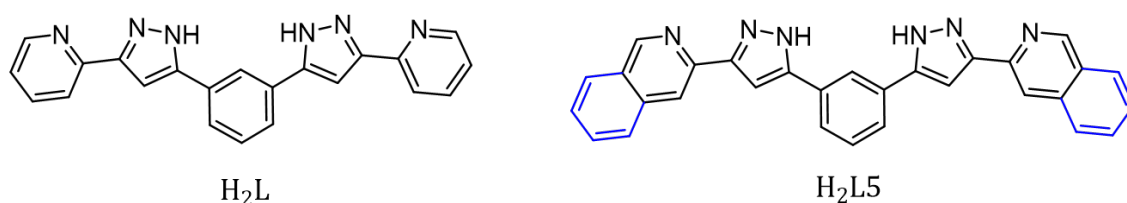


Figure 8.3. Molecular drawing of ligand H<sub>2</sub>L1 and H<sub>2</sub>L5. The additional aromatic rings of the latter are highlighted in blue.

### Inorganic Synthesis

#### Synthesis of the helicate assemblies **12**, **19**, **20** and **23**

Compounds ([X@Fe(H<sub>2</sub>L)<sub>3</sub>]<sub>2</sub>)<sup>3+</sup> (X: Cl and Br, for compounds **19** and **20**, respectively) were synthesized following the previously reported procedure.<sup>1</sup> As previously seen in chapter 6, and as part of the preliminary data analysis of this work, the preparation of the respective [ZnZn] derivatives were pursued in order to estimate precisely the diamagnetic shift. Thus, the synthesis of ([Cl@Zn<sub>2</sub>(H<sub>2</sub>L)<sub>3</sub>]<sup>3+</sup> (**12**) is already described in chapter 6. Compound [Br@Zn<sub>2</sub>(H<sub>2</sub>L)<sub>3</sub>]<sup>3+</sup> (**23**) was obtained with an analogue procedure to **12** from a methanolic solution using ZnBr<sub>2</sub> as a metallic source. Here, we do not require to estimate the paramagnetic contribution to achieve chemical shifts very precise. Thus, diamagnetic shifts can be subtracted from the pure ligand. In any case, the diamagnetic contribution to the observed chemical shift is nearly the same for the HS and LS states, thus, they cancel each other.<sup>14</sup> Nevertheless, the characterization and analysis of both [ZnZn] analogues are reported in Appendix 8.

**Synthesis of the “jellyfish” assemblies 24, 25, 26 and 27**

The reaction of  $\text{FeX}_2$  ( $\text{X}=\text{I}, \text{Br}$  and  $\text{Cl}$ ) salts with ligand  $\text{H}_2\text{L}_5$  (2:3 stoichiometry) in pure methanol or acetone (depending on the compound) treated with a pure methanolic or acetone solution of  $\text{NBu}_4\text{PF}_6$  ( $\text{NBu}_4\text{ClO}_4$  for **27**), led to the crystallization of the corresponding compounds  $(\text{X}@\text{[Fe}(\text{H}_2\text{L}_5)_3]_2)^{3+}$ . Despite that the iron source and the pure solvents (without using water) are the same used previously in the synthetic coordination procedures for preparing helicates, we only crystallized the different supramolecular “jellyfish” systems when using ligand  $\text{H}_2\text{L}_5$ . Therefore, the  $\text{H}_2\text{L}_5$  ligand design is crucial to force the exclusive formation of the jellyfish-like complexes even under the reaction conditions usually conducive to the helicates. This prevents the competition between both types of complexes as seen before for ligand  $\text{H}_2\text{L}$ . The formation of these dimerized  $(\text{X}@\text{[Fe}(\text{H}_2\text{L}_5)_3]_2)^{3+}$  architectures seems to be more stabilized due to the extended aromatic rings of  $\text{H}_2\text{L}_5$  respect to  $\text{H}_2\text{L}$  (see the crystallographic details below).

**Analysis of the NMR spectra for the  $\text{Fe}_2(\text{H}_2\text{L})_3$  helicates (19 and 20)**

As the  $(\text{X}@\text{Fe}_2(\text{H}_2\text{L})_3)^{3+}$  helicates (**19** and **20**) have two iron (II) ions, three spin states are plausible—[LS-LS], [LS-HS] and [HS-HS]. Nevertheless, only two of them—[HS-HS] and [HS-LS]—were accessible, presumably, as a consequence of the temperature range limitation in solution. The solvents freeze at temperatures before reaching the [LS-LS] state of the iron (II) helicates, which was seen to form below 100K in the solid state.<sup>1</sup> At very high temperatures, the  $(\text{X}@\text{Fe}_2(\text{H}_2\text{L})_3)^{3+}$  helicate is in the fully HS state with two-fold symmetry; thus, the  $^1\text{H}$  NMR spectrum exhibits a set of eight signals (paramagnetically shifted peaks between -6 and 60 ppm). Upon gradual decrease of temperature, one of the two iron (II) centres switches to the LS state (Figure 8.4). Thus, the number of molecules in the [HS-HS] state decreases and the number of [LS-LS] ones increases in the solution. For the latter, the symmetry is broken (there is no  $\text{C}_2$  symmetry axis between the two metal ions) and 16 signals should appear. However, it produces 14 new signals since the proton signals for the NH groups are not detected. These protons are located close to the Fe(II) centre and may exchange with the protons of the deuterated methanol used as solvent. Among all protons, the signals of the terminal pyridine-pyrazole moiety coordinated to the Fe(II) in the HS should be strongly shifted by the nearby

paramagnetism, while the ones coordinated to the Fe(II) in the LS might be barely shifted due to their large distance from the paramagnetic centre. Thus, distant protons show almost diamagnetic shifts that do not undergo temperature changes (Figure 8.4, middle).<sup>10</sup>

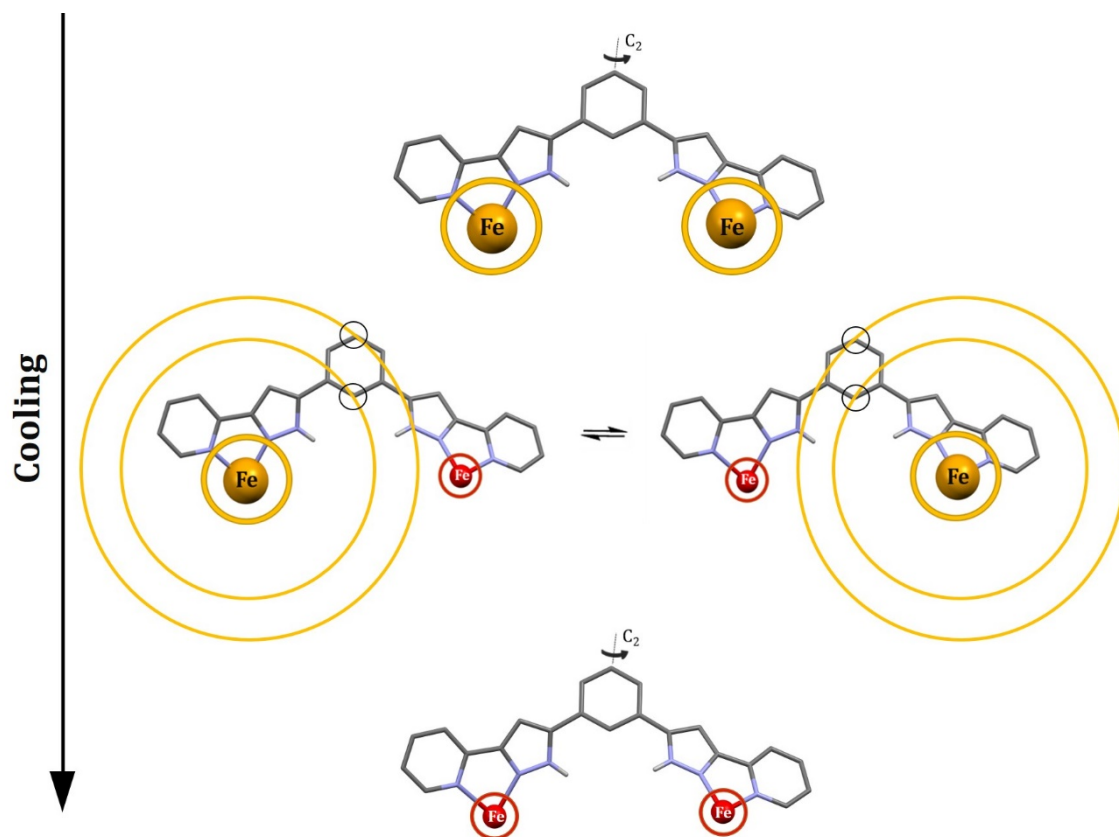


Figure 8.4. Representation of the structural transformation of helicates  $[X@Fe_2(H_2L)_3]^{3+}$  (**19** and **20**) upon SCO transition. Yellow spheres and circles indicate HS, while the red ones are the LS of the Fe(II). The middle schematic drawing represents the effect of the paramagnetism (yellow concentric circles) of the Fe(II) ions in the HS for the two possible broken-symmetry states [HS-LS] and [LS-HS]. Only one ligand  $H_2L$  is shown for clarity. The protons displaying the same chemical shifts are highlighted in black circles for both of the states.

Interestingly, there is evidence in our data to argue that the unsymmetrical state [HS-LS] is itself involved in a dynamic exchange as a result of the intramolecular spin-state interconversion between both Fe (II) centres of the  $[X@Fe_2(H_2L)_3]^{3+}$  helicates in solution (Figure 8.4, middle). Since the [HS-LS] and [LS-HS] states are thermodynamically equivalent, only kinetic activation is necessary for the exchange process between them. In contrast to the localized  $HS \leftrightarrow LS$  switching, which is usually fast in the NMR timescale, the  $[HS-LS] \leftrightarrow [LS-HS]$  equilibrium should involve large structural rearrangements. Therefore, eight signals would be expected for the

[HS-LS] state of the  $[X@Fe_2(H_2L)_3]^{3+}$  helicate only if the  $[HS-LS] \leftrightarrow [LS-HS]$  exchange is fast in the NMR timescale. Otherwise, there should be 14 proton signals in the NMR which is the case. In addition, we can clearly see that two protons of the central phenyl group of  $H_2L$  (shown by black circles in Figure 8.4, middle) do not change the paramagnetic shifts when this exchange takes place. It is expected since they are equidistant to both metal ions, and therefore, should be unaltered by the  $[HS-LS] \leftrightarrow [LS-HS]$  exchange dynamics.

The exchange dynamics by the Fe(II) centres in  $[X@Fe_2(H_2L)_3]^{3+}$  (**19** and **20**) was studied through variable-temperature NMR spectroscopy (Figure 8.5) in deuterated solutions of methanol and acetonitrile for accessing a wide temperature range. In the 320-260K range, eight signals were observed, which became substantially wider upon cooling, most disappearing below 240K (Figure 8.5 B). However, some signals appear again, with higher chemical shift values, when the temperature reaches 220K. The only exceptions to these effects were the two signals assigned to the protons of the central phenyl moiety that have the same paramagnetic shifts in both  $[Fe^{HS}-Fe^{LS}]$  and  $[Fe^{LS}-Fe^{HS}]$  complexes. Thus, these signals can be followed over the whole temperature range and could be used to study the SCO and exchange behaviour (Figure 8.5C).

The only plausible explanation for this magnetic behavior in solution is detailed below. Starting the initial cooling from 320K to 260K, the expected transition  $[HS-HS] \rightarrow [HS-LS]$ , and a concomitant dynamic process corresponding to the  $[HS-LS] \leftrightarrow [LS-HS]$  exchange, which is fast in the NMR timescales, is detected. Accordingly, eight signals are observed obeying the highest possible symmetry of the molecule, so the chemical shift is one averaged signal (Figure 8.5C). Since the [HS-LS] state with only one HS Fe(II) ion is less paramagnetic than the fully [HS-HS] state, the chemical shifts in NMR decrease with temperature differently than expected from the Curie law.<sup>14</sup> Further temperature decrease leads to the exchange  $[HS-LS] \leftrightarrow [LS-HS]$  entering an intermediate regime,<sup>16</sup> so that most lines broaden and disappear, with the exception of the two central protons. At this point, the difference between the paramagnetically shifted protons close to the HS Fe(II) ion and the nearly diamagnetic protons close to LS Fe(II) is very large. Despite determining the

temperature at which the signals disappear is arduous, the coalescence temperature<sup>16</sup> is around 210K. This implies a millisecond dynamics at 600 MHz. The central protons for the bridging phenyl moiety display the same chemical shift in both intermediate states [HS-LS and [LS-HS], and as previously predicted (Figure 8.2), their temperature dependence (Figure 8.5D) follows the expected tendency. Finally, at temperature below 220K, only both [HS-LS] and [LS-HS] are populated and distinguished since the protons signals near the HS Fe(II) ion reappear with strong paramagnetic shifts (Figure 8.5 B) indicating the [HS-LS]↔[LS-HS] exchange becomes slow in the NMR timescale.

The typical Curie behaviour of the paramagnetic signals indicates that [HS-HS]→[HS-LS] transition is complete below 220K. For the intermediate [HS-LS] state, the signals for the protons close to the LS Fe(II) ion fall in the diamagnetic region of the spectra. Thus, the complete assignment of for all the protons is nearly impossible in view of both observed dynamics and the crowded diamagnetic region with additional minor mixtures of the free ligand and possibly diamagnetic (X@[Fe(H<sub>2</sub>L)<sub>3</sub>]<sub>2</sub>)<sup>3+</sup> (**21** and **22**) jellyfish-like species<sup>2</sup> and broadening caused at low temperatures.

The signals for protons 7 and 9 (as labeled in Figure 8.5 A) in the central phenyl moiety follow the expected behavior for the [HS-LS] ↔[LS-HS] process (Figure 8.5 D), therefore, they can be used to qualitatively analyse the SCO for the [X@Fe<sub>2</sub>(H<sub>2</sub>L)<sub>3</sub>]<sup>3+</sup> (**19** and **20**) helicates. Among them, the use of the signal of external proton 9 is most appropriate for this goal since it is farthest from HS ion and only undergoes small interferences from different mechanisms of hyperfine interactions.<sup>17</sup>

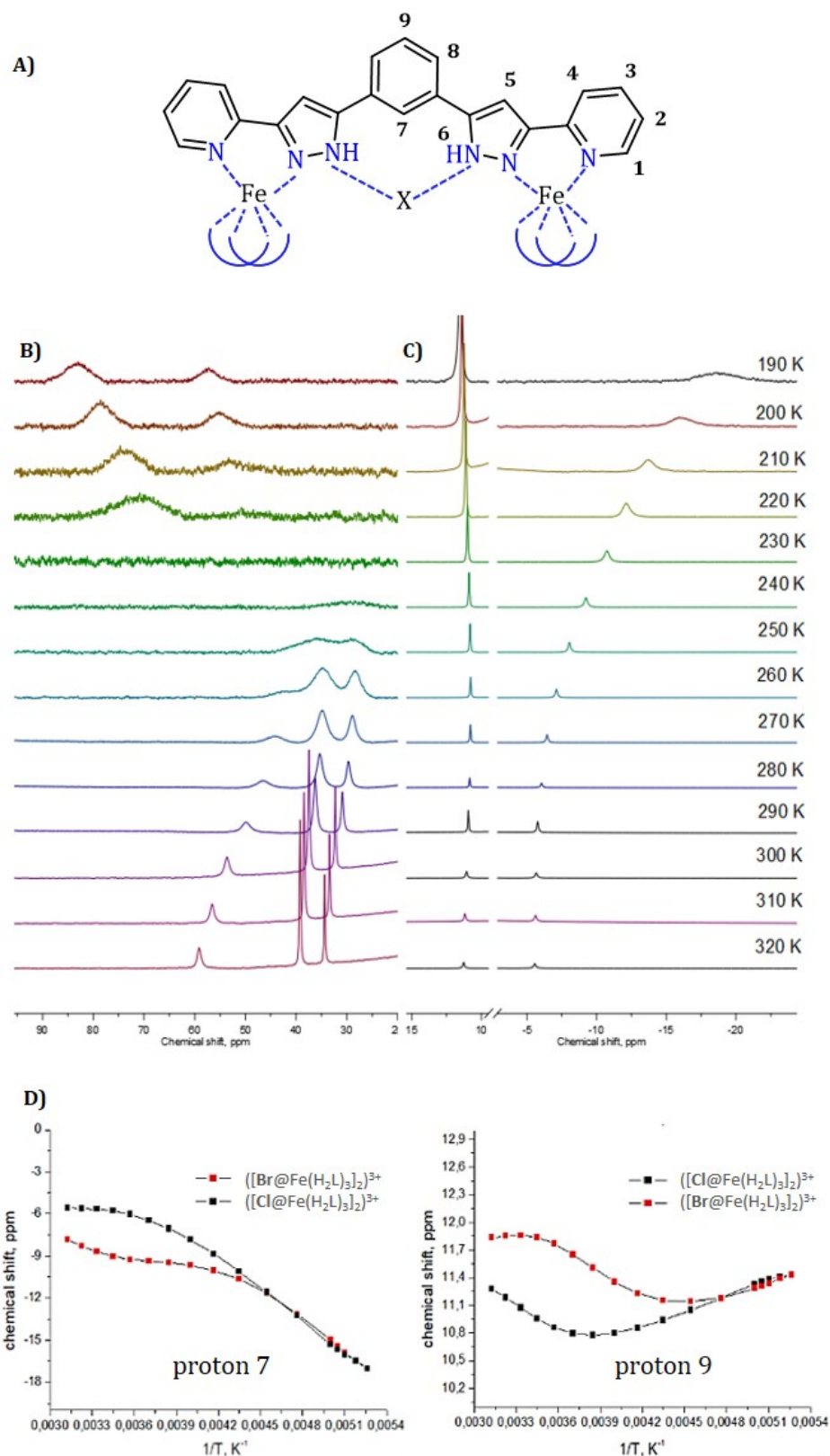


Figure 8.5. A) Representation of the coordination of ligand  $H_2L$  in  $[X@Fe_2(H_2L)_3]^{3+}$  helicates (**19** and **20**) with the labelled protons.  $^1H$  NMR spectra of **19** and **20** collected in methanol- $d_4$  at the selected temperatures in B) weak and C) strong field regions. D) Paramagnetic shift vs.  $1/T$  for the invariant protons of the central phenyl moiety). See Figures A8.4-A8.11 in Appendix 8 for other signals and  $^1H$  NMR in  $[X@Fe_2(H_2L)_3]^{3+}$  (**19** and **20**) at variable temperatures.

The SCO curves from the variable temperature NMR spectra (Figure 8.6) for both  $[\text{Cl@Fe}_2(\text{H}_2\text{L})_3]^{3+}$  (**19**) and  $[\text{Br@Fe}_2(\text{H}_2\text{L})_3]^{3+}$  (**20**) were appropriately accessed by simultaneously analyzing the temperature dependence of their respective chemical shifts in their deuterated solutions of methanol and acetonitrile. These SCO curves show a strong anion- and solvent dependence. The thermodynamic parameters obtained (Table A8.2; Appendix 8), which are typical for thermally induced SCO iron (II) complexes,<sup>18,19</sup> were compared with solid-state measurements.<sup>1</sup> Thus, correlation between the two encapsulated anion (Cl and Br) were revealed. As observed in the solid-state,<sup>1</sup> the difference between the  $T_{\text{SCO}}$  for  $[\text{Cl@Fe}_2(\text{H}_2\text{L})_3]^{3+}$  (**19**) and  $[\text{Br@Fe}_2(\text{H}_2\text{L})_3]^{3+}$  (**20**) in methanol- $d_4$  is close to the reported 40K. These results confirm that the influence of the halogen anion encapsulated inside the helicates on the SCO behavior is ascribed to intramolecular interaction rather than arising from crystal packing effects. Using acetonitrile as solvent allows to further modify this behavior by shifting the SCO curves by additional 20 to 40K (Figure 8.5).

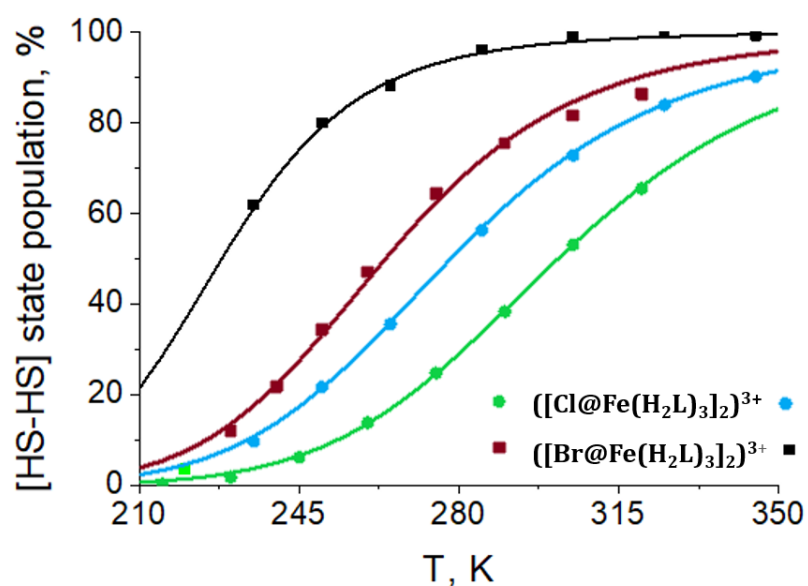


Figure 8.6. Percentage of [HS-HS] state population for  $[\text{X@Fe}_2(\text{H}_2\text{L})_3]^{3+}$  (**19** and **20**) in methanol- $d_4$  (green and brown dots) and acetonitrile- $d_3$  (black and blue dots) at selected temperatures resulting from the paramagnetic shift of proton 9 of the central phenyl moiety. The lines correspond to the best fittings using a regular solution model.<sup>20</sup>



**Crystal structures of (I@[Fe(H<sub>2</sub>L5)<sub>3</sub>]<sub>2</sub>)(PF<sub>6</sub>)<sub>3</sub> (**24**), (Br@[Fe(H<sub>2</sub>L5)<sub>3</sub>]<sub>2</sub>)(PF<sub>6</sub>)<sub>3</sub> (**25**), (Cl@[Fe(H<sub>2</sub>L5)<sub>3</sub>]<sub>2</sub>)(PF<sub>6</sub>)<sub>3</sub> (**26**) and (Cl@[Fe(H<sub>2</sub>L5)<sub>3</sub>]<sub>2</sub>)(ClO<sub>4</sub>)<sub>3</sub> (**27**)**

Due to the the poor diffraction of the crystals for the series of jellyfish-like complexes (**24**), (**25**) and (**26**) encapsulating different halides and (**27**) with a different counterion, only the accurate composition of complexes **24** and **27** was elucidated. However, a preliminary solution and crystallographic data for complexes **25** and **26** are given in Appendix 8.

**Crystal structure of (I@[Fe(H<sub>2</sub>L5)<sub>3</sub>]<sub>2</sub>)(PF<sub>6</sub>)<sub>3</sub> (**24**)**

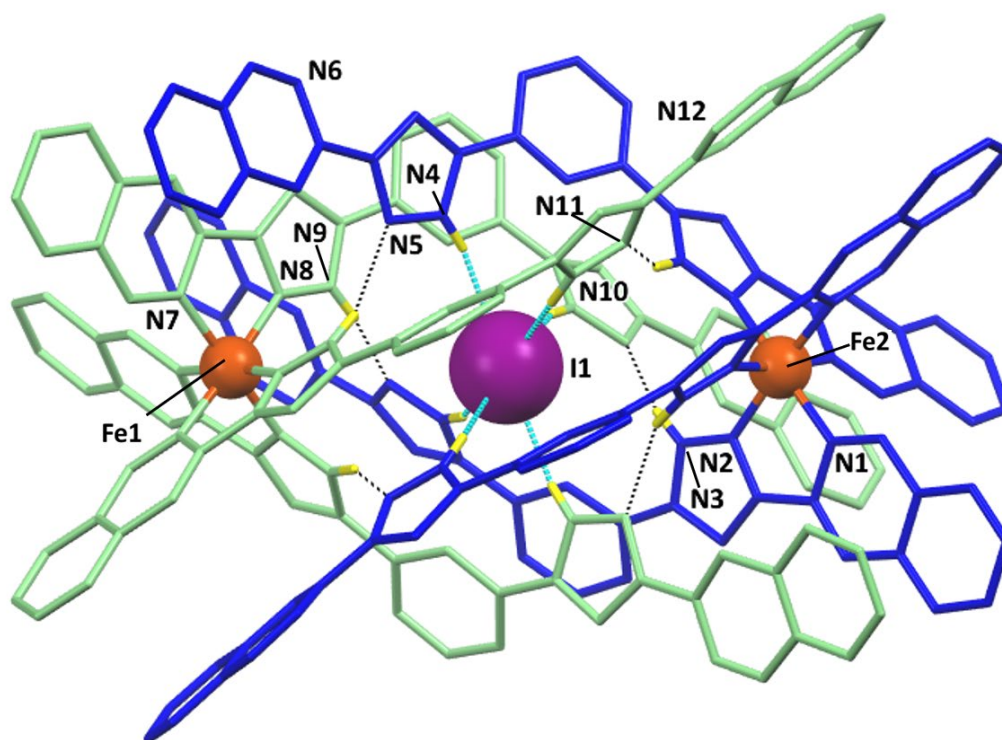


Figure 8.7. Representation of the (X@[Fe(H<sub>2</sub>L5)<sub>3</sub>]<sub>2</sub>)<sup>3+</sup> supramolecular assembly in **24** (X: I). The ligands of each [Fe(H<sub>2</sub>L5)<sub>3</sub>]<sup>2+</sup> unit are shown in different colors (blue and green). Unique heteroatoms are labels and the N-H groups are only one shown in yellow. The six N-H...I hydrogen bonds are highlighted in dashed cyan lines while the six N-H...N interactions are in dashed black.

At 100K, compound **24** crystallizes in the trigonal space group *R*-3*c* (Table A8.3; Appendix 8). The asymmetric unit contains two [Fe(H<sub>2</sub>L5)<sub>3</sub>]<sup>2+</sup> moieties, a central iodine as guest and three disordered PF<sub>6</sub><sup>-</sup> anions compensating the overall charge (Figure A8.12, Appendix 8). The whole supramolecular assembly (I@[Fe(H<sub>2</sub>L5)<sub>3</sub>]<sub>2</sub>)<sup>3+</sup> (Figure 8.7 and A8.13 in Appendix 8) is formed by two discrete mononuclear complexes with the formula [Fe(H<sub>2</sub>L5)<sub>3</sub>]<sup>2+</sup> that interact creating a central cavity with an iodine anion encapsulated. The unit cell encloses twenty-four

of such supramolecular ensembles. Each mononuclear unit consist in one Fe(II) center bounded to three H<sub>2</sub>L5 offering a pseudo-octahedral environment around the Fe(II) center. For the [FeN<sub>6</sub>] cores, the Fe-N distances (average of 1.967 and 1.973 for Fe1 and Fe2, respectively) at 100K indicating the LS state for both irons (Table A8.4.; Appendix 8). Thus, the ditopic ligand only coordinates from one chelating pocket, while the other side is not coordinated (Figure 8.8 and A8.14 in Appendix 8). The resulting pendant arms of the three H<sub>2</sub>L5 ligands interact with their counterparts for the other [Fe(H<sub>2</sub>L5)<sub>3</sub>]<sup>2+</sup> unit, yielding the helical supramolecular architecture with the encapsulated halide. The anion exhibits six N-H...I hydrogen bonds, one with each of the six H<sub>2</sub>L5 ligands. Additionally, each ligand H<sub>2</sub>L5 displays strong N-H...N interactions with the equivalent ligand from the opposite mononuclear unit (Figure 8.7 and Table A8.5 in Appendix 8).

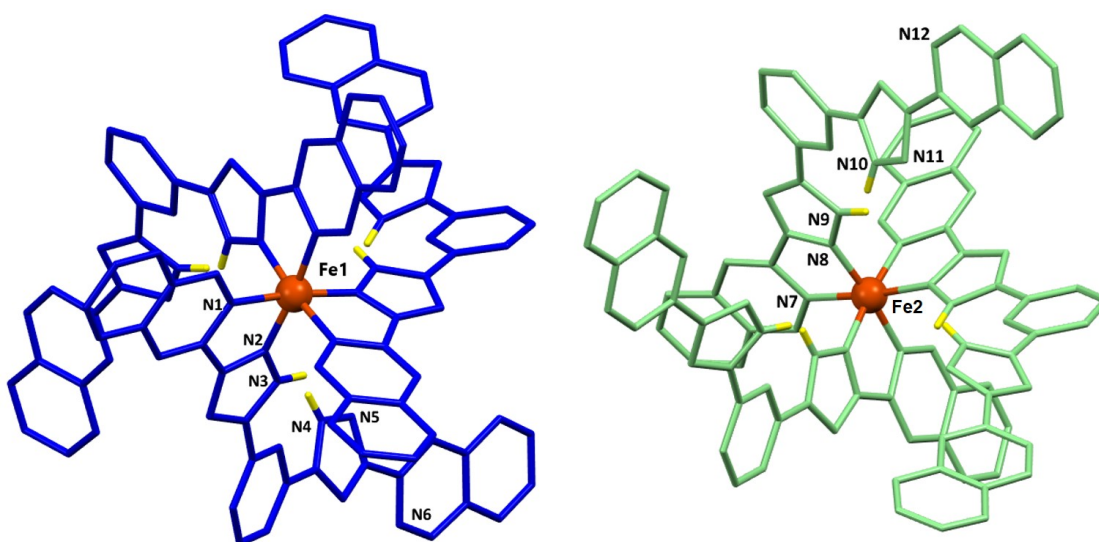


Figure 8.8. Representation of the individualized mononuclear units  $\text{Fe}[\text{H}_2\text{L5}]_3^{2+}$  of the dimerized complex found for **24** in the same special position (blue ligands point away from the reader and green ligands toward the reader). Counter ions, encapsulated I<sup>-</sup> and solvent are omitted for clarity. Only the hydrogen atoms of the N-H groups are shown.

Besides these twelve hydrogen bonds, the supramolecular architecture is also fastened by a vast series of  $\pi\cdots\pi$  interactions between parallel pairs of H<sub>2</sub>L5 ligands forming part of the two opposite [Fe(H<sub>2</sub>L5)<sub>3</sub>]<sup>2+</sup> units. The aromatic rings of each H<sub>2</sub>L5 are engaged in seven  $\pi\cdots\pi$  connections. Therefore, the whole (I@[Fe(H<sub>2</sub>L5)<sub>3</sub>]<sub>2</sub>)<sup>3+</sup> host-guest assembly is stabilized by a total of twenty-one

$\pi$ -stacking interactions (Figure 8.9 and Table A8.6 in Appendix 8). These features allow to rationalize the formation of this jellyfish-like structure (**24**) even in the reaction conditions used to prepare the triple-stranded helicates (such as **19** and **20**) with the similar but shorter H<sub>2</sub>L1 ligand. H<sub>2</sub>L5 has two terminal naphthyl groups instead of a phenyl for H<sub>2</sub>L1, which in turns, increases the number of  $\pi\cdots\pi$  stacking interactions between the pendant arms of the mononuclear jellyfish units. In this case, six additional  $\pi\cdots\pi$  interactions hold the whole (I@[Fe(H<sub>2</sub>L5)<sub>3</sub>]<sub>2</sub>)<sup>3+</sup> (**24**) jellyfish-like assembly compared to the similar ([X@Fe(H<sub>2</sub>L)<sub>3</sub>]<sub>2</sub>)<sup>3+</sup> (X= Cl and Br, for compounds **21** and **22**, respectively) jellyfish-like complexes. Therefore, the formation (**24**) is preferred over its putative triple-stranded helicate derivative.

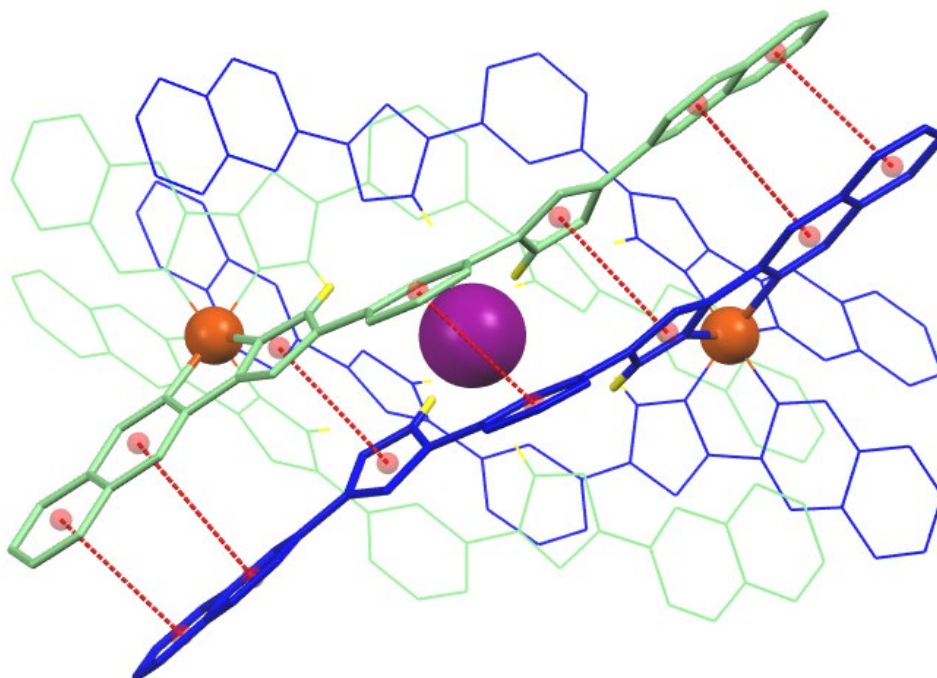


Figure 8.9. Representation of the  $\pi\cdots\pi$  stacking interactions between the seven aromatic rings of the parallel H<sub>2</sub>L5 ligands from the [Fe(H<sub>2</sub>L5)<sub>3</sub>]<sup>2+</sup> components of **24** (shown in different colors). Small red balls are the calculated centroid for each aromatic ring and the distance between them highlighted in dashed red lines.

In addition to the described intra-dimer interactions, the dimers interact with external components. The intermolecular interactions and the crystal packing are depicted in Appendix 8. The crystal lattice of **24** is formed by rods of (I@[Fe(H<sub>2</sub>L5)<sub>3</sub>]<sub>2</sub>)<sup>3+</sup> units with the irons parallelly aligned (Figure A8.15; Appendix 8). The jellyfish-like complexes within the rods are involved in six C-H $\cdots\pi$  interactions between the pyridyl rings (Figure A8.16).

**Crystal structure of  $(\text{Cl}@\text{[Fe}(\text{H}_2\text{L5})_3]_2)(\text{ClO}_4)_3$  (**27**)**

At 100K, compound **27** crystallizes in the trigonal space group  $P\bar{3}$  (Table A8.3; Appendix 8). The asymmetric unit contains six crystallographic independent iron ions each of them involved in one third of the  $[\text{Fe}(\text{H}_2\text{L5})_3]^{2+}$  moiety, three perchlorates, three encapsulated chlorides with one third of the occupation that compensate the overall charge, two molecules of water and two water molecules occupying one third as a solvent (Figure A8.17; Appendix 8). The whole supramolecular assembly  $(\text{Cl}@\text{[Fe}(\text{H}_2\text{L5})_3]_2)^{3+}$  is also formed by two discrete complexes with the formula  $[\text{Fe}(\text{H}_2\text{L5})_3]^{2+}$  that interact creating the cavity with a chloride anion encapsulated (Figure 8.10). However, in this case, the compound is formed by three dimerized mononuclear triple-stranded (jellyfish-like) complexes (Figure A8.18 and Tables A8.3 and A8.4; Appendix 8).

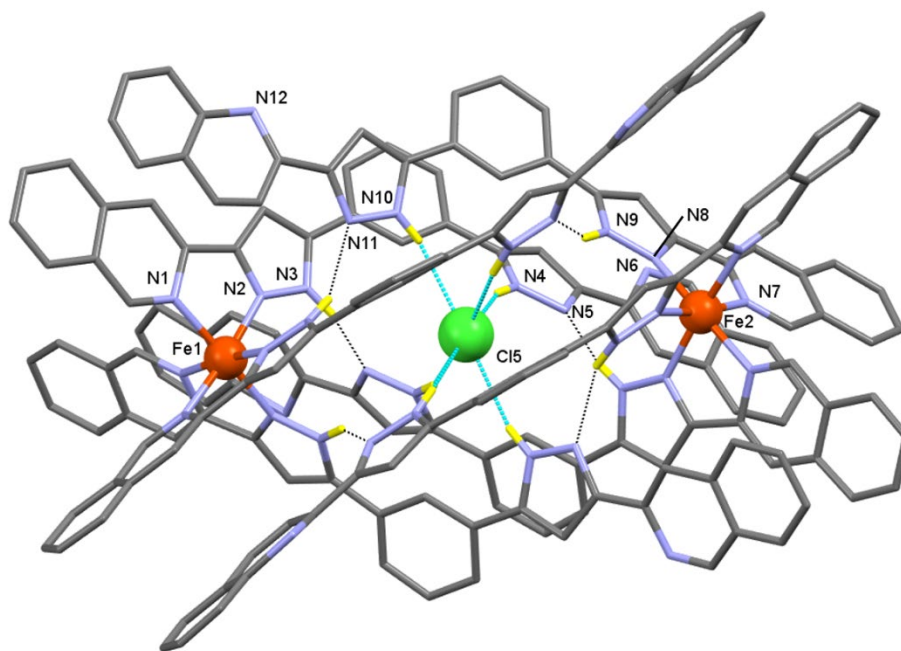


Figure 8.10. Representation of the  $([\text{X}@\text{Fe}(\text{H}_2\text{L})_3]_2)^{3+}$  supramolecular assembly in **27** (X: Cl). Unique heteroatoms are labels and the N-H groups are only one shown in yellow. The six N-H...I- hydrogen bonds are highlighted in dashed cyan lines while the six N-H...N interactions are in dashed black.

All iron ions are in the LS state (See Table A8.4; Appendix) at this temperature. The anion also exhibits six N-H...X (X=Cl) hydrogen interactions and six N-H...N interactions with the equivalent ligand from the opposite mononuclear unit (Table A8.5; Appendix 8). In the same way, the supramolecular architecture is fastened by seven  $\pi\cdots\pi$  interactions between parallel pairs of H<sub>2</sub>L5 ligands (Figure A8.19; Appendix 8).

Compounds **25** and **26** display the same space group, crystallographic arrangement of the dimerized mononuclear complexes. Thus, their preliminary elucidation of their crystalline structure allows to establish some sort of isostructurality despite the different counterion containing. Further refinement is required (Figure A8.20).

### 8.3. Conclusions

In this chapter we report the first attempt to identify the dynamics of a broken symmetry state system, [HS-LS] and [LS-HS], of binuclear  $X@[Fe_2(H_2L)_3]^{3+}$  (**19** and **20**) helicates on the millisecond timescale by using paramagnetic NMR spectroscopy. The contribution made here could have implications for the search of double-dot quantum cellular automata (QCA) by exploiting two degenerated but distinguishable states within one molecule.<sup>21,22</sup> If these two states are contemplated as two individual bits for information storage and processing, the observed fast [HS-LS]↔[LS-HS] equilibrium would result in their deleterious scrambling unless they are additionally stabilized by external factors. It is clearly attainable in the solid state by crystal packing effects.<sup>1,5,6</sup> However, there are some chances to reduce the exchange rate at the single-molecule level. Of them, the rigidity increase of the ligand by rational design should increase the kinetic barrier between the [HS-LS] and [LS-HS] states, and thus resulting in slower enough dynamics to use such kind of binuclear SCO-active complexes for data-processing applications.<sup>23</sup>

In addition, we demonstrate that the desired “jellyfish” supramolecular architecture is accessed through the rational design of ligand H<sub>2</sub>L5. The specific addition of two aromatic rings in the terminal location of the previously reported H<sub>2</sub>L ligand (two terminal naphthyl groups instead of the phenyl ones) is crucial to promote the formation of this scarce type of supramolecular assemblies. The results demonstrate that the favoured self-assembly of the dimerized mononuclear  $[X@Fe(H_2L5)_3]_2^{3+}$  (**24** to **27**) with respect to the triple-stranded helicate product is due to the enhancement of  $\pi\cdots\pi$  interactions between the pendant arms of the mononuclear  $[Fe(H_2L5)_3]^{2+}$  counterparty units.

## 8.4. Experimental

### Synthesis

The bis(pyrazolylpyridin) ligand H<sub>2</sub>L and the iron(II) helicates **19** and **20** were synthesized following the previously reported procedure by our group. The ligand 1,3-bis(3-(isoquinolin-3-yl)-1*H*-pyrazol-5-yl)benzene, H<sub>2</sub>L5, was prepared according to the procedure previously reported in chapter 5.

**Cl@[Fe<sub>2</sub>(H<sub>2</sub>L)<sub>3</sub>] (19).** <sup>1</sup>H NMR (600 MHz, methanol-d<sub>4</sub>, 290 K): 50.2 (1H, br. s.), 36.4 (4/5H, br. s.), 31.0 (2H, br. s.), 10.9 (9H, t, <sup>3</sup>J<sub>H-H</sub> = 7 Hz), 4.5 (8H, d, <sup>3</sup>J<sub>H-H</sub> = 7 Hz), 3.5 (3H, br. s.), -5.8 (7H, br. s.). <sup>1</sup>H NMR (600 MHz, acetonitrile-d<sub>3</sub>, 285 K): 56.9 (1H, br. s.), 39.5 (4/5H, br. s.), 33.9 (2H, br. s.), 11.4 (9H, br. s.), -6.4 (7H, br. s.), 16.3 (6H, br. s.), 4.2 (8H, br. s.), 2.9 (3H, br. s.).

**Br@[Fe<sub>2</sub>(H<sub>2</sub>L)<sub>3</sub>] (20).** <sup>1</sup>H NMR (600 MHz, methanol-d<sub>4</sub>, 290 K): 66.5 (1H, br. s.), 46.0 (4H, br. s.), 45.4 (5H, br. s.), 39.3 (2H, br. s.), 11.8 (9H, br. s.), 4.2 (8H, br. s.), 2.6 (3H, br. s.), -9.0 (7H, br. s.). <sup>1</sup>H NMR (600 MHz, acetonitrile-d<sub>3</sub>, 285 K): 72.5 (1H, br. s.), 49.5 (4H, br. s.), 48.9 (5H, br. s.), 42.1 (2H, br. s.), 14.8 (6H, br. s.), 12.3 (9H, br. s.), 4.1 (8H, br. s.), -9.9 (7H, br. s.).

**[Br@Zn<sub>2</sub>(H<sub>2</sub>L)<sub>3</sub>]Br(PF<sub>6</sub>)<sub>2</sub>·0.5C<sub>4</sub>H<sub>10</sub>O·4CH<sub>4</sub>O (23).** A suspension of H<sub>2</sub>L (25 mg, 0.069 mmol) in methanol (10 mL) was added dropwise to a methanolic solution (10 mL) of ZnBr<sub>2</sub> (10.35 mg, 0.046 mmol). An uncoloured solution formed, which was stirred for 45 minutes, filtered and the filtrate treated with a methanolic (10 mL) solution of NBu<sub>4</sub>PF<sub>6</sub> (14 mg, 0.036 mmol) and stirred for ten minutes. The resulting solution was poured in small vials for vapor diffusion with ether in the fridge, which yielded white crystals after a few days.

**(I@[Fe(H<sub>2</sub>L)<sub>3</sub>]<sub>2</sub>)(PF<sub>6</sub>)<sub>3</sub>·[7CH<sub>3</sub>OH] (24):** A suspension of ligand H<sub>2</sub>L5 (10 mg, 0.021 mmols) in methanol/acetone (1:1, 20ml) was added dropwise to a solution of FeI<sub>2</sub> (4.4 mg, 0.014 mmols) in methanol/acetone (1:1, 10 ml). The yellow solution formed, was stirred for 45 min, filtered, and the filtrate mixed with a solution of NBu<sub>4</sub>PF<sub>6</sub> (4.3 mg, 0.011 mmol) in methanol/acetone (1:1, 4ml). The resulting solution was layered with toluene and yielded red crystal after one month.

**(Br@[Fe(H<sub>2</sub>L<sub>5</sub>)<sub>3</sub>]<sub>2</sub>)(PF<sub>6</sub>)<sub>3</sub> (25)**: A suspension of ligand H<sub>2</sub>L<sub>5</sub> (10 mg, 0.021 mmols) in methanol (10 ml) was added dropwise to a solution of FeBr<sub>2</sub> (3.1 mg, 0.014 mmols) in methanol (5 ml). An orange solution formed, which was stirred for 45 min, filtered, and the filtrate mixed with a solution of NBu<sub>4</sub>PF<sub>6</sub> (4.3 mg, 0.011 mmol) in methanol (2 ml). Vapor diffusion of diethyl ether into the resulting solution yielded red crystals after a week.

**(Cl@[Fe(H<sub>2</sub>L<sub>5</sub>)<sub>3</sub>]<sub>2</sub>)(PF<sub>6</sub>)<sub>3</sub> (26)**. A suspension of ligand (10 mg, 0.021 mmols) in methanol (10 ml) was added dropwise to a solution of FeCl<sub>2</sub>·4H<sub>2</sub>O (2.9 mg, 0.014 mmols) in methanol (5 ml). An orange solution formed, which was stirred for 45 min, filtered, and the filtrate mixed with a solution of NBu<sub>4</sub>PF<sub>6</sub> (4.3 mg, 0.011 mmol) in methanol (2 ml). Vapor diffusion of diethyl ether into the resulting solution yielded red crystals after a week.

**(Cl@[Fe(H<sub>2</sub>L<sub>5</sub>)<sub>3</sub>]<sub>2</sub>)(ClO<sub>4</sub>)<sub>3</sub> (27)**. A suspension of ligand (10 mg, 0.021 mmols) in methanol (10 ml) was added dropwise to a solution of FeCl<sub>2</sub>·4H<sub>2</sub>O (2.9 mg, 0.014 mmols) in methanol (5 ml). An orange solution formed, which was stirred for 45 min, filtered, and the filtrate mixed with a solution of NBu<sub>4</sub>ClO<sub>4</sub> (4.3 mg, 0.011 mmol) in methanol (2 ml). Vapor diffusion of diethyl ether into the resulting solution yielded red crystals after a week.

## 8.5. References

- (1) Darawsheh, M.; Barrios, L. A.; Roubeau, O.; Teat, S. J.; Aromí, G. *Chem. - A Eur. J.* **2016**, *22*, 8635–8645.
- (2) Darawsheh, M. D.; Barrios, L. A.; Roubeau, O.; Teat, S. J.; Aromí, G. *Chem. Commun.* **2017**, *53*, 569–572.
- (3) Ortega-Villar, N.; Muñoz, M.; Real, J. *Magnetochemistry* **2016**, *2*, 16.
- (4) Moussa, N. O.; Trzop, E.; Mouri, S.; Zein, S.; Molnár, G.; Gaspar, A. B.; Collet, E.; Buron-Le Cointe, M.; Real, J. A.; Borshch, S.; Tanaka, K.; Cailleau, H.; Bousseksou, A. *Phys. Rev. B - Condens. Matter Mater. Phys.* **2007**, *75*, 1–8.
- (5) Klingele, M. H.; Moubaraki, B.; Cashion, J. D.; Murray, K. S.; Brooker, S. *Chem. Commun.* **2005**, *2*, 987–989.
- (6) Hogue, R. W.; Feltham, H. L. C.; Miller, R. G.; Brooker, S. *Inorg. Chem.* **2016**, *55*, 4152–4165.

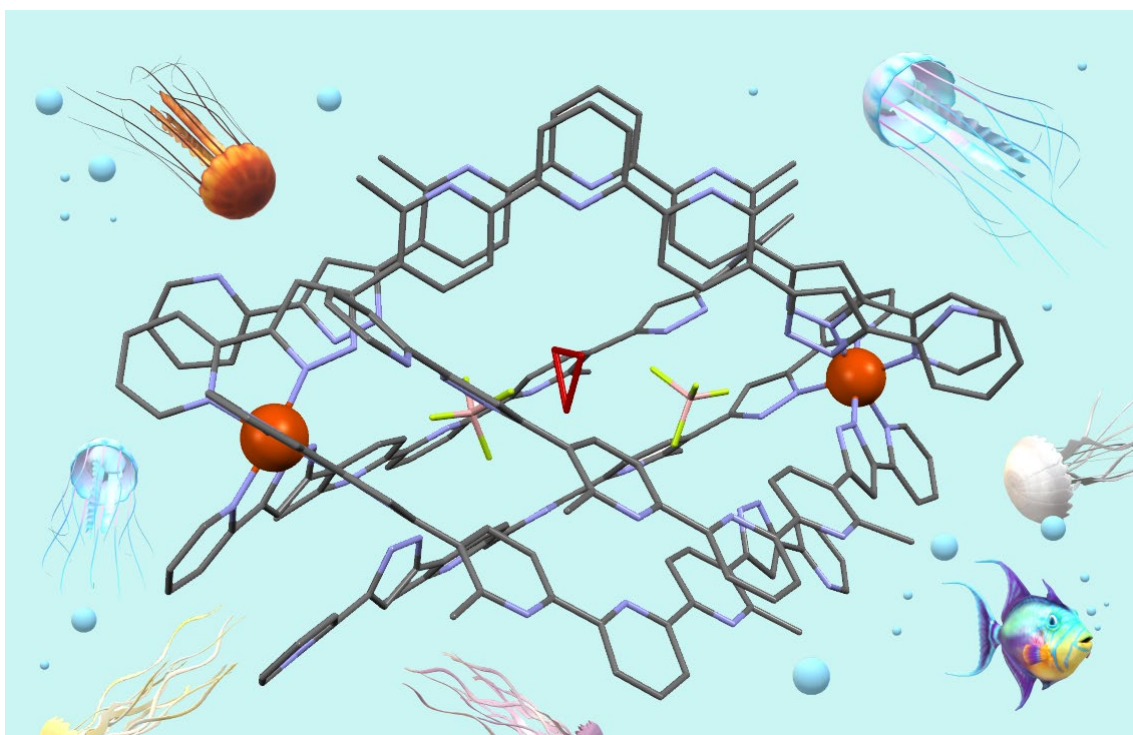
- (7) Amoore, J. J. M.; Kepert, C. J.; Cashion, J. D.; Moubaraki, B.; Neville, S. M.; Murray, K. S. *Chem. - A Eur. J.* **2006**, *12*, 8220–8227.
- (8) Telfer, S. G.; Bocquet, B.; Williams, A. F. *Inorg. Chem.* **2001**, *40*, 4818–4820.
- (9) Halcrow, M. *Crystals* **2016**, *6*, 58.
- (10) Diego, R.; Pavlov, A.; Darawsheh, M.; Aleshin, D.; Nehr Korn, J.; Nelyubina, Y.; Roubeau, O.; Novikov, V.; Aromí, G. *Inorg. Chem.* **2019**, *58*, 9562–9566.
- (11) Parigi, G.; Ravera, E.; Luchinat, C. *Prog. Nucl. Magn. Reson. Spectrosc.* **2019**, *114–115*, 211–236.
- (12) Petzold, H.; Hörner, G.; Schnaubelt, L.; Ruffer, T. *Dalt. Trans.* **2018**, *47*, 17257–17265.
- (13) Petzold, H.; Djomgoue, P.; Hörner, G.; Speck, J. M.; Ruffer, T.; Schaarschmidt, D. *Dalt. Trans.* **2016**, *45*, 13798–13809.
- (14) Pavlov, A. A.; Denisov, G. L.; Kiskin, M. A.; Nelyubina, Y. V.; Novikov, V. V. *Inorg. Chem.* **2017**, *56*, 14759–14762.
- (15) Pankratova, Y.; Aleshin, D.; Nikovskiy, I.; Novikov, V.; Nelyubina, Y. *Inorg Chem* **2020**, *59*, 7700–7709.
- (16) Range, D. *Dynamic NMR Spectroscopy*; Diehl, P., Fluck, E., Kosfeld, R., Eds.; Springer Science & Business Media, 2012.
- (17) Pavlov, A. A.; Nehr Korn, J.; Zubkevich, S. V.; Fedin, M. V.; Holldack, K.; Schnegg, A.; Novikov, V. V. *Inorg. Chem.* **2020**, *59*, 10746–10755.
- (18) Kershaw Cook, L. J.; Kulmaczewski, R.; Mohammed, R.; Dudley, S.; Barrett, S. A.; Little, M. A.; Deeth, R. J.; Halcrow, M. A. *Angew. Chem., Int. Ed.* **2016**, *55*, 4327–4331.
- (19) Galadzhun, I.; Kulmaczewski, R.; Cespedes, O.; Yamada, M.; Yoshinari, N.; Konno, T.; Halcrow, M. A. *Inorg. Chem.* **2018**, *57*, 13761–13771.
- (20) Weber, B.; Walker, F. A. *Inorg. Chem.* **2007**, *46*, 6794–6803.
- (21) Schneider, B.; Demeshko, S.; Neudeck, S.; Dechert, S.; Meyer, F. *Inorg. Chem.* **2013**, *52*, 13230–13237.
- (22) Lu, Y.; Lent, C. S. *Nanotechnology* **2008**, *19*.
- (23) Matsumoto, T.; Newton, G. N.; Shiga, T.; Hayami, S.; Matsui, Y.; Okamoto, H.; Kumai, R.; Murakami, Y.; Oshio, H. *Nat. Commun.* **2014**, *5*, 1–8.



# CHAPTER 9

---

## CONCLUSIONS AND FUTURE PERSPECTIVES





The results obtained along this thesis clearly contribute to the molecular magnetism area related to spin crossover or single-molecule magnetism, being some of them new and unique in the field. Despite the extensive library of versatile compounds exhibiting SCO and SMM behaviour, continuous growth in the knowledge of such molecular magnetic complexes is pursued at the time in order to understand fundamental insights of both phenomena. Therefore, we mainly contribute on expanding notions explored in previous works and unveiling crucial aspects on the foundations of their magnetic properties.

Starting from the ligand design and synthesis of several 3-bpp derivatives, whose organic moieties display the appropriate crystal field and almost systematically lead to active-SCO compounds of Fe(II), diverse novel mononuclear compounds were accessed. The magnetic study of these compounds offered fruitful opportunities to unveil specific insights related to the SCO (Chapters 2 to 4). The structure of all compounds has been solved allowing to intensively study the influence of the different interactions within the crystals on the magnetic properties of the compounds.

In chapter 2, we can drastically modulate the SCO temperature for a series of three Fe(II) derivatives of 1,3-bpp of (2-(pyrazol-1-yl)-6-(1H-pyrazol-3-yl)pyridine:  $[\text{Fe}(1,3\text{-bpp})_2](\text{ClO}_4)_2$  (**1**),  $[\text{Fe}(\text{met}1,3\text{-bpp})_2](\text{ClO}_4)_2$  (**2**),  $[\text{Fe}(\text{dimet}1,3\text{-bpp})_2](\text{ClO}_4)_2$  (**3**), (containing none, one or two methyl substituents, respectively). The direct influence of the methyl substituents on the SCO temperature (with  $T_{\text{SCO}}(\mathbf{3}) > T_{\text{SCO}}(\mathbf{1}) > T_{\text{SCO}}(\mathbf{2})$ ), was observed through by magnetic studies in solid-state and in solution. From the solution studies and the rationalized origin of their effect by DFT calculations, the crystal packing was excluded as a contributor to their overall macroscopic properties, being the  $T_{1/2}$  tuned through ligand design.

In Chapter 3, we studied the metal composition effects on the SCO thermal transition of compound  $[\text{Fe}(\text{met}1,3\text{-bpp})_2](\text{ClO}_4)_2$  (**2**). For such purpose, the isostructural  $[\text{Zn}(\text{met}1,3\text{-bpp})_2](\text{ClO}_4)_2$  (**4**) complex and the series  $[\text{Fe}_{1-x}\text{Zn}_x(\text{Me-1,3bpp})_2](\text{ClO}_4)_2$  (**5x**; 0.1, 0.153, 0.219, 0.333, 0.412, 0.476, 0.559 and 0.636) were synthesized as a pure homogeneous solids. The structural study unveils the gradual evolution of the

crystallographic parameters with the metal composition at three levels: at the local, at the level of intermolecular interactions and in terms of the crystal lattice parameters. From the magnetic data, we analysed the effect of the composition for **5x** in terms of cooperativity and thermodynamic parameters of the SCO. We observed a decrease on the SCO temperature and an increase of the residual HS Fe (II), which can be ascribed to the negative chemical pressure that Zn(II) induces into the iron lattice. Additionally, we quenched the samples at 2K, observing that the relaxation temperature of the metastable state,  $T(\text{TIESST})$ , is unaffected by the composition.

In Chapter 4, an unprecedented heteroleptic compound,  $[\text{FeL}(\text{bpp})](\text{ClO}_4)_2$  (**6**), showing four markedly different magnetic responses (depending on the thermal history) at the same temperature range (300-340K) near room temperature is achieved. This molecular material is accessed after the diffusion of acetone out of the crystal lattice of **6·ac**, creating a template effect for the novel **6** phase. Thus, the system is flexible enough to undergo a succession of irreversible phase transitions  $\mathbf{6}\cdot\text{ac} \rightarrow \mathbf{6}^\alpha \rightarrow \mathbf{6}^\beta \rightarrow \mathbf{6}^\gamma$  in the solid-state upon several warming and cooling cycles. In turn, compound **6** is a robust enough system that allows to establish an intimate connection between the SCO and structural phase transitions (SPTs) through single-crystal X-ray diffraction (SCXRD) since it does not lose crystallinity. A similar compound (**7·ac**) is presented as a good candidate for further SCO exploration. Additionally, we tried to elucidate some insights on the importance of the N-H interaction within complex **6** by using its methylated derivative. Nevertheless, the direct effect of disrupting hydrogen bonds interactions could not be reached. Instead, a series of homoleptic  $[\text{FeL}_2](\text{ClO}_4)_2 \cdot 2\text{H}_2\text{O}$  (**8**),  $[\text{Fe}(\text{Me}_2\text{bbp})_2](\text{ClO}_4)_2$  (**9**) complexes and the  $[\text{FeL}(\text{H}_2\text{O})_2(\text{C}_3\text{H}_6\text{O})](\text{ClO}_4)_2 \cdot 2\text{C}_3\text{H}_6\text{O}$  (**10**) were obtained.

The results obtained from the fifth chapter mainly demonstrate the importance of the rational ligand design to access different supramolecular architectures with potential SCO behaviour. Thus, the design of the appropriate polytopic ligands containing pyrazolyl-pyridine moieties is first discussed in chapter 5. Five new organic ligands (**H<sub>2</sub>L3**, **H<sub>2</sub>L4**, **H<sub>2</sub>L5**, **H<sub>2</sub>L6** and **H<sub>2</sub>L7**) were designed, synthesized and fully characterized. For all of them, a Claisen condensation of the appropriate

starting materials, followed by the ring closure of the obtained  $\beta$ -bis-diketone, which is the standardized procedure in our research group, were used. However, some synthetic issues were faced when designing more complex multitopic ligands. Thus, a new promising synthetic route to access multitopic ligands is proposed. Ligand **H<sub>2</sub>L8** is satisfactorily synthesized using this new synthetic approach. Future optimization of the procedure should aim to replicate the results in a larger scale. Once optimized, more complex and large ligands may be obtained through only two-step route (a click-reaction followed by coupling-reaction). This, in turns, has an important host-guest chemistry repercussion since larger hosts structures can encapsulate bigger and more interesting guests, as well as leading to bi-functional systems.

By exploring the coordination chemistry of ligand H<sub>2</sub>L with Co (II) ions, which often behaves as SMM, the triple-stranded helicate [Co<sub>2</sub>(H<sub>2</sub>L)<sub>3</sub>]<sup>4+</sup> (**11**) was synthesized (Chapter 6). The six-coordinated Co(II) ions display an adequate geometry between the trigonal prismatic (TP) and the trigonal antiprismatic (TAP) to study and rationalize its small axial anisotropy, which was previously predicted, through solution paramagnetic <sup>1</sup>H NMR and solid-state magnetometry. Additionally, the study of the [CoZn(H<sub>2</sub>L)<sub>3</sub>]<sup>4+</sup> (**13**) helicate allows to discard the intramolecular magnetic interactions as a source of the low magnetic anisotropy. By modifying rationally the phenylene core or introducing capping fragments into the pyridine groups of H<sub>2</sub>L the local Co(II) geometry could be tuned to the ideal TP, and therefore higher axial anisotropy.

Two new [Fe<sub>9</sub>] grid-like supramolecular clusters composed of an unprecedented flat nanosheet with the formula [Fe<sub>9</sub>O<sub>4</sub>(OH)<sub>8</sub>] as an inorganic core and six H<sub>2</sub>L ligands acting as “pincers” are prepared and described in Chapter 7. Both polynuclear coordination complexes with the proposed molecular formula Fe<sub>9</sub>O<sub>4</sub>(OH)<sub>10</sub>(H<sub>2</sub>L)<sub>6</sub>(H<sub>2</sub>O)<sub>4</sub>](BF<sub>4</sub>)<sub>5</sub> (**17**) and [Fe<sub>9</sub>O<sub>4</sub>Cl<sub>6</sub>(OH)<sub>8</sub>(H<sub>2</sub>L)<sub>6</sub>]<sub>4</sub>(Cl) (**18**) display an interesting magnetic behaviour. However, further characterization, such as Mössbauer spectroscopy, is required to confirm with certainty the oxidation states of the iron metal centres. Considering its first formation together with triple-stranded helicates with the general formula Fe(C<sub>2</sub>O<sub>4</sub>)<sub>3</sub>@[Fe<sub>2</sub>(H<sub>2</sub>L)<sub>3</sub>] (**14**, **15** and

**16**), their obtaining and isolation is discussed. Regarding the latest compounds, the ferrioxalate guest seems to provide an effect template on the obtention of the helical structures since it is mainly crystallized after screening several different coordination chemistry conditions.

In chapter 8, we describe the first attempt on identifying the dynamics of a broken symmetry states, [HS-LS] and [LS-HS], of a binuclear  $X@[Fe_2(H_2L)_3]^{3+}$  (**19** and **20**) helicates on the millisecond timescale by using paramagnetic NMR spectroscopy. The contribution made here have a wide applicability on double-dot quantum cellular automata (QCA) by exploiting the two degenerated but distinguishable states. Additionally, new synthetically addressed jellyfish-like compounds,  $[(X@Fe(H_2L_5)_3)_2]^{3+}$  (**24**, **25** and **26**) were obtained by using the appropriate ligand  $H_2L_5$  with additional aromatic groups concerning the original ditopic  $H_2L$  ligand. Such compounds are attractive for studying in solution.

A jellyfish-like structure was obtained for ligand  $H_2L_4$  coordinated with Fe(II). The structure is depicted in Figure 9.1. Since its discovery was recent, we only give a preliminary description. Despite the judicious design to achieve a large and coordinating central unit by introducing the terpyridine moiety, this coordinating pocket do not participate on any M-L ligand. Instead, the C-C bonds of the terpyridine rotate, being some of the nitrogen pointing out to the central cavity created by the dimerized mononuclear unit. The central cavity encapsulates two  $BF_4^-$  and a distorted water over 3 sites. This is the largest jellyfish-like structure synthesised. The ongoing and future work is focused on reproduce and study the magnetic behaviour or this unique supramolecular structure.

Finally, it will be important that future research explore the coordination chemistry of ligands  $H_2L_3$ ,  $H_2L_6$  and  $H_2L_7$ . Despite several tries have been done during this thesis, any supramolecular architecture was achieved with them.

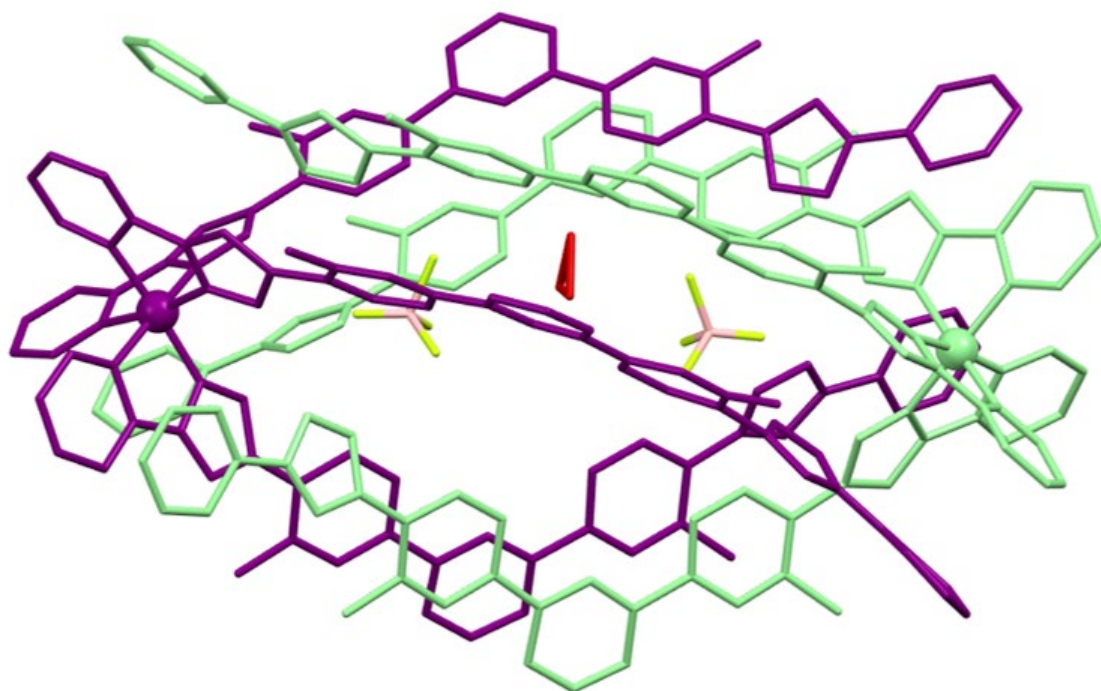


Figure 9.1. Representation of the  $(2\text{BF}_4\cdot\text{H}_2\text{O}@[Fe(\text{H}_2\text{L}_4)_3]_2)^{2+}$  supramolecular assembly. The ligands of each  $[Fe(\text{H}_2\text{L}_4)_3]^{2+}$  unit are shown in different colors (purple and green).





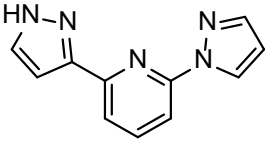
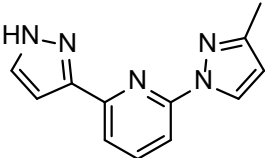
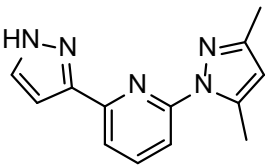
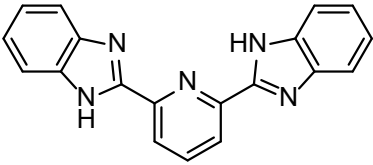
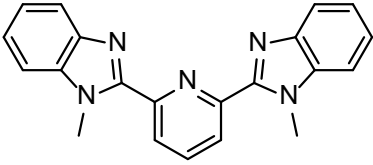
# APPENDIX

---

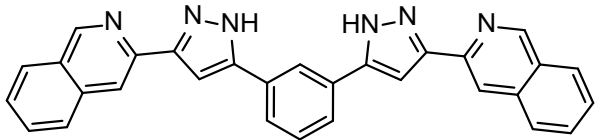
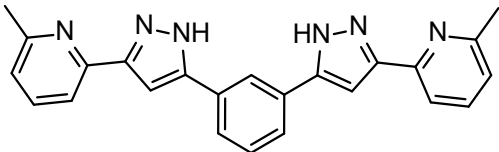
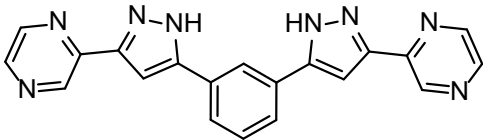
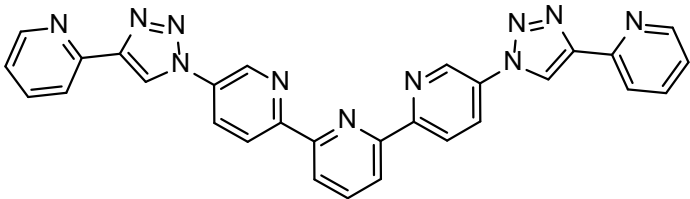


**APPENDIX 1 - CHAPTER 1. OVERVIEW OF THE SYNTHESIZED MATERIALS UNDER STUDY**

**Table A1.1.** List of ligands

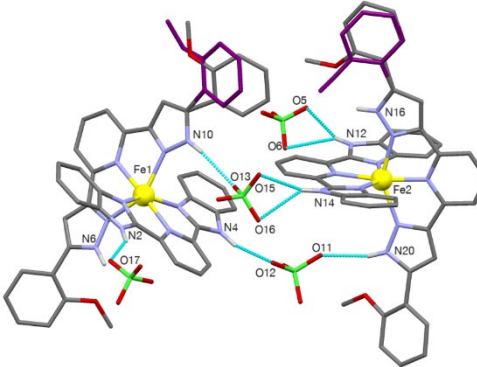
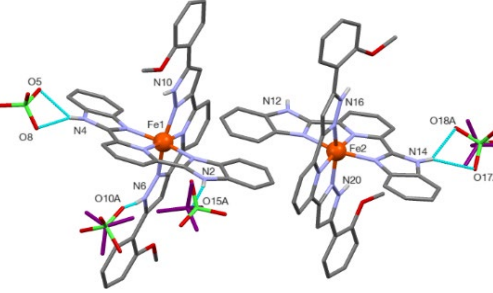
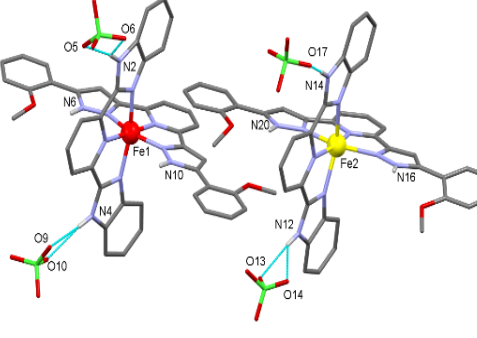
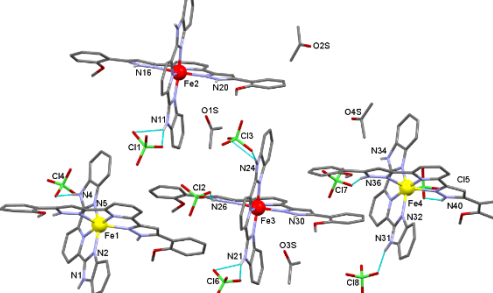
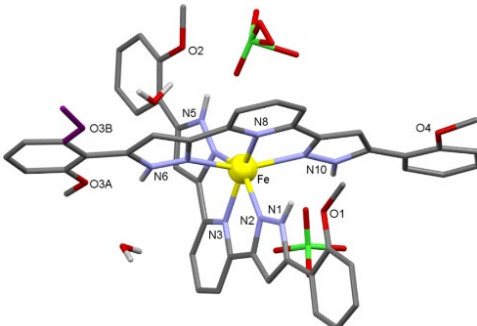
Ligand	Name	Structure
1,3-bpp	(2-(pyrazol-1-yl)-6-(1H-pyrazol-3-yl)pyridine	
Me-1,3-bpp	2-(3-methylpyrazol-1-yl)-6-(1H-pyrazol-3-yl)pyridine	
Me <sub>2</sub> -1,3-bpp	2-(3,5-dimethylpyrazol-1-yl)-6-(1H-pyrazol-3-yl)pyridine	
bbp	2,6-bis-(benzimidazol-2-yl)-pyridine	
NMe <sub>2</sub> bbp	2,6-bis-(1-methylbenzimidazol-2-yl)-pyridine	

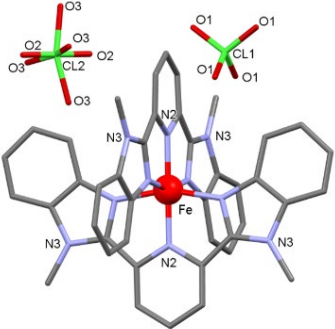
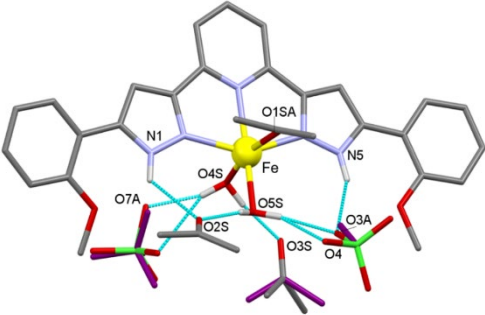
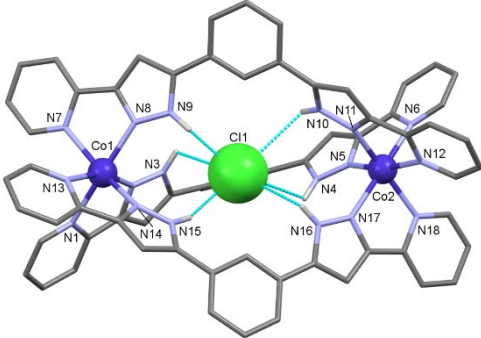
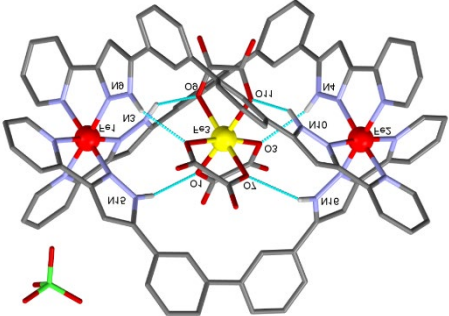
L	2,6-bis-(5-(2-methoxyphenyl)-pyrazol-3-yl)-pyridine	
H <sub>2</sub> L	1,3-bis(3-(pyridin-2-yl)-1H-pyrazol-5-yl)benzene	
H <sub>2</sub> L <sub>2</sub>	3,3'-bis(3-(pyridin-2-yl)-1H-pyrazol-5-yl)-1,1'-biphenyl	
H <sub>2</sub> L <sub>3</sub>	4,4''-bis(3-(pyridin-2-yl)-1H-pyrazol-5-yl)-1,1':3',1''-terphenyl	
H <sub>2</sub> L <sub>4</sub>	6,6''-dimethyl-5,5''-bis(3-(pyridin-2-yl)-1H-pyrazol-5-yl)-2,2':6',2''-terpyridine	

H <sub>2</sub> L5	1,3-bis(3-(isoquinolin-3-yl)-1H-pyrazol-5-yl)benzene	
H <sub>2</sub> L6	1,3-bis(3-(6-methylpyridin-2-yl)-1H-pyrazol-5-yl)benzene	
H <sub>2</sub> L7	1,3-bis(3-(pyrazin-2-yl)-1H-pyrazol-5-yl)benzene	
H <sub>2</sub> L8	5,5''-bis(4-(pyridin-2-yl)-4,5-dihydro-1H-1,2,3-triazol-1-yl)-2,2':6',2''-terpyridine	

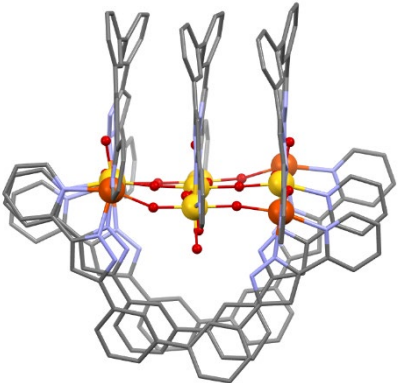
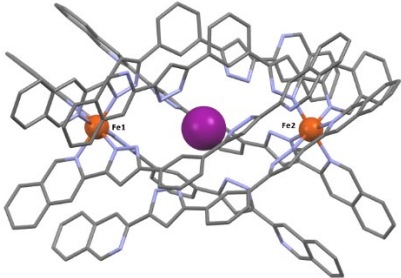
**Table A1.2.** List of complexes

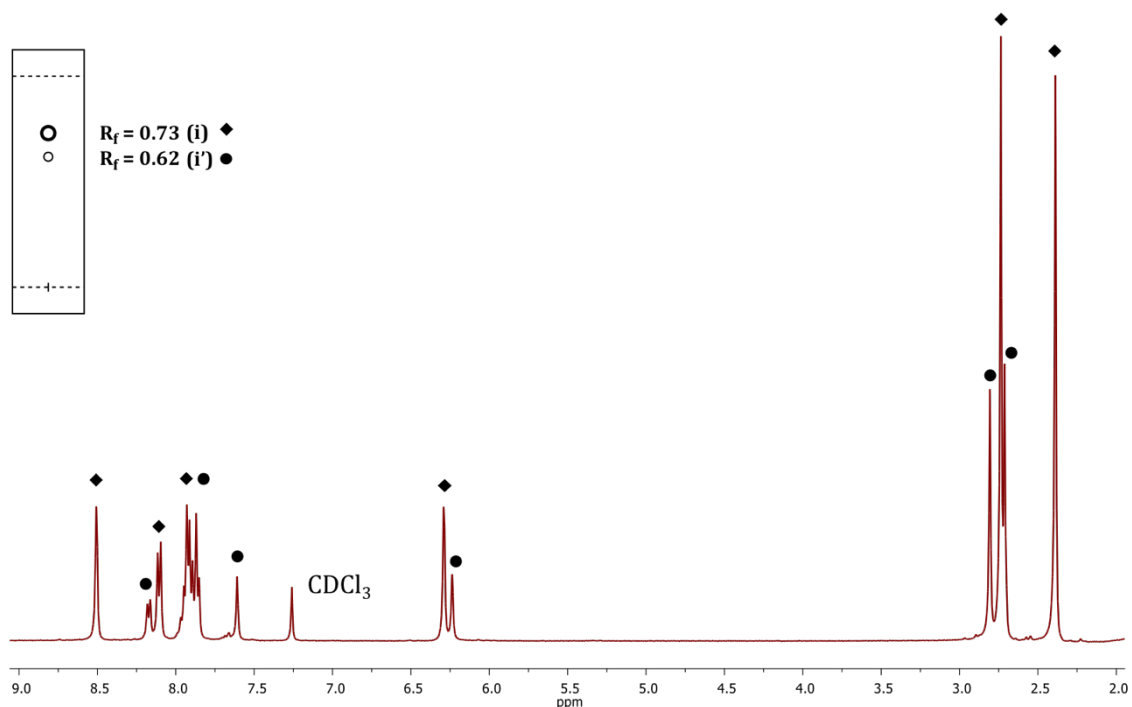
Number and chapter	Ligand	Complex formulation	Molecular representation
(1), <u>Chapter 2</u>	1,3-bpp	$[\text{Fe}(1,3\text{bpp})_2](\text{ClO}_4)_2$	
M= Fe (2), <u>Chapter 2</u>  M=Zn (4), <u>Chapter 3</u>  M=Fe <sub>1-x</sub> Zn <sub>x</sub> (5x; x=0.1, 0.153, 0.219, 0.333, 0.412, 0.476, 0.559 and 0.636) <u>Chapter 3</u>	Me <sub>1</sub> -1,3- bpp	$[\text{M}(\text{Me}-1,3\text{bpp})_2](\text{ClO}_4)_2$	
(3), <u>Chapter 2</u>	Me <sub>2</sub> -1,3- bpp	$[\text{Fe}(\text{Me}_2-1,3\text{bpp})_2](\text{ClO}_4)_2$	
(6•ac), <u>Chapter 4</u>	bbp and L	$[\text{FeL}(\text{bbp})](\text{ClO}_4)_2 \cdot \text{ac}$	

(6 <sup>α</sup> ), Chapter 4	bbp and L	*Series of Polymorphs: [FeL(bbp)](ClO <sub>4</sub> ) <sub>2</sub>	
(6 <sup>β</sup> ), Chapter 4	bbp and L	*Series of Polymorphs: [FeL(bbp)](ClO <sub>4</sub> ) <sub>2</sub>	
(6 <sup>γ</sup> ), Chapter 4	bbp and L	*Series of Polymorphs: [FeL(bbp)](ClO <sub>4</sub> ) <sub>2</sub>	
(7 <sup>ac</sup> ), Chapter 4	Na <sub>2</sub> -bbp and L	[FeL(bbp)](ClO <sub>4</sub> ) <sub>2</sub> ·ac	
(8), Chapter 4	L	[FeL <sub>2</sub> ](ClO <sub>4</sub> ) <sub>2</sub> ·2H <sub>2</sub> O	

(9), Chapter 4	NMe <sub>2</sub> bbp	[Fe(NMe <sub>2</sub> bbp) <sub>2</sub> ](ClO <sub>4</sub> ) <sub>2</sub>	
(10), Chapter 4	L	[FeL(H <sub>2</sub> O) <sub>2</sub> (C <sub>3</sub> H <sub>6</sub> O)](ClO <sub>4</sub> ) <sub>2</sub> · 2C <sub>3</sub> H <sub>6</sub> O	
[Co <sub>2</sub> ] (11), [Zn <sub>2</sub> ] (12), [Co Zn] (13), Chapter 6 [Fe <sub>2</sub> ] (19 and 20) Chapter 8	H <sub>2</sub> L	X@[M <sub>2</sub> (H <sub>2</sub> L) <sub>3</sub> ]Cl(PF <sub>6</sub> ) <sub>2</sub> X: Br, Cl	
(14) (15) (16) Chapter 7	H <sub>2</sub> L2	Fe(C <sub>2</sub> O <sub>4</sub> ) <sub>3</sub> @[Fe <sub>2</sub> (H <sub>2</sub> L2) <sub>3</sub> ](BF <sub>4</sub> )	



<p>(17) (18) <u>Chapter 7</u></p>	<p>H<sub>2</sub>L2</p>	<p><math>[\text{Fe}_9\text{O}_4(\text{OH})_{10}(\text{H}_2\text{L}2)_6(\text{H}_2\text{O})_4](\text{BF}_4)_5</math> and <math>[\text{Fe}_9\text{O}_4\text{Cl}_6(\text{OH})_8(\text{H}_2\text{L}2)_6](\text{Cl})_4</math></p>	
<p>(24, 25 and 26) (27) <u>Chapter 8</u></p>	<p>H<sub>2</sub>L5</p>	<p><math>(\text{X}@)\text{Fe}(\text{H}_2\text{L}5)_3]_2(\text{PF}_6)_3</math> X: I, Br, Cl <math>(\text{Cl}@)\text{Fe}(\text{H}_2\text{L}5)_3]_2(\text{ClO}_4)_3</math></p>	

**APPENDIX 2 - CHAPTER 2. THE EFFECT OF LIGAND SUBSTITUENTS ON THE SPIN CROSSOVER OF Fe (II) COMPLEXES**

**Figure A2.1.**  $^1\text{H-NMR}$  of N-arylation crude between 2-acetyl-6-bromopyridine and the asymmetric 3-methyl-pyrazole. Both regioisomeric compounds are distinguished in the spectrum. Black rhombus ( $\blacklozenge$ ) belongs to compound with the methyl in position 3 (i). Black dot ( $\bullet$ ) belongs to the compounds with the methyl in position 5 (i').  $i/i' = 2.33:1$  ratio. The inset on the top shows the TLC of the crude when hexane/ethyl acetate (8:2) is used as eluent. Same mixture of solvents has used to separate the regioisomers.

**Table A2.1.** Crystal data, average of Fe–N bond lengths and distortion parameter for compounds **2** and **3**.

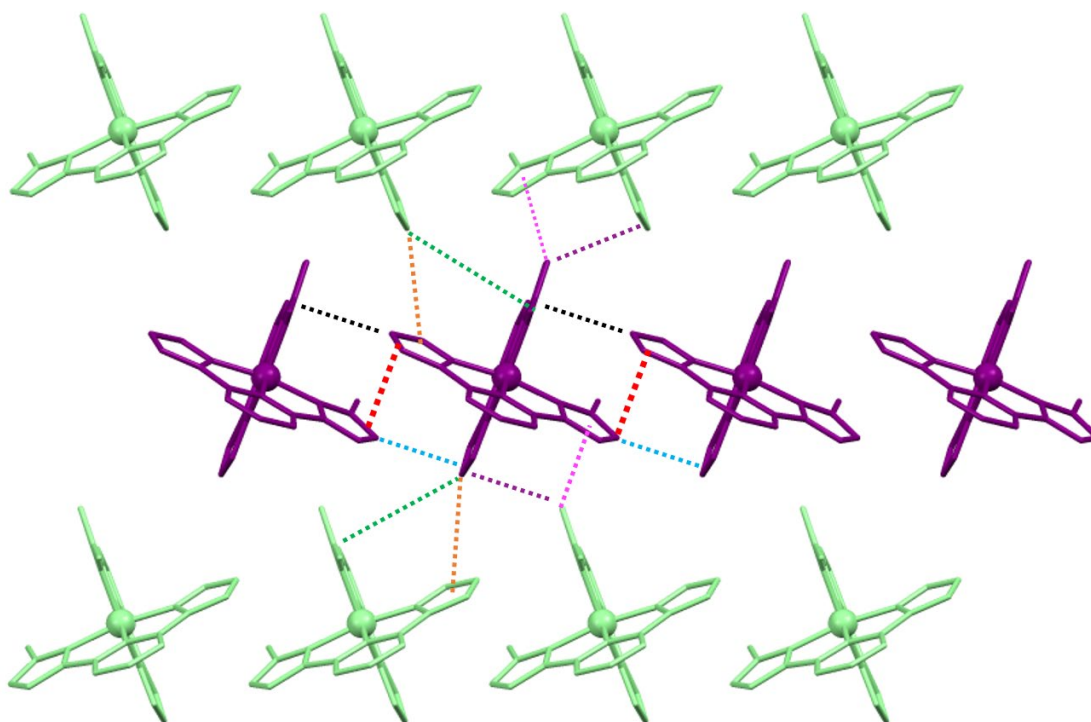
	<b>2</b>		<b>3</b>	
Formula	C <sub>24</sub> H <sub>22</sub> Cl <sub>2</sub> FeN <sub>10</sub> O <sub>8</sub>		C <sub>26</sub> H <sub>26</sub> Cl <sub>2</sub> FeN <sub>10</sub> O <sub>8</sub>	
FW (g mol <sup>-1</sup> )	705.26		733.32	
T(K)	100(2)	300(2)	100(2)	298(2)
Wavelength (Å)	0.71073			
Crystal system	monoclinic			
Space group	C2/c		P2 <sub>1</sub> /n	
<i>a</i> (Å)	41.290(9)	42.2075(12)	8.2654(3)	8.3260(5)
<i>b</i> (Å)	8.0448(15)	8.1769(3)	37.8383(12)	38.4690(19)
<i>c</i> (Å)	17.843(4)	18.2952(5)	9.05096(3)	9.6130(5)
β (°)	108.946(14)	111.307(2)	96.203(2)	95.768(3)
<i>V</i> (Å <sup>3</sup> )	5606(2)	5882.6(3)	2956.7(2)	3063.4(3)
<i>Z</i>	8		4	
ρ <sub>calcd</sub> (g cm <sup>-3</sup> )	1.671	1.593	1.647	1.590
μ (mm <sup>-1</sup> )	0.798	0.760	0.760	0.733
Independent reflections ( <i>R</i> <sub>int</sub> )	3428(0.2227)	4843(0.0427)	7394(0.0564)	3964 (0.0766)
Restraints/parameters	82 / 415	82 / 414	0/428	197 / 471
Goodness-of-fit on <i>F</i> <sup>2</sup>	1.059	1.051	1.031	1.019
Final <i>R</i> <sub>1</sub> / <i>wR</i> <sub>2</sub> [ <i>I</i> > 2σ( <i>I</i> )]	0.0700 / 0.1355	0.0579 / 0.1610	0.0462 / 0.0969	0.0591 / 0.1483
Final <i>R</i> <sub>1</sub> / <i>wR</i> <sub>2</sub> [all data]	0.1200 / 0.1553	0.0838 / 0.1806	0.0669 / 0.1066	0.1004 / 0.1749
Largest diff. peak and hole (e Å <sup>3</sup> )	0.881 / - 0.412	0.640 / - 0.599	0.948 / - 0.555	0.406 / - 0.523
<Fe–N>	1.96(4)	2.16(2)	1.95(4)	1.95(4)
Σ	93.2	147.5	88.7	90.0
Θ	367.8	378.2	367.2	367.1

**Table A2.2.** Hydrogen bonding in the structures of compounds **2** and **3** at 100K.

D–H...A	D–H (Å)	H...A (Å)	D–A (Å)	D–H...A (°)
<b>2 (100 K)</b>				
N5–H5...O5	0.90(2)	1.87(3)	2.759(9)	172(8)
N10–H10...O3	0.90(2)	2.27(6)	2.999(10)	138(7)
N10–H10...O4	0.90(2)	2.20(4)	3.017(10)	151(7)
<b>3 (100 K)</b>				
N5–H5...O8	0.88	1.96	2.832(3)	175.0
N10–H10...O1	0.88	2.24	3.004(0)	122.4
N10–H10...O4	0.88	2.00	2.878(3)	172.7

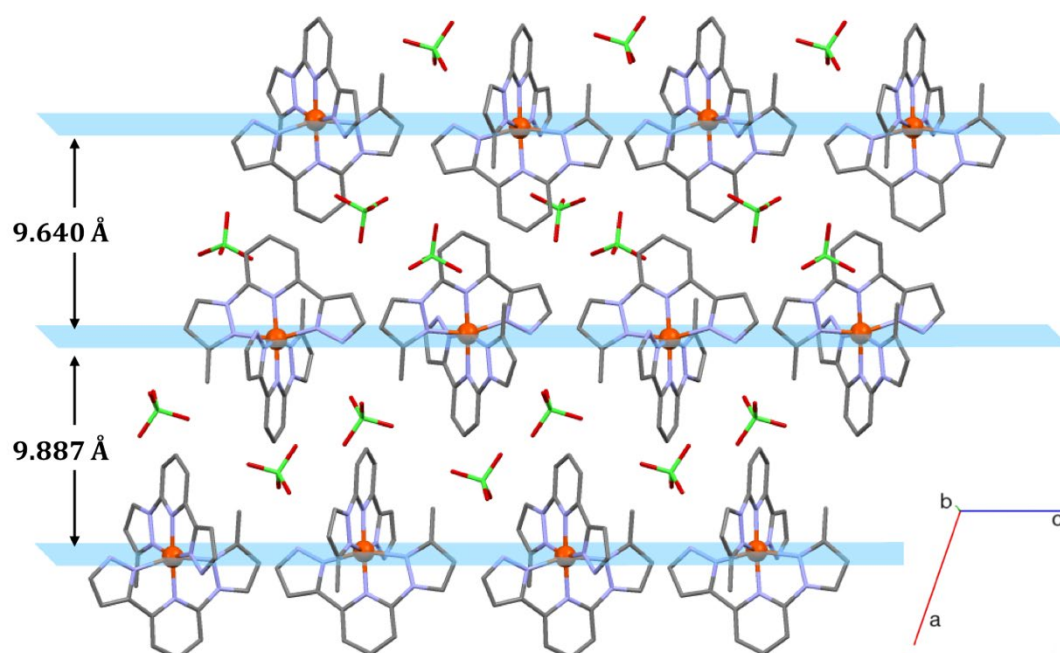
**Table A2.3.** Selected  $\pi\cdots\pi$  and C–H $\cdots\pi$  interactions in the structures of compounds **2** and **3** at 100 K.

interaction	labels		Distance (Å) ( $\pi$ : centroid)	Compd.
$\pi\cdots\pi$ (1)	Cg(N1 N2 C2 C3 C4) $\cdots$ Cg(N4 N5 C10 C11 C12)	■ ■ ■ ■	3.566	<b>2</b>
C–H $\cdots\pi$ (1)	C1–H1B $\cdots$ Cg(N9 N10 C22 C23 C24)	■ ■ ■ ■ ■ ■ ■ ■	3.272	<b>2</b>
C–H $\cdots\pi$ (2)	C12–H12 $\cdots$ Cg(N6 N7 C14 C15 C16)	■ ■ ■ ■ ■ ■ ■ ■	2.584	<b>2</b>
C–H $\cdots\pi$ (2)	C24–H24 $\cdots$ Cg(N4 N5 C10 C11 C12)	■ ■ ■ ■ ■ ■ ■ ■	3.320	<b>2</b>
C–H $\cdots\pi$ (2)	C24–H24 $\cdots$ Cg(N6 N7 C14 C15 C16)	■ ■ ■ ■ ■ ■ ■ ■	4.219	<b>2</b>
C–H $\cdots\pi$ (2)	C15–H15 $\cdots$ Cg(N1 N2 C2 C3 C4)	■ ■ ■ ■ ■ ■ ■ ■	3.154	<b>2</b>
C–H $\cdots\pi$ (2)	C15–H15 $\cdots$ Cg(N9 N10 C22 C23 C24)	■ ■ ■ ■ ■ ■ ■ ■	3.070	<b>2</b>
$\pi\cdots\pi$ (1)	Cg(N6 N7 C15 C16 C18) $\cdots$ Cg(N9 N10 C23 C24 C25)		3.635	<b>3</b>
C–H $\cdots\pi$ (1)	C25–H25 $\cdots$ Cg(N1 N2 C2 C3 C5)		2.978	<b>3</b>
C–H $\cdots\pi$ (2)	C16–H16 $\cdots$ Cg(N4 N5 C11 C12 C13)		3.118	<b>3</b>
C–H $\cdots\pi$ (3)	C3–H3 $\cdots$ Cg(N6 N7 C15 C16 C18)		3.321	<b>3</b>

**Figure A2.2.** Sheet organization of the cation for complex **2**, emphasizing the intermolecular interactions formed by each complex with its intermediate neighbors (different colors correlate with the ones in the table below). The two orientation of the cation are emphasized in green and purple colors.

**Table A2.4.** Selected bond distances (Å) in the structures of compounds **2** and **3**.

	<b>2</b> (100K)	<b>2</b> (300K)	<b>3</b> (100K)	<b>3</b> (298K)
Fe1–N3	1.900(6)	2.121(4)	1.908(2)	1.909(5)
Fe1–N8	1.913(6)	2.117(3)	1.907(2)	1.912(5)
Fe1–N4	1.960(6)	2.175(4)	1.965(2)	1.965(5)
Fe1–N9	1.972(6)	2.184(4)	1.966(2)	1.968(5)
Fe1–N1	1.987(6)	2.191(4)	1.9682(19)	1.968(5)
Fe1–N6	2.013(6)	2.197(3)	1.975(2)	1.985(5)

**Figure A2.3.** View of the lattice of [Fe(Me-1,3bpp)<sub>2</sub>](ClO<sub>4</sub>)<sub>2</sub> (**2**), quasi perpendicular to the *ac* crystallographic plane and thus, along the sheets of cations, emphasizing the two interlayer separation. Code balls, Fe; red, O; green, Cl, grey, C. Hydrogen not shown.

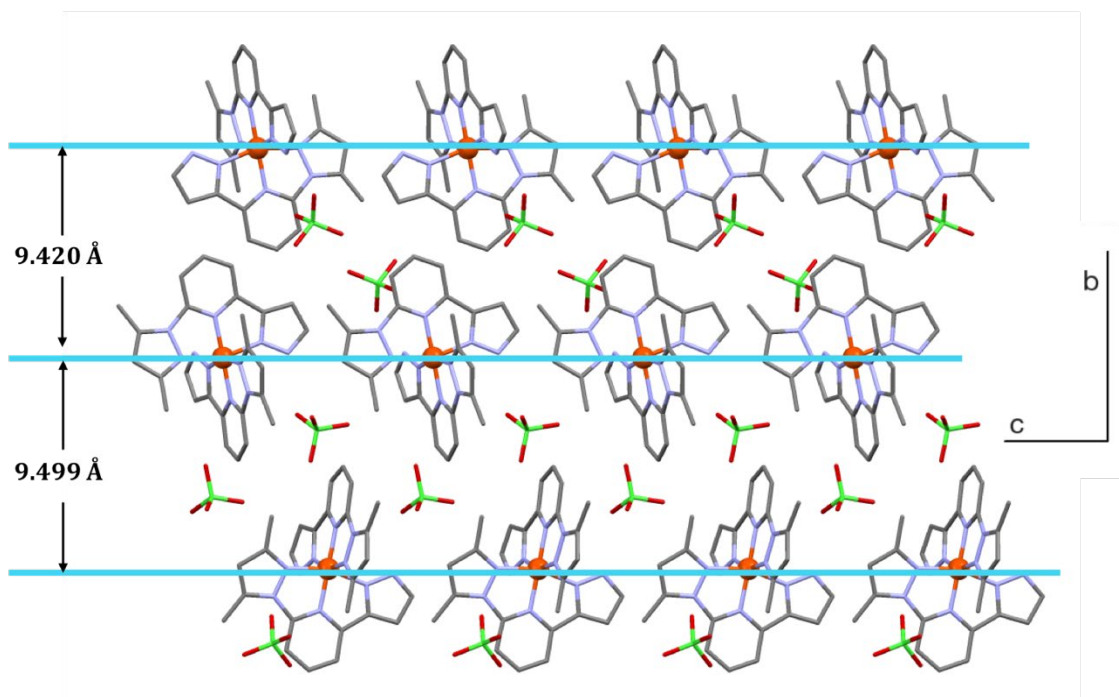


**Figure A2.4.** View of the lattice of [Fe(Me<sub>2</sub>-1,3bpp)<sub>2</sub>](ClO<sub>4</sub>)<sub>2</sub> (**3**), perpendicular to the *bc* crystallographic plane and thus, along the sheets of cations, emphasizing the two interlayer separation. Code balls, Fe; red, O; green, Cl, grey, C. Hydrogen not shown.

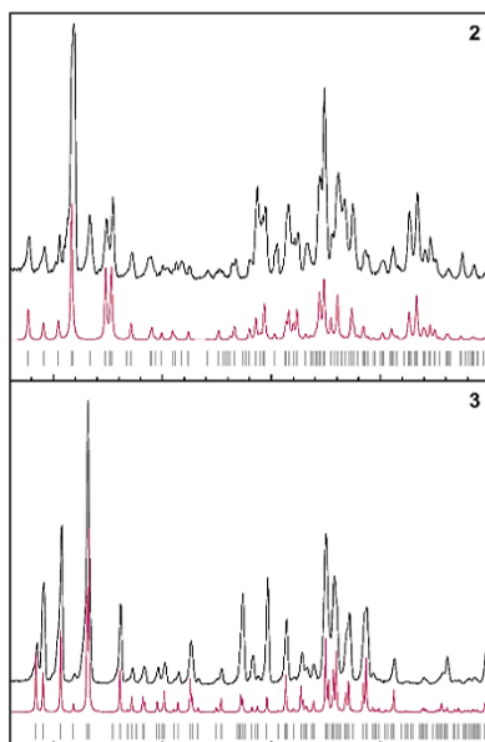


**Figure A2.5.** Experimental powder X-ray diffraction (PXRD) patterns for compound **2** and **3** in black traces. The corresponding diagrams simulated from the single crystal X-ray diffraction data are red traces and vertical lines.

## Heat capacity measurements and detailed modelization data to Sorai's domain model.

The excess of heat capacity  $\Delta C_p$  associate whit the SCO anomalies was estimated for all compounds (Figure A2.XXX). The integration of  $\Delta C_p$  with respect to  $T$  and  $\ln T$  gives the excess enthalpy ( $\Delta H$ ) and entropy ( $\Delta S$ ) due to the SCO, respectively.

Sorai's domain model was used to investigate the cooperativity of the SCO for all compounds. It is commonly used where calorimetric data are available. The model considers the crystal lattice as an assemblage of non-interacting domains with uniform size which contain  $n$  complexes. The measure of cooperativity is given by the number of complexes with SCO centres ( $n$ ) per interacting domain. As the number  $n$  increases, the cooperativity of the transition increases. According to this model, Equation S1 is used to determine the value of  $n$  when the thermal dependence of  $\Delta C_p$  is fitted:

$$\Delta C_p = \frac{n(\Delta H_{SCO})^2}{RT^2} \frac{\exp\left[\frac{n\Delta H_{SCO}}{R}\left(\frac{1}{T} - \frac{1}{T_{SCO}}\right)\right]}{\left\{1 + \exp\left[\frac{n\Delta H_{SCO}}{R}\left(\frac{1}{T} - \frac{1}{T_{SCO}}\right)\right]\right\}^2} \quad \text{Eq. S1}$$

Thus, the experimental data were fitted to Eq. S1 using  $\Delta H_{SCO}$  as derived from integration of  $\Delta C_p$  vs  $T$ . The best-fitting results are given in Table 1 and Figure 5 (full red lines). If  $n=1$ , no cooperative effects are considered.

Two fits were performed for compound **2**. At first attempt  $\Delta C_p$  data were fit to Eq. S1 as mentioned above (blue line in Figure 2.6; right-bottom). This fit reproduced quite well the sharp peak giving a  $n$  and  $T_{SCO}$  values of 118.74 and 182.1K, respectively. However, the broader anomaly below it was not well-fitted. For this reason, a second fit considering two components (two terms as in Eq. S1 with different  $n$  and  $T_{SCO}$ ) was used. The good simulation reached through this fit is shown in red line in Figure 2.6; right-bottom, which gave the values  $n_1=128.7$  and  $T_{SCO}= 182.1K$  and  $n_2=128.7$  and  $T_{SCO}= 185.6K$ . This sharp anomaly could be associate to the large structural changes upon SCO, since the cell parameters varies sharply at the same temperature. Values for this sharp component are given in Table 2.1.

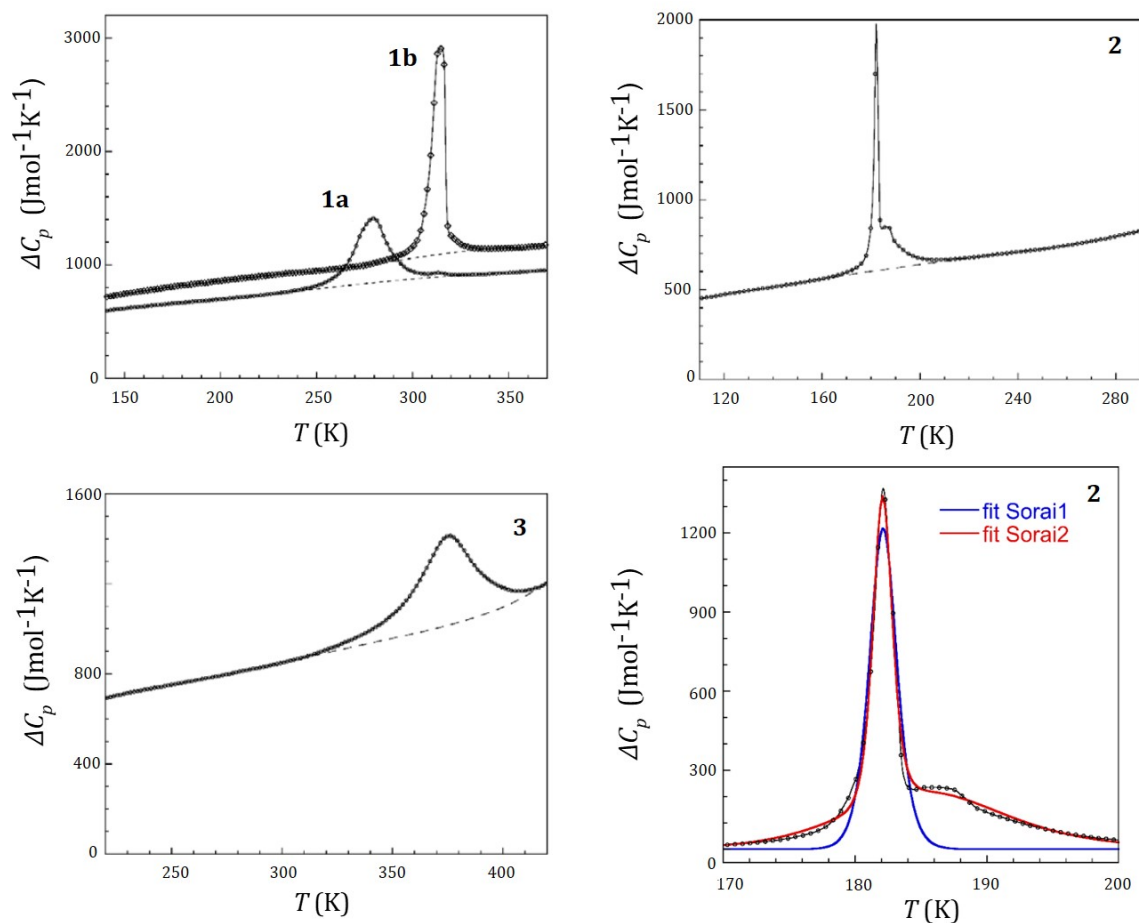


**Figure A2.6.** Molar heat capacity of compound **1a** and **1b** (previously reported), **2** and **3** as derived from DSC measurements. The dashed lines are the estimate lattice heat capacity used to access the excess heat capacity. (Right-bottom): Fits to Sorai's domain model for compound **2** with one (blue line) and two components as mentioned above.



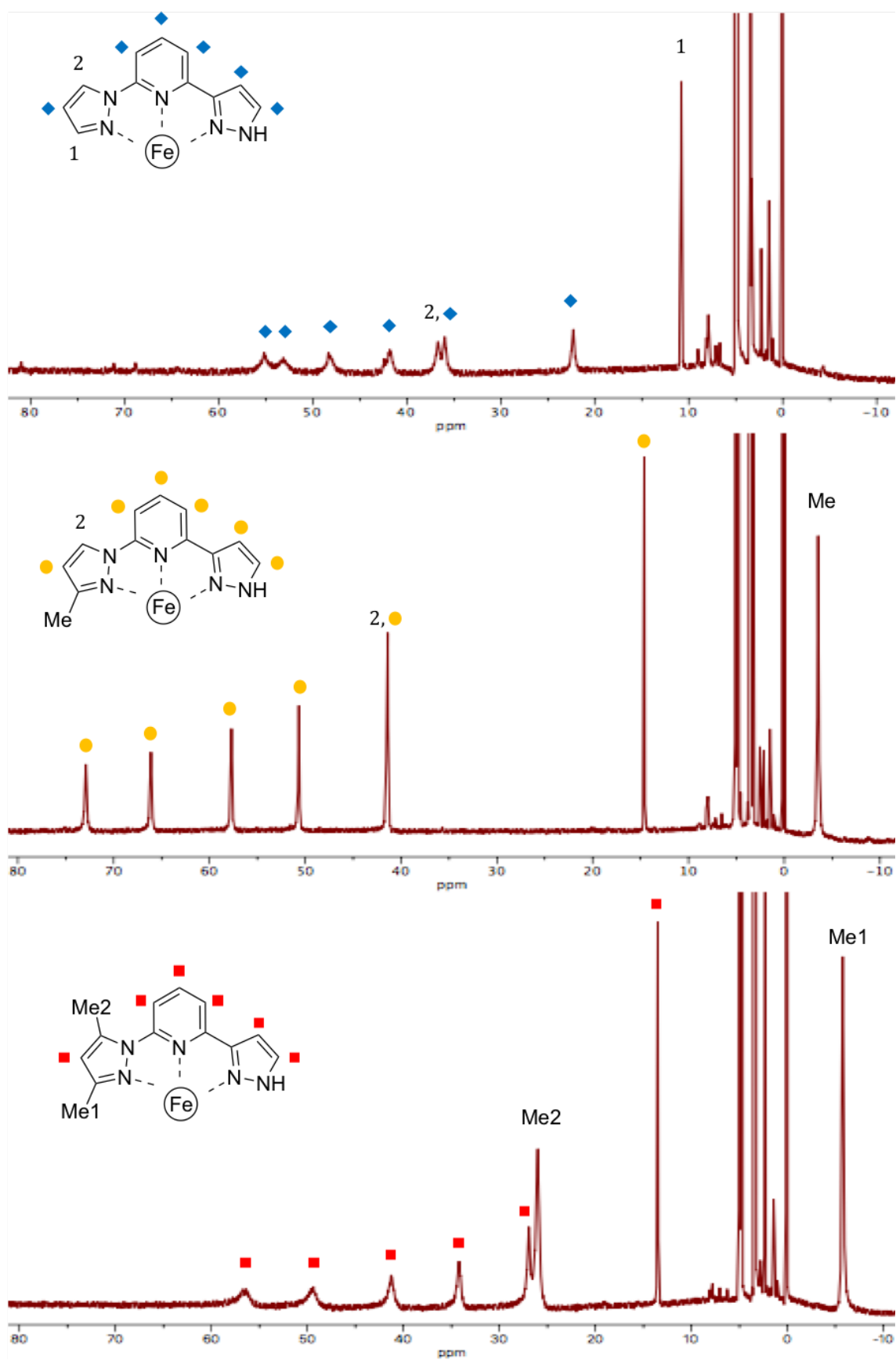


**Figure A2.7.**  $^1\text{H-NMR}$  spectra of complexes 1 (top), 2 (middle) and 3 (bottom) in methanol- $d_4$  collected at room temperature.

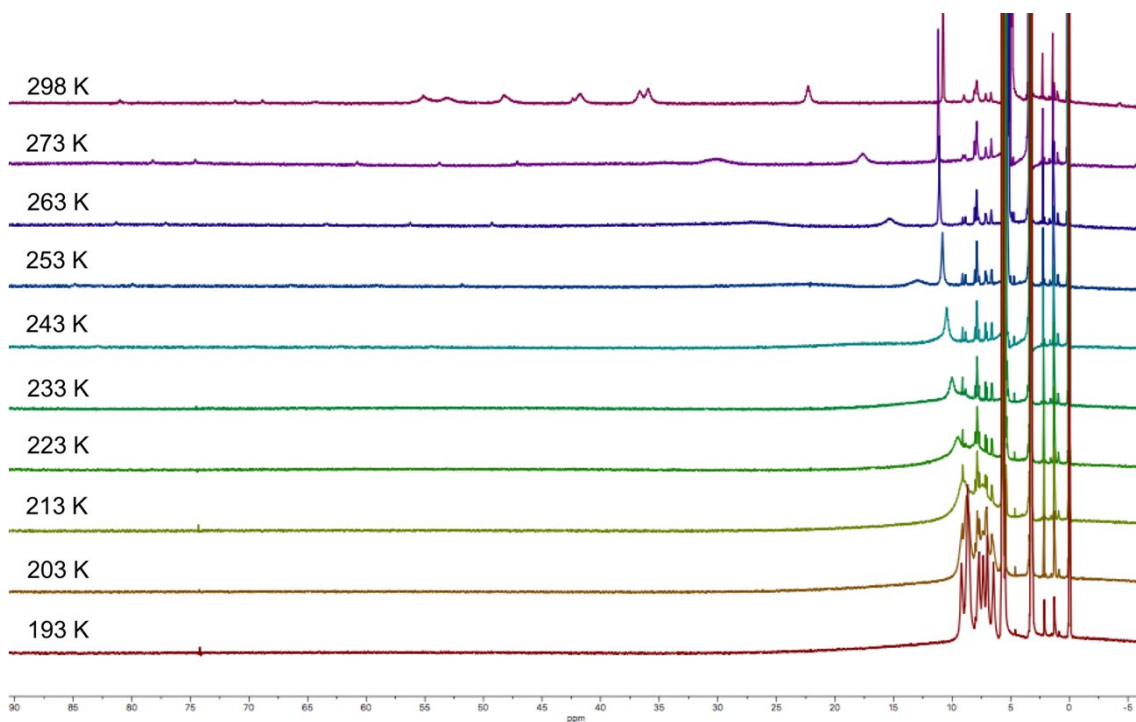


**Figure A2.8.** Complete stacked spectra, obtained by the Evans  $^1\text{H-NMR}$  method, from 193 to 298K for the complex  $[\text{Fe}(\text{1,3-bpp})_2](\text{ClO}_4)_2$  (**1**) in methanol- $d_4$ .

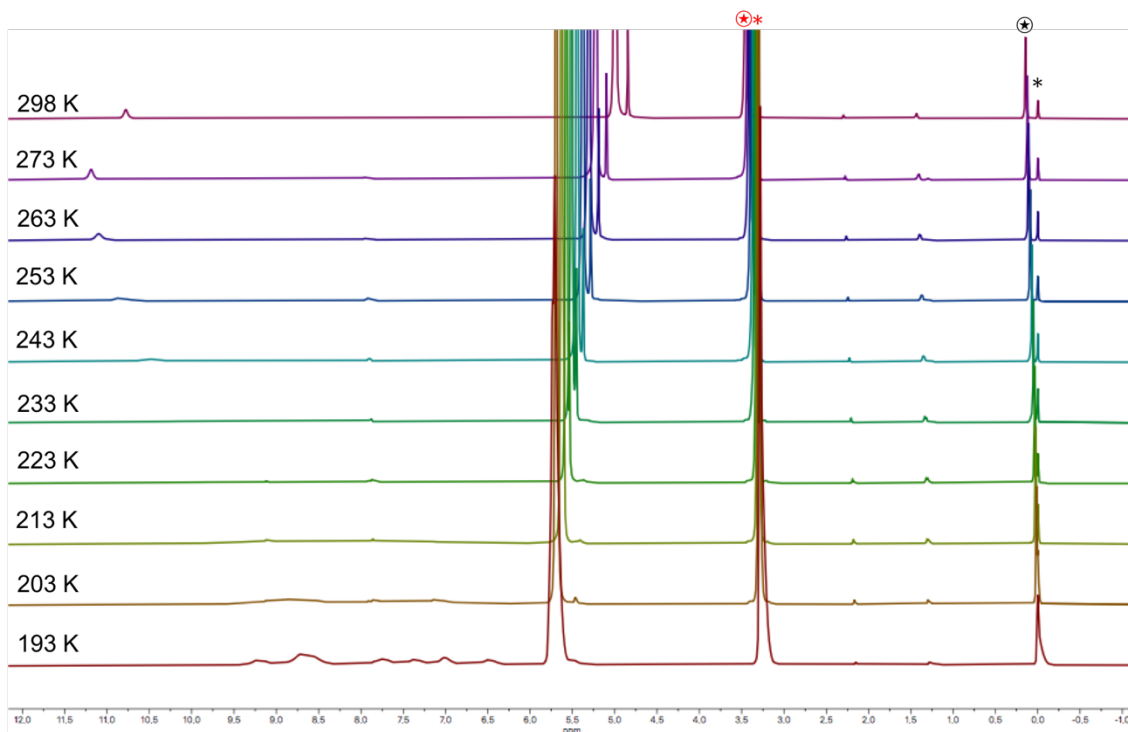


**Figure A2.9.** Stacked spectra (Zoom), obtained by the Evans  $^1\text{H-NMR}$  method, from 193 to 298K for the complex  $[\text{Fe}(\text{1,3-bpp})_2](\text{ClO}_4)_2$  (**1**) in methanol- $d_4$ .

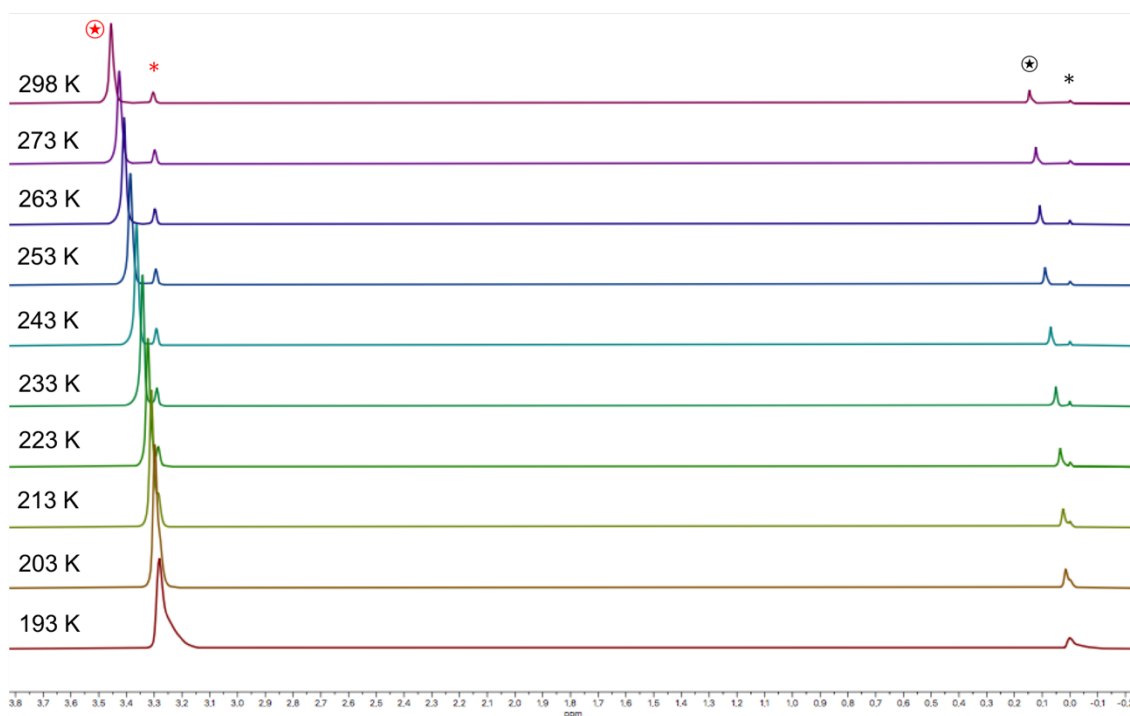


**Figure A2.10.** Stacked spectra (Zoom), obtained by the Evans  $^1\text{H-NMR}$  method, from 193 to 298K for the complex  $[\text{Fe}(\text{1,3-bpp})_2](\text{ClO}_4)_2$  (**1**) in  $\text{methanol-}d_4$ . (\*) The black star indicates the TMS peak for the inner capillary vs (⊛) outer solution containing the complex. (\* and ⊛) The red stars represent the solvent peaks.

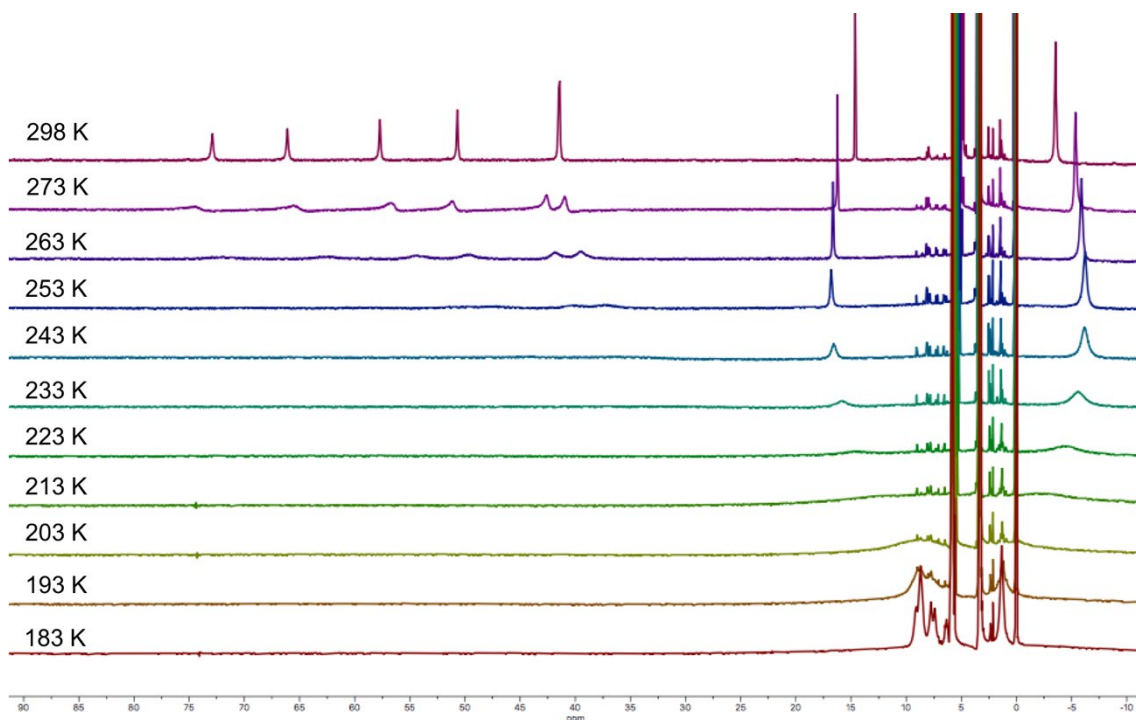


**Figure A2.11.** Complete stacked spectra, obtained by the Evans  $^1\text{H-NMR}$  method, from 193 to 298K for the complex  $[\text{Fe}(\text{Me-1,3-bpp})_2](\text{ClO}_4)_2$  (**2**) in  $\text{methanol-}d_4$ .

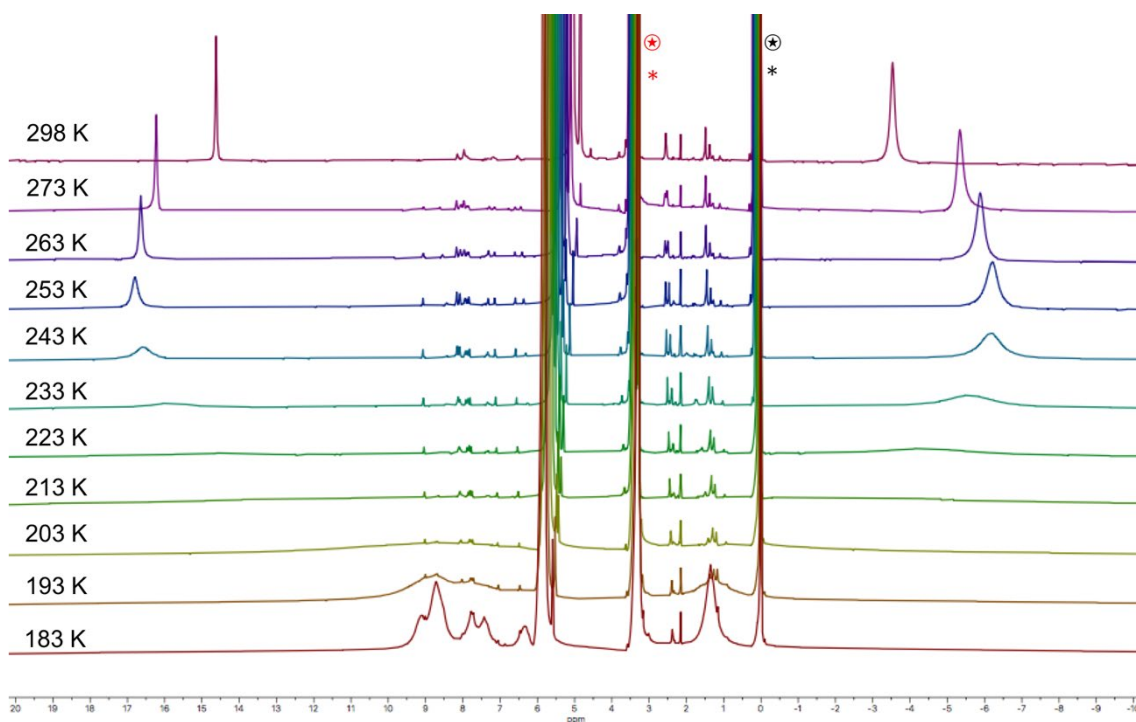


**Figure A2.12.** Stacked spectra, obtained by the Evans  $^1\text{H-NMR}$  method, from 193 to 298K for the complex  $[\text{Fe}(\text{Me-1,3-bpp})_2](\text{ClO}_4)_2$  (**2**) in methanol- $d_4$ .

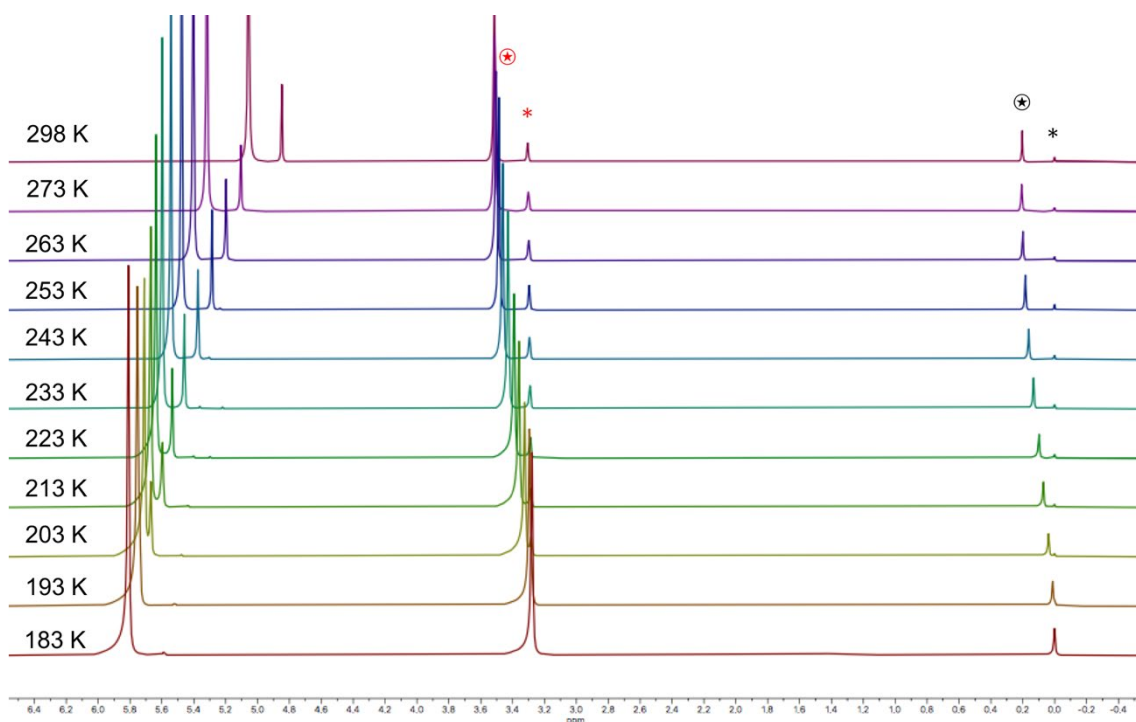


**Figure A2.13.** Stacked spectra (Zoom), obtained by the Evans  $^1\text{H-NMR}$  method, from 193 to 298K for the complex  $[\text{Fe}(\text{Me-1,3-bpp})_2](\text{ClO}_4)_2$  (**2**) in methanol- $d_4$ . (\*) The black star indicates the TMS peak for the inner capillary vs ( $\otimes$ ) outer solution containing the complex. (\* and  $\otimes$ ) The red stars represent the solvent peaks.

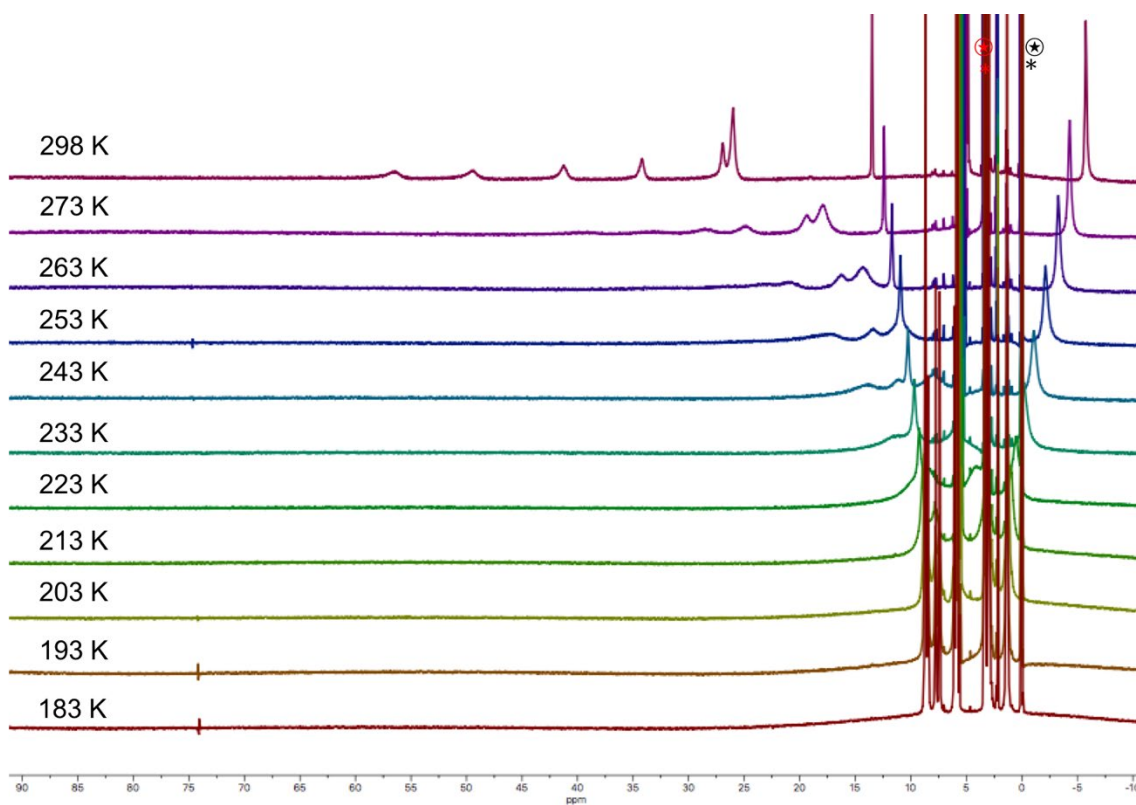


**Figure A2.14.** Stacked spectra (Zoom), obtained by the Evans  $^1\text{H-NMR}$  method, from 193 to 298K for the complex  $[\text{Fe}(\text{Me}_2\text{-1,3-bpp})_2](\text{ClO}_4)_2$  (3) in methanol- $d_4$ .

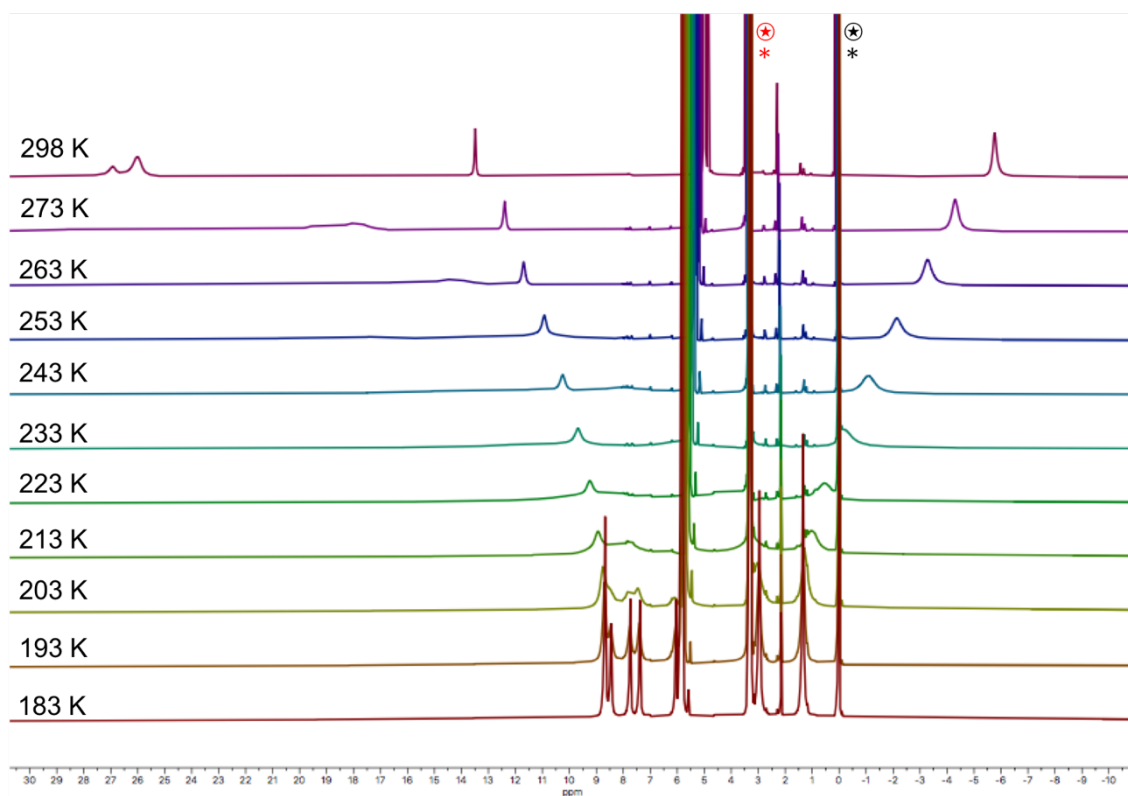


**Figure A2.15.** Stacked spectra, obtained by the Evans  $^1\text{H-NMR}$  method, from 193 to 298K for the complex  $[\text{Fe}(\text{Me}_2\text{-1,3-bpp})_2](\text{ClO}_4)_2$  (3) in methanol- $d_4$ .

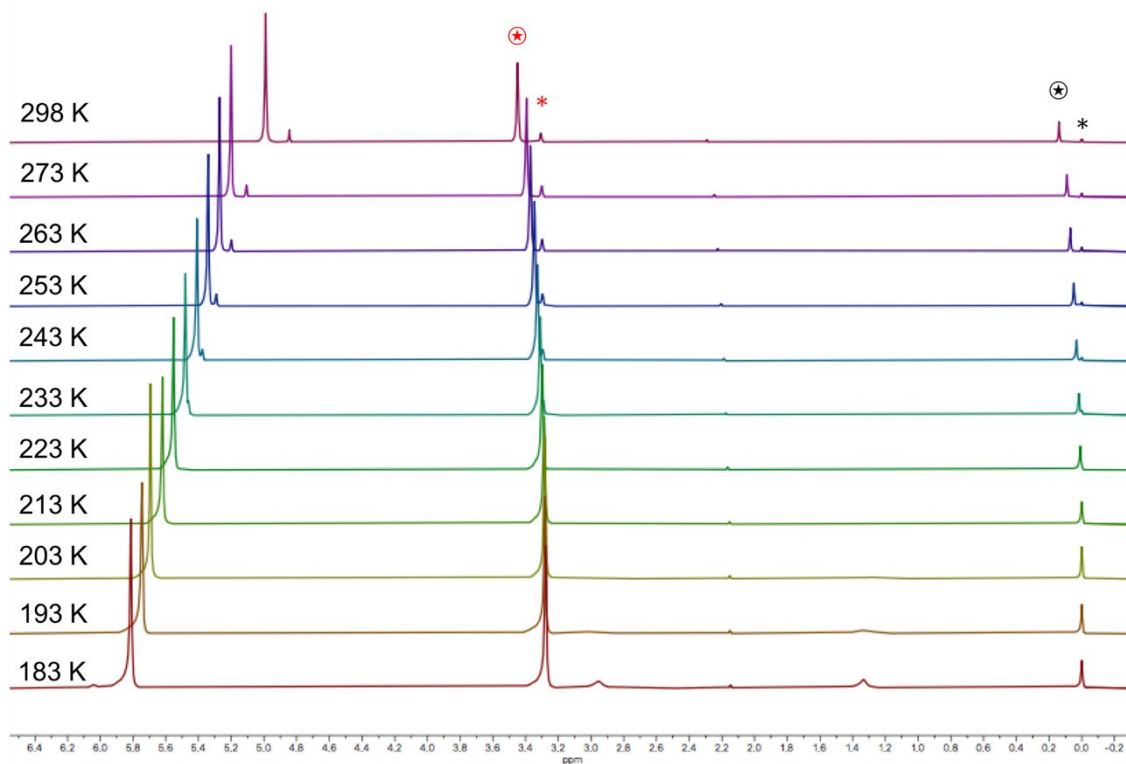


**Figure A2.16.** Stacked spectra, obtained by the Evans  $^1\text{H-NMR}$  method, from 193 to 298K for the complex  $[\text{Fe}(\text{Me}_2\text{-1,3-bpp})_2](\text{ClO}_4)_2$  (**3**) in  $\text{methanol-}d_4$ . ( $\blackstar$ ) The black star indicates the TMS peak for the inner capillary vs ( $\odot$ ) outer solution containing the complex. ( $\star$  and  $\odot$ ) The red stars represent the solvent peaks.

**Table A2.5.** Paramagnetic shifts measured for TMS at different temperatures on a 600MHz spectrometer, by  $^1\text{H-NMR}$  in 0.005M methanol- $d_4$  solutions, for complexes **1**, **2** and **3**, and the corresponding  $\chi\text{T}$  values calculated with Evans method.

T(K)	Complex 1			Complex 2			Complex 3		
	$\chi\text{pT}$	$\Delta\nu$ (Hz)	$\Delta\delta$ (ppm)	$\chi\text{pT}$	$\Delta\nu$ (Hz)	$\Delta\delta$ (ppm)	$\chi\text{pT}$	$\Delta\nu$ (Hz)	$\Delta\delta$ (ppm)
298	2.24	87.6	0.146	2.96	121.8	0.203	2.02	83.4	0.139
273	1.75	74.4	0.124	2.76	124.2	0.207	1.22	54	0.09
263	1.49	65.4	0.109	2.57	119.4	0.199	0.93	42	0.07
253	1.18	53.4	0.089	2.29	110.4	0.184	0.63	28.8	0.048
243	0.9	42	0.07	1.95	97.8	0.163	0.42	18.6	0.031
233	0.64	30	0.05	1.53	79.2	0.132	0.26	10.8	0.018
223	0.44	21	0.035	1.09	58.2	0.097	0.15	5.4	0.009
213	0.32	15	0.025	0.78	42.6	0.071	0.06	0.15	0.00025
203	0.2	9	0.015	0.42	22.8	0.038	--	--	--
193	--	--	--	0.15	6.6	0.011	--	--	--

**Table A2.6.** Data obtained from fitting the datasets obtained for complexes **1**, **2** and **3** with the regular solution model.

Model	SCOfit (User)		
Equation	A_MAX/(1+exp(-H/(R*T))+S/R)		
Reduced Chi-Sqr	0.00116		
Adj. R-Square	0.99763		
		Value	Standard Error
[Fe(1,3-bpp) <sub>2</sub> ](ClO <sub>4</sub> ) <sub>2</sub> ( <b>1</b> )	S	-65.86049	1.41248
	H	-18071.6428	360.81506
	R	8.14	0
	A_MAX	3.15	0

Model	SCOfit (User)		
Equation	A_MAX/(1+exp(-H/(R*T))+S/R)		
Reduced Chi-Sqr	0.00565		
Adj. R-Square	0.99443		
		Value	Standard Error
[Fe(Me-1,3-bpp) <sub>2</sub> ](ClO <sub>4</sub> ) <sub>2</sub> ( <b>2</b> )	S	-86.96918	2.72838
	H	-20780.45877	650.2193
	R	8.14	0
	A_MAX	3.15	0

Model	SCOfit (User)		
Equation	A_MAX/(1+exp(-H/(R*T))+S/R)		
Reduced Chi-Sqr	1.28E-04		
Adj. R-Square	0.99968		
		Value	Standard Error
[Fe(Me <sub>2</sub> -1,3-bpp) <sub>2</sub> ](ClO <sub>4</sub> ) <sub>2</sub> ( <b>3</b> )	S	-85.55271	0.68972
	H	-24732.0179	183.72097
	R	8.14	0
	A_MAX	3.15	0



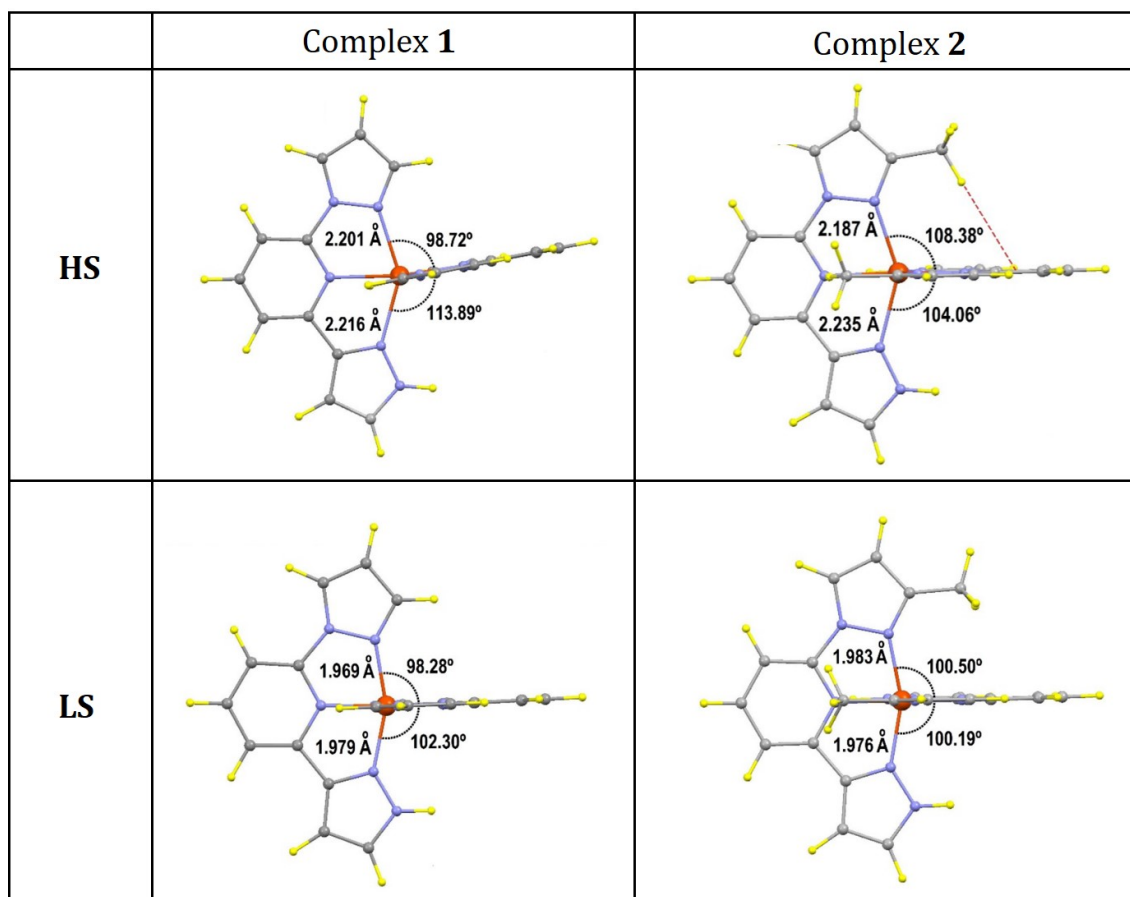


**Figure A2.17.** DFT optimized structures of the HS and LS states for compounds **1** and **2**.

**APPENDIX 3 - CHAPTER 3. THE EFFECT OF METAL DILUTION ON THE THERMAL SPIN TRANSITIONS OF  $[\text{Fe}(\text{Me-bppp})_2(\text{ClO}_4)_2$**

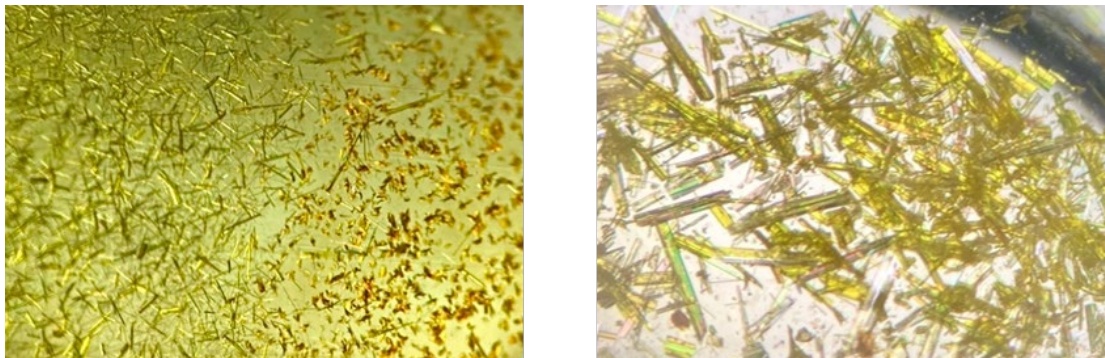


**Figure A3.1.** (Left) Non-homogenous (mixture of small yellow needles and light orange needles) crystalline samples from reactions of  $\text{Zn}(\text{ClO}_4)_2$ ,  $\text{Fe}(\text{ClO}_4)_2$  and Me-1,3bpp in amounts aiming at  $x > 0.333$  while using dry acetone as solvent. (Right) Homogenous crystalline sample of  $[\text{Fe}_x\text{Zn}_{1-x}(\text{Me-1,3bpp})_2](\text{ClO}_4)_2$  (**5x**) obtained from the same reactions as above, in a mixture of dry acetone and ethanol (1:1 vol.).

**Table A3.1.** Analytical results from ICP-OES metal analysis for  $[\text{Zn}(\text{Me-1,3bpp})_2](\text{ClO}_4)_2$  (**4**) and solid-solutions  $[\text{Fe}_x\text{Zn}_{1-x}(\text{Me-1,3bpp})_2](\text{ClO}_4)_2$  (**5x**;  $x = 0.10, 0.15, 0.22, 0.33, 0.41, 0.48, 0.56, 0.64$ ).

Empirical Formula	Fe/Zn stoichiometry used (expected weight %)	Expected av. MW [g/mol]	Metal content by ICP-OES [mass%]		Fe/Zn ratio by ICP-OES	Experimental av. MW [g/mol]
			Fe	Zn		
$\text{Fe}_{0.10}\text{Zn}_{0.90}\text{C}_{24}\text{H}_{22}\text{N}_{10}\text{Cl}_2\text{O}_8$	10/90 (0.78/8.24)	713.829	0.76	8.03	10/90	713.829
$\text{Fe}_{0.15}\text{Zn}_{0.85}\text{C}_{24}\text{H}_{22}\text{N}_{10}\text{Cl}_2\text{O}_8$	20/80 (1.57/7.34)	712.875	1.12	7.18	15.3/84.7	713.323
$\text{Fe}_{0.22}\text{Zn}_{0.78}\text{C}_{24}\text{H}_{22}\text{N}_{10}\text{Cl}_2\text{O}_8$	30/70 (2.35/6.43)	711.992	1.59	6.69	21.9/78.1	712.694
$\text{Fe}_{0.33}\text{Zn}_{0.67}\text{C}_{24}\text{H}_{22}\text{N}_{10}\text{Cl}_2\text{O}_8$	40/60 (3.14/5.52)	710.968	2.51	5.89	33.3/66.7	711.607
$\text{Fe}_{0.41}\text{Zn}_{0.59}\text{C}_{24}\text{H}_{22}\text{N}_{10}\text{Cl}_2\text{O}_8$	50/50 (3.93/4.6)	710.015	3.08	5.14	41.2/58.8	710.854
$\text{Fe}_{0.48}\text{Zn}_{0.52}\text{C}_{24}\text{H}_{22}\text{N}_{10}\text{Cl}_2\text{O}_8$	60/40 (4.73/3.69)	709.061	3.57	4.60	47.6/52.4	710.243
$\text{Fe}_{0.56}\text{Zn}_{0.44}\text{C}_{24}\text{H}_{22}\text{N}_{10}\text{Cl}_2\text{O}_8$	70/30 (5.52/2.77)	708.108	4.21	3.90	55.9/44.1	709.508
$\text{Fe}_{0.64}\text{Zn}_{0.36}\text{C}_{24}\text{H}_{22}\text{N}_{10}\text{Cl}_2\text{O}_8$	80/20 (6.32/1.85)	707.154	4.88	3.26	63.6/36.4	708.718

**Table A3.2.** C, N, H elemental analysis results for  $[\text{Zn}(\text{Me-1,3bpp})_2](\text{ClO}_4)_2$  (**4**) and solid-solutions  $[\text{Fe}_x\text{Zn}_{1-x}(\text{Me1,3bpp})_2](\text{ClO}_4)_2$  (**5x**;  $x = 0.10, 0.15, 0.22, 0.33, 0.41, 0.48, 0.56, 0.64$ ).

Best fit formula	Best fit composition	Element	Found (%)	Calculated (%)
$[\text{Zn}(\text{Me1,3bpp})_2](\text{ClO}_4)_2 \cdot 0.37 \text{H}_2\text{O}$	$\text{ZnC}_{24}\text{H}_{22.74}\text{N}_{10}\text{Cl}_2\text{O}_{8.37}$	C	40.63	39.96
		H	3.30	3.18
		N	18.74	19.41
$[\text{Fe}_{0.1}\text{Zn}_{0.9}(\text{Me1,3bpp})_2](\text{ClO}_4)_2 \cdot 0.69 \text{H}_2\text{O}$	$\text{Fe}_{0.1}\text{Zn}_{0.9}\text{C}_{24}\text{H}_{23.38}\text{N}_{10}\text{Cl}_2\text{O}_{8.69}$	C	40.27	39.7
		H	3.16	3.24
		N	18.71	19.29
$[\text{Fe}_{0.153}\text{Zn}_{0.847}(\text{Me1,3bpp})_2](\text{ClO}_4)_2 \cdot 0.75 \text{H}_2\text{O}$	$\text{Fe}_{0.153}\text{Zn}_{0.847}\text{C}_{24}\text{H}_{23.5}\text{N}_{10}\text{Cl}_2\text{O}_{8.75}$	C	40.39	39.66
		H	3.2	3.26
		N	18.54	19.27
$[\text{Fe}_{0.219}\text{Zn}_{0.781}(\text{Me1,3bpp})_2](\text{ClO}_4)_2 \cdot 0.69 \text{H}_2\text{O}$	$\text{Fe}_{0.219}\text{Zn}_{0.781}\text{C}_{24}\text{H}_{23.38}\text{N}_{10}\text{Cl}_2\text{O}_{8.69}$	C	40.53	39.75
		H	3.19	3.25
		N	18.53	19.31
$[\text{Fe}_{0.333}\text{Zn}_{0.667}(\text{Me1,3bpp})_2](\text{ClO}_4)_2 \cdot 0.24 \text{H}_2\text{O}$	$\text{Fe}_{0.333}\text{Zn}_{0.667}\text{C}_{24}\text{H}_{22.48}\text{N}_{10}\text{Cl}_2\text{O}_{8.24}$	C	40.51	40.27
		H	3.19	3.16
		N	19.32	19.56
$[\text{Fe}_{0.412}\text{Zn}_{0.558}(\text{Me1,3bpp})_2](\text{ClO}_4)_2 \cdot 0.35 \text{H}_2\text{O}$	$\text{Fe}_{0.412}\text{Zn}_{0.558}\text{C}_{24}\text{H}_{22.7}\text{N}_{10}\text{Cl}_2\text{O}_{8.35}$	C	40.46	40.2
		H	3.15	3.19
		N	19.27	19.53
$[\text{Fe}_{0.476}\text{Zn}_{0.524}(\text{Me-1,3bpp})_2](\text{ClO}_4)_2 \cdot 0.26 \text{H}_2\text{O}$	$\text{Fe}_{0.476}\text{Zn}_{0.524}\text{C}_{24}\text{H}_{22.52}\text{N}_{10}\text{Cl}_2\text{O}_{8.26}$	C	40.51	40.32
		H	3.14	3.18
		N	19.4	19.59
$[\text{Fe}_{0.559}\text{Zn}_{0.441}(\text{Me1,3bpp})_2](\text{ClO}_4)_2 \cdot 0.58 \text{H}_2\text{O}$	$\text{Fe}_{0.559}\text{Zn}_{0.441}\text{C}_{24}\text{H}_{23.16}\text{N}_{10}\text{Cl}_2\text{O}_{8.58}$	C	40.35	40.04
		H	3.16	3.24
		N	19.14	19.45
$[\text{Fe}_{0.636}\text{Zn}_{0.364}(\text{Me1,3bpp})_2](\text{ClO}_4)_2 \cdot 0.21 \text{H}_2\text{O}$	$\text{Fe}_{0.636}\text{Zn}_{0.364}\text{C}_{24}\text{H}_{22.42}\text{N}_{10}\text{Cl}_2\text{O}_{8.21}$	C	40.74	40.46
		H	3.13	3.17
		N	19.38	19.66

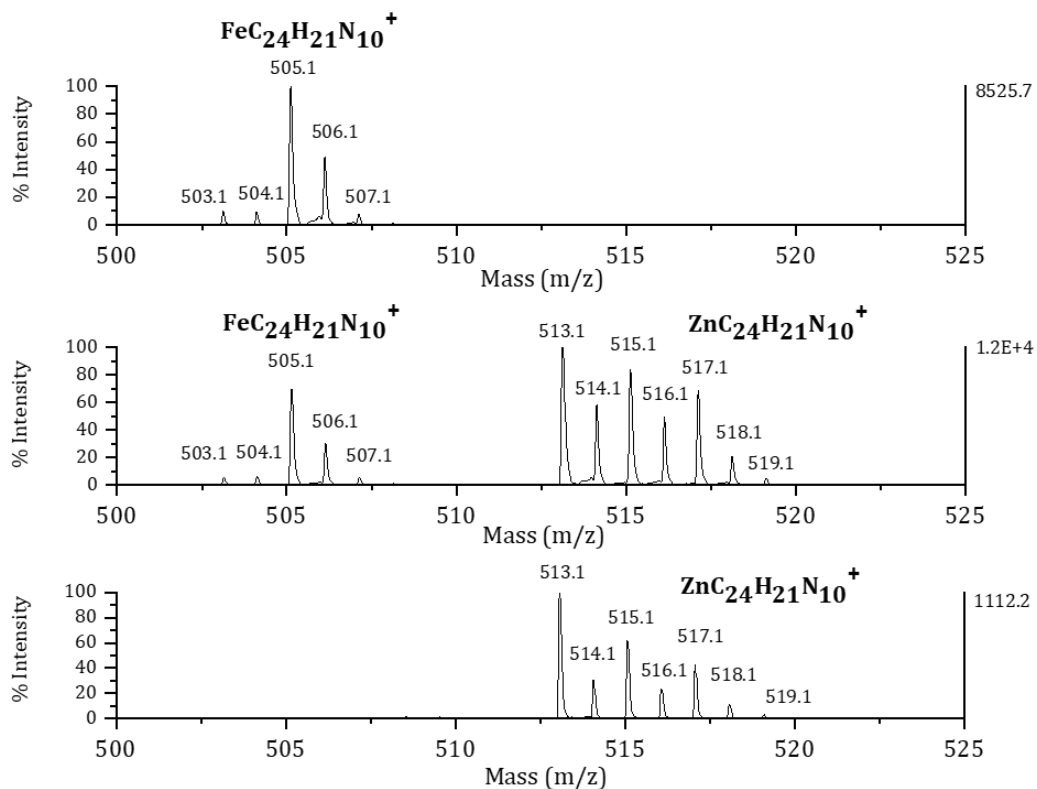


**Figure A3.2.** Selected region of the positive-ion MALDI mass spectrograms for  $[\text{Fe}(\text{Me}1,3\text{bpp})_2](\text{ClO}_4)_2$  (**2**, top),  $[\text{Fe}_x\text{Zn}_{1-x}(\text{Me}1,3\text{bpp})_2](\text{ClO}_4)_2$  (**5x**;  $x = 0.2$ , middle) and  $[\text{Zn}(\text{Me}1,3\text{bpp})_2](\text{ClO}_4)_2$  (**4**, bottom). The corresponding peaks at 505.1 and 513.1 exhibited by  $5x$  ( $x = 0.2$ ) corroborate the presence of both complexes (that of **2** and **4**, respectively) in the solid solution.

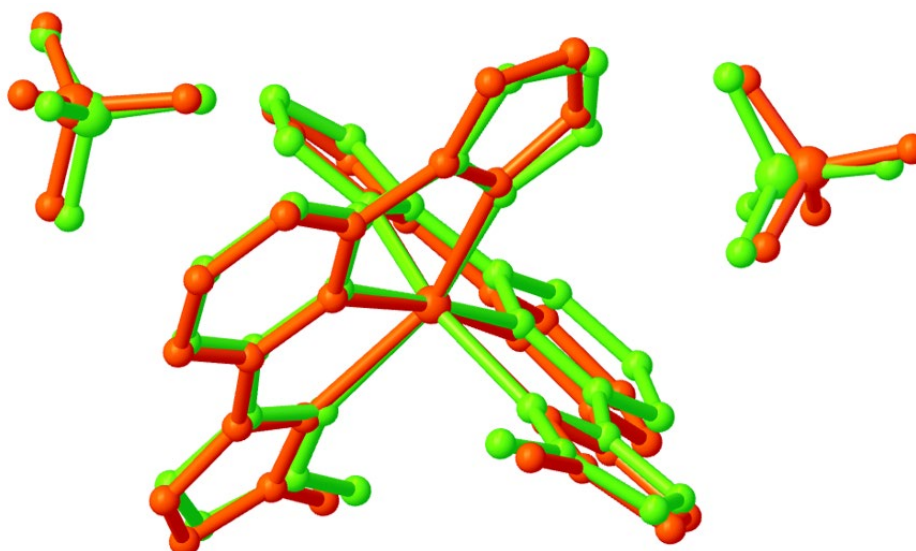


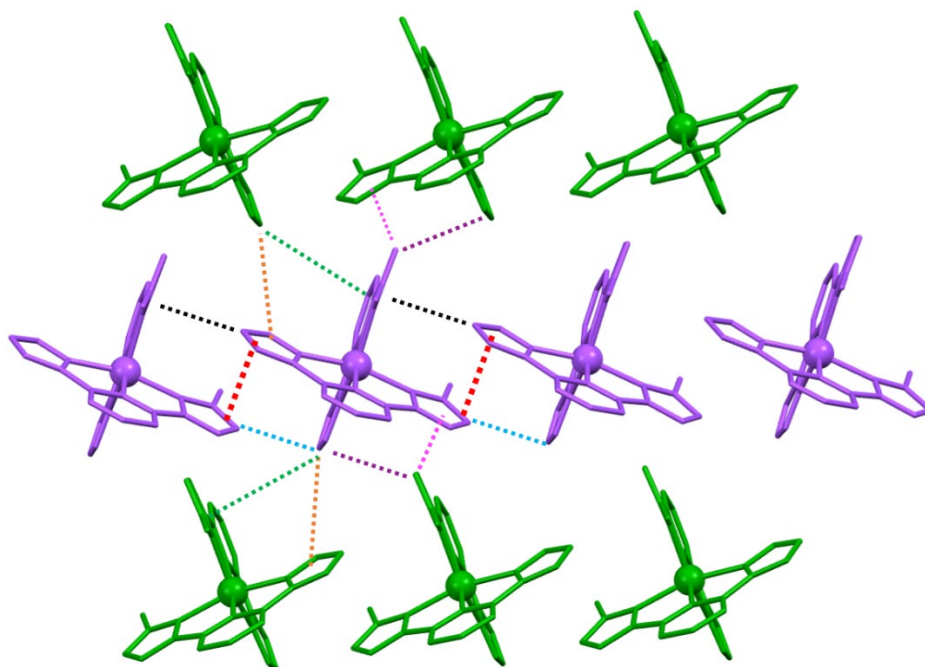
**Figure A3.3.** Overlaid crystal structures of reported  $[\text{Fe}(\text{Me}1,3\text{bpp})_2](\text{ClO}_4)_2$  (**2**, orange) and  $[\text{Zn}(\text{Me}1,3\text{bpp})_2](\text{ClO}_4)_2$  (**4**, green) at 100K.

**Table A3.3.** Crystallographic data, average Fe-N bond lengths and distortion parameters for [Zn(Me1,3bpp)<sub>2</sub>](ClO<sub>4</sub>)<sub>2</sub> (**4**) and (for comparison) Fe(Me-1,3bpp)<sub>2</sub>](ClO<sub>4</sub>)<sub>2</sub> (**2**).

Compound	<b>2</b>	<b>4</b>
Formula	C <sub>24</sub> H <sub>22</sub> Cl <sub>2</sub> FeN <sub>10</sub> O <sub>8</sub>	C <sub>24</sub> H <sub>22</sub> Cl <sub>2</sub> ZnN <sub>10</sub> O <sub>8</sub>
FW (g mol <sup>-1</sup> )	705.26	714.78
T(K)	100	
Wavelength (Å)	0.71073	
Crystal system	monoclinic	
Space group	C2/c	
<i>a</i> (Å)	41.290(9)	41.768(3)
<i>b</i> (Å)	8.0448(15)	8.1368(5)
<i>c</i> (Å)	17.843(4)	17.9388(11)
β (°)	108.946(14)	112.214(3)
<i>V</i> (Å <sup>3</sup> )	5606(2)	5644.2(6)
<i>Z</i>	8	8
ρ <sub>calcd</sub> (g cm <sup>-3</sup> )	1.671	1.682
μ (mm <sup>-1</sup> )	0.798	1.128
Independent reflections (R <sub>int</sub> )	3428(0.2227)	6498 (0.0411)
Restraints/parameters	82 / 415	0 / 416
Goodness-of-fit on <i>F</i> <sup>2</sup>	1.059	1.036
Final <i>R</i> <sub>1</sub> / <i>wR</i> <sub>2</sub> [ <i>I</i> > 2σ( <i>I</i> )]	0.0700 / 0.1355	0.0361 / 0.0801
Final <i>R</i> <sub>1</sub> / <i>wR</i> <sub>2</sub> [all data]	0.1200 / 0.1553	0.0491 / 0.0855
Largest diff. peak and hole (e Å <sup>-3</sup> )	0.881 / -0.412	0.609 / -0.551
<Fe-N>	1.96(4)	2.16(0)
Σ	93.3(1)	137.1(3)
Θ	367.8	445.7(6)

**Table A3.4.** Distances of selected  $\pi\cdots\pi$  and C-H $\cdots\pi$  interactions within compounds **2** and **4** at 100k.

interaction	Labels		Distance (Å) to centroid	Com pd.
$\pi\cdots\pi$ (1)	Cg(N1N2C2C3C4) $\cdots$ Cg(N4N5C10C11C12)	■ ■ ■ ■	3.566	<b>2</b>
C-H $\cdots\pi$ (1)	C1-H1B $\cdots$ Cg(N9N10C22C23C24)	■ ■ ■ ■	3.272	<b>2</b>
C-H $\cdots\pi$ (2)	C12-H12 $\cdots$ Cg(N6N7C14C15C16)	■ ■ ■ ■	2.584	<b>2</b>
C-H $\cdots\pi$ (2)	C24-H24 $\cdots$ Cg(N4N5C10C11C12)	■ ■ ■ ■	3.320	<b>2</b>
C-H $\cdots\pi$ (2)	C24-H24 $\cdots$ Cg(N6N7C14C15C16)	■ ■ ■ ■	4.219	<b>2</b>
C-H $\cdots\pi$ (2)	C15-H15 $\cdots$ Cg(N1N2C2C3C4)	■ ■ ■ ■	3.154	<b>2</b>
C-H $\cdots\pi$ (2)	C15-H15 $\cdots$ Cg(N9N10C22C23C24)	■ ■ ■ ■	3.070	<b>2</b>
$\pi\cdots\pi$ (1)	Cg(N1N2C2C3C4) $\cdots$ Cg(N4N5C10C11C12)	■ ■ ■ ■	3.474	<b>4</b>
C-H $\cdots\pi$ (1)	C1-H1B $\cdots$ Cg(N9N10C22C23C24)	■ ■ ■ ■	3.145	<b>4</b>
C-H $\cdots\pi$ (2)	C12-H12 $\cdots$ Cg(N6N7C14C15C16)	■ ■ ■ ■	2.756	<b>4</b>
C-H $\cdots\pi$ (2)	C24-H24 $\cdots$ Cg(N4N5C10C11C12)	■ ■ ■ ■	3.548	<b>4</b>
C-H $\cdots\pi$ (2)	C24-H24 $\cdots$ Cg(N6N7C14C15C16)	■ ■ ■ ■	4.164	<b>4</b>
C-H $\cdots\pi$ (2)	C15-H15 $\cdots$ Cg(N1N2C2C3C4)	■ ■ ■ ■	3.550	<b>4</b>
C-H $\cdots\pi$ (2)	C15-H15 $\cdots$ Cg(N9N10C22C23C24)	■ ■ ■ ■	2.972	<b>4</b>

**Figure A3.4.** Sheet organization of the cations of **4**, emphasizing the intermolecular **interactions** formed by each complex with its first-neighbors (shown in colors for reference in Table A3.4). The two different orientations of the cations are shown in green and purple.

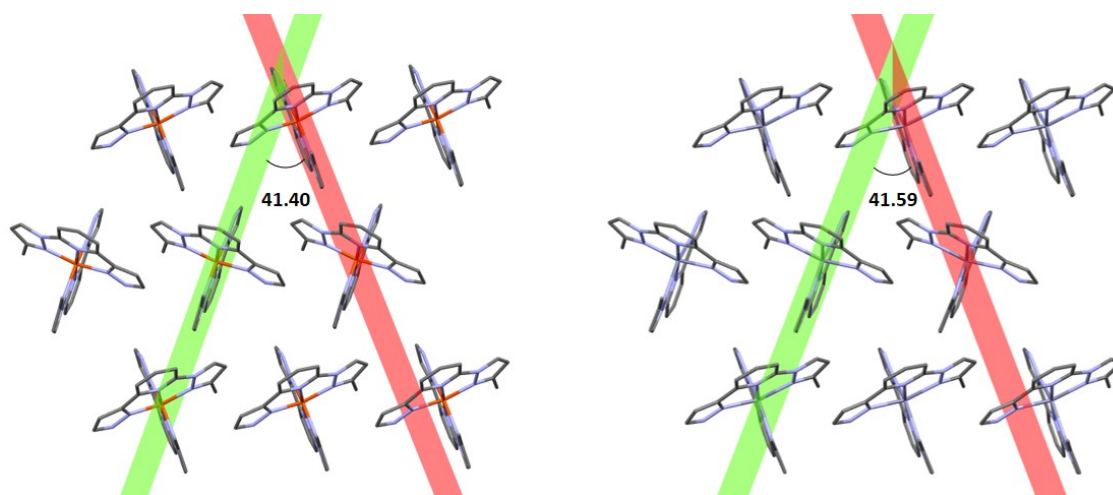
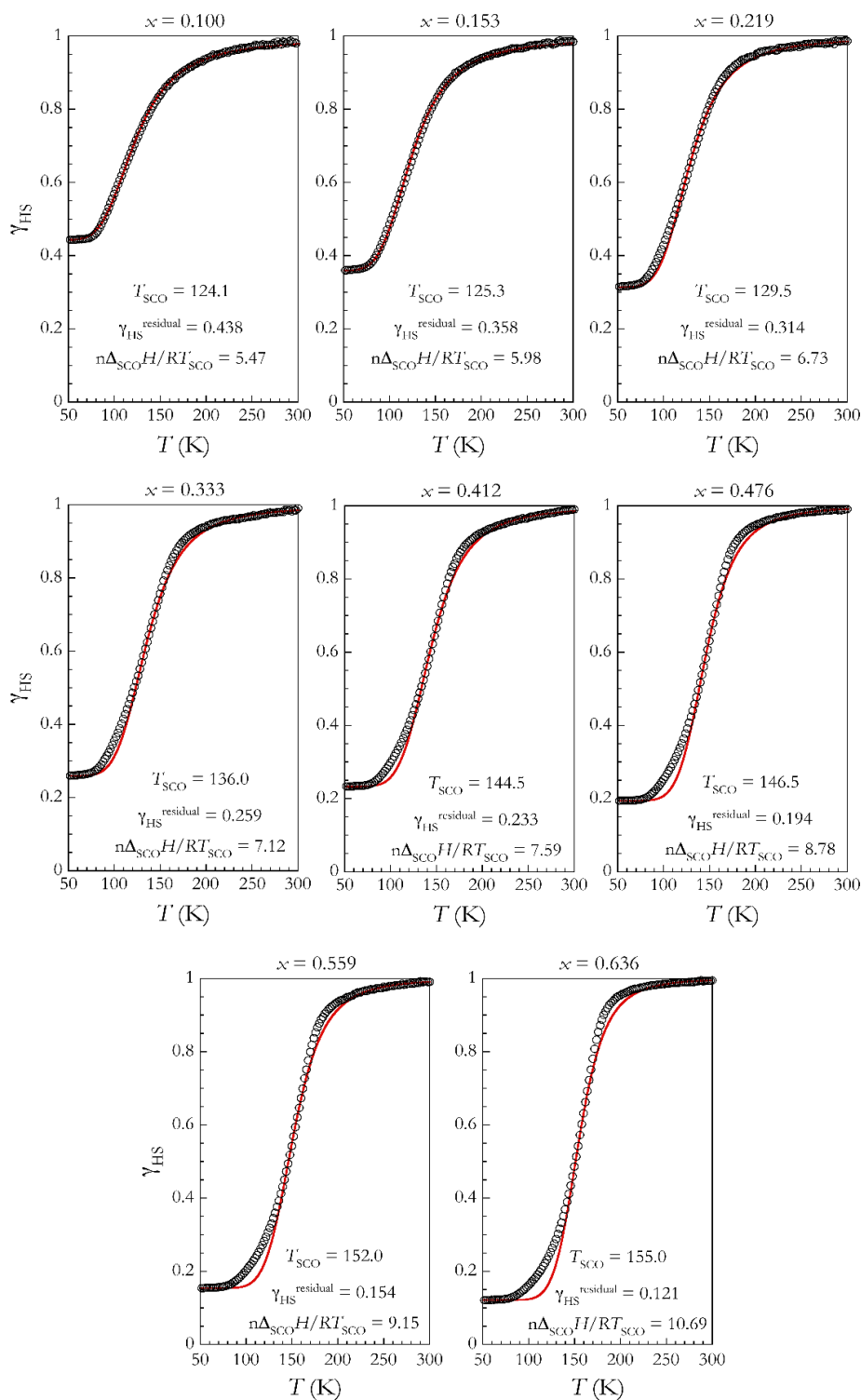


**Figure A3.5.** Angle between complexes in the two different orientations for  $\text{Fe}(\text{Me-1,3bpp})_2(\text{ClO}_4)_2$  (**2**, left) and  $\text{Fe}(\text{Me-1,3bpp})_2(\text{ClO}_4)_2$  (**4**, right), measured using idealized planes of two equivalent ligands.

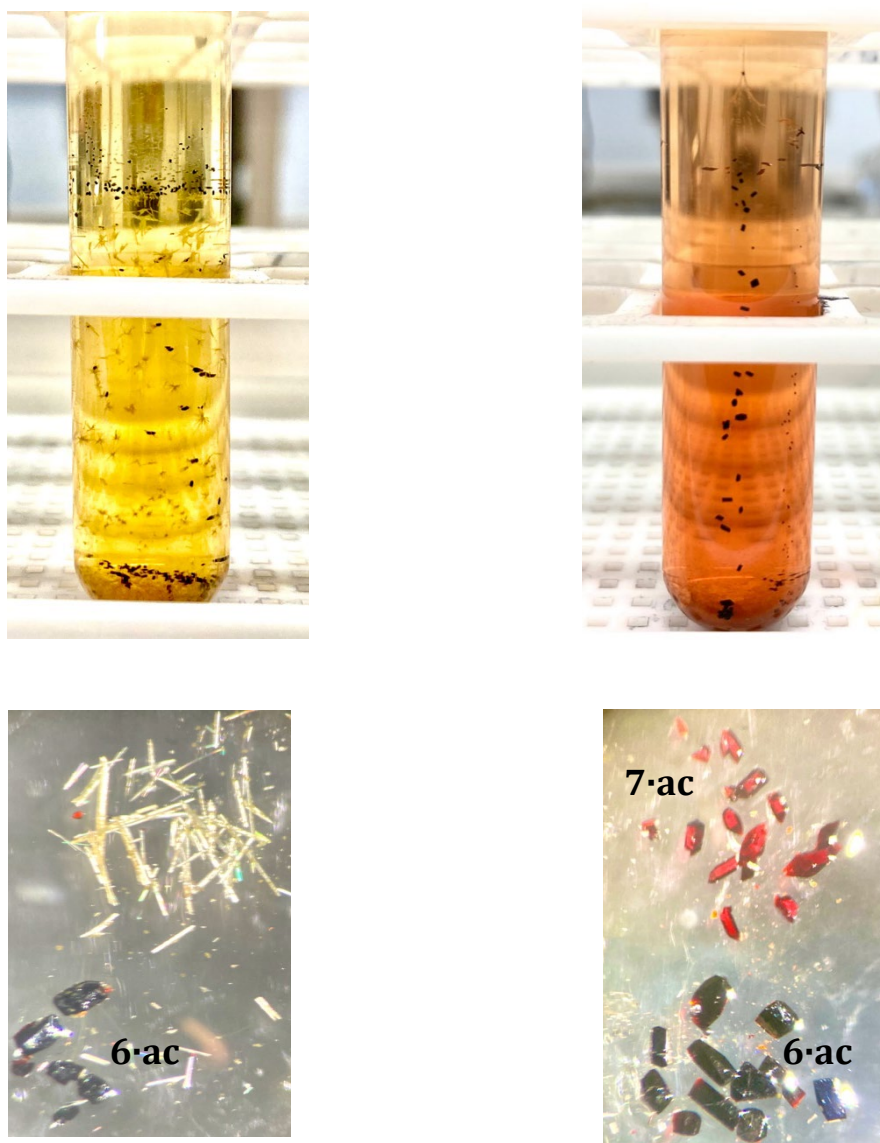


x	x:0.10	x:0.15	x:0.22	x:0.33	x:0.41	x:0.48	x:0.56	x:0.64
Formula	C24 H22 Fe0.164 N10 Zn0.836, 2(ClO4)	C24 H22 Fe0.19 N10 Zn0.81, 2(ClO4)	C24 H22 Fe0.166 N10 Zn0.834, 2(ClO4)	C24 H22 Fe0.381 N10 Zn0.619, 2(ClO4)	C24 H22 Fe0.498 N10 Zn0.502, 2(ClO4)	C24 H22 Fe0.618 N10 Zn0.382, 2(ClO4)	C24 H22 Fe0.664 N10 Zn0.336, 2(ClO4)	C24 H22 Fe0.655 N10 Zn0.345, 2(ClO4)
FW (g mol <sup>-1</sup> )	713.21	712.96	713.20	711.16	710.05	708.89	708.47	708.55
T(K)	100K							
Wavelength (Å)	0.71073							
Crystal system	monoclinic							
Space group	C 2/c							
a (Å)	41.8400(14)	41.7962(11)	41.853(5)	41.717(3)	41.6935(17)	41.601(2)	41.5382(14)	41.5818(15)
b (Å)	8.1139(3)	8.1127(2)	8.1030(10)	8.0829(8)	8.0820(4)	8.0751(5)	8.0675(3)	8.0616(3)
c (Å)	17.9721(6)	17.9490(5)	17.949(2)	17.9611(15)	17.9300(8)	17.9077(10)	17.8837(6)	17.9002(6)
β (°)	112.037(2)	112.017(2)	112.073(5)	111.545(5)	111.141(3)	110.962(3)	110.542(2)	110.605(2)
V (Å <sup>3</sup> )	5655.5(3)	5642.3(3)	5640.8(12)	5633.2(9)	5635.2(5)	5617.7(6)	5611.9(3)	5616.6(4)
Z	8							
ρ <sub>calcd</sub> (g cm <sup>-3</sup> )	1.675	1.679	1.680	1.677	1.674	1.676	1.677	1.676
μ (mm <sup>-1</sup> )	1.071	1.065	1.073	1.002	0.963	0.925	0.911	0.913
Independent reflections (R <sub>int</sub> )	6465 (0.0455)	8360(0.0542)	5231(0.0545)	5743(0.0845)	5742 (0.0636)	6881(0.0618)	5982(0.0495)	7562(0.0463)
Restraints/parameters	14/419	28/433	14/ 419	14/ 419	14/ 419	14/ 420	14/ 419	28/ 429
Goodness-of-fit on F <sup>2</sup>	1.024	1.025	1.022	1.046	1.049	1.037	1.039	1.047
Final R <sub>1</sub> /wR <sub>2</sub> [I>2σ(I)]	0.0385/0.0813	0.0421/ 0.0890	0.0391/ 0.0843	0.0499/ 0.0980	0.0489/ 0.0969	0.0485/ 0.1110	0.0441/ 0.1000	0.0429/ 0.0891
Final R <sub>1</sub> /wR <sub>2</sub> [all data]	0.0593/0.0914	0.0675/0.0991	0.0581/ 0.0925	0.0922/ 0.1144	0.0969/ 0.1097	0.0758/ 0.1240	0.0613/ 0.1078	0.0648/ 0.0972
Largest diff. peak and hole (e Å <sup>-3</sup> )	0.584/ -0.515	0.400/-0.542	0.318/ -0.350	0.354/ -0.507	0.623/ -0.511	0.486/ -0.650	0.478/ -0.604	0.392/ -0.432
<Fe-N>	2.155	2.155	2.156	2.127	2.104	2.089	2.066	2.070
Σ	136.9(3)	136.8(2)	137.8(3)	131.6(4)	126.6(4)	123.4(3)	117.3(3)	119.3(3)
θ	444.5(7)	444.1(6)	447.3(8)	425.7(10)	409.7(9)	399.5(8)	378.6(8)	385.0(7)

**Table A3.5.** Crystallographic data, average Fe-N bond lengths and distortion parameters for [Fe<sub>x</sub>Zn<sub>1-x</sub>(Me1,3bpp)<sub>2</sub>](ClO<sub>4</sub>)<sub>2</sub> (**5x**). Anisotropic data.



**Figure A3.6.** Temperature dependence of the HS fraction  $\gamma_{HS}$  in compounds  $3x$  and fits of Eq. 1 (see main text) to these (full red lines) for the given value of  $T_{SCO}$ ,  $\gamma_{HS}^{residual}$  and  $n\Delta_{SCO}H/RT_{SCO}$ .

**APPENDIX 4 - CHAPTER 4. A MONONUCLEAR SPIN-CROSSOVER COMPLEX  
DESCRIBING FOUR DISTINCT THERMAL ROUTES**

**Figure A4.1.** (Left). Pictures of the co-crystallization of **6·ac** (dark red crystals) and the protonated bbbp,  $[\text{Na}_2\text{bbp}](\text{ClO}_4)_2$ , (yellow-orange needles) from a stoichiometric reaction of ligands L and bbbp in dry acetone, using diethyl ether as the crystallization medium. (Right) Pictures of the co-crystallization of **6·ac** (dark red crystals) and the **7·ac** (shining red crystals) from a stoichiometric reaction of ligands L and the disodium salt of bbbp in dry acetone, using diethyl ether as the crystallization medium. (Top pictures) Pictures of the crystallization tubes after 5 days of diffusion for the respective reactions. (Down pictures). Pictures from microscope of the co-crystallized compounds separated manually.

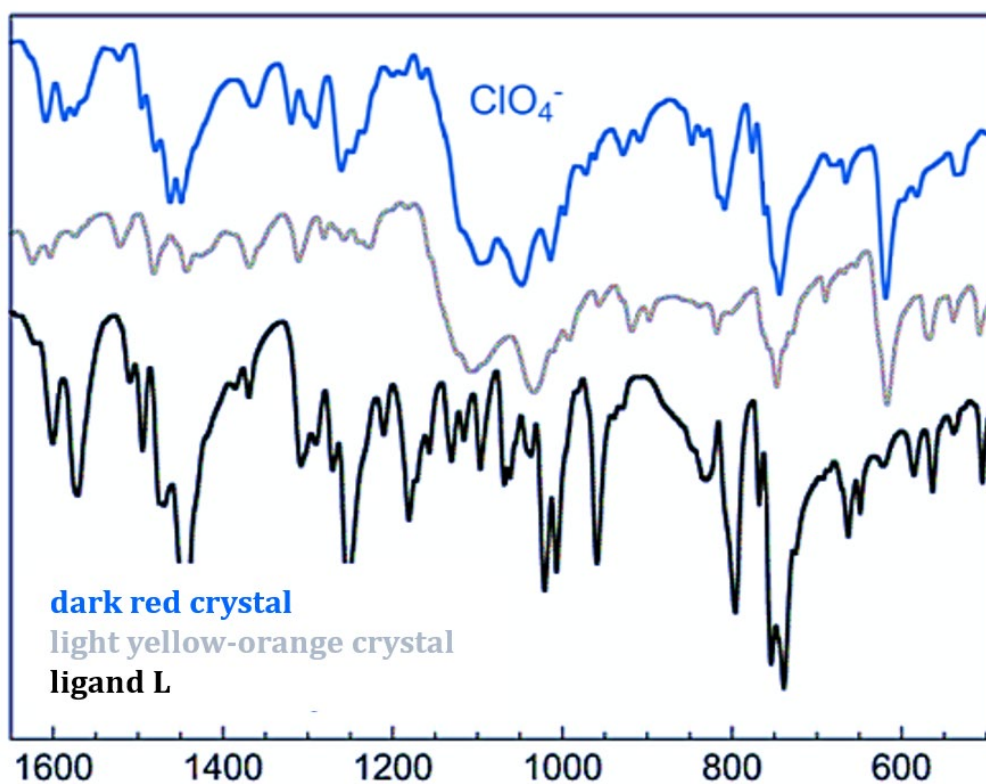


**Figure A4.2.** IR spectra of 6·ac (dark red crystals), the yellow-orange crystals; and ligand L. The IR for yellow-orange needles (grey line) is completely different to ligand L. Furthermore, it seems to contain perchlorate.

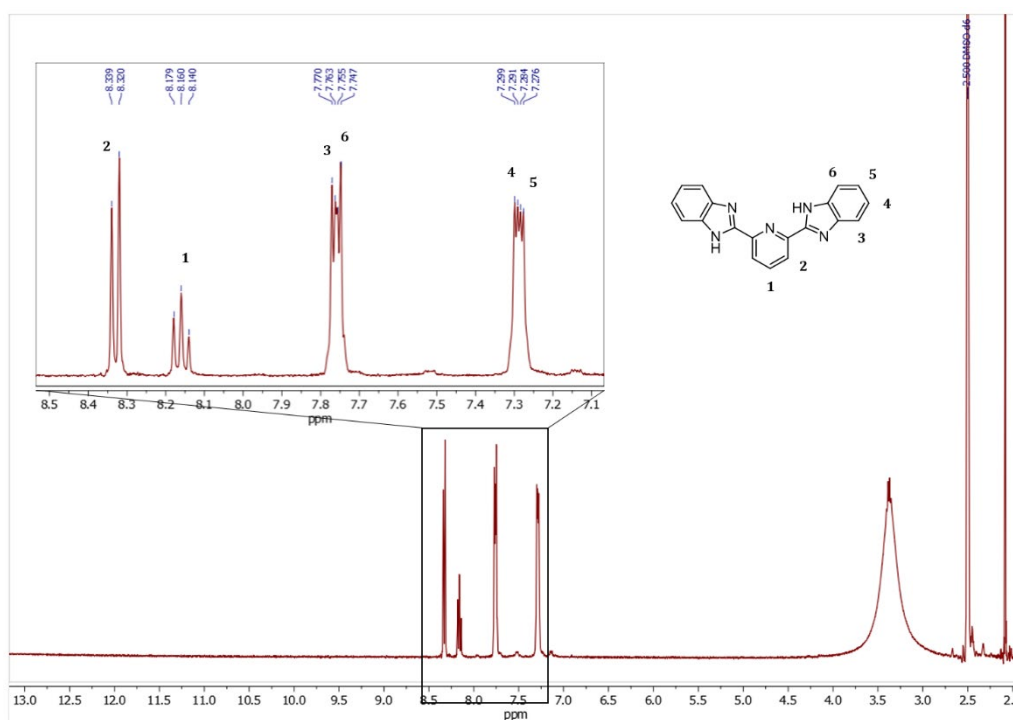


**Figure A4.3.** <sup>1</sup>H NMR of the light yellow-orange needles, which suggest the bbp ligand containing of the sample.

**Table A4.1.** Crystallographic table, average Fe-N bond lengths and distortion parameter of **6·ac**. Description of the thermal transition **6·ac** → **6 $\alpha$** . All structures were collected in one sequence on the same single crystal (except data at 30K).

	<b>6·ac</b>						<b>6<math>\alpha</math></b>			
Formula	C <sub>94</sub> H <sub>80</sub> Cl <sub>4</sub> Fe <sub>2</sub> N <sub>20</sub> O <sub>22</sub>						C <sub>88</sub> H <sub>68</sub> Cl <sub>4</sub> Fe <sub>2</sub> N <sub>20</sub> O <sub>20</sub>			
FW (g mol <sup>-1</sup> )	2095.28						1979.12			
T (K)	30(5)	100(2)	150(2)	200(2)	250(2)	280(2)	320(2)	340(2)	360(2)	390(2)
Wavelength (Å)	0.7749									
Crystal system	triclinic									
Space group	P-1									
a (Å)	12.4124(6)	12.4111(5)	12.4351(5)	12.4624(5)	12.4947(5)	12.5238(5)	12.6524(6)	13.008(4)	13.5526(13)	13.5487(11)
b (Å)	17.8190(8)	17.8454(7)	17.8748(7)	17.8925(7)	17.9022(7)	17.9008(8)	17.8660(9)	17.610(5)	17.630(2)	17.659(2)
c (Å)	22.7733(10)	22.8090(9)	22.8722(10)	22.9508(9)	23.0336(9)	23.1022(10)	23.2179(12)	23.247(7)	22.071(2)	21.983(2)
$\alpha$ (°)	68.239(2)	68.355(2)	68.422(2)	68.522(2)	68.664(2)	68.733(2)	68.823(2)	68.76(2)	109.215(7)	109.146(6)
$\beta$ (°)	79.811(2)	79.941(2)	79.870(2)	79.841(2)	79.808(2)	79.824(2)	79.647(2)	78.43(2)	106.870(7)	106.652(6)
$\gamma$ (°)	86.024(2)	86.244(2)	86.307(2)	86.436(2)	86.564(2)	86.661(2)	86.602(2)	85.54(2)	97.551(7)	97.606(6)
V (Å <sup>3</sup> )	4604.2(4)	4623.4(3)	4653.9(3)	4687.6(3)	4723.3(3)	4750.5(4)	4814.2(4)	4863(3)	4612.7(8)	4609.0(8)
Z	2									
$\rho_{\text{calcd}}$ (g cm <sup>-3</sup> )	1.511	1.505	1.495	1.484	1.473	1.465	1.445	1.431	1.425	1.426
$\mu$ (mm <sup>-1</sup> )	0.650	0.647	0.643	0.638	0.633	0.630	0.621	0.615	0.641	0.642
Independent reflections ( $R_{\text{int}}$ )	22766 (0.0644)	23851 (0.0465)	24985 (0.0489)	25171 (0.0456)	20782 (0.0416)	19403 (0.0494)	14250 (0.0420)	3916 (0.1304)	4371 (0.0953)	4597 (0.0848)
param. / restraints	1311 / 0	1311 / 0	1311 / 0	1311 / 126	1311 / 192	1311 / 192	1311 / 238	1137 / 1438	1310 / 1270	1311 / 1198
Goodness-of-fit	1.041	1.037	1.024	1.014	1.019	1.014	1.020	1.256	1.050	1.035
Final R1 / wR2 [I > 2 $\sigma$ (I)]	0.0466 / 0.1300	0.0388 / 0.0934	0.0416 / 0.1024	0.0451 / 0.1137	0.0476 / 0.1282	0.0521 / 0.1366	0.0631 / 0.1754	0.3036 / 0.6279	0.1068 / 0.2555	0.0927 / 0.2044
Final R1 / wR2 [all data]	0.0530 / 0.1358	0.0538 / 0.1017	0.0592 / 0.1131	0.0651 / 0.1276	0.0662 / 0.1429	0.0766 / 0.1549	0.0843 / 0.1950	0.3763 / 0.6646	0.1726 / 0.3248	0.1558 / 0.2618
largest diff. peak / hole (e Å <sup>3</sup> )	0.828 / -0.799	0.803 / -0.601	0.643 / -0.591	0.634 / -0.616	0.769 / -0.549	0.683 / -0.612	0.719 / -0.906	0.737 / -0.752	0.497 / -0.646	0.426 / -0.544
<Fe1-N> (Å)	2.171(9)	2.172(9)	2.173(9)	2.175(10)	2.175(12)	2.175(12)	2.18(21)	2.2(4)	2.19(13)	2.18(13)
<Fe2-N> (Å)	1.956(9)	1.956(8)	1.958(8)	1.960(9)	1.963(11)	1.969(12)	2.03(21)	2.1(4)	2.15(14)	2.14(12)
$\Sigma$ Fe1 / Fe2	137 / 89	137 / 90	137 / 90	138 / 90	139 / 92	139 / 93	140 / 108	137 / 115	138 / 150	141 / 221

**Table A4.2.** Crystallographic table, average Fe-N bond lengths and distortion parameters for the  $6^\alpha \rightarrow 6^\beta \rightarrow 6^\gamma$  phase transition. All structures were collected in the same single crystal as used to follow the  $6\text{-ac} \rightarrow 6^\alpha$  (except the structures at 100 and 460K; obtained through the same thermal history on a different crystal).

	$6^\alpha$		$6^\beta$		$6^\gamma$			
Formula	$\text{C}_{88}\text{H}_{68}\text{Cl}_4\text{Fe}_2\text{N}_{20}\text{O}_{20}$							
FW (g mol <sup>-1</sup> )	1979.12							
T (K)	280(2)	250(2)	280(2)	330(2)	360 (2)	400(2)	460(2)	100(2)
Wavelength (Å)	0.7749							
Crystal system	triclinic							
Space group	P-1							
a (Å)	13.4514(11)	11.9458(5)	11.9586(4)	11.9855(4)	11.9943(5)	12.0364(11)	12.1096(13)	11.7737(5)
b (Å)	17.6667(14)	18.7208(7)	18.7168(6)	18.7405(7)	17.2248(7)	17.256(2)	17.255(2)	17.0662(7)
c (Å)	21.724(2)	22.5705(9)	22.6188(8)	22.6945(8)	23.3508(9)	23.450(2)	23.520(2)	22.6962(9)
$\alpha$ (°)	109.064(5)	67.005(2)	67.058(2)	67.094(2)	98.696(3)	98.815(6)	98.725(7)	97.611(3)
$\beta$ (°)	106.922(5)	77.709(3)	77.756(2)	77.724(2)	97.990(3)	98.240(6)	98.710(7)	97.009(3)
$\gamma$ (°)	97.541(5)	84.423(3)	84.491(2)	84.545(2)	98.576(3)	98.538(7)	97.996(8)	99.037(3)
V (Å <sup>3</sup> )	4519.6(7)	4539.4(3)	4555.7(3)	4587.8(3)	4650.6(3)	4690.5(8)	4735.1(9)	4416.3(3)
Z	2							
$\rho_{\text{calcd}}$ (g cm <sup>-3</sup> )	1.454	1.448	1.443	1.433	1.413	1.401	1.388	1.488
$\mu$ (mm <sup>-1</sup> )	0.654	0.651	0.649	0.645	0.636	0.630	0.625	0.670
Independent reflections ( $R_{\text{int}}$ )	5167 (0.0892)	10050 (0.0995)	9228 (0.0810)	9043 (0.0820)	7687 (0.0853)	6919 (0.707)	6305 (0.0748)	10111 (0.0744)
param. / restraints	1311 / 1135	1331 / 606	1331 / 624	1331 / 674	1249 / 550	1249 / 583	1246 / 814	1239 / 290
Goodness-of-fit	1.060	1.079	1.051	1.024	1.020	1.030	1.035	1.102
Final R1 / wR2 [I > 2 $\sigma$ (I)]	0.0983 / 0.2152	0.0869 / 0.1857	0.0743 / 0.1572	0.0857 / 0.2087	0.1143 / 0.2744	0.1451 / 0.3359	0.1512 / 0.3600	0.0859 / 0.1885
Final R1 / wR2 [all data]	0.1631 / 0.2710	0.1419 / 0.2361	0.1353 / 0.2003	0.1536 / 0.2716	0.1803 / 0.3359	0.2103 / 0.3930	0.2208 / 0.4224	0.1331 / 0.2231
largest diff. peak / hole (e Å <sup>-3</sup> )	0.493 / -0.538	0.633 / -0.520	0.633 / -0.524	0.670 / -0.629	0.853 / -0.803	0.883 / -1.032	0.850 / -0.958	1.273 / -0.892
<Fe1-N> (Å)	2.16(13)	1.95(4)	1.95(4)	1.95(5)	1.95(8)	1.95(11)	1.95(12)	1.94(4)
<Fe2-N> (Å)	2.11(11)	1.95(4)	1.95(4)	1.96(5)	2.11(8)	2.15(11)	2.14(12)	1.96(4)
$\Sigma$ Fe1 / Fe2	147 / 146	87 / 89	87 / 89	88 / 90	84 / 131	79 / 140	88 / 138	86 / 88

**Table A4.3.** Hydrogen bonding in the structure of **6·ac**, **6<sup>α</sup>**, **6<sup>β</sup>** at 280 K and **6<sup>γ</sup>** at the respective temperatures.

D-H...A	D-H (Å)	H...A (Å)	D-A (Å)	D-H...A (°)
<b>6·ac (280 K)</b>				
N2-H2...O6	0.95(4)	1.95(4)	2.893(4)	176(3)
N4-H4...O10	0.81(4)	2.28(4)	3.084(6)	171(4)
N6-H6...O14	0.81(4)	2.22(4)	3.007(4)	163(4)
N10-H10...O1S	0.83(4)	2.14(4)	2.949(4)	165(3)
N12-H12...O19	0.76(4)	2.12(4)	2.856(5)	165(4)
N14-H14...O13#1	0.83(4)	2.05(4)	2.878(4)	176(4)
N16-H16...O5#1	0.84(4)	2.12(4)	2.937(4)	164(3)
N20-H20...O4	0.90(4)	2.10(4)	2.618(3)	115(3)
<b>6<sup>α</sup> (280 K)</b>				
N2-H2B...O15A	0.87	2.02	2.84(2)	156.2
N4-H4B...O5	0.87	2.15	2.883(13)	141.0
N6-H6A...O10A	0.87	2.04	2.889(12)	164.1
N10-H10B...O2	0.87	1.96	2.569(10)	125.6
N12-H12A...O11A#1	0.87	2.28	3.058(15)	149.4
N14-H14A...O17A	0.87	2.35	3.16(2)	154.2
N14-H14A...O18A	0.87	2.41	3.17(2)	146.6
N16-H16B...O14A#1	0.87	2.12	2.942(19)	156.6
N20-H20A...O4	0.87	2.04	2.622(10)	123.9
<b>6<sup>β</sup> (280 K)</b>				
N2-H2B...O15A	0.86	2.03	2.84(2)	155.5
N4-H4B...O5	0.86	2.14	2.868(13)	141.6
N6-H6A...O10A	0.86	2.05	2.888(12)	163.6
N10-H10B...O2	0.86	1.98	2.575(11)	125.4
N12-H12A...O11A#1	0.86	2.32	3.084(14)	148.8
N14-H14A...O17A	0.86	2.38	3.18(2)	153.4
N14-H14A...O18A	0.86	2.42	3.18(2)	147.4
N16-H16B...O14A#1	0.86	2.14	2.945(19)	156.5
N20-H20A...O4	0.86	2.04	2.620(10)	123.7
<b>6<sup>γ</sup> (100 K)</b>				
N2-H2B...O5	0.88	2.01	2.885(10)	170.4
N4-H4B...O9	0.88	2.09	2.933(11)	160.9
N4-H4B...O10	0.88	2.32	3.011(11)	135.7
N6-H6A...O1	0.88	1.98	2.586(9)	125.0
N12-H12A...O13	0.88	2.01	2.843(10)	158.1
N14-H14A...O17	0.88	1.99	2.850(10)	166.6
N16-H16B...O3	0.88	2.30	2.776(9)	113.9
N20-H20D...O4	0.88	1.99	2.588(9)	124.2

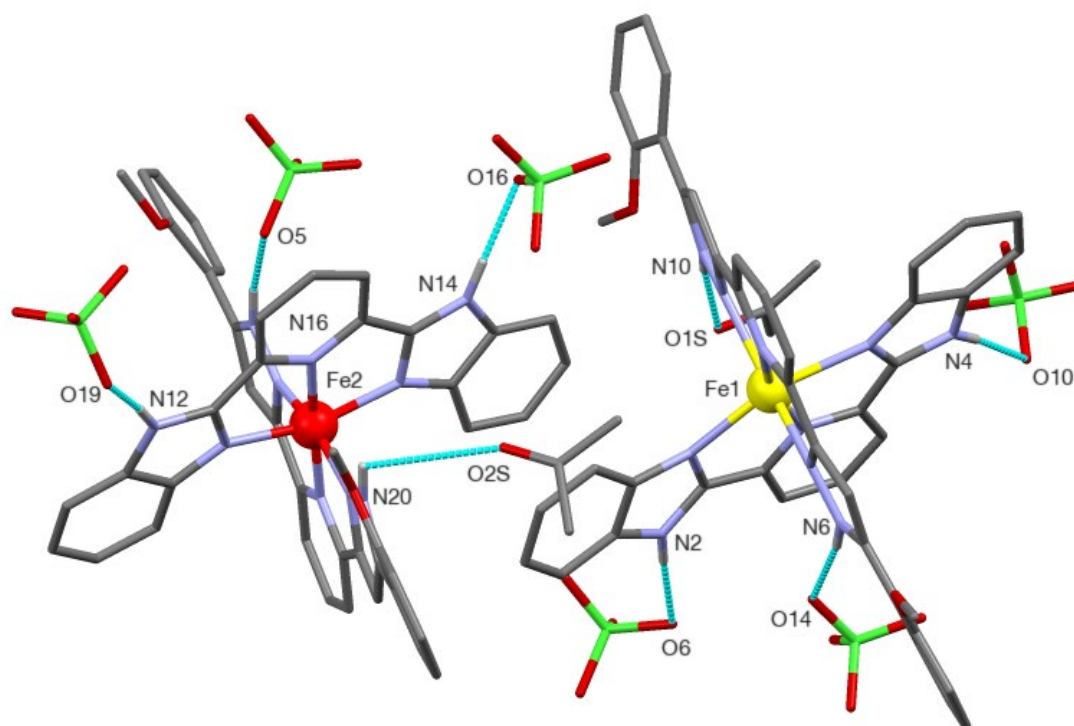


**Figure A4.4.** Molecular representation of one asymmetric unit of  $[\text{FeL}(\text{bbp})](\text{ClO}_4)_2 \cdot \text{ac}$  (**6·ac**), emphasizing the hydrogen bonds between perchlorate ions or acetone molecules and the N–H groups of the complexes (dashed cyan lines). Carbon, oxygen The HS Fe is in yellow while the LS one is red.



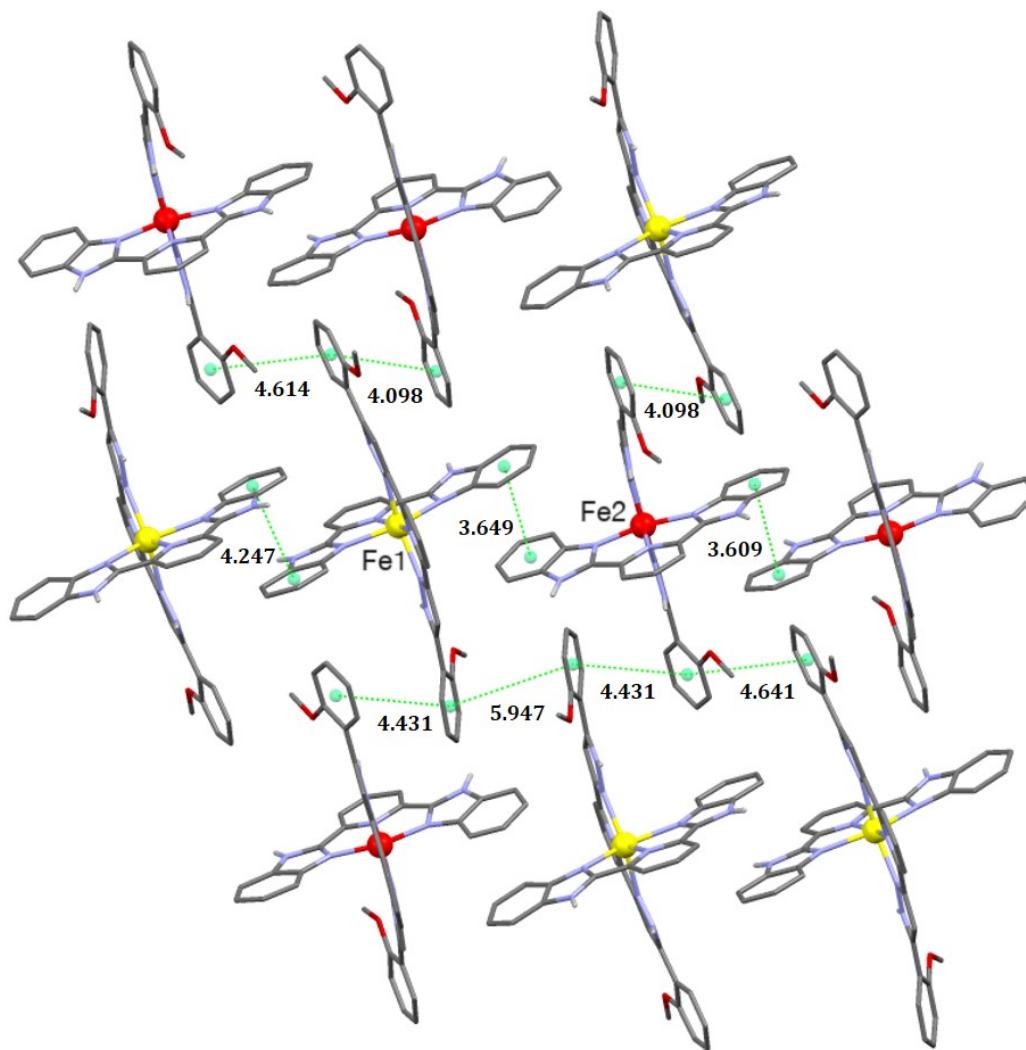


**Figure A4.5.** Sheet organization of the [FeL(bbp)]<sup>2+</sup> cations in 6·ac, emphasizing the π···π intermolecular interactions (dashed green lines) around the complexes of one asymmetric unit within these sheets. The HS Fe(II) centers are in yellow, while the LS ones are in red. All distances under the marked interactions are in angstroms.

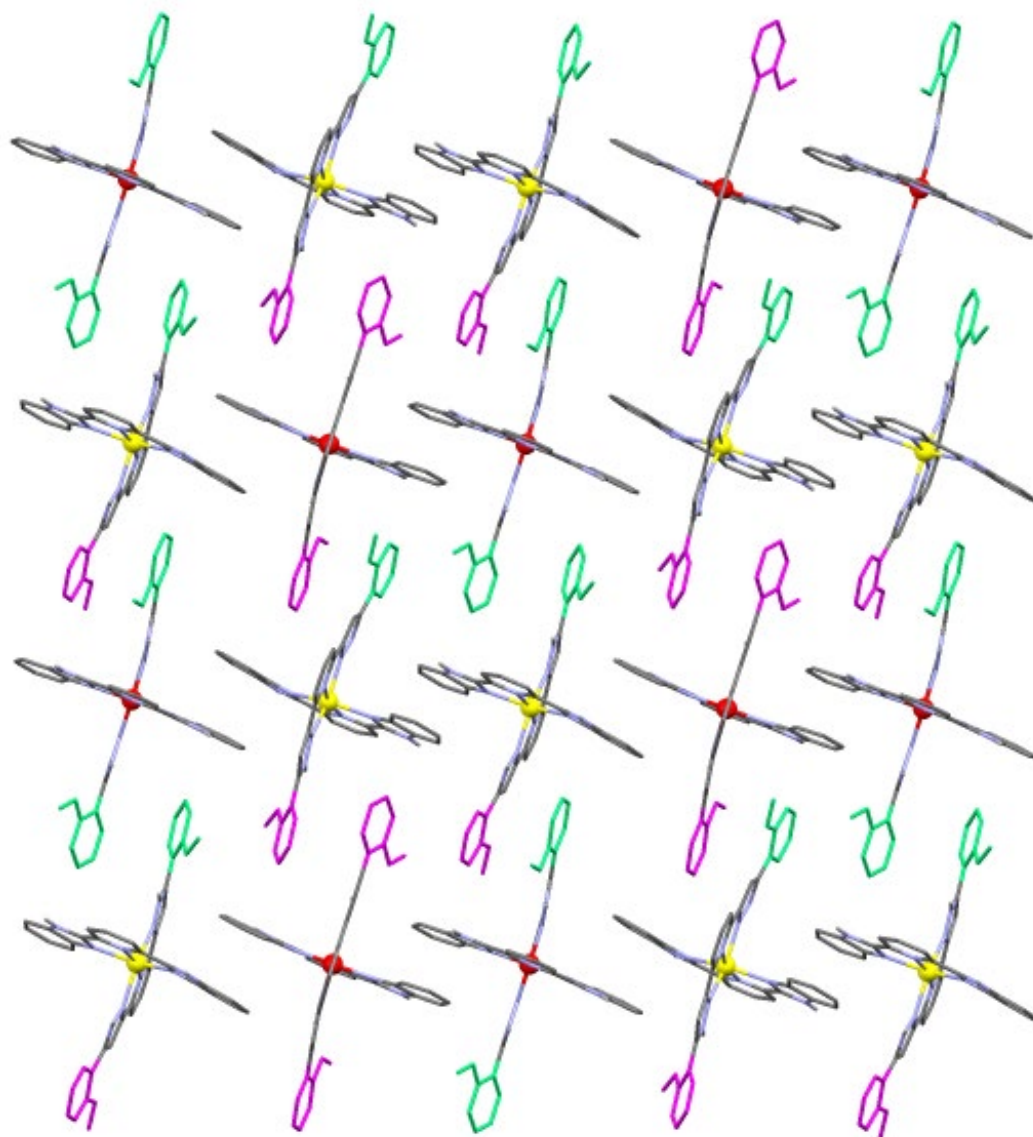


**Figure A4.6.** Sheet organization of the  $[\text{FeL}(\text{bbp})]^{2+}$  cations in **6-ac**, emphasizing the two orientations (different colors) of the methoxyphenyl groups with respect to the plane of the sheet made up by the complex cations (green towards the reader and violet away from the reader). The HS Fe(II) centers are in yellow, while the LS ones are in red.

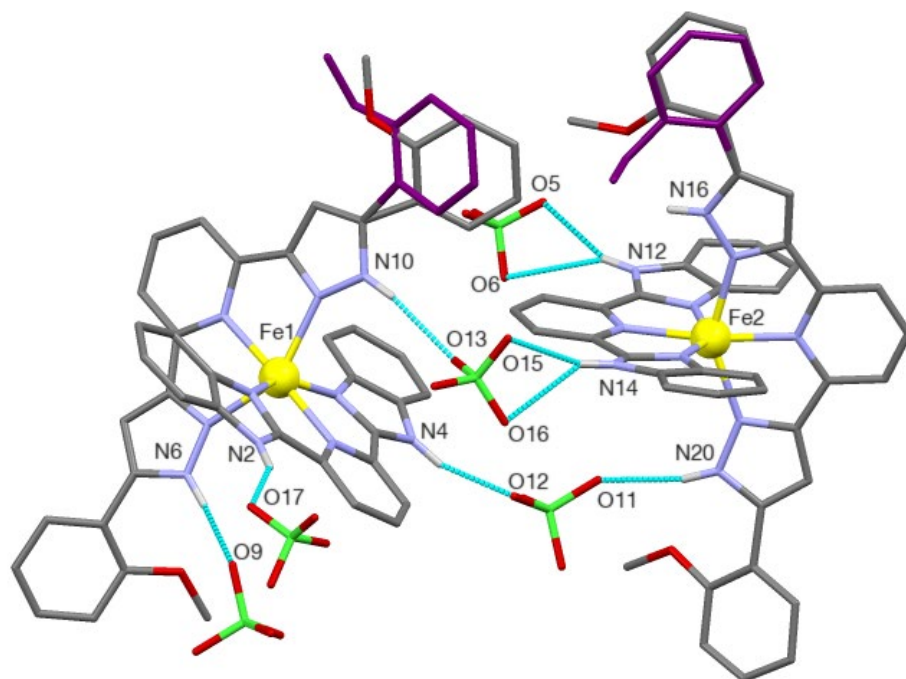


**Figure A4.7.** Molecular representation of one asymmetric unit of [FeL(bbp)](ClO<sub>4</sub>)<sub>2</sub> (**6<sup>a</sup>**), emphasizing the hydrogen bonds between perchlorate ions or acetone molecules and the N–H groups of the complexes (dashed cyan lines). Carbon, oxygen and nitrogen atoms are shown in grey, red and blue, respectively. The HS Fe is in yellow while the LS one is red.

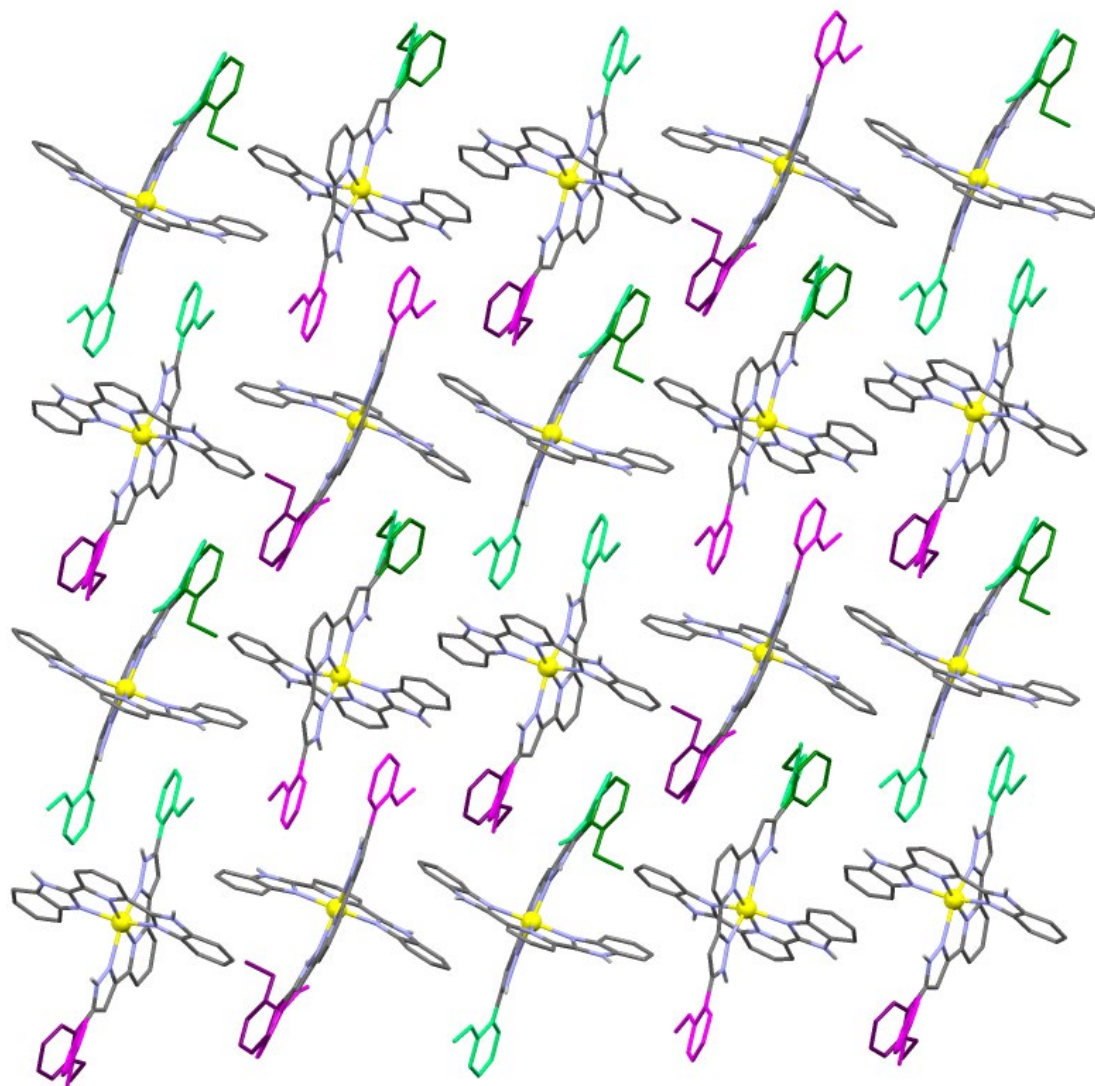


**Figure A4.8.** Sheet organization of the  $[\text{FeL}(\text{bbp})]^{2+}$  cations in  $6^\alpha$ , emphasizing the two orientations (different colors) of the methoxyphenyl groups with respect to the plane of the sheet made up by the complex cations (green towards the reader and red away from the reader). The disorder present on 50% of the phenyl rings is also shown with darker colours. (Dark green and dark violet for phenyl rings towards the reader and away from the reader, respectively). The HS Fe(II) centers are in yellow.

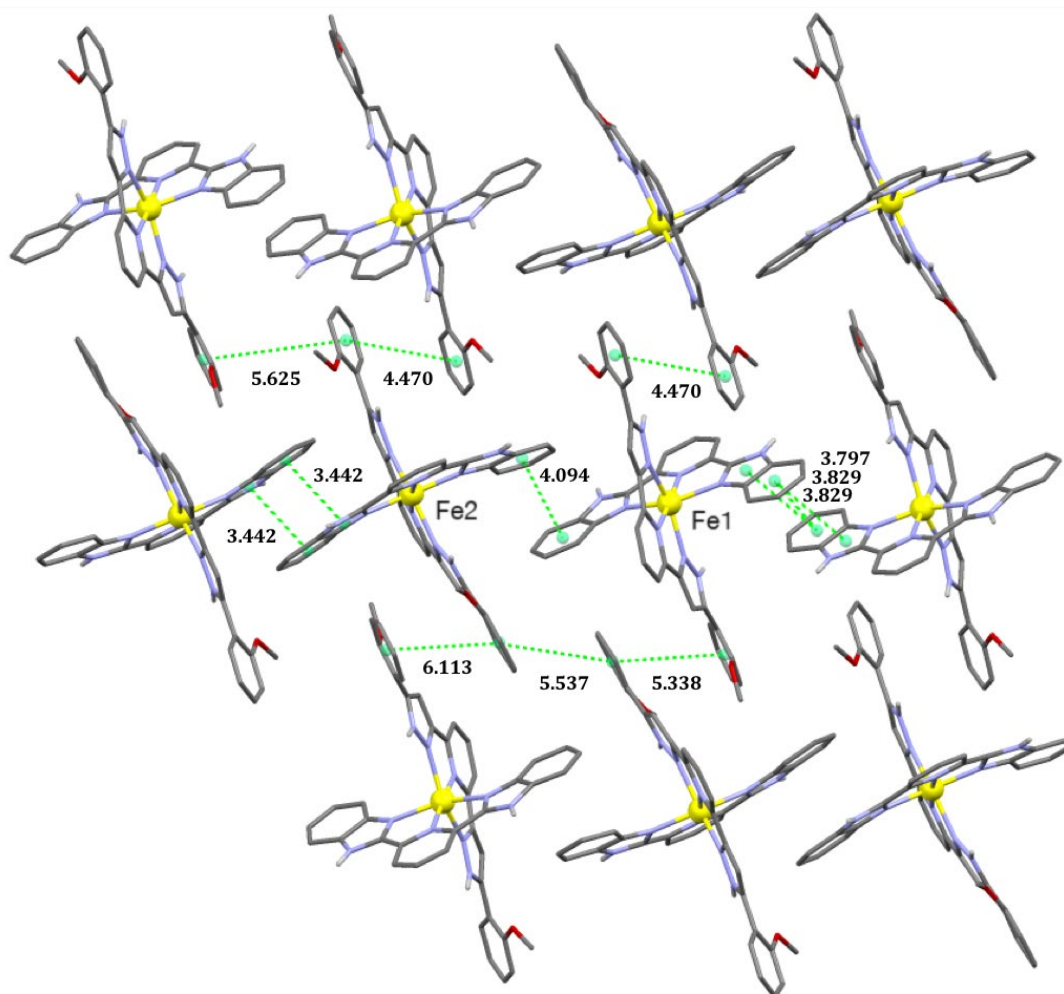


**Figure A4.9.** Sheet organization of the  $[\text{FeL}(\text{bbp})]^{2+}$  cations in  $6^\alpha$ , emphasizing the  $\pi \cdots \pi$  intermolecular interactions (dashed green lines) around the complexes of one asymmetric unit within these sheets. The HS Fe(II) centers are in yellow. All distances under the marked interactions are in angstroms.

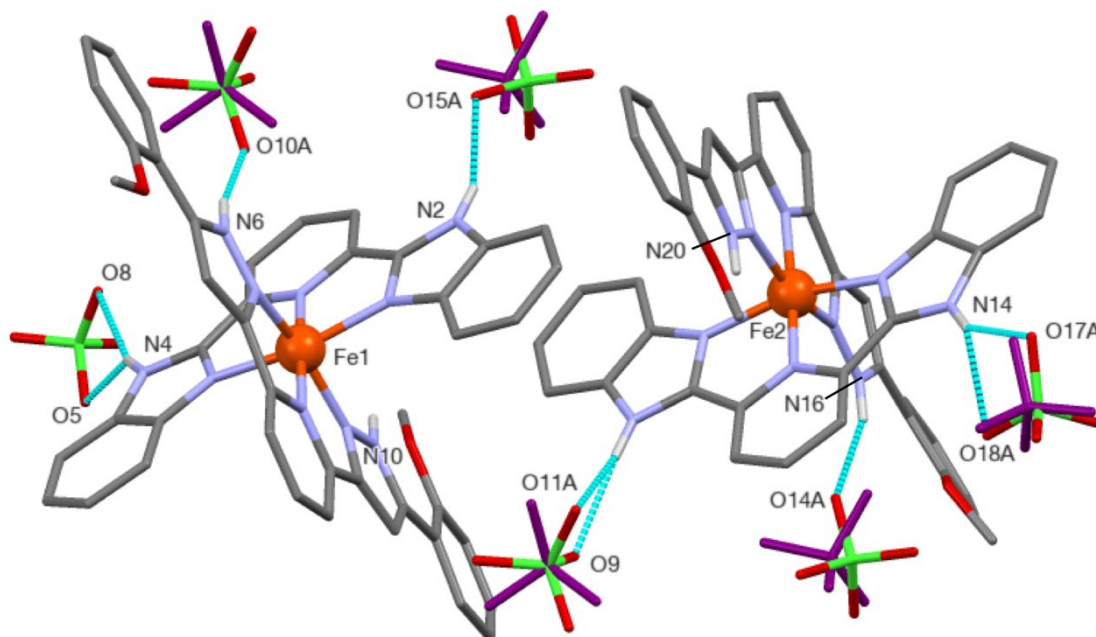


**Figure A4.10.** Representation of one asymmetric unit of the molecular structure of [FeL(bbp)](ClO<sub>4</sub>)<sub>2</sub> (**6<sup>β</sup>**,LS), emphasizing the hydrogen bonds between perchlorate ions and the N-H groups of the complexes, and (in purple) the disorder of some of these anions. Only hydrogen atoms on heteroatoms are shown.

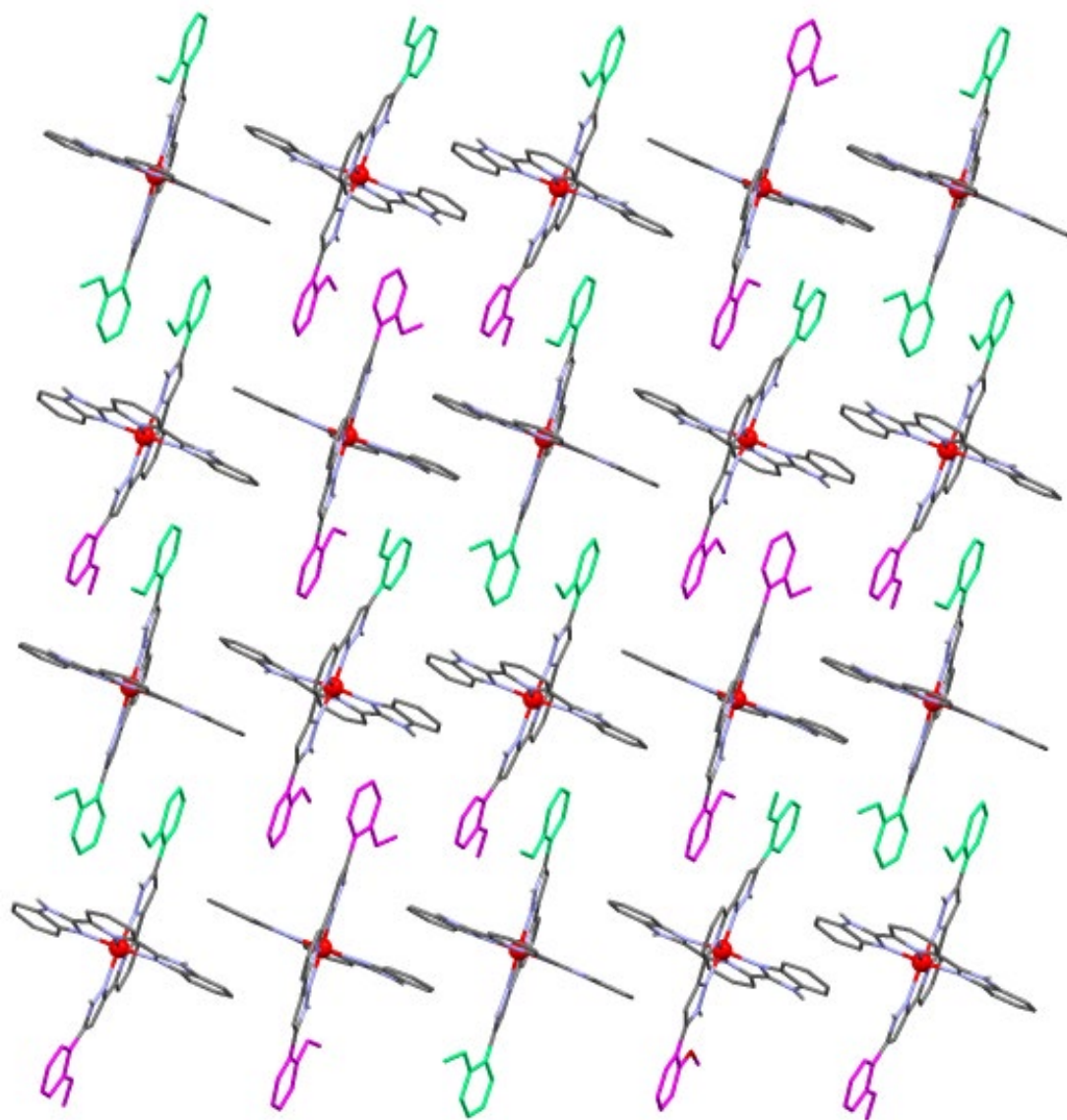


**Figure A4.11.** Sheet organization of the  $[\text{FeL}(\text{bbp})]^{2+}$  cations in  $6\beta$ , emphasizing the two orientations (different colors) of the methoxyphenyl groups with respect to the plane of the sheet made up by the complex cations (green towards the reader and violet away from the reader). The LS Fe(II) centers are in red.

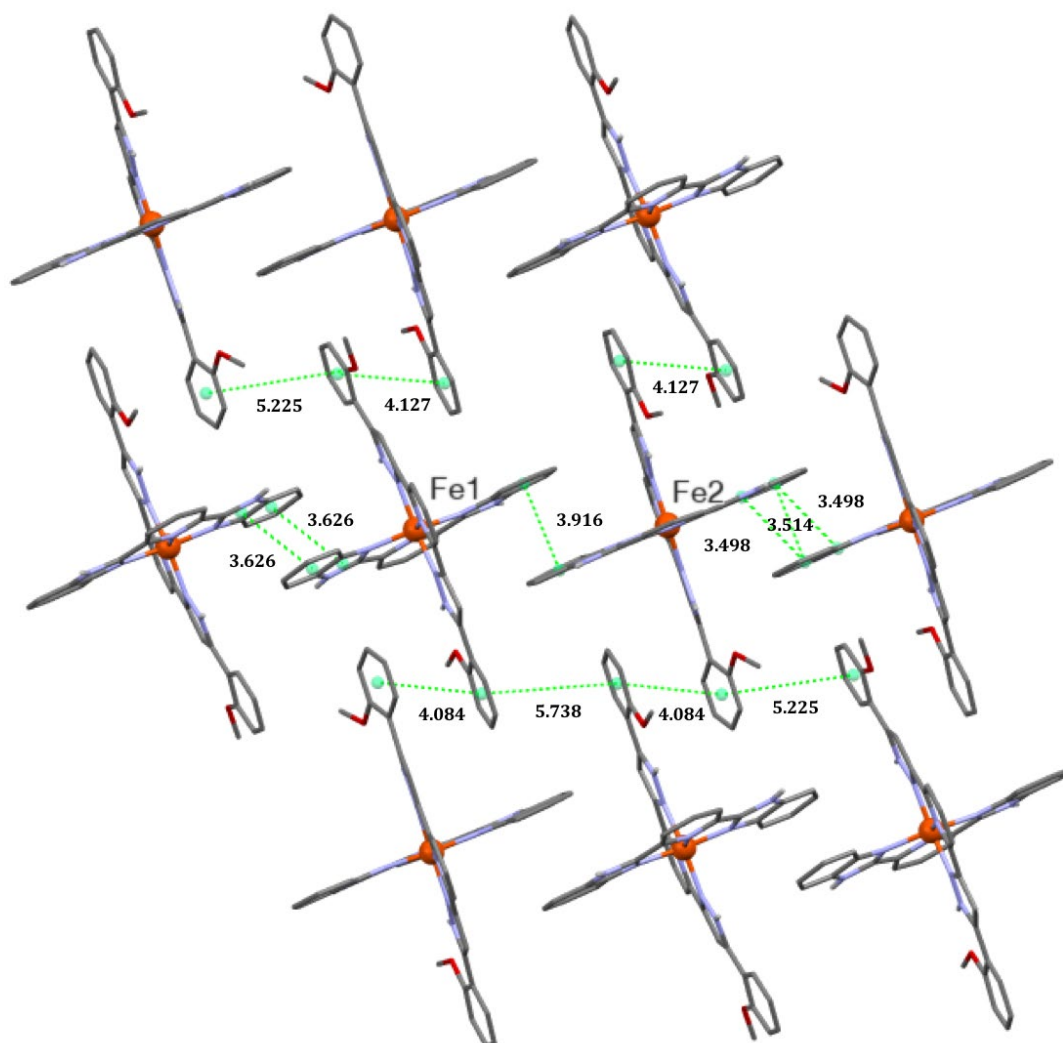


**Figure A4.12.** Sheet organization of the  $[\text{FeL}(\text{bbp})]^{2+}$  cations in  $6\beta$ , emphasizing the  $\pi\cdots\pi$  intermolecular interactions (dashed green lines) around the complexes of one asymmetric unit within these sheets. The HS Fe(II) centers are in yellow. All distances under the marked interactions are in angstroms.



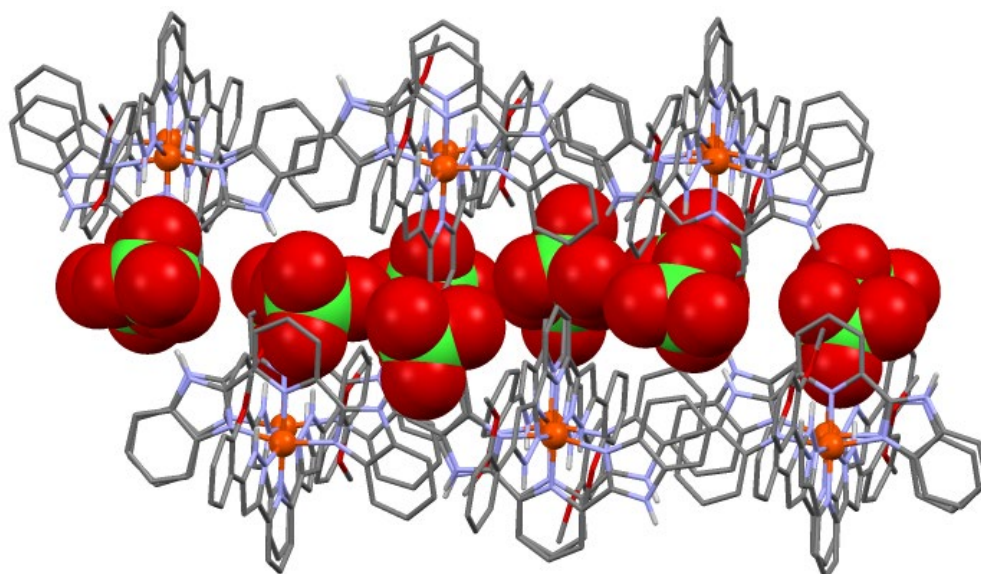


**Figure A4.13.** View of two sheets of  $[\text{FeL}(\text{bbp})]^{2+}$  cations in the structure of **6<sup>B</sup>** down direction parallel to them, emphasizing in spacefill style the perchlorate counter ions of the compound lying in between.

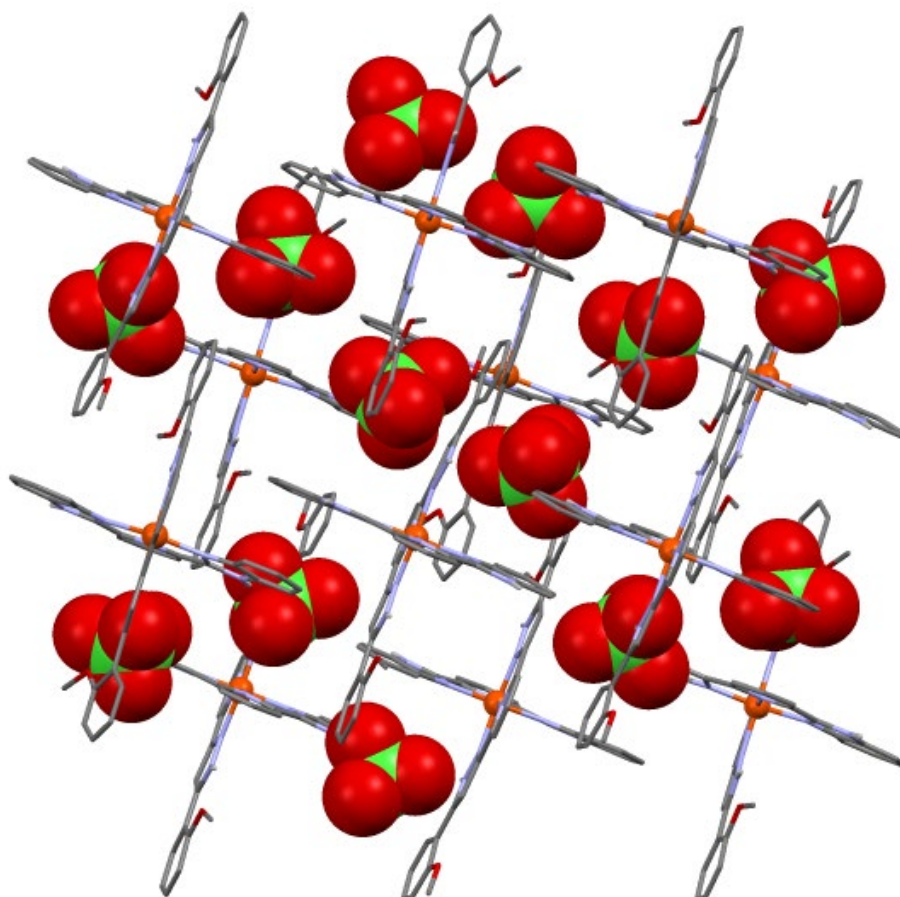


**Figure A4.14.** View of two sheets of  $[\text{FeL}(\text{bbp})]^{2+}$  cations in the structure of **6<sup>B</sup>** down a direction perpendicular to them, emphasizing in spacefill style the  $\text{ClO}_4^-$  counter ions of the compound lying in between.

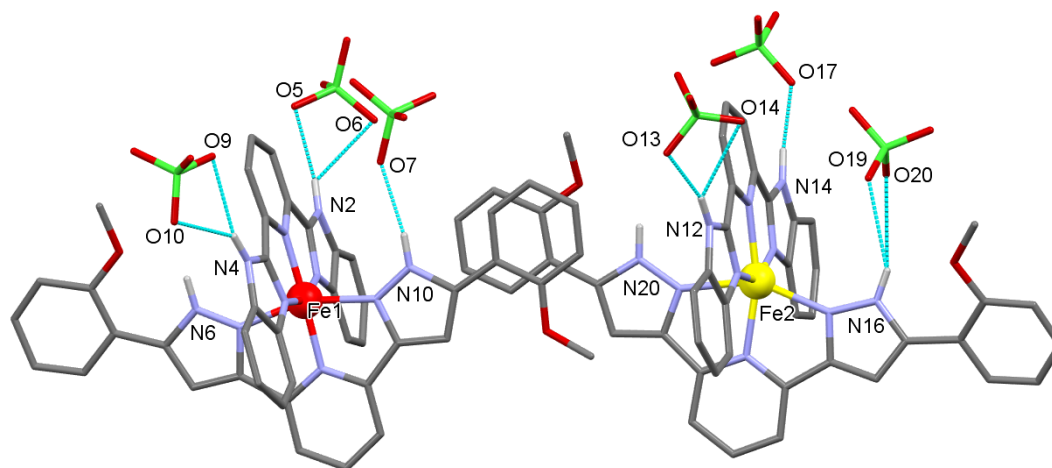


**Figure A4.15.** Molecular representation of one asymmetric unit of [FeL(bbp)](ClO<sub>4</sub>)<sub>2</sub> (6v,[LS-HS]), emphasizing the hydrogen bonds between perchlorate ions or acetone molecules and the N-H groups of the complexes (dashed cyan lines). Carbon, oxygen The HS Fe is in yellow while the LS one is red.

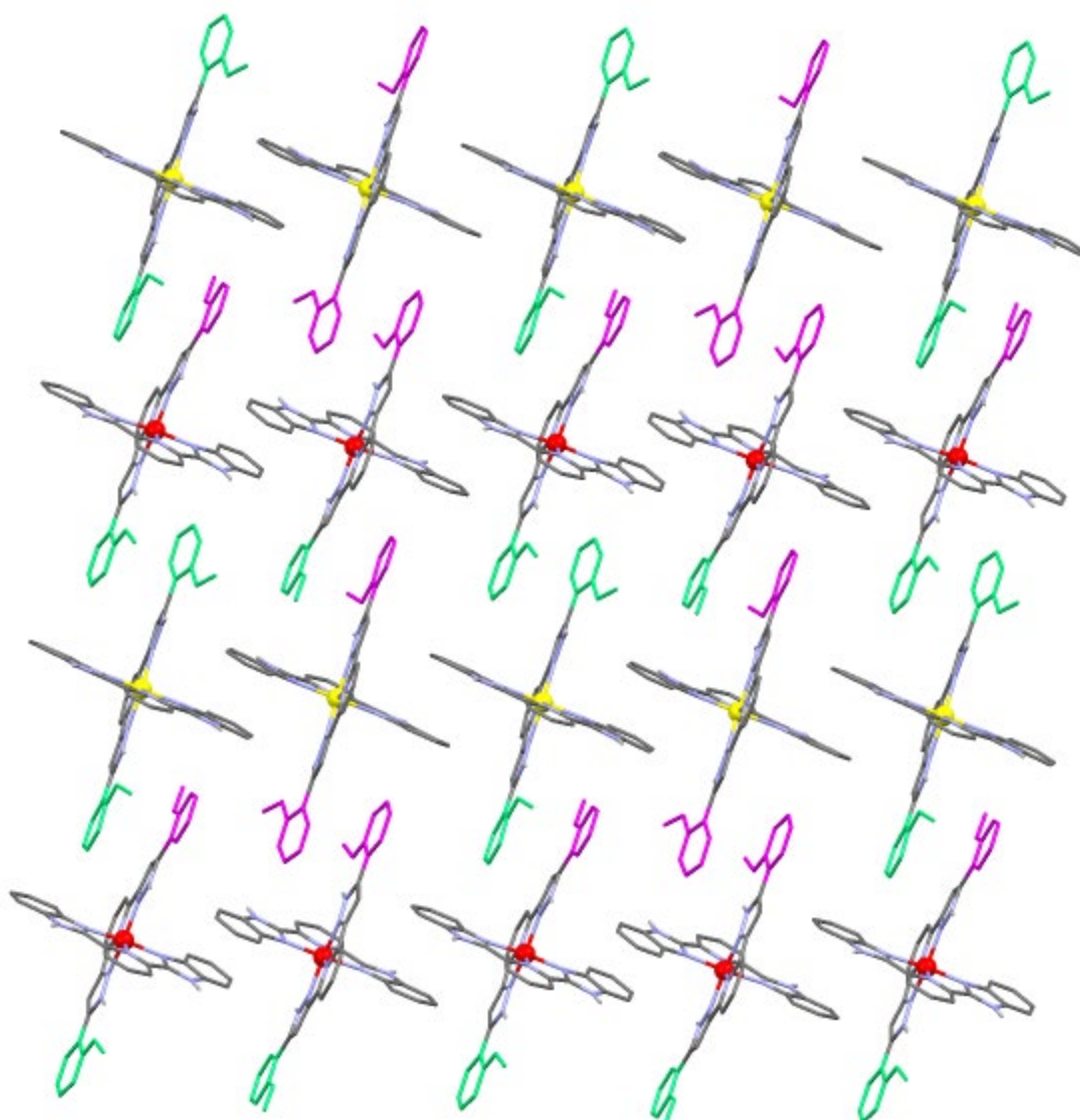


**Figure A4.16.** Sheet organization of the  $[\text{FeL}(\text{bbp})]^{2+}$  cations in **6<sub>v</sub>**, emphasizing the two orientations (different colors) of the methoxyphenyl groups with respect to the plane of the sheet made up by the complex cations (green towards the reader and violet away from the reader). The HS Fe(II) centers are in yellow, while the LS ones are in red.

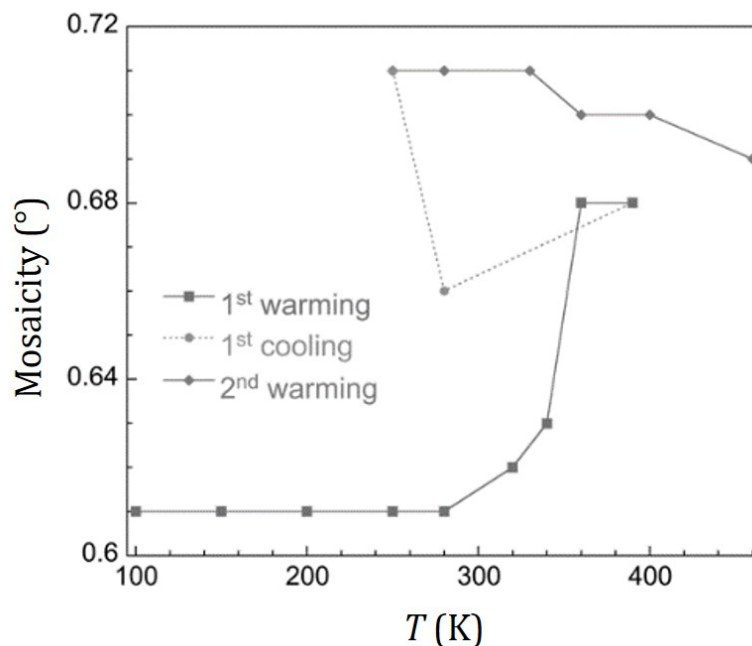


**Figure A4.17.** Evolution of the mosaicity as function of temperature where the succession of crystallographic transformations takes place is plotted. The first warming corresponds to  $6 \cdot ac \rightarrow 6^\alpha$ , the first cooling to  $6^\alpha \rightarrow 6^\beta$  and the second warming to  $6^\beta \rightarrow 6^\gamma$ . The mosaicity of the crystal was estimated by SAINT while integrating data through the average diffraction spot mosaicity and using rocking curves.

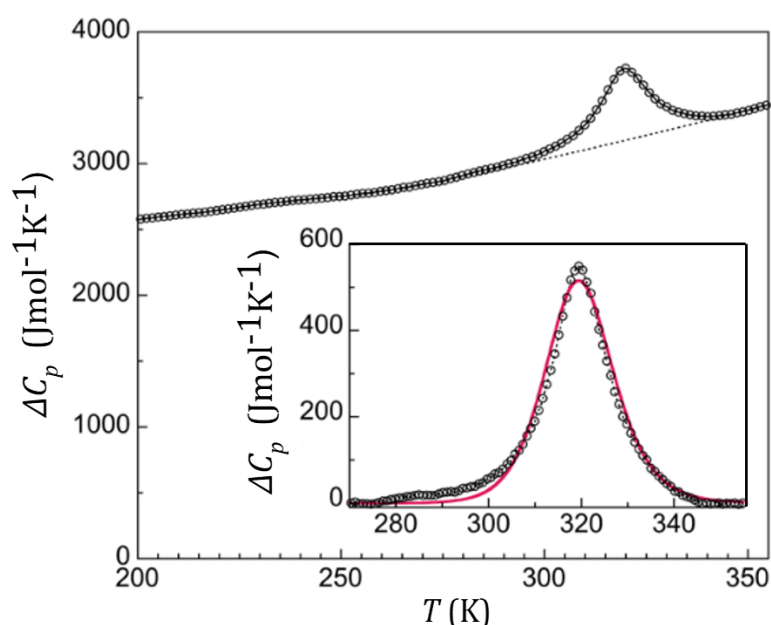


**Figure A4.18.** Molar heat capacity of  $6^\gamma$  derived from DSC measurements at constant pressure. The estimated lattice heat capacity (dashed line) is used to obtain the excess heat capacity. Inset: Anomaly fitted with Sorai's domain model (as previously used in chapter 2, Equation 2.1) shown as red line.

### Extended DFT Calculation Details

Equation S3.1 was used to evaluate the free energy ( $G$ ). Several terms, such as the electronic, rotational, vibrational and translational, contribute to the enthalpy and entropy. Nevertheless, only electronic and vibrational terms are considered in this study due to the small significance expected for the rotational and translational ones. Thus, the total enthalpy and entropy are considered as shown in equations S3.2 and S3.3:

$$G_{tot}(T) = H_{tot}(T) - TS_{tot}(T) \quad Eq.S3.1$$

$$H_{tot}(T) = H_{elec} + H_{vib}(T) \quad Eq.S3.2$$

$$S_{tot}(T) = S_{elec} + S_{vib}(T) \quad Eq.S3.3$$

The harmonic-oscillator (HO) approximation in equation S3.4 has been used to evaluate the  $H_{vib}$ :

$$H_{vib} = \sum_{i=1}^{N_{vib}} \left( \frac{1}{2} h\nu_i + \frac{h\nu_i e^{-h\nu_i/k_B T}}{1 - e^{-h\nu_i/k_B T}} \right) \quad Eq.S3.4$$

The  $S_{vib}$  is evaluated by using a mixed methodology: frequencies below 100 cm<sup>-1</sup> are treated with the free-rotor (FR) approximation (Equation S3.5), frequencies above 100 cm<sup>-1</sup> are treated with the HO approximation (Equation S3.6). The  $S_{elec}$  (Equation S3.7) with values 13.38 and 0 J K<sup>-1</sup> mol<sup>-1</sup> for HS (S=2) and LS (S=0), respectively, is a good temperature-independent approximation. The [LS-HS] state has been treated as a mixture of HS and LS molecules. Thus, the mixing entropy  $S_{mix}$  (Equation S3.8) is considered in equation S3.3 for this case.

$$S_{vib}^{FR} = \sum_{i=1}^{N_{vib}} k_B \left( \frac{1}{2} + \ln \left( \frac{8\pi^3 \mu' kT}{h^2} \right)^{1/2} \right) \quad Eq.S3.5$$

$$S_{vib}^{HO} = \sum_{i=1}^{N_{vib}} \left( \frac{h\nu_i}{T} \frac{1}{e^{h\nu_i/k_B T} - 1} - k_B \ln(1 - e^{-h\nu_i/k_B T}) \right) \quad Eq.S3.6$$

$$S_{elec} = k_B \ln(2S + 1) \quad Eq.S3.7$$

$$S_{mix} = -k_B [\gamma_{HS} \ln(\gamma_{HS}) + (1 - \gamma_{HS}) \ln(1 - \gamma_{HS})] \quad Eq.S3.8$$

**Table A4.4.** Unit cell parameters and volume obtained from the computed calculations. The volume expansion associated to the SCO form the LS stat is given in brackets. Distances, angles and volume are given in Å, ° and Å<sup>3</sup>, respectively.

		a	b	c	$\alpha$	$\beta$	$\gamma$	Volume
	LS	12.07	17.96	22.53	86.00	79.60	67.30	4430
<b>6·ac</b>	[HS-LS]	12.30	17.72	22.52	86.30	80.30	68.00	4484 (+1.2%)
	HS	12.37	17.46	22.81	88.30	82.40	69.30	4568 (+3.1%)
	LS	12.66	18.10	21.01	95.50	108.50	108.40	4227
<b>6<math>\alpha</math></b>	[HS-LS]	12.80	17.28	21.84	93.00	110.60	107.10	4254 (+0.6%)
	HS	12.99	16.91	22.19	92.90	110.50	107.00	4297 (+1.7%)
	LS	11.94	18.85	21.62	84.30	76.20	66.90	4345
<b>6<math>\beta</math></b>	[HS-LS]	12.05	19.21	21.71	83.80	74.80	66.40	4443 (+2.2%)
	HS	12.01	19.75	21.70	83.80	72.90	66.90	4521(+4.0%)
	LS	11.67	17.04	22.76	100.73	96.54	98.84	4345
<b>6</b>	[HS-LS]	11.70	17.04	23.20	101.13	96.86	99.35	4423 (+1.8%)
	HS	12.03	17.14	23.08	99.40	98.42	97.00	4590 (+5.6%)

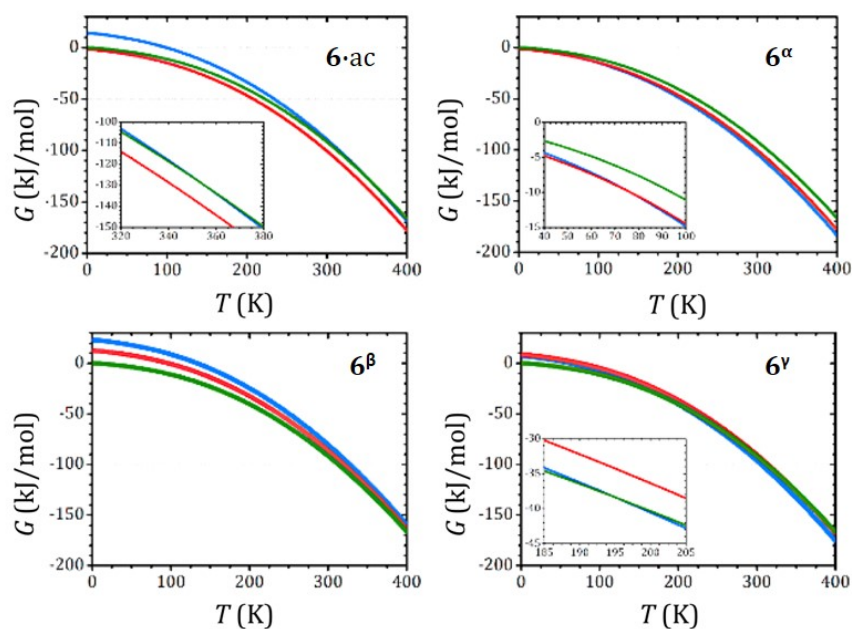


**Figure A4.19.** Free-Energy ( $G$ ) associate with the [HS-HS] (blue), [LS-HS] (red) and [LS-LS] (green) states of  $6\cdot ac$ ,  $6^\alpha$ ,  $6^\beta$  and  $6^\gamma$ . The [LS-LS] state  $G$  at 1K is used as reference. Insets highlight the significant crossings.

Table A4.5. Crystallographic table, average Fe-N bond lengths and distortion parameter of 7·ac.

<b>7·ac</b>	
Formula	C <sub>188</sub> H <sub>160</sub> Cl <sub>8</sub> Fe <sub>4</sub> N <sub>40</sub> O <sub>44</sub>
FW (g mol <sup>-1</sup> )	4190.55
T (K)	100
Wavelength (Å)	0.7749
Crystal system	triclinic
Space group	P-1
a (Å)	17.9783(18)
b (Å)	21.868(2)
c (Å)	23.635(2)
α (°)	82.015(6)
β (°)	85.007(5)
γ (°)	89.481(5)
V (Å <sup>3</sup> )	9166.9(16)
Z	2
ρ <sub>calcd</sub> (g cm <sup>-3</sup> )	1.518
μ (mm <sup>-1</sup> )	0.521
Independent reflections (R <sub>int</sub> )	41777 (0.1338)
param. / restraints	1161 / 0
Goodness-of-fit	1.137
Final R1 / wR2 [I>2σ(I)]	0.2668 / 0.6276
Final R1 / wR2 [all data]	0.3464 / 0.6556
largest diff. peak / hole (e Å <sup>3</sup> )	4.330 / -3.178
<Fe1-N> (Å)	2.17
<Fe2-N> (Å)	1.98
<Fe3-N> (Å)	2.0
<Fe4-N> (Å)	2.165
Σ Fe1 / Fe2 / Fe3 / Fe4	142 / 92 / 92 / 141

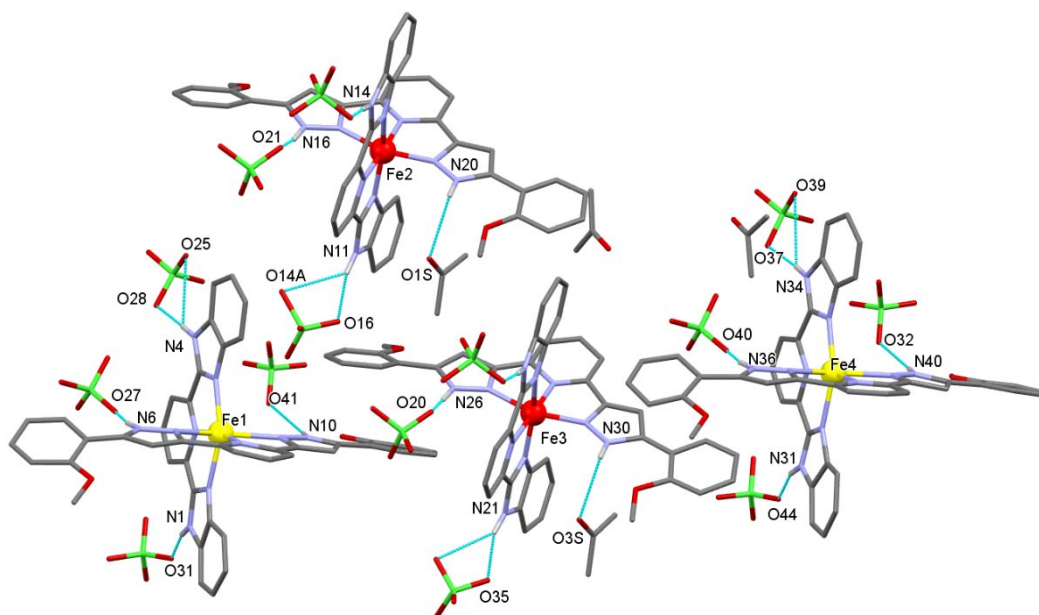


**Figure A4.20.** Representation of one asymmetric unit of the molecular structure of  $[\text{FeL}(\text{bbp})](\text{ClO}_4)_2$  (**7-ac**), emphasizing the hydrogen bonds between perchlorate ions or acetone molecules and the N–H groups of the complexes. Only hydrogen atoms on heteroatoms are shown.

**Table A4.6.** Specific hydrogen bonding for the cationic complexes of each iron (Fe1-F4) of compound **7** at 100k.

D–H...A	D–H (Å)	H...A (Å)	D–A (Å)	D–H...A (°)
<b>Fe1</b>				
N1–H1...O31_1 *	0.88	1.94	2.81(3)	169.1
N6–H6...O27_1 *	0.88	1.94	2.79(3)	162.1
N10–H10...O2 *	0.88	2.03	2.63(3)	124.0
<b>Fe2</b>				
N11–H11A...O16	0.88	1.96	2.83(3)	165.8
N20–H20...O4	0.88	2.09	2.66(3)	121.8
<b>Fe3</b>				
N21–H21...O35_2	0.88	1.93	2.78(3)	159.8
N26–H26...O20	0.88	2.06	2.89(3)	157.5
N30–H30...O6	0.88	2.05	2.61(3)	120.5
<b>Fe4</b>				
N31–H31A...O44	0.88	2.02	2.88(3)	164.4
N36–H36A...O40	0.88	1.95	2.80(3)	160.9
N40–H40A...O32_3	0.88	2.06	2.86(3)	150.8

\*Analyzed bond distances with maximum distance of 2.9 Å and minimum angle of 120° by processing HTAB Olex2.



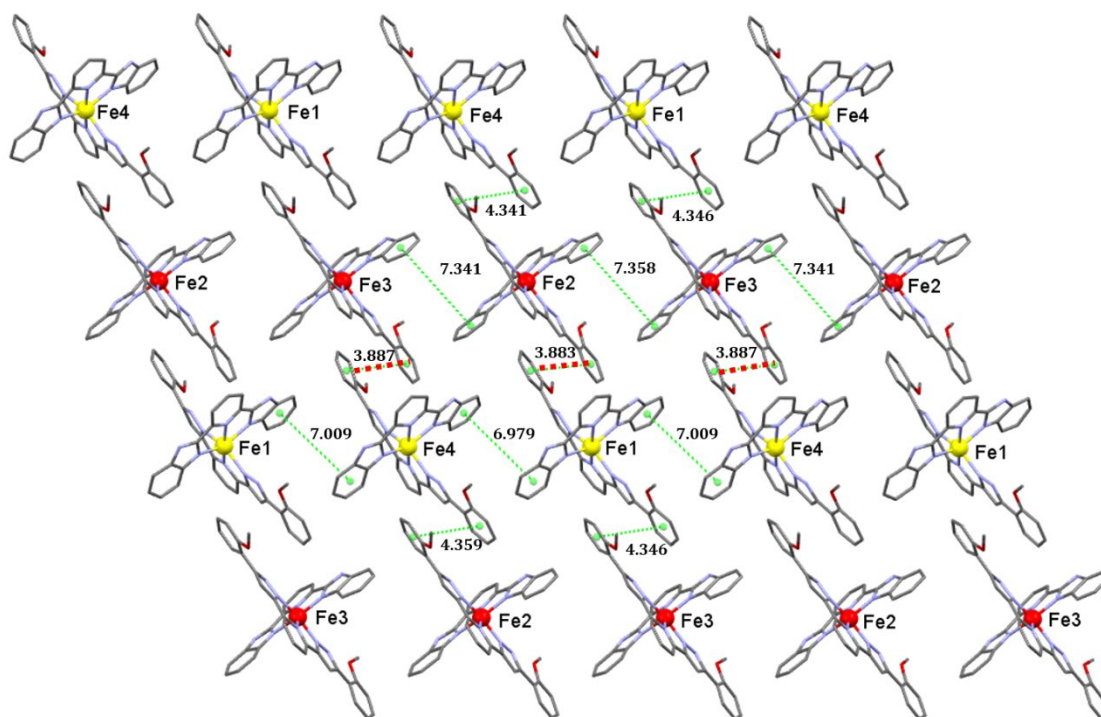


**Figure A4.21.** Sheet organization of the  $[\text{FeL}(\text{bbp})]^{2+}$  cations in **7-ac**, emphasizing the distances between selected centroids (dashed green lines) around the complexes of one asymmetric unit within these sheets. Red lines highlight the  $\pi\cdots\pi$  intermolecular interactions analyzed through Olex2. The HS Fe(II) centers are in yellow, while the LS ones are in red. All distances under the marked interactions are in angstroms.

**Table A4.7.** Selected  $\pi\cdots\pi$  interactions in the structure of compound **7-ac** at 100 K.

interaction	labels	■■■■■	Distance (Å) ( $\pi$ : centroid)
$\pi\cdots\pi$ (1)	Cg(C26 C25 C24 C23 C22 C21) $\cdots$ Cg(C87 C86 C85 C84 C83 C82)		3.883
$\pi\cdots\pi$ (2)	Cg(C131 C130 C129 C128 C127 C126) $\cdots$ Cg(C157 C156 C155 C154 C153 C152)		3.887

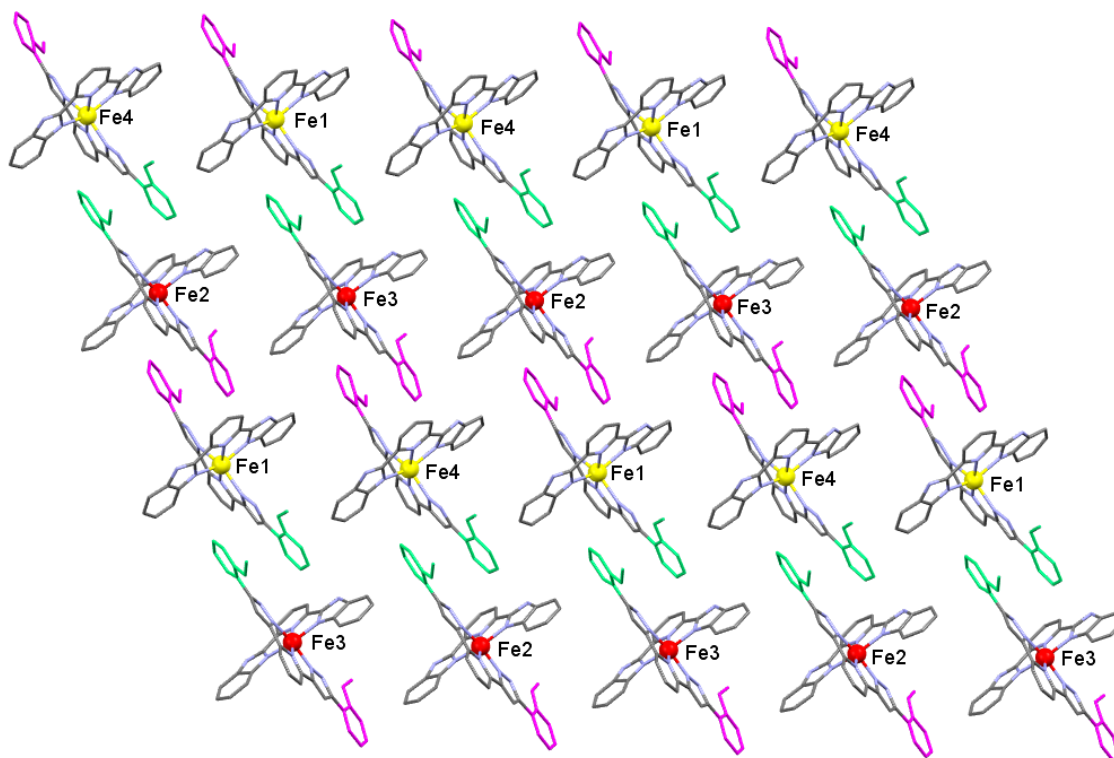


**Figure A4.22.** Sheet organization of the  $[\text{FeL}(\text{bbp})]^{2+}$  cations in 7-ac, emphasizing the two orientations (different colors) of the methoxyphenyl groups with respect to the plane of the sheet made up by the complex cations (green towards the reader and violet away from the reader). The HS Fe(II) centers are in yellow, while the LS ones are in red.

**Table A4.8.** Crystallographic table, average Fe-N bond lengths and distortion parameters for compounds **8**, **9** and **10**.

	<b>8</b>	<b>9</b>	<b>10</b>
Formula	C <sub>50</sub> H <sub>42</sub> Cl <sub>2</sub> FeN <sub>10</sub> O <sub>12</sub>	C <sub>42</sub> H <sub>34</sub> Cl <sub>2</sub> FeN <sub>10</sub> O <sub>6.61</sub>	C <sub>34</sub> H <sub>37</sub> Cl <sub>2</sub> FeN <sub>5</sub> O <sub>15</sub>
FW (g mol <sup>-1</sup> )	1101.68	911.22	882.43
T (K)		100	
Wavelength (Å)		0.71073	
Crystal system	triclinic	tetragonal	monoclinic
Space group	<i>P</i> -1	<i>P</i> -4b2	<i>P</i> 2 <sub>1</sub> / <i>c</i>
a (Å)	12.0245(14)	13.2538(11)	10.2474(4)
b (Å)	12.9106(15)	13.2538(11)	29.3813(10)
c (Å)	18.929(2)	12.7887(15)	13.7786(5)
α (°)	89.319(4)	90	90
β (°)	79.412(4)	90	108.136(2)
γ (°)	77.275(4)	90	90
V (Å <sup>3</sup> )	2816.3(6)	2246.5(5)	3942.4(3)
Z	2	2	4
ρ <sub>calcd</sub> (g cm <sup>-3</sup> )	1.299	1.347	1.487
μ (mm <sup>-1</sup> )	0.428	0.513	0.593
Independent reflections (R <sub>int</sub> )	7302 (0.0684)	1194(0.0578)	11885 (0.0499)
param. / restraints	305/ 6	151/0	593 / 35
Goodness-of-fit	2.509	1.113	1.035
Final R1 / wR2 [I > 2σ(I)]	0.2288/ 0.5604	0.0933/0.2475	0.0480/ 0.1189
Final R1 / wR2 [all data]	0.2565/ 0.5818	0.1131/ 0.2656	0.0707/ 0.1318
largest diff. peak / hole (e Å <sup>3</sup> )	3.821/ -2.603	0.651/ -0.512	0.613/ -0.512
<Fe1-N> (Å)	2.18(8)	1.93(8)	2.15(1)
Σ Fe	171.4(16)	81(4)	94.11(9)

**Table A4.9.** Specific hydrogen bonding for compound **8** at 100k.

D-H...A	D-H (Å)	H...A (Å)	D-A (Å)	D-H...A (°)
O5S-H5SB...O3A <sup>a</sup>	0.87	2.11	2.861(10)	143.1
O5S-H5SA...O2S	0.87	1.85	2.683(3)	158.4
O4S-H4SA...O7A <sup>a</sup>	0.87	1.90	2.716(4)	154.8
O4S-H4SA...O7B <sup>b</sup>	0.87	1.95	2.811(7)	168.0
O4S-H4SB...O3S	0.88	1.85	2.707(2)	165.5
N1-H1...O1	0.88	2.06	2.625(2)	121.4
N5-H5...O2	0.88	2.04	2.629(2)	122.9
N5-H5...O3B <sup>b</sup>	0.88	2.16	2.880(13)	138.8

**APPENDIX 5 - CHAPTER 5. DESIGN, SYNTHESIS AND CHARACTERIZATION OF NEW BIS-PYRAZOLYL BASED LIGANDS TO ACCESS METALLOSUPRAMOLECULAR ARCHITECTURES**

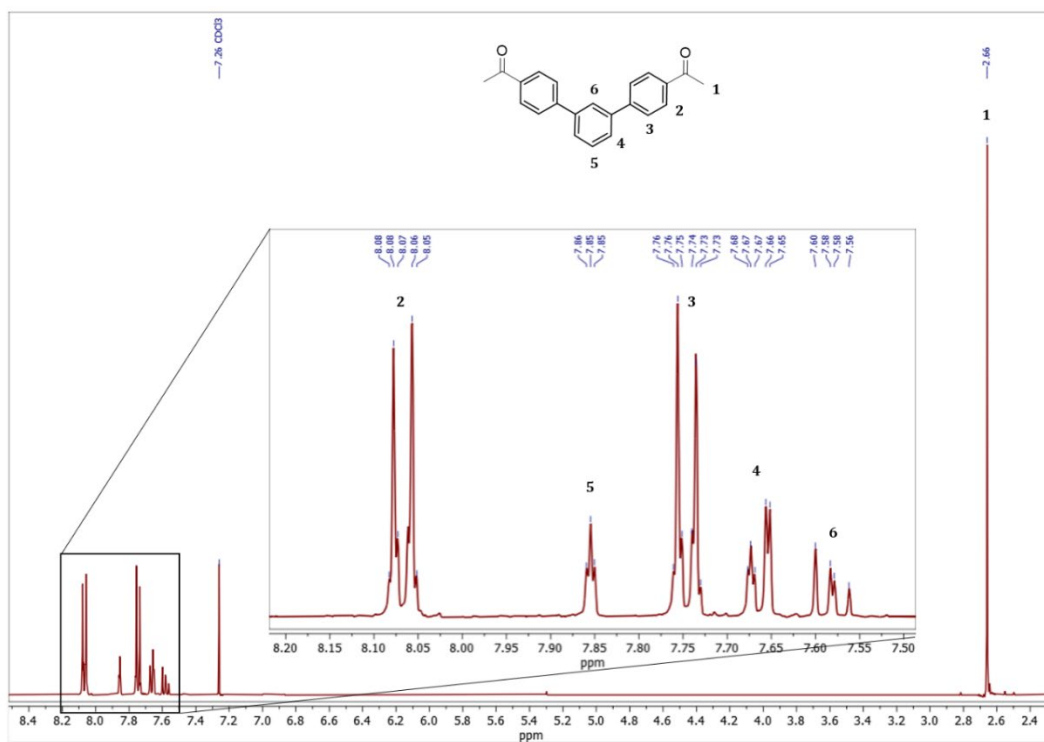


**Figure A5.1.**  $^1\text{H}$  NMR spectrum (zoom in aromatic region) of **A1** in chloroform-*d*.

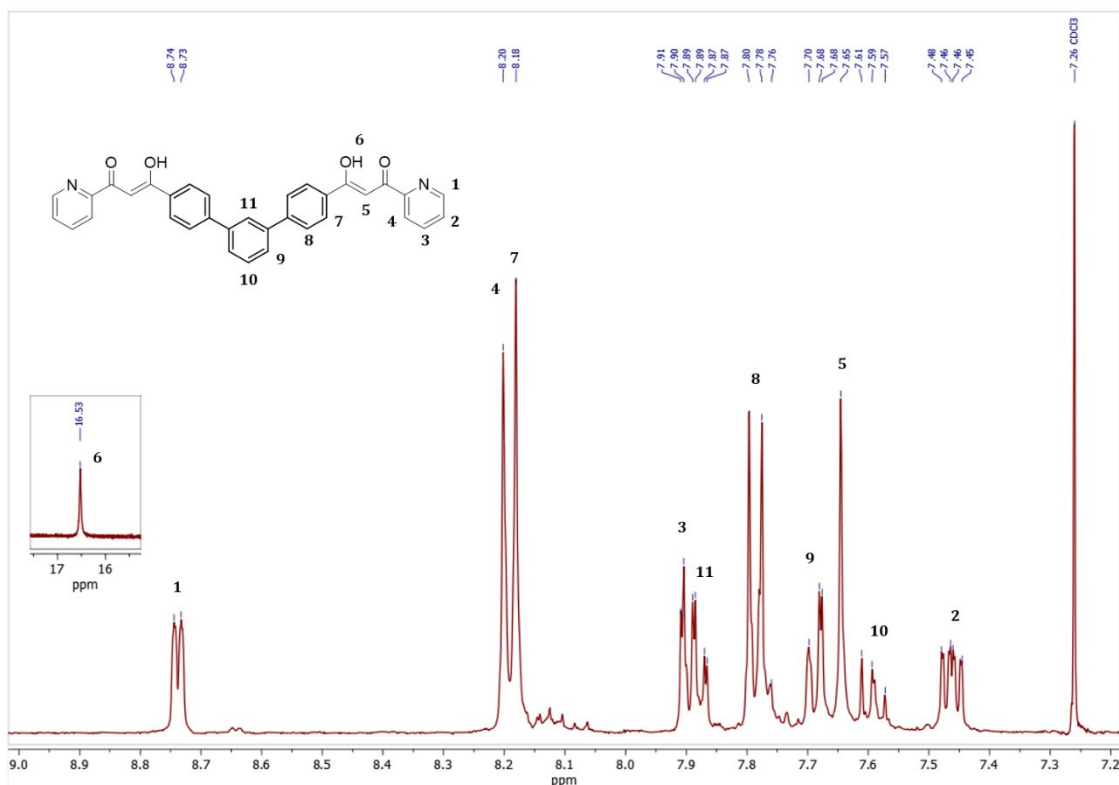


**Figure A5.2.**  $^1\text{H}$  NMR spectrum (aromatic region) of **A2** in chloroform-*d*.

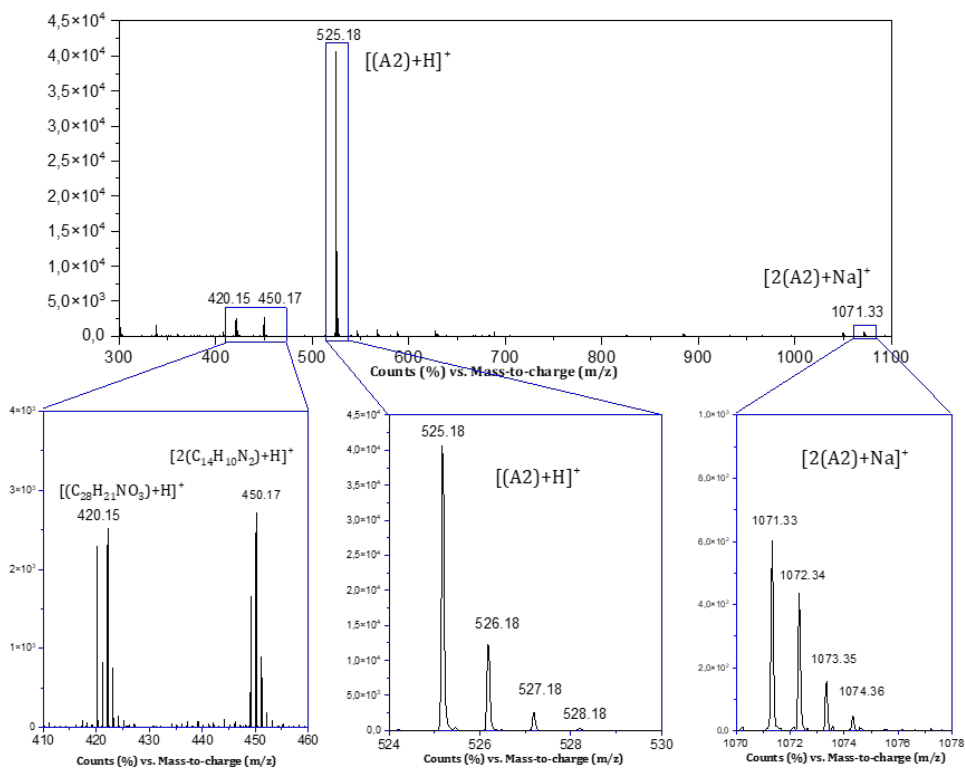


**Figure A5.3.** Positive ion ESI mass spectrum at 175V of **A2** dissolved in  $\text{CH}_2\text{Cl}_2$ . Zoom in ligand peaks and proposed fragments.

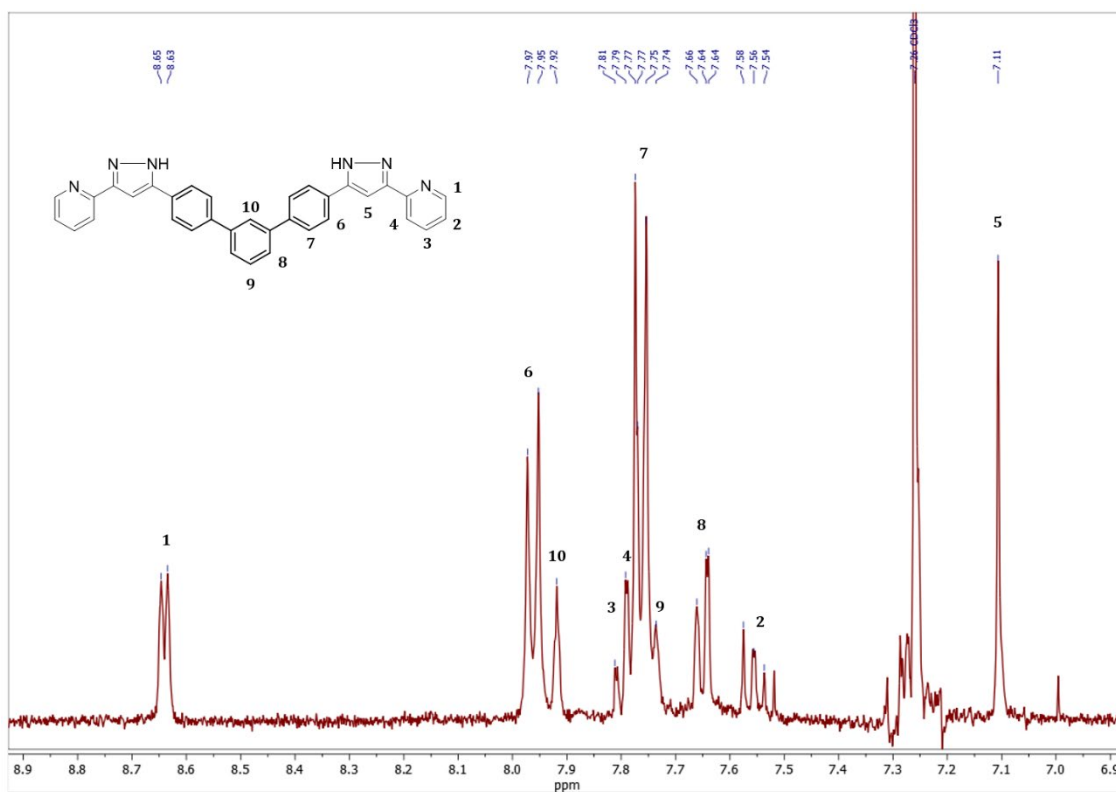


**Figure A5.4.** <sup>1</sup>H NMR spectrum (aromatic region) of **H<sub>2</sub>L3** in chloroform-*d*.

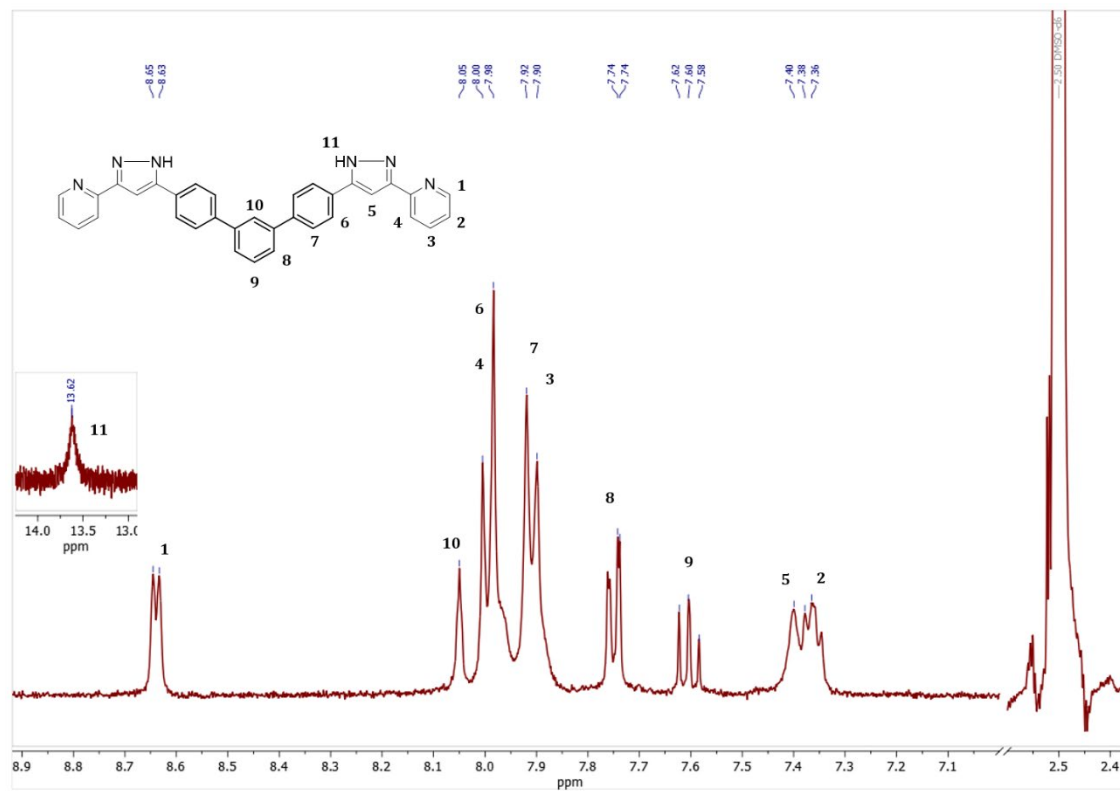


**Figure A5.5.** <sup>1</sup>H NMR spectrum (aromatic region) of **H<sub>2</sub>L3** in dmsu-*d*<sub>6</sub>.

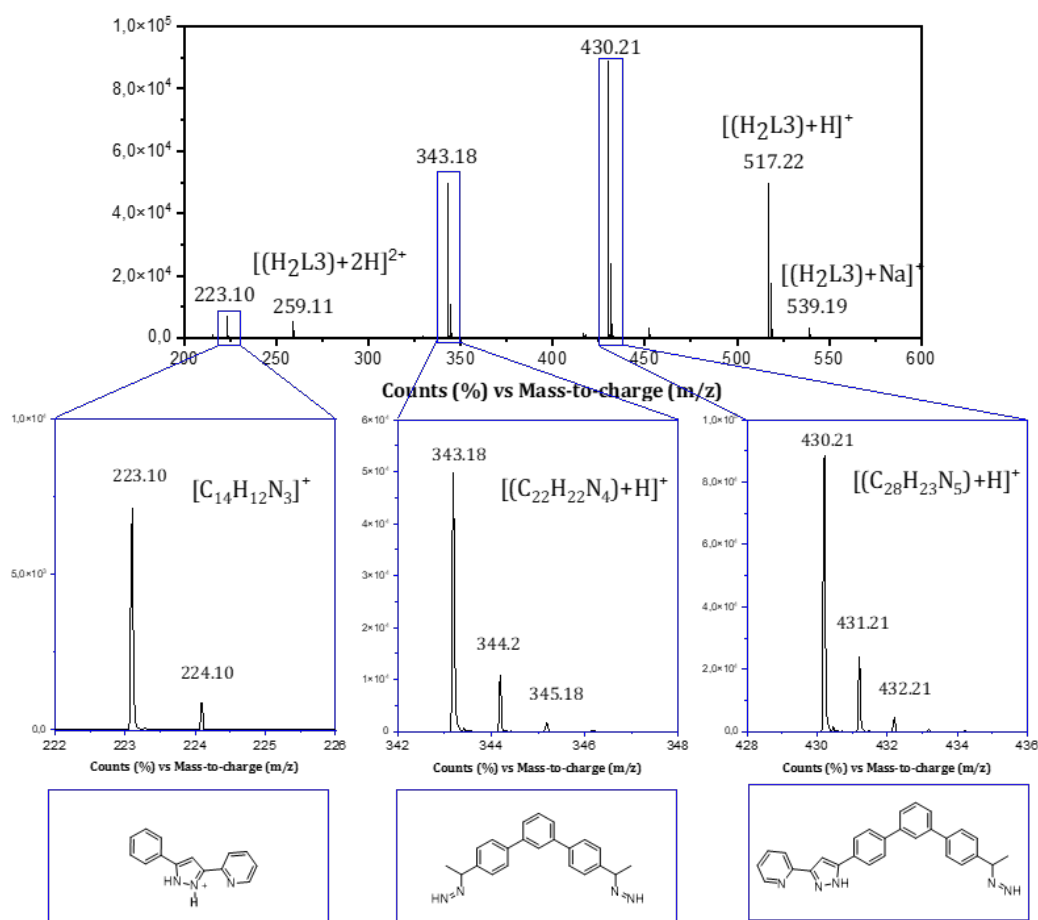


**Figure A5.6.** Positive ion ESI mass spectrum at 175V of  $H_2L3$  broken (24h cyclization) dissolved in a mixture of MeOH/CH<sub>2</sub>Cl<sub>2</sub>. Zoom in ligand peaks and proposed fragments.



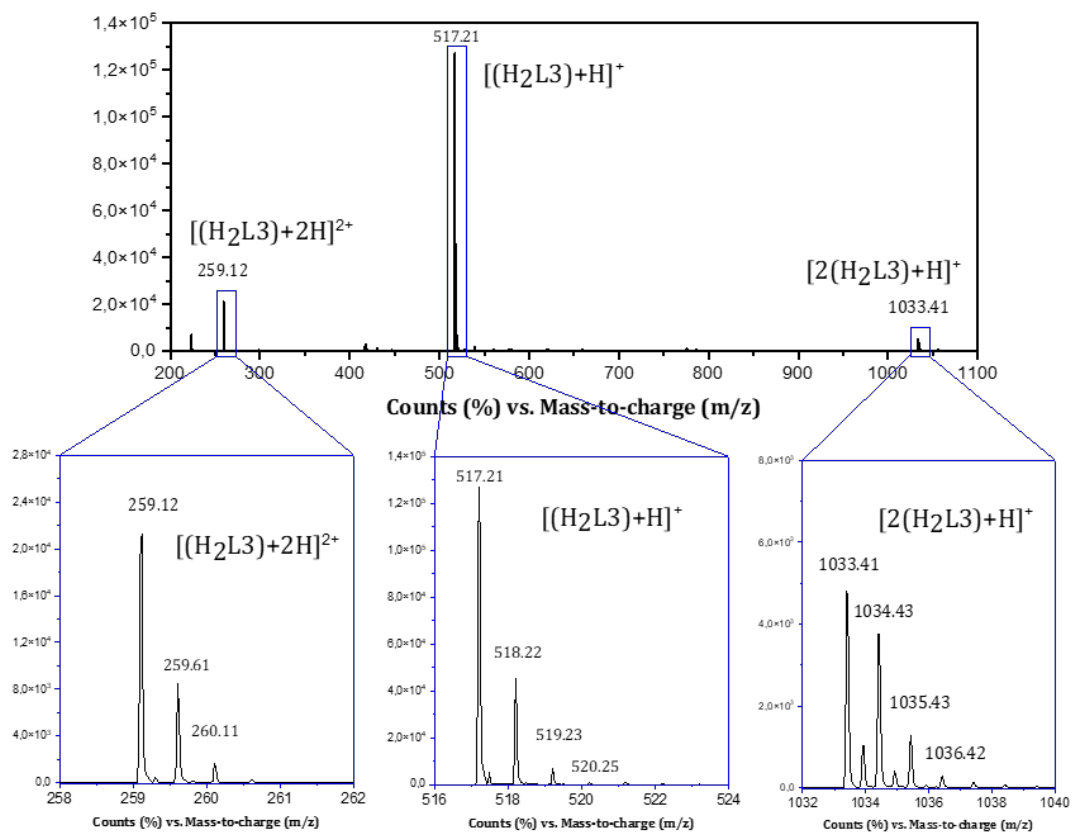


**Figure A5.7.** Positive ion ESI mass spectrum at 175V of  $\text{H}_2\text{L}_3$  (complete reaction) dissolved in a mixture of MeOH/ $\text{CH}_2\text{Cl}_2$ . Zoom in ligand peaks and proposed fragments.

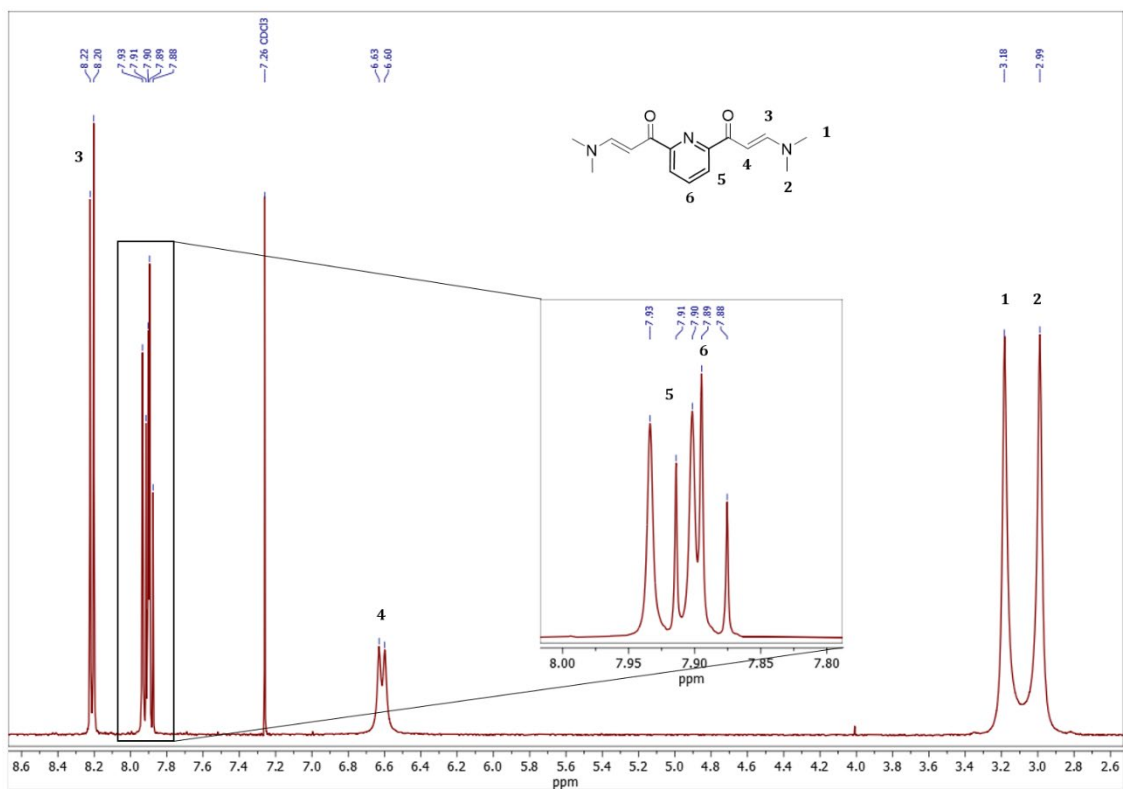


Figure A5.8.  $^1\text{H}$  NMR spectrum (zoom in aromatic region) of **B1** in chloroform-*d*.

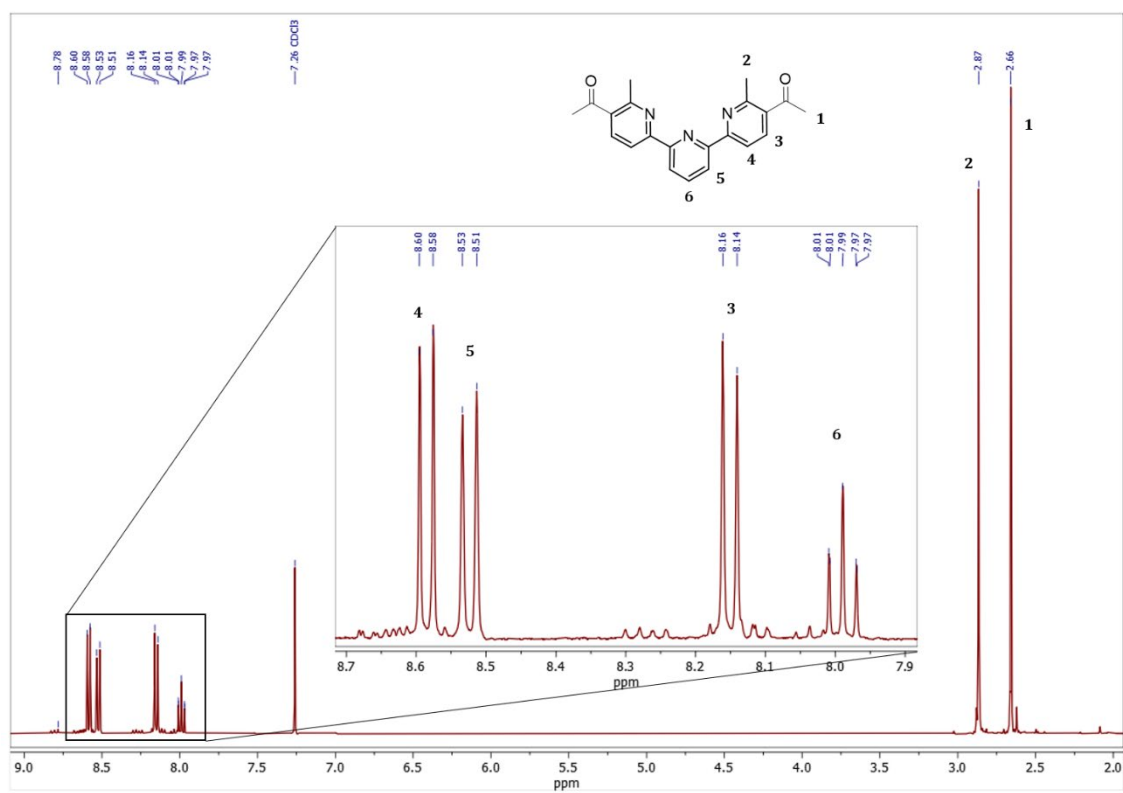
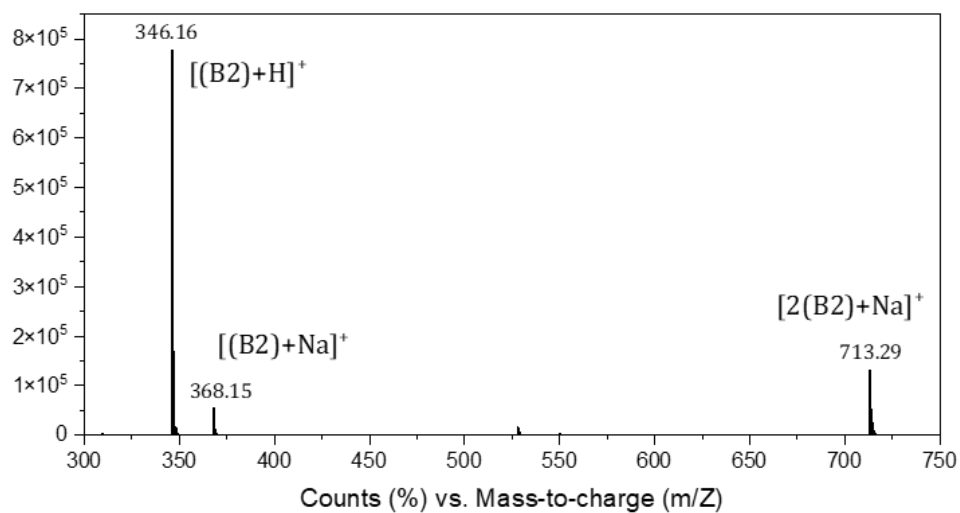
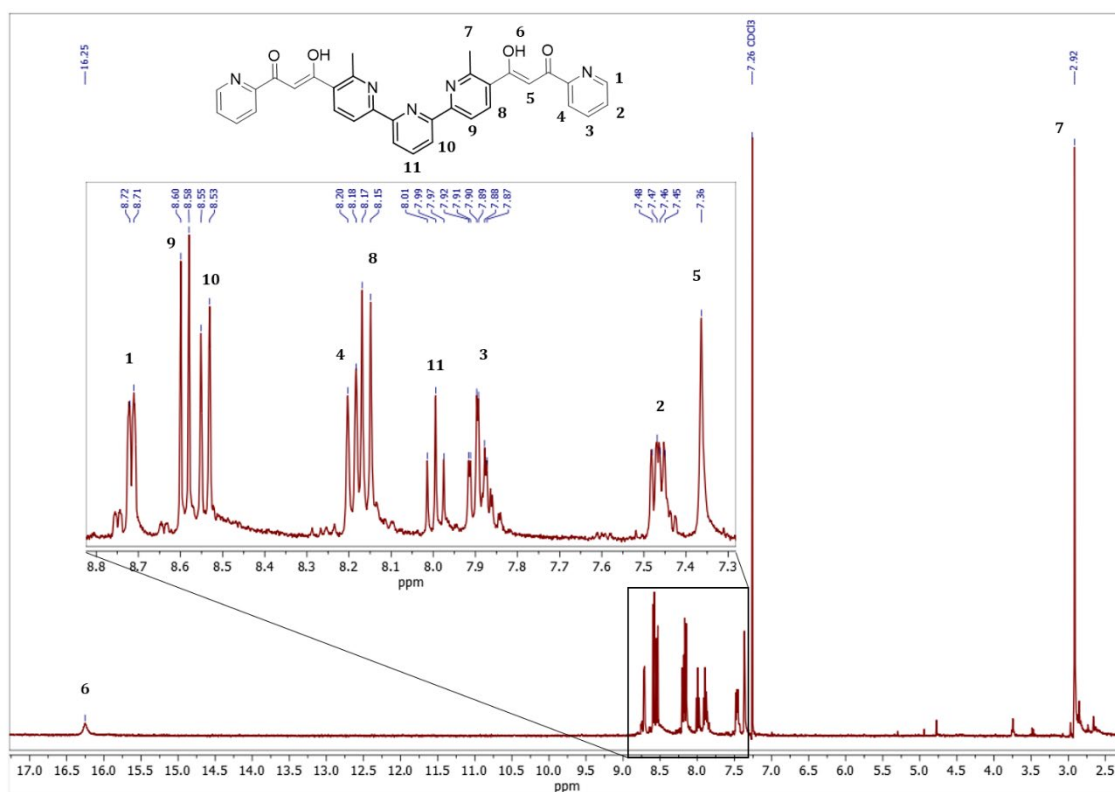


Figure A5.9.  $^1\text{H}$  NMR spectrum (zoom in aromatic region) of **B2** in chloroform-*d*.



**Figure A5.10.** Positive ion ESI mass spectrum at 175V of **B2** dissolved in a mixture of MeOH/CH<sub>2</sub>Cl<sub>2</sub>. Zoom in ligand peaks and proposed fragments.



**Figure A5.11.** <sup>1</sup>H NMR spectrum (zoom in aromatic region) of **B3** in chloroform-*d*.

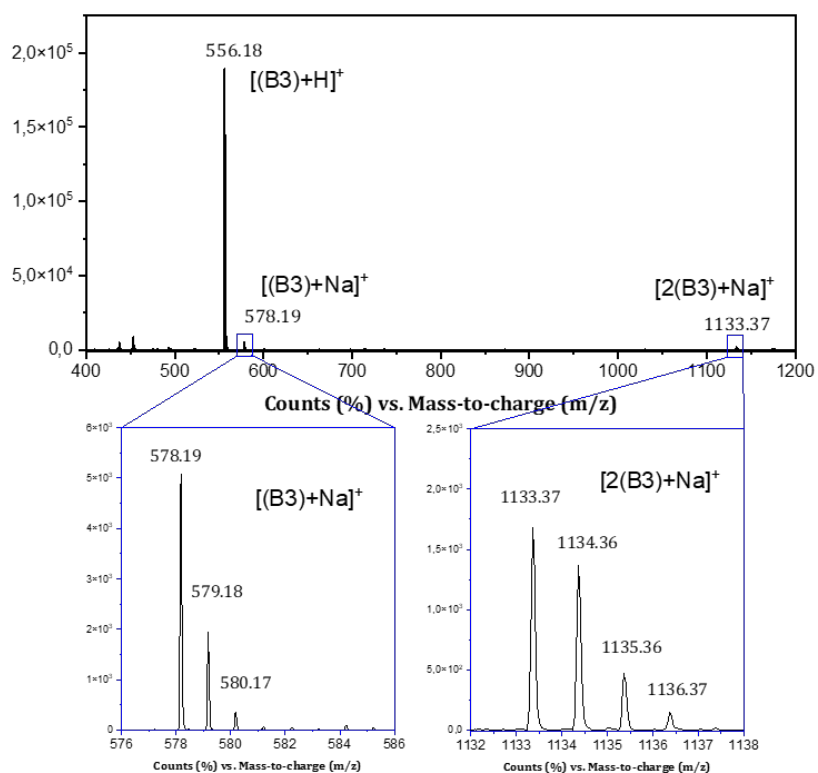


Figure A5.12. Positive ion ESI mass spectrum at 175V **B3** dissolved in  $\text{CH}_2\text{Cl}_2$ .

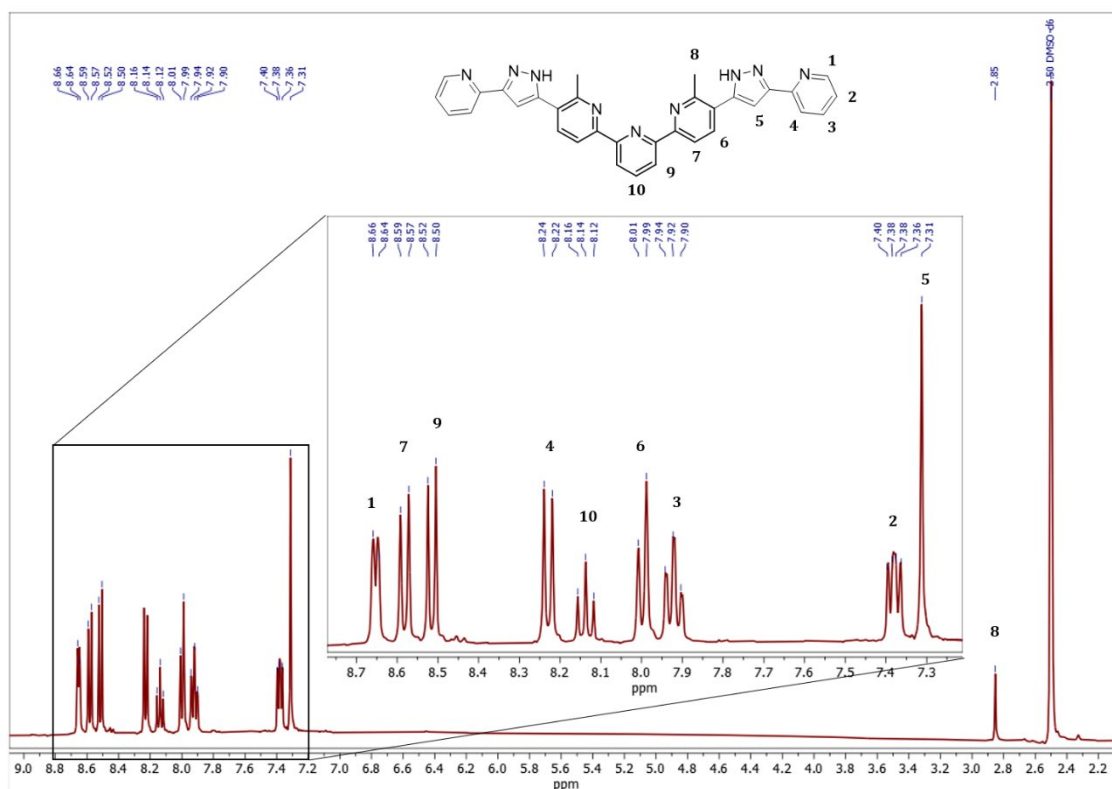
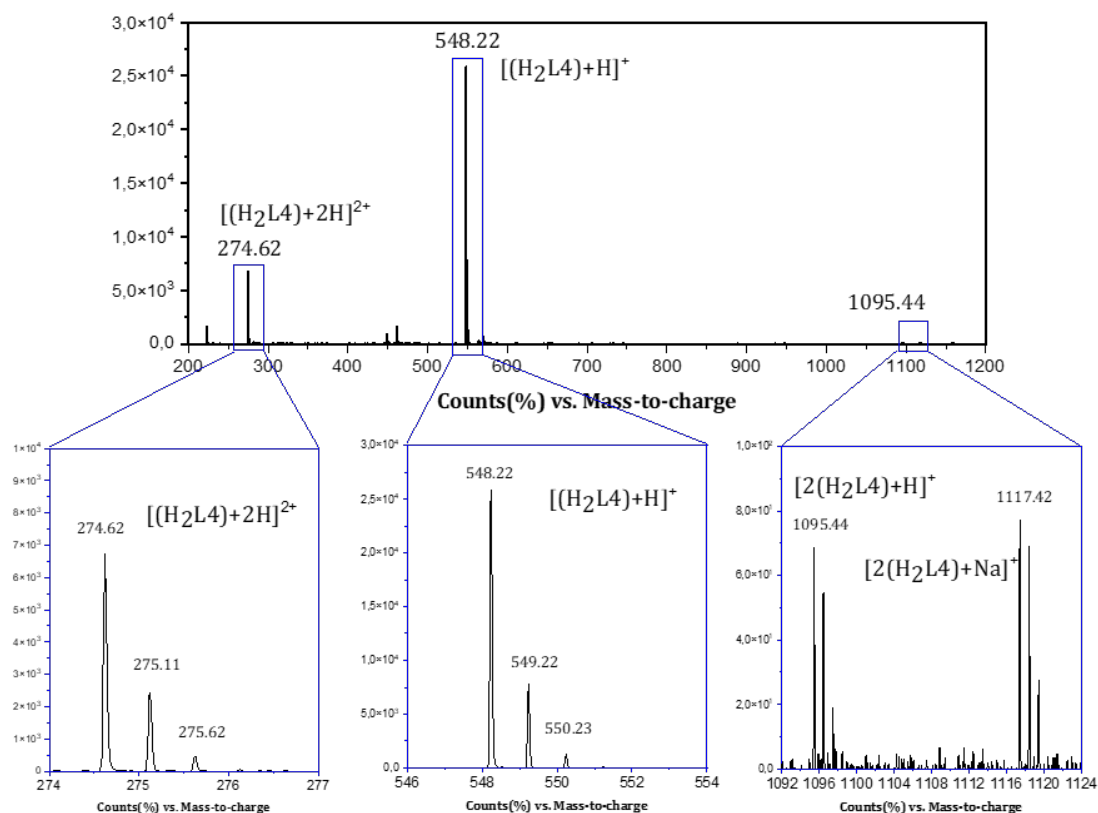
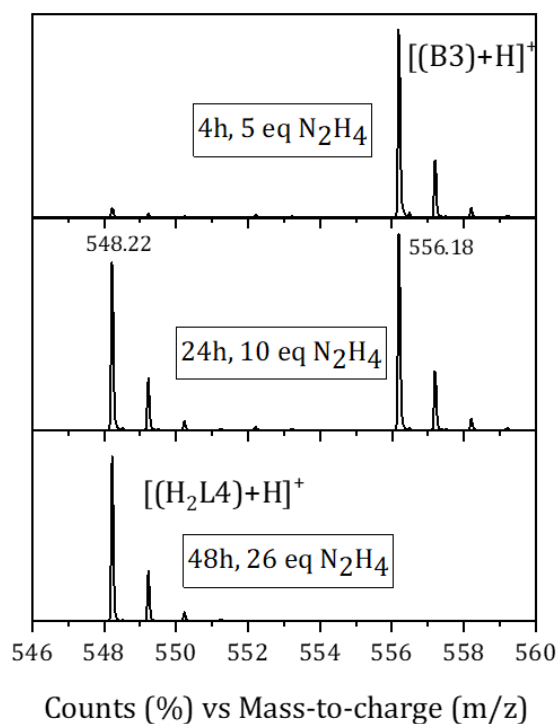


Figure A5.13.  $^1\text{H}$  NMR spectrum (aromatic region) of **H<sub>2</sub>L4** in  $\text{dmsO}-d_6$ .



**Figure A5.14.** Positive ion ESI mass spectrum at 175V  $\text{H}_2\text{L}_4$  dissolved in  $\text{CH}_2\text{Cl}_2$ .



**Figure A5.15.** Positive ion ESI mass spectrum at 175V  $\text{B}_3$  dissolved in  $\text{CH}_2\text{Cl}_2$ .

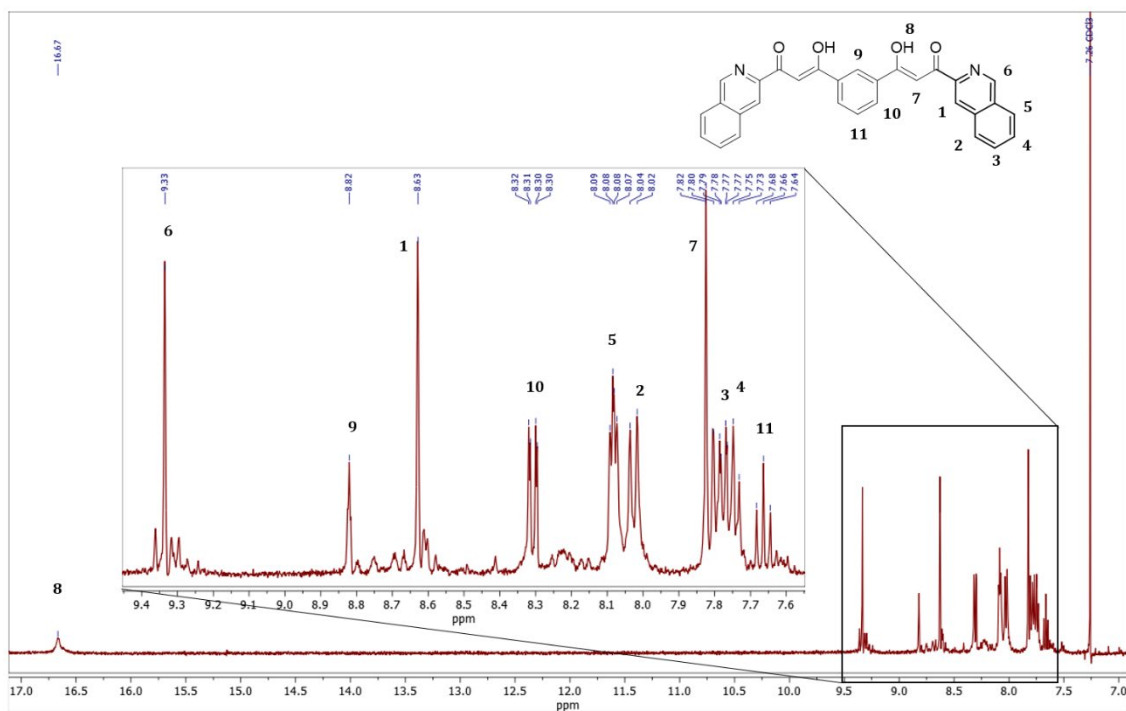


Figure A5.16.  $^1\text{H}$  NMR spectrum (aromatic region) of **C1** in chloroform- $d$ .

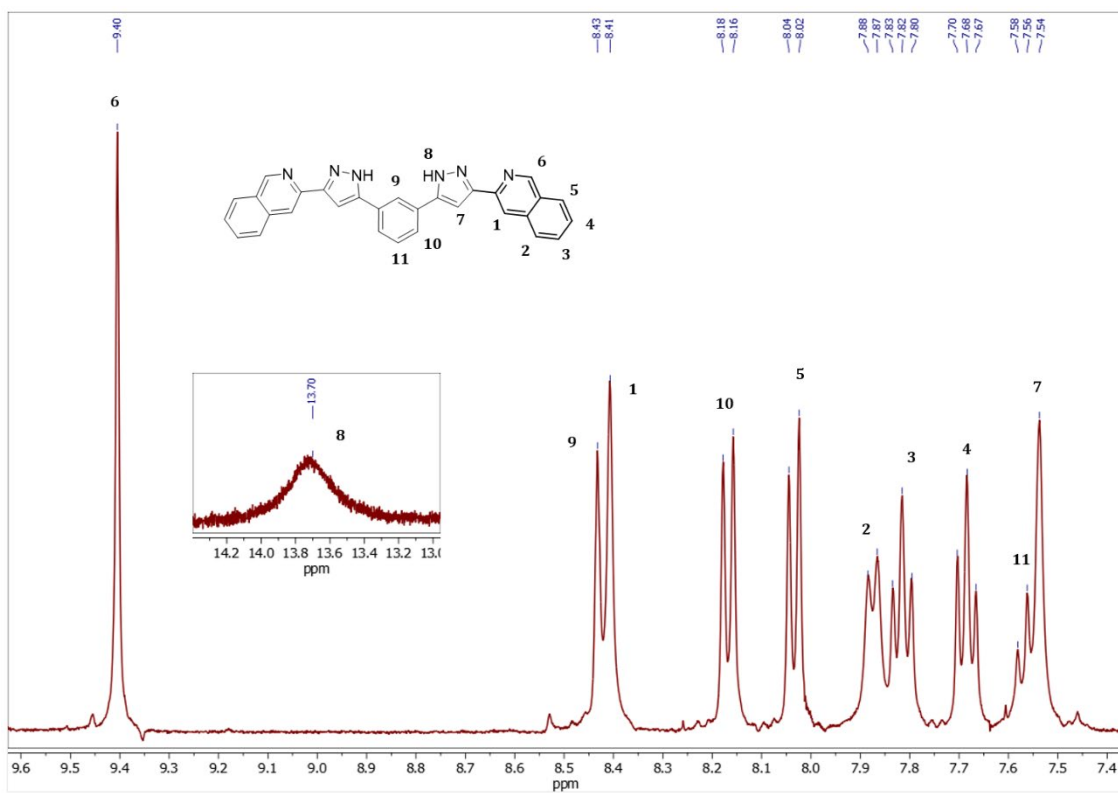
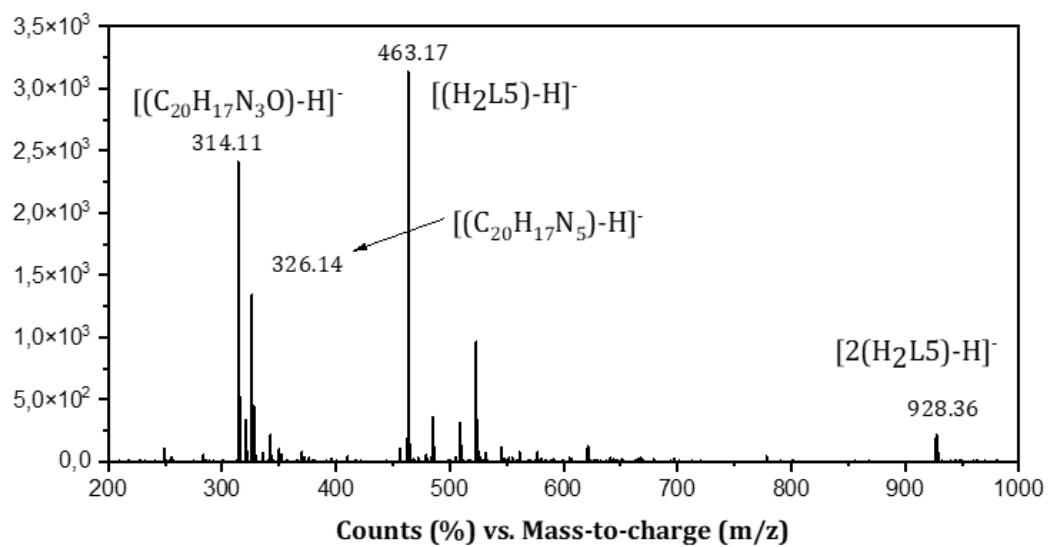
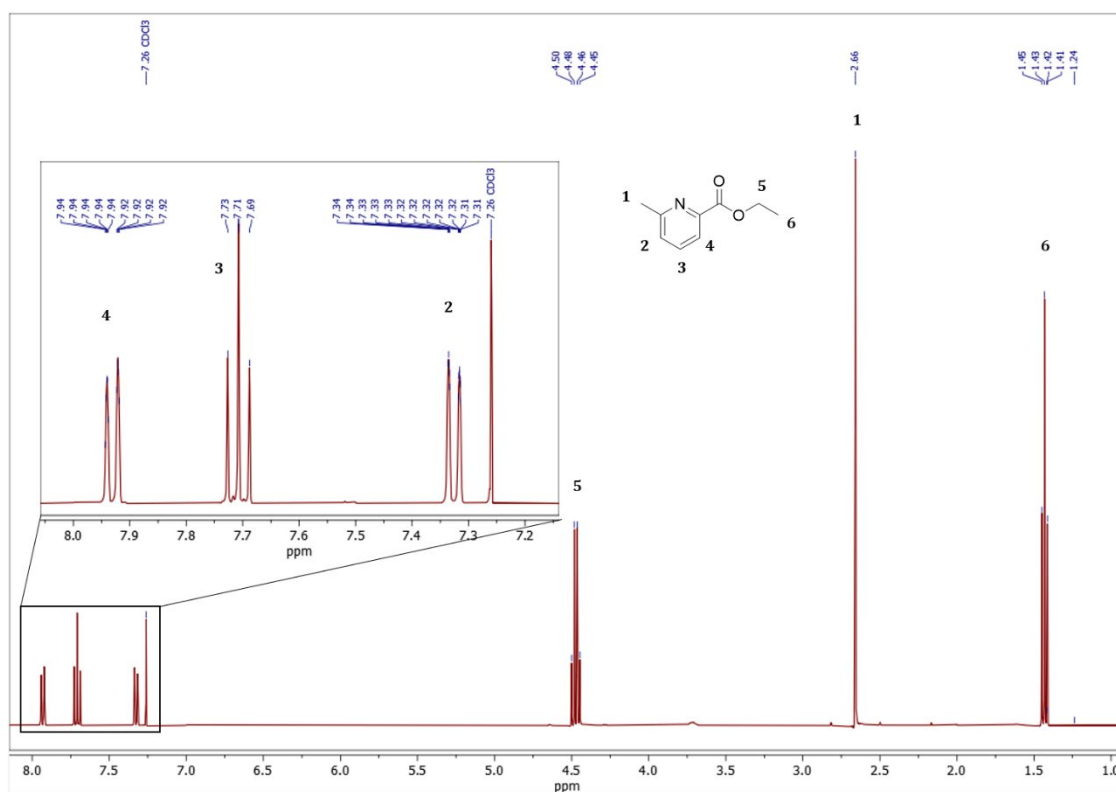


Figure A5.17.  $^1\text{H}$  NMR spectrum (aromatic region) of **H<sub>2</sub>L5** in dms0- $d_6$ .



**Figure A5.18.** Negative ion ESI mass spectrum at 175V **H<sub>2</sub>L5** dissolved in CH<sub>2</sub>Cl<sub>2</sub>.



**Figure A5.19.** <sup>1</sup>H NMR spectrum (aromatic region) of **D1** in chloroform-*d*.

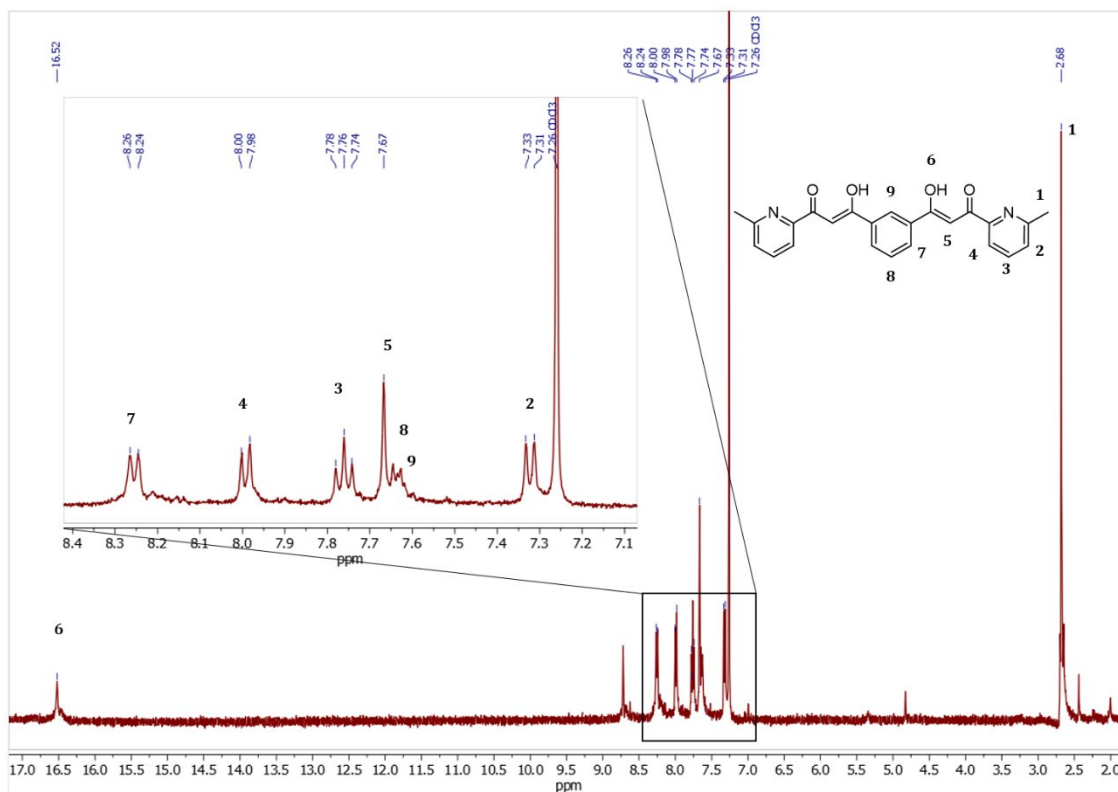


Figure A5.20.  $^1\text{H}$  NMR spectrum (aromatic region) of D2 in chloroform-*d*.

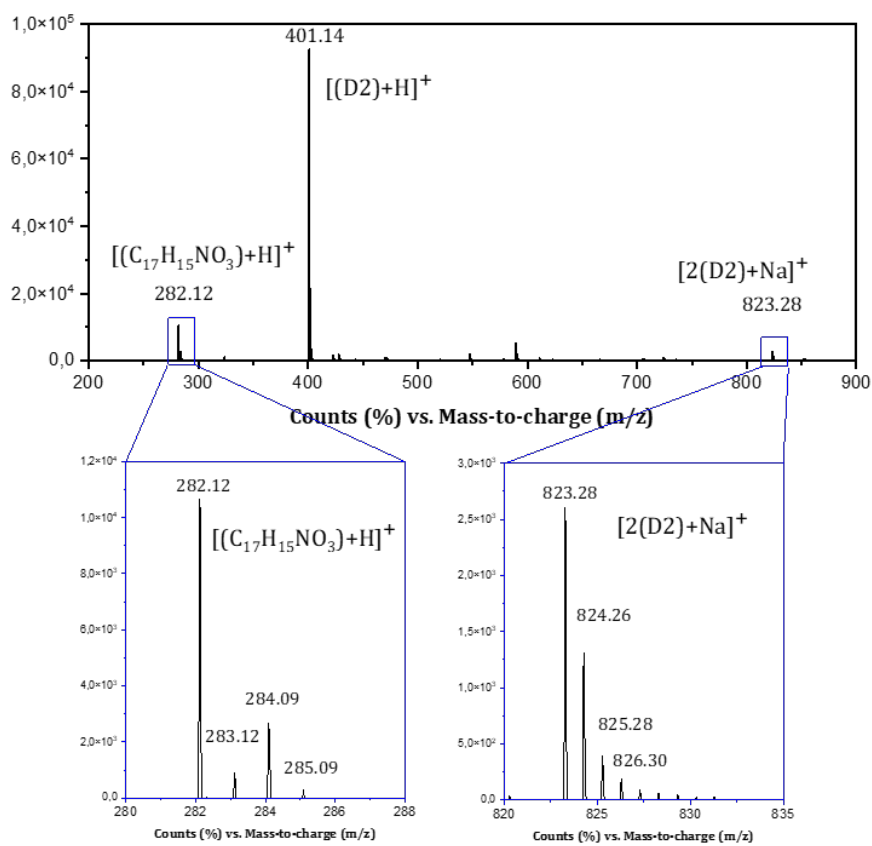


Figure A5.21. Positive ion ESI mass spectrum at 175V D2 dissolved in  $\text{CH}_2\text{Cl}_2$ .



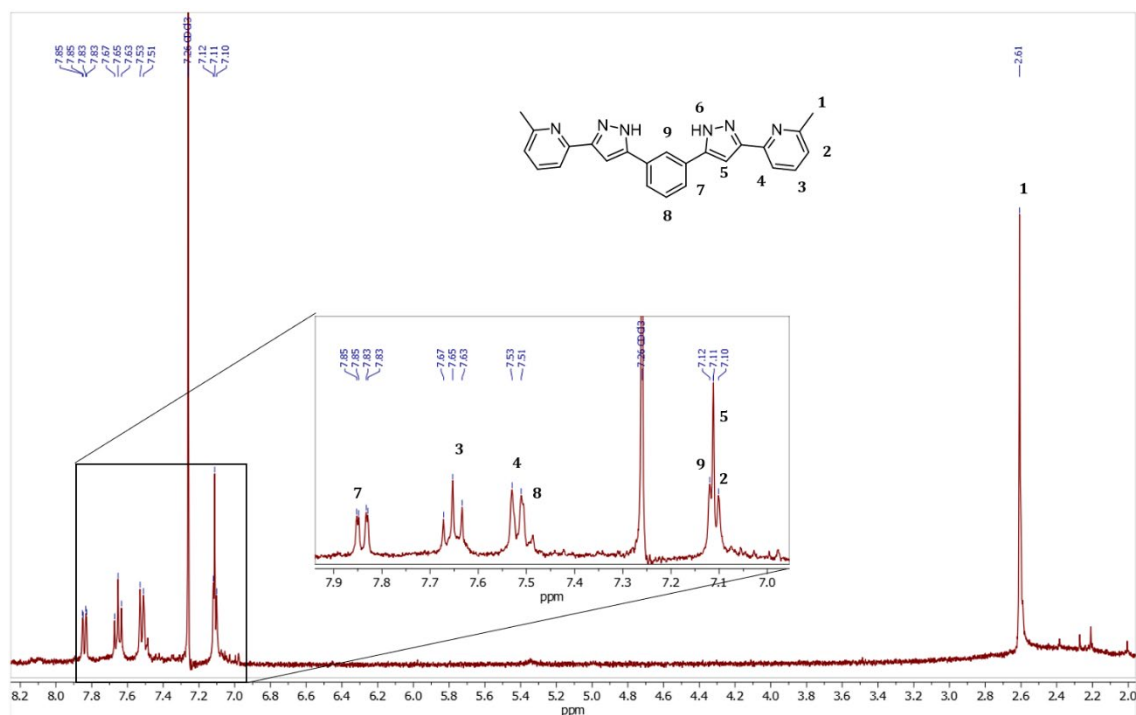


Figure A5.22.  $^1\text{H}$  NMR spectrum (aromatic region) of  $\text{H}_2\text{L6}$  in  $\text{CDCl}_3$ .

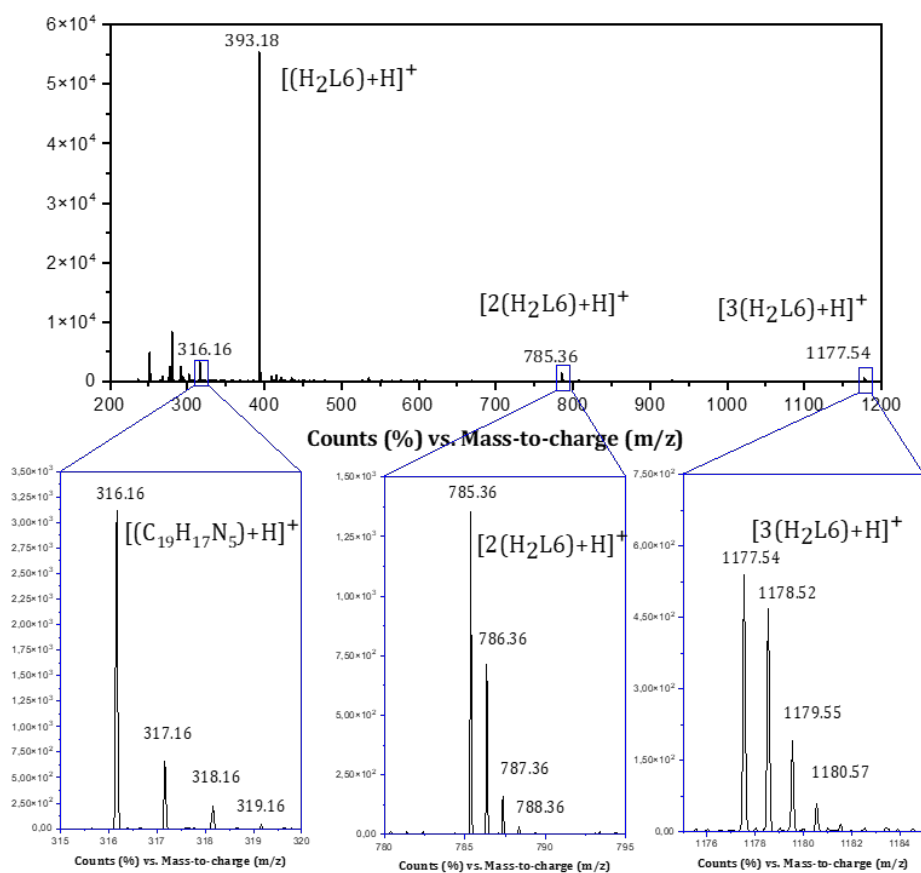


Figure A5.23. Positive ion ESI mass spectrum at 175V  $\text{H}_2\text{L6}$  dissolved in  $\text{CH}_2\text{Cl}_2$ .

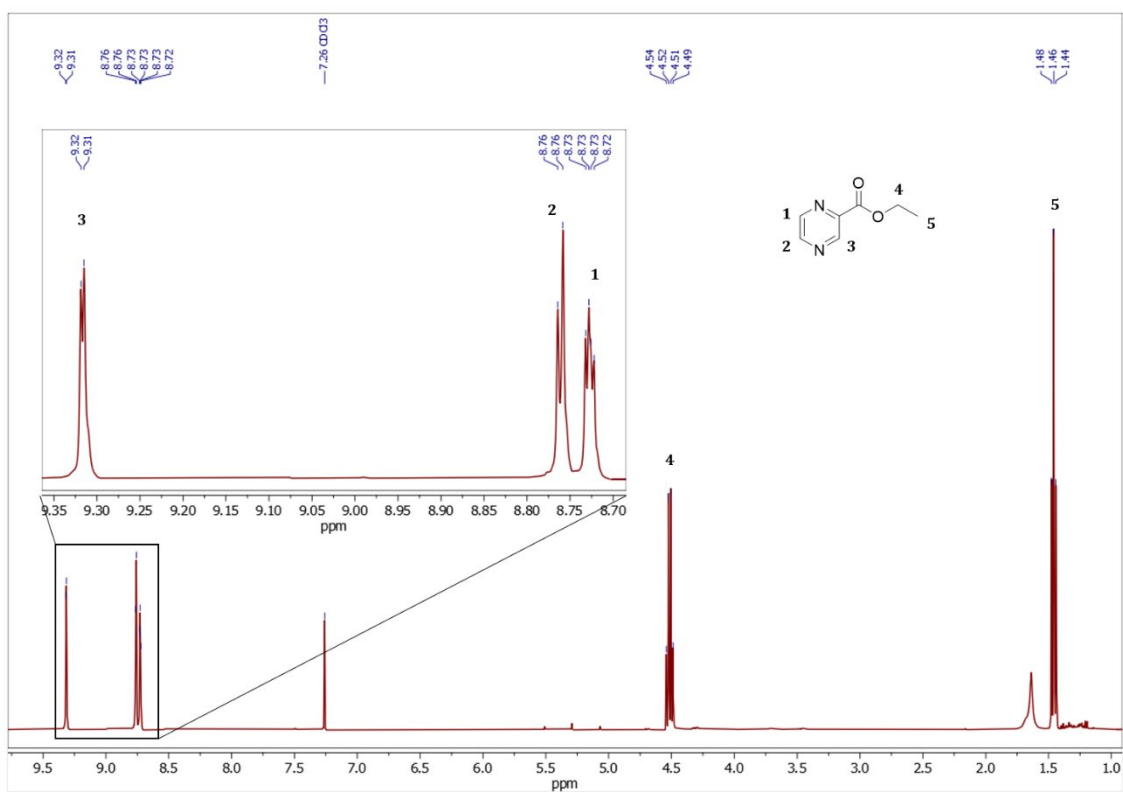


Figure A5.24. <sup>1</sup>H NMR spectrum (aromatic region) of E1 in chloroform-d.

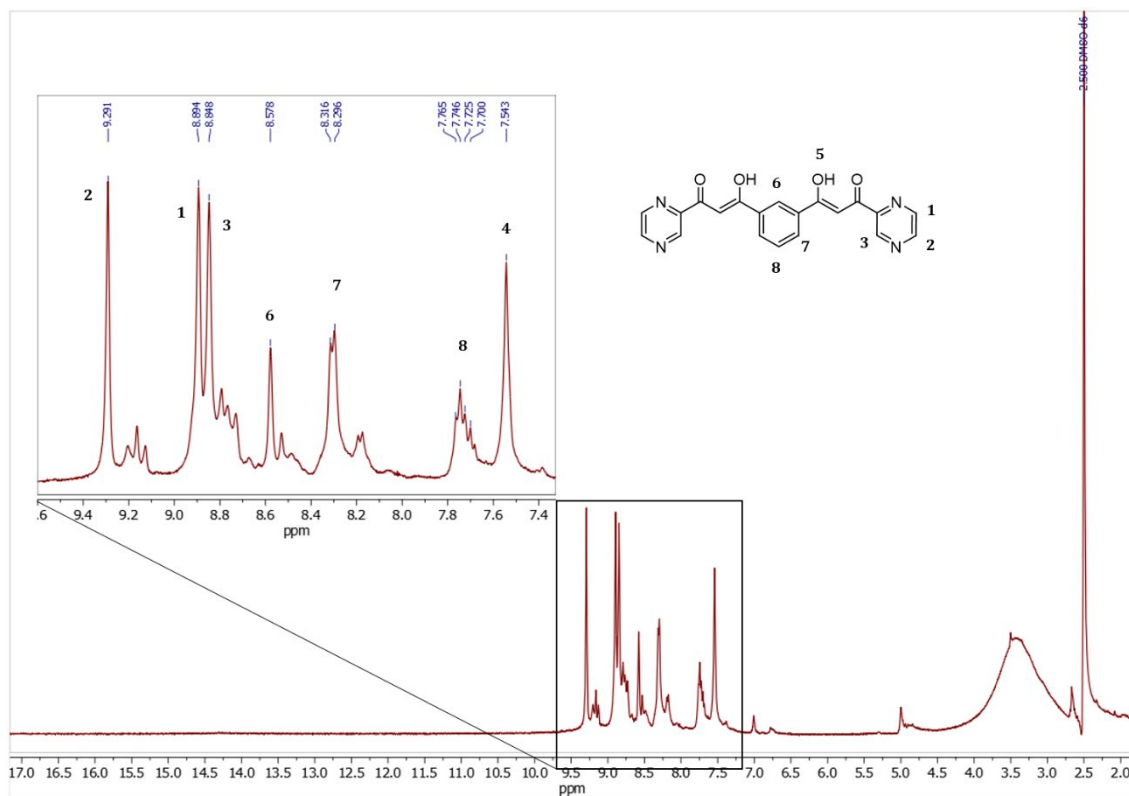
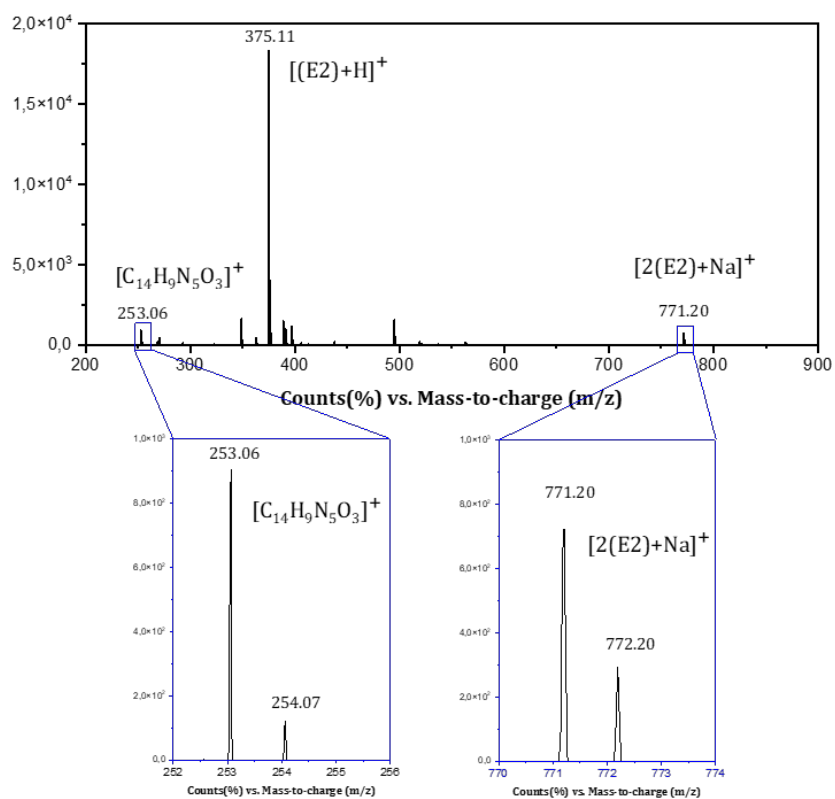
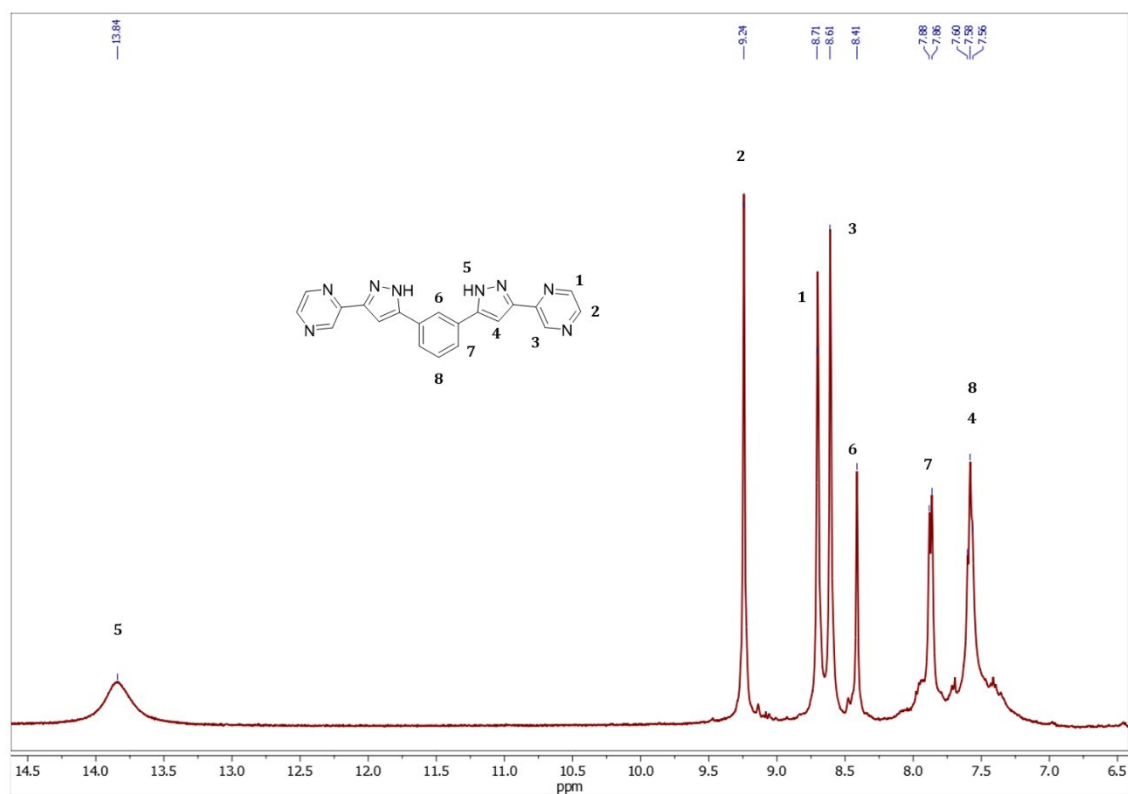


Figure A5.25. <sup>1</sup>H NMR spectrum (aromatic region) of E2 in dmsO-d<sub>6</sub>.



**Figure A5.26.** Positive ion ESI mass spectrum at 175V E2 dissolved in a mixture of  $CHCl_3$  and  $CH_3OH$ .



**Figure A5.27.**  $^1H$  NMR spectrum (aromatic region) of  $H_2L7$  in  $dms0-d_6$ .

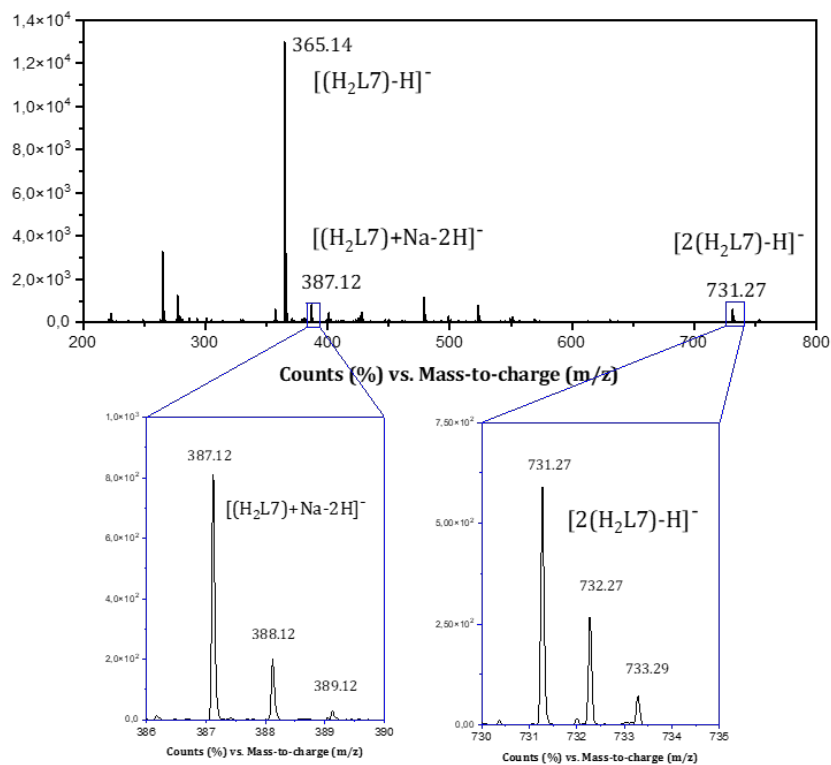


**Figure A5.28.** Negative ion ESI mass spectrum at 175V **E2** dissolved in a mixture of CHCl<sub>3</sub> and CH<sub>3</sub>OH.

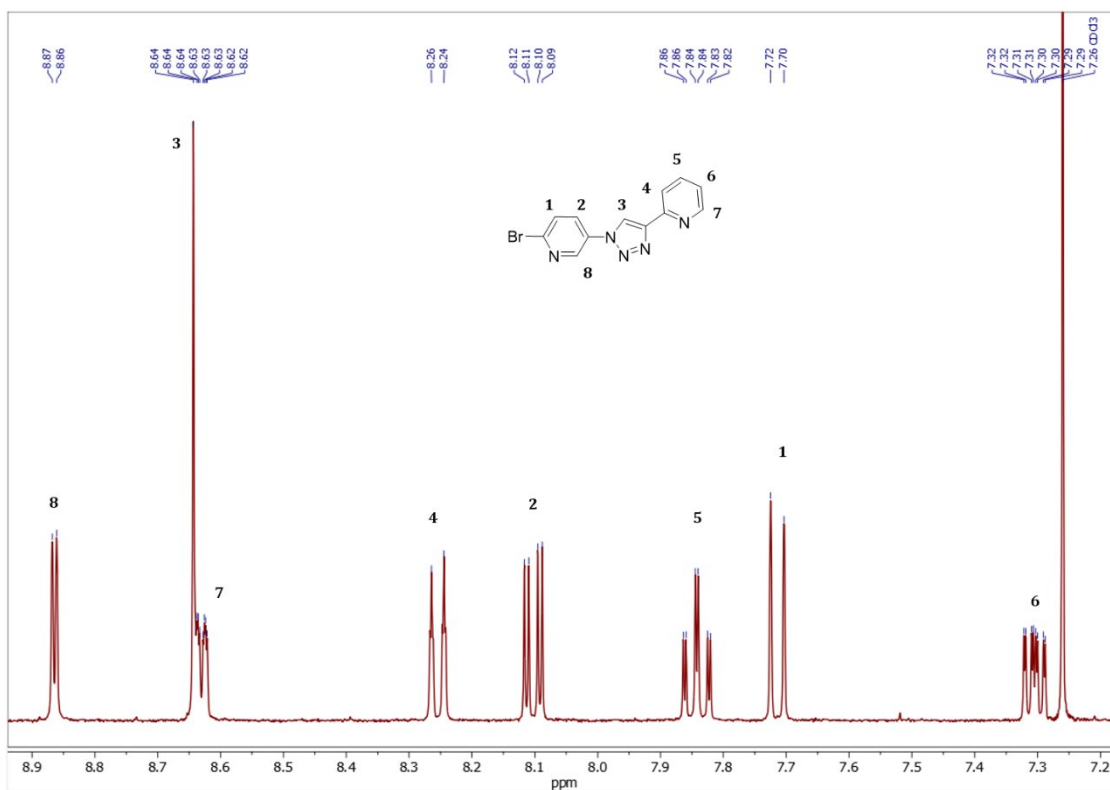


**Figure A5.29.** <sup>1</sup>H NMR spectrum (aromatic region) of **F1** in chloroform-*d*.

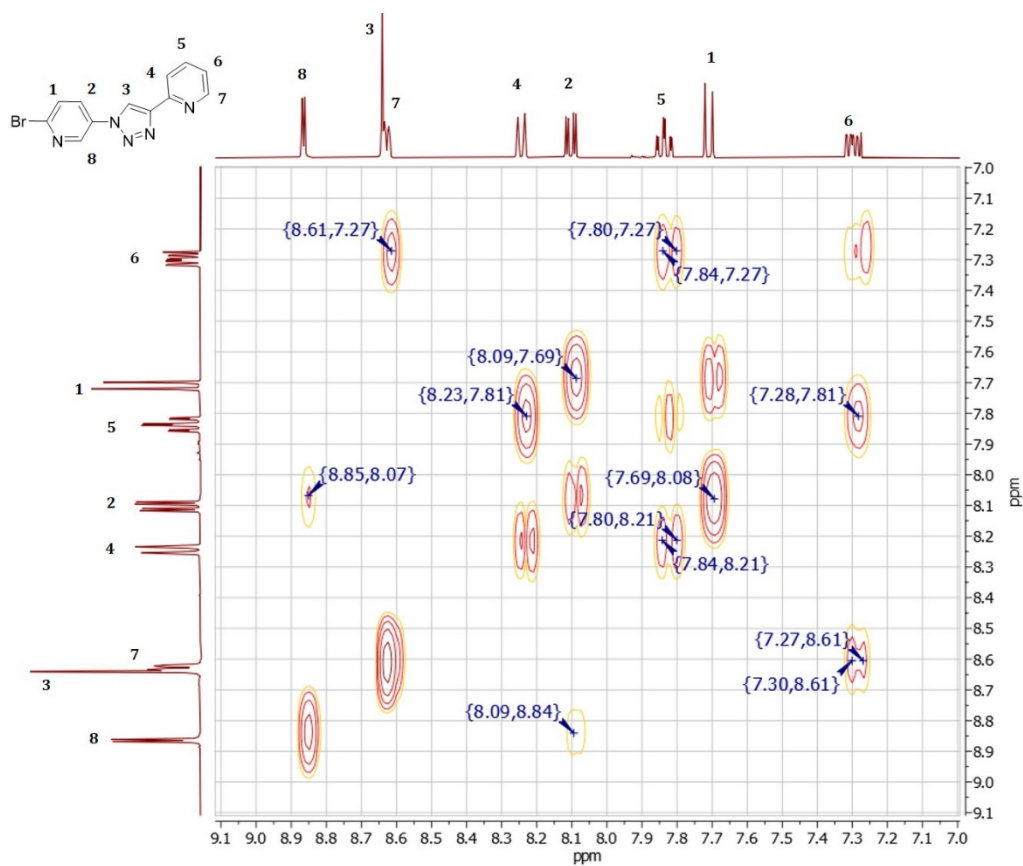


Figure A5.30. COSY spectrum of **F1** in chloroform-*d*.

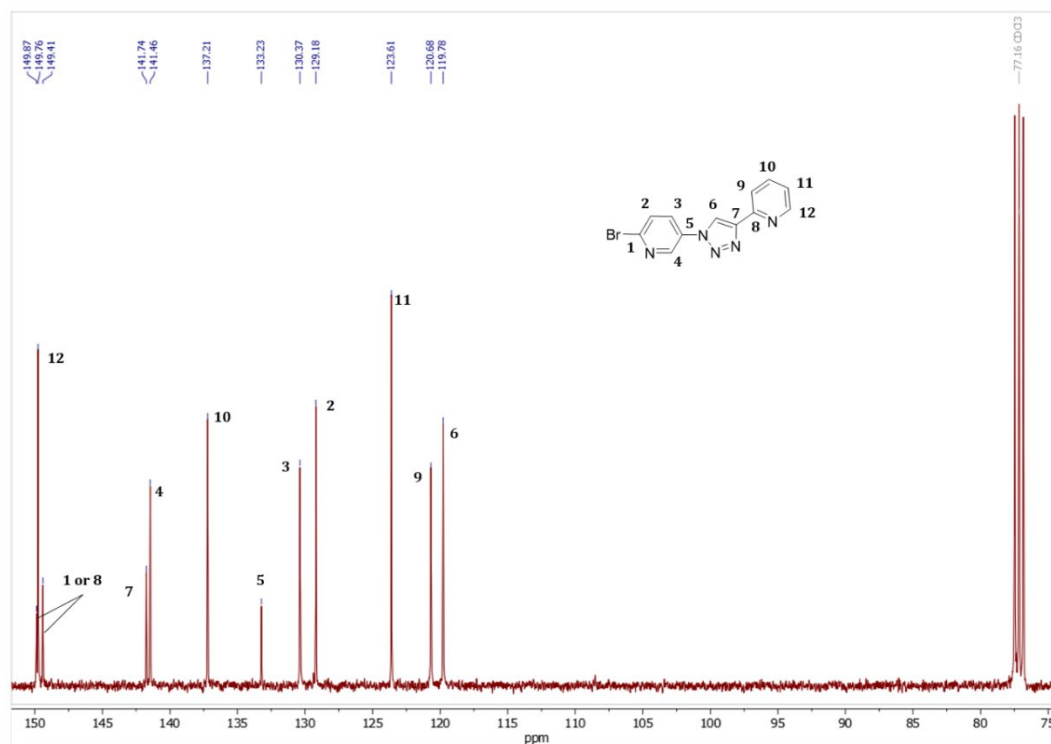
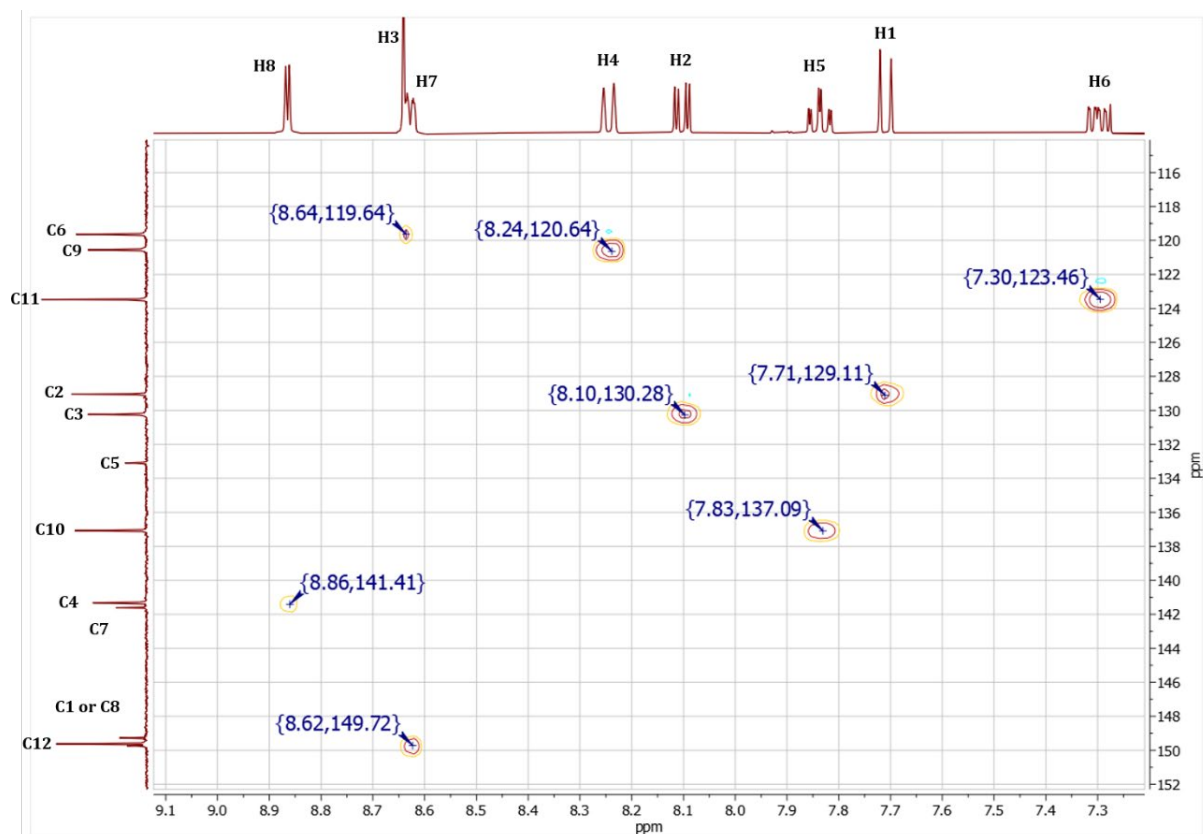
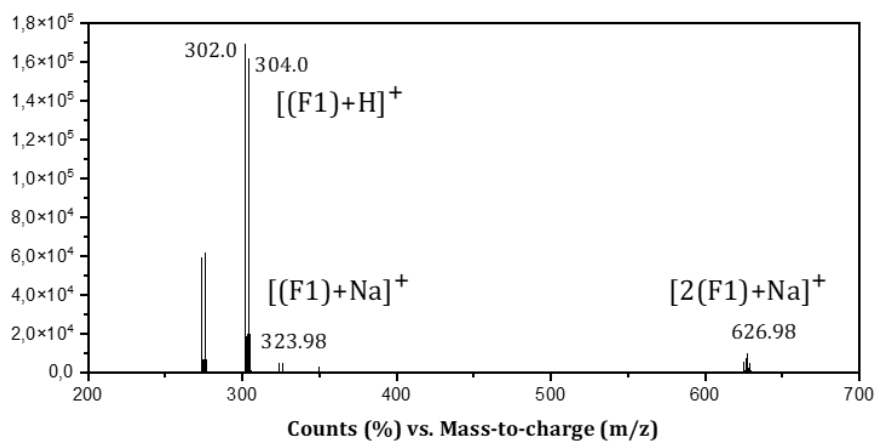


Figure A5.31.  $^{13}\text{C}$  NMR spectrum of **F1** in chloroform-*d*.



**Figure A5.32.** HSQC spectrum of **F1** in chloroform-d.



**Figure A5.33.** Positive ion ESI mass spectrum at 175V **F1** dissolved in a mixture of  $\text{CHCl}_3$  and  $\text{CH}_3\text{OH}$ .

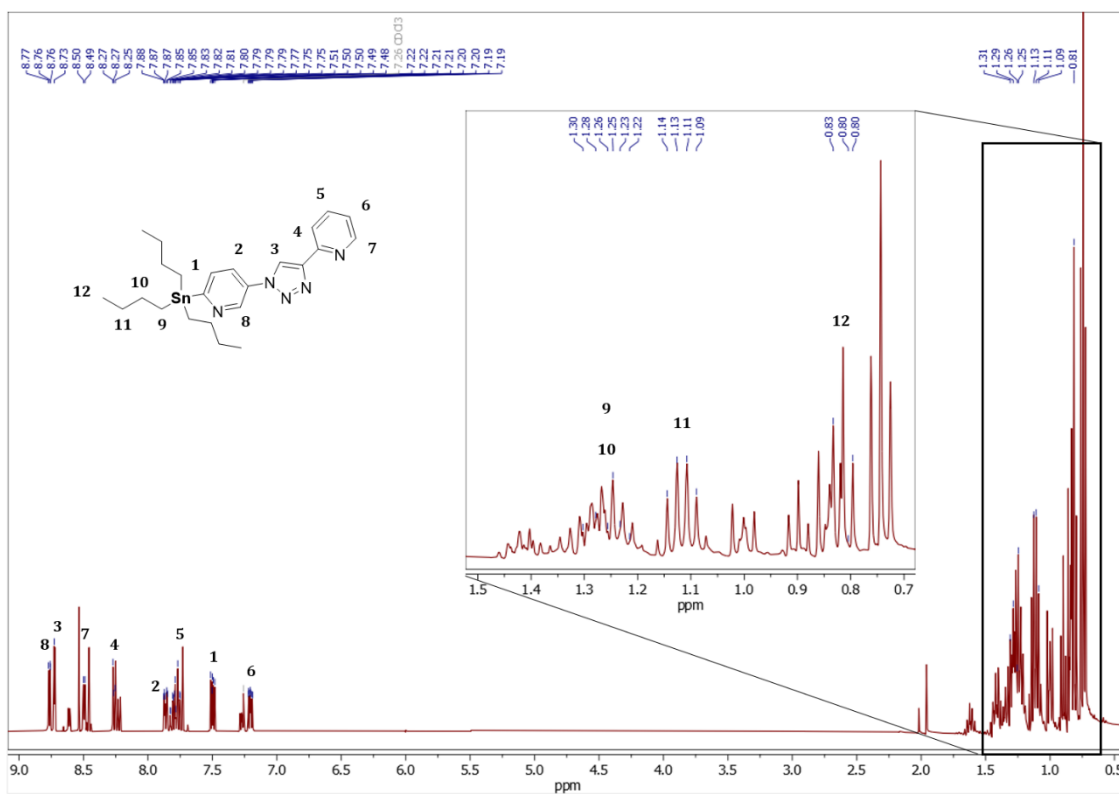


Figure A5.34.  $^1\text{H}$  NMR spectrum of F2 in chloroform-*d*.

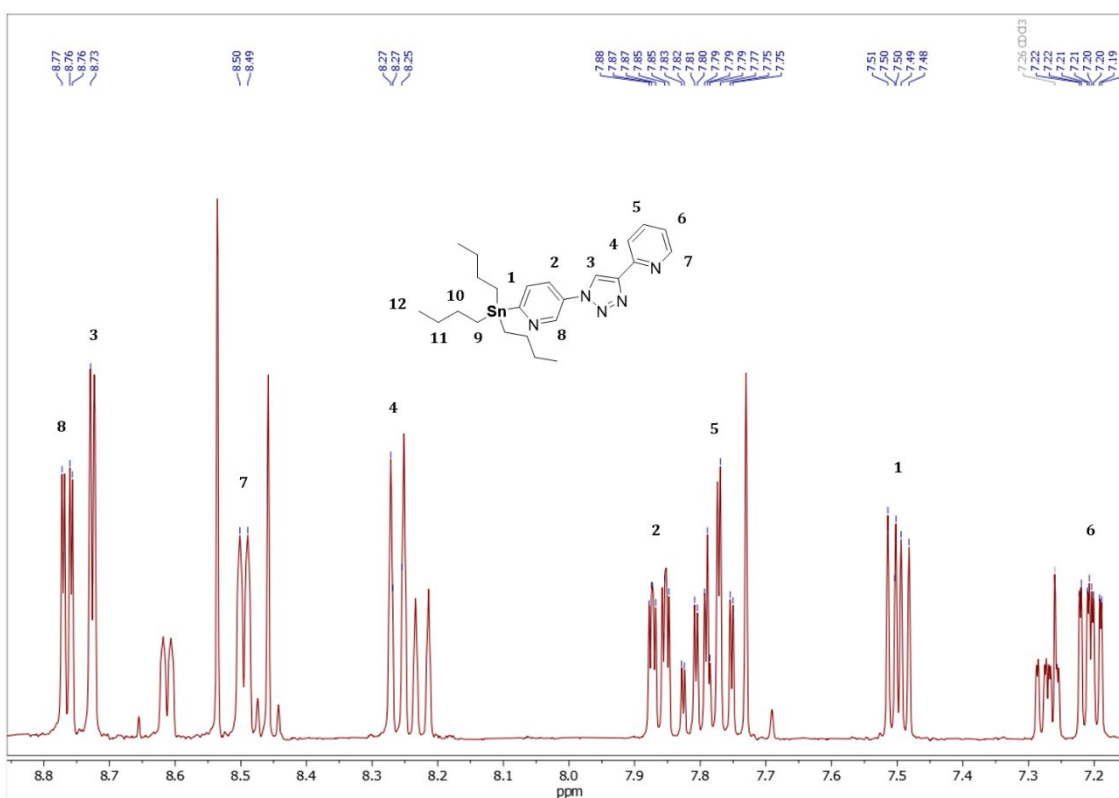


Figure A5.35.  $^1\text{H}$  NMR spectrum (aromatic region) of F2 in chloroform-*d*.

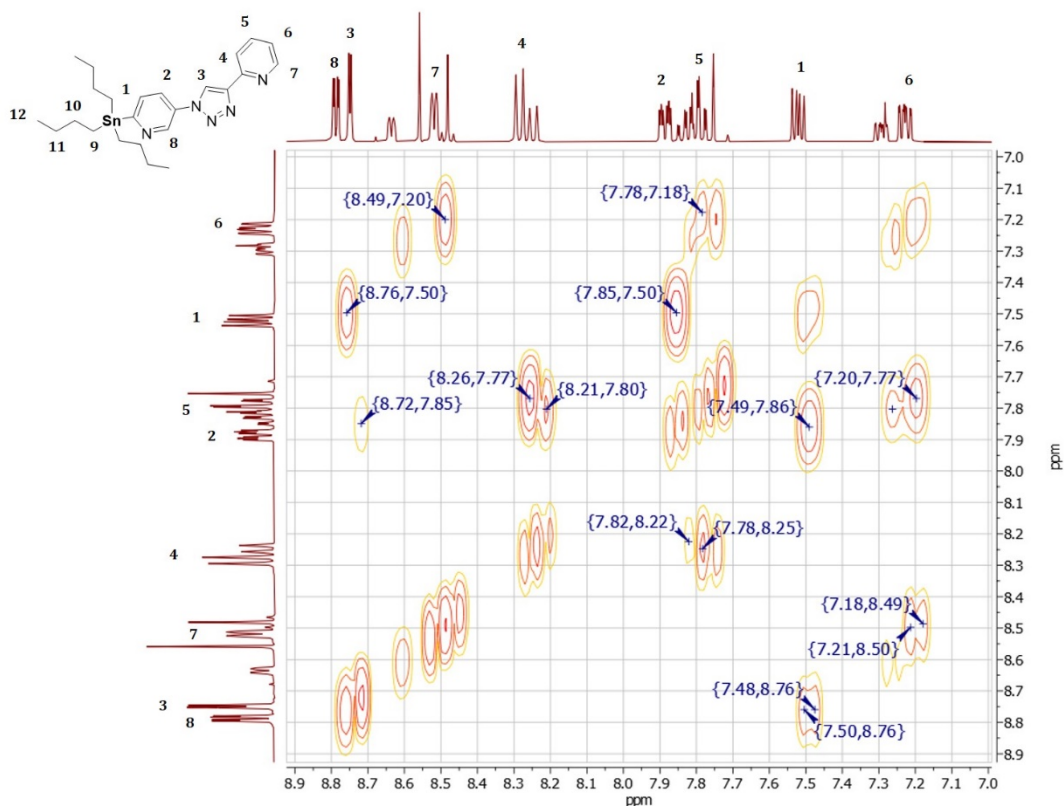


Figure A5.36. COSY spectrum of F2 in chloroform-*d*.

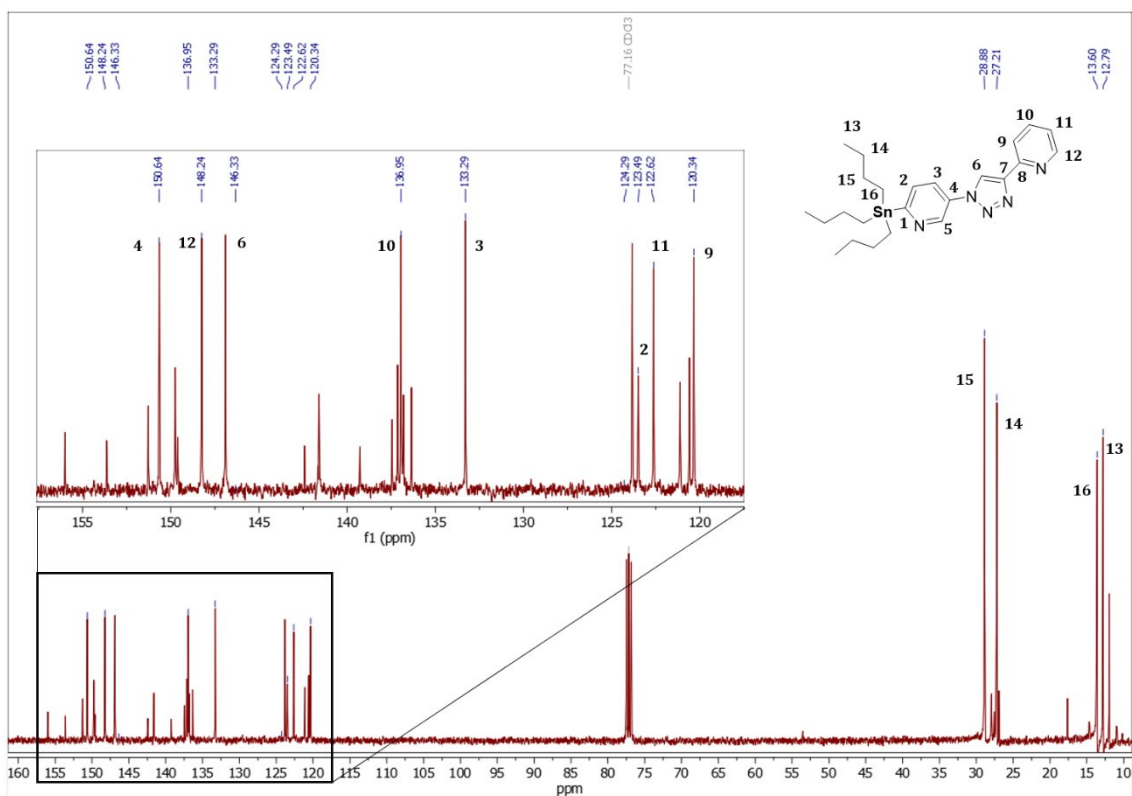


Figure A5.37.  $^{13}\text{C}$  NMR spectrum of F2 in chloroform-*d*.



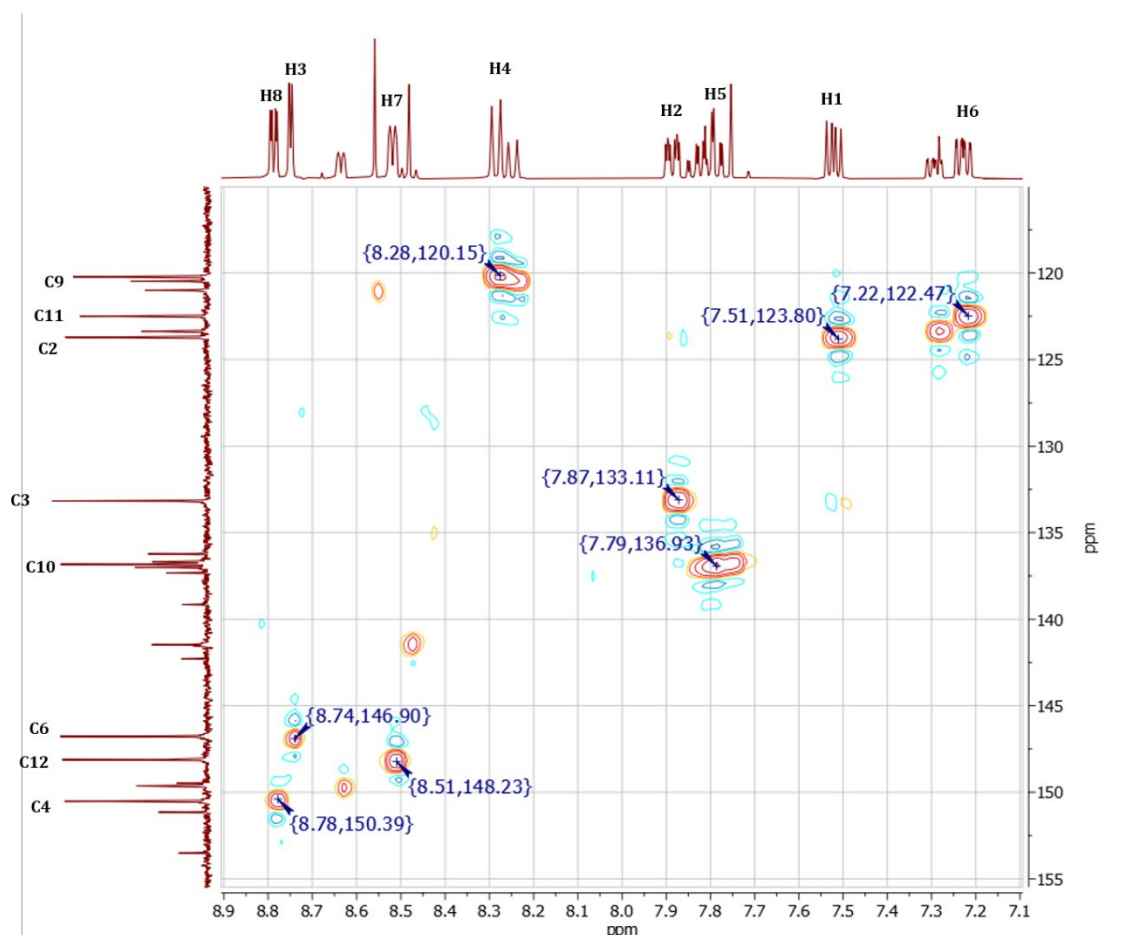


Figure A5.38. HSQC spectrum of F2 in chloroform-*d*.

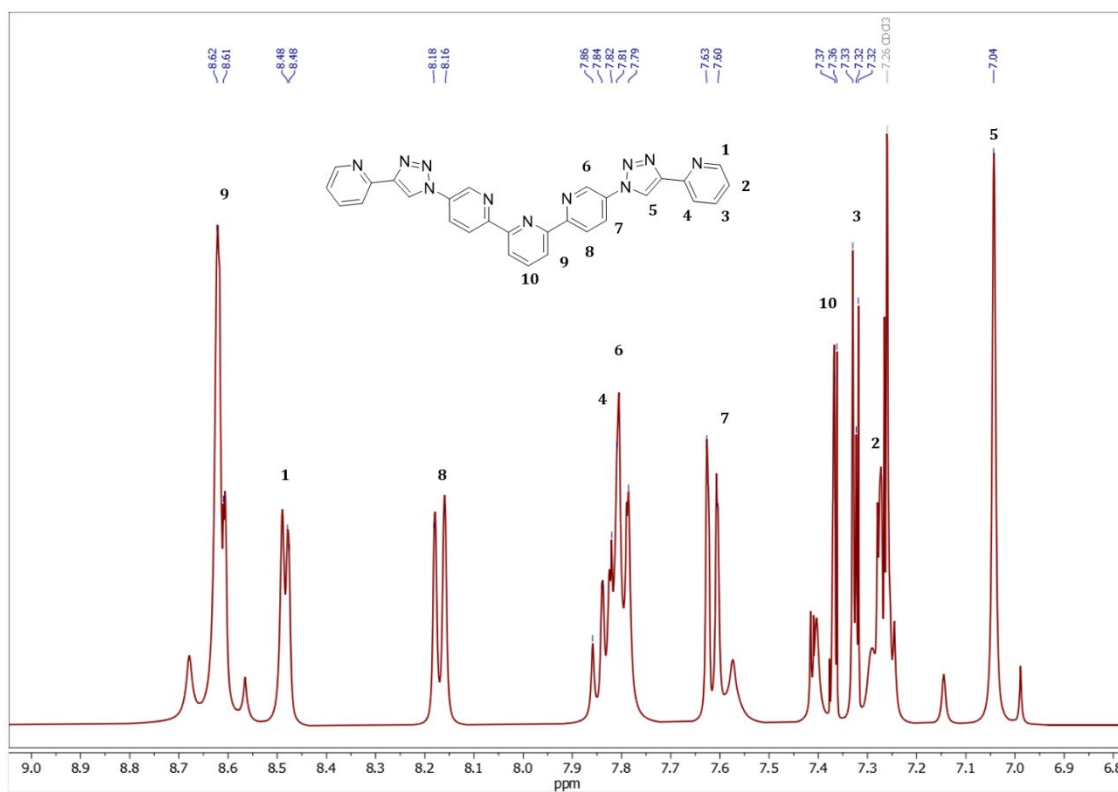
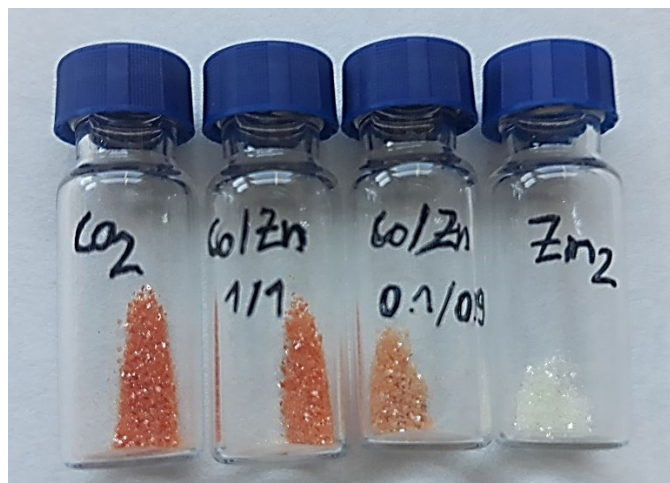
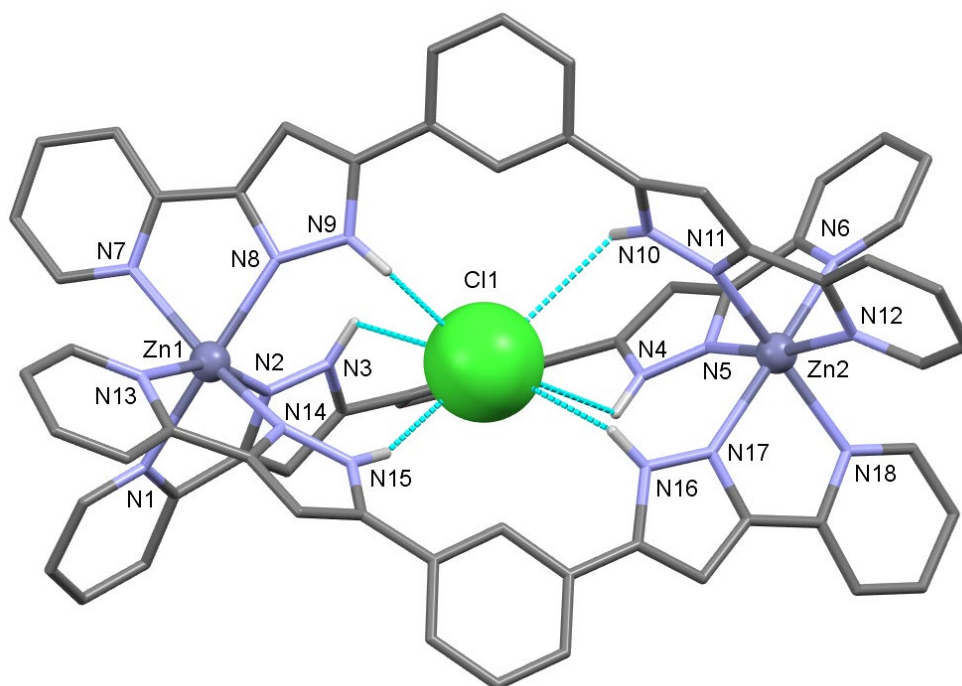


Figure A5.39.  $^1\text{H}$  NMR spectrum (aromatic region) of H<sub>2</sub>L8 in chloroform-*d*.

APPENDIX 6 - CHAPTER 6.  $\text{Cl}@\text{[Co}^{\text{II}}_2(\text{H}_2\text{L})_3]^{3+}$  AND  $\text{Cl}@\text{[Co}^{\text{II}}\text{Zn}^{\text{II}}(\text{H}_2\text{L})_3]^{3+}$   
TRIPLE-STRANDED HELICATES SHOWING SLOW MAGNETIC RELAXATION



**Figure A6.1.** Picture of the crystals obtained from the reaction conditions described in the experimental section. From left to right: The ratios of Co(II) and Zn(II) salts used are: (1:0) giving  $[\text{Co}_2]$  (**11**), (0.5:0.5) labelled as Co/Zn (1/1) for the first attempt on obtaining  $[\text{CoZn}]$  and giving also  $[\text{Co}_2]$  (**11**), (0.1:0.9) leading to  $[\text{CoZn}]$  (**13**) and (0:1) giving  $[\text{Zn}_2]$  (**12**).



**Figure A6.2.** Molecular representation of the cationic  $\text{Cl}@\text{[Zn}_2(\text{H}_2\text{L})_3]^{3+}$  assembly in compound **12**.  $\text{PF}_6^-$  and  $\text{Cl}^-$  counterions and MeOH and diethyl ether molecules are omitted for clarity. Only heteroatoms are labelled and H atoms that are part of N-H groups shown. H-bonds are shown with dashed cyan lines.

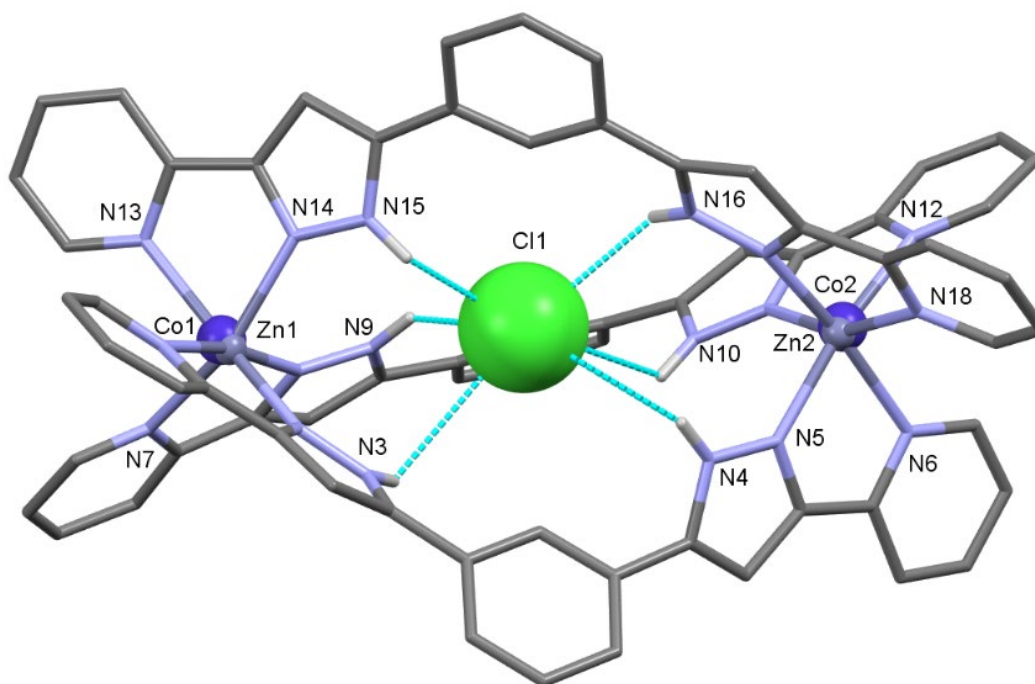


**Figure A6.3.** Molecular representation of the cationic mixture of the  $(\text{Cl}@[CoZn(\text{H}_2\text{L})_3])^{3+}$  and  $(\text{Cl}@[Zn_2(\text{H}_2\text{L})_3])^{3+}$  assemblies in compound **13**.  $\text{PF}_6^-$  and  $\text{Cl}^-$  counterions and  $\text{MeOH}$  and water molecules are omitted for clarity. Only heteroatoms are labelled and H atoms that are part of N–H groups shown. H–bonds are shown with dashed cyan lines.

### Crystallographic details on solving the structure of compound **13**

Since compound **13** contains essentially a mixture of  $[CoZn]$ ,  $[Zn_2]$  and an insignificant extent of  $[Co_2]$  (based on MS, EA and magnetic properties), the structure was refined by splitting each metal site into two positions, one for Zn and one for Co. Nevertheless, this refining attempt is poorly reliable due to the fairly high refined occupancy of Co with respect to other characterization techniques and the fact that several Co–N distances are longer than the corresponding Zn–N distances. Consequently, the structure for **3** was additionally refined excluding the Co atoms. For this refinement, the resulting Zn–N distances are shorter than the ones from the structure of **2** (pure  $[Zn_2]$ ). Thus, these comparative results found clear support for the mixture composition of  $[CoZn]$  and  $[Zn_2]$  molecules within the crystal. For further information of both refinements see table Table A6.1 where each is reported as **13** and **13'**, respectively. Supplementary crystallographic data can be found in CCDC 1912241-1912242-1912243-1912244 (**11-12-13-13'**).

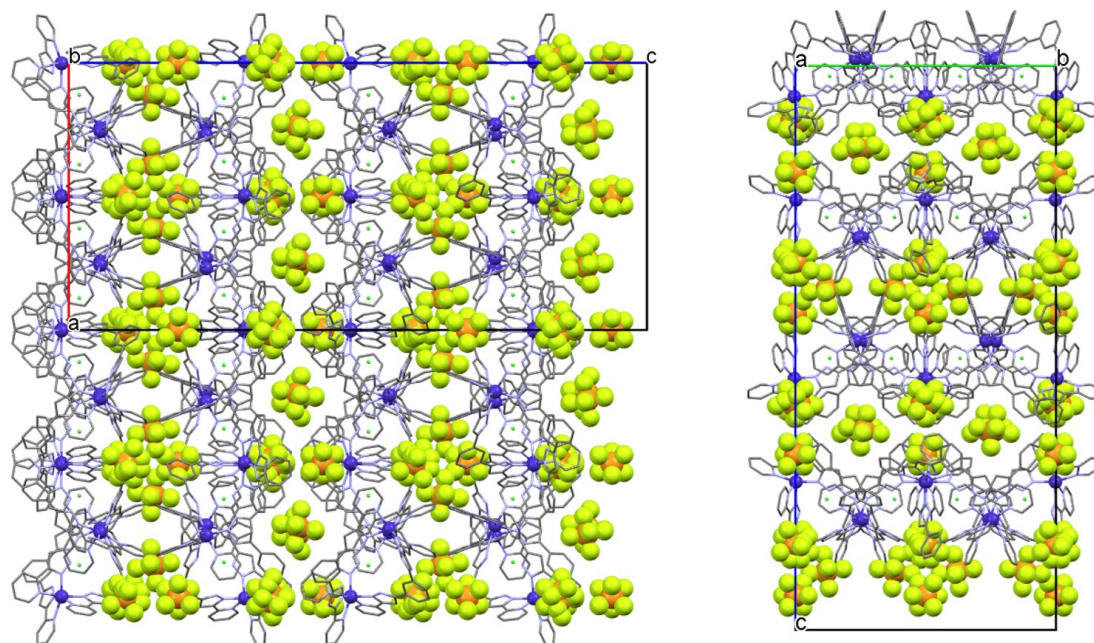


**Figure A6.4.** Representation of the  $\text{Cl}@\text{[Co}_2(\text{H}_2\text{L})_3\text{]}^{3+}$  moieties of **11** (purple and grey) within the lattice. Sheet along the *ab* crystallographic plane is represented. The  $\text{PF}_6^-$  anions are depicted in green and orange. Two of them display some disorder. H atoms are omitted for clarity.

**Table A6.1.** Summarized crystallographic data for compounds Cl@[Co<sub>2</sub>(H<sub>2</sub>L)<sub>3</sub>]Cl(PF<sub>6</sub>)<sub>2</sub>·4CH<sub>3</sub>OH·0.25 C<sub>4</sub>H<sub>10</sub>O (**11**), Cl@[Zn<sub>2</sub>(H<sub>2</sub>L)<sub>3</sub>]Cl(PF<sub>6</sub>)<sub>2</sub>·4CH<sub>3</sub>OH·C<sub>4</sub>H<sub>10</sub>O·H<sub>2</sub>O(**12**) and Cl@[Zn<sub>1.15</sub>Co<sub>0.85</sub>(H<sub>2</sub>L)<sub>3</sub>]Cl(PF<sub>6</sub>)<sub>2</sub>·2CH<sub>3</sub>OH·3H<sub>2</sub>O (**3**). Additionally, a refinement for compound **13** without including an heterometallic composition is detailed and reported as **13'**.

Compound	<b>11</b>	<b>12</b>	<b>13'</b>	<b>13</b>
Formula	C <sub>71</sub> H <sub>68</sub> Cl <sub>2</sub> F <sub>12</sub> N <sub>18</sub> O <sub>4.25</sub> P <sub>2</sub> Co <sub>2</sub>	C <sub>72</sub> H <sub>71</sub> Cl <sub>2</sub> F <sub>12</sub> N <sub>18</sub> O <sub>5.50</sub> P <sub>2</sub> Zn <sub>2</sub>	C <sub>68</sub> H <sub>62</sub> Cl <sub>2</sub> F <sub>12</sub> N <sub>18</sub> O <sub>5</sub> P <sub>2</sub> Zn <sub>2</sub>	C <sub>68</sub> H <sub>62</sub> Cl <sub>2</sub> F <sub>12</sub> N <sub>18</sub> O <sub>5</sub> P <sub>2</sub> Co <sub>0.85</sub> Zn <sub>1.15</sub>
FW (g mol <sup>-1</sup> )	1720.13	1768.04	1702.93	1697.46
Wavelength (Å)	0.7749	0.71073		0.71073
T (K)	100	100		100
Crystal system	tetragonal	tetragonal		tetragonal
Space group	I41cd	I41cd		I41cd
a = b (Å)	24.4100(8)	24.699(7)		24.223(7)
c (Å)	52.846(2)	53.777(16)		52.9655(16)
α=β=γ (°)	90	90		90
V (Å <sup>3</sup> )	31488(2)	32806(21)		31078(18)
Z	16	16		16
ρ <sub>calcd</sub> (g cm <sup>-3</sup> )	1.451	1.432	1.456	1.451
μ (mm <sup>-1</sup> )	0.764	0.776	0.816	0.735
Independent reflections (R <sub>int</sub> )	13907 (0.0247)	7280 (0.0436)	13264 (0.0468)	13272 (0.0468)
param. / restraints	1022/ 159	995/ 241	993/ 178	1000/ 178
Flack param.	0.45(2)	0.56(4)	0.32(3)	0.29(3)
Goodness-of-fit	1.031	1.062	1.048	1.049
R1 [I>2σ(I)]	0.0555	0.0634	0.0754	0.0733
wR2 [I>2 σ (I)]	0.1569	0.1721	0.2099	0.2052
R1 [all data]	0.0607	0.0729	0.0925	0.0906
wR2 [all data]	0.1636	0.1817	0.2262	0.2212
largest diff. peak / hole (e Å <sup>-3</sup> )	1.622 / -0.599	0.904 / -0.544	1.230/ -0.875	1.205 / -0.767

**Table A6.2.** Hydrogen bonding in the structures of compound **11**, **12** and **13**.

<b>D-H...A</b>	<b>D-H (Å)</b>	<b>H...A (Å)</b>	<b>D-A (Å)</b>	<b>D-H...A (°)</b>
<b>11</b>				
N4-H4B...O2S	0.88	1.97	2.779(10)	152.3
N9-H9A...Cl1	0.88	2.49	3.257(6)	145.8
N10-H10B...O1S	0.88	1.88	2.693(8)	153.2
N15-H15A...Cl1	0.88	2.38	3.136(6)	144.1
O1S-H1S...Cl2	0.84	2.26	3.080(6)	163.9
O2S-H2S...O4S	0.87(3)	1.77(4)	2.592(18)	156(10)
O3S-H3S...Cl2	0.91(3)	2.26(7)	3.080(16)	150(12)
<b>12</b>				
N3-H3B...Cl2	0.88	2.28	3.104(16)	155.2
N4-H4B...O2S	0.88	2.01	2.82(2)	151.2
N9-H9A...Cl1	0.88	2.51	3.289(15)	148.0
N10-H10B...O1S	0.88	1.89	2.714(19)	155.4
N15-H15A...Cl1	0.88	2.45	3.201(15)	144.2
N16-H16B...Cl1	0.88	2.74	3.450(15)	138.5
O1S-H1S...Cl2	0.84	2.32	3.117(14)	159.0
O2S-H2S...O6S	0.84	1.61	2.32(3)	140.4
O4S-H4S...Cl2	0.84	2.21	2.97(2)	151.4
O6S-H6S...O3W	0.84	1.55	2.21(3)	132.0
<b>13</b>				
N3-H3B...Cl2	0.88	2.18	3.014(10)	157.2
N4-H4B...O2S	0.88	1.86	2.735(18)	171.8
N9-H9A...Cl1	0.88	2.51	3.263(10)	143.6
N10-H10B...O1S	0.88	2.04	2.832(16)	149.5
N15-H15A...Cl1	0.88	2.54	3.241(11)	136.8
N16-H16B...Cl1	0.88	2.78	3.444(11)	133.2
O1S-H1S...Cl2	0.84	2.20	3.031(12)	166.9

**Table A6.3.** Bond lengths (Å) describing the coordination environments for the metal centres and intramolecular metal...metal separations in the structures of compounds **11**, **12** and **13**. Additionally, a refinement for compound **13** without including an heterometallic composition is detailed and reported as **13'**.

	<b>11(M=Co)</b>	<b>12(M=Zn)</b>	<b>13'(M= Zn)</b>	<b>13(M=Co/Zn)</b>
M1-N14	2.099(6)	2.148(14)	2.111(11)	2.12(4) / 2.12(2)
M1-N8	2.100(7)	2.149(17)	2.105(12)	2.08(4) / 2.12(3)
M1-N2	2.106(6)	2.158(14)	2.103(9)	2.26(3) / 2.01(2)
M1-N7	2.141(6)	2.198(14)	2.138(10)	2.09(4) / 2.17(2)
M1-N13	2.204(6)	2.261(13)	2.211(10)	2.08(3) / 2.30(2)
M1-N1	2.213(6)	2.295(16)	2.225(10)	2.30(4) / 2.19(2)
M2-N11	2.099(6)	2.134(15)	2.092(10)	1.98(3) / 2.159(19)
M2-N5	2.104(6)	2.146(14)	2.132(9)	2.25(2) / 2.066(19)
M2-N17	2.119(7)	2.187(16)	2.124(12)	2.21(3) / 2.076(19)
M2-N18	2.128(6)	2.168(14)	2.148(9)	2.24(3) / 2.094(18)
M2-N6	2.173(6)	2.216(15)	2.186(10)	2.14(3) / 2.214(19)
M2-N12	2.180(6)	2.231(13)	2.189(10)	2.05(2) / 2.272(19)
M1...M2	9.771(6)	9.881(12)	9.818(9)	9.94(2) - 9.75(2)

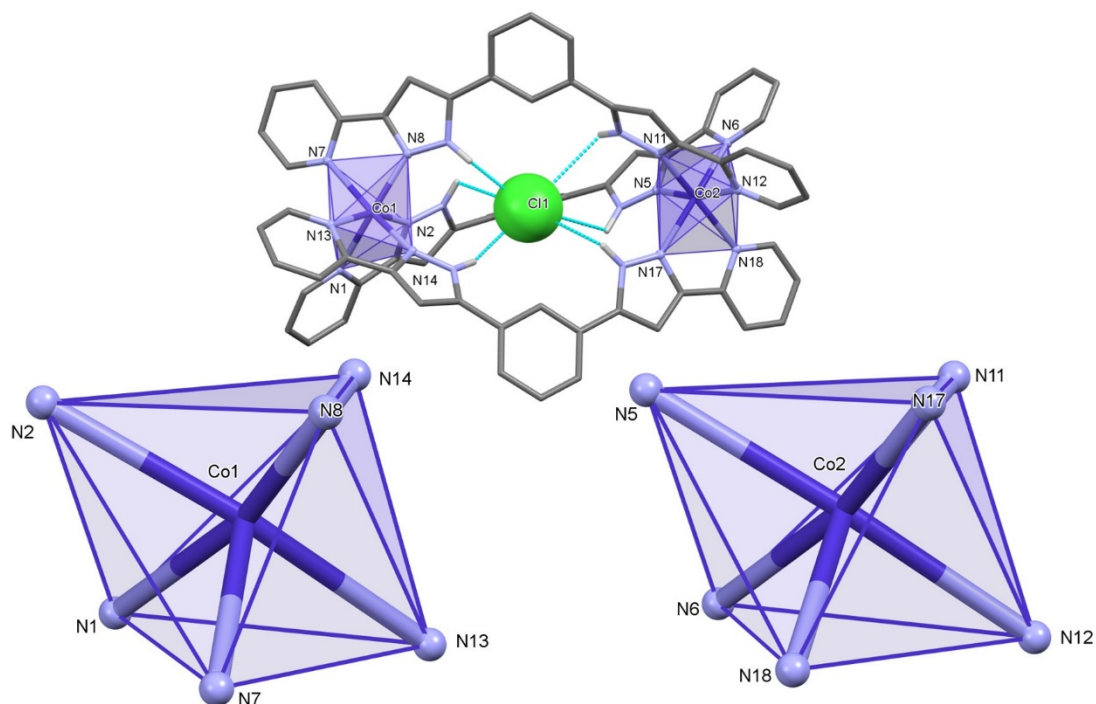


**Figure A6.5.** (Top) Molecular structure of  $\text{Cl}@[Co_2(H_2L)_3]^{3+}$  in compound two with the corresponding polyhedra around each metal center. (Bottom). Distorted coordination geometry for each cobalt in compound **11**.

**Table A6.4.** Continuous shape measures calculation (CShM) for six vertex polyhedra of compounds **11**, **12** and **13** calculated with SHAPE software. For each metal center, the displayed coordination polyhedra was compared with the ideal TP and TAP geometries.

	[Co <sub>2</sub> ] ( <b>11</b> )		[CoZn] ( <b>13</b> and <b>13'</b> )				[Zn <sub>2</sub> ] ( <b>12</b> )	
	Co1	Co2	Co1	Co2	Zn1	Zn2	Zn1	Zn2
<b>TAP</b>	2.789	1.765	2.517	2.157	2.501	2.158	3.059	1.959
<b>TP</b>	9.279	11.463	10.093	10.948	10.079	10.949	8.970	11.344

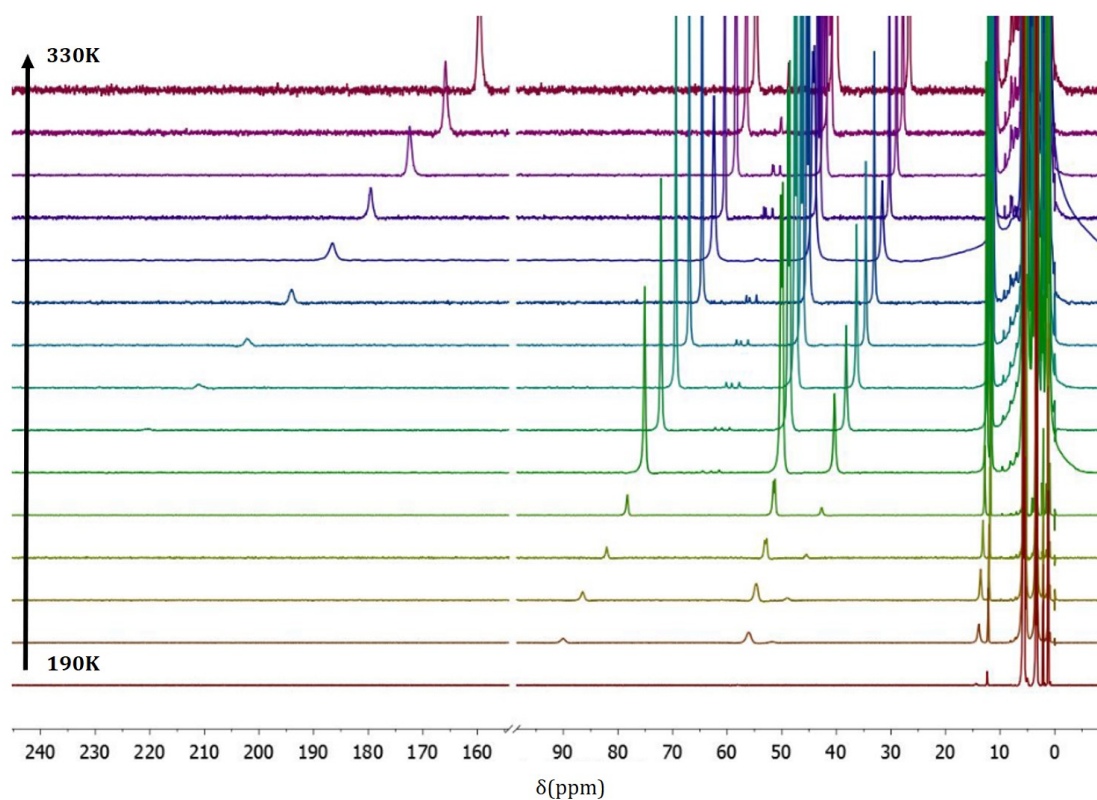


**Figure A6.6.** VT- <sup>1</sup>H NMR spectra of [Co<sub>2</sub>], (**11**), from 190 to 330K in methanol-*d*<sub>4</sub>.



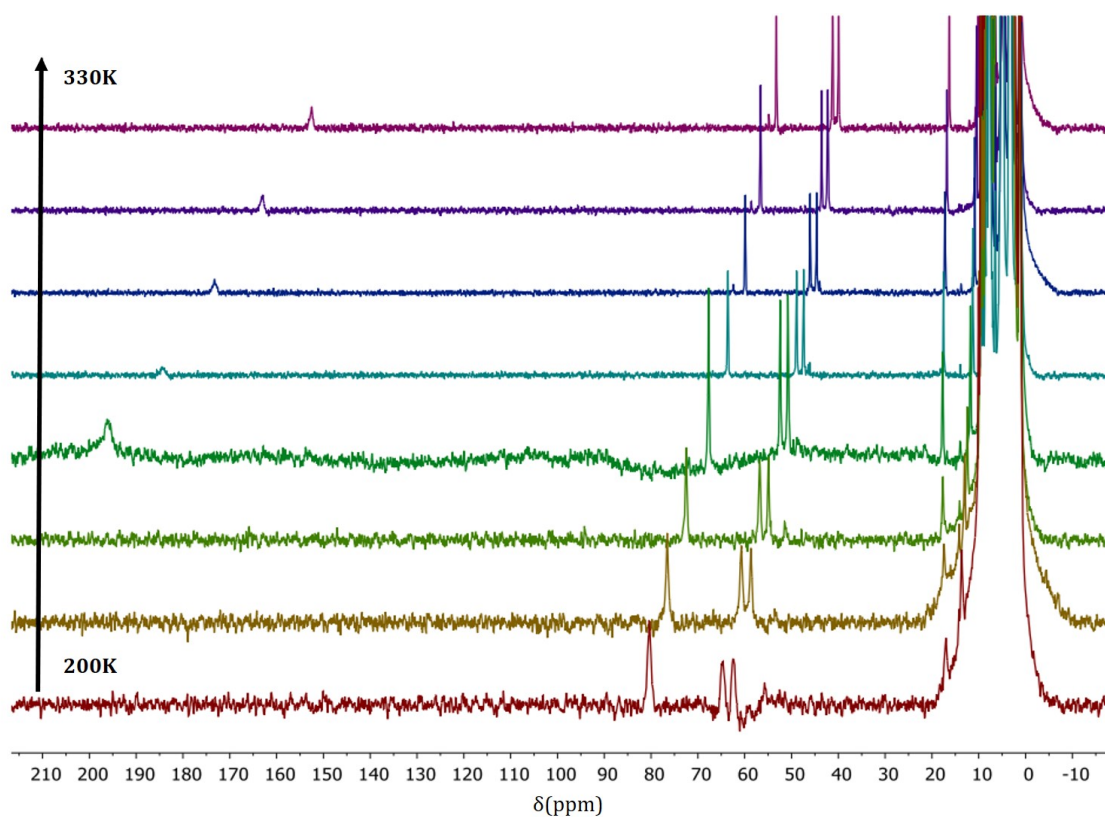


**Figure A6.7.** VT- <sup>1</sup>H NMR spectra of [CoZn], (**13**), from 190 to 330K in methanol-*d*<sub>4</sub>.

### Quantum chemical calculation related to analysis of paramagnetic shifts

All quantum chemical calculations were performed using the ORCA package, v. 4.0.<sup>1</sup> For geometry optimization, the x-ray diffraction molecular geometry was used as a starting point with the PBE0 functional, the ZORA<sup>2</sup> approximation, Grimme's DFT-D3 dispersion correction<sup>3</sup> and (SARC)<sup>4</sup> version of the def2-TZVP basis set. The resulting optimized geometry was used to compute the g-value and isotropic values of  $A_{\text{iso}}$ .<sup>5</sup>

### Analysis of the paramagnetic shifts in the $^1\text{H}$ NMR spectra

The presence of the paramagnetic Co(II) ions in  $[\text{Co}_2]$  and  $[\text{CoZn}]$  results in observable paramagnetic shifts ( $\delta_{\text{obs}}$ ) of the signals in the  $^1\text{H}$  NMR spectrum, which include the diamagnetic ( $\delta_{\text{dia}}$ ), contact ( $\delta_{\text{C}}$ ) and pseudocontact ( $\delta_{\text{PC}}$ ) contributions:

$$\delta_{\text{obs}} = \delta_{\text{dia}} + \delta_{\text{C}} + \delta_{\text{PC}} \quad \text{Eq. S6.1}$$

The diamagnetic contribution is directly measured by  $^1\text{H}$  NMR of the  $[\text{Zn}_2]$  diamagnetic isosturctural to  $[\text{Co}_2]$ .

The contact contribution arises form spin polarization brought through molecular orbitals and follows directly form the spin-density distribution which is accessible computationally by DFT calculations. Thus, for the contact shift evaluation, the  $\delta_{\text{C}}$  was calculated by using the following equation:

$$\delta_{\text{C}} = \frac{S(S+1)\mu_{\text{B}}}{3kTg_{\text{N}}\mu_{\text{N}}} \cdot \bar{g} \cdot A_{\text{iso}} \quad \text{Eq. S6.2}$$

where  $S$ : electron spin,  $\mu_{\text{B}}$ : Borh magneton,  $kT$ : thermal energy,  $g_{\text{N}}$ : nuclear g-value,  $\mu_{\text{N}}$ : nuclear magneton,  $\bar{g}$ : DFT-calculated rotationally averaged electronic g-value,  $A_{\text{iso}}$ : DFT-calculated isotropic value of the hyperfine interaction tensor.

The pseudocontact contribution comes from dipolar coupling between the magnetic moments of a nucleus and of an unpaired electron.  $\delta_{\text{PC}}$  depends on the axial anisotropy of the magnetic susceptibility tensor ( $\chi$ -tensor) and its computational value is hard to access. However, an estimation by fitting the  $\delta_{\text{obs}}$  to the geometrically optimized and known structure of the compound by equation Eq. S6.3, gives a reliable approximation of the values:

$$\delta_{\text{PC}} = \frac{1}{12\pi r^3} [\Delta\chi_{\text{ax}}(3\cos^2\theta - 1)] \quad \text{Eq. S6.3}$$

$\theta$  and  $r$  are the polar coordinates of the nuclei in the coordinate structure taken form the DFT-optimized geometry, which are access through the X-ray diffraction geometries. For Co(II) in the HS state, the  $\Delta\chi_{\text{ax}}$  can be really large due to the large ZFS energy. Therefore, it implies a large pseudocontact contribution.

The fittings of the calculated and the experimental chemical shifts for  $[\text{Co}_2]$  at selected temperatures are depicted in the following Figure A6.8:

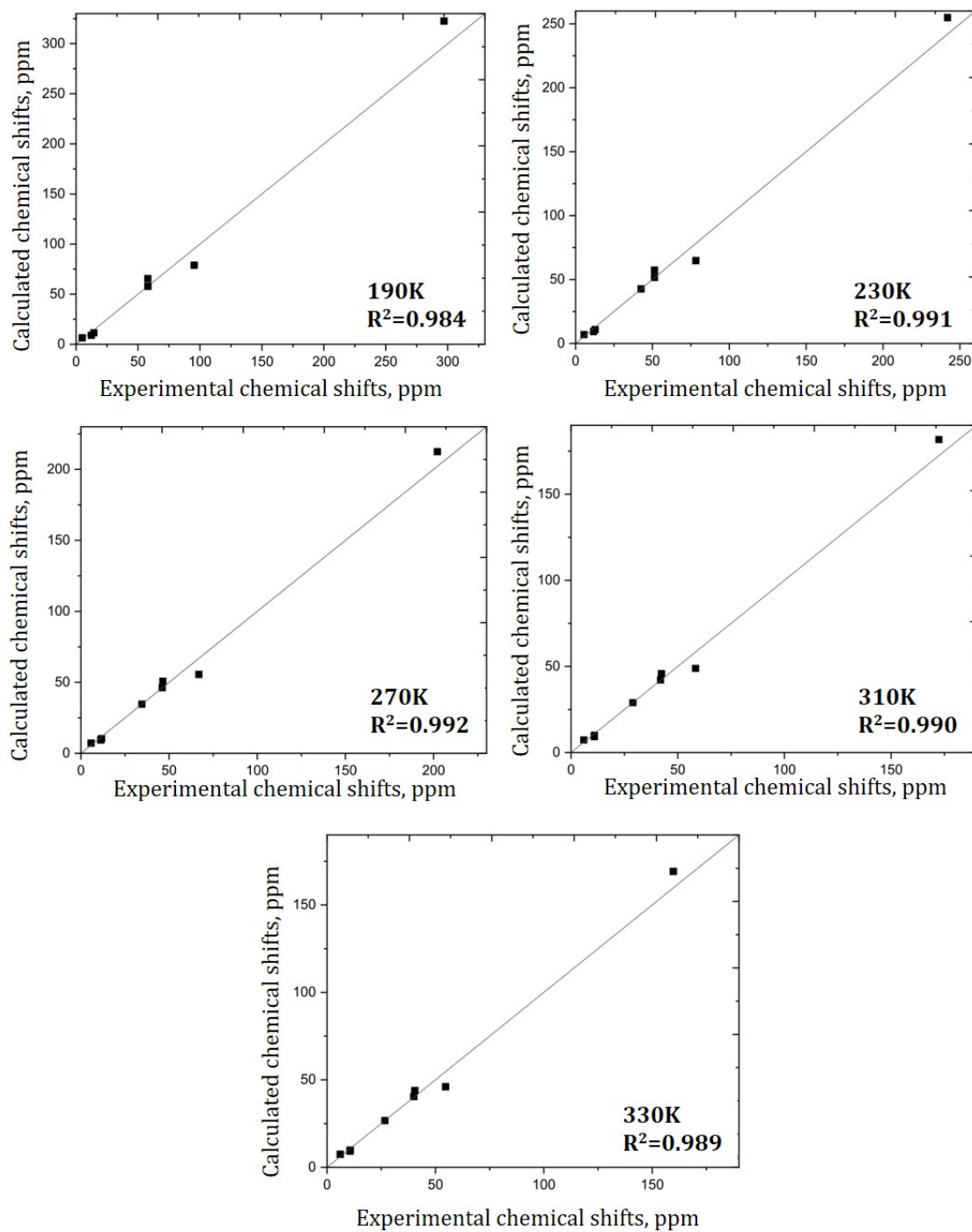


**Figure A6.8.** Calculated vs experimental chemical shifts in the paramagnetic  $^1\text{H}$  NMR for  $[\text{Co}_2]$  at 190, 230, 270, 310 and 330K.

### Fitting details of dc-Magnetometry and NMR data

The NMR spectroscopy data:

- Temperature dependence of the  $\Delta\chi_{ax}$ - Figure A6.9

And the dc-magnetometry data:

- Temperature dependence of the isotropic magnetic susceptibility- Figures 6.8 (right) and A6.12 (right)
- Field dependence of the magnetization – Figures 6.8 (left) and A6.12 (left)

Were fitted using the suitable Hamiltonian for HS six-coordinated Co(II) complexes<sup>6</sup>. Since there is spin-orbit contribution (an effective orbital angular momentum L of 1), an elaborated Hamiltonian given in equation S6.4 has to be used:

$$\hat{H} = \sigma\lambda\hat{L} \cdot \hat{S} + \Delta(3\hat{L}_z^2 - \hat{L}^2) + \mu_B B_0(-\sigma\hat{L} + g\hat{S}) \quad Eq.S6.4$$

where,  $\sigma$  is an orbital reduction factor,  $\lambda$  is the SOC parameter,  $\Delta$  parametrizes the crystal field splitting of the ground term of the six-coordinated Co(II)  $^4T_{1g}$  (S=3/2 and L=1), and g is the g-tensor. The other parameters have their usual meanings.

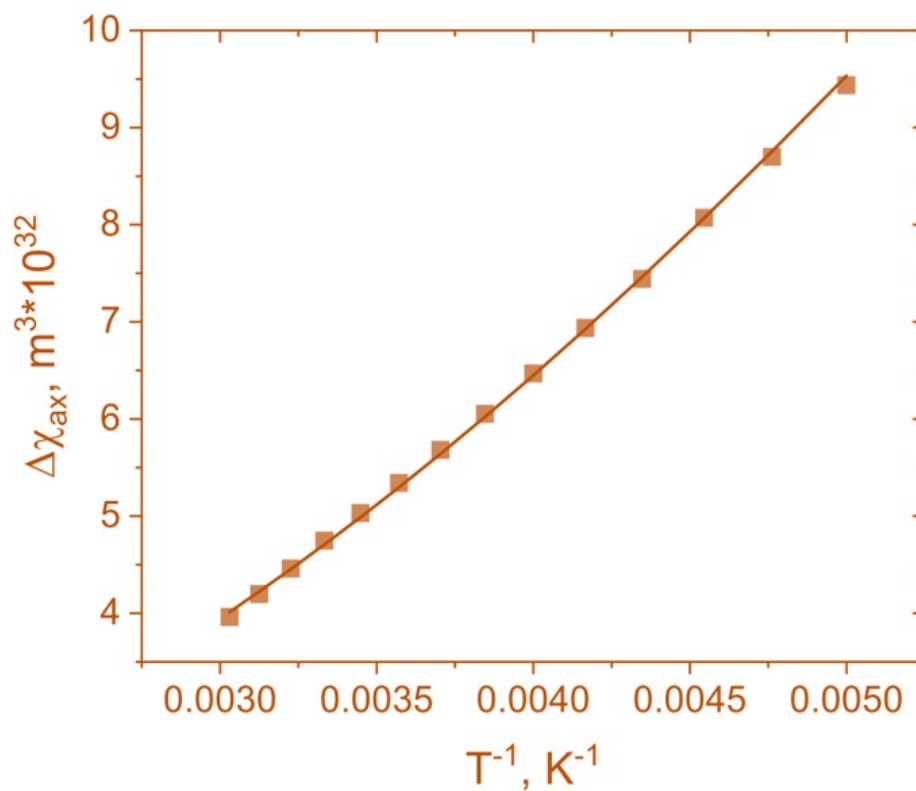


**Figure A6.9.** Temperature dependence of the  $\Delta\chi_{ax}$  for a solution of  $[Co_2]$ . Solid line shows the fit to Equation S6.4. Details on the NMR data fitting, as well as dc-magnetometry are described below.

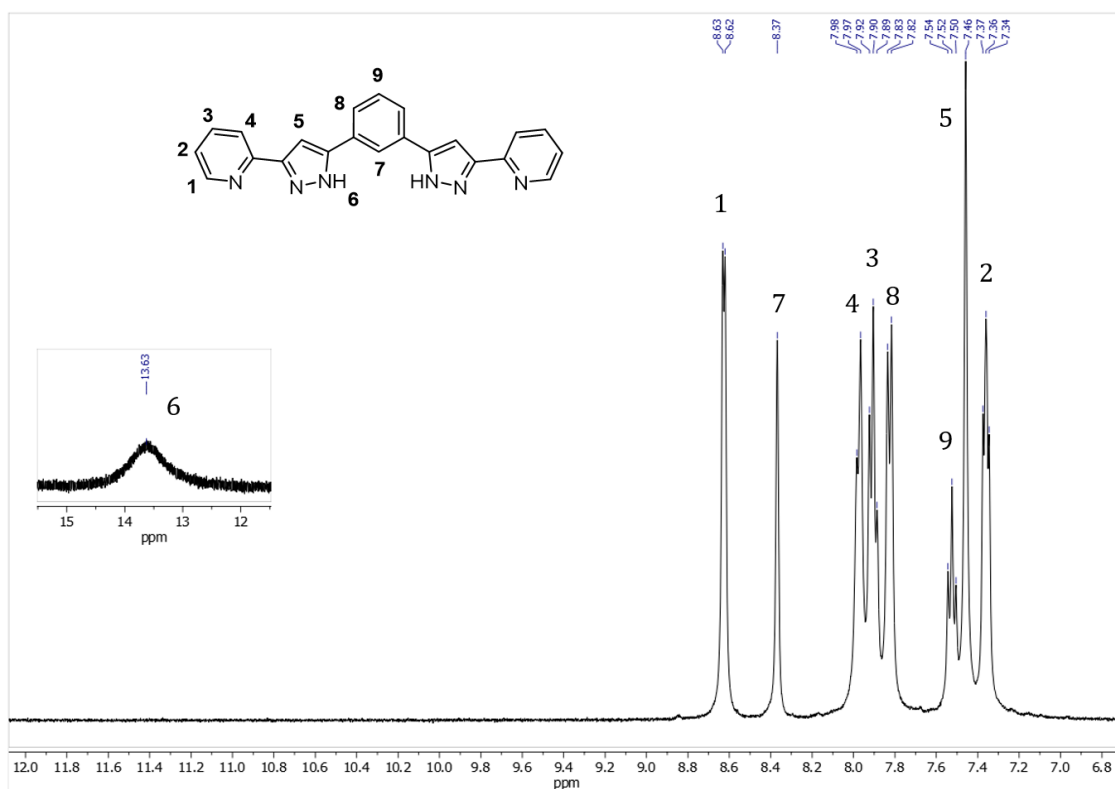


**Figure A6.10.** <sup>1</sup>H NMR of ligand **H<sub>2</sub>L** in *dmsol-d<sub>6</sub>* at room temperature. Comparative signals for the diamagnetic [Zn<sub>2</sub>] complex.

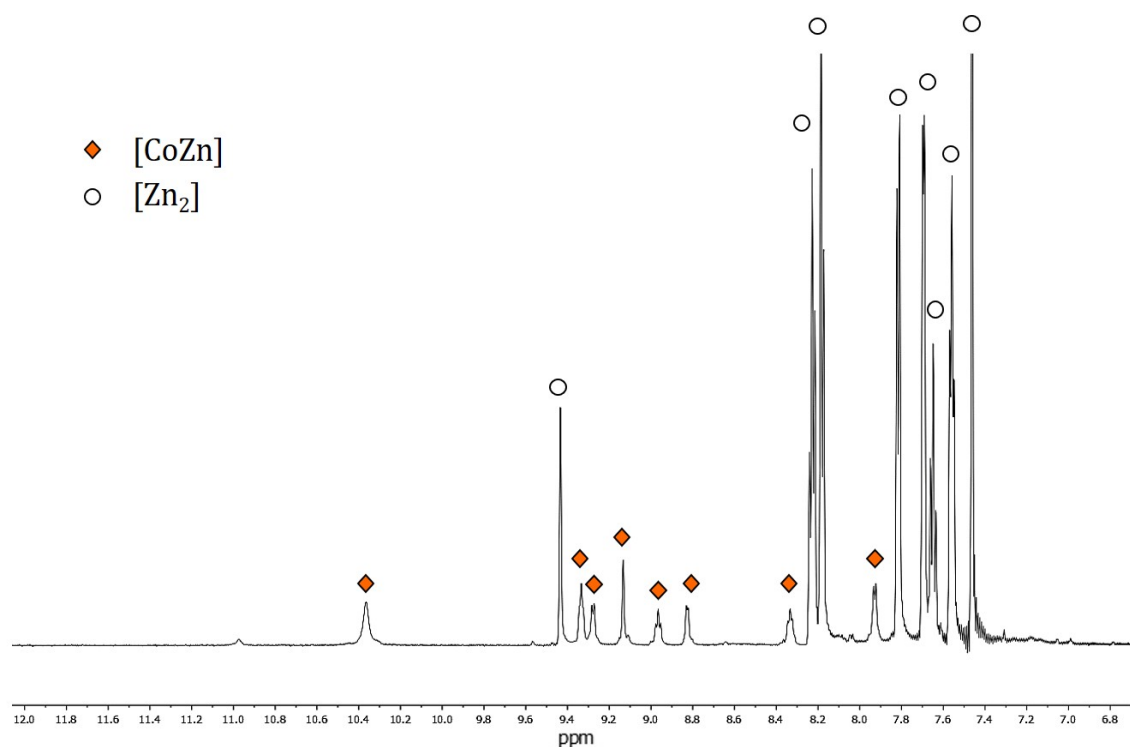


**Figure A6.11.** Diamagnetic part of the <sup>1</sup>H NMR spectrum for [CoZn] in *methanol-d<sub>4</sub>* at room temperature.

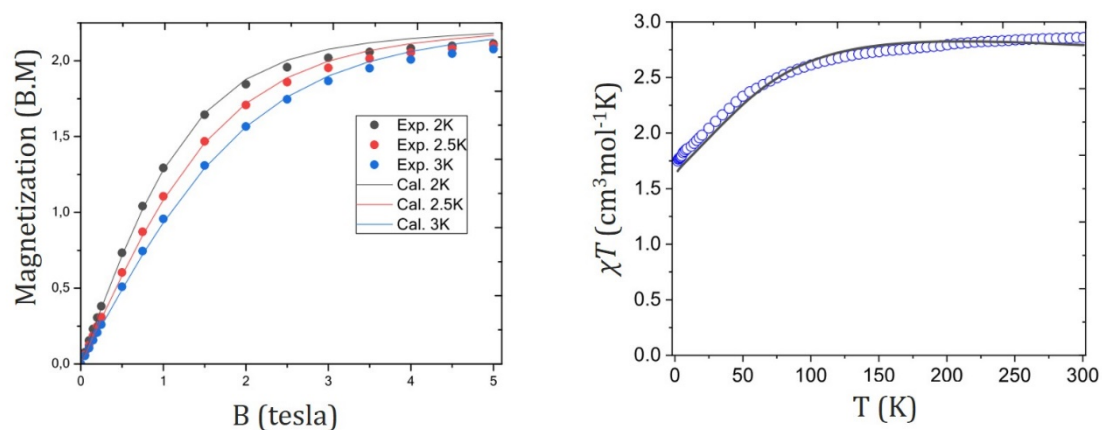


**Figure A6.12.** (Left) VT-magnetic magnetization versus magnetic field of  $\text{Cl}@\text{[CoZn(H}_2\text{L)}_3\text{]}^{3+}$  (**13**) at 2K (black), 2.5K (red) and 3K (blue). (Right) VT-magnetic susceptibility under an applied dc field of 1kOe. Solid line corresponds to the fit to equation S6.4.

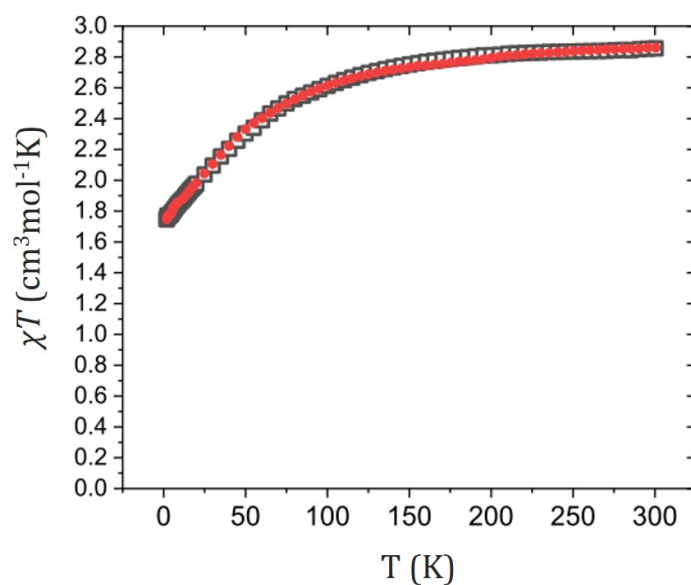


**Figure A6.13.** Superimposed VT-magnetic susceptibility data for  $[\text{Co}_2]$  (**11**) and  $[\text{CoZn}]$  (**13**). Data normalized to one Co(II).

**Table A6.5.** The parameter values obtained by fitting simultaneously the NMR and magnetometry data for [Co2] (**11**) with the Hamiltonian (Eq. S6.4)

$g_{\perp}$	2.10
$g_{\parallel}$	2.27
$\lambda, \text{cm}^{-1}$	171.5
$\sigma$	0.7852
$\Delta, \text{cm}^{-1}$	-45.03

**Table A6.6.** Resulting energies of Kramers doublets obtained by fitting simultaneously the NMR and magnetometry data for [Co2] (**11**) with the Hamiltonian (Eq. S6.4).

$E_1, \text{cm}^{-1}$	0 (as set)
$E_2, \text{cm}^{-1}$	174
$E_3, \text{cm}^{-1}$	232
$E_4, \text{cm}^{-1}$	502
$E_5, \text{cm}^{-1}$	569
$E_6, \text{cm}^{-1}$	591

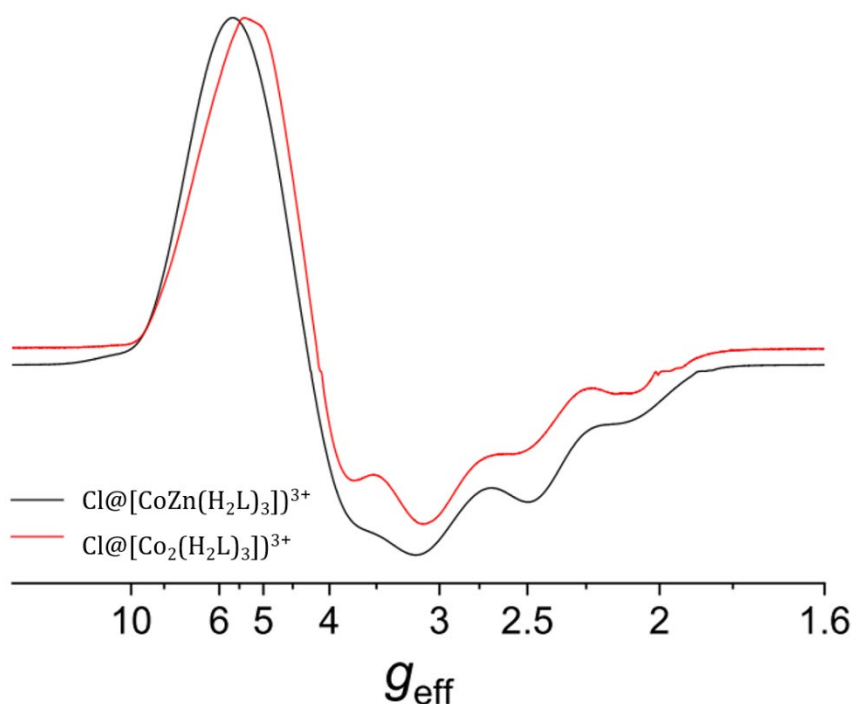


**Figure A6.14.** X-Band EPR for [Co2] and [CoZn] at 5K. Microwave frequency was 9.64GHz, 0.2 mW power and field modulation of 100kHz and 7G amplitude. Spectra are normalized to the maximum measured value. Spectra are shown as function for the effective g value (calculated from  $h\nu = \mu_B g_{\text{eff}}$ ).



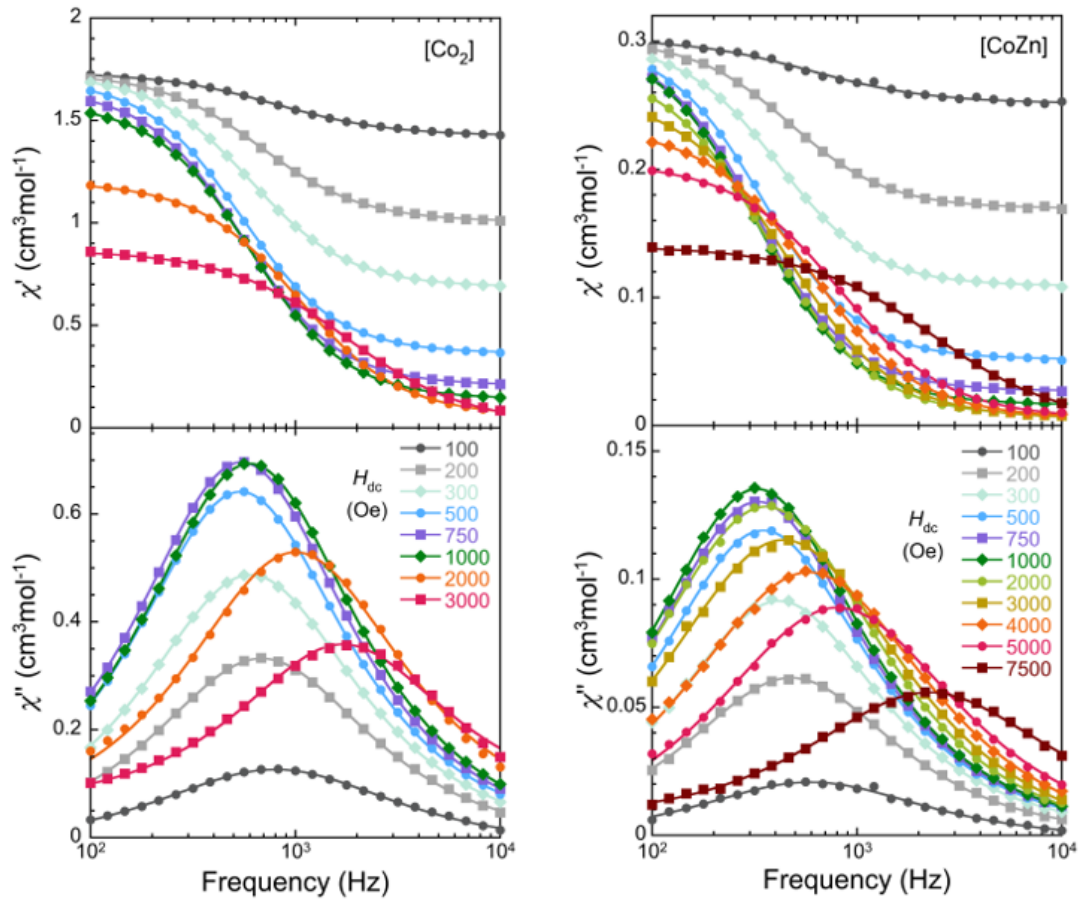


**Figure A6.15.** Field dependence study of the spin dynamics. In-phase ( $\chi'$ ) and out-of-phase ( $\chi''$ ) ac magnetic susceptibility for **[Co<sub>2</sub>]** (left) and **[CoZn]** (right) at 2K and various dc external magnetic fields.

### Analysis of the relaxation time

The relaxation time  $\tau$  was extracted from the frequency dependence of the real and imaginary components of the ac susceptibility  $\chi'$  and  $\chi''$  using the generalized Debye model (Equations S6.5 and S6.6):

$$\chi'(\omega) = \chi_S + (\chi_T - \chi_S) \frac{1 + (\omega\tau)^\beta \cos\left(\frac{\pi\beta}{2}\right)}{1 + 2(\omega\tau)^\beta \cos\left(\frac{\pi\beta}{2}\right) + (\omega\tau)^{2\beta}} \quad \text{Eq. S6.5}$$

$$\chi''(\omega) = (\chi_T - \chi_S) \frac{(\omega\tau)^\beta \sin\left(\frac{\pi\beta}{2}\right)}{1 + 2(\omega\tau)^\beta \cos\left(\frac{\pi\beta}{2}\right) + (\omega\tau)^{2\beta}} \quad \text{Eq. S6.6}$$

were  $\omega$  is the angular frequency,  $\chi_T$  the isothermal susceptibility,  $\chi_S$  the adiabatic susceptibility and  $\beta$  describes the distribution of relaxation times. Similar  $\beta$  values ranging from 0.89 to 0.98 were found, indicating a very limited distribution of the relaxation times.

The temperature and field dependence of the relaxation time for [Co<sub>2</sub>] and [CoZn] from the AC-magnetometry measurements were simultaneously fitted using equation S6.7, where QTM, direct, Raman and Orbach processes are considered:

$$\tau^{-1} = \frac{B_1}{1 + B_2 H^2} + AH^n T + CT^m + \tau_0^{-1} \exp\left(\frac{-U}{k_B T}\right) \quad \text{Eq. S6.7}$$

**Table A6.7.** Parameters used to fit the Arrhenius plot from figure A6.8 using equation S6.7.

Parameter	[Co <sub>2</sub> ]	[CoZn]
B <sub>1</sub> , s <sup>-1</sup>	2876	1939
B <sub>2</sub> , T <sup>-1</sup>	2996	2048
A, S <sup>-1</sup> K <sup>-1</sup> T <sup>-n</sup>	60880	25440
N	2.24	3.64
C, S <sup>-1</sup> K <sup>-m</sup>	306.8	289.7
M	3.19	2.78
$\tau_0^{-1}$ , s <sup>-1</sup>	0	5.00·10 <sup>7</sup>
U, K	0	45.0

## References

- (1) Neese, F. *Wiley Interdiscip. Rev. Comput. Mol. Sci.* **2012**, *2*, 73–78.
- (2) Van Wüllen, C. *J. Chem. Phys.* **1998**, *109*, 392–399.
- (3) Grimme, S.; Antony, J.; Ehrlich, S.; Krieg, H. *J. Chem. Phys.* **2010**, *132*.
- (4) Pantazis, D. A.; Chen, X. Y.; Landis, C. R.; Neese, F. *J. Chem. Theory Comput.* **2008**, *4*, 908–919.
- (5) Weigend, F.; Ahlrichs, R. *Phys. Chem. Chem. Phys.* **2005**, *7*, 3297–3305.
- (6) Pavlov, A. A.; Nehr Korn, J.; Pankratova, Y. A.; Ozerov, M.; Mikhalyova, E. A.; Polezhaev, A. V.; Nelyubina, Y. V.; Novikov, V. V. *Phys. Chem. Chem. Phys.* **2019**, *21*, 8201–8204.

**APPENDIX 7 – CHAPTER 7. EXPLORATION OF H<sub>2</sub>L2 COORDINATION CHEMISTRY. THE DISCOVERY OF [Fe<sub>9</sub>] SQUARED GRIDS.**

**Table A7.1.** Summarized reaction conditions for the obtention of dinuclear Fe<sub>2</sub> triple-stranded helicates encapsulating trisoxalate Fe(III), compound **14**, **15** and **16** (see below and chapter 10 for detailed explanation).

Compound	Reaction	Solvent	Crystallization	Formula
<b>14</b>	Fe(BF <sub>4</sub> ) <sub>2</sub> · xH <sub>2</sub> O + H <sub>2</sub> L2	MeOH	slow evaporation with acetonitrile	Fe <sub>2</sub> C <sub>84</sub> H <sub>60</sub> N <sub>18</sub> , FeC <sub>6</sub> O <sub>12</sub> , BF <sub>4</sub> , 5(C <sub>2</sub> H <sub>3</sub> N), CH <sub>4</sub> O, 3(H <sub>2</sub> O)
<b>15</b>	Fe(BF <sub>4</sub> ) <sub>2</sub> · xH <sub>2</sub> O + H <sub>2</sub> L2 (under N <sub>2</sub> conditions)	MeOH	layering with K <sub>3</sub> V(OX) <sub>3</sub> in water	Fe <sub>2</sub> C <sub>84</sub> H <sub>60</sub> N <sub>18</sub> , FeC <sub>6</sub> O <sub>12</sub> , BF <sub>4</sub> , 3(CH <sub>4</sub> O), 4.75(H <sub>2</sub> O)
<b>16</b>	Fe(ClO <sub>4</sub> ) <sub>2</sub> ·6H <sub>2</sub> O + H <sub>2</sub> L2	MeOH	layered with NBu <sub>4</sub> I in water	Fe <sub>2</sub> C <sub>84</sub> H <sub>60</sub> N <sub>18</sub> , FeC <sub>6</sub> O <sub>12</sub> , ClO <sub>4</sub> , 1(H <sub>2</sub> O), 28[ H <sub>2</sub> O]

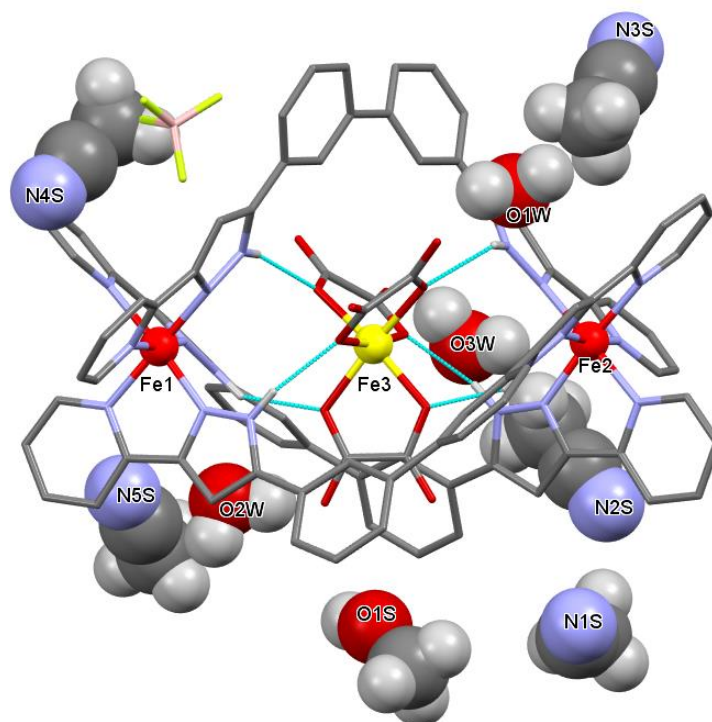


**Figure A7.1.** Molecular representation of the asymmetric unit of Fe(C<sub>2</sub>O<sub>4</sub>)<sub>3</sub>@[Fe<sub>2</sub>(H<sub>2</sub>L2)<sub>3</sub>](BF<sub>4</sub>)·5(C<sub>2</sub>H<sub>3</sub>N)·CH<sub>4</sub>O·3(H<sub>2</sub>O), (**14**) at 100K, emphasizing the hydrogen bonds between the encapsulated [Fe(C<sub>2</sub>O<sub>4</sub>)<sub>3</sub>]<sup>3-</sup> and the N–H groups of the complexes (dashed cyan lines). Carbon, oxygen, nitrogen, boron and fluoride are in grey, red, blue, pink and grey, respectively. Only hydrogen atoms in white are shown for the free N–H and the solvents. The LS Fe (II) is red, while the Fe (III) in yellow.

	Helical compound 14		Helical compound 15		Helical compound 16
<b>Formula</b>	Fe <sub>2</sub> C <sub>84</sub> H <sub>60</sub> N <sub>18</sub> , FeC <sub>6</sub> O <sub>12</sub> , BF <sub>4</sub> , 5(C <sub>2</sub> H <sub>3</sub> N), CH <sub>4</sub> O, 3(H <sub>2</sub> O)	Fe <sub>2</sub> C <sub>84</sub> H <sub>60</sub> N <sub>18</sub> , FeC <sub>6</sub> O <sub>12</sub> , BF <sub>4</sub> , 5(C <sub>2</sub> H <sub>3</sub> N), CH <sub>4</sub> O, 3(H <sub>2</sub> O)	Fe <sub>2</sub> C <sub>84</sub> H <sub>60</sub> N <sub>18</sub> , FeC <sub>6</sub> O <sub>12</sub> , BF <sub>4</sub> ,3(CH <sub>4</sub> O), 4.75(H <sub>2</sub> O)	Fe <sub>2</sub> C <sub>84</sub> H <sub>60</sub> N <sub>18</sub> , FeC <sub>6</sub> O <sub>12</sub> , BF <sub>4</sub> ,3(CH <sub>4</sub> O), 4.75(H <sub>2</sub> O)	Fe <sub>2</sub> C <sub>84</sub> H <sub>60</sub> N <sub>18</sub> , FeC <sub>6</sub> O <sub>12</sub> , ClO <sub>4</sub> , 1(H <sub>2</sub> O), 28[ H <sub>2</sub> O]
<b>FW (g mol<sup>-1</sup>)</b>	2130.27	2130.27	2021.62	2021.62	1870.57
<b>T (K)</b>	100	280	100	280	100
<b>Wavelength (Å)</b>	0.7288	0.7288	0.7288	0.7288	0.7288
<b>Crystal system</b>	triclinic	triclinic	monoclinic	monoclinic	monoclinic
<b>Space group</b>	P -1	P -1	P 21/n	P2 <sub>1</sub> /n	P2 <sub>1</sub> /n
<b>a (Å)</b>	14.814(2)	14.777(5)	19.6737(16)	20.122(8)	19.711(3)
<b>b (Å)</b>	18.257(2)	17.996(6)	16.6758(13)	16.557(6)	16.337(2)
<b>c (Å)</b>	18.779(2)	19.013(6)	28.868(3)	28.572(12)	28.722(4)
<b>α (°)</b>	75.876(4)	79.786(10)	90	90	90
<b>β (°)</b>	85.073(4)	86.407(10)	109.814(3)	109.976(3)	109.988(5)
<b>γ (°)</b>	79.765(4)	81.236(10)	90	90	90
<b>V (Å<sup>3</sup>)</b>	4842.2(10)	4915(3)	8910.2(14)	8946(6)	8692(2)
<b>Z</b>	2	2	4	4	4
<b>ρ<sub>calcd</sub> (g cm<sup>-3</sup>)</b>	1.461	1.440	1.507	1.501	1.429
<b>μ (mm<sup>-1</sup>)</b>	0.565	0.556	0.611	0.608	0.642
<b>Independent reflections (R<sub>int</sub>) param. / restraints</b>	26050 (0.0839)	10537 (0.0765)	21201 (0.0417)	10834 (0.0504)	10610 (0.0711)
<b>Goodness-of-fit</b>	1.030	1.022	1.026	1.058	1.665
<b>Final R1 / wR2 [I&gt;2σ(I)]</b>	0.1115 / 0.3195	0.1610 / 0.4202	0.0742 / 0.2172	0.1234 / 0.3373	0.1344 / 0.3756
<b>Final R1 / wR2 [all data]</b>	0.1428 / 0.3483	0.1750 / 0.4295	0.0796 / 0.2214	0.1359 / 0.3599	0.1492 / 0.3911
<b>largest diff. peak / hole (e Å<sup>3</sup>)</b>	0.001/0.000	0.000 /0.000	0.001/0.000	0.002 /0.000	2.117/ -1.064
<b>&lt;Fe1-N&gt; (Å)</b>	1.97(0)	1.97(1)	1.96(7)	1.96(5)	1.97(4)
<b>&lt;Fe2-N&gt; (Å)</b>	1.96(7)	1.96(6)	1.98(4)	2.14(6)	1.99(9)
<b>&lt;Fe3-O&gt; (Å)</b>	2.03(4)	2.04(4)	2.04(5)	2.02(7)	2.06
<b>Σ Fe1/ Fe2/Fe3</b>	65.2(7) / 64.5(7)/63.0(5)	76(2) / 69(2)/56.7(16)	61.9(5)/ 59.6(6) /63.2(4)	62.1(11) / 83.2(11)/ 46.3(8)	62.5(12)/62.4(13)/ 57.0(12)

**Table A7.2.** Crystal data, average Fe-N bond lengths and distortion parameters for compounds **14**, **15** and **16**.

**Table A7.3.** List of the angle twist around the C-C bonds between the aromatic rings of ligand H<sub>2</sub>L<sub>2</sub> in compound **14** at 100K.

Compound 14	labels	dihedral angle (°)
<b>phen-phen</b>	phen (C9C10C11C12C13C14)-phen (C15C16C17C18C19C20)	35.98
	phen (C65C66C67C68C69C70)-phen (C71C72C73C74C75C76)	39.62
	phen (C43C44C45C46C47C48)-phen (C37C38C39C40C41C42)	38.68
<b>phen-pz</b>	phen (C65C66C67C68C69C70)-pz (N14N15C62C63C64)	12.81
	phen (C37C38C39C40C41C42)-pz (N8N9C34C35C36)	22.79
	phen (C9C10C11C12C13C14)-pz (N2N3C6C7C8)	18.75
	phen(C15C16C17C18C19C20)-pz (N4N5C21C22C23)	19.84
	phen (C71C72C73C74C75C76)-pz (N16N17C77C78C79)	24.72
	phen (C43C44C45C46C47C48)-pz (N10N11C49C50C51)	14.51
<b>pz-py</b>	pz (N2N3C6C7C8) -py (N1C1C2C3C4C5)	9.79
	pz (N14N15C62C63C64)-py (N13C57C58C59C60C61)	12.08
	pz (N8N9C34C35C36)-py (N7C29C30C31C32C33)	10.95
	pz (N10N11C49C50C51)-py (N12C52C53C54C55C56)	10.39
	pz (N4N5C21C22C23)-py (N6C24C25C26C27C28)	10.60
	pz (N16N17C77C78C79)-py (N18C80C81C82C83C84)	9.78

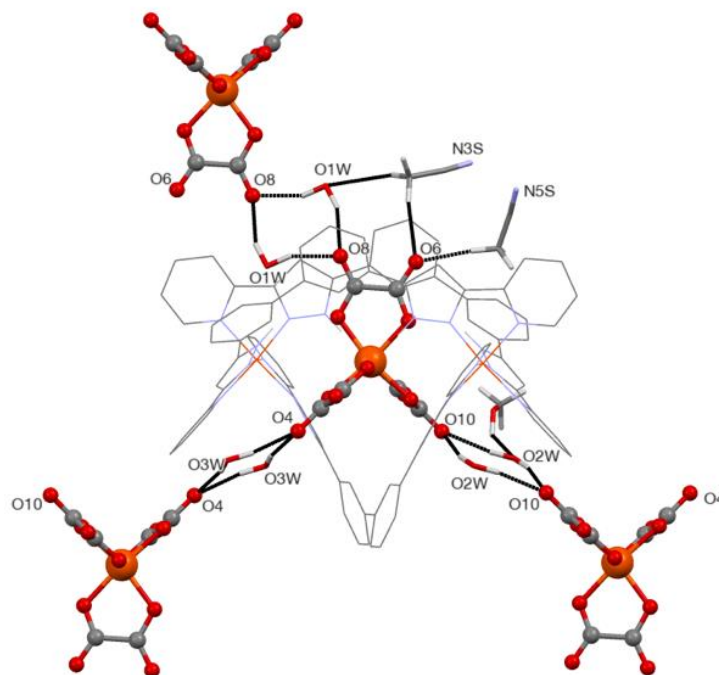


**Figure A7.2.** Molecular representation of the supramolecular bridging in compound **14** of the central  $[\text{Fe}(\text{C}_2\text{O}_4)_3]^{3-}$  guest with three closest neighbors via water molecules.

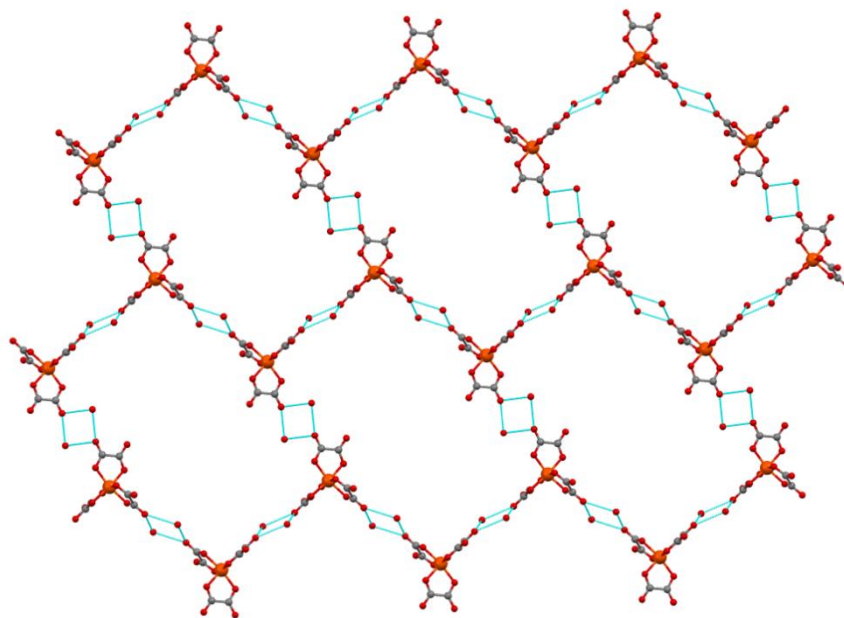


**Figure A7.3.** 2D packing network of the  $[\text{Fe}(\text{C}_2\text{O}_4)_3]^{3-}$  anions of compound **14** established through the supramolecular interactions assisted by water molecules.

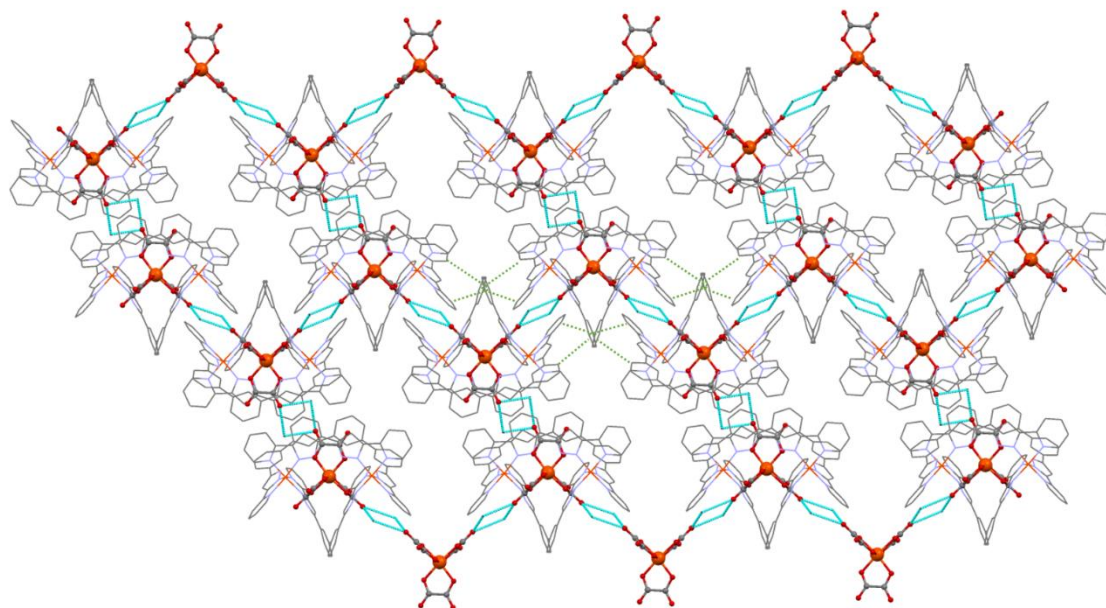


**Figure A7.4.** Representation of the  $\pi$ - $\pi$  interactions (dashed lines in green) between the cationic  $[\text{Fe}_2(\text{H}_2\text{L}_2)_3]^{4+}$  helicates of compound **14** together with the 2D supramolecular network described by the ferrioxalate guests.

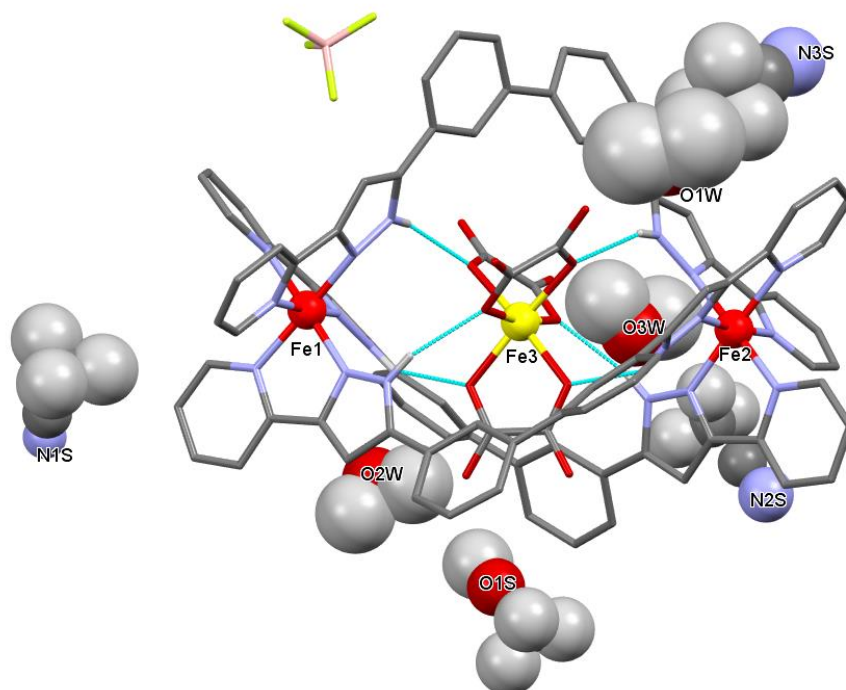


**Figure A7.5.** Molecular representation of the asymmetric unit of  $\text{Fe}(\text{C}_2\text{O}_4)_3@[\text{Fe}_2(\text{H}_2\text{L}_2)_3](\text{BF}_4) \cdot 5(\text{C}_2\text{H}_3\text{N}) \cdot \text{CH}_4\text{O} \cdot 3(\text{H}_2\text{O})$ , (**14**) at 280K, emphasizing the hydrogen bonds between the encapsulated  $[\text{Fe}(\text{C}_2\text{O}_4)_3]^{3-}$  and the N-H groups of the complexes (dashed cyan lines). Code labels are the same used through the thesis.

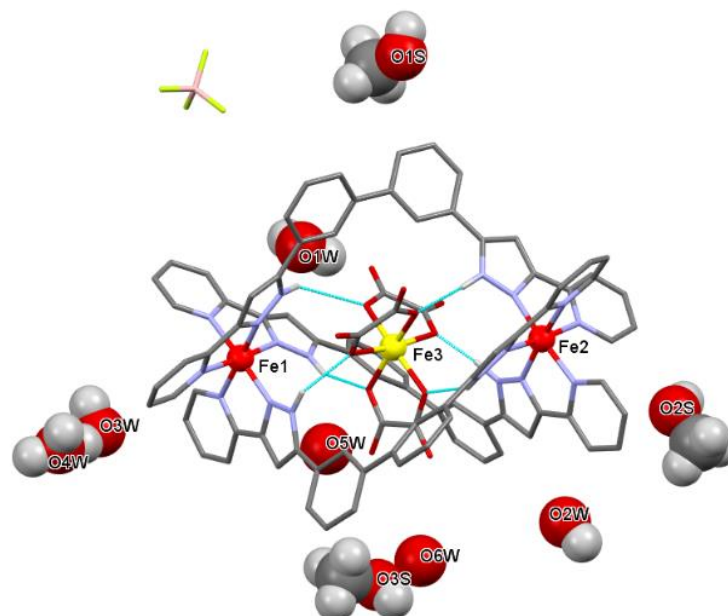


**Figure A7.6.** Molecular representation of the asymmetric unit of  $\text{Fe}(\text{C}_2\text{O}_4)_3@[\text{Fe}_2(\text{H}_2\text{L}_2)_3](\text{BF}_4) \cdot 3(\text{CH}_4\text{O}) \cdot 4.75(\text{H}_2\text{O})$ , (**15**) at 100K, emphasizing the hydrogen bonds between the encapsulated  $[\text{Fe}(\text{C}_2\text{O}_4)_3]^{3-}$  and the N–H groups of the complexes (dashed cyan lines). Carbon, oxygen, nitrogen, boron and fluoride are in grey, red, blue, pink and grey, respectively. Only hydrogen atoms in white are shown for the free N–H and the solvents. The LS Fe (II) is red, while the Fe (III) in yellow.

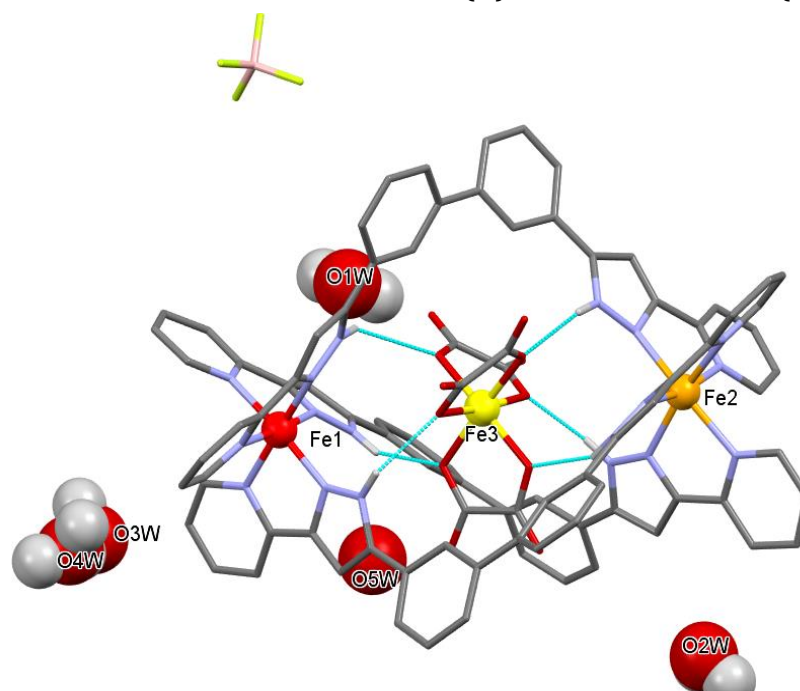


**Figure A7.7.** Molecular representation of the asymmetric unit of  $\text{Fe}(\text{C}_2\text{O}_4)_3@[\text{Fe}_2(\text{H}_2\text{L}_2)_3](\text{BF}_4) \cdot 3(\text{CH}_4\text{O}) \cdot 4.75(\text{H}_2\text{O})$ , (**15**) at 280K, emphasizing the hydrogen bonds between the encapsulated  $[\text{Fe}(\text{C}_2\text{O}_4)_3]^{3-}$  and the N–H groups of the complexes (dashed cyan lines). The LS Fe (II) is red, the HS Fe (II) in orange, while the Fe (III) in yellow.



**Table A7.4.** List of the angle twist around the C-C bonds between the aromatic rings of ligand H<sub>2</sub>L<sub>2</sub> in compound **15** at 100K.

<b>Compound 15</b>	<b>labels</b>	<b>dihedral angle (°)</b>
<b>phen-phen</b>	phen (C9C10C11C12C13C14)-phen (C15C16C17C18C19C20)	41.65
	phen (C65C66C67C68C69C70)-phen (C71C72C73C74C75C76)	30.62
	phen (C43C44C45C46C47C48)-phen (C37C38C39C40C41C42)	39.60
<b>phen-pz</b>	phen (C65C66C67C68C69C70)-pz (N14N15C62C63C64)	22.73
	phen (C37C38C39C40C41C42)-pz (N8N9C34C35C36)	12.29
	phen (C9C10C11C12C13C14)-pz (N2N3C6C7C8)	23.79
	phen(C15C16C17C18C19C20)-pz (N4N5C21C22C23)	14.78
	phen (C71C72C73C74C75C76)-pz (N16N17C77C78C79)	22.46
	phen (C43C44C45C46C47C48)-pz (N10N11C49C50C51)	18.14
<b>pz-py</b>	pz (N2N3C6C7C8) -py (N1C1C2C3C4C5)	11.30
	pz (N14N15C62C63C64)-py (N13C57C58C59C60C61)	13.72
	pz (N8N9C34C35C36)-py (N7C29C30C31C32C33)	9.89
	pz (N10N11C49C50C51)-py (N12C52C53C54C55C56)	10.90
	pz (N4N5C21C22C23)-py (N6C24C25C26C27C28)	10.50
	pz (N16N17C77C78C79)-py (N18C80C81C82C83C84)	7.98

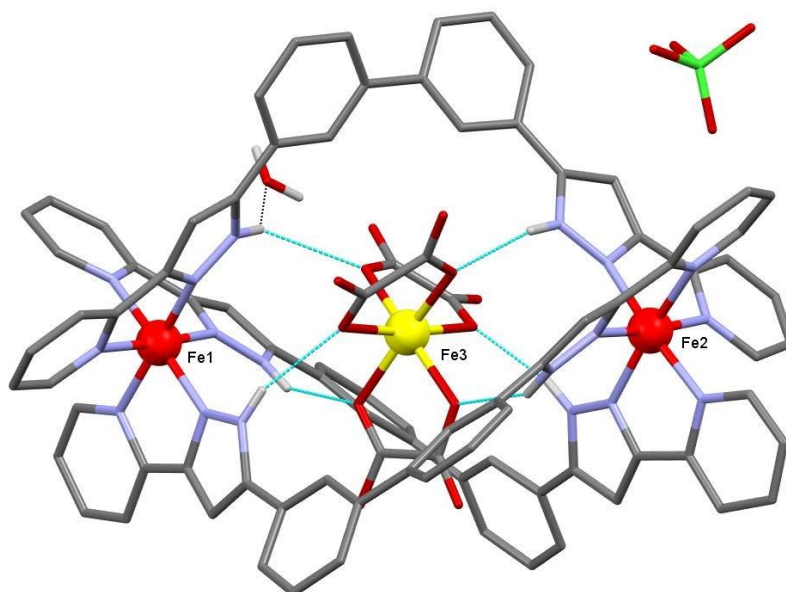


**Figure A7.8.** Molecular representation of the asymmetric unit of  $\text{Fe}(\text{C}_2\text{O}_4)_3@[\text{Fe}_2(\text{H}_2\text{L}_2)_3](\text{ClO}_4)\cdot(\text{H}_2\text{O})$ , (**16**) at 100K, emphasizing the hydrogen bonds between the encapsulated  $[\text{Fe}(\text{C}_2\text{O}_4)_3]^{3-}$  and the N-H groups of the complexes (dashed cyan lines). Carbon, oxygen, nitrogen, boron and fluoride are in grey, red, blue, pink and grey, respectively. Only hydrogen atoms in white are shown for the free N-H and the solvents. The LS Fe (II) is red, while the Fe (III) in yellow.

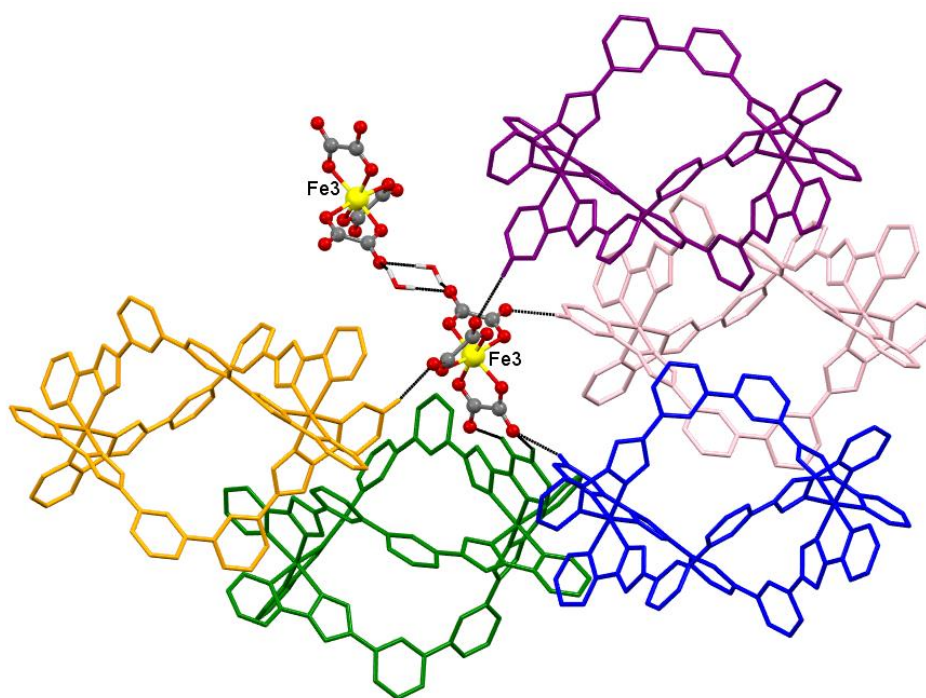


**Figure A7.9.** Molecular representation of the supramolecular bridging in compound **16** of the central  $[\text{Fe}(\text{C}_2\text{O}_4)_3]^{3-}$  guest with the six closest neighbors.

**Table A7.5.** List of the angle twist around the C-C bonds between the aromatic rings of ligand H<sub>2</sub>L<sub>2</sub> in compound **16** at 100K.

<b>Compound 16</b>	<b>labeles</b>	<b>dihedral angle (°)</b>
<b>phen-phen</b>	phen (C9C10C11C12C13C14)-phen (C15C16C17C18C19C20)	42.45
	phen (C65C66C67C68C69C70)-phen (C71C72C73C74C75C76)	29.68
	phen (C43C44C45C46C47C48)-phen (C37C38C39C40C41C42)	41.25
<b>phen-pz</b>	phen (C65C66C67C68C69C70)-pz (N14N15C62C63C64)	24.30
	phen (C37C38C39C40C41C42)-pz (N8N9C34C35C36)	8.97
	phen (C9C10C11C12C13C14)-pz (N2N3C6C7C8)	22.94
	phen(C15C16C17C18C19C20)-pz (N4N5C21C22C23)	14.45
	phen (C71C72C73C74C75C76)-pz (N16N17C77C78C79)	21.96
	phen (C43C44C45C46C47C48)-pz (N10N11C49C50C51)	18.62
<b>pz-py</b>	pz (N2N3C6C7C8) -py (N1C1C2C3C4C5)	12.80
	pz (N14N15C62C63C64)-py (N13C57C58C59C60C61)	14.51
	pz (N8N9C34C35C36)-py (N7C29C30C31C32C33)	8.46
	pz (N10N11C49C50C51)-py (N12C52C53C54C55C56)	10.89
	pz (N4N5C21C22C23)-py (N6C24C25C26C27C28)	11.71
	pz (N16N17C77C78C79)-py (N18C80C81C82C83C84)	6.61

**Table A7.6.** Crystallographic table for the [Fe<sub>9</sub>] compound **17** at 100K.

Compound 17	
Formula	Fe <sub>9</sub> C <sub>168</sub> H <sub>134</sub> N <sub>36</sub> O <sub>18</sub> , 5BF <sub>4</sub> , CH <sub>4</sub> O, 7H <sub>2</sub> O
FW (g mol <sup>-1</sup> )	4039.96
T (K)	100
Wavelength (Å)	0.7288
Crystal system	monoclinic
Space group	<i>P 2<sub>1</sub>/c</i>
a (Å)	19.2398(9)
b (Å)	21.2585(10)
c (Å)	41.578(2)
α (°)	90
β (°)	92.775(2)
γ (°)	90
V (Å <sup>3</sup> )	16985.8(14)
Z	4
ρ <sub>calcd</sub> (g cm <sup>-3</sup> )	1.580
μ (mm <sup>-1</sup> )	0.904
Independent reflections (R <sub>int</sub> )	23739 (0.0605)
param. / restraints	2450 / 443
Goodness-of-fit	1.043
Final R1 / wR2 [I > 2σ(I)]	0.0786 / 0.2155
Final R1 / wR2 [all data]	1.071 / 0.2314
largest diff. peak / hole (e Å <sup>3</sup> )	1.287 / -0.998

**Table A7.7.** Selected bond distances (Å) of [Fe<sub>9</sub>] grid 17.

<b>Atom pair</b>	<b>distance (Å)</b>	<b>Atom pair</b>	<b>distance (Å)</b>	<b>Atom pair</b>	<b>distance (Å)</b>
Fe1- N1	2.223	Fe2- O1	1.908	Fe3- N13	2.201
Fe1- N2	2.086	Fe2- O2	1.89	Fe3- N14	2.111
Fe1- N19	2.199	Fe2- O9	1.927	Fe3- N23	2.095
Fe1- N20	2.107	Fe2- O13	1.925	Fe3- N24	2.244
Fe1- O1	2.051	Fe2- N7	2.181	Fe3- O2	2.075
Fe1- O7	2.036	Fe2- N8	2.111	Fe3- O11	2.054
Fe4- O3	1.932	Fe5- O3	1.954	Fe6- O4	1.939
Fe4- O7	1.905	Fe5- O4	1.96	Fe6- O11	1.91
Fe4- O8	1.883	Fe5- O9	1.975	Fe6- O12	1.892
Fe4- O14	1.903	Fe5- O10	1.971	Fe6- O17	1.893
Fe4- N25	2.192	Fe5- O15	1.95	Fe6- N29	2.107
Fe4- N26	2.106	Fe5- O16	1.951	Fe6- N30	2.195
Fe7- N5	2.084	Fe8- O5	1.932	Fe9- N17	2.116
Fe7- N6	2.177	Fe8- O6	1.902	Fe9- N18	2.198
Fe7- N31	2.215	Fe8- O10	1.955	Fe9- N35	2.116
Fe7- N32	2.115	Fe8- O18	1.893	Fe9- N36	2.186
Fe7- O5	2.016	Fe8- N11	2.091	Fe9- O6	2.073
Fe7- O14	2.084	Fe8- N12	2.23	Fe9- O12	2.046

### The Bond Valence Sum (BVS) method for estimating the oxidation state in [Fe9] grids

This is an empirical method for estimating the oxidation state of a metal ion from the metal-ligand distances.<sup>1,2</sup> The expression is:

$$BV_i = \exp((R_o - R)/0.37) \quad (\text{Eq. A10.1})$$

$$\text{Estimated oxidation state (BVS)} = \sum_i BV_i \quad (\text{Eq. A10.2})$$

where  $R_o$  is an empirical parameter associated with the metal in a given coordinating environment a oxidation state and  $R$  is the experimental bond length.

**Table A7.8.** Empirical parameters of  $R_o$  considered for the BVS calculation in **4**.<sup>2</sup>

	$R_o$
Fe <sup>III</sup> -N (HS)	1.820
Fe <sup>III</sup> -N (LS)	1.700
Fe <sup>III</sup> -O	1.759
Fe <sup>II</sup> -N (HS)	1.760
Fe <sup>II</sup> -N (LS)	1.660
Fe <sup>II</sup> -O	1.734

**Table A7.9.** Bond-valence sum calculations in **4** for +2 and +3 oxidation states and HS and LS magnetic states for each type of iron metal centre. The experimental  $R$  values are reported in table A10.7.

Metal centre	Oxidation state +3		Oxidation state +2		Conclusions
	HS	LS	HS	LS	
Fe1	2.57	2.11	2.26	1.93	Fe1= Fe <sup>II</sup> (HS)
Fe2	3.47	3.25	3.18	1.93	Fe2= Fe <sup>III</sup> (HS)
Fe3	2.48	2.03	2.18	1.86	Fe3= Fe <sup>II</sup> (HS)
Fe4	3.52	3.29	3.22	3.05	Fe4= Fe <sup>III</sup> (HS)
Fe5	3.48		3.26		Fe5= Fe <sup>III</sup>
Fe6	3.50	3.27	3.2	3.03	Fe6= Fe <sup>III</sup> (HS)
Fe7	2.58	2.12	2.27	1.93	Fe7= Fe <sup>II</sup> (HS)
Fe8	3.40	3.18	3.11	2.94	Fe8= Fe <sup>III</sup> (HS)
Fe9	2.38	2.18	2.16	2.02	Fe9= Fe <sup>II</sup> (HS)

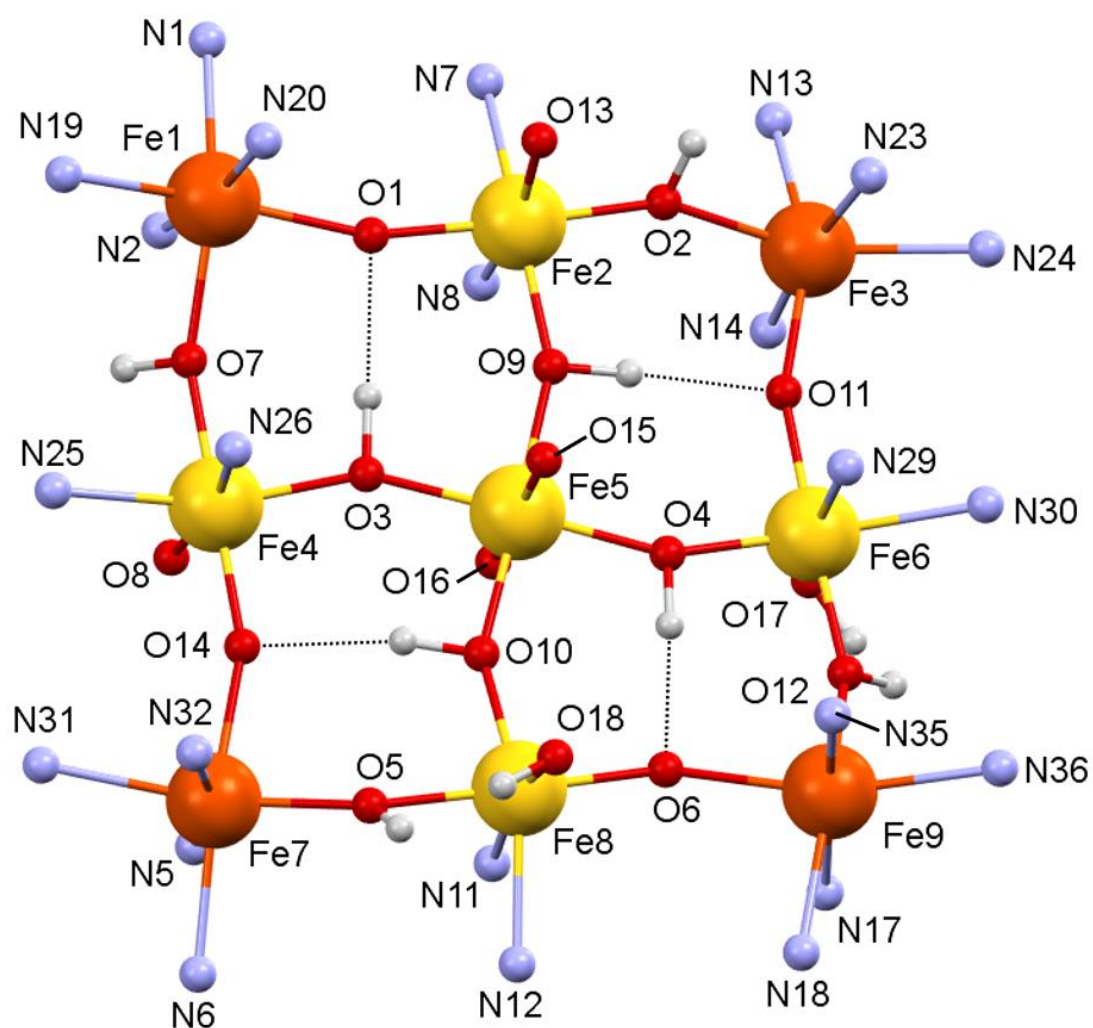


**Figure A7.10.** Representation of the  $[\text{Fe}_9\text{O}_4(\text{OH})_{10}(\text{H}_2\text{L}_2)_6(\text{H}_2\text{O})_4]^{5+}$  core in grid **17** with the atoms labelled. White, blue, red and grey are hydrogen, nitrogen, oxygen and carbon. Big red and yellow spheres are Fe(II) and Fe(III) atoms, respectively. Dashed black lines are hydrogen bonds between pairs of OH<sup>-</sup>/O<sup>2-</sup> atoms within the core.

**Table A7.10.** Series of Fe-O-Fe angles in grid 17.

labels	Distance (Å) ( $\pi$ : centroid)
Fe1-O1-Fe2	161.8(2)
Fe1-O7-Fe4	158.0(2)
Fe2-O2-Fe3	153.6(2)
Fe4-O3-Fe5	154.2(2)
Fe4-O14-Fe7	160.1(2)
Fe5-O9-Fe2	155.5(2)
Fe5-O4-Fe6	154.0(2)
Fe6-O11-Fe3	158.7(2)
Fe6-O12-Fe9	150.5(2)
Fe7-O5-Fe8	151.3(2)
Fe8-O10-Fe5	152.5(2)
Fe9-O6-Fe8	158.9(2)

**Table A7.11.** Series of Fe...Fe distances in grid 17.

labels	Distance (Å) ( $\pi$ : centroid)
Fe1...Fe2	3.911(1)
Fe2...Fe3	3.856(1)
Fe1...Fe4	3.865(1)
Fe2...Fe5	3.811(1)
Fe3...Fe6	3.897(1)
Fe4...Fe5	3.785(1)
Fe5...Fe6	3.795(1)
Fe4...Fe7	3.928(1)
Fe5...Fe8	3.809(1)
Fe6...Fe9	3.806(1)
Fe7...Fe8	3.821(1)
Fe8...Fe9	3.909(1)



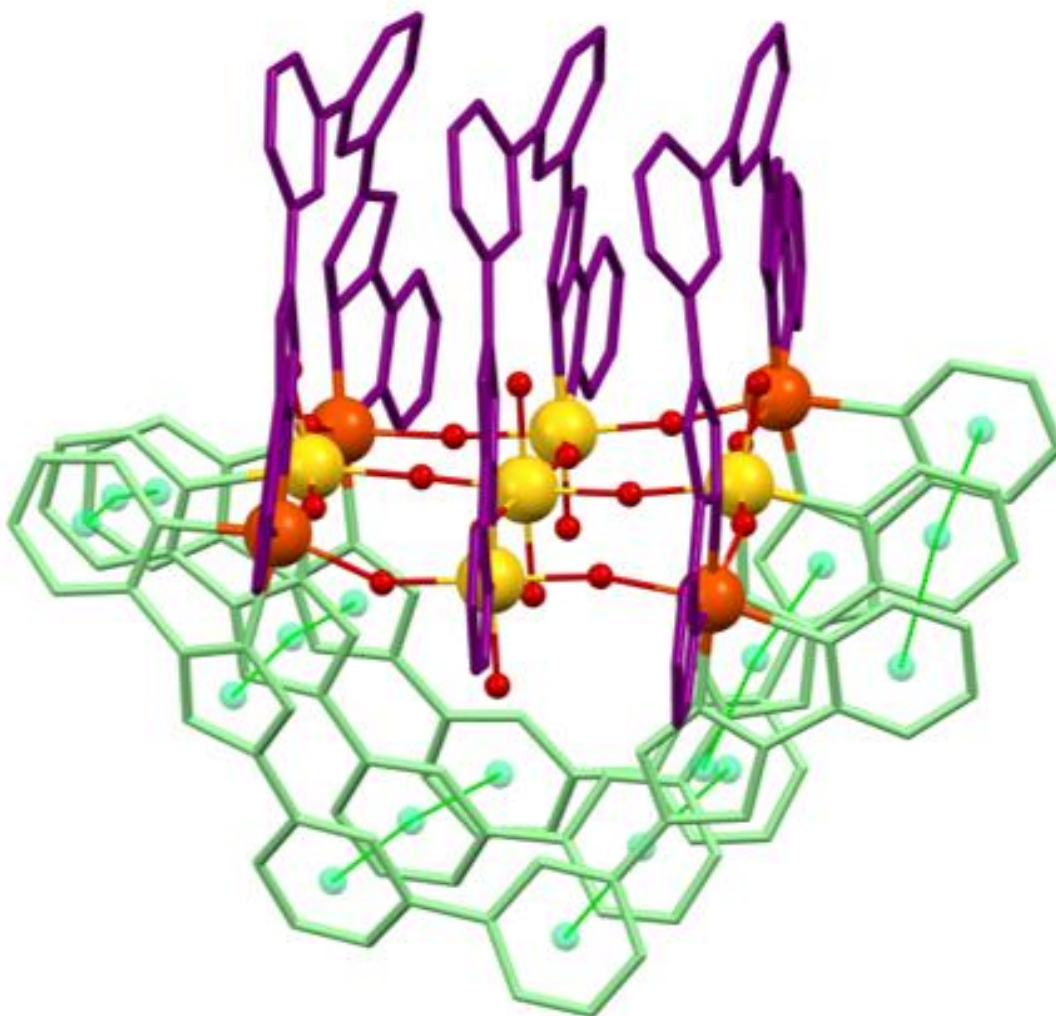


**Figure A7.11.** Illustration of  $[\text{Fe}_9\text{O}_4(\text{OH})_{10}(\text{H}_2\text{L}_2)_6(\text{H}_2\text{O})_4]^{5+}$  of grid **17**, emphasizing six  $\pi\cdots\pi\cdots\pi$  intramolecular interactions within three  $\text{H}_2\text{L}_2$  ligands that are part of the same set, highlighted in green dashed lines joining the centroids (green balls) of the aromatic rings. The two different sets of ligands are coloured in green and purple. There are 6 equivalent interactions within the other set of three ligands (in purple) not shown. Big red and yellow spheres are Fe(II) and Fe(III), respectively.

**Table A7.12.** Series of  $\pi\cdots\pi$  stacking interactions in compound **17**.

labels	Distance (Å) ( $\pi$ : centroid)
Cg(N1 C1 C2 C3 C4 C5) ... Cg(N7 C31 C32 C33 C34 C35)	3.532
Cg(N7 C31 C32 C33 C34 C35) ... Cg(N13 C61 C62 C63 C64 C65)	3.744
Cg(N2 N3 C6 C7 C8) ... Cg(N8 N9 C36 C37 C38)	3.939
Cg(N8 N9 C36 C37 C38) ... Cg(N14 N15 C66 C67 C68)	3.771
Cg(C9 C10 C11 C12 C13 C14) ... Cg(C39 C40 C41 C42 C43 C44)	3.688
Cg(C39 C40 C41 C42 C43 C44) ... Cg(C69 C70 C71 C72 C73 C74)	3.625
Cg(C15 C16 C17 C18 C19 C20) ... Cg(C45 C46 C47 C48 C49 C50)	3.719
Cg(C45 C46 C47 C48 C49 C50) ... Cg(C75 C76 C77 C78 C79 C80)	3.743
Cg(N4 N5 C21 C22 C23) ... Cg(N10 N11 C51 C52 C53)	3.780
Cg(N10 N11 C51 C52 C53) ... Cg(N16 N17 C81 C82 C83)	3.985
Cg(N6 C24 C25 C26 C27 C28) ... Cg(N12 C54 C55 C56 C57 C58)	3.849
Cg(N12 C54 C55 C56 C57 C58) ... Cg(N18 C84 C85 C86 C87 C88)	3.563

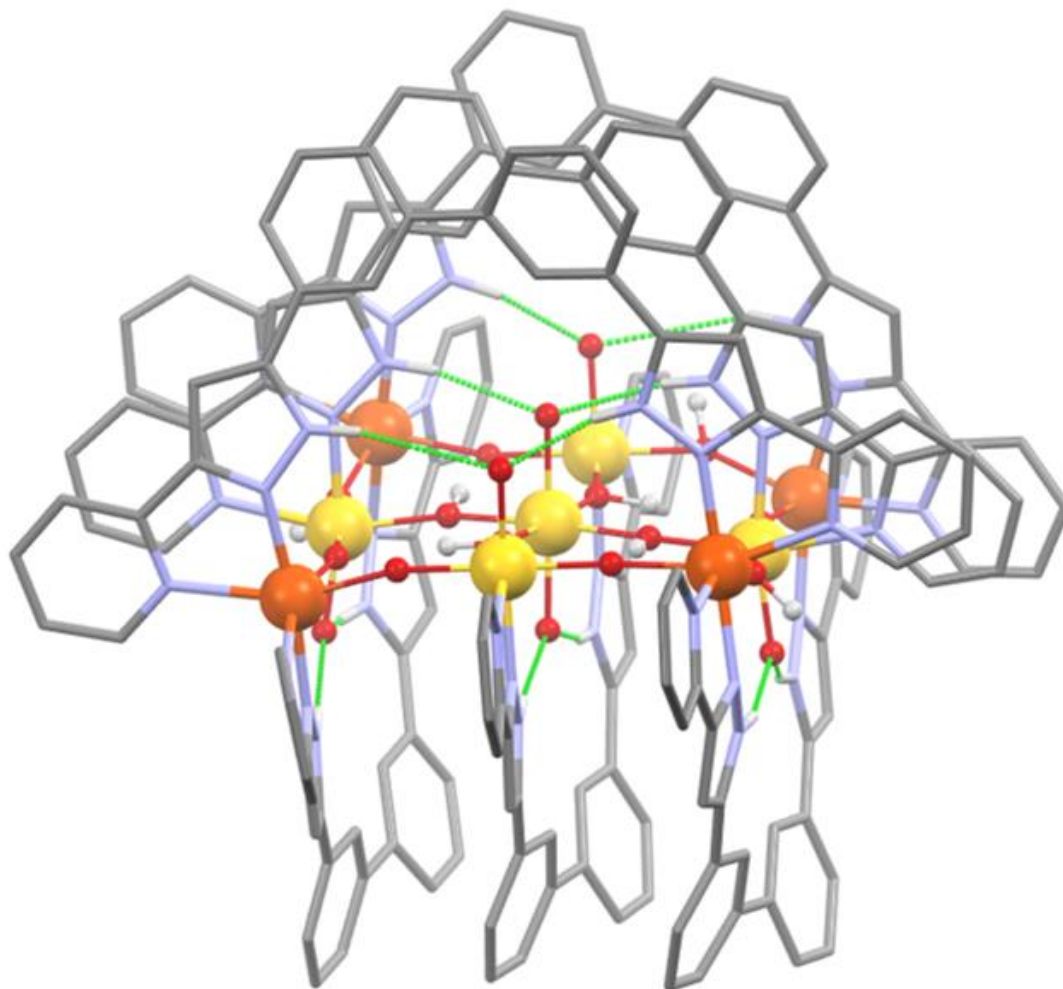


**Figure A7.12.** Representation of the  $[\text{Fe}_9\text{O}_4(\text{OH})_{10}(\text{H}_2\text{L}_2)_6(\text{H}_2\text{O})_4]^{5+}$  of grid **17**, highlighting the twelve N-H $\cdots$ O intramolecular hydrogen bonds between the free N-H groups of the  $\text{H}_2\text{L}_2$  ligands and the oxygen atoms ( $\text{H}_2\text{O}$  or  $\text{OH}^-$ ) at the axial positions of the core. Only H atoms of the N-H moieties are shown.

**Table A7.13.** Series of N–H···O intramolecular hydrogen bonds in grid **17**.

labels	Distance (Å)( $\pi$ : centroid)
N3-H3B ... O8	2.520
N4-H4B ... O8	2.113
N9-H9B ... O16	2.064
N10-H10I ... O16	2.476
N15-H15F ... O17	1.922
N16-H16I ... O17	2.907
N21-H21A ... O13	1.946
N22-H22B ... O13	2.693
N27-H27B ... O15	2.250
N28-H28B ... O15	2.206
N33-H33B ... O18	2.981
N34-H34B ... O18	1.926

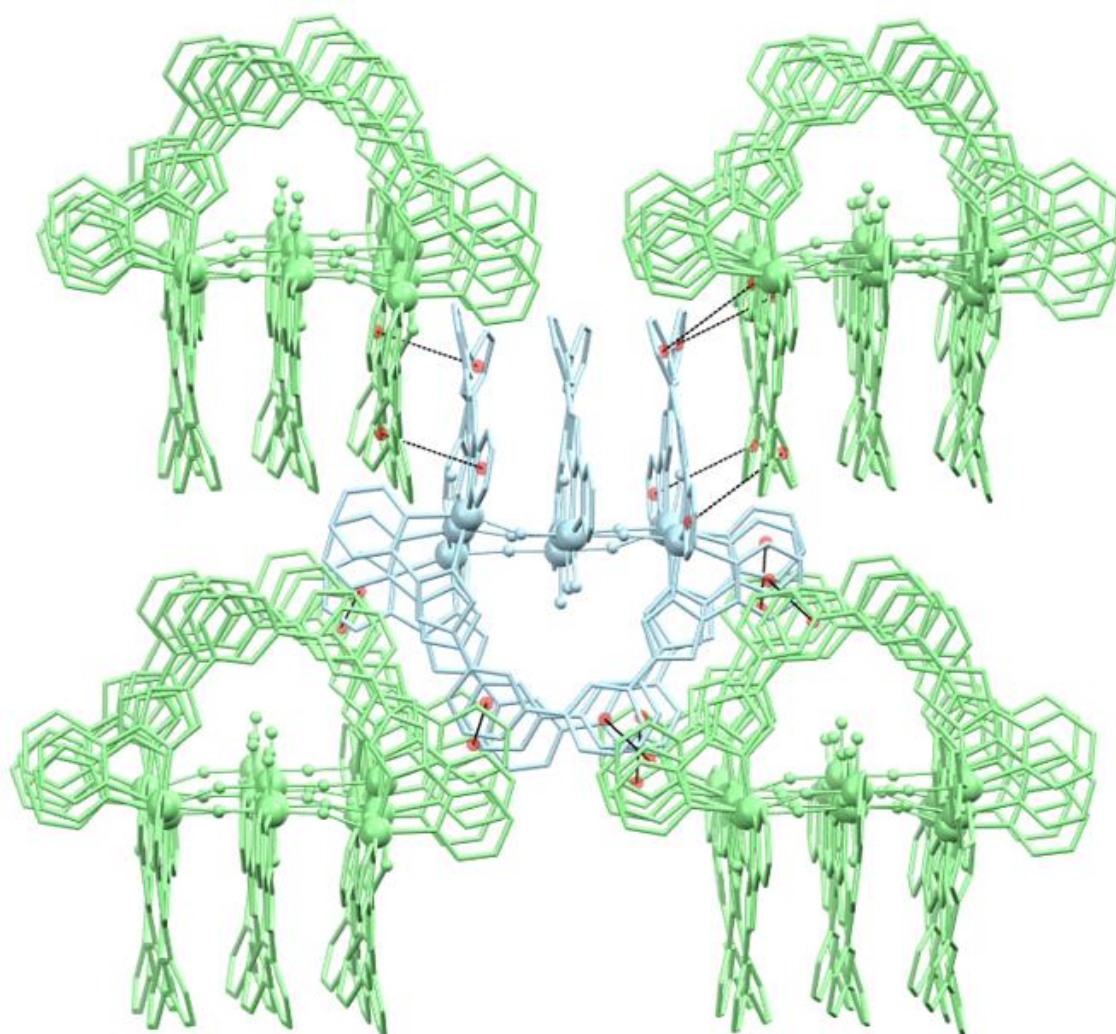


**Figure A7.13.** Representation of the cationic  $[\text{Fe}_9\text{O}_4(\text{OH})_{10}(\text{H}_2\text{L}2)_6(\text{H}_2\text{O})_4]^{5+}$  complex of grid **14** in light blue with its closest eighth neighbours in light green. Twelve  $\pi\cdots\pi$  interactions are shown as dashed lines connecting the centroids (red balls) of the aromatic rings involved.

**Table A7.14.** Twelve  $\pi\cdots\pi$  interactions between the eight cationic neighbours of compound **17**.

labels	Distance (Å) ( $\pi$ : centroid)
(2) Cg(C75 C76 C77 C78 C79 C80) ... Cg(N6 C24 C25 C26 C27 C28)	3.713
(2) Cg(C9 C10 C11 C12 C13 C14) ... Cg(N1 C1 C2 C3 C4 C5)	4.197
(2) Cg(C69 C70 C71 C72 C73 C74) ... Cg(N13 C61 C62 C63 C64 C65)	4.080
(2) Cg(C105 C106 C107 C108 C109 C110) ... Cg(N24 C114 C115 C116 C117 C118)	4.292
(2) Cg(C99 C100 C101 C102 C103 C104) ... Cg(N19 C91 C92 C93 C94 C95)	4.067
(2) Cg(N36 C174 C175 C176 C177 C178) ... Cg(C159 C160 C161 C162 C163 C164)	3.839

**Table A7.15.** Crystallographic table for compound **18** at 100K.

Compound <b>18</b>	
Formula	Fe <sub>9</sub> C <sub>168</sub> H <sub>124</sub> Cl <sub>6</sub> N <sub>36</sub> O <sub>12</sub> , 4Cl, 28[CH <sub>3</sub> OH]
FW (g mol <sup>-1</sup> )	3700.21
T (K)	100
Wavelength (Å)	0.7288
Crystal system	cubic
Space group	I -4 3 d
a (Å)	38.702(3)
b (Å)	38.702(3)
c (Å)	38.702(3)
$\alpha$ (°)	90
$\beta$ (°)	90
$\gamma$ (°)	90
V (Å <sup>3</sup> )	57969(14)
Z	12
$\rho_{\text{calcd}}$ (g cm <sup>-3</sup> )	1.272
$\mu$ (mm <sup>-1</sup> )	0.855
Independent reflections ( $R_{\text{int}}$ )	6403 (0.0655)
param. / restraints	539 / 4
Goodness-of-fit	1.046
Final R1 / wR2 [ $I > 2\sigma(I)$ ]	0.0491 / 0.1221
Final R1 / wR2 [all data]	0.0660 / 0.1457
largest diff. peak / hole (e Å <sup>3</sup> )	0.374 / -0.527

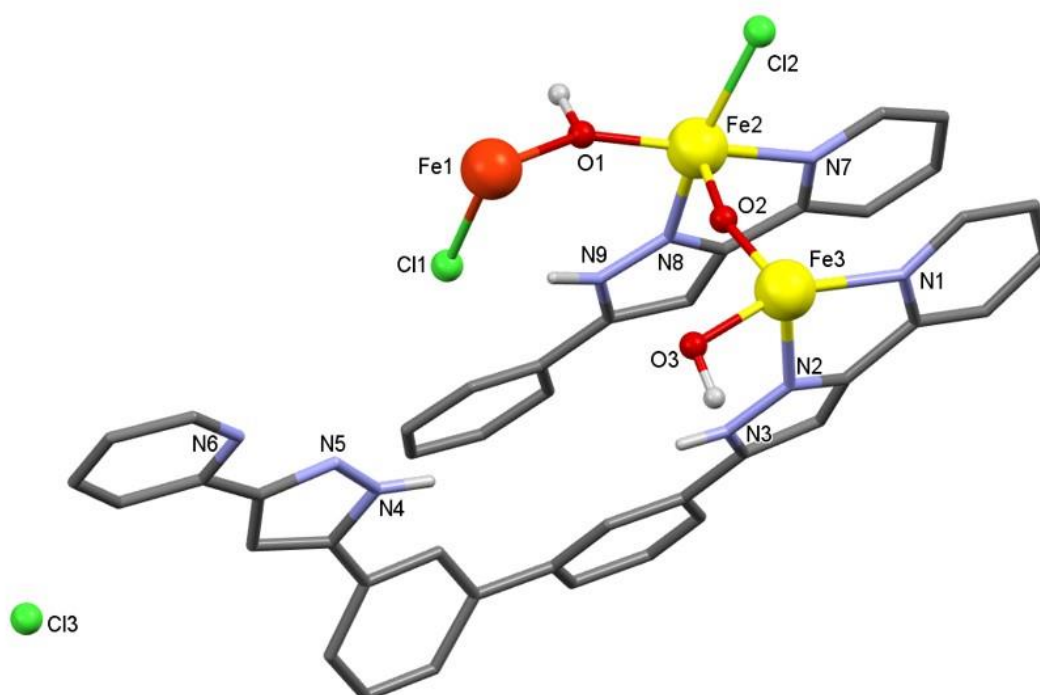


**Figure A7.14.** Molecular representation of the asymmetric unit for grid **18**. Big red and yellow spheres are Fe(II) and Fe(III), respectively.

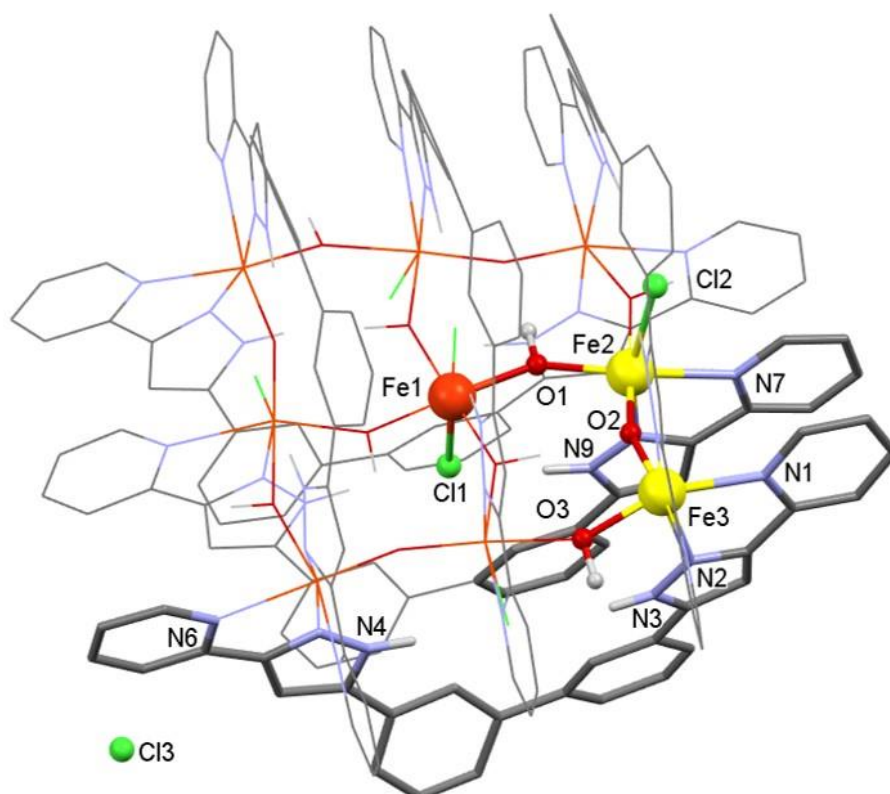


**Figure A7.15.** Grown molecular representation of the whole grid **18** with the formula  $[\text{Fe}_9\text{O}_4\text{Cl}_6(\text{OH})_8(\text{H}_2\text{L}_2)_6]\text{Cl}_4$  from the asymmetric unit.

**Table A7.16.** Final coordinates, atomic occupation and anisotropic displacement parameters for the heteroatoms of grid **18**.

atom	x	y	z	occ	U <sub>11</sub>	U <sub>22</sub>	U <sub>33</sub>	U <sub>23</sub>	U <sub>13</sub>	U <sub>12</sub>
Fe1	0.62500	0.50000	0.25000	10.25000	0.01714	0.03000	0.03000	-0.00000	-0.00000	-0.00000
Fe2	0.62499	0.49837	0.34675	11.00000	0.02338	0.03762	0.02735	0.00116	-0.00322	0.00008
Fe3	0.60971	0.40753	0.34530	11.00000	0.02623	0.03030	0.02735	0.00291	0.00171	-0.00268
Cl1	0.68789	0.50000	0.25000	10.50000	0.01577	0.08797	0.03863	0.00219	-0.00000	0.00000
Cl2	0.56505	0.50976	0.36108	11.00000	0.02572	0.04504	0.03647	-0.00389	0.00050	0.00073
O1	0.62671	0.51367	0.29901	11.00000	0.03152	0.03390	0.03297	0.00164	0.00429	-0.00742
O2	0.61655	0.45338	0.33762	11.00000	0.02872	0.03372	0.04757	0.00811	-0.00629	-0.00833
O3	0.62064	0.39260	0.29919	11.00000	0.02752	0.02478	0.01024	0.00576	0.00552	-0.00753
N1	0.60912	0.40793	0.40110	11.00000	0.03457	0.02288	0.04804	0.00706	0.00183	-0.01071
N2	0.66083	0.39655	0.36003	11.00000	0.03779	0.03115	0.02987	0.00404	-0.01387	-0.00056
N3	0.69043	0.39905	0.34105	11.00000	0.02478	0.03418	0.03615	0.00492	0.00136	0.00881
N4	0.71537	0.40914	0.18793	11.00000	0.02957	0.04169	0.03281	-0.01078	0.00514	-0.00094
N5	0.69383	0.40891	0.16074	11.00000	0.03754	0.02613	0.03174	-0.00091	0.00933	0.00333
N6	0.66101	0.40374	0.10208	11.00000	0.03949	0.02165	0.04850	-0.00748	0.01545	-0.00740
N7	0.63753	0.49566	0.40400	11.00000	0.04347	0.03541	0.03124	-0.00165	-0.00853	0.00124
N8	0.67992	0.49568	0.35057	11.00000	0.02850	0.03370	0.04007	0.00329	-0.00465	0.00683
N9	0.70592	0.49756	0.32710	11.00000	0.02534	0.02282	0.04474	0.00198	-0.01670	0.00025
Cl3	0.8048	0.4305	0.0608	11.00000	0.2529	0.26310	0.2078	-0.0437	0.1067	-0.1058



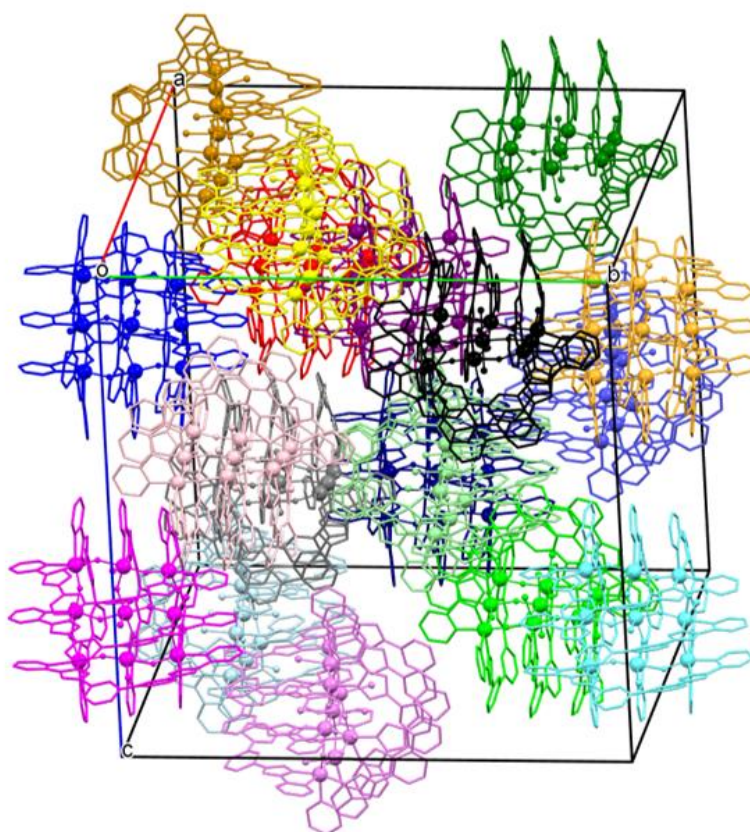


**Figure A7.16.** Unit cell for compound **18** enclosing eighteen  $[\text{Fe}_9\text{O}_4\text{Cl}_6(\text{OH})_8(\text{H}_2\text{L}2)_6]4(\text{Cl})$  moieties.

**Table A7.17.** Selected bond distances ( $\text{\AA}$ ) of grid **18**.

Atom pair	distance ( $\text{\AA}$ )	Atom pair	distance ( $\text{\AA}$ )	Atom pair	distance ( $\text{\AA}$ )
(4) Fe1- O1	1.991	Fe2- O1	1.937	Fe3- N1	2.280
(2) Fe1- Cl1	2.431	Fe2- O2	1.820	Fe3- N2	2.090
		Fe2- O3	2.014	Fe3- N5	2.100
		Fe2- Cl2	2.416	Fe3- N6	2.180
		Fe2- N7	2.290	Fe3- O2	1.810
		Fe2- N8	2.140	Fe3- O3	1.945

**Table A7.18.** Empirical parameters of  $R_0$  considered for the BVS calculation in **18**.<sup>2</sup>

	$R_0$
Fe <sup>III</sup> -N (HS)	1.820
Fe <sup>III</sup> -N (LS)	1.700
Fe <sup>III</sup> -O	1.759
Fe <sup>II</sup> -N (HS)	1.760
Fe <sup>II</sup> -N (LS)	1.660
Fe <sup>II</sup> -O	1.734
Fe <sup>III</sup> -Cl	2.090
Fe <sup>II</sup> -Cl	2.060

**Table A7.19.** Bond-valence sum calculations in **18** for +2 and +3 oxidation states and HS and LS magnetic states for each type of iron metal centre. The experimental R values are reported in table A7.17.

Metal centre	Oxidation state +3		Oxidation state +2		Conclusions
	HS	LS	HS	LS	
Fe1	2.93*	2.41	2.73*	2.24	Fe1= Fe <sup>II</sup> (LS)
Fe2	3.08	2.89	2.82	2.68	Fe2= Fe <sup>III</sup> (HS)
Fe3	3.09	2.65	2.75	2.43	Fe3= Fe <sup>III</sup> (HS)

\* Weak-field ligands, like Cl<sup>-</sup>, results in HS state.

**Table A7.20.** Selected Fe-O-Fe angles for grid **18**.

labels	Distance (Å) ( $\pi$ : centroid)
(4) Fe1-O1-Fe2	164.4
(4) Fe2-O2-Fe3	159.2(4)
(4) Fe2-O3-Fe2	169.6(3)

**Table A7.21.** Fe...Fe distances for grid **18**.

labels	Distance (Å)( $\pi$ : centroid)
(4) Fe1...Fe2	3.745
(4) Fe2...Fe3	3.801(2)
(4) Fe2...Fe3	3.566(2)

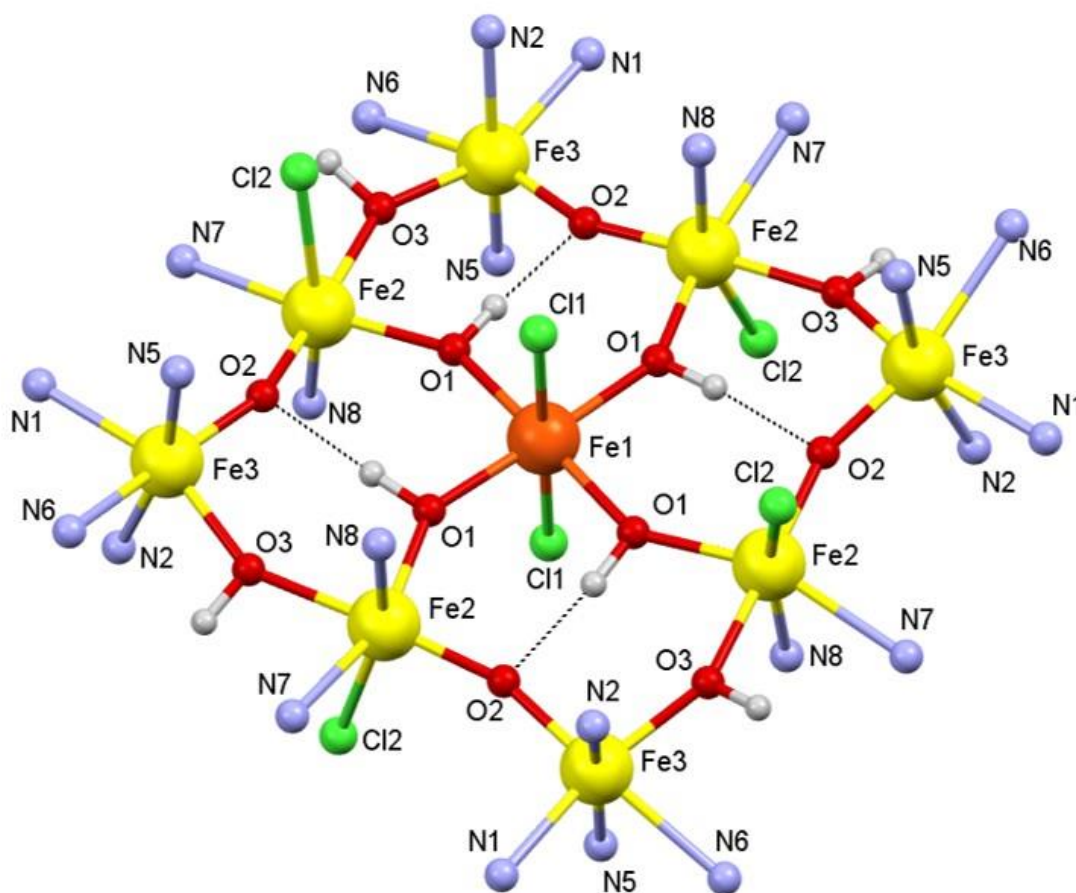


**Figure A7.17.** Representation of the  $[\text{Fe}_9\text{O}_4\text{Cl}_6(\text{OH})_8(\text{H}_2\text{L}_2)_6]^{4+}$  core in grid **18** with the atoms labelled. Big red and yellow spheres are Fe(II) and Fe(III), respectively. Dashed black lines are hydrogen bonds between pairs of OH $^-$ /O $^{2-}$  atoms within the core.

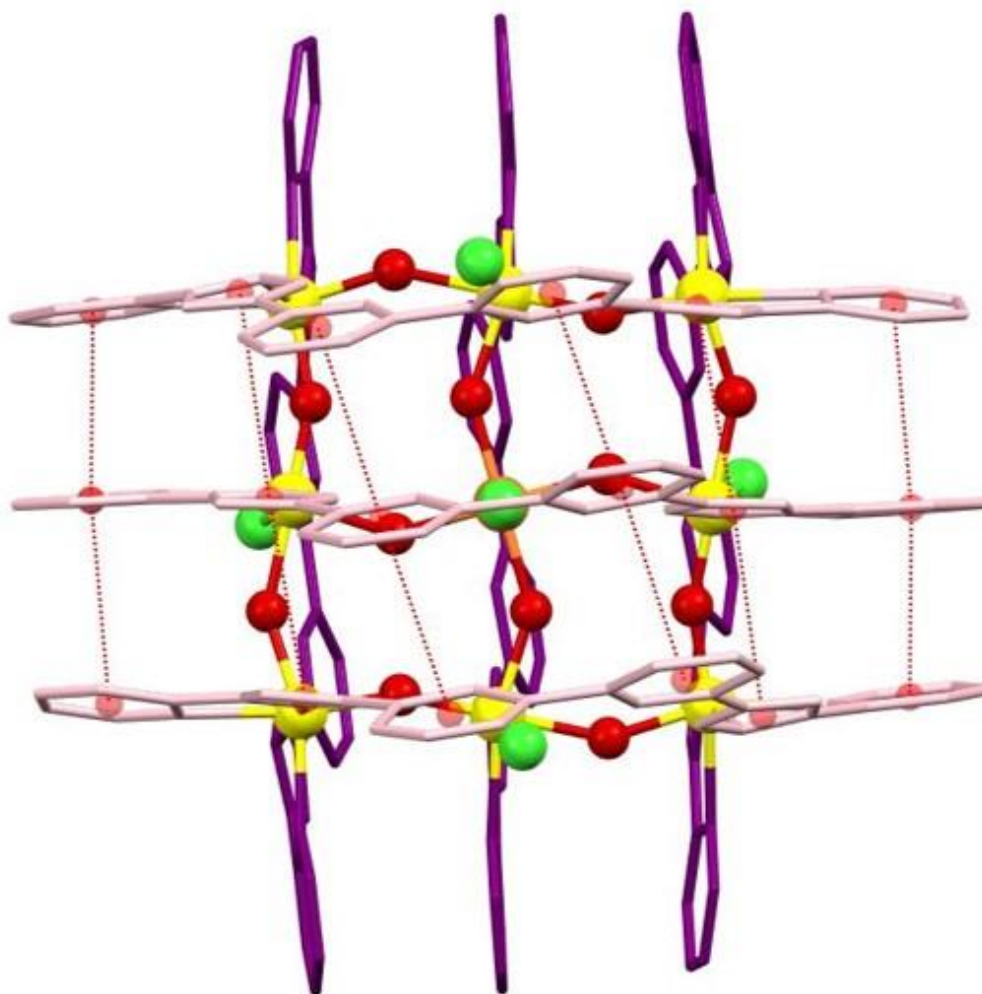


**Figure A7.18.** Illustration of  $[\text{Fe}_9\text{O}_4\text{Cl}_6(\text{OH})_8(\text{H}_2\text{L}2)_6]^{4+}$  of grid **18**, emphasizing six  $\pi\cdots\pi\cdots\pi$  intramolecular interactions within three  $\text{H}_2\text{L}2$  ligands that are part of the same set, highlighted in green dashed lines joining the centroids (green balls) of the aromatic rings. The two different sets of ligands are coloured in green and purple. There are 6 equivalent interactions within the other set of three ligands (in purple) not shown.

**Table A7.22.** Series of  $\pi\cdots\pi$  stacking interactions in compound **18**.

labels	Distance (Å) ( $\pi$ : centroid)
(2) Cg(N1 C1 C2 C3 C4 C5) $\cdots$ Cg(N7 C29 C30 C31 C32 C33)	3.643
(2) Cg(N2 N3 C6 C7 C8) $\cdots$ Cg(N8 N9 C34 C35 C36)	3.798
(2) Cg(N4 N5 C21 C22 C23) $\cdots$ Cg(N8 N9 C34 C35 C36)	3.642
(2) Cg(N6 C24 C25 C26 C27 C28) $\cdots$ Cg(N7 C29 C30 C31 C32 C33)	3.777
(2) Cg(C9 C10 C11 C12 C13 C14) $\cdots$ Cg(C37 C38 C39 C40 C41 C42)	3.665
(2) Cg(C15 C16 C17 C18 C19 C20) $\cdots$ Cg(C37 C38 C39 C40 C42 C41)	3.636

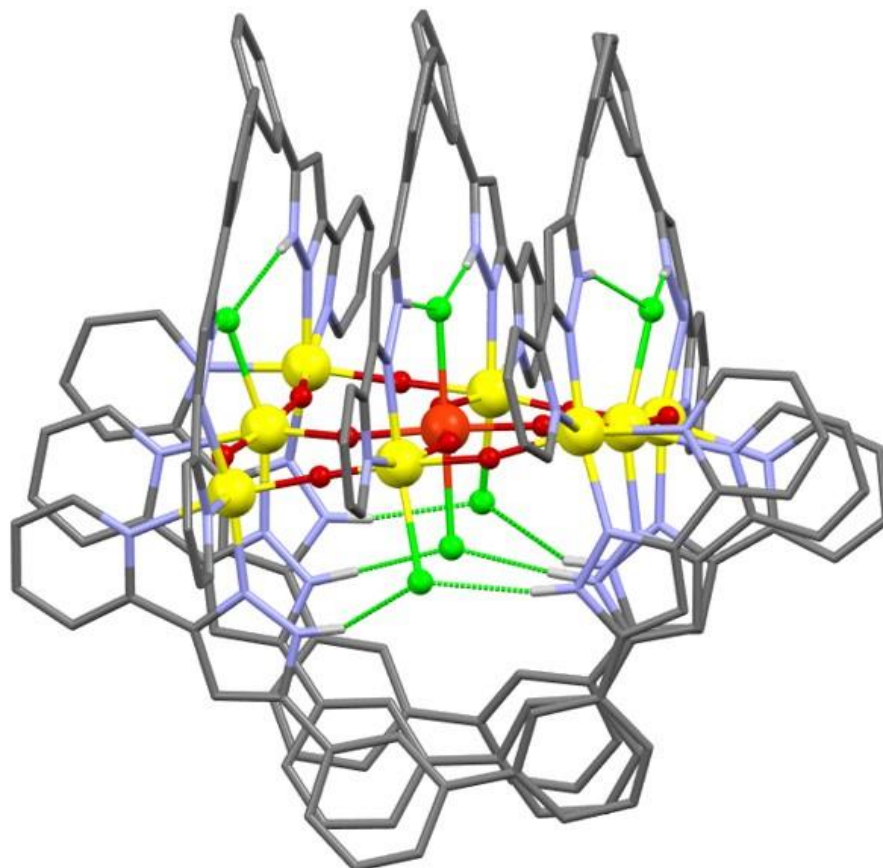


**Figure A7.19.** Representation of the  $[\text{Fe}_9\text{O}_4\text{Cl}_6(\text{OH})_8(\text{H}_2\text{L}_2)_6]^{4+}$  of grid **18**, highlighting the twelve N-H $\cdots$ Cl intramolecular hydrogen bonds between the free N-H groups of the  $\text{H}_2\text{L}_2$  ligands and the chloride atoms at the axial positions of the core. Only H atoms of the N-H moieties are shown.

**Table A7.23.** Twelve N-H $\cdots$ O intramolecular hydrogen bonds between the free N-H groups of the  $\text{H}_2\text{L}_2$  ligand and the axial chloride ligands in compound **18**.

labels	Distance ( $\text{\AA}$ ) ( $\pi$ : centroid)
(4) N3-H3B $\cdots$ Cl2	2.314
(4) N4-H4 $\cdots$ Cl2	2.284
(4) N9-H9 $\cdots$ Cl2	2.127

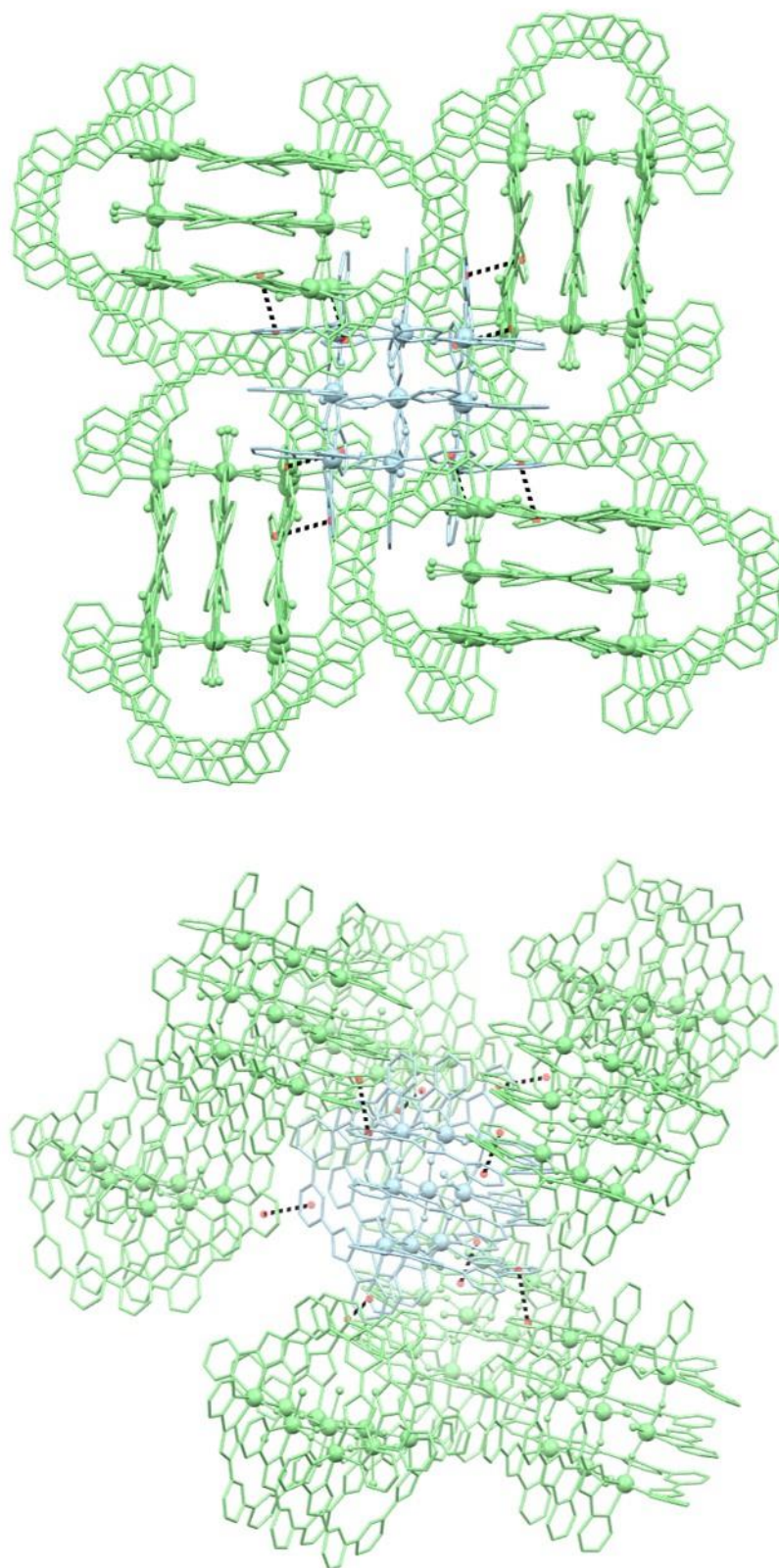


**Figure A7.20.** Two views of the representation of the cationic  $[\text{Fe}_9\text{O}_4\text{Cl}_6(\text{OH})_8(\text{H}_2\text{L}_2)_6]^{4+}$  complex of grid **18** in light blue with its closest eighth neighbours in light green. Eight  $\pi\cdots\pi$  interactions are shown as dashed lines connecting the centroids (red balls) of the aromatic rings involved.

**Table A7.24.** Eight  $\pi \cdots \pi$  interactions between the eight cationic neighbours of compound **18**.

labels	Distance (Å) ( $\pi$ : centroid)
(8) Cg(CN1 C1 C2 C3 C4 C5) ... Cg(C9 C10 C11 C12 C13 C14)	3.483

**Description of the magnetization behaviour. Brillouin function approximation.**<sup>3</sup>

The molar magnetization of a compound is defined as the average magnetization of the whole molecules and is defined by the product between the magnetic moment ( $\mu$ ) and the Avogadro's number ( $N_A$ ) (Eq. A10.3):

$$M = N_A * \langle \mu \rangle \quad (\text{Eq. A10.3})$$

For a system without orbital contribution and a defined spin ( $S$ ), the Boltzman distribution is applied to the magnetization expression giving Eq. A10.4, which is known as the Brillouin function (only spin contribution):

$$M = N_A g \mu_B S [B_S(x)] \quad (\text{Eq. A10.4})$$

where

$$[B_S(x)] = \frac{2S+1}{2S} \coth\left(\frac{2S+1}{2} x\right) - \frac{1}{2S} \coth\left(\frac{x}{2}\right) \quad \text{and} \quad x = \frac{g \mu_B H}{k_B T}$$

The parameter  $g$  represents the measurement of the states  $\pm M_S$  or  $\pm M_J$  splitting. For a free electron,  $g$  is considered as  $g_e = 2.0023$ , also known as Landé's factor. Nevertheless, each electron belongs to an atom in a specific orbital, giving rise to an orbital contribution. The  $g$  value varies depending on the spin-orbit coupling nature. The orbital contribution can be neglected for organic radicals or inorganic molecules with an electron on the  $s$  or  $p$  orbitals.  $\mu_B$  is the Bohr magneton and  $k_B$  is the Boltzman constant.



Brillouin law provides important information of the magnetic system. For  $x \gg 1$  (strong fields and/or low temperatures),  $B_s(x)$  is 1, and thus,  $M = N_A g \mu_B S$ . The molar magnetization tends to a constant value called saturation magnetization (only spin dependent). By representing  $M/N_A \mu_B$  vs. field (B), considering  $g$  close to  $g_e$  ( $\approx 2.00$ ), the saturation magnetization indicates the number of unpaired electrons, and therefore, elucidates the fundamental state of the system (S).

#### REFERENCES

- (1) Kanowitz, S. M.; Palenik, G. J. Bond Valence Sums in Coordination Chemistry Using Oxidation-State-Independent  $R_0$  Values. A Simple Method for Calculating the Oxidation State of Iron in Fe-O Complexes. *Inorg. Chem.* **1998**, *37*, 2086–2088.
- (2) Brese, N. E.; O’Keeffe, M. Bond-Valence Parameters for Solids. *Acta Cryst. Sect. B.* **1991**, *47*, 192–197.
- (3) Gispert, J. R. *Coordination Chemistry*; Wiley-VCH, Ed.; Weinheim, 2008.

**APPENDIX 8- CHAPTER 8. MAGNETIC STUDY OF TRIPLE-STRANDED HELICATES [X@Fe<sub>2</sub>(H<sub>2</sub>L)<sub>3</sub>]<sup>4+</sup> IN SOLUTION AND ACCEST TO ([X@Fe(H<sub>2</sub>L5)<sub>3</sub>]<sub>2</sub>)<sup>3+</sup> (X=Br, Cl) COMPLEXES**

**Crystal structure description of [Br@Zn<sub>2</sub>(H<sub>2</sub>L)<sub>3</sub>]Br(PF<sub>6</sub>)<sub>2</sub>·0.5C<sub>4</sub>H<sub>10</sub>O·4CH<sub>4</sub>O (23)**

At 100K, compound [Br@Zn<sub>2</sub>] crystallizes in the tetragonal space group *I4<sub>1</sub>cd* (see Figure A8.1 and Table A8.1). The asymmetric unit consists in one [Zn<sub>2</sub>(H<sub>2</sub>L)<sub>3</sub>]<sup>4+</sup> helical cation with one Br<sup>-</sup> in the provided cavity of the cation, one external Br<sup>-</sup>, two PF<sub>6</sub><sup>-</sup> anions (with one PF<sub>6</sub><sup>-</sup> disordered over two positions), four solvent molecules of methanol (one disordered over two positions) and half solvent molecule of diethyl ether. The unit cell contains sixteen of such ensembles. The helical structure is composed by two Zn<sup>II</sup> metal centres and three H<sub>2</sub>L ligands which chelate through their terminal pyrazolyl and pyridine moieties completing the ZnN<sub>6</sub> coordination sphere. Thus, each helical cation displays both Δ-Δ and Λ-Λ configurations, being a racemic mixture of these enantiomeric species in the crystal. The bromide guest is held in the cavity through six hydrogen bonds with the free N-H groups of the pyrazolyl rings of the ligands. The structure is completely similar to the previously reported [Fe<sup>II</sup><sub>2</sub>] helicites.

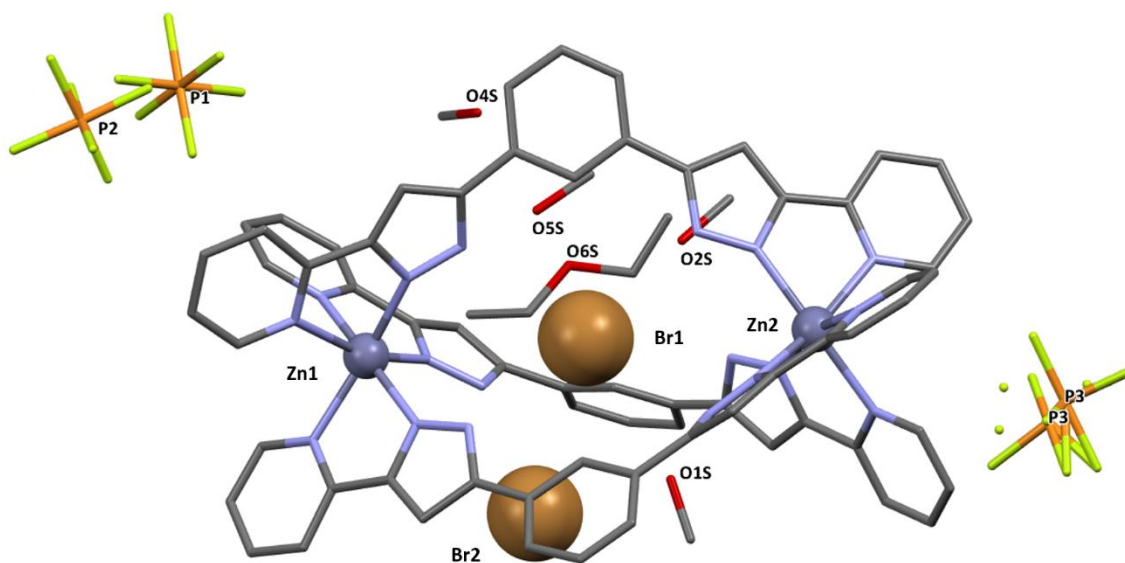


**Figure A8.1.** Molecular representation of the diamagnetic helicate **23** at 100K. Hydrogen atoms are omitted for clarity.

**Table A8.1.** Crystal data for the diamagnetic helicate [Br@Zn<sub>2</sub>(H<sub>2</sub>L)<sub>3</sub>] (**23**).

<b>Compound 23</b>	
<b>Formula</b>	Zn <sub>2</sub> C <sub>66</sub> H <sub>48</sub> N <sub>18</sub> , 2(Br), 2(PF <sub>6</sub> ), 0.5(C <sub>4</sub> H <sub>10</sub> O), 4(CH <sub>4</sub> O)
<b>FW (g mol<sup>-1</sup>)</b>	1838.95
<b>T (K)</b>	100
<b>Wavelength (Å)</b>	0.72932
<b>Crystal system</b>	tetragonal
<b>Space group</b>	<i>I4<sub>1</sub>cd</i>
<b>a (Å)</b>	24.511(3)
<b>b (Å)</b>	24.511(3)
<b>c (Å)</b>	53.260(6)
<b>α (°) = β (°) = γ (°)</b>	90
<b>V (Å<sup>3</sup>)</b>	31998(9)
<b>Z</b>	16
<b>ρ<sub>calcd</sub> (g cm<sup>-3</sup>)</b>	1.527
<b>μ (mm<sup>-1</sup>)</b>	1.840
<b>Independent reflections (R<sub>int</sub>)</b>	15609 (0.0872)
<b>param. / restraints</b>	1021 / 27
<b>Goodness-of-fit</b>	1.061
<b>Final R1 / wR2 [I &gt; 2σ(I)]</b>	0.0753 / 0.1843
<b>Final R1 / wR2 [all data]</b>	0.1158 / 0.2097
<b>largest diff. peak / hole (e Å<sup>-3</sup>)</b>	1.214 / -1.056

### Analysis of the NMR spectra for the $Zn_2(H_2L)_3$ helicates, (12) and (23)

For both complexes, 12 and 23, two set of signals were observed, a majoritarian one assigned to the dinuclear helicate (symmetric compound) and minoritarian one for the dimerized mononuclear complex called also jellyfish (unsymmetrical compound).

For  $[Br@Zn_2(H_2L)_3]^{3+}$  (23), the ratio of 34/66% is assigned for the jellyfish/helicate complexes. The mononuclear complex (jellyfish, labelled as **M**), which display a lower symmetry, has a double set of signals in comparison to the binuclear (helicate, labelled as **D**) one. We can clearly see it for the NH protons (Figure A8.2). Two NH signals are found for the mononuclear, in contrast, only one is ascribed to the binuclear helicate. Many signals of the mononuclear are assigned, however, some peaks are overlapped.

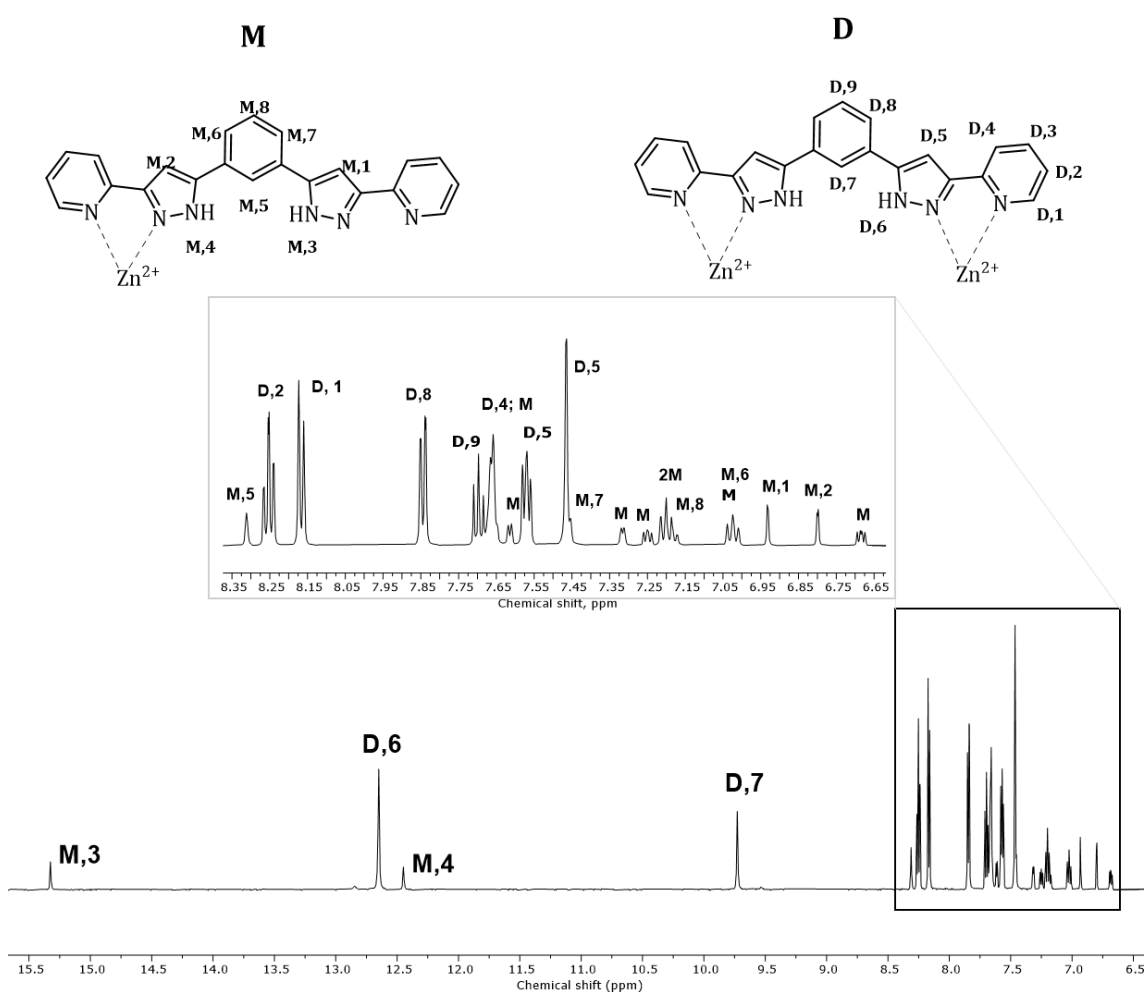


**Figure A8.2.**  $^1H$  NMR spectrum of  $[Br@Zn_2(H_2L)_3]^{3+}$  (23).

The  $^1\text{H}$  NMR spectrum of  $[\text{Br}@\text{Zn}_2(\text{H}_2\text{L})_3]^{3+}$  (**23**) is similar to the analogue  $[\text{Cl}@\text{Zn}_2(\text{H}_2\text{L})_3]^{3+}$  (**12**) (previously reported in chapter 6). However, some differences are observed due to the different halide in their respective cavity (Figure A8.3). Thus, the encapsulating anion effects are shown since they affect the electron structure of the complex in solution.

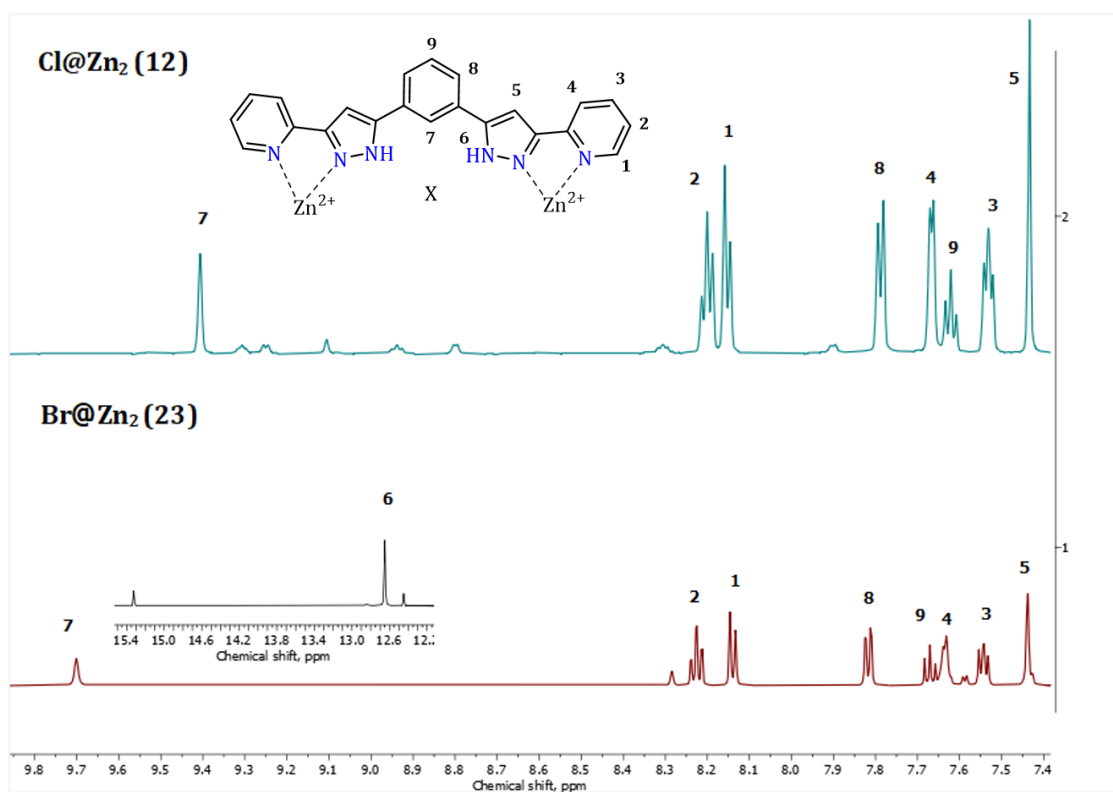


**Figure A8.3.** Comparison of the  $^1\text{H}$  NMR for the diamagnetic helicates **12** and **23**.

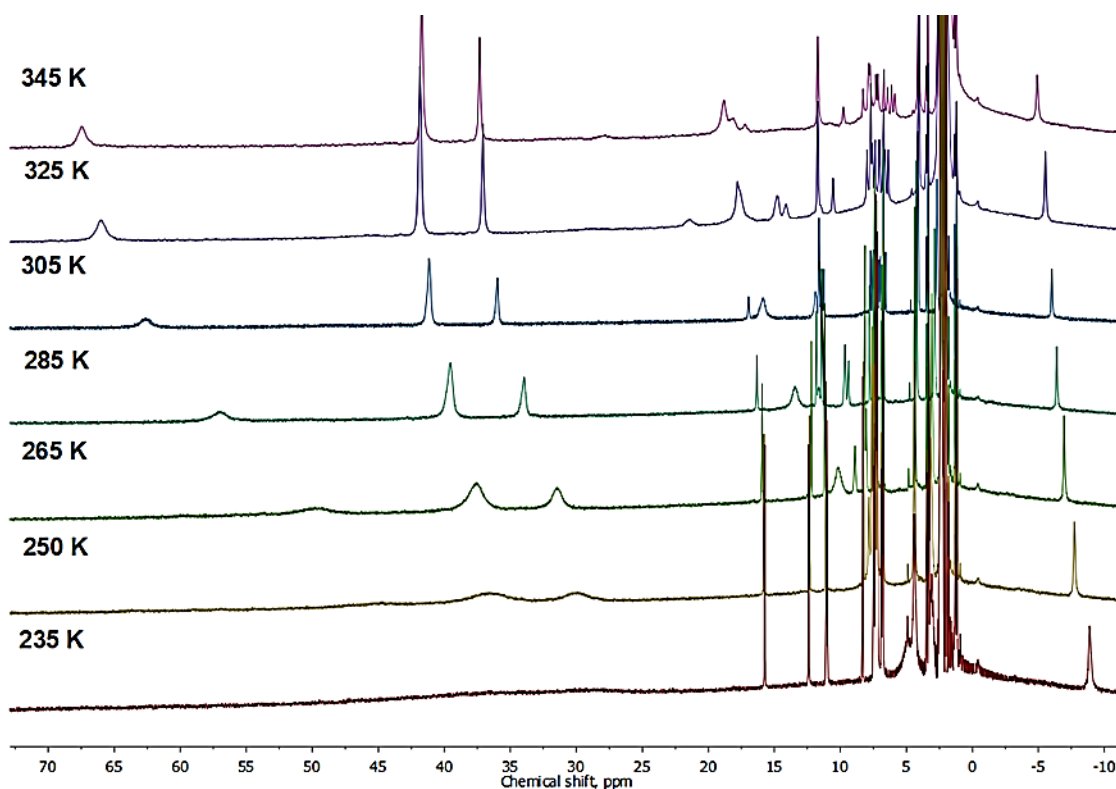


**Figure A8.4.** VT- $^1\text{H}$  NMR spectra collected for  $[\text{Cl@Fe}(\text{H}_2\text{L})_3]_2^{3+}$  (**12**) in acetonitrile- $d_3$ .

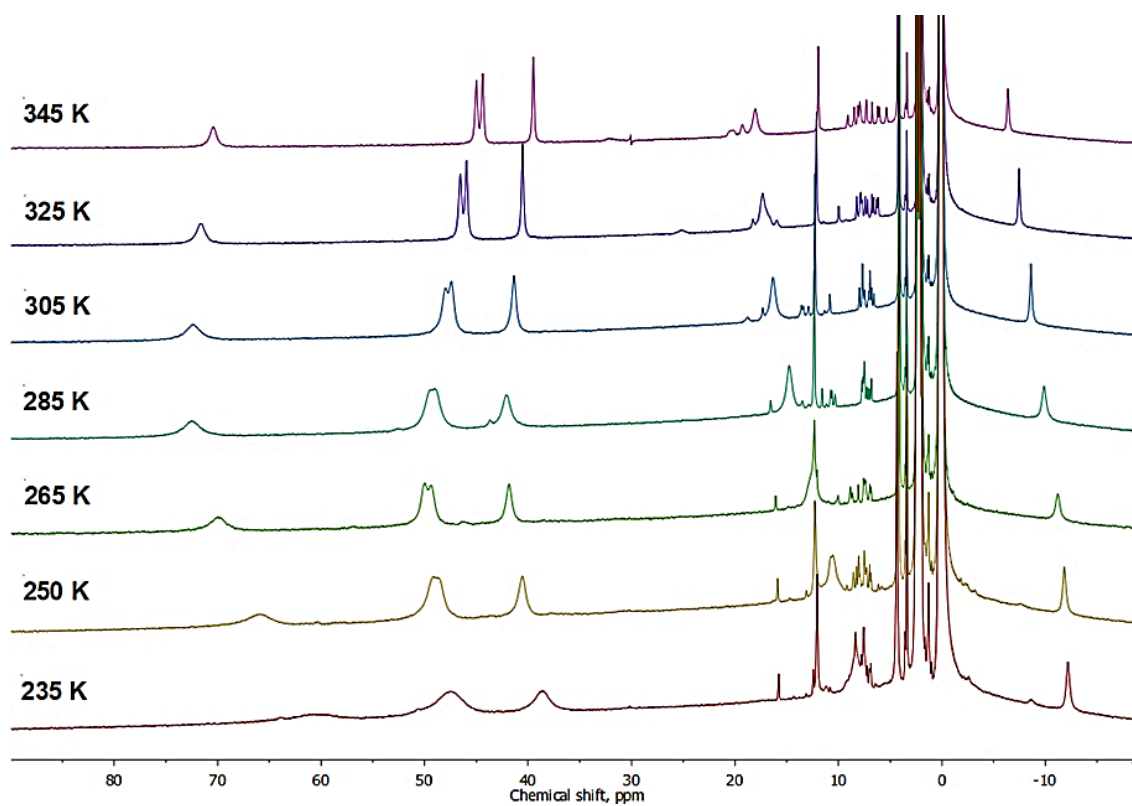


**Figure A8.5.** VT- $^1\text{H}$  NMR spectra collected for  $[\text{Br@Fe}(\text{H}_2\text{L})_3]_2^{3+}$  (**23**) in acetonitrile- $d_3$ .

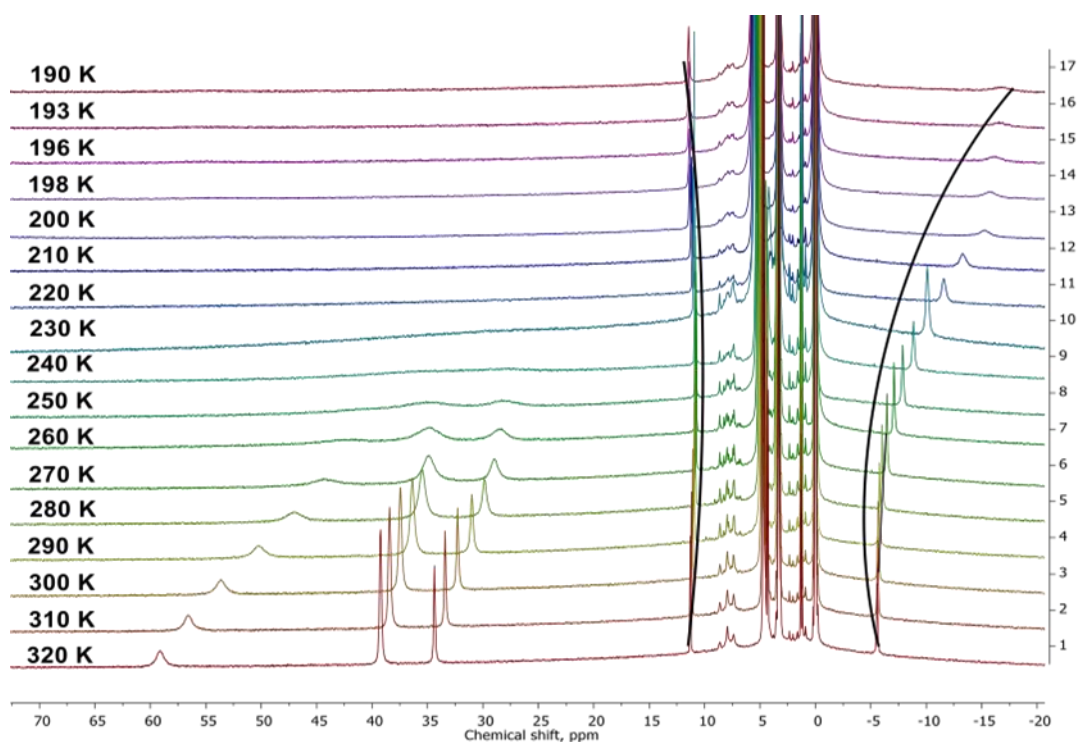


**Figure A8.6.** VT-<sup>1</sup>H NMR spectra collected for  $[\text{Cl@Fe}(\text{H}_2\text{L})_3]^{3+}$  (**12**) in methanol-*d*<sub>4</sub>. Black curves highlight the signals for the two protons (7 and 9) on the central phenyl moiety that are observed over the whole temperature range.

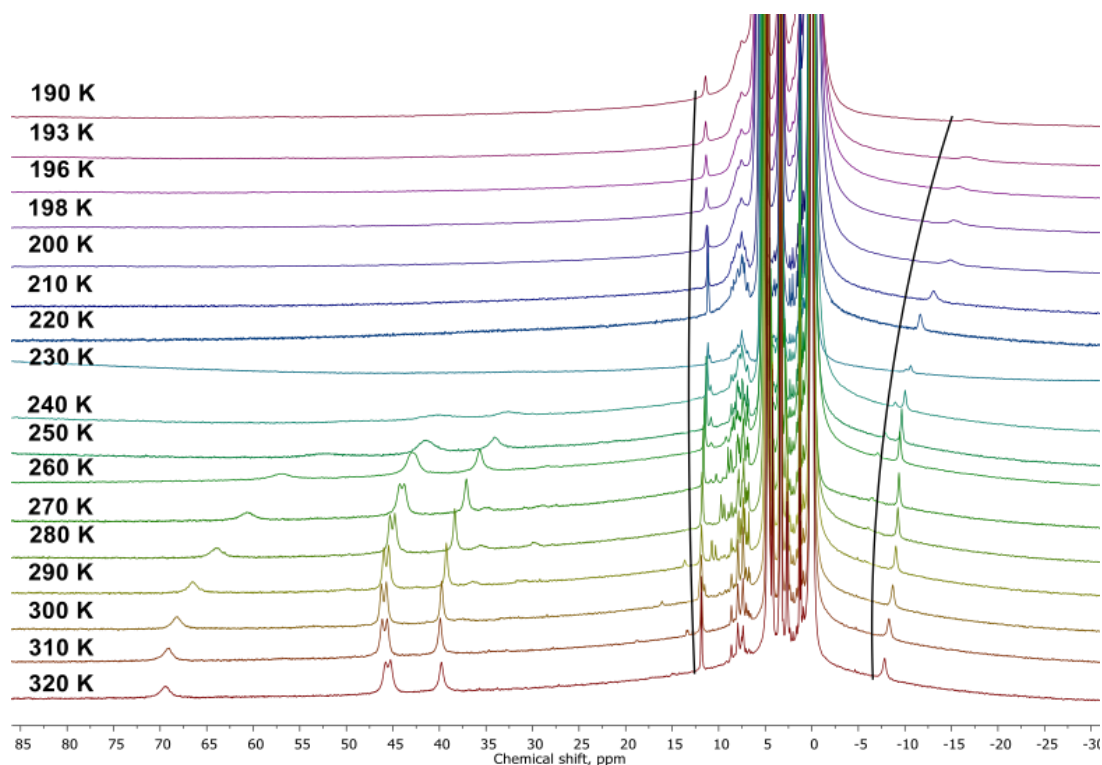


**Figure A8.7.** VT-<sup>1</sup>H NMR spectra collected for  $[\text{Br@Fe}(\text{H}_2\text{L})_3]^{3+}$  (**23**) in methanol-*d*<sub>4</sub>. Black curves highlight the signals for the two protons (7 and 9) on the central phenyl moiety that are observed over the whole temperature range.

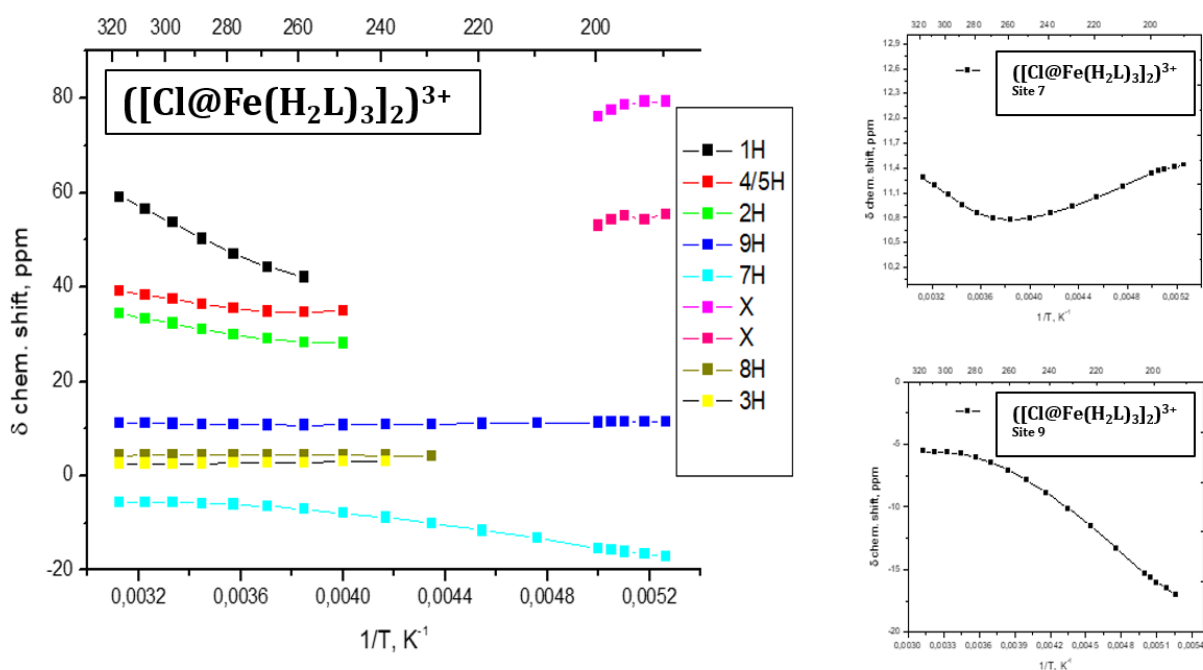


**Figure A8.8.** Temperature dependence of the chemical shift for  $[(\text{Cl}@\text{Fe}(\text{H}_2\text{L})_3)_2]^{3+}$  (**12**) in methanol- $d_4$ . Results for protons 7 and 9 of the central phenyl moiety are given in the two right insets.

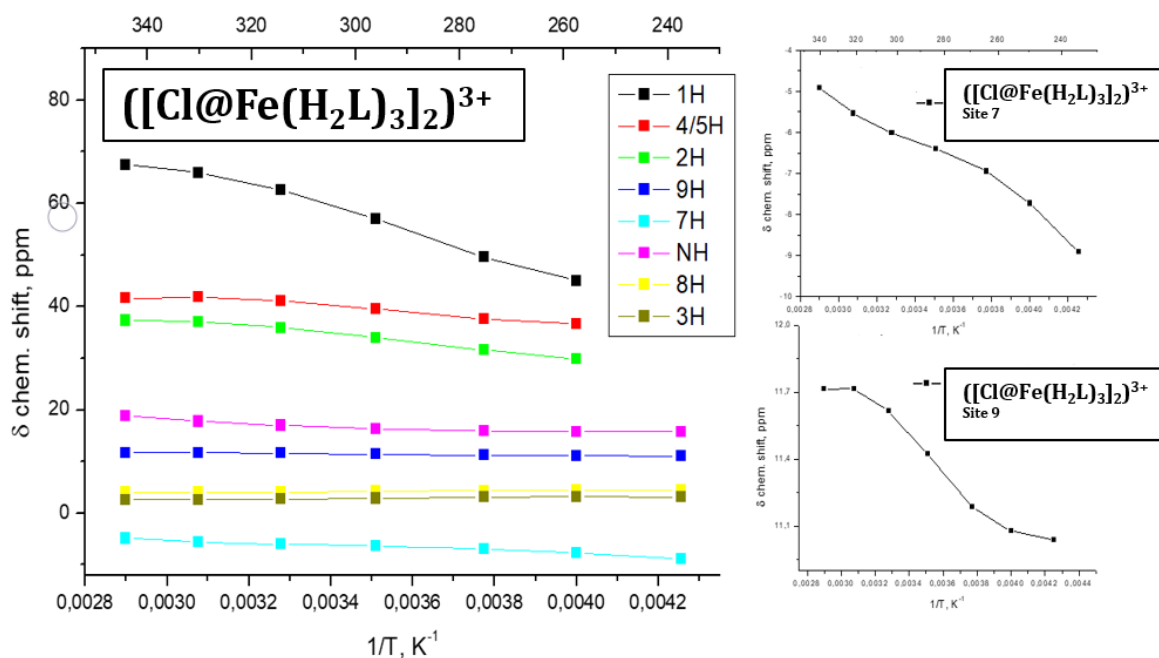


**Figure A8.9.** Temperature dependence of the chemical shift for  $[(\text{Cl}@\text{Fe}(\text{H}_2\text{L})_3)_2]^{3+}$  (**12**) in acetonitrile- $d_3$ . Results for protons 7 and 9 of the central phenyl moiety are given in the two right insets.



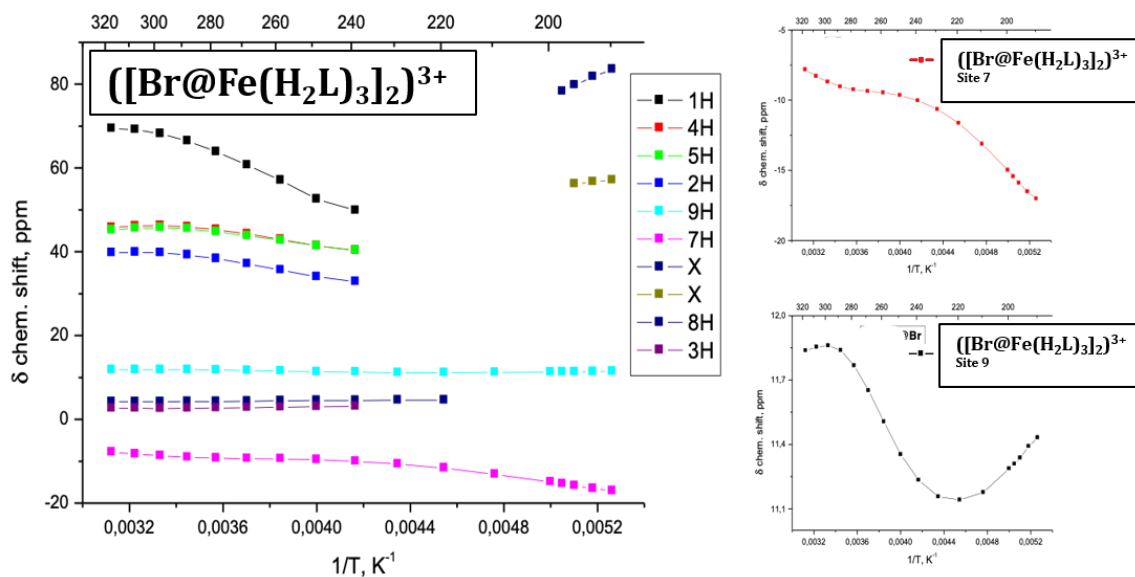


**Figure A8.10.** Temperature dependence of the chemical shift for  $[\text{Br@Fe}(\text{H}_2\text{L})_3]_2^{3+}$  (**23**) in methanol- $d_4$ . Results for protons 7 and 9 of the central phenyl moiety are given in the two right insets.

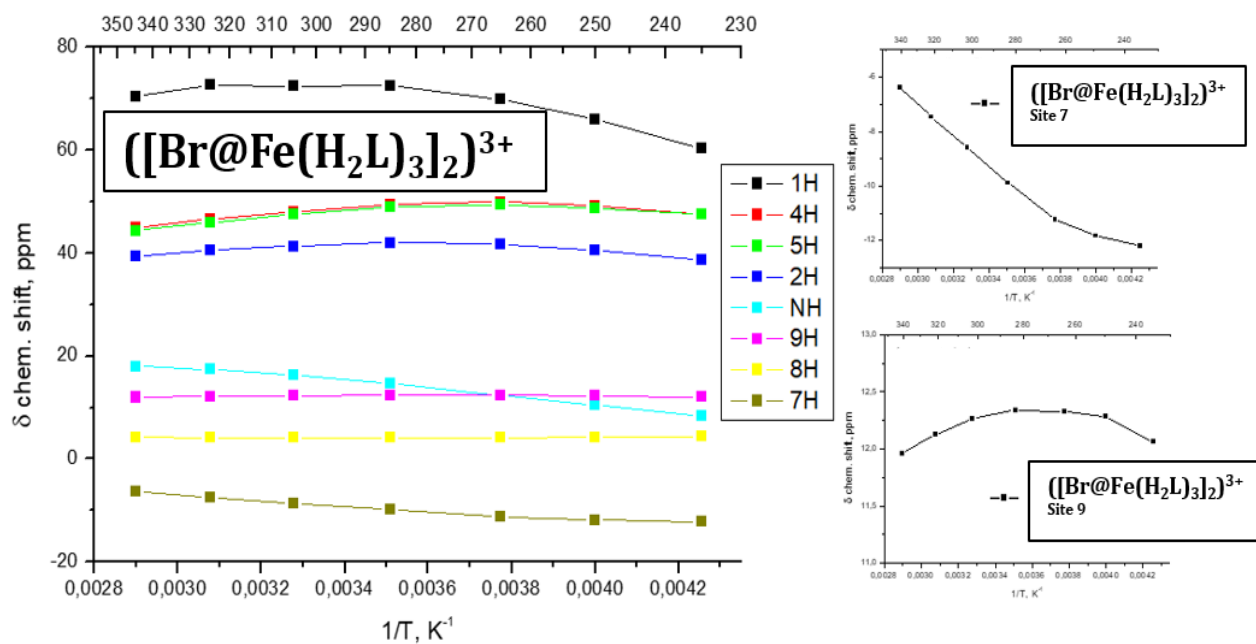


**Figure A8.11.** Temperature dependence of the chemical shift for  $[\text{Br@Fe}(\text{H}_2\text{L})_3]_2^{3+}$  (**23**) in acetonitrile- $d_3$ . Results for protons 7 and 9 of the central phenyl moiety are given in the two right insets.

**Table A8.2.** Thermodynamic parameters\* for the SCO transition of helicates X@[Fe<sub>2</sub>(H<sub>2</sub>L)<sub>3</sub>]<sup>3+</sup> obtained from the NMR data.

	$\Delta H$ , kJ/mol	$\Delta S$ , J/(mol*K)	$\Delta S$ , J/(mol*K)
Cl@[Fe <sub>2</sub> (H <sub>2</sub> L) <sub>3</sub> ] <sup>3+</sup> (12) in acetonitrile-d <sub>3</sub>	26.7	96	278
Cl@[Fe <sub>2</sub> (H <sub>2</sub> L) <sub>3</sub> ] <sup>3+</sup> (12) in methanol-d <sub>4</sub>	29.0	96	302
Br@[Fe <sub>2</sub> (H <sub>2</sub> L) <sub>3</sub> ] <sup>3+</sup> (23) in acetonitrile-d <sub>3</sub>	28.7	126	228
Br@[Fe <sub>2</sub> (H <sub>2</sub> L) <sub>3</sub> ] <sup>3+</sup> (23) in methanol-d <sub>4</sub>	27.7	105	264

\* Parameters obtained by fitting the observed chemical shifts in Vt-NMR spectra by a regular solution model.

	Compound 24	Compound 25	Compound 26	Compound 27
<b>Formula</b>	1(I), 2(FeC <sub>90</sub> H <sub>60</sub> N <sub>18</sub> ), 3(PF <sub>6</sub> ), 9[C <sub>3</sub> H <sub>6</sub> O], 7[CH <sub>3</sub> OH]	3(Br),6(FeC <sub>90</sub> H <sub>60</sub> N <sub>18</sub> ),9(PF <sub>6</sub> )	3(Cl),6(FeC <sub>90</sub> H <sub>60</sub> N <sub>18</sub> ),9(PF <sub>6</sub> )	3(Cl),6(FeC <sub>90</sub> H <sub>60</sub> N <sub>18</sub> ),9(ClO <sub>4</sub> ), 8(H <sub>2</sub> O)
<b>FW (g mol<sup>-1</sup>)</b>	6103.93	10132.28	10107.52	9841.97
<b>T (K)</b>	293	100	100	100
<b>Wavelength (Å)</b>	0.72931	0.7288	0.7288	0.7749
<b>Crystal system</b>	trigonal	trigonal	trigonal	trigonal
<b>Space group</b>	<i>R</i> -3 <i>c</i>	<i>P</i> -3	<i>P</i> -3	<i>P</i> -3
<b>a (Å)</b>	27.347	25.95(2)	26.3076(12)	26.340(12)
<b>b (Å)</b>	27.347	25.95(2)	26.3076(12)	26.340(12)
<b>c (Å)</b>	93.6216(3)	42.41(4)	42.546(3)	42.707(17)
<b>α (°)</b>	90	90	90	90
<b>β (°)</b>	90	90	90	90
<b>γ (°)</b>	120	120	120	120
<b>V (Å<sup>3</sup>)</b>	60633.59(19)	24733(51)	25501(3)	25660(26)
<b>Z</b>	12	2	2	2
<b>ρ<sub>calcd</sub> (g cm<sup>-3</sup>)</b>	2.006	1.316	1.316	1.274
<b>μ (mm<sup>-1</sup>)</b>	0.483	0.316	0.316	0.381
<b>Independent reflections (R<sub>int</sub>)</b>	23073 (0.0338)	18019 (0.0341)	18019 (0.0341)	12428 (0.0636)
<b>param. / restraints</b>	751 / 16	2165/18019	2165 / 2547	2123/ 2731
<b>Goodness-of-fit</b>	1.452	4.000	4.000	0.4697
<b>Final R1 / wR2 [I&gt;2σ(I)]</b>	0.1019/ 0.3481	0.3982 / 0.6830	0.3982 / 0.6830	0.2143 / 0.3867
<b>Final R1 / wR2 [all data]</b>	0.1191/ 0.3613	0.4614 / 0.7577	0.4614/ 0.7577	0.3639/ 0.4697
<b>largest diff. peak / hole (e Å<sup>3</sup>)</b>	2.087/ -6.665	23.236 / -2.801	23.236 /-2.801	2.101 /-1.152

Table A8.3. Crystal data for compounds 24-27.

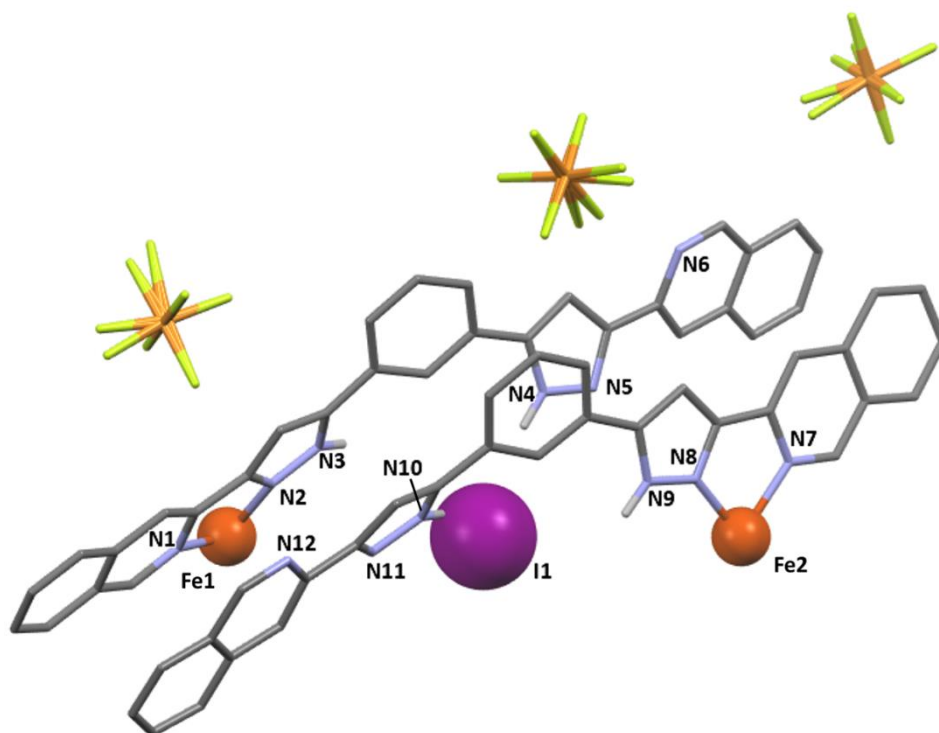


**Figure A8.12.** Asymmetric unit for the jellyfish-like compound **24**.

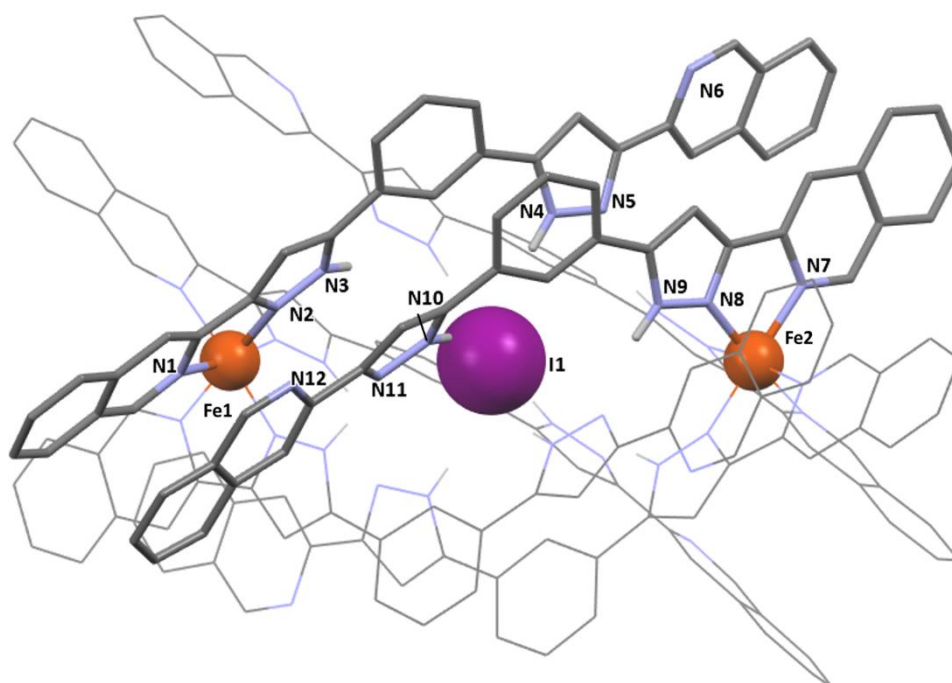


**Figure A8.13.** Complex moiety grown from the asymmetric unit of compound **24**.

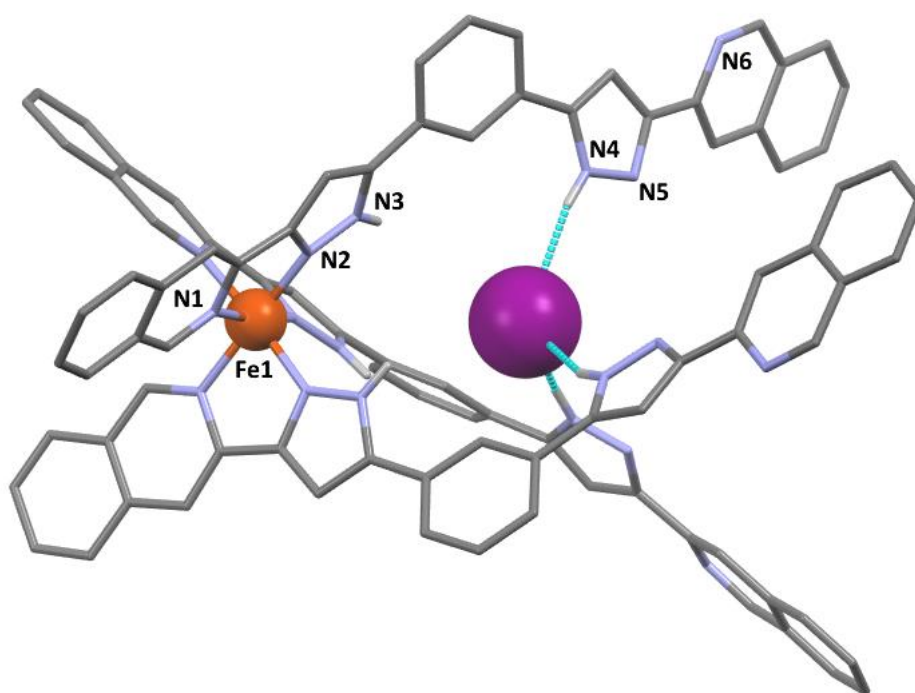


**Figure A8.14.** Monomeric moiety of the dimerized complex **24**.

**Table 8.4.** Fe-N bond lengths, average Fe-N bond lengths and distortion parameters, Fe...Fe and Fe...X lengths within the supramolecular X@[Fe(H<sub>2</sub>L5)<sub>3</sub>]<sub>2</sub><sup>2+</sup> assemblies in the structure of compounds **24** and **27**.

Compound	Pair of atoms	Lengths (Å)
<b>24</b>	(3) Fe1-N1	1.9917
	(3) Fe1-N2	1.9438
	(3) Fe2-N7	1.9950
	(3) Fe2-N8	1.9519
	<Fe1-N> (Å)	1.96(7)
	<Fe2-N> (Å)	1.97(3)
	Σ Fe1/ Fe2/	60.0(6)/ 58.9(8)
	Fe1...Fe2	11.388
	Fe1...I1	5.683
	Fe2...I1	5.705
	<b>27</b>	(3) Fe1-N1
(3) Fe1-N2		1.96
(3) Fe2-N7		2.03
(3) Fe2-N8		1.97
(3) Fe3-N13		1.99
(3) Fe3-N14		1.97
(3) Fe4-N19		2.01
(3) Fe4-N20		1.94
(3) Fe5-N25		1.97
(3) Fe5-N26		1.97
(3) Fe6-N31		2.02
(3) Fe6-N32		1.94
<Fe1-N> (Å)		1.985
<Fe2-N> (Å)		2.00
<Fe3-N> (Å)		1.98
<Fe4-N> (Å)		1.975
<Fe5-N> (Å)		1.97
<Fe6-N> (Å)		1.98
Σ Fe1/ Fe2/ Fe3/ Fe4/ Fe5/ Fe6/		51(5)/55(5)/
Fe1...Fe2		11.645
Fe3...Fe4		11.683
Fe5...Fe6		11.648
Fe1...Cl1		5.891
Fe2...Cl1	5.753	
Fe3...Cl4B	4.893	
Fe4...Cl4	5.919	
Fe5...Cl6B	4.187	
Fe6...Cl6	5.796	

**Table 8.5.** Hydrogen bonding in the structures of compounds compounds **24** and **27**.

Compound	D-H...A	D-H (Å)	H...A (Å)	D...A (Å)	D-H...A (°)
<b>24</b>	(3) N4-H4...I1	0.860	2.566	3.474	159.64
	(3) N10-H10...I1	0.860	2.643	3.473	163.60
	(3) N3-H3...N11	0.860	2.140	2.923	151.19
	(3) N9-H9...N5	0.860	2.144	2.951	156.20
<b>27</b>	(3) N4-H4...Cl1	0.879	2.550	3.398	162.20
	(3) N10-H10...I1	0.880	2.581	3.429	161.86
	(3) N3-H3...N11	0.880	2.089	2.884	149.88
	(3) N9-H9...N5	0.882	2.119	2.931	152.94

**Table 8.6.** Selected  $\pi\cdots\pi$  interactions in between the parallel ligands of compounds **24**, **25** and **26**.

Comp.	labels	Distance (Å) ( $\pi$ : centroid)
24	Cg(C36 C34 C32 C33 C37 C35)···Cg(C25 C24 C26 C27 C29 C28)	3.766
24	Cg(N7 C31 C39 C38 C32 C37)···Cg(C23 N6 C24 C22 C29 C30)	4.055
24	Cg(N9 N8 C41 C42 C40)···Cg(N4 N5 C20 C19 C21)	3.549
24	Cg(C45 C43 C47 C44 C46 C48)···Cg(C16 C15 C14 C18 C13 C17)	3.599
24	Cg(N10 C49 N11 C51 C50)···Cg(N2 N3 C12 C11 C10)	3.552
24	Cg(C52 N12 C59 C60 C53 C54)···Cg(C7 C9 N1 C1 C2 C8)	4.041
24	Cg(C55 C56 C59 C58 C57 C54)···Cg(C7 C6 C2 C3 C4 C5)	3.677
27	Cg(C36 C34 C32 C33 C37 C35)···Cg(C25 C24 C26 C27 C29 C28)	3.595
	Cg(N7 C31 C39 C38 C32 C37)···Cg(C23 N6 C24 C22 C29 C30)	3.893
	Cg(N9 N8 C41 C42 C40)···Cg(N4 N5 C20 C19 C21)	3.532
	Cg(C45 C43 C47 C44 C46 C48)···Cg(C16 C15 C14 C18 C13 C17)	3.799
	Cg(N10 C49 N11 C51 C50)···Cg(N2 N3 C12 C11 C10)	3.575
	Cg(C52 N12 C59 C60 C53 C54)···Cg(C7 C9 N1 C1 C2 C8)	3.763
	Cg(C55 C56 C59 C58 C57 C54)···Cg(C7 C6 C2 C3 C4 C5)	3.826



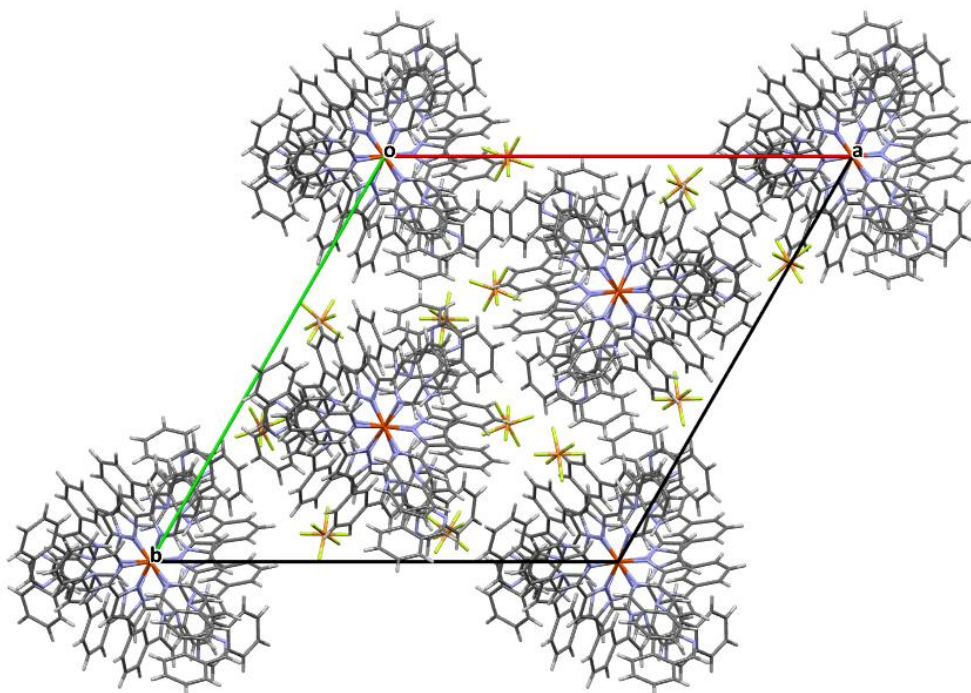


**Figure A8.15.** Representation of the lattice of **24** along the crystallographic *c* direction. The rods are along the crystallographic *c* direction.

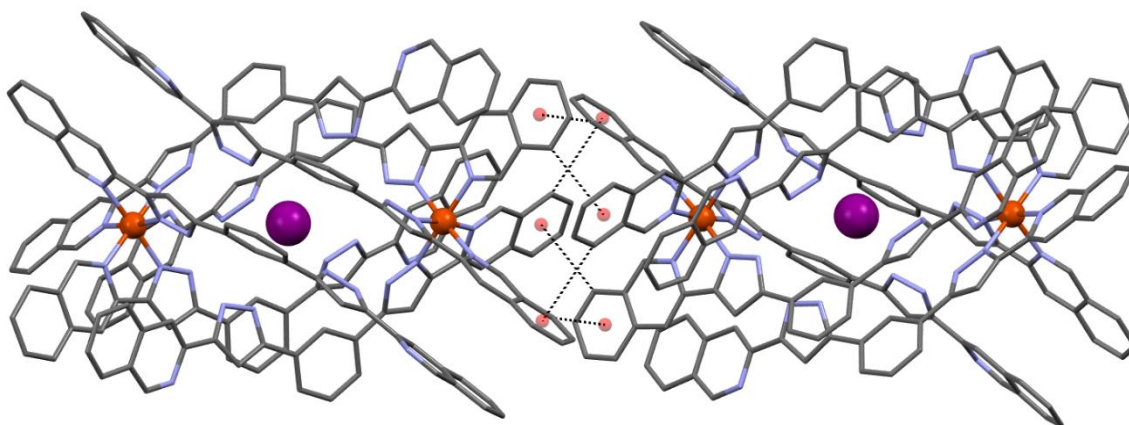


**Figure A8.16.** Representation of two jellyfish-like complexes of **24** within the rod packing. The six C-H... $\pi$  intermolecular interactions that link the pairwise along the crystallographic *c* direction are highlighted in black dashed lines.

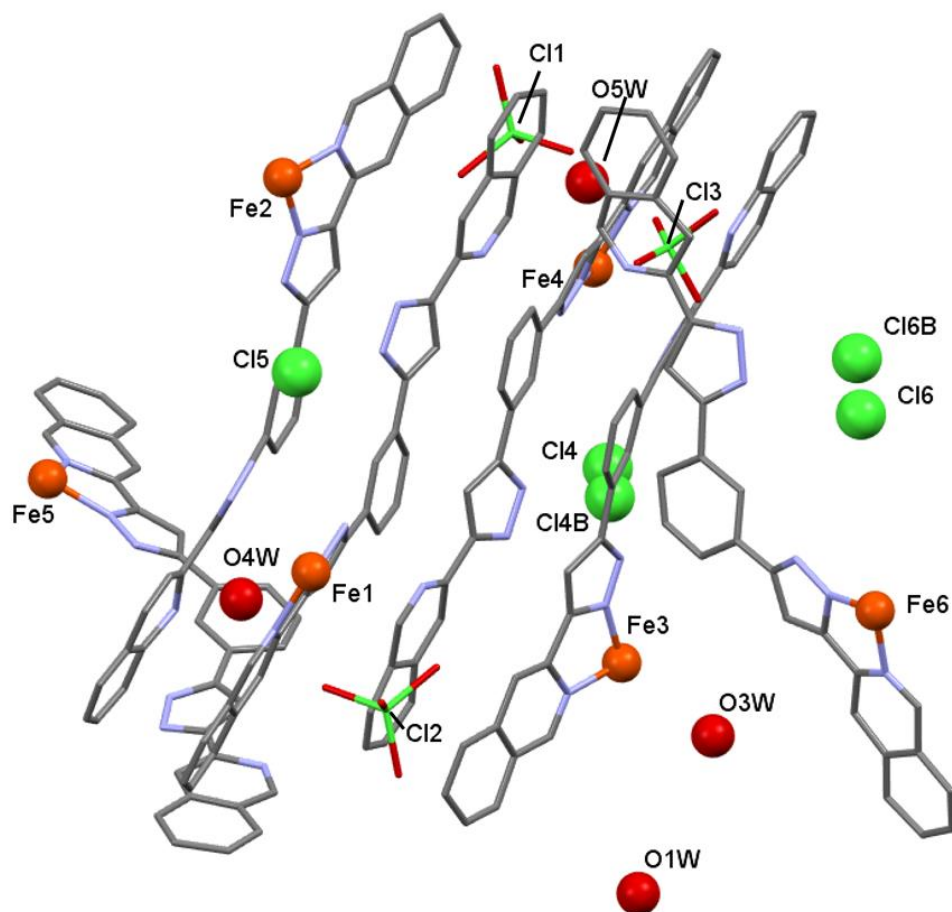


**Figure A8.17.** Asymmetric unit for the jellyfish-like compound **27**.

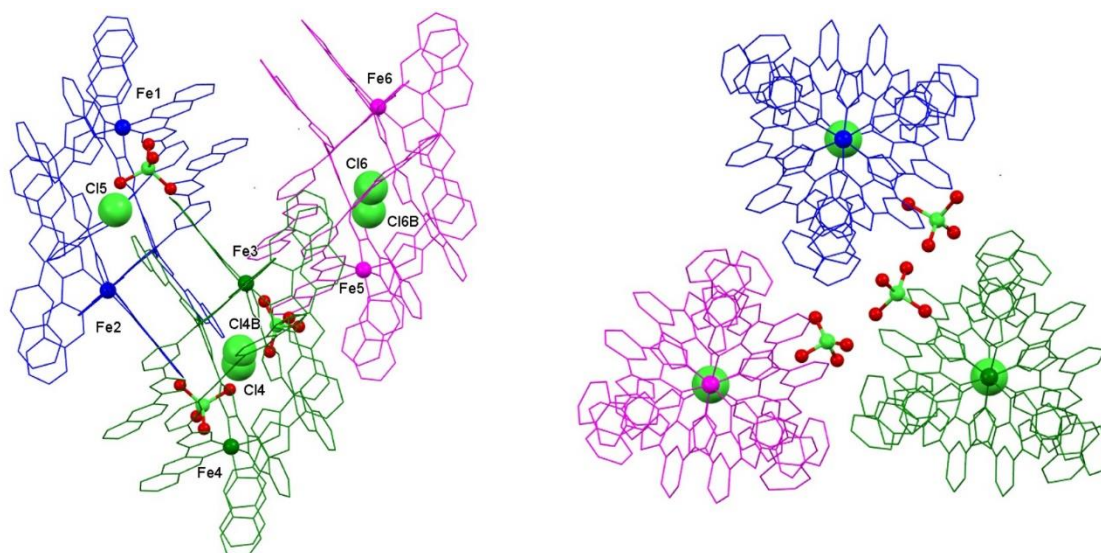


**Figure A8.18.** Illustration of the three jellyfish-like complexes in different colours for **27**.

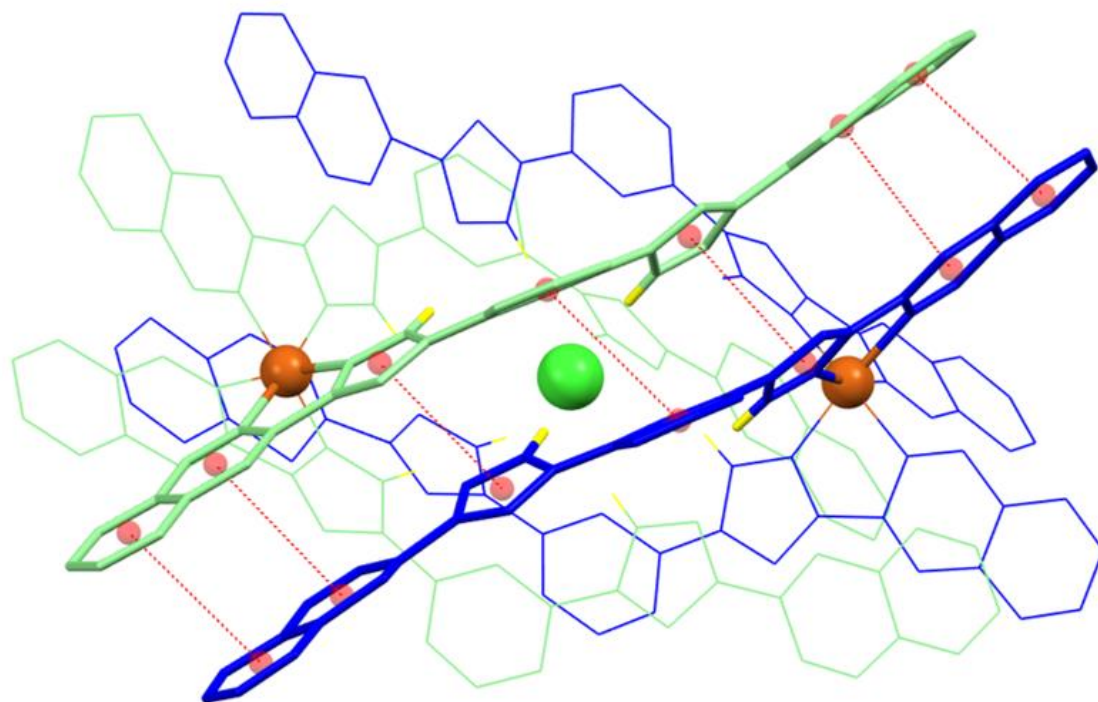


**Figure A8.19.** Representation of the  $\pi\cdots\pi$  stacking interactions between the seven aromatic rings of the parallel H<sub>2</sub>L5 ligands from the [Fe(H<sub>2</sub>L5)<sub>3</sub>]<sup>2+</sup> components of **27** (shown in different colors). Small red balls are the calculated centroid for each aromatic ring and the distance between them highlighted in dashed red lines.

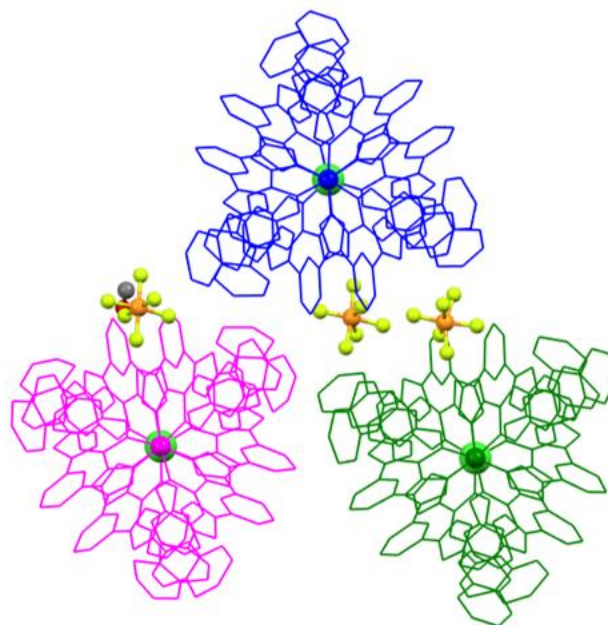


**Figure A8.20.** Illustration of the three jellyfish-like complexes in different colours for **26**.



## PHYSICAL TECHNIQUES

**Crystallographic data** were collected:

- Bruker APEX II QUIZAR diffractometer with  $\text{MoK}\alpha$  radiation ( $\lambda = 0.71037 \text{ \AA}$ ) and equipped with microfocus multilayer monochromator.

- Bruker APEX II CCD diffractometer on the Advanced Light Source. Beamline 11.3.1 at Lawrence Berkeley National Laboratory equipped with a PHOTON 100 CCD detector and using silicon 111 monochromated synchrotron radiation ( $\lambda = 0.7749 \text{ \AA}$ ).

- Synchrotron X-ray diffractometer ALBA, Cerdanyola del Vallès, Barcelona. Beamline BL13- XALOC (radiation ( $\lambda = 0.72931 \text{ \AA}$ )).

**Elemental analysis** (C, H, N): was performed with an Elemental Microanalyzer (A5), model Flash 1112 at the Servei de Microanàlisi of CSIC, Barcelona, Spain.

**NMR:** Spectra were recorded on Bruker AVQ Spectrometer (400 MHz) or Varian Mercury Spectrometer (400 MHz) at the Unitat de RMN at the Universitat de Barcelona.

**Paramagnetic NMR** experiments were carried out by Valentin Novikov's group using a Bruker Avance 600 spectrometer (600.15 MHz) at Nesmeyanov Institute of Organoelement Compounds RAS, Moscow, Russia; (chapters 6 and 8) or Bruker Digital Avance 800 MHz (2000) at the Unitat de RMN at the Universitat de Barcelona; (Chapter 2).

**Magnetic measurements:** Quantum Design MPMS-XL SQUID magnetometer at the "Unitat de Mesures Magnetiques" of the Universitat de Barcelona or MPMS5 or MPMS-XL SQUID magnetometers through the Physical Measurements unit of the Servicio de Apoyo a la Investigación-SAI, Universidad de Zaragoza.

**Mass spectrometry: Positive ion ESI TOF mass spectrometry** experiments were performed on a LC/MSD-TOF (Agilent Technologies) at the Unitat d'Espectrometria de Masses de Caracterització Molecular (CCiT) of the University of Barcelona.

**Infrared spectroscopy:** spectra were collected on KBr pellet samples on a Nicolet 5700 FTIR spectrometer.

**Analysis of metals** were performed by using by ICP-OES (Inductively coupled plasma - optical emission spectrometry) with a Perkin Elmer (Optima 8300) instrument in standard conditions.

**EPR experiments** were measured in d in continuous-wave (cw) mode using a Bruker E500 ELEXSYS spectrometer with a dual-mode cavity (Bruker ER4116DM, the perpendicular mode was used) and an helium flow cryostat (Oxford Instruments, ER4116DM). The magnetic field was calibrated with an NMR field probe (Bruker ER035M).

**Differential scanning calorimetry (DSC)** experiments were done at a scanning rate of 10 K min<sup>-1</sup> with a Q1000 calorimeter from TA Instruments equipped with the LNCS accessory.

## LIST OF PUBLICATIONS

- Variations to Spin Crossover in  $[\text{Fe}_x\text{Zn}_{(1-x)}(\text{Me}1,3\text{bpp})_2(\text{ClO}_4)_2]$  molecular alloys examined by Magnetometry and Single Crystal X-Ray Diffraction.  
Rosa Diego, Olivier Roubeau and Guillem Aromí. **Chem<sup>2</sup>**, 2021, 1-5 (**Accepted**)
- Designed asymmetric coordination helicates with bis- $\beta$ -diketone ligands.  
Rosa Diego, Mohanad Darawsheh, Leoní A. Barrios, Anna Sadurní, Jordi García, Paul Lloyd-Williams, Simon J. Teat, Olivier Roubeau, David Aguilà and Guillem Aromí. **Dalton. Trans.**, 2019, **48**, 16844-16847. DOI: 10.1039/c9dt03398j
- Coordination  $[\text{Co}^{\text{II}}_2]$  and  $[\text{Co}^{\text{II}}\text{Zn}^{\text{II}}]$  Helicates Showing Slow Magnetic Relaxation.  
Rosa Diego, Alexander Pavlov, Mohanad Darawsheh, Dmitry Aleshin, Joscha Nehr Korn, Yulia Nelyubina, Olivier Roubeau, Valentin Novikov and Guillem Aromí, **Inorg. Chem.**, 2019, **58**, 15, 9562-9566. DOI: 10.1021/acs.inorgchem.9b01334
- Exploració d'efectes estèrics de substituents en lligands a l'spin crossover de complexos de Fe(II).  
Carlos Bartual-Murgui, Sergi Vela, Mohanad Darawsheh, Rosa Diego, Simon J. Teat, Olivier Roubeau and Guillem Aromí, **Revista de la Societat Catalana de Química [Recurs electrònic]**, 2018, **17**, 96-106. DOI: 10.2436/20.2003.01.100
- A Spin-Crossover Molecular Material Describing Four Distinct Thermal Pathways.  
Carlos Bartual-Murgui, Rosa Diego, Sergi Vela, Simon J. Teat, Olivier Roubeau and Guillem Aromí, **Inorg. Chem.**, 2018, **57**, 11019-11026. DOI: 10.1021/acs.inorgchem.8b01625
- A probe of steric substituent effects on the spin crossover of Fe (II) complexes.  
Carlos Bartual-Murgui, Sergi Vela, Mohanad Darawsheh, Rosa Diego, Simon J. Teat, Olivier Roubeau and Guillem Aromí, **Inorg. Chem. Front.**, 2017, **4**, 1374-1383. DOI: 10.1039/C7QI00347A





## **AGRAÏMENTS (ACKNOWLEDGEMENTS)**

En aquest moment d'escriptura no em puc estar de començar amb els agraïments. Sou molts els que m'heu ajudat i acompanyat en aquesta etapa tan bonica i enriquidora. Diuen que lo bo dura poc, i quanta raó tenen. Heu fet que estigui molt a gust i gaudeixi diàriament de la meva feina fins al punt que no vulgui marxar. A tots vosaltres, gràcies per permetre'm que m'endugui el millor de cadascú.

En primer lloc, us vull donar les gràcies, Dr. Guillem Aromí i Dr. Jordi García, per la vostra confiança dipositada em mi, el vostre suport i tot el coneixement que m'heu transmès durant aquest temps. **Guillem**, t'apassiona la recerca i fas que es contagií fàcilment a tots els que t'envoltem. Gràcies per carregar estratosfèricament el meu nivell de motivació, per les discussions científiques i les oportunitats d'aprenentatge. Aconsegueixes que em quedi meravellada amb poques paraules. Veus el got mig ple i no pas mig buit, i tot serveix per aprendre. Així que, també gràcies pels teus consells personals. **Jordi**, ets un sol!! Com a tal, un professor i persona brillant. Gràcies per posar llum en la meva trajectòria acadèmica. Predisposat i entusiasta en emprendre i dissenyar noves rutes sintètiques. Així doncs, gràcies per les discussions orgàniques. Gràcies també per compartir diàlegs personals molt enriquidors, aprecio molt la teva proximitat.

Gràcies al Dr. **David** Aguilà o el nostre "Hot David" del departament pel suport incondicional. Tant científicament com personalment m'has ajudat molt durant el transcurs de la tesi. David, sempre hi ets. Gràcies a la teva generositat m'he enriquit i he après molt. Per tot l'esmentat "breument" i molt més que podria escriure (et vaig prometre moltes pàgines d'agraïments, que saps que podria emplenar, però personalment crec que ja saps el molt que t'aprecio), ets una de les persones que tothom voldria sempre al seu costat. M'emporto un gran amic.

Gràcies a la Dra. Leoní Barrios amb qui he compartit "synthetic tricks" i bons moments tan fins com fora del laboratori. **Leo**, ets la canya!! Sempre agradable i atenta amb mi. Gràcies per la teva humanitat i el constant positivisme que desprens. Et fas estimar.

Gràcies a la Dra. **Carolina** Sañudo per les seves aportacions i discussions científiques en respecte a la meva tesi en els diversos “group meetings”. Gràcies pel teu criteri rigorós i sincer, i la teva sublim organització.

Gràcies a la resta de components del grup GMMF. Gràcies als més veterans que em van acollir i ajudar diàriament quan vaig entrar al grup. Al **Raúl**, mi alma gemela, novio del pueblo y gran amigo. A la **Lidia**, la super tringle de l'agrupació musical “Fardatxo”, amb qui hem compartit molts bons moments futbolístics, festius, socials... Com vas dir, hem de tornar a Canàries, però no de congrés. PD: esperant uns seïtons que em vas prometre. A la **Mariona**, la cerverina super eficaç que sempre t'ajuda i algun cop s'indigna (en raó). Al **Mohanad**, per els seus consells i ajuda als meus inicis. A la **Vero**, pel seu suport i visites esporàdiques al lab. A l'**Ivana**, amb qui vaig descobrir l'art de pescar el millor cristall per difractar i compartir interessant discussions científiques.

Als nouvinguts, el **Guillem Gabarró** (el cryptoman) i la **Manto** (Llamaduleee), gràcies pel suport donat durant els últims moments d'aquesta tesi i els bons moments al lab. Guillem, ens deus un dinar a la Manto i a mi quan et forris. Manto, Είμαι τυχερή που συναντώ ένα τόσο δυνατό άτομο. Tots dos sou molt macos. La tieta Rosa desitja que gaudiu i espremeu al màxim aquesta oportunitat.

Thanks to the International students as **Oliver Lineneberg**, **Willem Aarts**, **Yannick Tulaseket**, who visited our group and left their personal mark. Specially, thanks to **Lucy Parkins** who was deeply dedicated to the project's work. Apart from the promising results obtained during her internship, we had enjoyable moments.

Gràcies al Dr. **Olivier Roubeau** per les estructures cristal·lines i la seva paciència a l'ensenyar-me cristal·lografia. Oliver, gràcies per les tardes de classes personalitzades i els dubtes resolts electrònicament. Gràcies també pel teu interès, suport i les discussions i aportacions científiques.

Gràcies al Dr. **Paul Lloyd-Williams**, que em va acollir al Departament d'Orgànica per realitzar les pràctiques internes ja fa un temps. Gràcies a aquesta oportunitat vaig descobrir la meva passió per la recerca.

Gràcies a les meves nenes del departament i les meves amigues per sempre. **Andrea**, **Ari** i **Araceli**: me dais la vida. Andrea, hem compartit el moment d'escriptura de tesi

i diverses crisis existencials arrelades a aquesta. Amb elles també, la **Valentina**. Nenes gràcies pels bons moments que m'heu regalat i pel vostre suport. També del grup, gràcies al **Romo** per els bons moments i anècdotes que ens has delectat. El noi mexicà introvertit i tímid, que quan es solta a casa i agafa confiança, és molt divertit.

També, donar gràcies a tots els del departament amb qui he compartit molt bons moments i anècdotes. Veterans, **Beltzane, Saskia, Berta, Júlia, Fran, Guillermito, Arnald** i la **Helen**. En especial, gràcies pels ànims del **Jan Romano** i la **Laia Ràfols**.

Moltes gràcies als tècnics de la UB per les mesures respectives, l'ajuda en la caracterització i les discussions. En especial a Dra. **Núria Clos** pel magnetisme, a la Dra. **Irene Fernández** i la **Laura Ortiz** pels masses, al Dr. **Albert Gutiérrez** pels EA i l'ajuda en el departament, i el **Victor Meriel**, que a banda dels rmns és un bon amic. També agrair a la **Teresa**, la **Cristina** i l'**Anna Ruiz** per la seva ajuda administrativa i proximitat.

Thanks to Dr. **Valentin Novikov** for the magnetic study and measurements in solution. Also, thank you for your kind explanations of the work.

Regarding my visiting research at the University of Otago, I would like to firstly thank Dra. **Sally Brooker** for accepting me with kind hospitality into her international lab. Thanks for your professional and personal support.

Among all the amazing people who helped me during my placement in New Zealand (including the covid lockdown), I would like to thank **Luca**. È il ragazzo italiano più estroverso, divertente, amico stretto, intelligente e lavoratore che ho conosciuto a livello internazionale. Grazie per avermi accolta nel gruppo di ricerca e in quella che è stata la nostra famiglia kiwi con **Adeel, Carmen, Francesca** e **Isa**. Grazie per il tuo aiuto e per le lezioni di "fittings" e per preoccuparti sempre per me. Ci ho guadagnato un buon amico. A tutti dico grazie per i bei momenti vissuti, i super pranzi italiani (mangiando a tutte le ore) e i viaggi del fine settimana.

Als vells amics de la carrera, **Victor (Trip)**, la **Fer** i el **Fero**, la **Maria Avián**, la **Marta Galindo** i el **Tomàs**, amb qui sempre hem passat bons moments i s'han preocupat per mi.

Gràcies al super mix de nenes maques i cuquis amb qui hem fet pinya. Entre pixurris orgàniques i comiditas, la **Mar**, la **Noe**, l'**Eva** i la **Carol**.

Gràcies a tots els meus amics de fora el departament. En especial a les meves frígides. Sí, així som les dotze amigues de sempre de "LO POBLE". **Laura, Lidia, Elga, Natàlia, Mercè, Anna** (Pantereta), **Anna** (Tarragona), **Maria, Marta, Rosa i Roser**, gràcies per ser-hi sempre. Encara que de vegades hem estat separades per molts quilòmetres i temps, m'heu acompanyat i ens hem acompanyat entre nosaltres sense que ho notem. Màgic, i seguim! Frígides, les meves conselleres, les meves confidents. Celebrant victòries, rient de les mateixes tonteries, compartint les meves pors i aixecant-me quan he tocat fons. Em doneu molta tranquil·litat, pau i felicitat. De tot cor xiques, gràcies per la vostra amistat.

Gràcies a l'**Anna**, qui m'ha donat suport incondicional durant aquest últim any. Gràcies també pel TOC del capítol 5. Gràcies per aparèixer en el meu camí.

Gràcies a la família que sempre esteu amb mi. **Iaia Rosi, tia Tere, Carmel i Marta, Tere i Dani**, pel vostre suport, ànims i estima. Gràcies als petits de casa, **Dani, Joan i Maria**, que son l'alegria de casa i amb un somriure t'alegren un mal dia. Al padrí **Carmelo**, que sempre tinc molt present. Sempre encuriós amb la meva feina i la ciència. Imagino el content i orgullós que estaries de la "filaberquina".

I per últim, i no pas perquè siguin menys important, sinó més aviat al contrari, perquè han estat el pilar de la meua vida: gràcies al meu pare, la meua mare i el meu germà. **Papa, mama i Pep**, sempre heu confiat en mi i m'heu donat molt de suport i força. Gràcies per cuidar-me, mimar-me i suportar-me en els moments no tan bons (el caràcter fort es treu a casa). Papis, gràcies pel valors d'esforç i perseverança que m'heu inculcat i la gran llibertat que sempre m'heu donat.